Characterisation of the bidirectional reflectance distribution function (BRDF) of sea ice in response to deposited black carbon and mineral aerosols

Maxim L. Lamare

A thesis submitted in fulfillment of the requirements for the degree of Doctor of Philosophy

Department of Earth Sciences
Royal Holloway University of London

August 2017

Declaration of Authorship

I, Maxim L. Lamare, hereby declare that this thesis and the work presented in it are entirely my own. I confirm that:

- This work was done wholly or mainly while in candidature for a research degree at this University.
- Where I have consulted the published work of others, this is always clearly attributed.
- Where the thesis is based on work done by myself jointly with others, I have made clear exactly what was done by others and what I have contributed myself.

Signed:

Date:

Abstract

Optical satellite remote sensing is an ideal tool to monitor surface albedo over polar regions, facilitating synoptic observations of expansive areas with a high temporal coverage, which would be unachievable through *in situ* field measurements. Sea ice does not reflect solar radiation isotropically, therefore the knowledge of the bidirectional distribution function (BRDF) of sea ice is necessary to normalise the data obtained from different sensor viewing angles, and derive surface albedo products. Satellite sensors are limited by a discrete number of viewing angles and spectral bands, and rely on *a priori* knowledge of the angular distribution of the reflected radiation above the sea ice. Few studies have fully characterised the BRDF of bare sea ice, and the effects of anthropogenic and natural impurities deposited from the atmosphere on the BRDF of sea ice are poorly understood. This study investigates the effects of black carbon and mineral aerosol deposits on the BRDF of sea ice for the calibration and validation of Earth Observation satellite products, based on radiative-transfer modelling, laboratory experiments and field studies. Modelling the impact of different mineral aerosol deposits on the surface albedo of snow and sea ice shows that although mineral light-absorbing impurities significantly change the radiation budget, the type of snow or sea ice has a larger effect than the type of mineral aerosol deposited. The reflectance of a black carbon bearing surface layer of sea ice is recorded in an artificial sea ice laboratory. The reflectance of the doped sea ice is compared to radiative-transfer calculations performed by the TUV-snow radiative-transfer code, in order to validate the model against realistic sea ice conditions. Calculations of downwelling photosynthetically active radiation (PAR) throughout a layer of snow and sea ice help provide an explanation for the observations of an early algae bloom under sea ice in North-East Greenland. PlanarRad, a radiative-transfer model that calculates the angular distribution of radiance, is used to investigate the response of the BRDF of sea ice to varying physical properties. The results highlight the importance of surface roughness, which cannot be considered independently from other parameters. The BRDF of sea ice in response to increasing quantities of black carbon and mineral aerosol deposits in a surface layer are measured in the sea ice laboratory. The results, used to validate PlanarRad, show that the mineral aerosol deposits have a larger effect on the quasi-lambertian part of the hemisphere than on the typical forward scattering peak of the BRDF, however the pattern of the BRDF over the hemisphere does not change. The angular reflectance of bare young sea ice is measured for the first time in an outdoor artificial facility, providing controlled sea ice conditions with natural illumination. Radiative-transfer calculations provided further insight on the optical properties and impurity content of the sea ice. The work presented here provides a better understanding of the BRDF of sea ice, and the impact of atmospheric particulates deposited on the sea ice. Furthermore, the study validates a radiative-transfer model that is of use to the remote sensing community for more accurate satellite retrievals of sea ice.

Acknowledgements

First of all I would like to thank my supervisors Professor Martin King and Dr. Nigel Fox for the inspiration and support throughout the course of this Ph.D.. I am extremely grateful to Martin King for his guidance and encouragements during the entire project. I appreciate the academic freedom that I was given. I would also like to thank Claire Greenwell for putting up with me on fieldwork in Namibia and Canada, and helping with data processing, and Aga Bialek for providing excellent advice and passionate exchanges of ideas about BRDF. A further thank you goes to Jerry Morris, who could build anything that was needed for the field or the lab in an instant.

I would also like to thank the Natural Environment Research Council (NERC) and the National Physical Laboratory for financial support, the Earth Sciences department's research committee for supporting fieldwork and conference expenses, and NERC FSF for the equipment loan for my fieldwork in Canada. Additionally, I would like to thank Feiyue Wang and his team at the University of Manitoba for the warm welcome and access to their facility.
I would like to acknowledge my colleagues, with whom I shared pleasant moments in the office or over lunch. A special mention goes to Max and Ben who forced me to run an ultra-marathon with them; the hours spent training were a good way to clear my mind. Steph was always there to help and provide moral support in the last moments of the PhD. It was a great race! A particular thanks goes to Giovanni and Laura, who were always there to support me in this challenging and exciting adventure. Their friendship is invaluable.

Finally, I would like to thank my family for their patience and understanding. Thank you John and Nataliya, for all the great french cuisine and pleasant evenings. To Baptiste, who is like a brother to me: I hope we keep exploring the arctic together. Lastly, Pauline: thank you for your support and encouragements. This would not have been possible without you.

Contents

List of Figures

List of Tables

Chapter 1

Introduction

1.1 Background

Sea ice in the Arctic has been undergoing rapid changes over the last decades. Observations have shown a large decrease in the extent of the sea ice (e.g. Stroeve et al., 2007; Kwok et al., 2009; Stroeve et al., 2012; Serreze et al., 2016), with record minima in 2007 and 2012 (Kirchmeier-Young et al., 2016), leading to the idea of an ice-free Arctic Ocean in the close future (Wang and Overland, 2012). Associated with the loss in extent and volume of sea ice, transitions from thick multi-year sea ice to a thinner sea ice cover predominantly composed of first year sea ice (e.g. Rigor and Wallace, 2004; Maslanik et al., 2007; Nghiem et al., 2007) have been underlined. The changes occurring in the Arctic have a significant impact on the global climate system, affecting atmospheric circulation patterns in the northern hemisphere (e.g. Deser et al., 2010; Overland and Wang, 2010; Vihma, 2014), and potentially leading to extreme weather events (Simmonds and Keay, 2009). Furthermore, the loss of sea ice is predicted to have important socioeconomic impacts, with for example, new shipping route possibilities (Ho, 2010) and natural resource availabilities leading to the question of the ecological consequences of the human use of the Arctic (Post et al., 2013), as well as challenges faced by people living in the Arctic (Meier et al., 2014).

Developments in remote sensing technology have allowed increasingly accurate retrievals of the properties of sea ice, which in turn have lead to a better understanding of the processes occurring in polar regions. Indeed satellite observations of sea ice allow data assimilation with a high spatial coverage, and the repeat coverage has allowed to monitor trends in sea ice spanning over multiple decades (e.g. Cavalieri, 2003). Amongst the sea ice parameters observed from spaceborne platforms including cloud coverage, sea ice extent, surface temperature, and sea ice thickness, the surface albedo is of specific importance, having been shown to provide a significant positive-feedback effect on the climate (Curry et al., 1995). The high surface albedo of sea ice compared to open seawater is the principle driver of the radiative forcing in the Arctic, and is highly sensitive to the variations in the physical properties of the sea ice. Indeed, reductions in the sea ice

thickness, as well as changes in the type of sea ice, from multi-year to first-year, and enhanced melting of sea ice which leads to the formation of melt ponds, substantially lower the surface albedo (Hanesiak et al., 2001; Serreze et al., 2007; Perovich and Polashenski, 2012), and therefore lead to increased solar radiation absorption that in turn amplifies warming. The surface albedo of sea ice is also reduced by light-absorbing aerosols which are deposited on the surface of the sea ice, and warm the surface by absorbing solar radiation (Jacobson, 2004).

The light-absorbing particles typically found in the snow or sea ice in the Arctic originate from natural or anthropogenic sources, with the main contributions being black carbon or soot particles (Hansen and Nazarenko, 2004), mineral particles (Zdanowicz et al., 1998) and organic matter (Doherty et al., 2013). The black carbon particles, which are considered to be the most absorbing of carbonaceous aerosols (Koch and Hansen, 2005a) originate principally from the combustion of fossil fuels in industry, transport and residential sectors, as well as from open burning of biomass (Ramanathan et al., 2008; Bond et al., 2013a). Mineral aerosol deposits principally originate from arid and semi-arid regions, which are the most important source of mineral aerosols in the atmosphere (Ginoux et al., 2010), and high-latitude volcanic eruptions that frequently emit large quantities of ash into the Arctic (e.g. Young et al., 2012). Whilst coarse particles quickly drop out of the atmosphere, the smaller particles are prone to long-range transport, which may be transported to the Arctic. The particles are deposited onto the surface of the snow or sea ice either by direct deposition or by snow scavenging (Penner and Novakov, 1996). Aerosol deposits in snow and sea ice have been shown to significantly reduce the albedo, owing to the much larger absorption of the particles compared to ice in the ultraviolet and visible wavelengths (Wiscombe and Warren, 1980a). The absorption of light by black carbon aerosol deposits is significantly higher than by mineral aerosols (Lamare et al., 2016), however larger mass-ratios of mineral aerosol deposits are found in the Arctic due to seasonal deposition events (**ZDANOWICZ1998a**). The effect of the light-absorbing particles are enhanced in polar regions, as the particles increase melting through the albedo feedback effect (Doherty et al., 2010a).

Sea ice, as most natural surfaces, is not a lambertian scatterer, and therefore the albedo cannot be retrieved by measuring the nadir reflectance. The algorithms used to calculate surface albedo from satellite observations rely on the knowledge of the angular distribution of reflectance to provide accurate measurements of the sea ice. However, most satellite sensors are limited by the number of viewing angles and rely on semi-empirical models to compute surface albedo. Advances in remote sensing have enabled the development of remote sensing platforms that provide multi-angular measurements of the surface of the Earth. However, in the case of sea ice, the rapidly changing intensities in the forward scattering part of the hemisphere, cannot be accurately described by the

discrete number of viewing angles provided by these instruments. Current albedo algorithms rely on semi-empirical models, which in some cases use libraries of in-situ angular measurements to extrapolate the measurements over the hemisphere (Lucht et al., 2000). However, the radiative-transfer modelling used to generate albedo is based on a limited number of field measurements which do not account for the variability of sea ice conditions. Furthermore, field measurements are labour intensive and require multiple repeated measurements to account for varying sea ice conditions. The parameterisation of the Bidirectional Reflectance Distribution Function (BRDF), which provides information on the anisotropy of the radiation reflected for a surface is therefore essential to provide improved remote sensing products of sea ice. To do so, the effects of the physical and optical properties of sea ice on the BRDF of sea ice need to be characterised, and an assessment of the impact of impurities in the sea ice on the angular reflectance of the sea ice is necessary.

1.2 Research aims

The principal motivation behind the work presented here was to attempt to provide a parameterisation of the BRDF of sea ice, which will improve the semi-empirical models used to derive albedo products from multi-angular satellite data. A radiative-transfer model calculating directional radiance and irradiance fluxes was tailored to perform BRDF calculations for sea ice with varying physical and optical properties. The aim of the radiative-transfer calculations was to understand the effects of the individual parameters on the angular distribution and intensity of the reflected radiation from the surface of the sea ice. With the effects of the physical and optical properties of the sea ice constrained, the effects of anthropogenic and natural aerosol deposits on the BRDF of sea ice was investigated. The effects of different mineral aerosol sources on the light-absorption in snow and sea ice, and the effects of layering within the medium were not previously characterised. Therefore, a modelling study was performed to assess the importance of different mineral aerosol types on the radiative forcing of snow and sea ice, prior to the calculations of BRDF. The radiative-transfer model used to calculate the BRDF of sea ice was validated with empirical measurements of the bidirectional reflectance factor (BRF) performed in an interior sea ice laboratory, as an approximation for BRDF. Furthermore, the radiative-transfer calculation were compared to the measurements of the hemispherical-directional reflectance factor (HDRF), with natural solar illumination in a sea ice facility.

The work throughout the chapters was guided by three main scientific questions, which will be discussed in the concluding chapter.

- Which physical and optical parameters affect the BRDF of bare clean sea ice,and what are the individual effects of the parameters?
- How do impurities, which are know to strongly impact the nadir reflectance of sea ice, affect the anisotropy of sea ice?
- Can radiative-transfer modelling provide an accurate representation of the BRDF of sea ice for varying physical and optical parameters, to provide the remote sensing community with better inputs for satellite products, and can radiative-transfer modelling replace in-situ measurements?

1.3 Outline of the thesis

The present work is divided into nine chapters. The present introduction sets the overall background and defines the aims of the work presented in this thesis. The introduction is complemented by the individual introductions of the chapters 3 to 8. In chapter 2, the methods and instrumentation employed to collect and analyse the data used in this thesis are presented. Chapters 3 to 8 are presented as published peer-reviewed papers or paper drafts in preparation for publication. Chapter 3 focusses on the impact of different types of mineral aerosol deposits on the albedo of snow and sea ice, using the TUV-snow radiative-transfer model. Chapter 4 validates the radiative-transfer model by comparing the modelled reflectance of sea ice with measurements performed in the Royal Holloway sea ice laboratory, and investigates the effects of black carbon aerosol deposits on the reflectance of sea ice. Chapter 5 presents the first observations of an early onset of algae bloom under sea ice covered in a thick layer of snow. Radiative-transfer calculations provide an explanation on the amounts of light available for photosynthesis owing to a metamorphosing snow pack. In chapter 6, an extensive characterisation of the BRDF of sea ice is proposed for different types of sea ice with varying thicknesses as a function of surface roughness, using the PlanarRad radiative-transfer model. The model is compared to BRF measurements of sea ice acquired at the Royal Holloway sea ice laboratory in chapter 7. Known amounts of black carbon and volcanic ash particles were placed in a 5 cm surface layer of sea ice to investigate the angular dependance of impurities on the BRF of sea ice, and the PlanarRad model was used to reproduce the measurements, providing information on the optical characteristics of the laboratory sea ice, characterising the effects of impurities on the BRF of sea ice and validating the model. In chapter 8, the first in-situ measurements of the HDRF of bare sea ice for natural illumination conditions are presented. The measurements performed with afield goniometer at the University of Manitoba sea ice facility were reproduced with the PlanarRad radiative-transfer model to derive the optical properties of the sea ice, as well as the amount of black carbon deposits and algae present in the sea ice. A final discussion, recommendations for further work, and the conclusions of the thesis are included in chapter 9. At the end of the thesis,

the appendix presents further work that was carried out during the PhD project, where the initial characterisation of a new autonomous radiometric calibration target was performed in the Namib desert. The HDRF of the mineral desert surface was characterised using the field goniometer presented in chapter 8.

Chapter 2

Methods

In this chapter, the approaches used to produce the results discussed in chapters 3, 4, 5, 6, 7, and 8 are presented. Firstly, the experimental setup, instrumentation, testing, data collection, and data processing at the artificial sea ice laboratory located at Royal Holloway University of London (RHUL) are described. In a second step, the collection, instrumental setup and testing, and the processing of the multi-angular reflectance of the artificial sea ice at the Sea-ice Environmental Research Facility at the University of Manitoba, Winnipeg is reported. The third section of the chapter discusses the radiative-transfer models used to compute radiative fluxes in polar snow and sea ice, and explains the modelling methods employed to fit the observational data

2.1 Laboratory sea ice

The experiments reported in chapters 4 and 7 were performed on artificial sea ice generated in a sea ice simulator, located on the campus of Royal Holloway University of London. The facility and setup have been described by Marks (2014) (chapter 5), who participated in the construction of the sea ice simulator and performed *e*-folding depth and nadir reflectance measurements of sea ice doped with black carbon. A description of the sea ice simulator is also found in Ball (2015) who performed initial BRF measurements of clean sea ice. A short description of the facility and experimental setup are also present in chapters 4 and 7 . In this section, an overview of the sea ice simulator is presented, and the experimental setup which differs from the ones previously described (Marks, 2014; Ball, 2015), is described.

2.1.1 Sea ice simulator description

The RHUL sea ice simulator consists of a seawater tank, placed in an environmental chamber which allows control over the air temperature. A refrigerated international shipping container was used to house the seawater tank and provide polar temperatures during the experiments. A Daikin reefer with dimensions of 11.95 m (length) x 2.56 m (height) x 2.29 m (width) allowed the interior temperature to be controlled between $-25\,^{\circ}\mathrm{C}$ and $25\,^{\circ}\mathrm{C}$. The interior panels of the container are made of stainless steel sheets,

and an aluminium raised flooring grid allows a flow of air along the container. An air circulation system transports cold air beneath the flooring grid and back along the ceiling of the container, maintaining a constant flow of cold air in the reefer. The container is cooled using a compression refrigeration system with refrigerant flowing across a condenser and an evaporator. Episodically, the compressor system was automatically reversed to heat the cooling circuit, in order to remove the ice build-up on the system. Owing to the high levels of humidity in the container caused by the large body of water in the sea ice tank, the defrosting cycle was frequent, therefore the container was unable to maintain stable temperatures. Monitoring the air temperature inside the container highlighted the cycles: during the freezing cycle, a temperature of $-18\,^{\circ}\mathrm{C}$ was maintained in the container for a period of approximately seven hours, after which the room temperature rose rapidly to $-12\,^{\circ}\mathrm{C}$ over a period of 1 hour. Furthermore, the heat generated by the tungsten-halogen lamps (described in section 2.1.3) during the experiments caused an increase in ambient temperatures, typically reaching $-4\,^{\circ}\mathrm{C}$ and a maximum of $0\,^{\circ}\mathrm{C}$.

The sea ice was formed in a white polyethylene cylindrical tank ($132\,\mathrm{cm}$ in height, and $139\,\mathrm{cm}$ in diameter). A diagram of the sea ice simulator setup is presented in figure 2.1. The tank is supported by an aluminium structure that provides structural stability. In order to insulate the side walls and the bottom of the tank, and prevent the seawater from freezing at the base or on the sides of the tank (see section 2.1.2.1), a layer of neoprene and expanded foam is attached to the sides of the tank, between the tank and the supporting structure. Furthermore, the tank is raised on a wooden pallet and polystyrene insulation is placed between the tank and the floor, providing insulation to the base of the tank. The tank, insulation and aluminium structure was housed in a plywood housing, painted with black water-resistant paint. An aluminium frame with a black plywood ceiling was placed above the tank during previous experiments (Ball, 2015). The vertical struts of the frame were covered with matte black aluminium foil to eliminate reflections during the BRF measurements. Furthermore, matte black rubberised curtains were attached to the top of the frame on three sides of the tank, to prevent stray light from the stainless steel walls and the operator's clothing from affecting the measurements.

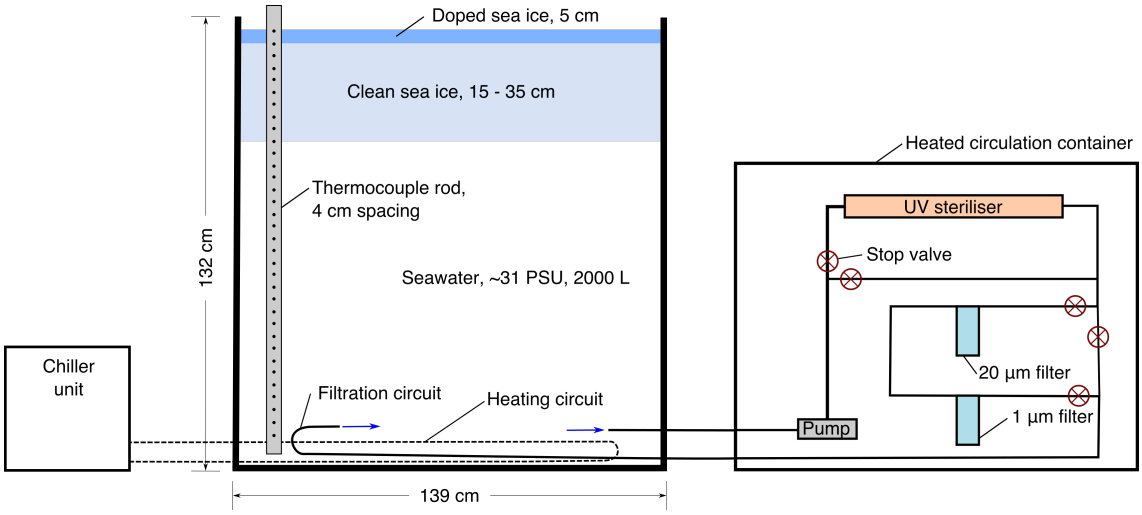

FIGURE 2.1: Schematic diagram of the seawater tank in the sea ice simulator, including the sterilisation and filtration system, and the heating circuit.

2.1.2 Creating artificial sea ice

The artificial sea ice was formed by subjecting the seawater in the tank to polar temperatures. In the following sections, the conditions necessary to form realistic sea ice are discussed.

2.1.2.1 Sea water

A proxy for seawater was created by mixing Tropic Marin salt with fresh water. Tropic Marin salt, designed for aquariums, is made of pharmaceutical pure salts and contains 70 trace elements found in natural seawater. The salt does not contain nitrates or phosphates, to limit algae growth. Atkinson and Bingman (1997) compared 8 types of artificial seawater created with commercially available salts (including Tropic Marin) with natural ocean seawater. The results showed that the major cations and anions were within approximately 10% of seawater.

The typical salinity of the upper layer of open seawater in the polar oceanic waters is between 30.4 and 34.4 practical salinity units (PSU) (Weeks, 2010). Although the surface layer salinity of the Arctic Ocean is not spatially homogeneous (Jones and Anderson, 1986), Aagaard et al. (1981) report a typical surface layer salinity of 32.5 PSU for the Arctic Ocean. During the experiments described in chapters 4 and 7, the salinity of the water was adjusted to 32 $\pm$1 PSU. The sea ice tank (described in section 2.1.1) was filled with approximately 2000 L of fresh tap water and Tropic Marin salt was added in known quantities over the period of a few days to reach the desired salinity. Marks (2014) compared solutions of Tropic Marin dissolved in ultra pure water ($>$18 mΩ)and tap water, showing that the difference between the two were negligible. Therefore, tap water was used out of convenience. An initial mass of 60 kg of Tropic Marin was added to the fresh water in

the tank over the period of 48 h. The water was stirred using a plastic oar, and the salt was left to dissolve over the period of 24 hours after each addition. The salinity was measured before each addition of salt using a Fisher Scientific seawater refractometer, which has previously been shown to be as accurate as the more widely used conductivity probe (Marks, 2014). Further smaller masses of salt were added until an average salinity of 32 PSU was achieved. Table 2.1 shows typical quantities of salt added to the water and the resulting salinity measured.

TABLE 2.1: Mass of Tropic Marin salt added to the seawater in the sea ice simulator tank, and the resulting salinity measured after dissolution.

Cumulative mass of Tropic Marin salt added to the tank / kg (Total = 78 kg)	Average salinity measured after dissolution / PSU
30	16.33
60	28
67	29
72	29.66
78	32

In order to limit the development of algae and remove particulates in suspension in the tank, the seawater was circulated through a sterilising and filtration system. The circuit, shown in figure 2.2, was powered with a 120 HP magnet-driven Iwaki MD-40 centrifugal pump, circulating the water at a rate of 10 $\mathrm{l\,min^{-1}}$. A non-metallic magnet-driven pump was selected to avoid corrosion by the seawater. The seawater was driven through a UV sterilising lamp followed by a series of two 10 inch water filter housings with 20 $\mu\mathrm{m}$ and 1$\mu\mathrm{m}$ spun polypropylene filters. The filters were replaced between each experiment. The pump, UV steriliser, and the filters were located in an enclosed heated cabinet, placed under an insulated foam and aluminium cover to avoid the water in the tubing to freeze.

In order to fit the BRF of the artificial sea ice grown in the sea ice simulator with a radiative-transfer model (see section 2.3), knowledge of the reflectance of the underlying water and tank are required. The reflectance of the seawater tank was measured and provided by A. Marks. The tank was filled with seawater, and reflectance measurements were performed at nadir under diffuse illumination conditions. The diffuse illumination was achieved by using an array of fluorescent lighting tubes placed above the tank in combination with white boards placed around the edges of the tank, as described by Marks (2014). The measurements, shown in figure 2.3 were provided over the wavelength range 300–800 nm.

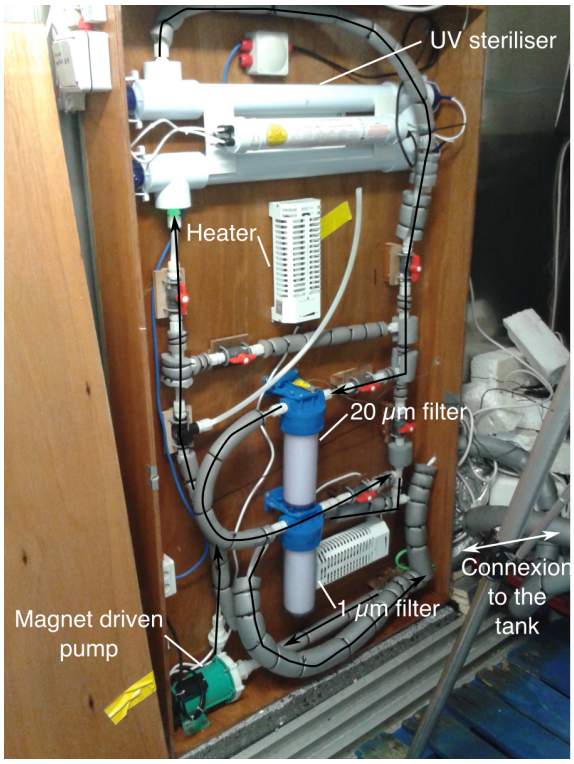

FIGURE 2.2: Sterilising and filtration system in a heated and insulated enclosure. The black arrows in the image indicate the direction of flow of the seawater.

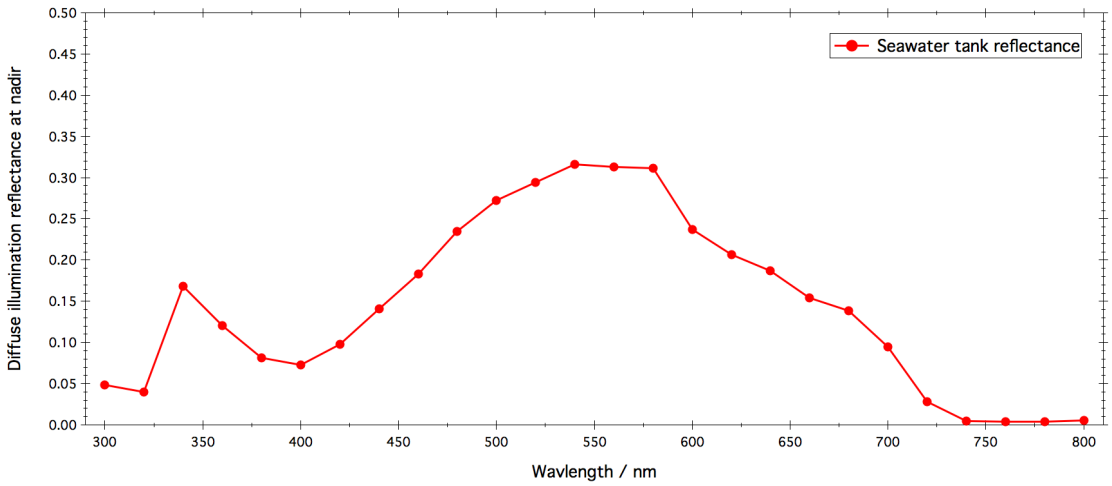

FIGURE 2.3: Nadir reflectance of the seawater tank under diffuse illumination conditions. Data provided by A. Marks.

2.1.2.2 Sea ice growth and thickness

The growth of the sea ice was initiated by setting the ambient temperature thermostat to -18°C in the sea ice simulator. As the air temperature dropped, frazil ice started developing on the surface of the seawater over a period of 48 h, forming a "skin" of dark nilas ice on the surface. As the ice grew to approximately $5\ \mathrm{cm}$ in thickness, surface brine expulsion was observed. The surface of the ice appeared wet and brinicles developed across the surface (figure 2.4 b). The features disappeared over the course of approximately 48 h. Furthermore, the brinicle events were only observed when the air circulation above the ice was low and the features did not appear consistently during each experiment. Over the three weeks following the formation of nilas, the thin elastic layer of sea ice grew vertically downwards, reaching thicknesses of 25 to $35\ \mathrm{cm}$. As the ice grew thicker, becoming grey ice, then thin first year ice, a change in the appearance of the sea ice was observable, with a whitening of the surface (figure 2.4 a). After an initial thin layer of ice formed, two electric air circulation fans were used to blow air on the surface of the ice, to remove heat by convection, facilitating heat transfer from the tank. The cold air blown on the surface, lead to a quicker formation of the ice. However, the air circulation contributed to forming surface roughness features, examples of which can be found in figure 2.34.

To ensure a realistic growth sequence of the artificial sea ice, with ice forming from the surface of the seawater, then growing vertically downwards, a heating system was placed in the bottom of the seawater tank. A Cole-Parmer temperature-controlled recirculator was connected to a closed circuit of pipes running (shown in figure 2.1 and 2.2) around the bottom of the tank. A solution of 1:1 water and glycol was pumped around the system with a flow rate of $5\ \mathrm{l\,min^{-1}}$ at +4°C. The closed loop circulation, in conjunction with the insulation around the tank (described in section 2.1.1) prevented the seawater from freezing at the bottom or on the sides of the tank. Furthermore, to insure mixing of the seawater below the ice and prevent temperature and salinity stratification, a circulation system was placed at the bottom of the tank. The circulation of the seawater in the tank, mimicking oceanic currents, was achieved by using the return flow from the sterilising and filtration system described in section 2.1.2.1. Originally, a rotating flow of seawater was observed in the tank because of the configuration of the circulation system, causing an uneven sea ice growth. To avoid the formation of an eddy under the ice, a diffuser head was attached to the output hose of the circulation system, spreading the flow of water in three directions. After the diffuser was installed, the sea ice grew homogeneously across the surface of the tank.

The thickness of the sea ice was monitored using a thermocouple array and confirmed by regular drilling of the sea ice. A polypropylene tube with holes drilled every centimetre was placed vertically in the tank and held in place with an aluminium clamp. Type-T

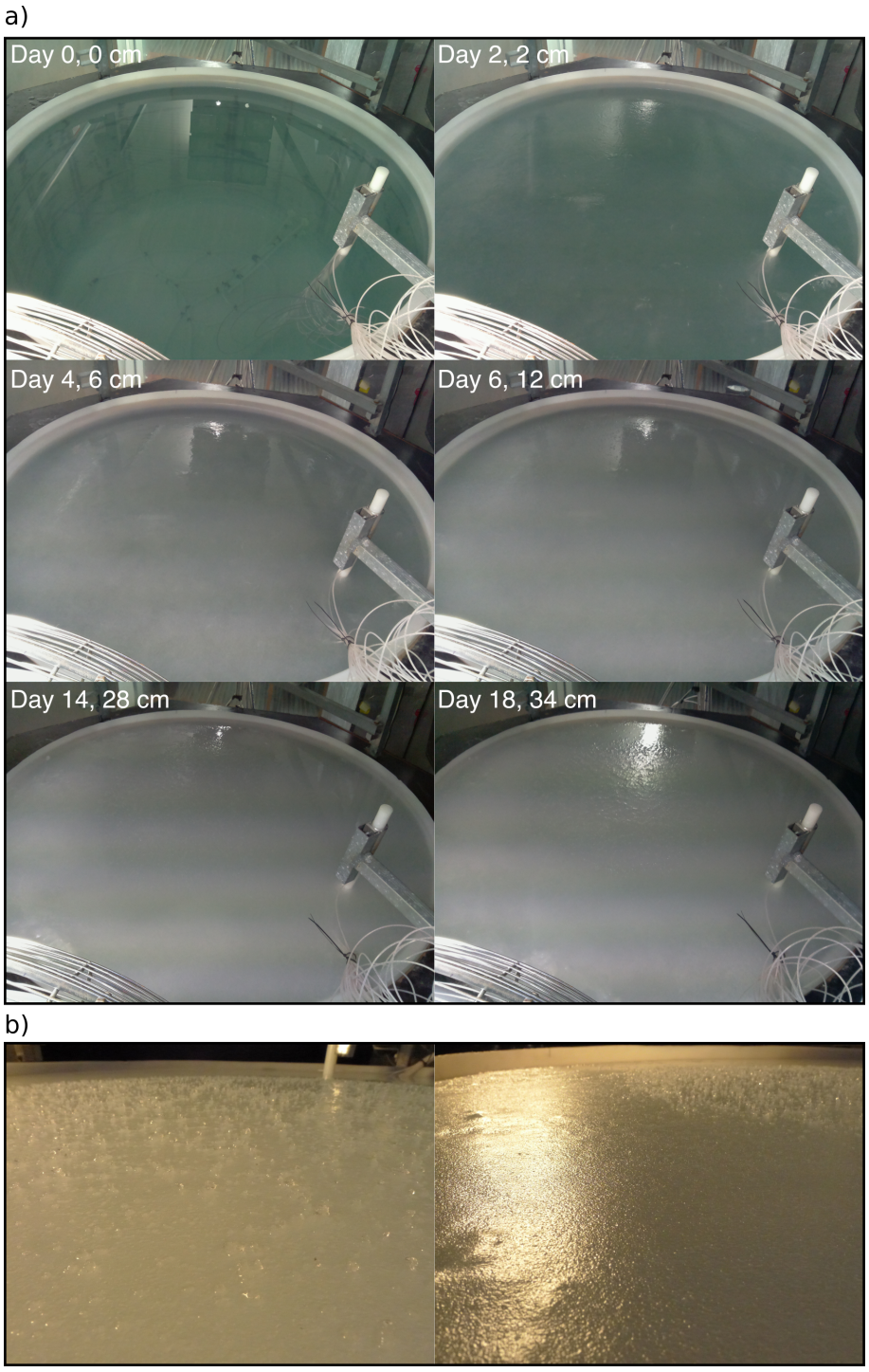

FIGURE 2.4: a) Time-lapse of the artificial sea ice growth over 18 days. The number of days since the start of the ice growth period and the ice thickness are indicated in each image. b) Left: example of a brinicle formation on the sea ice 5 days after the start of the sea ice growth. Right: 2 days after the appearance of the brinicles, the features disappeared.

thermocouples were threaded through the holes at varying intervals and connected to a switch box. In the work presented in chapter 7, 26 thermocouples were placed on the rod with a spacing of 20×2 cm, 4×4 cm and 6×10 cm, the last thermocouple being at a height of 16 cm from the bottom of the tank. The spacing was chosen to insure better resolution in the upper part of the tank to monitor the ice growth, whilst providing temperature information throughout the tank.The temperature profiles were recorded manually on a regular basis, using a handheld thermocouple data-logger. The recorded temperature profiles provided an estimate of the thickness of the artificial sea ice, and allowed to monitor its growth. The ice / water interface depth was estimated from the temperature profiles, from the discontinuity in the profile where the temperature became linear as a function of depth. An example of the evolution of the temperature profile during an experiment and the estimated thickness of the sea ice is shown in figure 2.5. The thickness of the ice was also assessed by drilling boreholes within 10 cm of the edge of the tank and marking the drill bit as it went through the ice. The main purpose of drilling holes in the ice during the growth phase, was to avoid excessive hydrostatic pressure build up under the ice, which leads to excessive brine rejection and may change the physical properties of the ice. Drilling was performed approximately 10 cm from the edge of the tank (away from the measurement area) with a 65 cm steel bit attached to a low-speed high-torque electric drill. The excess water was collected in a plastic container and removed to avoid disturbing the surface of the ice.

To investigate the effects of black carbon and mineral aerosol deposits on the BRF of the laboratory grown sea ice, a 5 cm layer of doped sea ice was formed on the surface of the existing artificial ice. At the start of each experiment, 75L of the artificial seawater were drained into sterilised polypropylene containers using an outlet valve in the filtration system. The containers were sealed and placed in a dark storage unit during the growth and measurements of the clean ice. After the BRF measurements of the clean ice were performed, a known aqueous solution of black carbon or volcanic ash was poured into the seawater containers. The provenance and properties of the particulates used, as well as the procedures of the preparation of the solutions are described in section 2.1.5. The laboratory goniometer was removed from the surface of the sea ice, and after being cooled in the sea ice simulator to prevent melting of the sea ice, the 75 L of seawater containing the impurities were poured onto the surface of the existing artificial sea ice. The water on the surface of the ice froze over a period of approximately 48 hours. For a period of approximately 5 days, brine rejection was observed on the surface of the ice, forming a wet layer on the surface of the new ice. Contrarily to the clean ice layer, the doped sea ice was not drilled to prevent impurities from being flushed out of the top layer into the seawater. The measurements of the BRF of the sea ice with a surface layer were performed approximately 7 days after the seawater was placed on the ice, after the surface was visually similar to the previous layer. The list of experiments performed with

a clean ice, followed by a poisoned layer is reported in chapter 7.

At the end of each experiment, an ice sample was collected using a 3 cm diameter ice core auger operated using the drill described above. The ice core was photographed, measured and cut into sections of 2 to 5 cm immediately after coring. The sections were placed in sealed teflon pots and left to melt at room temperature. Once melted, the salinity of the individual sections was recorded using the refractometer mentioned in section 2.1.2.1. Figure 2.6 shows a photograph of a typical core with a plot of the measured temperature (using the thermocouples in the tank before coring) and salinity. The salinity is plotted as a bar plot, where each bar represents the salinity of the section of the core. The figure shows a steep gradient in temperature throughout the sea ice layer, and constant temperature with depth in the underlying water. The sea ice was visually uniform throughout the core, consisting of columnar ice, with the exception of the top layer (corresponding to the added layer) which consisted of granular sea ice. The salinity profile of the ice forms a crude C shape, which is in agreement with the shape of in-situ salinity observations of first-year sea ice in the literature (e.g. Weeks and Lee, 1962; Tucker III et al., 1984). In the example shown here, the profile indicates a more saline subsurface layer located between 2 and 6 cm deep. The layer with a higher salinity corresponds to the surface layer containing impurities that was added in the second phase of the experiment.

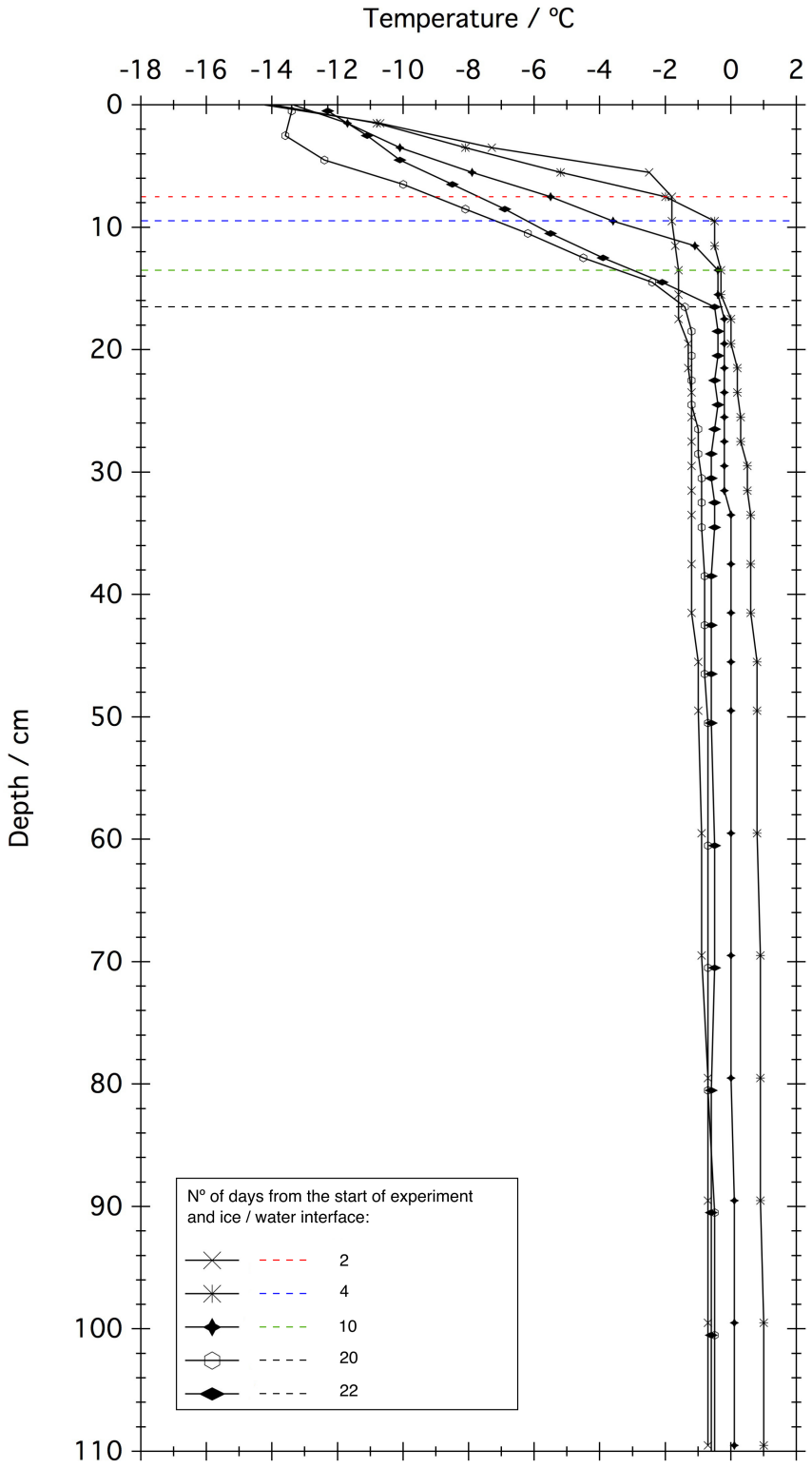

FIGURE 2.5: Example of temperature profiles in the tank measured over the course of 3 weeks. The thickness of ice is determined by the change in slope, and represented in dotted lines in the figure.

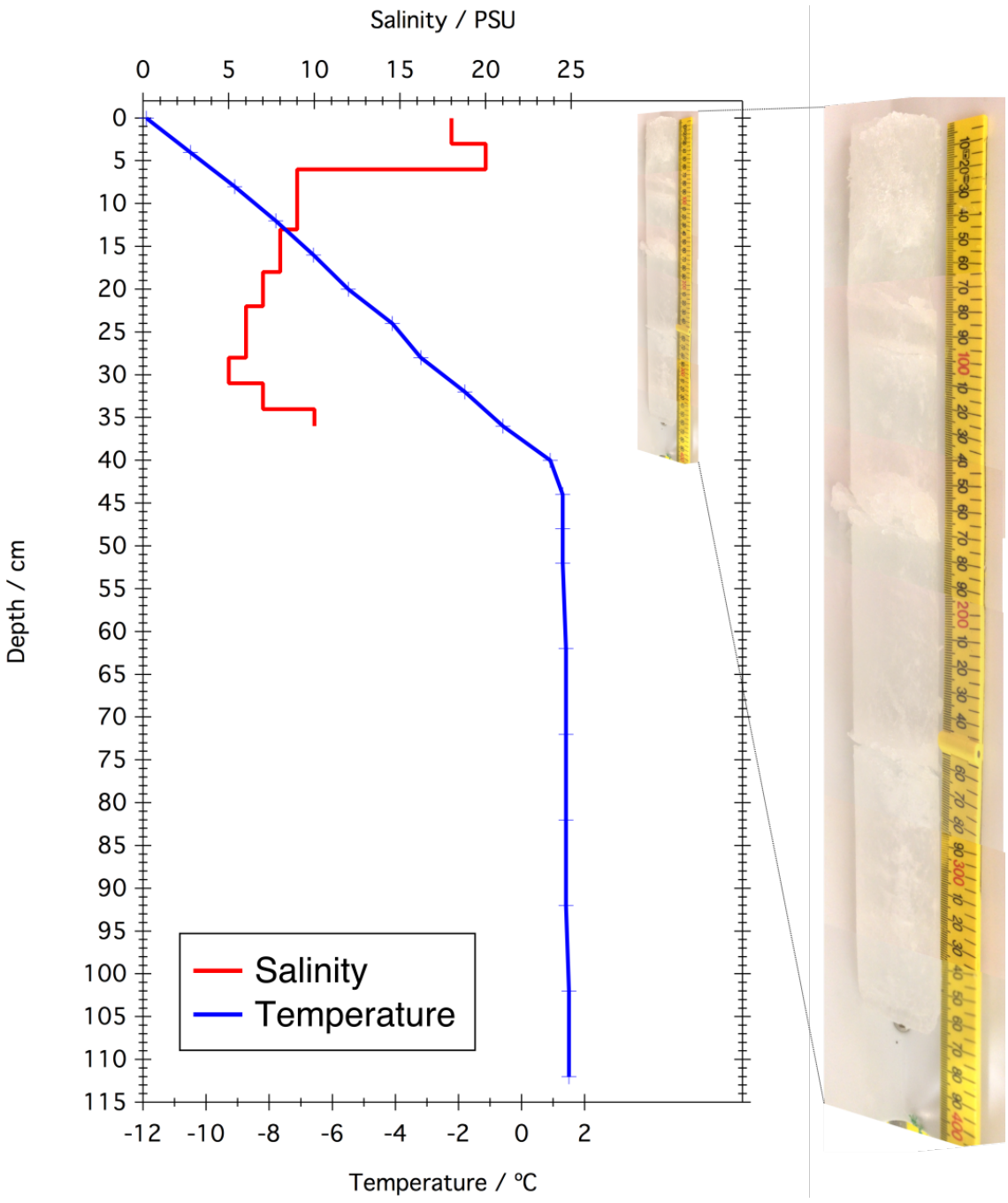

FIGURE 2.6: Typical ice core, salinity and temperature of the artificial sea ice at the end of an experiment. The salinity is plotted in red and the temperature in blue. Each vertical section of the salinity plot corresponds to the temperature for the section of the core that was melted.

2.1.3 Illumination

Laboratory BRF measurements require an artificial light source providing the incident irradiance flux. An ideal illumination source generates uniform and stable illumination across the measurement target (Sandmeier and Strahler, 2000), with the smallest possible solid angle and a parallel beam (Schaepman-Strub et al., 2006). However, owing to the weakly absorbing, highly scattering sea ice, the illumination was required over the largest possible area to account for the contribution of scattered light to the viewing target from the surrounding sea ice. In the following sections, the characteristics of the illumination source used in the sea ice simulator are presented.

2.1.3.1 Light source

To perform the BRF measurements reported in chapter 7, the artificial sea ice was illuminated using 9 tungsten-halogen floodlight lamps mounted as an array (figure 2.7). Each lamp had an output of 400 W, producing 9500 lumen with a colour temperature of 3000 K. The floodlight housings were mounted on a plywood board attached to a tripod, covering an area of 550 mm x 485 mm. The lamps provided a sufficiently strong signal for the detector in the electromagnetic spectrum region of 400 nm to 1000 nm.

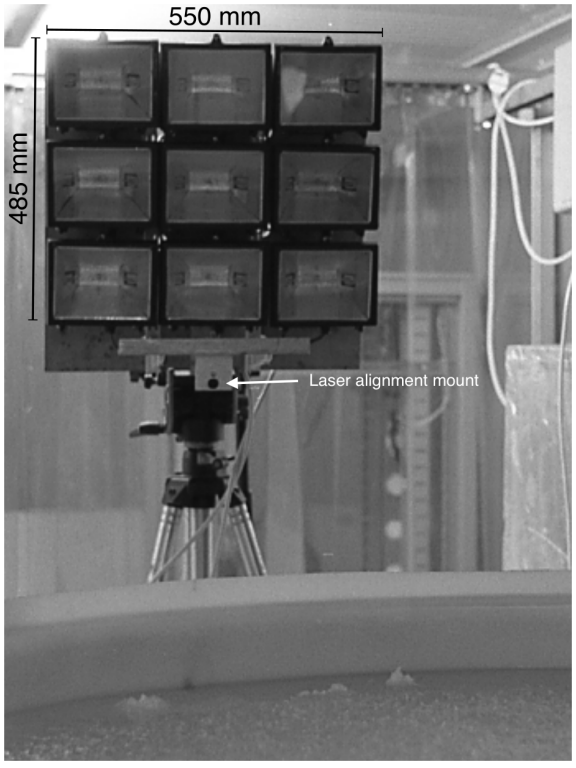

FIGURE 2.7: Illumination source for the BRF measurements.

2.1.3.2 Illumination angles and uncertainties

The moving tripod allowed the adjustment of the height and inclination of the plywood board supporting the lamps, and therefore the adjustment of the illumination angle. Throughout the BRF measurements, the illumination was set to a fixed zenith angle of $60°$. To ensure a consistent illumination angle of $60°$, the lamps were aligned using a laser. The laser pointer was inserted in a mount at the base of the lamp array (shown in figure 2.7), perpendicularly to the plane of the lamps. The lamp array was tilted forward to an angle of $30°$, using a digital angle reader with a precision of $\pm 0.1°$. The tripod was adjusted in height and distance so that the centre of the array was at a distance of 155 cm from the centre of the measurement target on the ice, and the beam of the laser illuminated a target on a measuring rod placed across the sea ice tank. The position of the target was calculated to take in account the offset between the centre of the lamps and the laser pointer.

2.1.3.3 Lamp stability

The drift in the illumination intensity was monitored by measuring the nadir radiance of a quasi-lossless lambertian panel. The lamps were turned on for 1 hour prior to the measurements to allow the power supply to stabilise. The radiance of a Spectralon panel was recorded over a period of 200 minutes using an Ocean Optics USB 2000+ spectrometer. The change in radiance over 200 minutes, shown in figure 2.8 for 3 example wavelengths, was less than 1.5% over the wavelength range 400 – 850 nm. The lamp stability was considered to be uniform over the duration of the measurements performed in the sea ice simulator, and therefore not corrected for.

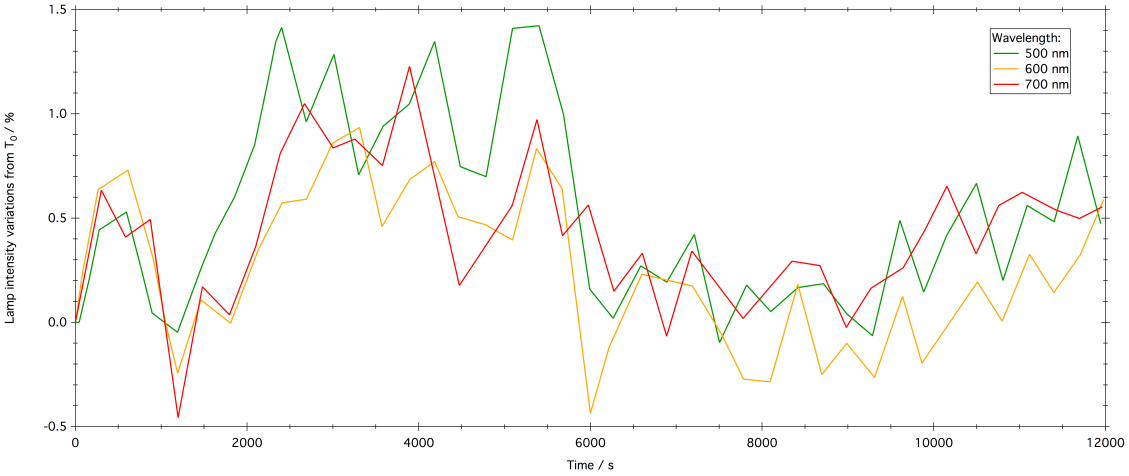

FIGURE 2.8: Change in the intensity of the illumination source output over a period of 200 minutes at wavelengths 500 nm, 600 nm and 700 nm.

The homogeneity of the illumination footprint was characterised to account for the variations in the sampling area of the sensor as a function of zenith and azimuth angles (described in section 2.1.4.2). Indeed, an uncollimated illumination beam and thus the heterogeneity of the footprint are a source of error for BRF measurements, particularly at high illumination zenith angles (Sandmeier et al., 1998). The irradiance homogeneity across the target surface was assessed by measuring the radiance from a Spectralon panel across a grid using an Ocean Optics USB 2000+ spectrometer. The footprint of the lamps was compared to the footprint using a series of collimating baffles. The experiment was produced in collaboration with C. Ball, and the results were reported in Ball (2015). Therefore, the characterisation will not be described in detail here. The test results showed an asymmetry of the illumination in the principal plane for the uncollimated lights. The direction of the inhomogeneity can be explained by the large illumination solid angle: owing to the non-parallelism of the beam, the surface closer to the lamps is more intensely illuminated. However, the addition of collimating baffles did not correct for the asymmetry, creating additional asymmetry in illumination in the orthogonal plane. Ball (2015) proposed a correction factor accounting for the non-uniformity of the illumination footprint. The theoretical footprint for five viewing zenith angles, over a viewing azimuth angle range of 360° was divided into a 400×400 pixel grid. The sum of the intensity of the lamp footprint for each pixel was normalised by the sum of the pixels of the viewing footprint at nadir, yielding a correction factor. Nevertheless, the correction factor provided by Ball (2015) was not applied to the measurements performed in chapter 7. Firstly, the correction factors were not provided for viewing zenith angle over 60°, owing to the characterisation area of the footprint being too small. Measurements of the BRF of the artificial sea ice (chapter 7) show a strong forward scattering maximum located close to the illumination zenith angle, in the forward part of the principal plane. Therefore, the area of interest on the hemisphere is located at high viewing zenith angles. Providing a correction factor for lower zenith angles only may lead to a misinterpretation of the intensity of the forward scattering maxima. Secondly, small changes in the setup and the alignment of the lamps to the sea ice surface may change the position of the lamp footprint on the surface of the sea ice, introducing significant errors in the correction factor. Furthermore, the pixel values within each viewing footprint area were interpolated over a 10×10 cm grid assuming a spatial linearity on the x and y axis of the illumination distribution, which was considered here too coarse to capture small spatial scale variations. Because the illumination footprint was quasi-symmetrical on each side of the centre of the viewing target in the principal plane, the changes in illumination over the viewing footprint may be partly nullified. However, the characterisation of the illumination inhomogeneities suggested uncertainties of up to 7%.

2.1.4 BRF measurements of artificial sea ice

The BRF of the artificial sea ice at the sea ice simulator in RHUL was acquired using a laboratory goniometer. A description of the instrument and the measurement procedures is found in the following sections.

2.1.4.1 Instrument design and setup

The laboratory goniometer, shown in figure 2.9 was designed and built at RHUL specifically for BRF measurements of the artificial sea ice in the sea ice simulator. The instrument consists of a steel base ring measuring 77 cm in diameter, supported by 8 steel bolts, that control the height of the base ring. The bolts are attached to polytetrafluoroethylene (PTFE) disks to limit the disruption of the surface of the ice and spread the load of the instrument. A black anodised circular sheet of aluminium was placed on the inside of the base ring during measurements to limit stray light reflections perturbing the sampling area. A carriage, clamped to the base ring with steel wheels supports the arm of the instrument. The carriage travels along the base ring and has a range of 360°. The azimuth angle of the carriage on the base ring is determined by using a digital angle reader with a precision of $\pm 0.1^\circ$ connected to the base ring with low friction gears. The angle of the carriage is measured relative to the forward principal plane by calculating the distance travelled along the ring. A pivoting arm is connected to the carriage and adjusted using a clamping lever. The arm is made of two square aluminium pieces of tubing forming an L shape. A diagonal supporting strut provides structural rigidity and stops the arm from flexing at high viewing zenith angles. The aluminium tubing is covered in matte black rubber to limit stray light reflections. The arm can be pivoted 180°, providing a sensor viewing zenith angle range 0° – 90°. The zenith angle is measured using a digital angle reader with an accuracy of $\pm 0.1^\circ$ mounted on a holder on the upright section of the arm. A signal collector is connected to the arm using an optics slip ring connected to an aluminium optical breadboard that is bolted to the end of the horizontal section of the arm. The position of the signal collector is adjustable, allowing the signal collector to be placed above the centre of the base ring. The alignment methodology is presented in section 2.1.4.2. The signal collector, placed at a height of 48 cm from the surface, consists of an 8° field of view lens, connected to a spectroradiometer with a fibre optic. The combination of the height and field of view were chosen as a compromise. On the one hand, the smallest field of view possible was required to approximate an infinitely small viewing solid angle and to keep the viewing footprint within the goniometer's base ring at high viewing zenith angles. On the other hand, a wide field of view was required to provide sufficient light to the spectroradiometer and ensure that the sampling area was larger than the roughness features observed. With the setup described above, the footprint at nadir was circular, with a diameter of 6.71 cm. At larger viewing zenith angles, the viewing footprint was larger and elliptical, with a field of view reaching a major axis

of 34.55 cm for a viewing zenith angle of 75°, taking in account the bias owing to the offset of 3 cm of the goniometer's arm pivot point from the surface of the ice.

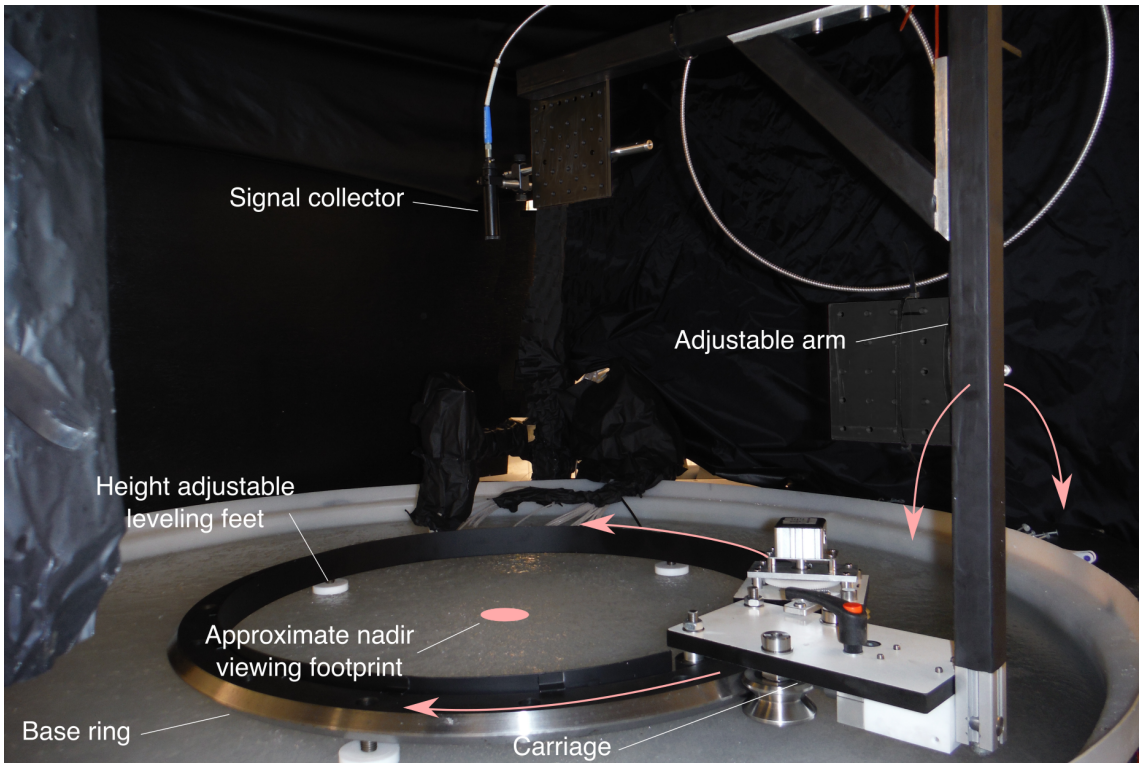

FIGURE 2.9: Goniometer setup for BRF measurements.

Over the course of the experiments, two different spectroradiometers were used with the laboratory goniometer. An Ocean Optics USB2000+ spectrometer was used for the experiments with black carbon, and an ASD FieldSpec pro was used during the experiments with the volcanic ash. The ASD spectroradiometer was obtained through a Natural Environment Research Council (NERC) Field Spectroscopy Facility (FSF) loan. The Ocean Optics spectrometer is an Ultra-Violet to Visible (UV-VIS) spectrometer that operates over a wavelength range 300–875 nm. The detector consists of a 2048 pixel silicon CCD array with an optical full width at half maximum (FWHM) optical resolution of 0.1 nm and a sampling resolution of 0.3 nm. The signal-to-noise ratio of the instrument of the instrument for a full signal is 250:1. The spectrometer was attached to the arm of the goniometer, and measurements were taken using the Ocean Optics SpectraSuite software on a Panasonic Toughbook ruggedised laptop. The ASD FieldSpec pro spectroradiometer covers a wavelength range of 400–2500 nm using three detectors. A 512 element silicon photodiode array is used between 350 nm and 1050 nm, and two separate thermoelectrically cooled, near-infrared indium gallium arsenide photodiodes measure incoming radiation between 900 nm and 1850 nm and between 1700 and 2500 nm respectively. The ASD has a FWHM resolution of 3 nm at 700 nm, 10 nm at 1400 nm and 12 nm at 2100 nm,

and a sampling resolution of 1 nm in the visible range and 2 nm in the near-infrared. The signal to noise ratio of the ASD is larger than the Ocean Optics spectrometer, with ratios of approximately 10000:1 at 600 nm, 1000:1 at 1500 nm and 350:1 at 2200 nm. The 8° field of view optic of the ASD was connected to the optical breadboard on the goniometer's arm and placed in the same position as the signal collector used with the Ocean Optics spectrometer. The ASD has been shown to stop operating at temperatures below $-10\,^\circ\mathrm{C}$ (Greenwell et al., 2015). As a consequence, the instrument was placed in an insulated polystyrene container. Measurements were recorded using the RS^3 software on a Dell laptop.

The measurements of the radiance of the artificial sea ice were normalised using a white reference Labsphere Spectralon panel. As defined in chapter 7, BRF requires the angular measurement of radiance to be ratioed by the radiance of a lossless lambertian reflector. Spectralon, made from pressed PTFE spheres, offers quasi-lossless and near-lambertian properties. A $20 \times 20\ \mathrm{cm}$ panel was placed on a horizontal perspex frame with three adjustable legs and a circular bullseye spirit level. The adjustable feet minimised the disruption of the sea ice surface and allowed the spectralon panel to be levelled, limiting the errors owing to the anisotropy of Spectralon (Sandmeier et al., 1998; Sandmeier and Strahler, 2000; Peddle et al., 2001). To correct the deviation from a lossless reflector, the Spectralon panel was calibrated by Ball (2015) at the National Physical Laboratory, Teddington, UK. The suggested broadband correction factor of 0.97 for an illumination zenith angle of 60° was applied to the BRF equations in chapter 7. During the measurements, the radiance of the panel at nadir was acquired immediately before or after each angular radiance measurement of the sea ice. Ideally, the panel measurements should have been performed at the same viewing angles as the ice measurements. However, a panel with minimum dimensions of $50 \times 50\ \mathrm{cm}$ would have been required to include the viewing footprint at high viewing zenith angles, and a full characterisation of the BDRF response of the panel, which is not feasible (Sandmeier et al., 1998) would have been necessitated. Further uncertainties would have also been introduced owing to the heterogeneity of the illumination (further from the centre of the illumination footprint). Owing to the intensity of each point on a Lambertian surface being reflected in a cosine response, and the surface being sampled by the signal collector proportionally to the reciprocal of the cosine of the viewing zenith angle, the radiance of the Spectralon panel was considered to be independent of the viewing angle. Therefore, nadir measurements of the Spectralon panel was used to normalise measurements for all viewing zenith angles. Moreover, the approach of normalising the measurements with a nadir viewing angle of the Spectralon panel has been widely followed for field angular measurements (e.g. Peltoniemi et al., 2005; Schopfer et al., 2007; Ball et al., 2015).

2.1.4.2 Measurement procedure

To ensure a good repeatability of the measurements, a standard protocol for setting up the experiments was developed. The different steps are listed below.

- **Goniometer**
  - Perform the geometrical calibration of the signal collector holder.
  - Place the goniometer on the ice and align the goniometer to the reference points.
  - Level the goniometer's base ring, whilst maintaining it as close as possible to the surface.
  - Verify that the alignment of the signal collector holder is correct.
  - Install the instruments (digital inclinometers, spectrometer, computer) and turn the instruments on for warm-up (minimum 1 hour).

The geometrical calibration and alignment of the signal collector holder was performed by using a laser pointer. The laser pointer was inserted in the signal collector holder. As the carriage was rotated around the ring, the position of the laser spot was traced on millimetre graph paper placed on the sampling surface, every 30° in azimuth. The tilt of the signal collector was adjusted until the spot deviation was within a circle with a diameter of 0.5 cm. The adjustments were carried out at nadir and at a viewing zenith angle of 45°. Once the goniometer was placed on the surface of the ice, the laser pointer was replaced with the signal collector. To ensure that the alignment was valid for the signal collector, the laser beam was shone reversely into the fibre optic cable connected to the signal collector and the laser footprint projected on the ice was recorded on millimetre paper. Figure 2.10 shows a digitalised example of the variation in the nadir footprint of the signal collector. The grey area represents the deviation in the centre of the footprints. Although the laser dot alignment was within 0.5 cm, the signal collector deviation was within a circle with a diameter of 1.8 cm. The extent of the footprint for a viewing zenith angle of 75° is also shown for comparison.

The goniometer base ring was aligned to reference marks on the sea ice tank. The centre of the base ring was placed as close as possible to the centre of the tank, whilst enabling the goniometer carriage and arm to be unobstructed by tank structures. However, the range of measurements over the hemisphere was restricted by the thermocouple rod. Therefore, the instrument was not able to perform BRF acquisitions between azimuth angles of 225° and 270° (with an illumination azimuth angle of 180°).The levelling of the base ring was achieved using a digital angle reader, placed on a rigid plastic support. The support was placed across the base ring of the goniometer and the height of the feet was adjusted until the base ring was within 0.1° of 0° (horizontal). The height of the ring

above the surface of the ice was kept as small as possible to minimise the offset of the pivot point of the goniometer's arm and reduce shadowing from the ring.

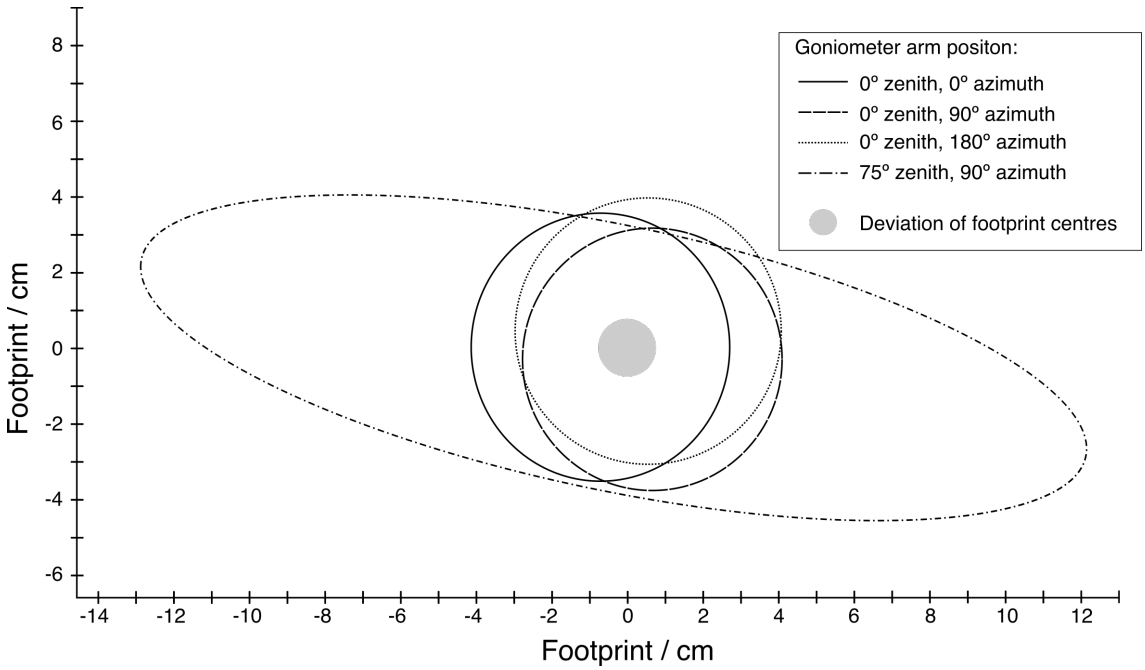

FIGURE 2.10: Digitalised outlines of the footprint of the signal collector traced on millimetre graph paper for different viewing azimuth angles. The viewing footprint of the signal collector at a azimuth angle of $90°$ and a zenith angle of $75°$ is also shown. The grey spot represents the maximum deviation of the centres of the nadir footprints over $360°$ in azimuth.

- **Illumination**
  - Position the lamps connected to the tripod on a designated platform on the side of the sea ice tank.
  - Adjust the inclination of the light board using a digital inclinometer to an angle of $30°$ to the horizontal, to obtain an illumination zenith angle of $60°$.
  - Adjust the position of the tripod so that the centre lamp is at a distance of 155 cm from the centre of the goniometer.
  - Align the laser pointer on the predetermined target on the measuring rod by adjusting the height and position of the tripod.
  - Place a shield between the lamps and the ice to limit melting of the sea ice, and turn the lamps on for warm-up (minimum 1 hour).

After the instruments and lamps were setup and stabilised, measurements of the BRF were performed over a discrete number of angles across the hemisphere. For the initial tests, the sampling was done in fixed steps in azimuth and zenith angles (figure 2.11 a).

Preliminary results of the angular distribution of the reflectance of the artificial sea ice highlighted a strong forward scattering peak centred across the forward principal plane and around the illumination zenith angle. The sampling distribution was modified (figure 2.11 b), with a higher sampling resolution in the forward direction to capture the rapid change of intensity. The number of sampling points varied between the experiments, with an average of 75 points for each BRF acquisition. The number of points was chosen to provide a sufficient coverage of the hemisphere whilst limiting the duration of the experiment. The acquisition time for the 75 points was approximately 4 hours. The measurements were performed in a sequential manner across the viewing zenith angles for each azimuth angle. However, the order of the measurements across the viewing azimuth angles was randomised. Regular nadir measurements of the sea ice were made during the experiment, to monitor changes to the sea ice surface and assess the reproducibility of the measurements. The goniometer was manually operated. The measurements sequence was as follows:

- Rotate the goniometer's arm to achieve a viewing zenith angle of 0° (nadir).
- Normalise with the Spectralon panel at nadir. The panel is placed in the centre of the goniometer's base ring making sure the panel is level.
- Remove the Spectralon panel, rotate the goniometer to the desired azimuth and zenith angle and acquire a measurement of the ice.

During the measurements, particular care was taken to shield the operators behind the optical curtains described in section 2.1.1 to prevent errors caused by the reflection of diffuse light from the operator's clothing, that can significantly impact radiometric measurements (Kimes, D S et al., 1983).

A total of six experiments were performed at the sea ice simulator, after the testing phase was completed. The results of the experiments are reported in chapter 7. Each experiment was broken down into 6 phases: (1) the preparation of the seawater, (2) the growth of a layer of clean sea ice, (3) the BRF measurements of the clean sea ice surface, (4) the growth of an additional overlying layer of poisoned sea ice, (5) the BRF measurements of the poisoned sea ice, and (6) the melting of the sea ice and the filtering / cleaning of the seawater tank. Each experiment lasted a period of approximately 2 months.
The six experiments were in turn divided into two stages. The first three experiments were performed using black carbon particles as impurities in the poisoned layer. In the second stage, the black carbon was replaced with varying mass-ratios of volcanic ash particles from the Eyjafjallajökull volcano. Table 2.2 reports the different mass-ratios of impurities placed in the sea ice, and the thickness derived from the temperature profiles at the time of the measurements.

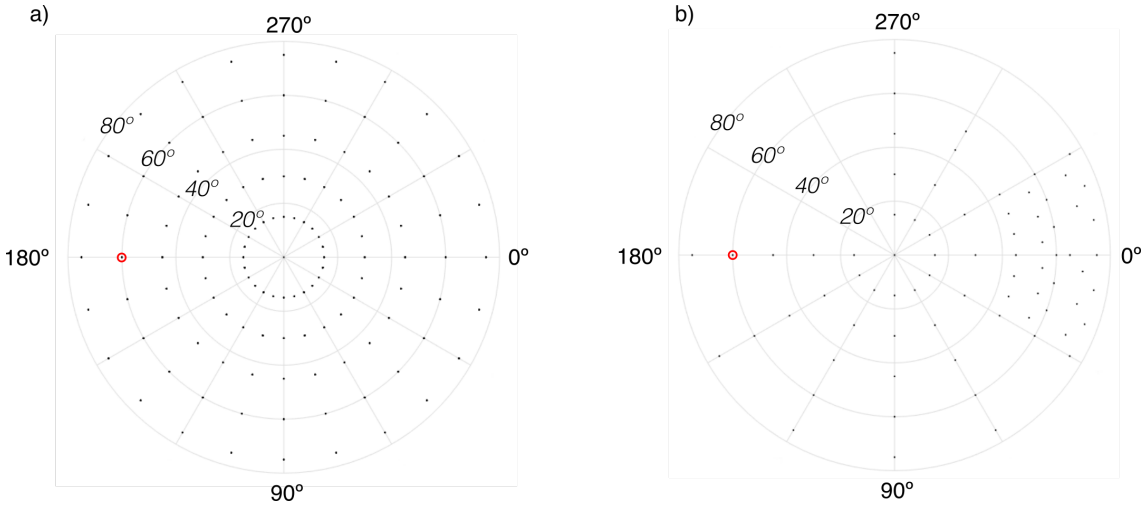

FIGURE 2.11: Polar plots of the distribution of the measurement points across the hemisphere. a) Original sampling distribution. b) Adjusted sampling distribution after initial tests. The red circles indicate the illumination zenith angle ($60°$).

TABLE 2.2: Summary of the experiments performed in the sea ice simulator at RHUL.

Experiment number	Type of impurity added to the upper layer of sea ice	Mass-ratio of the impurities in the top layer / ng g^{-1}	Thickness of the sea ice (Clean run/ Poisoned run) / cm
1	Black carbon	68.6	33.5 / 36
2	Black carbon	34.3	40 / 44
3	Black carbon	205.9	28 / 33
4	Volcanic ash	550	27.5 / 32
5	Volcanic ash	2202.6	35 / 46
6	Volcanic ash	5506.6	36 / 43.5

2.1.4.3 BRF calculations

Based on the definition of BRF found in chapter 7, the following procedure was used to calculate the values of the BRF of the artificial sea ice. The differences between the two spectrometer systems, meant that the procedure was adapted for each instrument. When processing the data collected with the Ocean Optics spectrometer, the raw radiance measurements of the surface of the ice and of the Spectralon panel were corrected for the baseline noise, by subtracting the dark spectrum for each integration time from the raw measurements. All measurements were divided by the integration time, which was set manually for each measurement to obtain the highest signal-to-noise ratio possible. The radiance of the ice was then divided by the radiance of the Spectralon panel, to which the correction factor described in section 2.1.4.1 was applied. The BRF of the laboratory sea ice was therefore expressed as:

$$BRF_\lambda(\theta_r, \phi_r) = \frac{\frac{L_\lambda^{raw}(\theta_r,\phi_r,IT)-D_\lambda(IT)}{IT}}{\frac{L_\lambda^{id}(IT)-D_\lambda(IT)}{IT}C_f}, \tag{2.1}$$

with L_λ^{raw} the raw surface radiance of the sea ice at the viewing zenith angle θ_r and the viewing azimuth angle ϕ_r for a wavelength λ, L_λ^{id} the raw radiance of the Spectralon panel, D_λ the dark spectrum at the integration time IT, and C_f the wavelength-independent Spectralon correction factor of 0.88.
The BRF values were derived differently for the ASD, which allowed a quicker and simplified acquisition of data points compared to the Ocean Optics spectrometer. The baseline noise was corrected in the acquisition software quasi-simultaneously to the radiance measurements, and the output files were corrected for the integration time (automatically set by the instrument). Therefore, the radiance of the ice directly output from the instrument was divided by the corrected Spectralon panel radiance.
The values of BRF across the hemisphere were visually represented using circular plots based on a polar coordinate system. The circumference of the polar plot represents the viewing azimuth angle relative to the forward principal plane increasing clockwise. In the work presented here, the illumination azimuth angle is fixed at $180°$ on the plots (oriented left), meaning that $0°$ represents the viewing point directly opposite the illumination source. The increasing radii of the plot represents the viewing zenith angles and ranges from $0°$ (nadir) to $80°$. To represent the complete hemisphere from a discrete number of measurements, the BRF values were interpolated between measurements. The interpolation was based on a triangulation natural neighbour method (Sibson et al., 1981).

2.1.5 Laboratory preparation of the impurities

The effect of two types of impurities of the BRF of sea ice were investigated in the RHUL sea ice simulator. Black carbon was used to simulate black carbon aerosol deposits that have been observed in naturally occurring sea ice (e.g. Koch and Hansen, 2005b; Doherty et al., 2010b; Bond et al., 2013b). Volcanic ash from the Eyjafjallajökull volcano, was used as a proxy for mineral aerosol deposits found in sea ice (e.g. VanCuren et al., 2012; Zdanowicz et al., 2016). The black carbon and volcanic ash samples were made into aqueous solutions that were placed in a known amount of seawater, that was frozen into a layer of sea ice over an existing clean sea ice layer. The solutions prepared in the chemistry laboratory of the RHUL Earth Sciences department are described in the following sections.

2.1.5.1 Black carbon

To recreate black carbon impurities that are representative of the black carbon atmospheric deposits found in snow or sea ice, the method described by Clarke (1982) was adapted. A commercial sample of Cabot Monarch 120 Carbon Black was used. Monarch 120 is oxidised carbon black that comes in an insoluble black power form with a density of 1.7–1.9 $\mathrm{g\,cm^{-3}}$. Firstly, 1 g of the carbon black was added to a solution of 1000 ml of

a 1:4 ratio of pure water and isopropyl alcohol. The isopropyl alcohol was added to facilitate the dispersal of the black carbon in the suspension. The solution was placed in a Decon FS200b ultrasonic bath at a temperature of 50 °C for 4 hours, to disperse the black carbon particles homogeneously in the solution. Following the sonication of the sample, the black carbon solution was filtered to obtain particle sizes that are representative of atmospheric transported black carbon. Atmospheric black carbon particle diameters range from 0.1 to 1 µm (Gottschalk, 2016). Clarke (1982) showed that filtering a solution of Cabot Monarch 71 Carbon Black throught 2 µm Nuclepore filters followed by 0.8 µm filters yielded a size distribution similar to atmospheric soot. Following the method of Clarke (1982), the black carbon solution was vacuum filtered through a 2 µm Whatman Nuclepore track-etched polycarbonate membrane in aliquots of 100 ml to prevent the filter from clogging (figure 2.14 a). The filtered solution was then filtered a second time, using a Nuclepore 0.8 µm filter. Known quantities of the filtered solution were added to the 75 L of seawater to generate a black carbon poisoned layer of sea ice.
The mass-ratio of black carbon in the solution was determined by performing a gravimetric analysis, thus allowing the calculation of the mass-ratio of black carbon in the sea ice. Three 50 ml glass beakers were cleaned and placed in an oven at 90 °C for 24 hours, to remove residual water. After cooling, the mass of each beaker was measured using a microbalance. After having been weighted, the beakers were placed in the 90 °C oven, and 50 ml aliquots of the black carbon solution were added every 24 hours to be evaporated. A total of 400 ml of solution was evaporated from each beaker. The mass of the beakers containing the precipitates was measured using the microbalance, allowing the mass-ratio of black carbon in the solution to be determined. The mass-ratio of the black carbon in the solution used in chapter 7 was 6.36 ± 0.22 µg ml^{-1} ($\pm$ 1 σ).

2.1.5.2 Volcanic ash

The modelling study on the effects of mineral aerosol deposits on the albedo of sea ice presented in chapter 3, showed that the change in albedo was more sensitive to the type of sea ice than to the optical properties of the mineral aerosol deposit in the sea ice. Therefore, in the work presented in chapter 7, a sample of volcanic ash from the Eyjafjallajökull eruption was considered to be representative of mineral aerosol deposits. A sample of volcanic ash was collected south of the Eyjafjallajökull volcano (approximately $63.545°$, $-19.633°$) and provided by C. Manning from RHUL. The sample was collected from the ground two months after the eruption after having removed a weathered dark surface layer of approximately 5 cm thick. The sample was composed of coarse particles that are not representative of long distance transported aerosol particles. To obtain a realistic particle size, a sample of the collected volcanic ash was placed in a vibrating mill at 1500 rpm for a duration of 3 minutes. Mineral dust particles deposited in snow have been shown to be typically 2–3 order of magnitude larger than black carbon particles (Flanner

et al., 2007). Zdanowicz et al. (2016) found a mean diameter of 2.3 µm for atmospheric dust deposited in snow in Baffin Island, Canada. The long-range transported (> 500 km) Eyjafjallajökull ash particle size was derived by Derimian et al. (2012), who showed a bimodal size distribution of the particles, with radii maxima at 0.1 µm and 1.5 µm. A similar bimodal distribution was derived from satellite observations of a plume 30 hours after the eruption (Waquet et al., 2014), with particle radii distributed around 0.25 µm and 1.75 µm. Therefore, the sample of Eyjafjallajökull ash was not filtered in the same way as the black carbon solution. Because the volcanic ash was placed in a layer of seawater, the rate of sedimentation of the ash particles had to be slower than the rate of the seawater freezing (48 hours). A aqueous solution of Eyjafjallajökull ash was prepared by adding a ratio of 1:50 of the milled ash sample to a ratio of 1:4 pure water and isopropyl alcohol. The solution was left to settle for 48 hours, the equivalent duration of the freezing of the upper layer of sea ice in the sea ice simulator. After 48 hours, the solution of volcanic ash was separated in two layers by decanting: the upper layer with suspended ash, and the lower layer consisting of the larger precipitated particles. The upper layer of the suspension was extracted under vacuum, and diluted with pure water with a 1:4 ratio. Known quantities of the suspension were placed in the 75 L containers of seawater in the second part of the experiments described in chapter 7. The mass-ratio of the volcanic ash in the suspension was determined with the gravimetric analysis described in the previous section. The mass-ratio of the Eyjafjallajökull ash solution was 413.00 $\pm$ 0.90 $\mu g\,ml^{-1}$ ($\pm$ 1 σ).

2.1.5.3 Determining the optical properties of black carbon and volcanic ash

To determine the mass absorption cross-section of the black carbon used in the sea ice simulator, a method using an integrating sandwich spectrometer, described by Grenfell et al. (2011), based on the method of Clarke (1982) was adapted. The integrating sandwich spectrometer measures the absorption spectrum of particulate matter on filter samples in a diffuse radiance environment. Two scattering diffusers "sandwiched" around the sample allow for multiple scattering which results in the attenuation of the light though the sample to be caused solely by the absorption of the sample, and not scattering or shadowing. An integrating spectrometer, shown in figure 2.14 b, was built at RHUL for the purpose of the experiments presented in chapter 4 and chapter 7. A Hitech Scientific stabilised quartz-halogen lamp, with an output between 300 and 760 nm was aligned with the input port of a 5 cm diameter Thor Labs Spectralon integrating sphere. A sapphire filter holder was mounted on the exit port of the integrating sphere. A weighted holder containing a second sapphire window placed against a diffusing quartz filter was designed to "sandwich" the Nuclepore filters between the two sapphire filters. The light transmitted through the system was recorded using an Ocean Optics USB 2000+ spectrometer, operated with the SpectraSuite software on a laptop computer. Using different calibration sheets (described below), the absorption spectra of multiple filters containing

black carbon loadings were converted to a mass absorption cross-section.
Six known aliquots of the filtered black carbon solution described in 2.1.5.1 were filtered through 0.4 µm Nuclepore filters, providing filter loadings of 10.076, 15.115, 20.153, 25.191, 50.383 and 100.765 $\mu g\,cm^{-2}$ (shown in figure 2.14 c). The absorbance spectra of the filters, shown in figure 2.13 b, was calculated as:

$$A(\sigma) = -ln\frac{I(\lambda)}{I_0(\lambda)}, \tag{2.2}$$

where I is the intensity measured from the loaded filter measured in the integrating sandwich spectrometer, and I_0 is a blank 0.4 µm filter measured following the same procedure as the loaded filter.

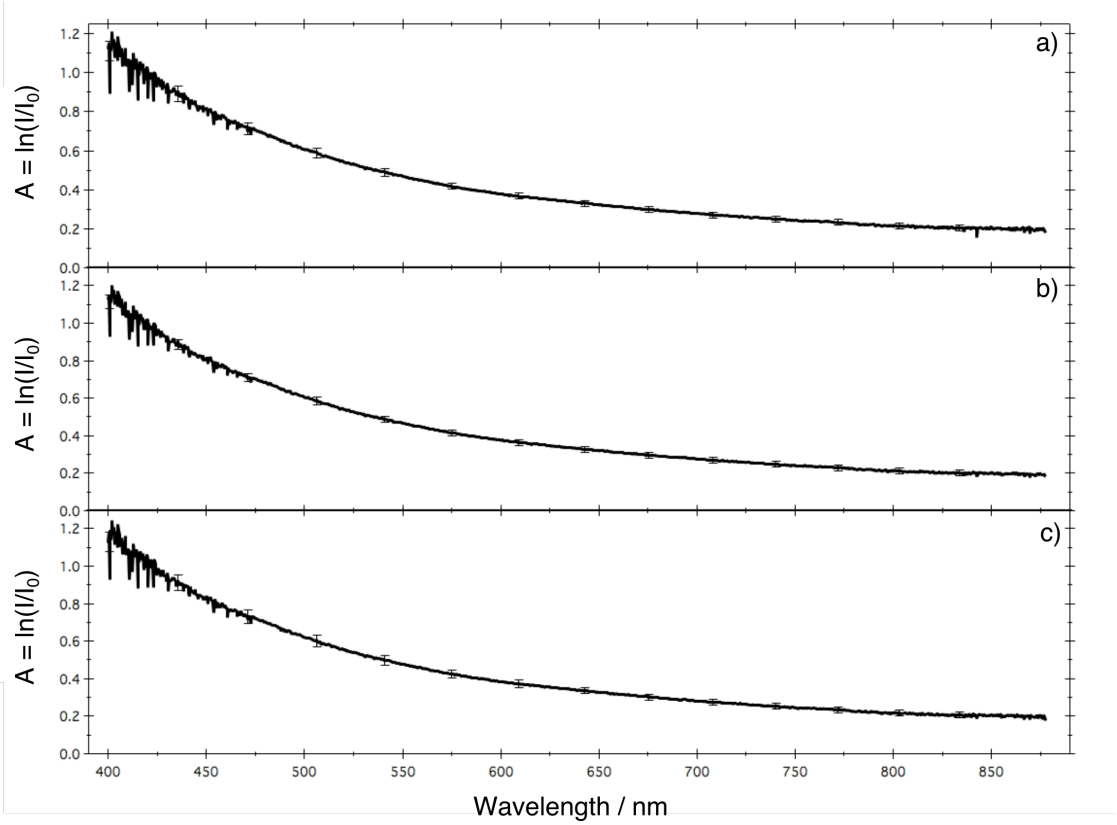

FIGURE 2.12: Integrating sandwich spectrometer initial tests. a) Mean absorbance of five different filters with loadings of 20.153 $\mu g\,cm^{-2}$. b) Mean absorbance of a filter with a loading of 20.153 $\mu g\,cm^{-2}$ measured five times with an interval of 10 minutes. c) Mean absorbance of a filter with a loading of 20.153 $\mu g\,cm^{-2}$ measured three time, rotating the filter by $90°$ between measurements. All error bars represent $\pm$ 1 σ.

The repeatability of the measurements in the integrating sphere and the lamp stability were tested prior the experiments. The lamps were left to warm up and stabilise for 2 hours before each experiment. The repeatability of the measurements were tested by

recording the absorbance (see equation 2.2) of five different filters with loadings of 20.153 $\mu g\,cm^{-2}$ (figure 2.12 a). The temporal repeatability of the measurements was investigated by recording the absorbance of a filter with a loading of 20.153 $\mu g\,cm^{-2}$, five times at 10 minute intervals (figure 2.12 b). The positioning accuracy of the filters in the holder was tested by measuring the absorbance of a filter with a loading of 20.153 $\mu g\,cm^{-2}$ three times, rotating the filter by $90°$ between each measurement (figure 2.12 c). The results showed a good repeatability of the measurements using multiple filters, as well as no significant drift over time. Furthermore, the positioning of the filter in the holder was not considered to be significant for the experiment.

To calibrate the response of the integrating sandwich spectrometer, two sets of standard materials were tested: translucent Light Blue Acetate film sheets, with a thickness of 150 μm and translucent Light Blue Polypropylene sheets, with a thickness of 100 μm. The sheets were placed on a 0.4 μm Nuclepore filter and measured in the integrating sandwich spectrometer using the same method as for the black carbon filters. Multiple sheets of each plastic type were stacked, providing mass-loadings of 0.0254, 0.0508, 0.0762 and 0.1016 $g\,cm^{-2}$ for the Acetate film and 0.011, 0.0219, 0.0329, 0.0439 and 0.0548 $g\,cm^{-2}$ for the Polypropylene plastic. The absorbance of the Acetate film is shown in figure 2.13 b.

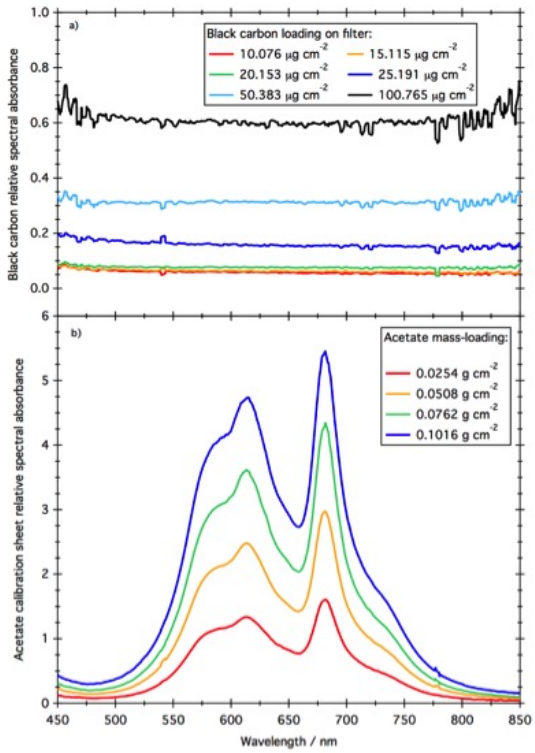

FIGURE 2.13: Spectral absorbance of: a) the black carbon filters with varying mass-loadings, b) the Light Blue Acetate film sheets, stacked to provide different mass-loadings.

Grenfell et al. (2011) showed that the mass loading of black carbon in the snow estimated from the filters, and the mass ratio determined using the integrating sandwich spectrometer initially have a linear relationship. In this study, the linear sensitivity between the black carbon mass loading on the filter and the black carbon absorbance was considered with the ratio between black carbon and plastic, and the ratio of sensitivities to the ratio of the mass absorption cross-section was equated. Therefore, the mass absorption cross-section of the black carbon was expressed as:

$$\sigma_{BC} = \sigma_{pl} \frac{m_{pl}}{m_{BC}}, \tag{2.3}$$

where m_{pl} is the slope of the linear regression between the mass loading of the plastic calibration sheets and the relative absorbance of the plastic measured in the integrating sandwich spectrometer, m_{BC} is the slope of the linear regression between the mass loading of the black carbon filters and the relative absorbance of the black carbon measured in the integrating sandwich spectrometer and σ_{pl} is the mass absorption cross-section of the plastic, given by the Beer-Lambert law:

$$\sigma_{pl} = \frac{A(\lambda)}{\rho l}, \tag{2.4}$$

with $A(\lambda)$, the absorbance measured with a absorbance spectrometer system, ρ is the density of the plastic and l is the geometric path length through the plastic. To measure σ_{pl}, a direct absorbance spectrometer system was setup. The instrument consists of a white light illumination from an Ocean Optics DT-MINI-2-GS tungsten-halogen lamp into a fibre optic cable connected to a lens mounted on a hollow holder. A second lens connected with a fibre optic cable to a spectrometer was aligned with the first lens. The plastic calibration sheets were placed in the slot between the two lenses and the transmitted light was normalised to the signal detected without the presence of a sheet of plastic. The resulting measured absorption was 45.77 $\pm$ 0.04 $\mathrm{cm^2\,g^{-1}}$, at a wavelength of λ = 610 nm for the Acetate plastic and 229.23 $\pm$ 0.02 $\mathrm{cm^2\,g^{-1}}$, at a wavelength of λ = 610 nm for the Polypropylene plastic.

A mass absorption cross-section between 0.58 and 2.1 $\mathrm{m^2\,g^{-1}}$ at a wavelength, λ = 610 nm was estimated for the black carbon placed in the artificial sea ice from the methods described above. The values found are a factor of 3–11 smaller than the black carbon mass absorption cross-section of 6.57 $\mathrm{m^2\,g^{-1}}$ at a wavelength λ = 610 nm (Flanner et al., 2007) typically used in radiative transfer calculations. Furthermore, Grenfell et al. (2011) reported a mass absorption cross-section of 6 $\mathrm{m^2\,g^{-1}}$ for the Monarch 71 Carbon Black solution. To validate the results obtained in the integrating sandwich spectrometer and obtain a closer estimation of the mass absorption cross-section of the black carbon and volcanic ash used in the sea ice simulator, Mie calculations (Bohren and Huffman, 2008) were performed.

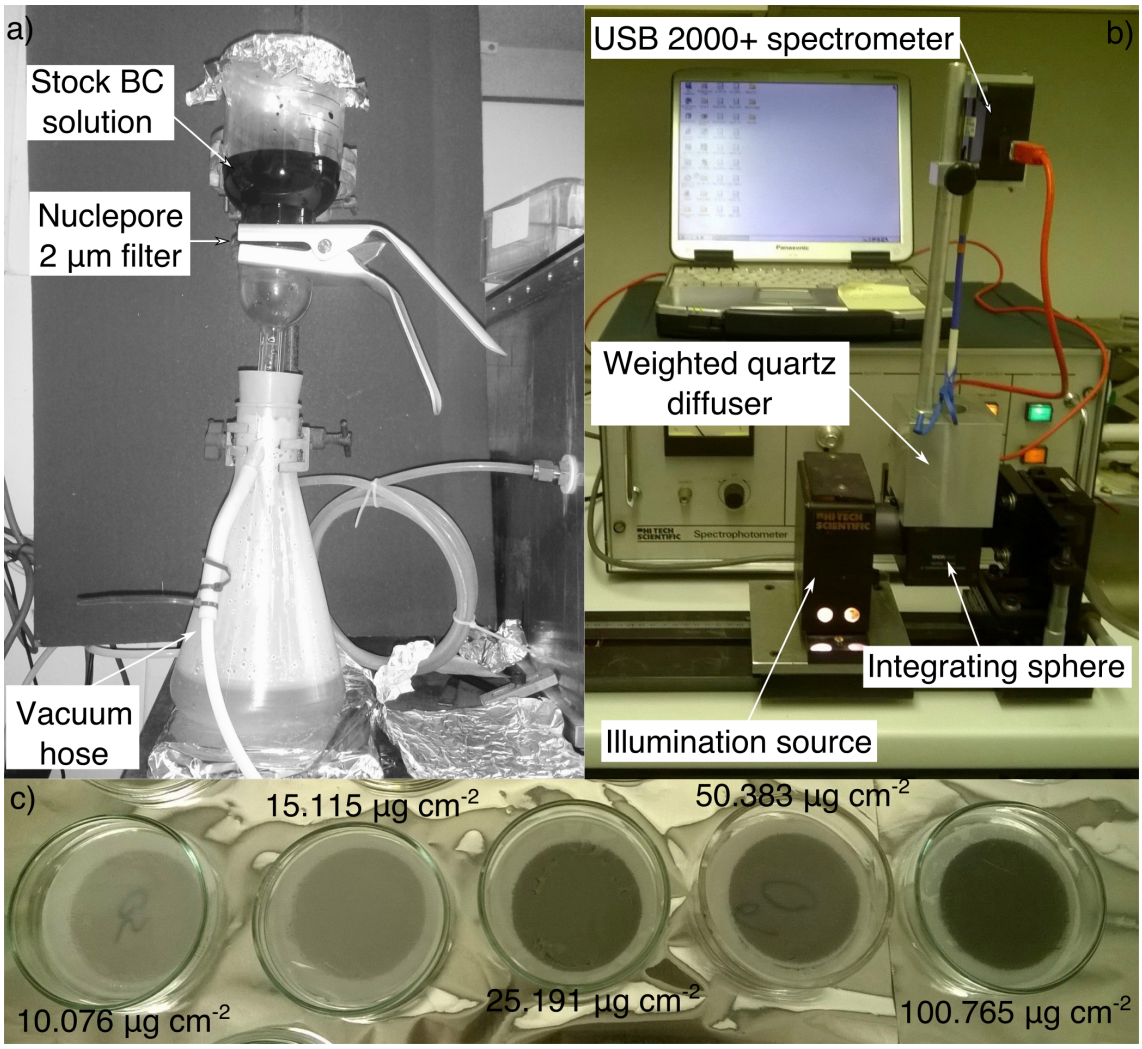

FIGURE 2.14: Laboratory setup for the measurements of the absorption cross-section of black carbon particles. a) The filtering setup of the black carbon on 2 µm Nuclepore filters. b) The integrating sandwich spectrometer. c) A selection of the filters containing different mass-loadings of black carbon.

The calculation of the absorption cross-section using Mie theory requires the knowledge of the particle size distribution, the particle shape, the density of the particles, and the refractive index of the particle and surrounding medium. An estimation of the size of the particles in the solutions poured onto the surface of the ice was obtained using a scanning electron microscopy (SEM). The solutions of black carbon and volcanic ash were filtered through Nuclepore 0.4 µm filters, and SEM images of the filters were taken. A further description of the SEM methods is found in chapter 4. The circularity of the particles, described in chapter 4 (Heilbronner and Barrett, 2013), and the Feret diameter was computed for the black carbon and volcanic ash particles from the SEM images using the image analysis software, Image J (Abràmoff and Magalhães, 2004). An example SEM

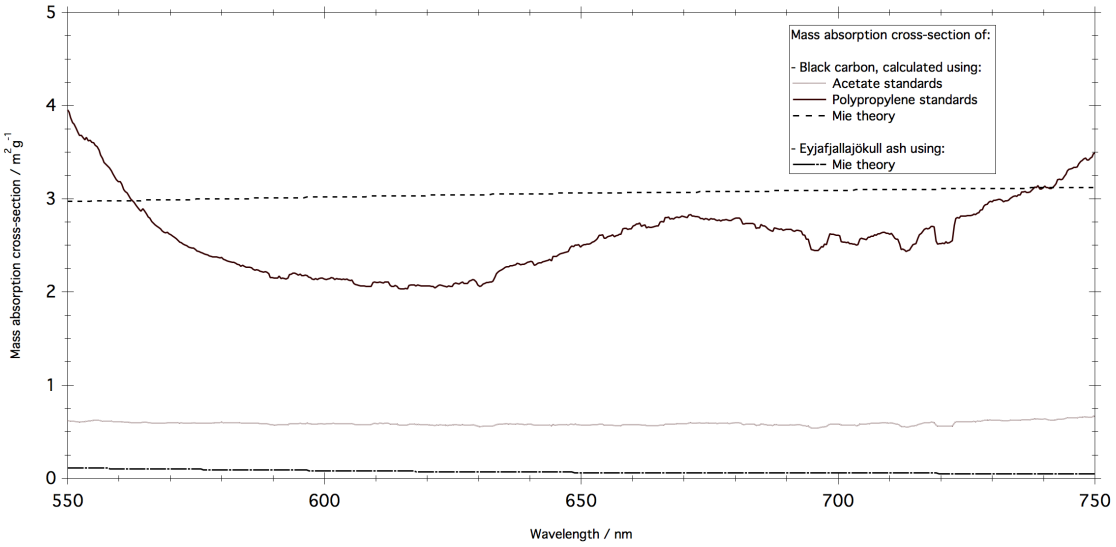

FIGURE 2.15: Mass absorption cross-section of Monarch 120 black carbon, calculated using the integrating sandwich spectrometer technique, with two different standards.

image is shown in chapter 4 and an image of the mineral dust is shown in figure 2.16. The average circularity of the black carbon particles was 0.842 $\pm$ 0.189 µm ($\pm 2\sigma$), indicating spherical-like particles. The average Feret diameter of the black carbon particles was 0.461 $\pm$ 0.331 µm ($\pm 2\sigma$). The average circularity of the volcanic ash particles was 0.731 $\pm$ 0.245 ($\pm 2\sigma$), indicating that although the particles were rounded, they were less rounded than the black carbon particles. The average maximum Feret diameter was 1.691 $\pm$ 1.270 µm ($\pm 2\sigma$). The volcanic ash particles Feret diameter varied between 0.559 and 3.053 µm, which was similar to the sizes observed by Derimian et al. (2012) and Waquet et al. (2014).

The black carbon absorption cross-section was calculated based on the Mie theory in the MiePlot software (Laven, 2006) using the BHMIE code (Bohren and Huffman, 2008), using a mean particle diameter of 0.461 µm, a density of 1.8 $\mathrm{g\,cm^{-3}}$ (mean range specified by the manufacturer), and a black carbon refractive index of 1.95 - 0.79 from Bond and Bergstrom (2006). The calculated mass absorption cross-section value of Monarch 120 carbon black was in agreement with the values obtained in the integrating sandwich spectrometer, with a value of 2.97 $\mathrm{m^2\,g^{-1}}$ at 550 nm. Therefore, the absorption cross-section obtained from the Mie calculations (shown in figure 2.15) was used for the radiative-transfer modelling of the black carbon in chapter 4 and chapter 7. The volcanic ash absorption was calculated in the same way as the black carbon, with a mean diameter of 1.691 µm was assumed in the calculations. A density of 2300 $\mathrm{kg\,m^{-3}}$ was obtained from Johnson et al. (2012). The refractive index of the Eyjafjallajökull, shown in chapter 3, was estimated by Derimian et al. (2012). The refractive index of pure ice was used for the sea ice (Warren and Brandt, 2008). The mass absorption cross-section of the Eyjafjallajökull ash, used in chapter 7 was calculated as 0.11 $\mathrm{m^2\,g^{-1}}$ at 550 nm.

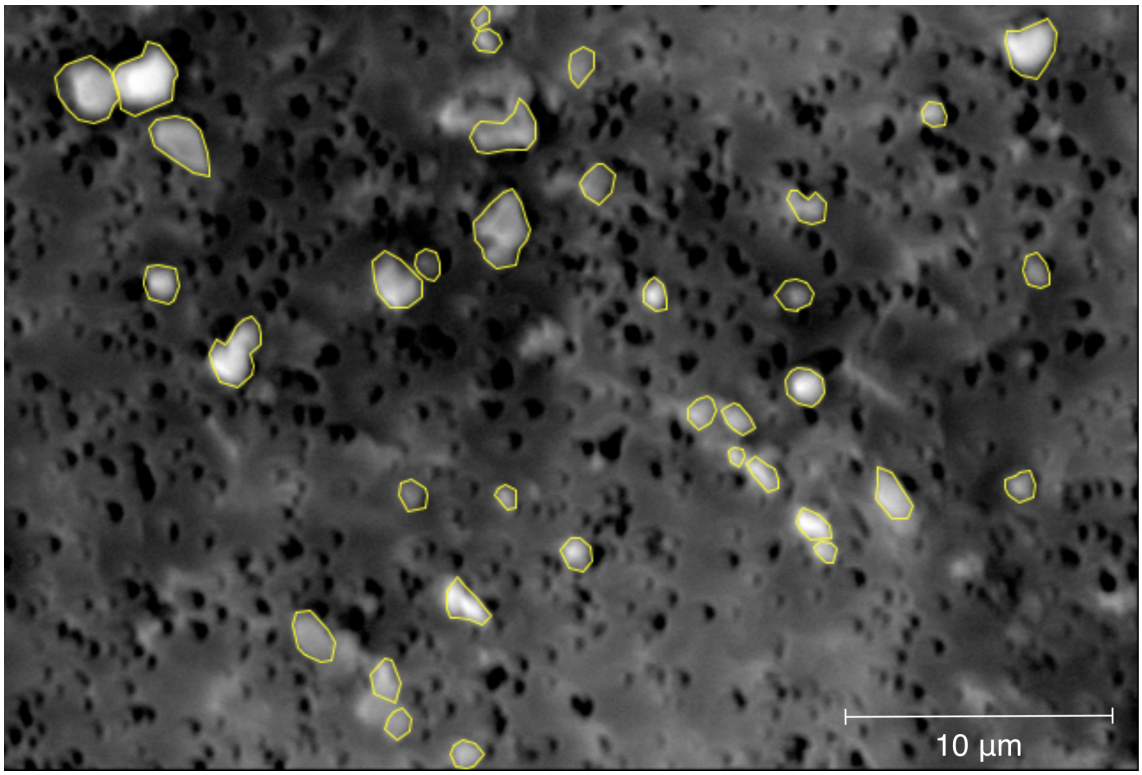

FIGURE 2.16: SEM photograph of the volcanic ash particles used in the sea ice simulator trapped on a Nuclepore 0.4 µm filter. The black circular features in the image are the holes in the filter paper.

2.2 HDRF of experimental first year sea ice

The HDRF measurements of thin first year sea ice reported in chaper 8 were performed at the Sea-ice Environmental Research Facility (SERF) in Canada. In this section, the facility and the instrumentation used are described, and the experimental protocol is reported.

2.2.1 Description of the artificial sea ice facility

SERF is a sea ice research facility, located on the campus of the University of Manitoba, Winnipeg, Canada ($49.80°$, $-97.14°$). The facility, shown in figure 2.17, features an outdoor pool with dimensions of $18.3\,\mathrm{m}$ (length) x $9.1\,\mathrm{m}$ (width) x $2.1\,\mathrm{m}$ (depth). The pool is covered by a removable roof on a set of tracks, allowing the sea ice to be protected from or exposed to snowfall events. At the start of the experiment campaign run over winter, the pool is filled with seawater mimicking the composition of natural seawater (Hare et al., 2013). The pool is heated using a closed hose circuit, through which warmed ethylene glycol is circulated. The heating system is turned off at the start of the experiments and the seawater, exposed to the cold outdoor temperatures, forms sea ice. Sensors are deployed in the pool before the experiments, providing ancillary information on the salinity and temperature of the sea ice and underlying seawater. SERF has been in operation since the beginning of 2012, and has been used to study the physical and chemical

properties of sea ice (e.g. Hare et al., 2013; Rysgaard et al., 2014; Galley et al., 2015; Landy et al., 2015) in a controlled environment. A detailed description of SERF can be found in the literature (e.g. Hare et al., 2013; Else et al., 2015).

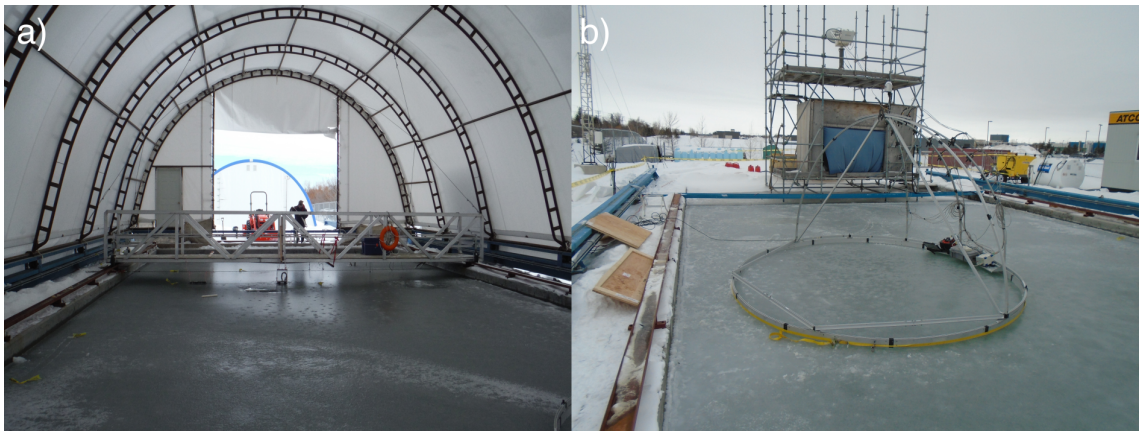

FIGURE 2.17: SERF, University of Manitoba, Canada. a) The sea ice pool with the retractable roof installed. b) GRASS on the artificial sea ice, with the roof removed.

The 2016 campaign at SERF was run from the beginning of January 2016 to the end of February 2016. Two experiments were planned, each carried out over three weeks. The work presented in chapter 8 was performed during the second experiment between the 15th Febraury 2016 and the 28th February 2016. At the end of the January experiment, the heaters in the sea ice pool were turned on and the sea ice was melted. The heaters were turned off for the second experiment on the 9th.February 2016. The sea ice grew to a thickness of 2.5 cm in 3 days, and reached $13\,\mathrm{cm}$ on the 17th February 2016, remaining constant thereafter, until the end of the experiment The monitoring of the sea ice thickness is described in section 2.2.2.5. HDRF measurements were performed on the sea ice in 4 locations on the ice. The number of HDRF acquisitions was dependent on the number of days with clear atmospheric conditions. A total of 9 HDRF acquisitions were carried out during the experiment. However, owing to overcast sky illumination, and instrument instabilities reported in section 2.2.3, only 4 HDRF measurements were usable.

2.2.2 HDRF measurements of the sea ice

The HDRF characterisation of the sea ice surface at SERF was performed with a field goniometer. In the following sections, the instrument setup is described, and the measurement procedures are reported.

2.2.2.1 Instrument design

HDRF measurements of the sea ice were performed with the Gonio RAdiometric Spectrometer System (GRASS), designed at the National Physical Laboratory, Teddington,

UK. The original concept and design of the instrument were described by Pegrum et al. (2006) and Pegrum-Browning et al. (2008). GRASS has previously been used to characterise the HDRF of a variety of natural surfaces. GRASS was first used to characterise the HDRF of a potential vicarious radiometric calibration site for optical satellites located on a salt lake in Turkey (Leigh et al., 2011) . The HDRF of snow was measured in Dome C, Antarctica (Marks et al., 2015), and compared with previous angular reflectance measurements at the same location (Hudson et al., 2006) to support the inter-comparison and inter-calibration of satellite optical sensors. The HRDF of windblown snow and the effects of surface roughness on HDRF were investigated in Ny-Ålesund (Ball et al., 2015). A new vicarious radiometric calibration site for optical satellites, which will be part of the Radiometric Calibration Network (RadCalNet) (Bialek et al., In preparation), was characterised using GRASS (Bialek et al., 2016) and the results will be compared to an automated station that will operate in 2017.

GRASS, shown in figure 2.18, consists of an aluminium base ring measuring 4 m in diameter. A structure formed by five curved arms and two straight supporting segments, connected to an upper base ring are mounted on a rail located on the lower base ring. The upper structure rotates 360° around the base ring, providing a full coverage of the azimuth angles (0° – 360°). Three of the curved arms are placed at 30° intervals on the upper base ring, and are used to support the signal collectors described below. The two other curved arms are used to support the structure and are each placed at an azimuth angle of 90° from the central measurement arm. For previous studies (Ball et al., 2015; Marks et al., 2015), the two straight arms providing structural support to the frame were placed at a relative azimuth angle of 150° on each side of the centre measurement arm. During some of the experiments at SERF, the supporting straight sections of the structure caused shadowing across the target surface. The arm were moved to a relative azimuth angle of 90° from the centre measurement arm, extending the range of measurements across the hemisphere. No change in stability of structure was noticeable.

For the purpose of the study presented in chapter 8, five signal collectors were mounted on each of the three curved measurement arms. The signal collectors were placed at viewing zenith angles of 0° (nadir), 15°, 30°, 40°, 50° and 60°. Measurements of the angular reflectance of artificial sea ice (chapter 7) and modelling of the BRDF of sea ice (chapter 6) have shown that sea ice has a quasi-lambertian response, except for a strong forward scattering peak located on the forward part of the principal plane, around the same zenith angle as the illumination zenith angle. Therefore, the positioning of the signal collectors was weighted towards larger viewing zenith angles, to measure the rapid changes in intensities around the forward scattering maximum. However, the position of the signal collectors was limited to a maximum viewing zenith angle of 60°, as Marks et al. (2015) showed that the base ring affected the measurements at larger viewing zenith angles. The signal collectors consist of an optical lens with a field-of-view of 8°, and are each connected to an Ocean Optics $400\,\mu\mathrm{m}$ ruggedised fibre optic. As it was shown for

the laboratory goniometer in section 2.1.4.1, the viewing footprint of the GRASS is circular at nadir, but becomes elliptical at larger zenith angles. With the setup described here, the nadir viewing footprint has a diameter of approximately 27.97 cm and the major axis of the viewing footprint of the signal collectors at 60° viewing zenith angle is approximately 56.77 cm. The optical lenses are mounted on aluminium brackets that slide along the curved arms, which have etched markings every 1° in zenith, allowing the signal collectors to be aligned to the desired viewing zenith angle. Ball et al. (2015) assessed the pointing accuracy of the goniometer in a dark room at RHUL by shining a laser pointer down the fibre optics connected to each signal collector and tranced the illuminated area on a white surface beneath GRASS. The results suggest a pointing accuracy of approximately $\pm$20 cm for signal collectors between 0° and 50° zenith angle. As shown in section 2.2.2.2, the sea ice at SERF was homogenous. Therefore the pointing accuracy of GRASS was considered to be acceptable. The ruggedised fibre optic cables attached to the signal collector are connected to a Ocean Optics MPM 2000 multiplexer. The multiplexer is in turn connected to the spectrometer system with an separate fibre optic cable, allowing sequential measurements of the radiance of the target with the signal collectors. A custom visible to shortwave infrared (V-SWIR) spectroradiometer was used to record the radiance of the sea ice. The V-SWIR spectrometer is composed of two separate spectrometers, operating over a wavelength range of 400–1700 nm with a spectral interval of $1\,\mathrm{nm}$. The visible part of the spectrum is recorded with an Ocean Optics 2000+ spectrometer, between $400\,\mathrm{nm}$ and $969\,\mathrm{nm}$. The same spectrometer model was used in the laboratory measurements at RHUL, described in section 2.1. The SWIR measurements were performed between $970\,\mathrm{nm}$ and $1700\,\mathrm{nm}$ using a BWTEK Sol 1.7 spectrometer. The incoming radiance was measured simultaneously with the two spectrometers, using a beam splitter. The wavelength dependence of the spectrometers was calibrated before the field campaign by Greenwell et al. (2015), who measured the response of the individual spectrometers to a stable illumination source. The GRASS spectrometer was piloted with a custom LabVIEW software, developed at NPL. A Panasonic Toughbook, that was able to function at polar temperatures, was used to operate the software.

After the measurements were performed in each location on the surface of the sea ice, the signal collectors / fibre optics were inter-calibrated, to minimise errors introduced by the individual response of each signal collector. The purpose of the calibration was to normalise the response of the spectrometer system for each signal collector and fibre optic, correcting for differences in radiance owing to changes in the alignment of the connections between the optics and the spectrometer system. Signal collector calibrations were performed after the measurements of the sea ice target were acquired in each location on the sea ice pool, rather than between each individual HDRF acquisition, because the calibration process required an operator to walk over the measurement target in order to access the signal collectors, disrupting the sea ice. To perform the calibration, a

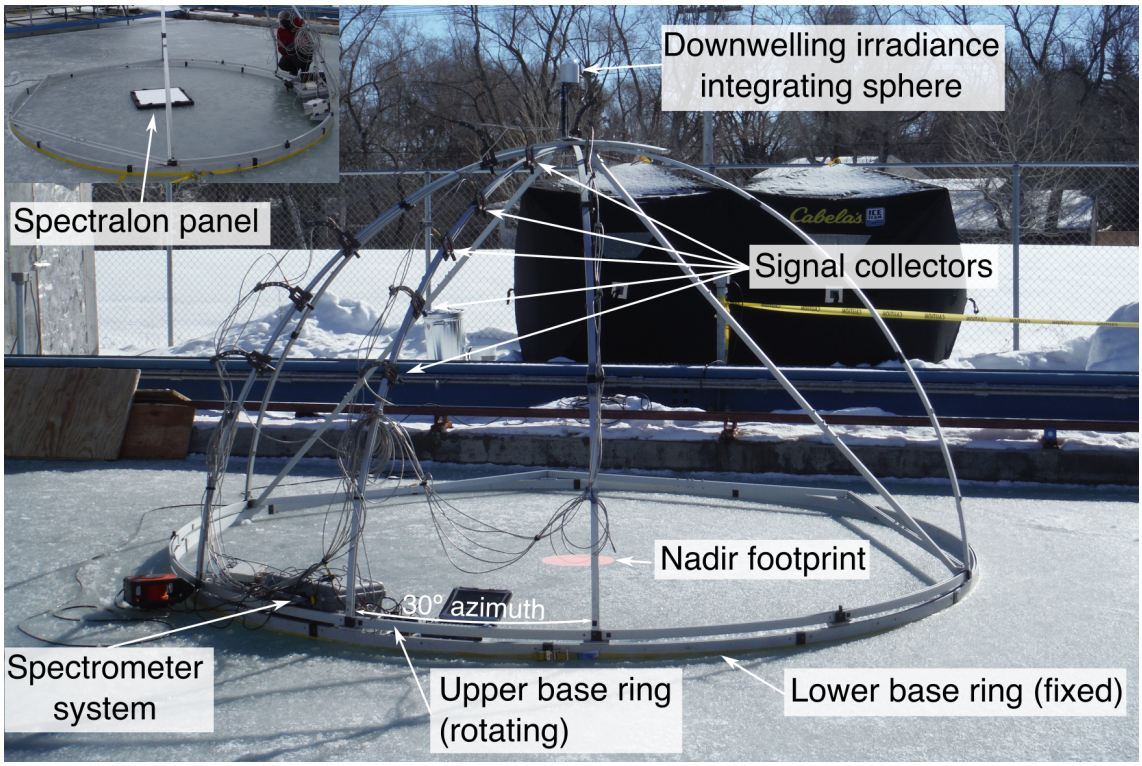

FIGURE 2.18: The Gonio RAdiometric Spectrometer System (GRASS). Inset: Spectralon reference panel used to derive HDRF.

stable light source was connected to each signal collector, and the radiance of the calibration lamp was recorded with the GRASS spectrometer system. The calibration lamp consists of a tungsten-halogen lamp connected to the input port of a Spectralon integrating sphere, providing a uniform and stable illumination source through the exit port of the integrating sphere. The calibration lamp was designed for the signal collectors to slot into the exit port of the integrating sphere, preventing stray light interference or intensity loss. Marks (2014) reported an average relative standard deviation of 3.1% for repeated measurements of the calibration lamp using the same detector. An example of the raw radiance response of the GRASS spectrometer system over the wavelength range 400–969 nm (for clarity) to the calibration lamp for each signal collector is shown in figure 2.19. The response of the spectrometer to the calibration lamp shows differences of up to 36.2 % between different signal collectors. The correction factor applied to the computation of the HDRF values is reported in chapter 8.

An integrating sphere with a cosine collector was attached to the top of the goniometer's frame above the downward looking nadir signal collector, as shown in figure 2.20. The integrating sphere was directly connected to the spectrometer with a $400\,\mu\mathrm{m}$ fibre optic. For each radiance acquisition, a measurement of the downwelling irradiance was obtained, using a flipping mirror that switched between the signal from the downward looking signal collectors and the upward looking integrating sphere. Downwelling irradiance and upwelling radiance measurements were quasi-simultaneous, allowing to

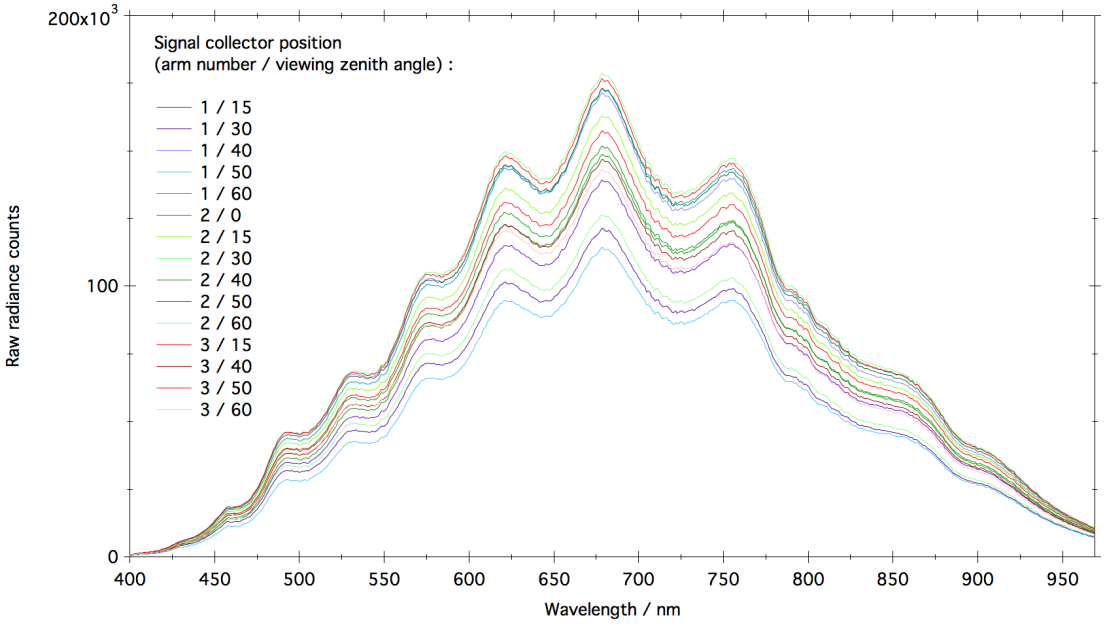

FIGURE 2.19: Raw radiance counts of the GRASS spectrometer system (400–969 nm) for each signal collector attached to the calibration lamp. The position of the signal collectors is described by the arm number (facing the instrument, from left to right) and the viewing zenith angle of each collector.

correct for small changes in illumination owing to changes in atmospheric conditions.

The Lambertian reference used to calculate HDRF (see chapter 8) was a 60×60 cm Labsphere Spectralon panel (shown in figure 2.20). After each set of HDRF measurements, the Spectralon panel was placed on a horizontal aluminium ladder laid across the base ring of GRASS. The setup allowed the Spectralon panel to be centred at the nadir of the downward facing signal collector with a viewing zenith angle of $0°$ without disrupting the surface of the sea ice. The ladder also guaranteed a constant level of the surface of the panel, limiting errors owing to the anisotropy of the panel. A measurement of the Spectralon panel should have been performed for every measurement of the sea ice and with each signal collector. However, a sampling of the panel after each set of measurements was performed to limit the acquisition time, and the changes in illumination during the HDRF acquisition were corrected for using the downwelling irradiance integrating sphere. Furthermore, the nadir measurement of the panel limited significant errors owing to the positioning of the panel because of the footprint size at larger viewing zenith angles. Based on the assumption of a Lambertian response of the radiance from the Spectralon panel, measurements were considered to be independent of the viewing angle. After the campaign, the response of the Spectralon panel was characterised at NPL by A. Bialek, using the National Reference Reflectometer (Williams, 1999), to correct for the departure of the panel from a lossless reflector. The panel was calibrated

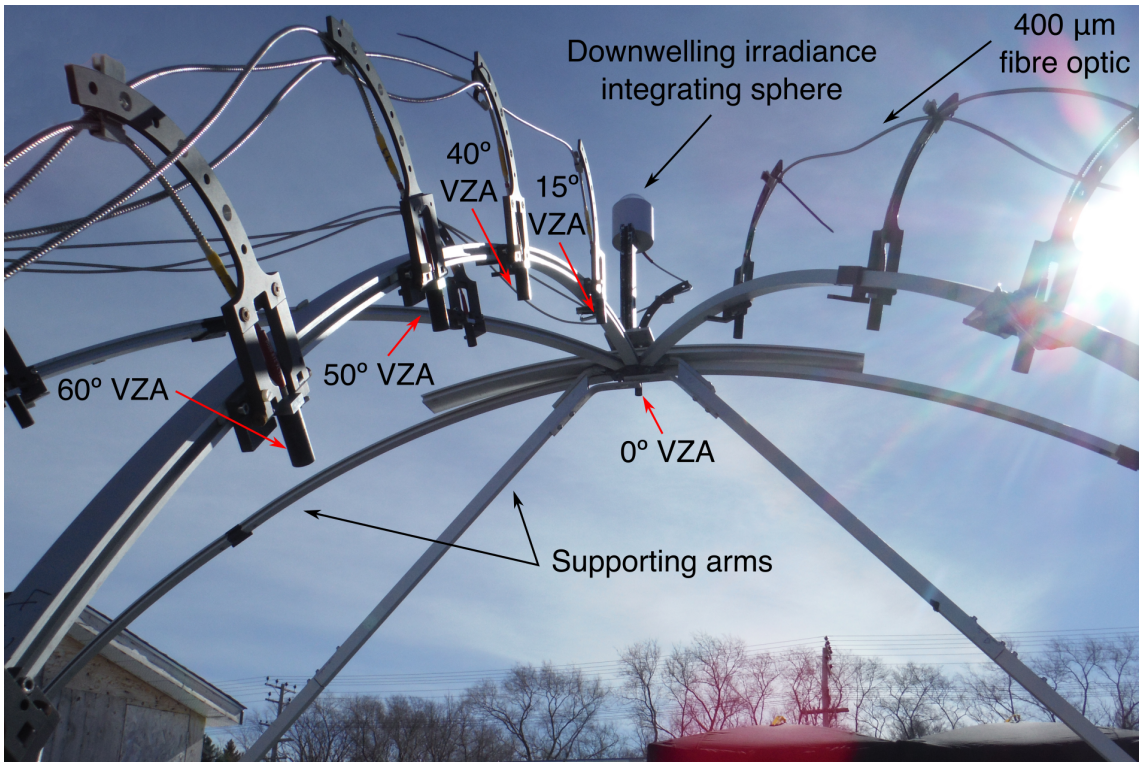

FIGURE 2.20: Signal collectors and downwelling cosine collector on the GRASS structure.

for a $0 - 60°$ configuration ($0°$ illumination zenith angle, $60°$ viewing zenith angle). The correction factor was considered to be representative of the Spectralon measurement conditions during the experiment ($0°$ viewing zenith angle, $60°$ illumination zenith angle), as the BRDF of Spectralon obeys Helmholtz's reciprocity theorem (Meister et al., 1996). A reflectance calibration factor for a wavelength range $409 - 1001\,\mathrm{nm}$ was expressed as (Williams, 1999):

$$\beta = \frac{R(2s/d)^2}{cos\theta}, \tag{2.5}$$

with R the measured ratio of reflected power to incident power, s the distance between the Spectralon panel and the detector of the National Reference Reflectometer, d the diameter of the viewing footprint of the detector on the spectralon panel and θ the viewing angle of the detector relative to the illumination beam. The calibration factor β, plotted in figure 2.21 as a function of wavelength, was measured over a discrete number of wavelengths. The correction values were linearly interpolated over the $1\,\mathrm{nm}$ step of the measurements with GRASS, and the value of β at the wavelength number $\lambda = 1001\,\mathrm{nm}$ was used for wavelengths between $1001\,\mathrm{nm}$ and $1700\,\mathrm{nm}$, as the variation of reflectance of Spectralon has been shown to be less than $1\,\%$ over the wavelength range $1000 - 1700\,\mathrm{nm}$ (Jackson et al., 1992).

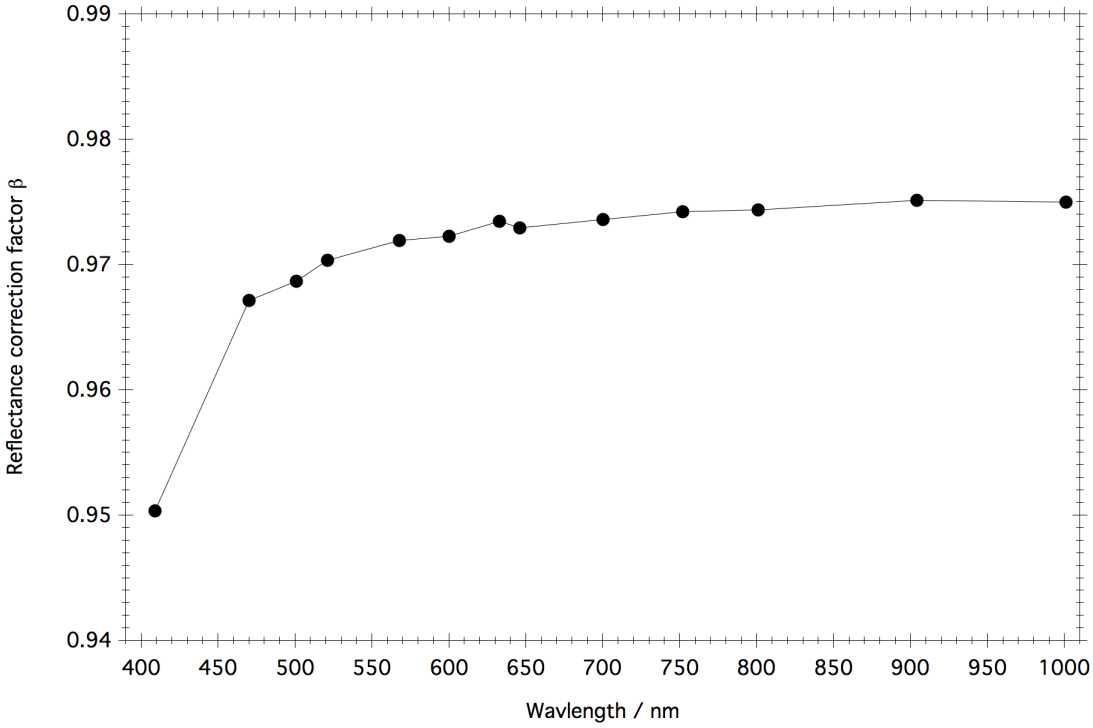

FIGURE 2.21: Reflectance correction factor for the Spectralon panel used during the Winnipeg experiments as a function of wavelength.

In addition to the measurements performed with GRASS, ancillary measurements of nadir reflectance and tests were carried out using an ASD FieldSpec 4 Hi-Res spectroradiometer. The ASD FieldSpec 4 performs radiance measurements over a wavelength range 350–2500 nm, although most measurements presented in this work are reported for wavelengths between 400 and 1700 nm. The wavelength step of the instrument was set to 1 nm. The spectroradiometer has a spectral resolution (FWHM) of 3 nm at 700 nm and 8 nm in the infrared. Similarly to the ASD FieldSpec Pro, described in section 2.1.4.1, the FieldSpec 4 is composed of three detectors. A 512 element silicon array operates between 350 and 100 nm, and two graded index InGaAs photodiode detectors operate over the wavelength ranges 1001–1800 nm and 1801–2500 nm. During the measurements reported in the following sections, the ASD spectroradiometer was placed in an insulated polystyrene box, preventing the instrument stopping operating owing to cold outdoor temperatures. The instrument was controlled using a laptop computer running the software RS^3 through a wifi link. Operating the ASD from a distance allowed to reduce the effects of the operators on the spectral measurements (Kimes, D S et al., 1983).

2.2.2.2 Homogeneity of the sea ice

Alongside the HDRF measurements obtained with GRASS, additional reflectance measurements were performed using the ASD FieldSpec Pro spectroradiometer to characterise the heterogeneity of the sea ice within the base ring of the goniometer. Firstly,

reflectance measurements at regular intervals across the sea ice were performed along the principal plane and the orthogonal plane (figure 2.22). The signal collector of the ASD spectroradiometer was attached to the end of a 1 m carbon fibre boom connected to a tripod at a height of 1 m above the surface of the sea ice. Reflectance measurements were performed along two transects with a relative azimuth angle of $90°$ across the base ring of GRASS every 40 cm, starting and ending 40 cm from the edge of the base ring. The viewing footprint of the instrument was circular with an approximate diameter of 13.98 cm. For each point along the transects, 10 nadir spectra of the raw radiance of the sea ice were acquired, immediately followed by 10 nadir radiance measurements of the Spectralon panel. The radiance of the sea ice was normalised to the corrected Spectralon panel. Figure 2.22 shows the relative change in reflectance from the centre of the goniometer ring (located at nadir from the $0°$ viewing zenith angle GRASS signal collector). At the points on the transect located 40 cm away from the centre (200 cm from the edge of the base ring) which represent the maximum footprint sampling distance from nadir, the change in reflectance was less than 10 % over all the wavelengths up to 1000 nm and less than 6 % for wavelengths between 400 and 800 nm. Across the full transects, the sea ice was more heterogenous, with a maximum change in reflectance of 22.49 % at 1000 nm and 12.62 % at 800 nm. The HDRF results presented in chapter 8 were spatially averaged across all the measurement sites at SERF to remove the effects of the small scale inhomogeneities.

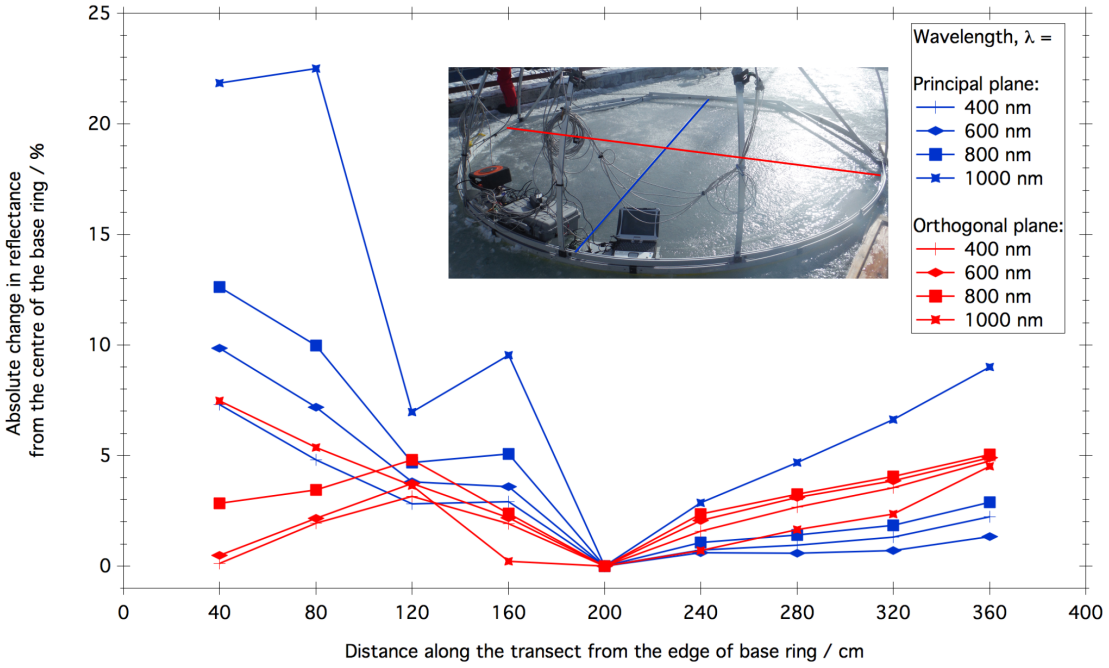

FIGURE 2.22: Absolute change in reflectance along two transects across the sea ice beneath GRASS. The reflectance was measured ever 40 cm and is shown normalised to the central point. Inset: photograph of the surface of the sea ice sampled.

TABLE 2.3: Nadir viewing footprint sizes for varying signal collector heights. The field of view of the signal collector was 8°.

Height of the ASD signal collector above the surface / cm	Equivalent viewing footprint diameter / cm
25	3.49
50	6.99
75	10.49
100	13.98
200	27.97

In a second step, the effect of the surface features on the reflectance in relation to the viewing footprint was investigated. Reflectance measurements were performed with the ASD spectroradiometer at varying heights, thus with a varying footprint size. The instrumental setup was identical to configuration described above. The signal collector was placed vertically above the centre of the goniometer base ring and the height of the tripod was adjusted so that the signal collector was at a height of 25, 50, 75 and 100 cm above the surface of the sea ice. An additional radiance measurement with the signal collector attached to the mount of the nadir GRASS signal collector (200 cm from the surface of the ice) was acquired, replicating the nadir footprint of GRASS. The raw radiances of the sea ice were normalised to the corrected Spectralon panel for each elevation. The equivalent viewing footprint diameters of the ASD on the surface of the sea ice for the different heights are reported in table 2.3. The relative change in reflectance from the reflectance measured at a height of 200 cm for each elevation is shown in figure 2.23. The change in reflectance as a function of sensor height is almost wavelength independent over the visible. At 400, 600 and 800 nm, the change in reflectance is less than 1.5% between 50 cm and 200 cm from the surface. The effect of a varying sampling footprint is more pronounced at 1000 nm with a change of 3.0% between a sensor height of 50 cm and 200 cm. The change in reflectance increases significantly for a lower sensor height, with a variation of 5.2 – 5.8 % over the wavelength range 400–800 nm between a sensor height of 25 cm and 200 cm, and 12.6% for a 1000 nm wavelength. The small change in reflectance between a sensor height of 25 and 200 cm indicates that the the viewing footprint size of the GRASS instrument was large enough to contain a representative distribution of surface roughness features.

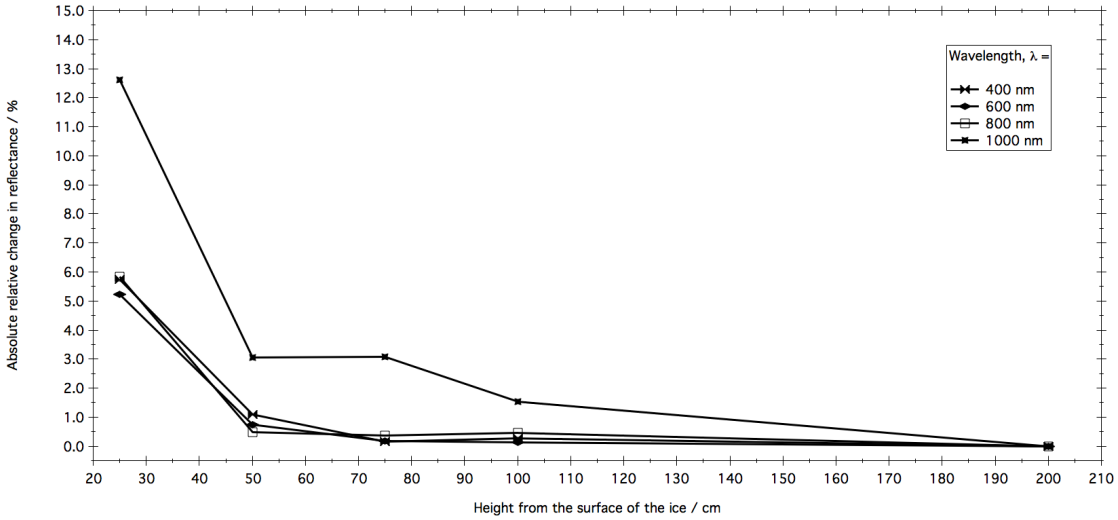

FIGURE 2.23: Absolute change in reflectance of the SERF artificial sea ice at nadir, measured with the ASD spectroradiometer. The measurements are reported for wavlengths 400, 600, 800 and 1000 nm.

2.2.2.3 Measurements procedure

To perform the HDRF measurements consistently, a measurement protocol was prepared, similarly to the procedure check-list created for the sea ice simulator in section 2.1.4.2. The steps of the procedure are listed hereafter.

- **Instrument set up**
  - Verify the structural integrity of the field goniometer frame.
  - Attach the signal collectors and fibre optics to the signal holder brackets on the arms of the instrument.
  - Connect the downwelling irradiance integration sphere to the summit of the structure, ensuring that the base of the integrating sphere is horizontal.
  - Move the ring to a new sampling location taking care not to disrupt the surface.

The order of the instrument preparation was essential to ensure that the instrument was sampling an undisrupted area of sea ice. On the account of the finite area of the pool, the instrument placement was prepared in advance to optimise the available area, and the sampling areas were cordoned off to limit access to the ice. The number of displacements to the instrument on the ice were limited to a minimum, using set paths on the ice.

- **Measurements**
  - Setup the instrumentation on the GRASS instrument holders, turn on and leave instruments to warm up for 1 hour.

- Record the all-sky illumination conditions using the ASD spectroradiometer described in section 2.2.2.1.
- Perform a measurement sequence (all signal collectors and quasi-simultaneous downwelling irradiance).
- Record the solar azimuth angle, rotate the upper part of the structure to a predetermined location, taking in account the change in solar azimuth angle.
- Perform nadir measurements of the Spectralon panel on the horizontal frame, placed below the nadir looking signal collector.
- When the measurements at the current location are finished, perform a signal collector inter-calibration.

After having connected the instruments to the structure and left the spectrometer system to stabilise, the HDRF measurements of the sea ice were performed. Owing to the changing illumination conditions, the solar azimuth angle was recorded for each rotation of the instrument (measurement sequence) and the angle of rotation of the frame was corrected as a consequence. The measurements were performed close to solar noon, when the rate of change of the solar zenith angle was minimal. Between 12h00 and 13h00 local time, the change in solar zenith angle was approximately $0.6°$, and therefore not accounted for in the data processing. Each HDRF acquisition was obtained with 4 rotations, generating 64 measurement angles (including 4 nadir repeats). Prior knowledge of the BRF of sea ice, led the measurements to be weighted with an emphasis on the forward scattering part of the hemisphere. The acquisition time for the four rotations was approximately 45 minutes in total. After the sampling of the sea ice surface was completed, the inter-calibration of the signal collectors was performed. Because of acquisition time constraints and because the inter-calibration process was destructive, as it required the operator to stand in the measured area, the calibration could not be performed between each rotation. Therefore, the corrections were assumed to hold true over multiple structure rotations. At then end of each measurement day, the instruments, signal collectors and fibre optics were dismantled to limit the exposure to the outdoor conditions.

2.2.2.4 HDRF data analysis

The HDRF of the sea ice was calculated based on equation 2, in chapter 8. The flowchart in figure 2.24 shows the different steps of the processing chain that was programatically implemented. The raw measurements were corrected for the errors reported in section 2.2.3. In a second step the radiance measurements were corrected for differences in the response of the signal collectors using the calibration lamp. The small changes in atmospheric conditions were corrected, using the downwelling irradiance measurements. The Spectralon panel readings were corrected for the non-lossless properties of the material. Finally, the corrected sea ice measurements were normalised to the reference panel,

yielding HDRF. The equation for the HDRF measurements at SERF is reported in chapter 8.

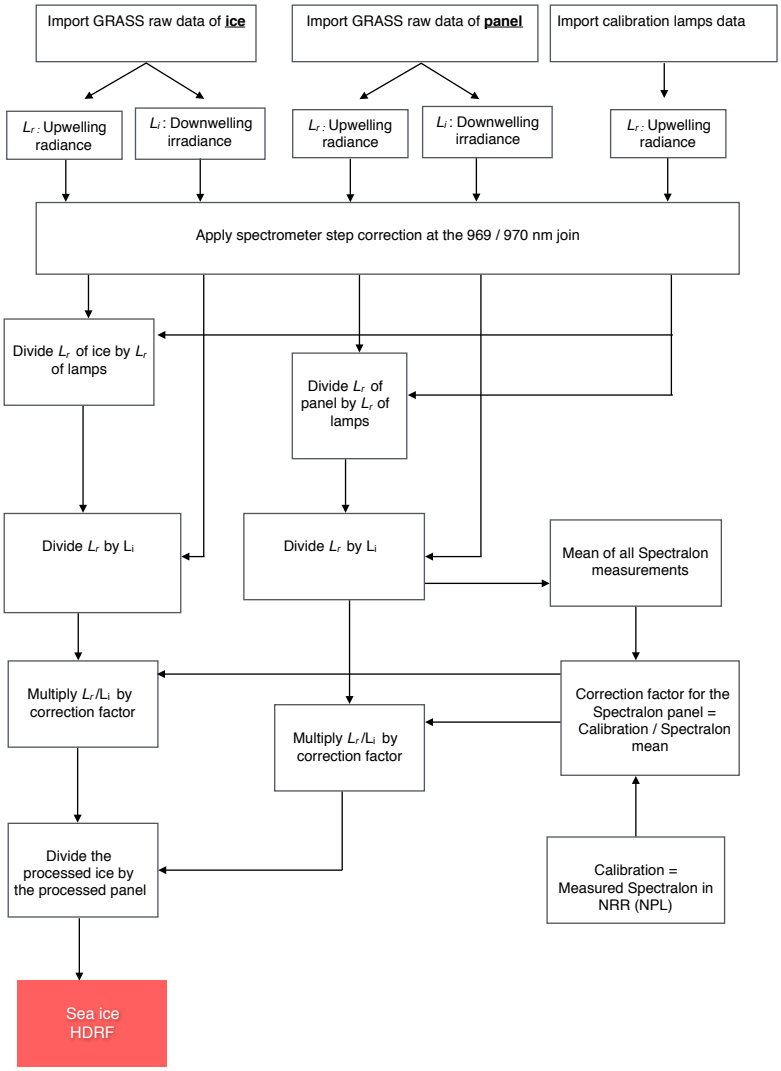

FIGURE 2.24: Flowchart describing the processing chain to generate HDRF quantities from raw measurements.

2.2.2.5 Ancillary measurements

During the HDRF measurements the atmospheric conditions were monitored using the upward looking ASD spectroradiometer described in section 2.2.2.1, and cloud cover was visually inspected in the post-processing phase using a GoPro camera that recorded sky conditions. To monitor changes in downwelling irradiance, a Remote Cosine Receptor (RCR) optic was connected to the fibre optic of the instrument. The RCR consists of a polymer diffuser disk attached to a fibre optic holder. The signal collector provides a cosine response of the radiant energy over a field of view of $180°$. The RCR was mounted

on a tripod (figure 2.25, inset), facing upwards and levelled using a circular bullseye spirit level. Daily measurements of the downwelling irradiance, plotted in figure 2.25, were carried out automatically over periods of 30 minutes, with a 30 second temporal acquisition interval over the duration of the campaign, at different times between 09h00 and 16h00 local time. The downwelling irradiance was acquired continuously between 10h45 and 15h15 on the 21st February 2016. The sky was cloud-free over the duration of the measurements, except for the presence of small cirrus clouds at approximately 11h50 and 12h45, which appear in the plotted data in figure 2.25. The continuous dataset was fitted with a second order polynomial, shown with the averaged residuals added and subtracted. The downwelling irradiance was monitored during the HDRF measurements with GRASS. Downwelling irradiance measurements synchronised with each HDRF acquisition were used to assess the atmospheric conditions. Measurements outside of the residuals (i.e. measurements affected by cloud cover) led to the HDRF acquisition to be discarded.

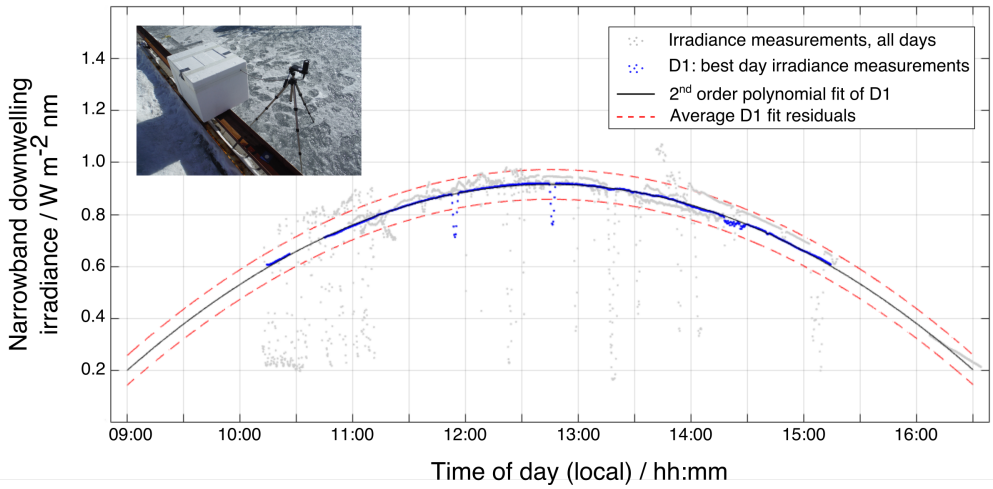

FIGURE 2.25: Daily composite of the narrowband downwelling irradiance for the wavelength 500 nm for the duration of the campaign. Measurements acquired on the 21st February 2016 are shown as blue markers and were fitted with a second order polynomial. The averaged residuals are shown as a red dashed line. The data presented in this figure was processed by C. Greenwell. Inset: The upward facing RCR on a tripod connected to the ASD spectrometer (in an insulation box).

Owing to technical difficulties with the ASD battery, a number of HDRF measurements did not have corresponding downwelling irradiance measurements. For the HDRF sets with missing downwelling irradiance, the sky conditions were monitored with a GoPro digital camera. The manufacturer specifications report a diagonal field of view of $149.2°$, a vertical field of view of $94.4°$ and a horizontal field of view of $122.6°$. The camera was placed on the end of a 1m carbon fibre boom facing upwards and images were

taken during each rotation of GRASS. The images were visually assessed, and only measurements without cumulus or less than 10 % cirrus were used in the study presented in chapter 8.

For the modelling of the sea ice observed at SERF with the radiative-transfer model PlanarRad, described in section 2.3.1.2, the reflectance of the seawater and the bottom of the pool below the sea ice was measured using the ASD spectrometer. A section of 2×2 m of the sea ice was cut out and and removed from a corner of the sea ice pool to avoid disrupting the measurements. The floating debris of ice in the water were removed with a surface skimming net before the measurements. The 8° field of view signal collector of the ASD was placed on the end of the carbon fibre boom that was connected to the tripod. The lens was placed at a height of 1m above the centre of the seawater, yielding a viewing footprint of 13.98 cm on the surface. A series of 10 measurements of the radiance of the water were acquired, immediately followed by measurements of the Spectralon panel. The reflectance of the seawater, shown in figure 2.26, was low in the visible, with a peak reflectance of 0.031 at 560 nm, and no signal was recorded past 750 nm. However, the reflectance values were not statistically different from zero, showing that the spectra recorded was at the limit of the sensitivity of the instrument.

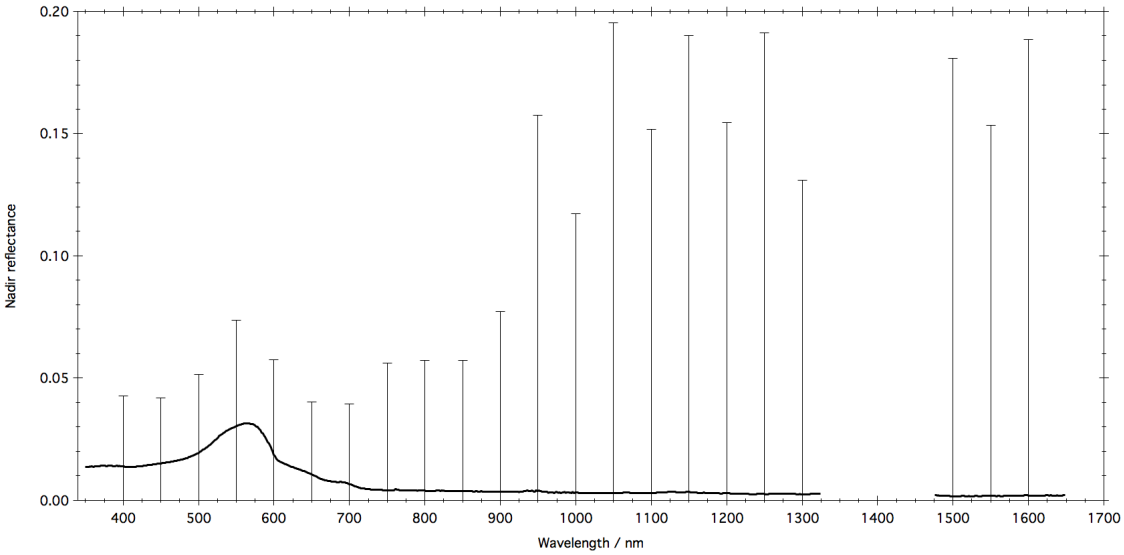

FIGURE 2.26: Open seawater nadir reflectance measurements with the ASD spectrometer at SERF. The error bars represent $\pm$ 2 σ.

The thickness of the sea ice was monitored by measuring the length of ice cores sampled with a Kovacs Mark II corer. Cores samples (figure 2.27 b) were taken from the sea ice pool close to the GRASS instrument, and measured using a graduated ruler. As shown in figure 2.27 e, the growth of the sea ice was rapid at the start of the experiment, reaching a thickness of 10 cm in five days. However, owing to day-time ambient temperatures ranging from -11.00 to $-0.18\,^{\circ}\mathrm{C}$, the sea ice did not grow thicker than 13.5 cm

over the course of the experiment. Measurements of the temperature profile throughout the ambient air, the sea ice and the underlying seawater were monitored at the facility using an automated type-T thermocouple array. However, owing to an operational error by the facility management, the data were overwritten, and therefore unavailable. The structure of the sea ice at SERF was similar to the typical ice texture found in naturally occurring first-year sea ice (Petrich and Eicken, 2010). A visual analysis of a 13 cm sea ice core, taken on the 21st February 2016 showed a top 2 cm layer of white granular ice, formed during the early stages of ice growth (frazil and nilas ice) (figure 2.27 c). Granular ice is composed of randomly orientated spherical-like ice crystals, generally less than 5 mm in diameter (Weeks, 2010) and is representative of rapid sea ice formation. Beneath the granular ice layer, congelation ice or columnar ice was formed as the ice grew downwards (figure 2.27 d). The texture of the sea ice was characterised by elongated grains, with a horizontal c-axis alignment. At the bottom of the ice core, a skeleton layer, with individual ice platelets extending into the seawater was observed. The salinity of six 13 cm long ice cores sampled at random locations of the sea ice pool was measured in the middle of the campaign. The ice cores were cut into three sections of 4 cm, 4 cm and 5 cm in length. The ice core sections were placed in sample bags and left to melt at room temperature. The salinity of the melted cores was measured using a seawater refractometer. The average salinity of each section is shown in figure 2.27 a. A C-shape profile of salinity as a function of depth is observable, typical of first-year sea ice (e.g. Weeks and Lee, 1962; Tucker III et al., 1984).

Two different methods were used to quantify the mass-ratio of algae in the sea ice and underlying seawater. Six samples of 100 ml of seawater were collected using a syringe connected to a plastic hose. The water was sampled through a borehole in the ice at a depth of 15 cm. Markers were placed on the weighted hose to ensure consistent measurements. Six ice cores were also taken with the Kovacs Mark II corer, from six random uncontaminated locations on the surface of the ice. Each core was cut into 2 equal size sections and placed in plastic sampling bags. The bags were placed in a light-sealed box in the SERF laboratory at room temperature, and the ice was left to melt for 24 hours. For each sample of seawater and ice, an aliquot of 100 ml was filtered through a $0.22\,\mu\mathrm{m}$ Millipore GSWP 025 00 biologically inert cellulose filter placed in a PTFE syringe filter. Half of the filters were folded, bagged and placed in a $-80\,^{\circ}\mathrm{C}$ freezer for further chlorophyll-*a* content analysis. At the time of the study presented in chapter 8, the samples were yet to be analysed by the University of Manitoba. The second half of the filters and a set of blank filters were shipped to RHUL within 48 hours of filtering, to limit the organic decay of the biological matter on the filters. The samples were placed at $-18\,^{\circ}\mathrm{C}$ upon arrival. The integrating sandwich spectrometer method described in section 2.1.5 was employed to estimate the mass absorption cross-section of the particulates on the filters. However, owing to the thickness of the filters, the recorded transmittance was too low to detect

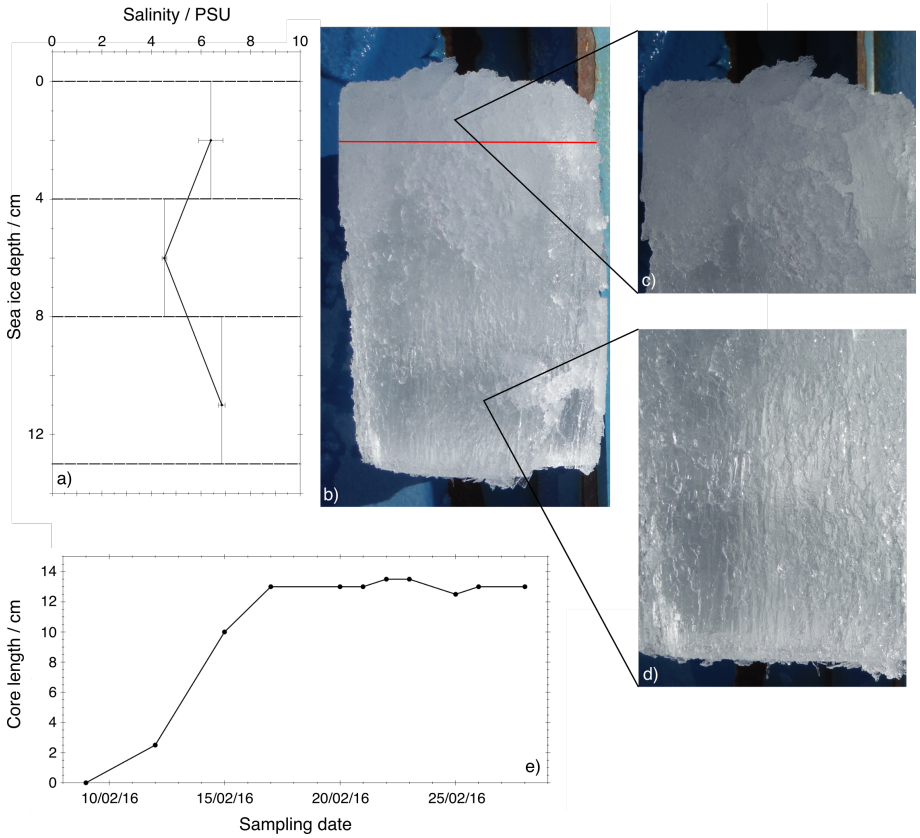

FIGURE 2.27: a) Salinity of 6 sea ice samples as a function of depth. The dashed lines represent the sections of the ice core. The data are plotted with 1σ error bars. b) Typical 13 cm long ice core. The red line marks the limit between granular ice, magnified in c) and columnar ice in d). e) Sea ice thickness measured as a function of time. HDRF measurements were performed between 21/02/16 and 28/02/16.

differences between the blank filters and the filter containing impurities. To replace the lack of measurements, the mass-ratio of algae in the sea ice at SERF was modelled using the radiative-transfer model PlanarRad. The description of the input parameters used for algae is found in section 2.3.3.1.

2.2.3 Instrument response characterisation

As described in section 2.2.2.1, a custom built spectrometer system was connected to GRASS, in order to measure the HDRF of the artificial sea ice at SERF. A LabVIEW software, with a graphical user interface was used to control the spectrometers and the multiplexer. The software was custom designed to operate the hardware in the Spectrometer system, allowing the operator to determine a measurement sequence by selecting the number and order of acquisitions from each signal collector connected to the multiplexer. For each acquisition, the integration times of the Ocean Optics USB2000+ and BWTEK Sol 1.7 spectrometers were set automatically by the software, as using manual settings caused the measurement sequence to crash. During the measurement campaign

at SERF, a number of anomalous acquisitions were observed, which appeared to occur randomly. During the post-campaign data processing phase, an in-depth study of the spectra recorded at SERF revealed further irregular measurements, owing to a firmware bug in the UV-VIS spectrometer. To assess the quality of the data, a characterisation of the spectral response of the instruments was performed.

The spectral response of the GRASS spectrometer system was characterised at NPL using the Transfer Standard Absolute Radiance Source (TSARS). TSARS is an integrating sphere illuminated with external stable lamps, and has a 75 mm exit port (Pegrum et al., 2004). TSARS is calibrated against the primary NPL blackbody (Chu et al., 1994), providing an illumination stability of less than $\pm 0.2\%$ over 4 hours (Woolliams et al., 2005) and a uniformity of less than $\pm 0.5\%$ across the exit port. The response of the ASD spectrometer was used for comparison purposes. The GRASS and ASD spectroradiometers used during the campaign at SERF were setup in the TSARS optics laboratory. The ASD fibre optic was connected to the 8° field of view signal collector used during the field measurements which was aligned with the TSARS exit port. The nadir GRASS signal collector, with a field of view of 8°, was aligned with the TSARS exit port, approximately 2 cm from the ASD signal collector, and connected to the GRASS spectrometer system via the multiplexer. A bare fibre optic, placed in parallel with the signal collectors facing the exit port of TSARS was connected to the downwelling input of the GRASS spectrometer system. The two signal collectors and the bare fibre optic were placed at an equal distance from the exit port. TSARS was turned on and left to warm up for a duration of 2 hours. Once the light source was stabilised, radiance measurements were performed with the two spectrometer systems. The intensity of the illumination was varied by placing different graded neutral density (ND) filters between the fore-optics and the light source. ND filters transmitting 64.56, 32.86, 10.15 and 2.75 % of the illumination were used. In a first step, the raw counts of the instruments were measured for different light intensities. In a second step, the response of the spectrometers was compared by normalising the radiance measurements with different intensities to the radiance of the TSARS without filters. Two types of anomalies in the response of the GRASS spectrometer system were detected and are discussed in the following sections.

2.2.3.1 Downwelling irradiance systematic error

The spectral response of the GRASS spectrometer system to different illumination intensities was analysed by measuring the output of TSARS with the different ND filters placed between the illumination source and the detectors. As shown in figure 2.28, the raw radiance counts of the instrument were quasi-linear as a function of illumination intensity for the measurements through the upwelling port (via the multiplexer). The response of the BWTEK spectrometer was also linear for measurements acquired through

the downwelling port (bare fibre). However, the response of the Ocean Optics spectrometer showed a non linear response of the intensity measured through the 32.86% ND filter. The downwelling port reading through the 32.86% ND filter was performed with an automatic integration time of 750 ms, which was identical to the integration time of the anomalous measurements observed during the experiments at SERF. The difference in the counts measured between the upwelling and the downwelling ports is explained by the difference in the signal collectors connected to the upwelling and downwelling ports of the spectrometer system (8° field of view signal collector for the upwelling and 25° field of view bare fibre for the downwelling). The difference in the slope of the response between the Ocean Optics Spectrometer (shown at 620 nm in figure 2.28) and the BWTEK spectrometer (shown at 1200 nm in figure 2.28) is due to a discrepancy between the two instruments, characterised in section 2.2.3.2.

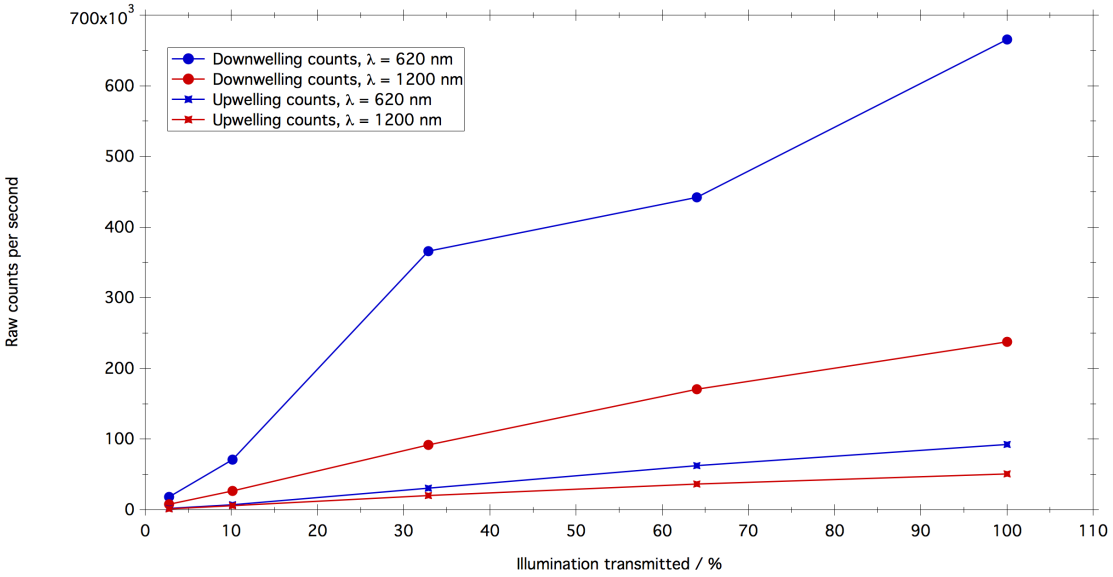

FIGURE 2.28: GRASS spectrometer system response to varying illumination intensities from TSARS. The response of the Ocean Optics spectrometer at 620 nm was plotted in blue for the downwelling measurements (circles) and the upwelling measurements (squares). The response of the BWTEK Sol spectrometer is shown in red.

The spectral response of the GRASS spectrometer system is shown in figure 2.29. An anomaly in the spectral shape of the measurement through the 32.86% ND filter with an integration time of 750 ms appeared consistently during the measurements in the optics laboratory. The shape of the spectrum suggests a saturation of the instrument, which may be caused by an error in the piloting software. However, an analysis of the LabVIEW code (in collaboration with C. Greenwell at NPL) did not reveal errors in the sequence sent to the hardware. Furthermore, the output spectrum of the spectrometer was identical when controlled with a VBA macro developed by the National Environmental Research Council (NERC) Field Spectroscopy Facility (FSF). Following the tests performed at NPL,

the instrument was recalled by FSF for further testing. The measurements of the artificial sea ice at SERF with a faulty downwelling measurement were discarded for the purpose of the study presented in chapter 8.

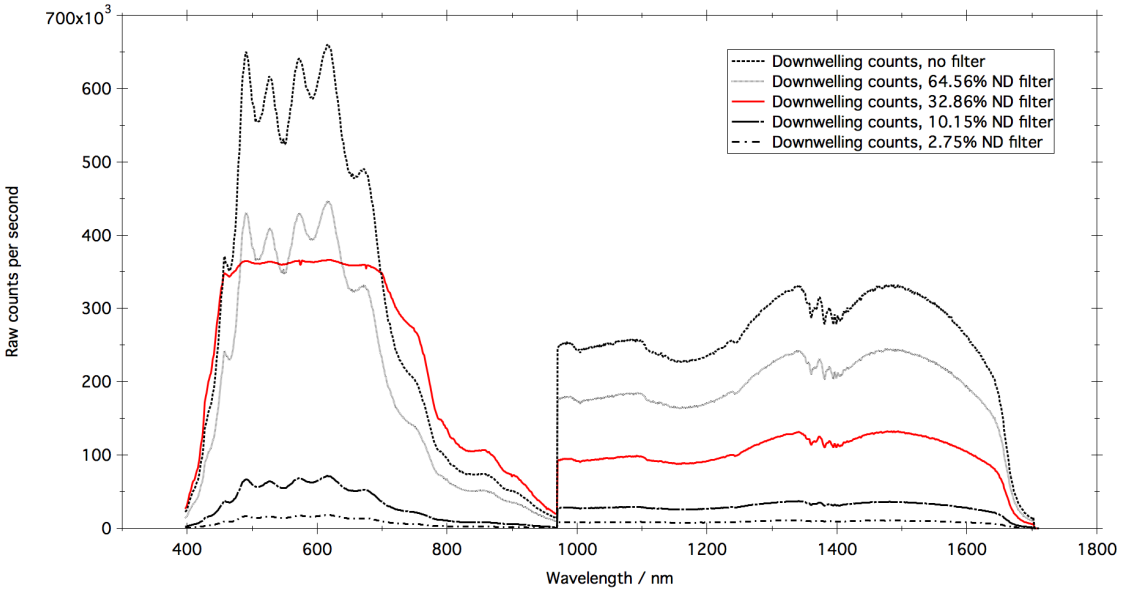

FIGURE 2.29: GRASS spectrometer system response to varying illumination intensities from TSARS as a function of wavelength. The plotted spectra was recorded through the downwelling port with a bare fibre optic. The erroneous measurement is highlighted in red.

2.2.3.2 Spectrometer radiance step

For all the measurements (upwelling and downwelling) performed with the GRASS spectrometer system, a jump in intensity was observed between the two spectrometers. To investigate the effects of the apparent misreading between the two spectrometers, the raw radiance counts measured with the different ND filters between TSARS and the instruments were normalised to the raw radiance counts measured without the presence of ND filters. The normalised measurements through the downwelling and the upwelling ports were compared to the response of the ASD spectrometer. The results are shown in figure 2.30. Measurements with the ASD, plotted with black lines, show a flat-like response with a slight spectral shape owing to the wavelength dependence of the absorption of the ND filters. The normalised intensity is consistent with intensity of the transmitted light through the ND filters. The measurements with GRASS through the downwelling port show a good agreement with the ASD for all the ND filters, except the 32.86%, owing to the problem described in the previous section. The NIR measurements with the BWTEK Sol spectrometer through the upwelling port are also in agreement with the ASD response. The difference between the normalised measurement using the 2.75% ND filter through the upwelling port, and the downwelling port and ASD was considered negligible. Figure 2.30 clearly highlights the spectral jump between the two spectrometers in the

GRASS system, with the visible spectrum measured by the Ocean Optics spectrometer underestimating the illumination intensity. However, over the multiple measurements performed at TSARS, the spectral jump was not systematic. As shown for for the 32.86% ND filter, the normalised raw radiance for the two GRASS spectrometers through the upwelling port is in agreement with the downwelling and the ASD measurements. For each ND filter, the observed spectral discrepancy between the two spectrometers appeared to be randomly occurring throughout the repeat measurements. The spectral jump, which had not been observed during the pre-campaign testing phase of the instrument, was present in a high number of measurements from the SERF campaign. Following the characterisation of the response of the GRASS spectrometer system with TSARS, a correction was applied to the data, using the stable NIR part of the spectrum. The correction factor was expressed as:

$$C_{j(400,969nm)} = \frac{\overline{L}_{(970,980nm)}}{\overline{L}_{(959,969nm)}}, \tag{2.6}$$

with C_j the correction factor applied to the subscripted wavelength range, and $\overline{L}$ the raw radiance counts averaged over the subscripted wavelength range. The correction factor assumes that the radiance from the NIR spectrometer is correct, as shown during the testing.

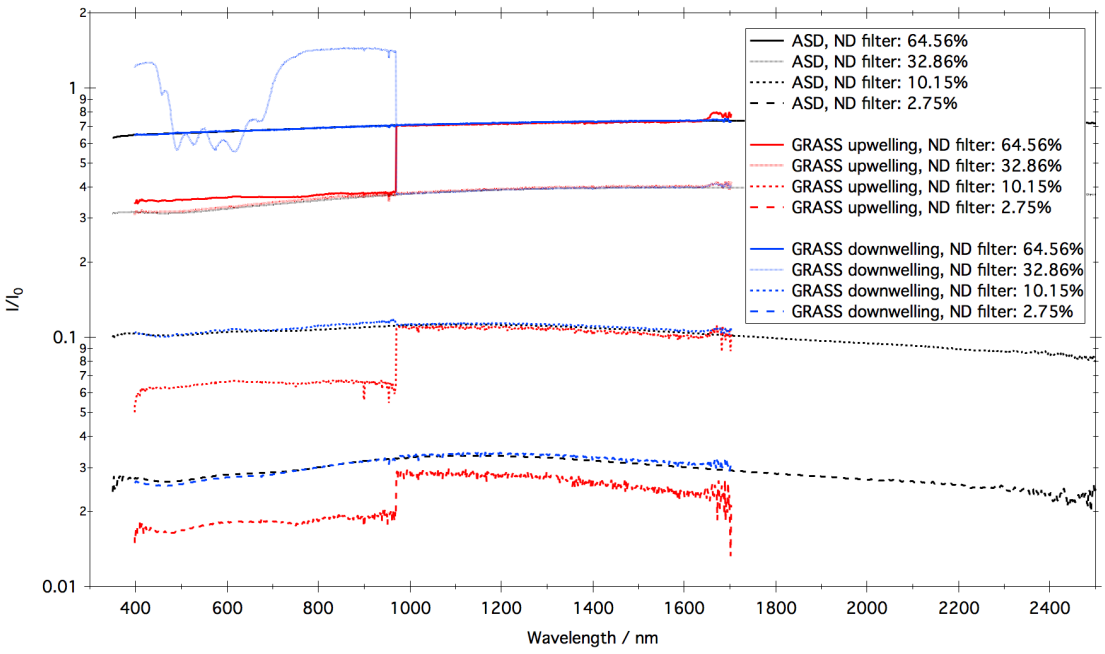

FIGURE 2.30: Wavelength dependent normalised radiance counts of the GRASS spectrometer system and the ASD spectrometer to TSARS for different illumination intensities. The y-axis is plotted on a log scale.

2.3 Radiative transfer modelling

To understand the effects of impurities on the radiative budget of snow and sea ice, radiative-transfer calculations were performed. Based on values found in the literature, the effect of mineral aerosol deposits on the albedo of snow and ice was investigated in chapter 3. The BRDF of sea ice was modelled from first principles in chapter 6, to understand the effects of surface roughness, sea ice thickness, and sea ice type on the angular distribution of reflectance, providing a base to later understand the effects of different impurities on the radiative budget of sea ice. The radiative-models were also used to provide an explanation of observed phenomena in the field. The downwelling PAR was computed throughout the snowpack and sea ice to highlight the effect of a changing snowpack on the primary production of sea ice algae in chapter 5. Furthermore, the radiative-transfer models provided a validation of laboratory experiments on artificial sea ice (chapter 4, 7, 8), allowing the isolation of the effects of impurities on the reflectance or BDRF of sea ice, and providing a tool for the remote sensing community. In the following sections, the approaches to the radiative-transfer modelling in this work are described.

2.3.1 Model descriptions

Two models based on different numerical methods were used in this work to solve the radiative-transfer calculations throughout the snow and sea ice. The following sections outline the characteristics and the quantities calculated by each of the models.

2.3.1.1 TUV-snow model

A modified version of the Tropospheric Ultraviolet Visible (TUV) model, developed at the National Centre for Atmospheric Research, USA (NCAR) was used to perform the radiative-transfer calculations in snow and sea ice. TUV is a one-dimensional radiative-transfer model, based on the discrete ordinate method for radiative-transfer (DISORT) code (Stamnes et al., 1988b) that calculates the electromagnetic radiation propagation through atmospheric layers in the ultra-violet and visible wavelength range. The modified version used in chapter 3 and chapter 5, called TUV-snow (Lee-Taylor and Madronich, 2002) , was optimised to perform radiative-transfer calculations throughout layers of snow or sea ice, placed below the atmosphere. A description of the model applied to highly scattering media can be found in Lee-Taylor and Madronich (2002). TUV-snow has been previously used to calculate the scattering and absorption cross-section of snow from field measurements (e.g. Fisher et al., 2005; King et al., 2005), and model the effects of black carbon deposits on the surface albedo of snow and sea ice (Marks and King, 2013a; Marks and King, 2014).
The snow / sea ice layers were input in the model in a similar manner to clouds. The model is based on the plane-parallel approximation, assuming that the atmosphere and

the snow or sea ice are vertically inhomogeneous but horizontally homogeneous. The atmosphere and snow or sea ice are computed as multilayered media, where the thickness of the layers can be adjusted. Each layer is defined by its thickness, the wavelength dependent absorption cross-section and scattering cross-section of the medium, the density, and the asymmetry parameter. The lower boundary of the model is defined by a specified BRDF, described in Stamnes et al. (1988b). The parameters describing the optical properties of the snow and sea ice in the model are described in section 2.3.2. For each layer throughout the model, the plane upwelling and downwelling spectral irradiance are computed, which in turn can be converted to albedo. In chapter 3 and chapter 4, albedo was calculated as the ratio of the plane upwelling spectral irradiance to the plane downwelling spectral irradiance for the surface layer of the snow or sea ice for the wavelengths range 350–650 and 350–800 nm. To solve the radiative-transfer equation, the DISORT method relies on calculating a gaussian integration, where the number of gaussian quadrature angles, called "streams" describe the phase function, resulting in higher precision calculations. For inhomogeneous layers with forward scattering, the computation requires a large number of streams. Kuo-Nan (1973), performed numerical computations of transmission and reflection of clouds using 2, 4, 8 and 16 streams, reporting the precision obtained and accuracies in the calculations. The author showed that for 16 streams the results were accurate to 3–4 digits. In this work, the computational resources allowed to perform the radiative-transfer calculations using 32 streams with short processing times.

Initial tests in collaboration with one of the authors of the TUV-snow model were performed to generate a bidirectional response of the upwelling radiance for each layer in the model. The implementation of the radiative-transfer code dealing with the boundary conditions for each layer and the continuity of intensity at the layer interfaces did not allow for sufficient precision in a rapidly changing medium (snow or ice / atmosphere interface), leaving the model unable to solve the eigenvalues. The computation methods of the eigenvalues are detailed in Stamnes et al. (1988a). Therefore, a different model, performing the radiative-transfer calculations of directional fluxes was used.

2.3.1.2 PlanarRad model

PlanarRad (Hedley, 2008) was used to perform the calculations of the BRF of sea ice in chapter 6, chapter 7 and chapter 8. PlanarRad is a numerical model that uses the invariant imbedded numerical integration technique to solve the radiative-transfer equation. PlanarRad is the open-source implementation of the Hydrolight model based on the method described in detail by Mobley (1994). Hydrolight was designed to compute the spectral irradiance distribution within natural bodies of water, such as lakes or oceans, and provide the directional upwelling radiance at the surface, taking in account waves.

Functions in PlanarRad were implemented to carry out the radiative-transfer calculations in highly scattering media such as sea ice for the purpose of the work presented here. As for the TUV-snow model, PlanarRad assumes that the media in the model is plane-parallel, therefore the variations of the optical properties of the layers occur vertically only, and the modelled media are horizontally infinite. However, unlike TUV-snow, the modelled media is not split into vertical layers with different properties, although the radiative flux quantities are computed throughout the medium in a number of defined levels. The optical properties of the medium in the model describe a single homogenous slab, placed on a lower boundary. Furthermore, the downwelling irradiance and the upwelling radiance are modelled at surface level, and therefore the model does not include an atmosphere. The quantities of interest generated by the model in the case of the work presented here are the directional radiance fields (upwelling and downwelling) at the sea ice / air boundary.

The computation of an infinite number of incident and scattering directions is impossible, thus the radiance in PlanarRad was directionally discretised, as described in Mobley (1994). Therefore, the irradiance and radiance were calculated over a sphere consisting of upward and downward hemispheres, by being averaged over a finite number of quadrilateral regions, called "segments" or "quads". A visual representation of the discretised hemispheres is shown in chapter 6. Each hemispheres were divided into 9×24 segments, with an additional polar segment. Therefore, the radiance was averaged over segments of 15° in azimuth and 10° in zenith, with the exception of the quads located between a zenith angle of 85° and 90° on the hemisphere, which were 5° wide. Tests were performed to increase the directional resolution of the model by doubling the amount of quads, however the computational resources required were too important, and a run with 18×48 segments plus the polar caps could not be completed by a modern desktop computer. For each model run, the quad-averaged radiance is computed by PlanarRad within each quad of the discretised hemisphere. The illumination in the model is set to a single quad, defined by the azimuth angle, ϕ and zenith angle, θ boundaries. Theoretically, to compute the full BRDF of the modelled surface, 217 iterations should be run, changing the illumination quad for each new run. However, the model was considered to be rotationally invariant, with the output being relative to the input illumination. Thus, the BRDF of a surface was fully characterised by 10 iterations over the zenith quads, keeping the azimuth fixed.

The surface of the sea ice is rarely perfectly smooth, having vertical features ranging from a few millimetres (e.g. brine rejections or frost flowers) to dozens of metres in height (e.g. pressure ridges). To represent surface roughness in the model, an interface was implemented based on Monte Carlo statistical modelling. The method used is similar to the procedure described by Mobley (1994) to represent capillary waves. For each quad, a mathematical representation of a random roughness interface between the air and a wind blown water surface is constructed. The surface is formed by a matrix of congruent

isosceles triangles with the base aligned along the wind direction. The mean elevation of the matrix nodes is set to 0, and the variance is determined using the statistical method described by Cox and Munk (1954). The size of the triangles is fixed, and the variance of the elevation of the nodes is varied to represent more or less roughness. The realisation of the surface is repeated, to generate a collection of a random surfaces. After the mathematical surface is generated, a Monte Carlo ray tracing simulation is applied to the surface. The paths of rays of photons are traced, as they intercept one or multiple facets of the realised surfaces. Each ray interacting with the surface generates a reflected and a refracted ray, which can in turn interact with the surface. For each ray, the path is calculated until the ray is either reflected back into the air, or transmitted into the water. For each ray, the irradiance reflectance is computed for a random surface realisation, and the total irradiance reflectance is averaged over the number of realisations, yielding a ratio of reflected radiance to incident irradiance. The result is then set as a surface condition for each quad in the model. The roughness model in PlanarRad differs from the model proposed by (Mobley, 1994), as equilateral triangles replace the isosceles triangles, to remove directionality effects from the surface roughness. Furthermore, rather than deriving the standard deviation of the height of the nodes from wind speed, the height of the nodes is set randomly to match a defined standard deviation. A representation of the construction of a randomised surface is shown in figure 2.31, and a visual representation of surfaces for different standard deviation values can be found in chapter 6. In the work presented here, 2000 random surface realisations were built, each containing 100×100 nodes, and the Monte Carlo calculations were carried out with 10 rays per quad. A refractive index of 1 was used above the surface, and the refractive index of ice was obtained from Warren and Brandt (2008) for the sea ice. A roughness parameter file for each wavelength was generated in approximately 10 hours using a modern desktop computer.

To describe the sea ice, PlanarRad requires the knowledge of the attenuation and absorption coefficients, the phase function, the surface roughness and the thickness of the sea ice. The optical properties used to described the sea ice in the model are referred to in each corresponding chapter.

2.3.2 Modelling snow and sea ice with TUV

In chapter 3, TUV-snow was used to model the effects of mineral aerosol deposits on the albedo of snow and sea ice. The model was also used by A. Marks to model the effect of black carbon impurities on the reflectance of sea ice in chapter 4. Downwelling PAR was calculated throughout the snow pack using TUV-snow in chapter 5. The following chapters will provide insight on the parameters used to model the albedo and PAR, as well as the modelling approach.

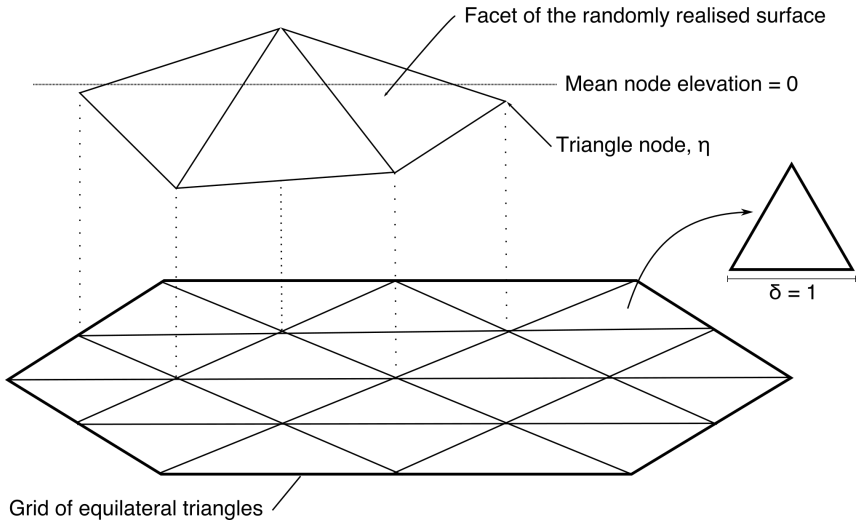

FIGURE 2.31: Representation of the construction of a random surface. The roughness parameter σ, is equal to the ratio of the distance, δ between the triangle nodes η (fixed to 1), and the standard deviation of the nodes η. The surface roughness is scale invariant. The diagram was modified from (Mobley, 1994).

2.3.2.1 TUV model parameterisation

For the radiative-transfer modelling presented in chapter 3, the optical and physical properties of the snow and sea ice were obtained from the literature. Similarly, the properties of the mineral aerosol deposits were calculated using Mie theory, based on values collected in the literature. The values of the different model parameters used are reported in chapter 3. In the work presented in chapter 3 and chapter 5, the distance between the bottom boundary and the top of the atmosphere was set to 90 km, which corresponds approximately to the top of the mesosphere, including the troposphere and the stratosphere where most of the scattering and absorption of solar radiation in the Earth's atmosphere occurs. The distance from the model's top-of-atmosphere to the sun was fixed at an arbitrary distance of 1 astronomical unit. The atmosphere in the model was considered to be aerosol-free for the purpose of the work presented here. A baseline value of 300 Dobson units was used for the ozone column. The solar zenith angle was fixed at 60°, to be representative of the high solar zenith angles observed in polar regions. For the purpose of the work reported in chapter 3, chapter 4, and chapter 5, a diffuse illumination was used. Indeed, because snow and sea ice are not isotropic reflectors, the response of the surface albedo or downwelling PAR throughout the snow and sea ice varies with the illumination angle (Wiscombe and Warren, 1980b; Simpson et al., 2002). Therefore, a diffuse illumination was set, to separate the effects of impurities on the reflectance or albedo of the sea ice or snow, and the effects of the metamorphosing snow on the downwelling PAR throughout the snow and underlying sea ice from the effects of a changing illumination. To generate a diffuse illumination, a cumulus cloud layer with a thickness of 1 km was placed at an altitude of 1 km above the lower boundary of the model. The cloud layer was

assigned a single scattering albedo of 0.9999, an optical depth of 32, and an asymmetry parameter, g of 0.85. The single scattering albedo is a measure of the amount of light extinction owing to scattering, which is expressed as the ratio between the scattering optical depth and the total optical depth. A single scattering albedo value of 0.9999 signifies that the absorption of solar radiation by the cloud is insignificant. The optical depth, which here defines the opacity of the cloud is a measure of the extinction of radiation. Marks (2014) computed the surface albedo of a 1 m thick snowpack, as a function of solar zenith angle using the same TUV-snow model setup as described above. The results showed that a cloud optical depth of 16 was sufficient to create a diffuse environment, where the albedo was insensitive to the illumination angle. The asymmetry parameter, g defines the scattering directionality of electromagnetic radiation hitting a particle. The asymmetry parameter varies from -1 to +1, where -1 represents scattering in a backwards direction relative to the incident light path, +1 represents forward scattering and 0 is indicative of isotropic scattering. Therefore, in the cumulus cloud layer used in the model, most of the incident illumination was forward scattering.

For the lower boundary of the model, a fixed wavelength-independent isotropic reflectance value of 0.1 was chosen, based on the work of Perovich (1991), Marks and King (2013b), and Marks and King (2014). Although the under-ice value was considered to be representative of seawater (Jin et al., 2004), a vast range of values is found in the literature. Rösel et al. (2012) used a wavelength-independent spectral radiance of 0.08 to represent open water in the Arctic, for a MODIS retrieval algorithm of melt ponds, based on values from Tschudi et al. (2008). Perovich (1996) used a slightly lower wavelength-integrated albedo of 0.05 for open water. In the sea ice radiative-transfer model developped by Grenfell (1983), and later used in Grenfell (1991), the lower boundary was set to a spectral radiance value of 0. Furthermore, measurements and calculations of the spectral reflectance of open seawater at high latitudes has been shown to be wavelength dependent, with values measured bewteen 0.01 and 0.1 at shorter wavelengths (400–550 nm) dropping to 0 – 0.01 in the near-infrared (Morel and Prieur, 1977; Morel and Maritorena, 2001; Siegel et al., 1994; Siegel et al., 2005). Owing to the large differences in seawater reflectance values, the sensitivity of the sea ice albedo to the variability of the underlying seawater reflectance was assessed by modelling the albedo of sea ice, using the thicknesses described in chapter 3 and chapter 6. The calculations were performed with a fixed wavelength-independent isotropic reflectance value of 0, 0.05, 0.08 and 0.1. The change in sea ice surface albedo relative to the same sea ice (identical optical properties and thickness) is shown in figure 2.32. Since the underlying surface reflectance does not change the surface albedo of sea ice in the case of an optically thick sea ice layer, the reflectance value for the modelled semi-infinite sea ice has no effect on the surface albedo, and therefore semi-infinite cases are not considered here. For the three types of sea ice, the effects of the undelying reflectance on the surface albedo are more important for thinner sea ice. At 400 nm, the albedo of first year sea ice changes by 5.5% when using an underlying reflectance

of 0 compared to 0.1 for 50 cm thick sea ice, 2.8% for 80 cm thick sea ice, and by 2% for 1 m thick sea ice. For multi-year sea ice, the albedo changes by 0.47% for 50 cm thick sea ice, 0.12% for 1 m thick ice, and 0.08% for 1.2 m thick sea ice. For melting sea ice, the surface albedo changes by 29% for 50 cm thick sea ice when using an underlying reflectance of 0 compared to 0.1, 16% for 1 m thick sea ice, and 13% for 1.2 m thick sea ice. Figure 2.32 also shows that the effect of the underlying reflectance is variable depending on the type of sea ice, which is linked to the *e*-folding depth of the sea ice. Indeed, changing the reflectance beneath the sea ice has a much smaller effect on the albedo of highly scattering multi-year sea ice, with a maximum change in albedo of 0.43%, than for melting sea ice with a maximum change in albedo of 29%. Therefore, with variations of less than 0.5% with the different underlying reflectance values and thickness for multi-year sea ice, the impact of the lower boundary may be considered as negligible. However, for first year sea ice and melting sea ice, where the impact of the lower boundary on the surface albedo is more important (5.5% and 29% respectively for 50 cm thick sea ice with a lower boundary reflectance of 0, compared to 0.1), the parameterisation of the lower boundary should be performed with care . Furthermore, the figure highlights the wavelength dependence of the effects of the under sea ice reflectance on the surface albedo of sea ice. Owing to the larger absorption of the ice at wavelengths above 700 nm, the albedo of the sea ice is more sensitive to the reflectance of the medium below the sea ice at shorter wavelengths than in the near-infrared. In the case of a 50 cm thick first year sea ice layer with an underlying reflectance of 0, compared to an underlying reflectance of 0.1 used in this work, the change in surface albedo is 5.5% at 350 nm and 0.7% at 800 nm. For multi-year sea ice in the same configuration, the change in albedo is 0.43% at 350 nm and no change is observed at 800 nm. For melting sea ice, which is more sensitive to the lower boundary, the change in albedo is 29% at 350 nm and 10% at 800 nm. When considering recent measurements of spectral reflectance of seawater (e.g. Morel and Maritorena, 2001), with values of 0.1 around 400 nm dropping to 0.0001 at 700 nm, the difference in surface albedo would be less pronounced than for the fixed wavelength-independent values presented in figure 2.32. Indeed, the change in albedo would be small at smaller wavelengths and would not exceed the values for an underlying surface reflectance of 0 presented in the figure at 700 nm. Therefore, for first-year sea ice, the change in albedo would not exceed 1% for sea ice thicker than 80 cm and 3.2% for 50 cm thick sea ice. For multi-year sea ice, the change in albedo would be less than 0.15% for sea ice thicker than 50 cm. For melting sea ice however, the change in albedo would be less than 10% for sea ice thicker than 1 m and approximately 25% for 50 cm thick sea ice. Therefore, although the impact of the underlying surface reflectance is less important for multi-year and first year sea ice than for melting sea ice, particular attention to the parameterisation of the lower boundary is recommended when modelling thin sea ice layers using a radiative-transfer model.

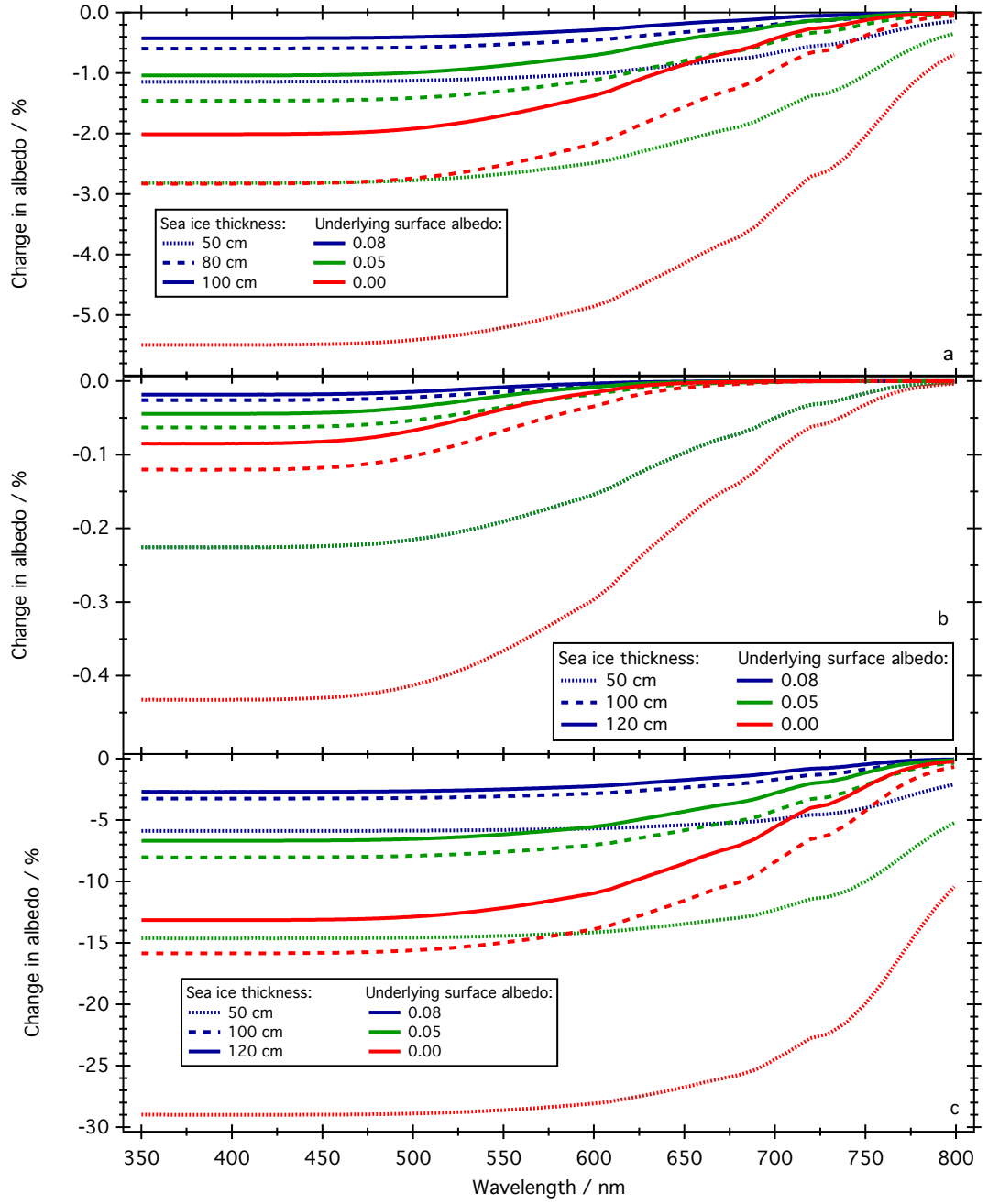

FIGURE 2.32: Change in albedo of a) first year sea ice, b) multi-year sea ice, c) melting sea ice, with varying thicknesses and underlying surface albedos, relative to sea ice with identical optical properties and thicknesses, and a fixed underlying reflectance of 0.1.

2.3.2.2 Modelling PAR in snow and sea ice

In chapter 5, the lead authors detected an early onset of an algae bloom under a layer of sea ice covered by a layer of snow in a Fjord in the North East of Greenland (Station North, 82.05, -19.35). The detection of the algae bloom occurred when 1 m of snow was still present on the surface of the sea ice, which was unusual, as it has been previously been considered in the literature that 40 cm of snow were sufficient to deprive under ice algae of available solar irradiance (e.g. Mundy et al., 2007a). To investigate the plausible causes of the early onset of algae in the sea ice, a collaboration was set up, providing insight on the radiative fluxes through the snow and ice using the TUV-snow radiative-transfer model. The physical parameters of the snow and sea ice that were measured in the field were used as model input parameters: a 1 m of snow was placed on a 1 m layer of sea ice, with an underlying albedo of 0.1 to represent the ocean below the ice. The model setup and parameters are further described in chapter 5, and a schematic diagram of the modelling conditions is shown in figure 2.33. The downwelling photosynthetically active radiation (PAR) was calculated for each snow and sea ice layer as:

$$PAR = \int_{\lambda=400\mathrm{nm}}^{\lambda=800\mathrm{nm}} I_\lambda d_\lambda, \tag{2.7}$$

with I the downwelling monochromatic irradiance and λ the wavelength. In a first step, the previously discussed setup was modelled as a function of scattering cross-section to represent different snow conditions. In a second step, the small decrease in the observed snow cover was modelled by changing the thickness of the snow pack in the model.

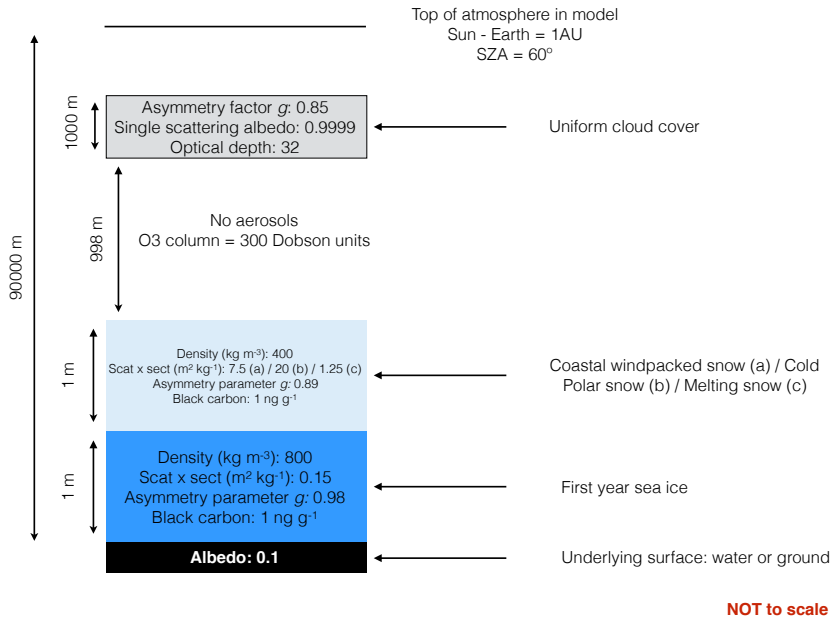

FIGURE 2.33: Diagram representing the TUV-snow model setup for the calculations of downwelling PAR through the snow and sea ice presented in chapter 5.

2.3.3 Fitting the observed sea ice using Planarrad

In chapter 6 the BRDF of sea ice was modelled as a function of surface roughness for different types of sea ice. In chapter 7 and chapter 8, PlanarRad was used to fit the measured BRF and HDRF of the artificial sea ice. The parameters used in the model were derived from physical measurements, values from the literature or were varied to fit the measurements. In the following sections, the model parameters are overseen and the fitting process is explained.

2.3.3.1 Model parameters justification

In the current section, the model parameters are described and the choice of the values is justified.

- Wavelength

PlanarRad computes radiance quantities over a discrete number of specified wavelength numbers. For each wavelength, the wavelength number and the band width are specified and an iteration is performed over the number of specified wavelengths. Therefore, a trade-off between computational time and spectral resolution is required. To fit the measured data in SERF, the wavelength range was set to match the instruments (400–1700 nm), with an interval of 100 nm, the wavelength 1400 nm was omitted from calculations, owing to the atmospheric absorption band removed from the measurements. The band width was set to 1 nm for all the wavelengths. To fit the measurements in the RHUL

sea ice simulator, a wavelength range of 400–850 nm with an interval of 50 nm was chosen. Although the ASD measurements covered the wavelength range 400–1700 nm, the output from the illumination source was not considered to provide sufficient intensity above 1000 nm. The Ocean Optics measurements were recorded over the wavelength range 300–875 nm. However, measurements below 400 nm were considered to be too noisy to be meaningful, owing to the stray light scattered in the spectrometer and the weak UV irradiance of the lamps.

- Input irradiance angles

As described in section 2.3.1.2, PlanarRad in rotationally invariant. Therefore, to calculate the BRF of sea ice for a fixed illumination angle, the input illumination angle is defined by the zenith angle only. During the measurements at SERF using GRASS, the instrument was rotated to compensate for a changing solar azimuth angle. The zenith angle of the sun at the time of each acquisition was calculated using the National Oceanic and Atmospheric Administration Solar Calculator (NOAA, 2017). The average solar zenith angle for the HDRF measurements at SERF of 61.5° was used as input in PlanarRad. Because of the quadrilateral discretisation of the model, the illumination was set to the quad bound by the zenith angles 55° and 65° and azimuth angles 175° and 185°. The BRF measurements in the sea ice simulator were performed with a fixed zenith angle of 60°. Therefore the same quad as for the SERF fitting was used.

- Sea ice thickness

The sea ice thickness was obtained from *in-situ* physical measurements. The thickness of the sea ice at SERF was obtained from coring, as described in section 2.1.2.2 and the thickness of the sea ice in the RHUL sea ice simulator was inferred from the temperature profile data, described in section 2.2.2.5. The thickness of the added layer of poisoned sea ice in the sea ice simulator was fixed to 5 cm. Additionally, the model allows the interval of the rate of change of the light field to be controlled, which is equivalent to the resolution of the model. For all the model runs, the interval was set to 1/100th of the thickness.

- Sea ice / air interface

The sea ice / air interface was varied to fit the observations. As described in section 2.3.1.2, the surface roughness was generated using the refractive index of air and the refractive index of pure ice from Warren and Brandt (2008). The standard deviation of the elevation of the triangular nodes was used to control the amount of surface roughness. The effect of a varying surface roughness is discussed in chapter 6. In chapter 7 and chapter 8, the standard deviation of the surface roughness parameter was varied in PlanarRad between values of 0.001 and 0.5 to fit the observed data. Photographs of examples of observed surface roughness features at SERF and in the sea ice simulator at

RHUL are presented in figure 2.34.

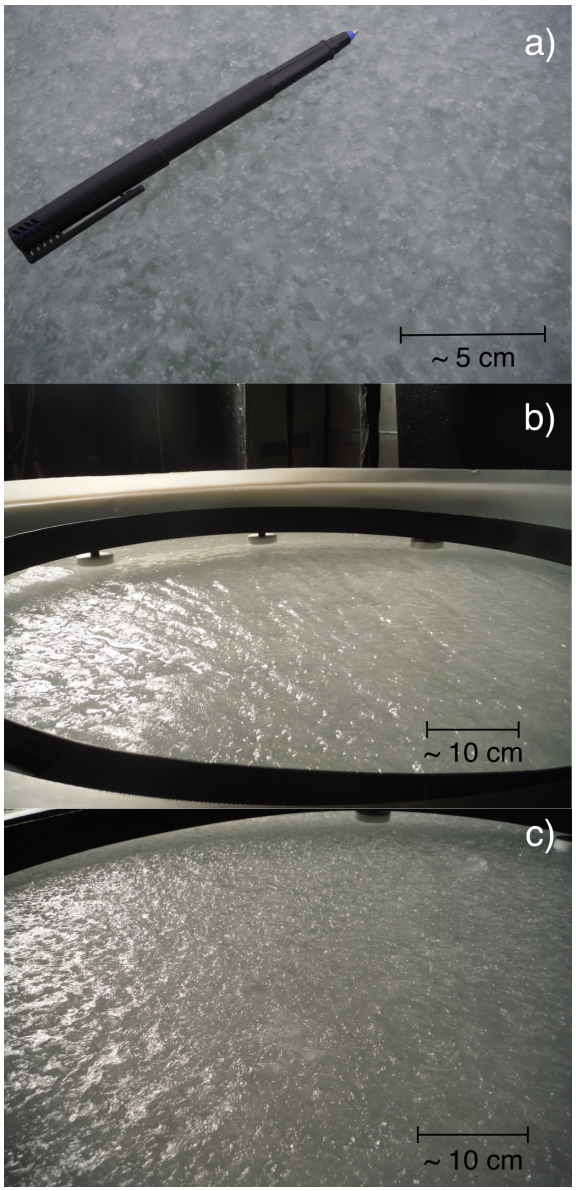

FIGURE 2.34: Examples of observed surface roughness of artificial sea ice. a) A smooth surface was observed at SERF. b, c) the air cooling of the sea ice grown at RHUL using fans generated varying amounts of surface roughness that were modelled with PlanarRad.

- Sea ice absorption and scattering

The optical properties of the sea ice in PlanarRad are described with the attenuation coefficient and the absorption coefficient. The attenuation coefficient, is expressed as (Petty, 2006):

$$\mu = \mu_a + \mu_s, \tag{2.8}$$

with μ_a, the absorption coefficient, and μ_s, the scattering coefficient. The absorption coefficient of the sea ice was considered to be the sum of the absorption by the sea ice and the absorption by the impurities present in the sea ice. The absorption values of Warren and Brandt (2008) were used for the absorption of the sea ice, using the Beer-Lambert law (Born and Wolf, 1980):

$$\alpha = \frac{4\pi k}{\lambda}, \tag{2.9}$$

with k, the imaginary refractive index, and λ the wavelength number. The use of the absorption coefficient of pure ice to represent the absorption of sea ice is discussed in chapter 6. The absorption coefficient of the impurities in the sea ice is discussed below.
For the work in chapter 7 and chapter 8, the scattering coefficient of the sea ice was used as a fitting parameter in the model. The scattering values were considered to be wavelength-independent (Lee-Taylor and Madronich, 2002). For the work in chapter 6, three scattering coefficients covering three typical types of snow were selected from the literature. The scattering coefficient has been shown to be density-dependent (Lee-Taylor and Madronich, 2002). Therefore, values of scattering cross-section found in the literature were converted to scattering coefficients, such as:

$$s = \sigma_{scatt}\rho, \tag{2.10}$$

with s, the scattering coefficient (per unit length), σ_{scatt} the scattering cross-section, and ρ, the density of sea ice. Based on the values reported in chapter 3, a scattering coefficient of 120 m^{-1} was used to represent first-year sea ice, 600 m^{-1} for multi-year sea ice, and 24 m^{-1} for melting sea ice.

- Absorption of the impurities in the sea ice

The impurities modelled in the sea ice were considerer to be purely absorbing, and not scattering. The absorbers described henceforth are estimated as bulk absorbers (Lee-Taylor and Madronich, 2002) within the snow or ice and will be referred to as the mass of absorber per mass of sea ice or snow. In chapter 6, a mass-ratio of 1 $\mathrm{ng\,g}^{-1}$ of black carbon was added to the sea ice in the model, representing the small quantities of atmospherically deposited black carbon occurring in natural sea ice (e.g. Doherty et al., 2010b). For the modelling of the sea ice at SERF (chapter 8), the amount of black carbon in the sea ice was used as a fitting parameter. In both modelling studies, the mass absorption cross-section of black carbon for a black carbon particle size of 0.13 $\mu\mathrm{m}$ in diameter was obtained from Dang et al. (2015). The mass absorption cross-section was converted to an absorption coefficient of black carbon in sea ice, by multiplying the mass absorption cross section by the mass-ratio of black carbon in sea ice and the density of sea ice. The absorption cross-section of black carbon and volcanic ash, used to fit the sea ice in the sea ice simulator (chapter 7), were calculated based on Mie theory, as described in section 2.1.5.3. The mass-ratio of black carbon or volcanic ash were likewise used as free fitting

parameters.
The spectral shape of nadir measurements of the sea ice at SERF and the RHUL sea ice simulator suggest that the sea ice was contaminated with small concentrations of algae. Indeed, algae typically found in sea ice exhibits a strong absorption in the UV–Visible part of the spectrum (Jeffrey et al., 1999), where small quantities of absorbers affect the reflectance of sea ice strongly owing to the small absorption of the ice at shorter wavelengths (400–600 nm). Therefore, the drop in reflectance observed in the measurements between 400 and 550 nm may suggest the presence of algae in the sea ice. Chlorophyl-*a* was used as a proxy for algae absorption. The mass absorption cross-section of chlorophyl-*a* was obtained from Mundy et al. (2011) and converted to an absorption coefficient, as described above. In chapter 7 and chapter 8, the quantities of algae are referred to as mass of algae per volume of sea ice, and were varied to fit the observational data.

- Phase function of the sea ice

The directionality of the scattering within the sea ice in the model is controlled by the scattering phase function. The scattering phase function provides knowledge of the angular distribution of electromagnetic radiation scattered by a particle in a medium, and is expressed as a function of the scattering angle between the direction of the incident and scattered radiation. The homogeneous sea ice slab modelled in PlanarRad is considered as a uniform ensemble of scattering particles, for which the interaction of the incident radiation is defined by the absorption and scattering coefficients defined above, and the phase function. To represent the scattering within the sea ice, the Henyey-Greenstein (HG) phase function was used (Henyey and Greenstein, 1941). The HG phase function, that was empirically derived to model the scattering of light by interstellar dust, is expressed as (Henyey and Greenstein, 1941):

$$\beta(g,\theta) = \frac{1}{4\pi}\frac{1-g^2}{[1+g^2-2gcos(\theta)]^{\frac{3}{2}}}, \tag{2.11}$$

where θ is the incident angle to the scattered angle, and g, the asymmetry parameter (see section 2.3.1.1). The HG phase function is a simple approximation of the angular dependance of light scattering by small particles relying on a single parameter, g. However, the function relies on the assumption of spherical particles that are located in a uniform medium, which may lead to errors. The HG parameter was used in the modelling of the sea ice with PlanarRad, as it has been shown that the phase function is adequate for the computation of the light field within sea ice (Maffione et al., 1998), and asymmetry parameter values for sea ice have been reported in the literature (Mobley et al., 1998). The asymmetry parameter was fixed, with a wavelength independent value of 0.98. Previous studies (Warren and Wiscombe, 1980; Marks and King, 2013a; Marks and King, 2014) have shown that g is near-wavelength independent for spherical ice grains, and small

variations in g have a negligible effect on the scattering cross-section of sea ice (France et al., 2012). Therefore, for consistency with chapter 3, the value of g = 0.98 was chosen.

- Bottom boundary

The lower boundary condition in PlanarRad is defined by an isotropic reflector. For the modelling study in chapter 6, a wavelength independent reflectance of 0.1 was chosen, as described in the previous section. When fitting the artificial sea ice at SERF, in chapter 8, the measured reflectance of an ice free patch on the artificial sea ice pool at nadir was used as a lower boundary. The reflectance is shown in figure 2.26. When fitting the artificial sea ice in the sea ice laboratory at RHUL, in chapter 7, the measured nadir reflectance of the tank full of sea water under diffuse illumination conditions was used. The reflectance of the bottom layer of the tank in the RHUL sea ice simulator is shown in figure 2.3. For wavelengths above 800 nm, the reflectance of the tank was considered to be 0. At a later stage of the development of the PlanarRad model, the option to add the BRF of an underlying medium was implemented, allowing for the vertical stratification of the modelled sea ice. In chapter 7, the BRF of clean ice was calculated for 10 illumination zenith angles, using the best-fit parameters described in section 2.3.3. The resulting BRF was compiled and placed as the lower boundary layer for the modelling of the poisoned 5 cm layer of sea ice placed over the clean ice layer.

2.3.3.2 Fitting procedure and assessment of the model fitting

To fit the angular reflectance of the artificial sea ice at SERF and in the RHUL sea ice simulator, the model parameters were divided in two categories. Firstly, the known physical properties of the sea ice and environmental conditions were fixed in the model. The properties were either obtained from ancillary measurements, such as the thickness of the sea ice or the illumination angles (described in 2.3.3.1), or from known values in the literature (e.g. the absorption coefficient of ice). The remaining parameters necessary to describe the sea ice conditions in the model were varied until the modelling results fitted the observational data. In the development stages of the model, each parameter was varied individually, whilst keeping the other parameters fixed in order to assess the individual effects of the parameters. To fit the HDRF measurements of the artificial sea ice at SERF, and the artificial sea ice in the RHUL sea ice simulator, the free parameters of the model were limited to the scattering coefficient of the sea ice, the mass-ratio of black carbon or volcanic ash in the ice and the mass-ratio of algae in the sea ice. The individual effects of the three parameters of the BRF at nadir are shown for illustrative purposes in figure 2.36. A sea ice layer of 1 m thick was modelled with an underlying medium with a lambertian reflectance of 0.1, and for a solar zenith angle of $60°$. The scattering coefficient, was varied between 100 and 600 m^{-1} without impurities present in the ice. The black carbon mass-ratio was varied for a fixed scattering coefficient of 300 m^{-1} and no algae.

Finally the algae mass-ratio was varied for a fixed scattering coefficient of 300 m^{-1} and no black carbon. Figure 2.36 highlights the spectral effects of the different parameters. The effects of further parameters such as surface roughness, sea ice thickness and sea ice type on the BRDF of sea ice were investigated and reported in chapter 6.

To fit the BRF of the layered artificial sea ice measured in the RHUL sea ice simulator (chapter 7), the modelling was performed in two stages. First, the measurements of the clean ice were fitted with PlanarRad, by varying the scattering coefficient, and small amounts of algae owing to tank contamination and black carbon owing to particles transported from the atmosphere through the air circulation system. When a satisfactory fit was obtained, the full BRF of the sea ice was calculated using the best fitting parameters, and varying the illumination zenith angle over the 10 zenith quads. The result was compiled into a boundary BRF file. In the second stage of the modelling, the computed BRF boundary file was placed below a new layer of sea ice. The know mass-ratio of black carbon or volcanic ash was fixed in the model and the scattering coefficient and the surface roughness of the new layer was varied until the model results fit the observed BRF.

To optimise the fit between the measured BRF or HDRF and the modelled BRF of the artificial sea ice, the modelling was performed in an iterative way. First the values of the free parameters were varied in coarse steps between realistic values for the quantities fitted. Firstly, the nadir BRF of the sea ice was computed without impurities, for varying scattering cross-section values. A visual comparison of the results with the measured nadir BRF or HDRF narrowed the range of values modelled. In a second step the absorption of impurities in the sea ice was added to the model, based on prior knowledge of the effects, shown in figure 2.36. After a visual fit determined a narrowed range of values for the different parameters, the model was run with a combination of the different parameters over the predetermined ranges of values with a fine interval. Figure 2.35 shows the nadir BRF modelled with a range of scattering coefficients, black carbon mass-ratios and algae mass-ratios. The mean nadir HDRF that the model was being fitted to is plotted over the model run for comparison.

To described how well the combination of modelled parameters explained the observed data, a quantitative assessment of the goodness of fit was performed. The χ^2 test (Snedecor and Cochran, 1967) was used to compare the modelled and observed data, providing a metric on the goodness-of-fit. The χ^2 test was originally used to test whether a sample of data originates from a population with a specific distribution. However, the χ^2 test statistic is the normalised sum of the squared difference between observed and

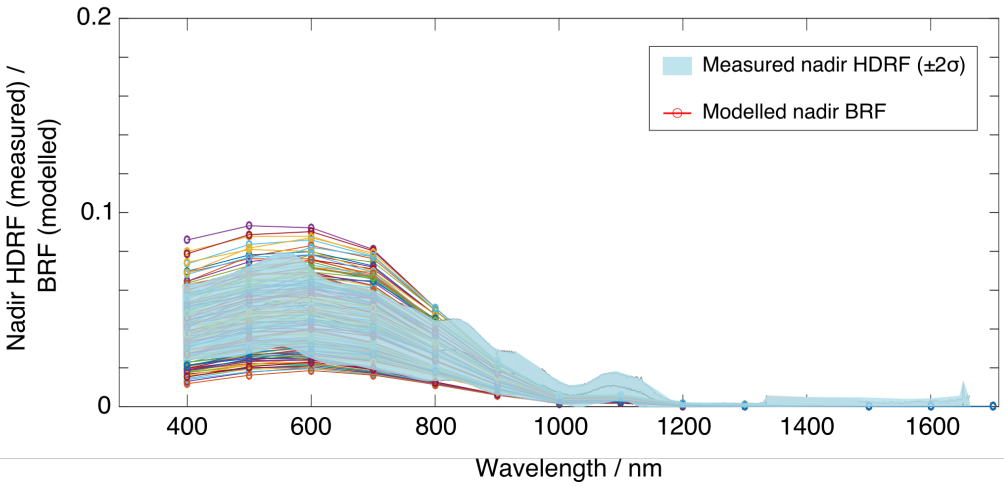

FIGURE 2.35: PlanarRad model results for the fitting of the mean nadir HDRF measured at SERF. The varying values are not reported for clarity, but can be found in chapter 8.

theoretical, and therefore can also be used to describe how well modelled data fit observations. The χ^2 test is expressed as:

$$\chi^2 = \sum_i \frac{(C_i - O_i)^2}{O_i}, \tag{2.12}$$

with O_i, the modelled data points and E_i the measured data points. The chi-square goodness of fit test was performed for the nadir observations, where a modelled value was fitted to the mean nadir observations. To take in account the uncertainties in the measurements, the reduced χ^2 test was used, expressed as (Wong, 1997) :

$$\chi^2 = \sum_i \frac{(C_i - O_i)^2}{\sigma_i^2}, \tag{2.13}$$

where the statistic is adjusted for the standard deviation σ_i of the data points. In chapter 7 and chapter 8, the goodness of fit test was performed over the modelled wavelength range i. The value of χ^2 was plotted for each model run with a combination of different values of the free parameters. The model results with the lowest value of χ^2 were considered to have the parameters that best described the observed sea ice. An example of χ^2 values for different model runs is shown in chapter 8.

After obtaining the best fit for the nadir BRF, the pattern of modelled BRF was compared to the measurements. Chapter 6 reports the effects of surface roughness on the BRDF of sea ice. Variations in the surface roughness have an important effect on the BRDF pattern of the sea ice. The surface roughness was varied in the model and the resulting BRF was compared with the laboratory measurements. The relative difference in the distribution of the angular reflectance was calculated, and assessed visually. After a good fit of the

BRF distribution was observed, the fit at nadir was assessed iteratively, ensuring that the previous parameter combination remained valid. If a difference in the χ^2 was observed, the process was repeated.

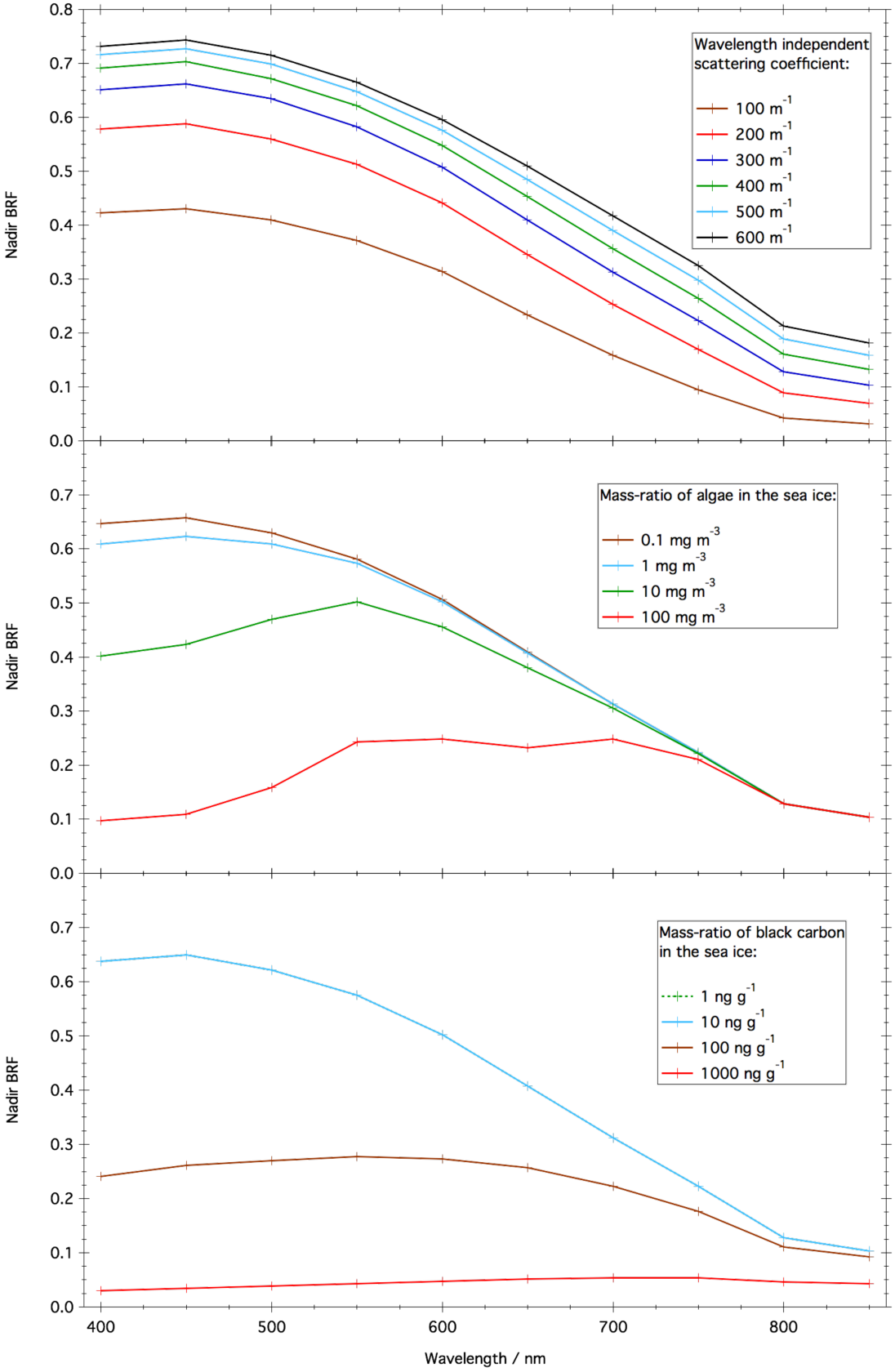

FIGURE 2.36: Nadir BRF of modelled sea ice for different model parameters. A 1 m thick sea ice layer was placed on a bottom boundary layer with a reflectance of 0.1. The illumination zenith angle was $60°$. Top: the sea ice was modelled with varying scattering coefficients. Middle: the scattering coefficient was fixed to 300 m^{-1} and the algae mass-ratio in the ice was varied. Bottom: the scattering coefficient was fixed to 300 m^{-1} and the black carbon mass-ratio in the sea ice was varied.

Chapter 3

The impact of atmospheric mineral aerosol deposition on the albedo of snow & sea ice: are snow and sea ice optical properties more important than mineral aerosol optical properties?

Citation:
Lamare, M. L., Lee-Taylor, J., & King, M. D. (2016). The impact of atmospheric mineral aerosol deposition on the albedo of snow & sea ice: are snow and sea ice optical properties more important than mineral aerosol optical properties? Atmospheric Chemistry and Physics, 16(2), 843–860.

Author contributions:
Lamare, M. performed the radiative-transfer calculations, did the data analysis, prepared the results and wrote the paper.

Lee-Taylor, J. designed the radiative-transfer model, helped with the debugging of the model code and proof-read the paper.

King, M.D. oversaw the study, and proof-read the paper.

Atmos. Chem. Phys., 16, 843–860, 2016
www.atmos-chem-phys.net/16/843/2016/
doi:10.5194/acp-16-843-2016

Atmospheric Chemistry and Physics
Open Access
EGU

The impact of atmospheric mineral aerosol deposition on the albedo of snow & sea ice: are snow and sea ice optical properties more important than mineral aerosol optical properties?

M. L. Lamare[1], J. Lee-Taylor[2,3], and M. D. King[1]

[1]Department of Earth Sciences, Royal Holloway University of London, Egham, Surrey, TW20 0EX, UK
[2]National Center for Atmospheric Research, Boulder, CO, USA
[3]Cooperative Institute for Research in Environmental Sciences, University of Colorado, Boulder, CO, USA

Correspondence to: M. D. King (m.king@es.rhul.ac.uk)

Received: 7 July 2015 – Published in Atmos. Chem. Phys. Discuss.: 27 August 2015
Revised: 8 January 2016 – Accepted: 11 January 2016 – Published: 25 January 2016

Abstract. Knowledge of the albedo of polar regions is crucial for understanding a range of climatic processes that have an impact on a global scale. Light-absorbing impurities in atmospheric aerosols deposited on snow and sea ice by aeolian transport absorb solar radiation, reducing albedo. Here, the effects of five mineral aerosol deposits reducing the albedo of polar snow and sea ice are considered. Calculations employing a coupled atmospheric and snow/sea ice radiative-transfer model (TUV-snow) show that the effects of mineral aerosol deposits are strongly dependent on the snow or sea ice type rather than the differences between the aerosol optical characteristics. The change in albedo between five different mineral aerosol deposits with refractive indices varying by a factor of 2 reaches a maximum of 0.0788, whereas the difference between cold polar snow and melting sea ice is 0.8893 for the same mineral loading. Surprisingly, the thickness of a surface layer of snow or sea ice loaded with the same mass ratio of mineral dust has little effect on albedo. On the contrary, the surface albedo of two snowpacks of equal depth, containing the same mineral aerosol mass ratio, is similar, whether the loading is uniformly distributed or concentrated in multiple layers, regardless of their position or spacing. The impact of mineral aerosol deposits is much larger on melting sea ice than on other types of snow and sea ice. Therefore, the higher input of shortwave radiation during the summer melt cycle associated with melting sea ice accelerates the melt process.

1 Introduction

The albedo of snow and sea ice has a large influence on the surface energy budget of polar regions, impacting the Earth's climate system (e.g. Barry et al., 1993; Curry et al., 1995; Jacobson, 2004; Serreze and Barry, 2005). Shortwave radiation is a key factor in the radiative balance at high latitudes, influencing the large-scale dynamics and the snow and sea ice cover. Variation in albedo is linked to several factors, such as the physical properties of snow and sea ice, morphology, surface roughness, thickness and light-absorbing impurities (e.g. Perovich et al., 1998).

The albedo of sea ice is strongly wavelength-dependent, owing to the light scattering and absorption by ice and brine. Previous studies have defined wavelength integrated and spectral albedos for a variety of snow and sea ice types (e.g. Langleben, 1969, 1971; Grenfell and Makyut, 1977; Grenfell and Perovich, 1984; Perovich et al., 1986; Perovich, 1996; Buckley and Trodahl, 1987; Grenfell, 1991; Wiscombe and Warren, 1980; Aoki et al., 1998; Hanesiak et al., 2001). Albedo is not only influenced by the physical structure of snow or sea ice but also by the amount and type of light-absorbing impurities in the snow and sea ice (Warren and Wiscombe, 1980). Only small amounts of light-absorbing impurities are needed to achieve changes in snow or sea ice albedo (e.g. Warren and Wiscombe, 1980; Warren, 1984; Light et al., 1998; Doherty et al., 2010; Marks and King, 2014). Indeed, mass ratios of less than 1 part per million are sufficient to reduce the albedo by 5 to 15 % (Warren and Wiscombe, 1980). Light-absorbing pollutants may be trans-

ported to the Arctic as fine particulate aerosols (Shaw, 1984). Once in the Arctic, the particles are deposited onto snow or sea ice from the atmosphere by precipitation or dry deposition (Fischer et al., 2007; Doherty et al., 2010). Dust from arid and semi-arid regions is the most important source of mineral aerosols in the atmosphere (e.g. Ginoux et al., 2010). Although gravitational processes remove larger particles (Westphal et al., 1987), finer particles can be transported over great distances and in some cases reach the Arctic (Prospero et al., 2002). The two main source areas of mineral dust deposited in the Arctic are Asia and North Africa (Pacyna and Ottar, 1989; Zdanowicz et al., 1998; Bory, 2003; VanCuren et al., 2012), with an estimated flux range between 1 and 21 $\mu g\,cm^{-2}\,yr^{-1}$ (Zdanowicz et al., 1998). After mineral dust, volcanic ash is the second largest type of mineral aerosols found in the Arctic (VanCuren et al., 2012). Indeed, high-latitude volcanic eruptions frequently emit large quantities of ash into the Arctic (e.g. Stone et al., 1993; Zielinski et al., 1997; Young et al., 2012) disturbing the Arctic's climate system. The analysis of core samples in Arctic sea ice has exposed the presence of volcanic ash through traces of silicate shards and aged tephra (Ram and Gayley, 1991). However, the complex nature of volcanic eruptions makes ash deposition in the Arctic difficult to assess.

Soot and black carbon are known to absorb light strongly, thus reducing the albedo of snow and sea ice (e.g. Chýlek et al., 1983; Warren, 1984; Clarke and Noone, 1985; Warren and Clarke, 1990; Grenfell et al., 2002; Lee Taylor and Madronich, 2002; Jacobson, 2004; Flanner et al., 2007; Doherty et al., 2010; Reay et al., 2012; Ye et al., 2012; Marks and King, 2013, 2014). Field observations and modelling simulations have also shown that increases in dust deposition to snow lead to radiative forcing that affects the energy balance of snow (Woo and Dubreuil, 1985; Aoki et al., 1998; Painter et al., 2007, 2012; Huang et al., 2011; Wang et al., 2013; Zhang et al., 2013; Zhao et al., 2014; Yasunari et al., 2014). However, although anthropogenic deposits in polar snow and ice have been well characterised, studies on the effects of natural mineral aerosol deposits are more scarce. Warren and Wiscombe (1980) modelled the impact of desert dust in snow, using a compilation of optical properties present in the literature. By varying particle size and concentration, they showed that the presence of dust reduces the albedo of natural snow at shorter wavelengths (300–800 nm), but the large absorption of snow in the infrared region means that the albedo of snow is insensitive to mineral dust in this region. Carmagnola et al. (2013) considered the impact of dust as well as black carbon on albedo of snow, comparing modelled results with in situ observations. They pointed out the importance of dust impurities due to their higher concentration within the snow compared with black carbon. However, Carmagnola et al. (2013) measured small concentrations of impurities to fit their observational data set, and did not take into account a larger range of values. Although volcanic ash has a local and instantaneous impact on snow and sea ice, its effects have been described as similar to soot (Warren, 1982). Warren (1982) modelled the effect of increasing Mount St. Helens ash on snow albedo for diffuse incidence. The results show a significant reduction of albedo in the visible wavelengths, and unimportant in the infrared. Conway et al. (1996) confirmed these results by showing that volcanic ash can reduce the albedo of snow up to 50 %. Flanner et al. (2007) and Flanner et al. (2009) developed a model that provides albedo of snow for different concentrations of black carbon, dust or volcanic ash, based on a two-stream radiative-transfer code (Toon et al., 1989). In the single-layer implementation of the model, SNICAR-online (Flanner et al., 2007), multiple snow types can be modelled by changing the snow grain radius. However, only a single type of volcanic ash derived from Patterson (1981) and combined mineral refractive indices as an approximation of mineral dust were used. Furthermore, SNICAR-online does not allow for calculations in sea ice. Impurities in sea ice have been considered by Light et al. (1998), who used a four-stream discrete-ordinates radiative-transfer model to determine how particulates (Saharan dust and sediments) alter the optical properties of sea ice. The authors analysed the sensitivity of albedo in relation to depth and thickness of a single dust layer within the ice, showing the importance of vertical distribution of deposited aerosols. Additionally, the effects of an increasing surface layer of snow containing a fixed mass of soot has been considered by Grenfell et al. (2002). However the study was limited to a single snow type and only a constant mass of soot. To the knowledge of the authors of this paper, no studies on the effects on albedo of multiple mineral dust or volcanic ash layers deposited at varying intervals in snow have been published. Studying the layering of mineral aerosol deposits in snow or sea ice enables to take into account the episodic nature of dust and volcanic ash deposition events. Moreover, the comparison of multiple sources of mineral aerosol deposits on multiple different types of snow and sea ice in an Arctic environment has not been investigated. Although Woo and Dubreuil (1985) proposed a characterisation of the relationship between dust content and Arctic snow albedo, the range of snow types and dusts was limited. Overall the understanding of the impact of mineral aerosol deposits on the albedo in the Arctic is hampered by the lack of comprehensive studies on the role of the snow or sea ice optical properties in relation to the optical properties of the mineral aerosol deposits. The work of Marks and King (2014) on the effects of the snow and sea ice type on the response of albedo to black carbon loadings suggests that the type of snow or sea ice is an important factor when considering the effects of impurities on the albedo of snow and sea ice. The conclusions from Marks and King (2014) led the authors of this paper to address the question of the importance of the type of snow or sea ice compared to the type of mineral dust or volcanic ash when evaluating the impact of mineral aerosol deposits on albedo. No studies

investigating the effects of light-absorbing impurities on the albedo of snow and ice have examined this question.

In this work an atmospheric and snow/sea ice radiative-transfer model (TUV-snow) was used to investigate the effects of mineral aerosol deposits on snow and sea ice. The main purpose was to evaluate the impact of different mineral dusts and volcanic ashes on albedo. To do so, different mass ratios of a selection of five different mineral aerosol deposits in multiple snow and sea ice types were modelled. The thickness of a single surface layer and the vertical distribution of multiple layers loaded with mineral deposits were then varied to explore the effects of layering.

2 Method

The description of the method is split into three sections: the radiative-transfer model is described, followed by a detailed section on the calculation of mineral absorption cross-sections and a final section describing the modelling experiment performed.

2.1 Radiative-transfer model

The radiative-transfer calculations of the penetration and reflection of light into snow and sea ice containing mineral aerosol deposits were performed using the Tropospheric Ultraviolet and Visible Radiation Model (TUV-snow), using the discrete-ordinates "DISORT" algorithm (Stamnes et al., 1988), as described by Lee Taylor and Madronich (2002). The model is a coupled atmospheric and snow/sea ice model that allows calculation of radiative-transfer parameters in snow and sea ice from the top of the atmosphere to the surface of the Earth and into a layer of snow or sea ice.

The model parameters simulating different types of snow and sea ice are controlled by an asymmetry factor g, a wavelength independent scattering cross-section, σ_{scatt}, a wavelength dependent absorption cross-section, σ_{ice} and the sea ice or snow density (Lee Taylor and Madronich, 2002; France et al., 2011a, b; Reay et al., 2012; Marks and King, 2013, 2014).

In this study, three types of sea ice were used: first-year ice, multi-year ice and melting ice, as well as three types of snow: cold polar snow, coastal wind packed snow and melting snow. The optical and physical parameters of the selected snows and sea ice are based on field studies and summarised in Table 1. A detailed description and justification of these values can be found in Marks and King (2014).

The wavelength independent albedo of the surface under the snow and sea ice layer was fixed to 0.1 to represent seawater or soil. Irradiance reflectance at the surface was calculated to approximate albedo, represented by Eq. (1):

$$A = \frac{E_{\text{u}}}{E_{\text{d}}}, \tag{1}$$

where E_{u} is the upwelling plane irradiance and E_{d} is the downwelling plane irradiance.

A layer of cumulus cloud was added to the model at an altitude of 1 km to provide diffuse illumination of the snow or sea ice surface and remove the solar zenith angle dependance. The cloud asymmetry factor g, was set to 0.85, the single scattering albedo was set to 0.9999 and the optical depth was set to 32. The atmosphere was added with an ozone column of 300 Dobsons containing no aerosols. The distance between the Earth and the Sun was fixed to 1 AU.

The modelled wavelength dependent albedo was produced over a spectrum ranging from 350 to 800 nm with a 1 nm interval.

2.2 Optical properties of mineral dust and volcanic ash

The snow and sea ice were modelled as media which are highly scattering and weakly absorbing of photons. The light-absorbing impurities were modelled as absorbers only and it was assumed that the ice matrix provides all the scattering. The total absorption in sea ice is

$$\sigma_{\text{total}} = \sigma_{\text{s}}(\lambda) + x_{\text{mn}}\sigma_{\text{mn}}(\lambda), \tag{2}$$

where $\sigma_{\text{s}}(\lambda)$ is the wavelength-dependant absorption cross-section of snow or sea ice, x_{mn} is the mass ratio of mineral aerosol deposits in the snow or sea ice and $\sigma_{\text{mn}}(\lambda)$ is the wavelength-dependant absorption cross-section by mineral aerosols.

The optical constants of ice were obtained from the work of Warren and Brandt (2008). The calculation of the absorption cross-section of the mineral aerosol deposits was calculated based on the Mie theory (Bohren and Huffman, 1983) in the Mieplot program (Laven, 2006) using the BHMIE computation code (Bohren and Huffman, 1983). The resulting absorption cross-sections of the mineral aerosol deposits were used in the radiative transfer model described in Sect. 2.1.

To calculate the absorption spectra of representative mineral aerosols from a Mie Calculation, values of the imaginary refractive index, density, size and size distribution are needed. The values of the imaginary refractive index for different mineral dusts and ashes vary significantly with wavelength and the medium's mineral composition (Tegen and Fung, 1994; Sokolik and Toon, 2007). A selection of the imaginary part of the refractive index values of mineral dust found in the literature was reported by Dang et al. (2015). Three different volcanic ashes and two dusts were chosen from the literature to represent the variety of mineral aerosols deposited in the Arctic. The work of VanCuren et al. (2012), was used for Asian dust, Saharan dust, fresh volcanic tephra and aged volcanic dust plumes as the four characteristic sources of aerosols deposited at Summit, Greenland.

A representative value of the imaginary component of the refractive index of Saharan dust was calculated as the average of eight measurements of the imaginary refractive index of

Table 1. Values of the input parameters used for snow and sea ice for the TUV-snow model, based on literature values and detailed in the work of Marks and King (2014).

Snow/sea ice	Density ($kg\,m^{-3}$)	Scattering cross-section ($m^2\,kg^{-1}$)	Asymmetry parameter (g)	e-folding depth (cm)	Typical depth modelled (cm)	Minimal optical thickness (cm)	Equivalent snow grain radius (μm)
Cold polar snow	400	20.0	0.89	15	40	45	85
Coastal windpacked snow	400	7.5	0.89	21	40	63	220
Melting snow	400	1.25	0.89	45	40	135	1400
First year sea ice	800	0.15	0.98	37	80	111	–
Multi year sea ice	800	0.75	0.98	75	250	225	–
Melting sea ice	800	0.03	0.98	400	250	1200	–

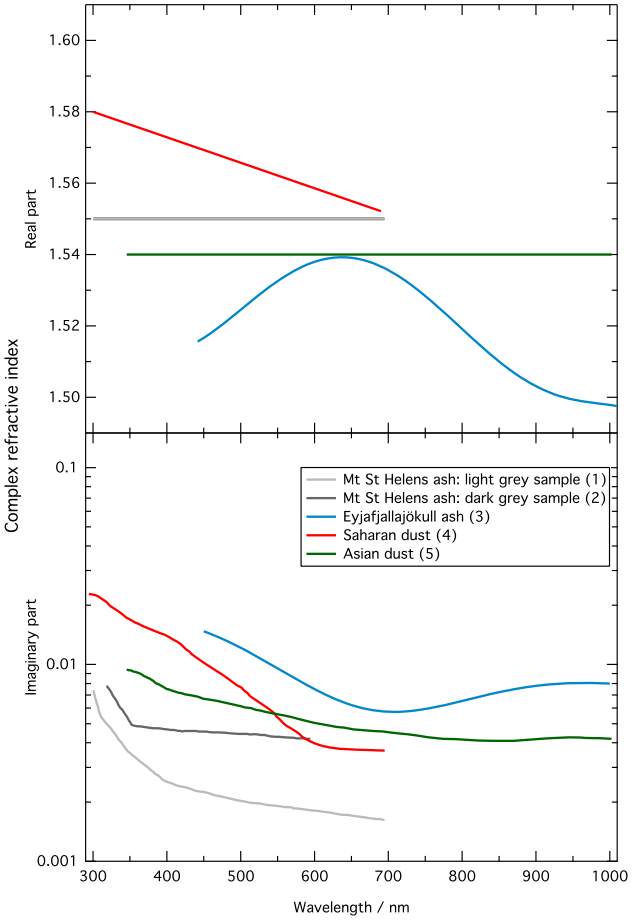

Figure 1. Complex refractive index (real and imaginary part) for mineral aerosol deposits as a function of wavelength. Values are based on work by Derimian et al. (2012) **(3)**, Patterson and Gillette (1977) **(4)**, Patterson (1981) **(1, 2)** and Sokolik et al. (1993) **(5)**.

airborne Saharan aerosols from eight locations in the Atlantic ocean (Patterson and Gillette, 1977).

The refractive index of a characteristic central Asian dust was taken from Sokolik et al. (1993). The dust samples that Sokolik et al. (1993) collected in Tadzhikistan, are a combination of airborne dust aerosols and surface dust. The imaginary refractive index of the dust aerosols was used, as it represents a better approximation of transported material. Three different volcanic ash sources were used, providing a variety of mineral and thus, optical properties. Two wavelength-dependent indices of refraction of Mount St. Helens ash from the 18 May 1980 eruption were obtained from Patterson (1981). The first sample, collected in Boulder, Colorado corresponds to the first pulse of the eruption and is characterised by a dark grey colour and a high absorption coefficient in the visible wavelengths. The second sample collected in Cheney, Washington has a pale grey appearance and a lower absorption coefficient by approximately a factor of 2 (Patterson, 1981). Direct measurements of volcanic ash optical properties are scarce. Therefore an estimate of the complex refractive index of Eyjafjallajökull ash calculated by Derimian et al. (2012) was used. The weighted combination of refractive indices of each aerosol component presented a good fit with AERONET data (Derimian et al., 2012) and was more realistic than the mineral dust data of Balkanski et al. (2007) that is more widely used (Johnson et al., 2012; Turnbull et al., 2012). The values of the complex refractive index of the aerosols as a function of wavelength considered in the study presented here are in Fig. 1.

For the calculation of the extinction coefficient of light-absorbing impurities, the mineral aerosol deposits were assumed to be spherical. Based on observations of atmospheric dust deposition in snow on the Penny ice cap on Baffin Island by Zdanowicz et al. (1998), the size distribution of the aerosols used in the calculations presented here was fixed to a log normal distribution peaking at a diameter of 2.3 μm with a standard deviation of 2.1 μm. The size distribution corresponds to a mean value for long-range transported dusts and is similar to those measured in Greenland (Koerner, 1977). Particle densities of 2600 $kg\,m^{-3}$ for Saharan dust (Hess et al., 1998), 2500 $kg\,m^{-3}$ for Asian dust (Fratini et al., 2007), 2300 $kg\,m^{-3}$ for Eyjafjallajökull ash (Johnson et al., 2012) and 1400 $kg\,m^{-3}$ for Mt St. Helens ash (Sarna-Wojcicki et al., 1981) were assumed in the calculation of absorption cross-sections. The refractive index of air was used as a surrounding medium for the Mie calculations in snow whereas values for pure ice (Warren and Brandt, 2008) were used for sea ice.

2.3 Calculation of albedo on snow and sea ice with different mineral loading schemes

Three types of modelling experiment were performed, as shown in Fig. 3. Initially, the surface albedo of snow and sea ice was calculated owing to increasing mineral dust mass ratios uniformly distributed in the snow and sea ice. To allow a fair comparison between the snowpack or the sea ice and the different dusts, the snow and sea ice was defined as semi-infinite, i.e. the thickness of the medium is large enough that the underlying layer does not affect the results. Secondly, the semi-infinite thickness was replaced by snowpacks and sea ice types with varying realistic thicknesses. Thirdly, the mineral aerosol deposits were constrained to layers in the snow and sea ice, as opposed to a uniform distribution. The third case reflects the episodic nature of mineral deposition.

Initially, the surface albedo of the different snow and sea ice types was calculated between 350 and 800 nm for an increasing mass ratio of mineral aerosol deposits. Based on the properties of the snow and sea ice used in this study, a depth of 1.5 m for snow and 15 m for ice was found to be sufficient to achieve a semi-infinite medium. Assuming the mineral aerosol deposits were distributed evenly through the medium, their mass ratio was varied between 10 and 10 000 ng g^{-1}. Typical mass ratio values on Baffin Island range from 78.2 to 193.2 ng g^{-1} (Zdanowicz et al., 1998), however much higher values can be found on glaciers close to volcanoes or on dust storm paths (Thorsteinsson et al., 2012; Schwikowski et al., 1995; Dong et al., 2014). Therefore a large range of values was included for completeness.

In order to determine the impact of different types of mineral aerosol deposits (with different absorption cross-sections), a semi-infinite snow and sea ice cover with a uniform mass ratio of 100 ng g^{-1} for each mineral sample was modelled.

In a second step, representative thicknesses for each type of snow and ice were used based on mean values found in the literature. A depth of 40 cm for snow (Warren et al., 1999; Serreze and Barry, 2005; Kohler et al., 2006) representing a maximum spring Arctic value, 2.5 m for multi-year and melting sea ice (Bourke and Garrett, 1987; Laxon et al., 2003; Weeks, 2010) and 80 cm for first-year sea ice (Weeks, 2010) were chosen. The albedo of the layer under the sea ice or snow was set to 0.1 to simulate a strongly absorbing medium similar to water or soil. Albedo, as a function of an increasing mass ratio of Asian mineral dust, was calculated (discussed in Sect. 3.2). By selecting realistic thicknesses of snow and sea ice, a comparison of the impact of mineral dust on different types of snow and sea ice was performed.

In a third step, a surface layer of 1 cm of snow or sea ice containing 100 ng g^{-1} of Asian dust was placed on the surface of each snow and sea ice type. The underlying snow or sea ice was modelled as a clean medium containing no black carbon or mineral aerosol deposits. The thickness of this top layer was increased to 10 cm in 1 cm steps. The variation in albedo was represented as a percentage of change relative to a pure medium at four different wavelengths (450, 550, 650 and 750 nm). The effects of multiple layers in snow were taken into account, simulating dust deposition by multiple storm events between snow falls. For three different 40 cm deep snowpacks, 100 ng g^{-1} of mineral deposits previously placed throughout the pack were concentrated to 5 cm layers of 800 ng g^{-1}. The distance between the five layers was increased from 1 to 8 cm with a 1 cm interval in eight different model combinations, alternating poisoned and clean snow. The albedo of the layered snow packs was compared to a clean snow pack containing 1 ng g^{-1} of mineral dust. Furthermore, the importance of buried layers containing mineral aerosol deposits was investigated by comparing multiple layers each with a dust mass ratio of 800 ng g^{-1} to

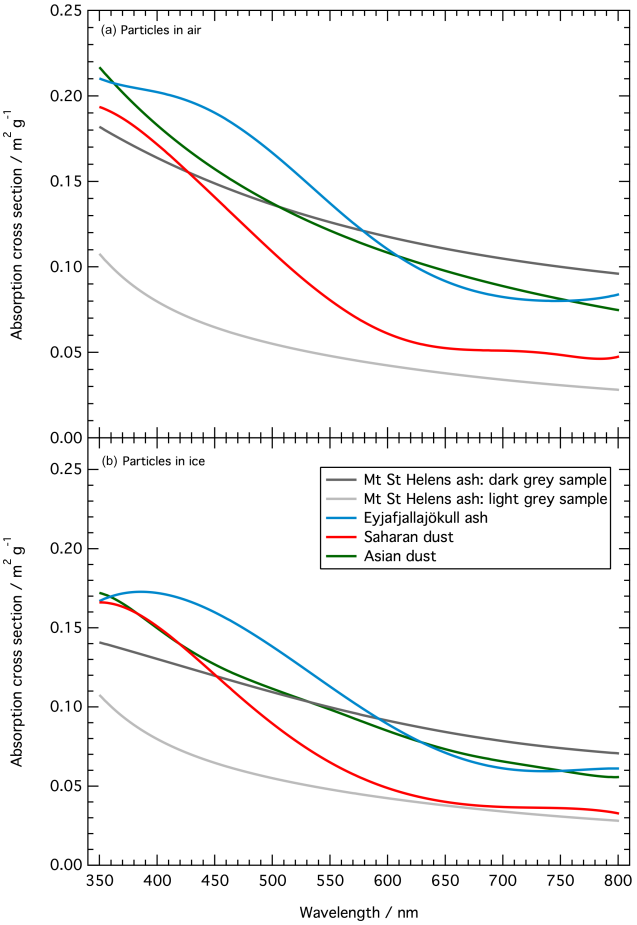

Figure 2. Absorption cross-section values based on Mie theory calculations undertaken here. Particles were considered to be surrounded by air at a temperature of 0 °C **(a)** for snow; and surrounded by ice **(b)**, using refractive index data for ice from Warren and Brandt (2008) for sea ice. The size distribution of the particles used in the Mie calculation was fixed to a log normal distribution peaking at 2.3 μm with a standard deviation of 2.1 μm. The data were smoothed with a polynomial fit to remove the fine wavelength structure.

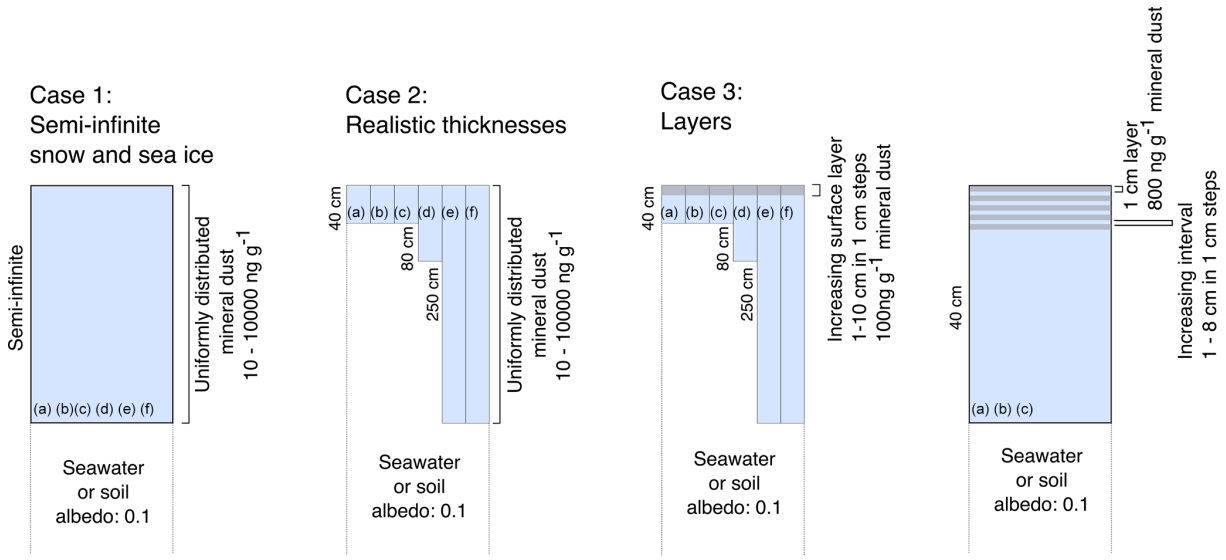

Figure 3. Snow and sea ice configurations modelled for **(a)** cold polar snow, **(b)** coastal windpacked snow, **(c)** melting snow, **(d)** first-year sea ice, **(e)** multi-year sea ice, **(f)** melting sea ice (not to scale).

one surface layer of 1 cm containing the same mass ratio of 800 ng g^{-1}. Although typical mass ratios are lower in polar regions (Zdanowicz et al., 1998), Dong et al. (2013) show values higher than 800 ng g^{-1} in snowpacks close to dust sources. The mass ratio of 800 ng g^{-1} was selected to provide a clear signal whilst remaining realistic.

Finally, the albedo of three semi-infinite snow types (cold polar snow, coastal wind packed snow and melting snow) with an increasing mass ratio of Asian dust and light coloured Mt St Helens volcanic ash, obtained from the TUV-snow model was compared to the SNICAR-online model (Flanner et al., 2007) for validation. Identical input parameters were used for snowpack thickness, density and the underlying ground albedo. The snow grain radius parameter was varied in SNICAR-online to fit three types of clean snowpacks to the output of TUV-snow. A snow grain radius of 85 μm was compared to the cold polar snow modelled in this study, 220 μm for coastal wind packed snow and 1400 μm for melting snow. In a second step, increasing concentrations of dust and volcanic ash were added to SNICAR-online, and the results were compared with TUV-snow.

3 Results

The results are presented in three sections: the effect of different types of mineral aerosol deposits on albedo of polar snow and sea ice, the variation of albedo with increasing loading of mineral aerosol deposits and the effect of layers of mineral aerosol deposits in snow.

3.1 The effect of different mineral aerosol deposit types on albedo

The absorption cross-sections of the different mineral aerosol deposits have a similar pattern with wavelength, but differ by a maximum of 77 %, as seen in Fig. 2, where the wavelength-dependant absorption cross-sections of different mineral aerosol deposits are plotted. The variation in the values of absorption cross-section has little effect on the albedo for most snow or ice types. As Fig. 4 indicates, variation in albedo between the different mineral dusts and volcanic ashes does not exceed 0.0080 for snow and 0.0788 for sea ice. For semi-infinite snow or sea ice with a mass ratio of 100 ng g^{-1}, the variation in albedo between the strongly light-absorbing Eyjafjallajökull ash and the less light-absorbing Mt. St. Helens light grey ash sample is 0.0024 for cold polar snow at 450 nm; a wavelength where the difference between mineral deposits is the largest. For comparison, the difference in albedo at 450 nm between a cold polar snowpack containing 1 ng g^{-1} of Mt. St. Helens light grey ash and 100 ng g^{-1} of the same ash is 0.0036. Different mineral aerosol deposits have a larger effect on melting sea ice, where the difference in albedo between Eyjafjallajökull ash and Mt. St. Helens light grey ash reaches 0.0749 at 450 nm. When increasing the mass ratio of mineral aerosol deposits to larger values in the snow or sea ice, the importance of their optical properties becomes more obvious. The variation in albedo between 10 000 ng g^{-1} of Eyjafjallajökull ash and Mt. St. Helens light grey ash reaches 0.0268 in cold polar snow (smallest change) and 0.1444 in first-year sea ice (largest change) as shown in Fig. 5, where the albedo of different snow and sea ice types is shown for an increasing mass ratio of mineral aerosol deposits.

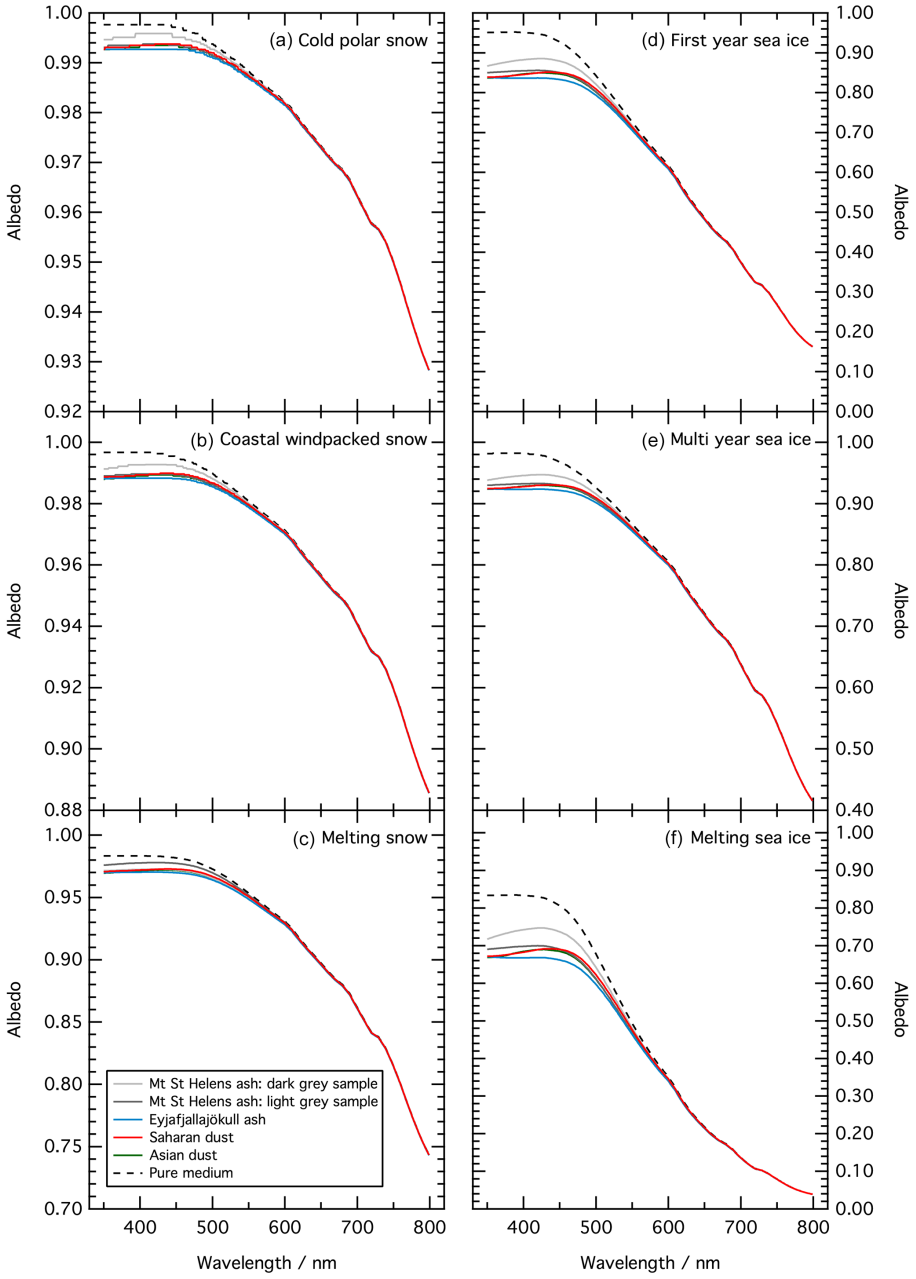

Figure 4. Wavelength-dependant albedo of three semi-infinite snow and sea ice types containing 100 ng g^{-1} of different mineral aerosol deposits (Mt St Helens ash, Eyjafjallajökull ash, Saharan dust and Asian dust). The albedo of a pure medium (containing 1 ng g^{-1} of Asian dust) has been included for comparison. The y axis has different scales in each panel to cover the large range of values.

The variation in the albedo of snow and sea ice is less sensitive to the type of mineral aerosol deposit and its optical properties than to the properties of the snow or sea ice themselves (Figs. 4 and 5). Indeed, where a maximum variation of 0.0788 is observed from one mineral deposit to another, the variation between the albedo of melting sea ice and cold polar snow for the same mass ratio of mineral dust reaches 0.8893. Thus, an important result of this work is that when considering the darkening of snow or sea ice, it may be more important to understand the optical properties of the snow or sea ice than the optical properties of the mineral aerosol deposits. Therefore, when observing the impact of an increasing mineral dust mass ratio on realistic thicknesses (Fig. 7), of surface layers (Fig. 9) and of multiple layers (Fig. 10) a single type of mineral deposit was picked. Asian dust was selected, being the most commonly found mineral dust in the Arctic (Zdanowicz et al., 1998; VanCuren et al., 2012) but

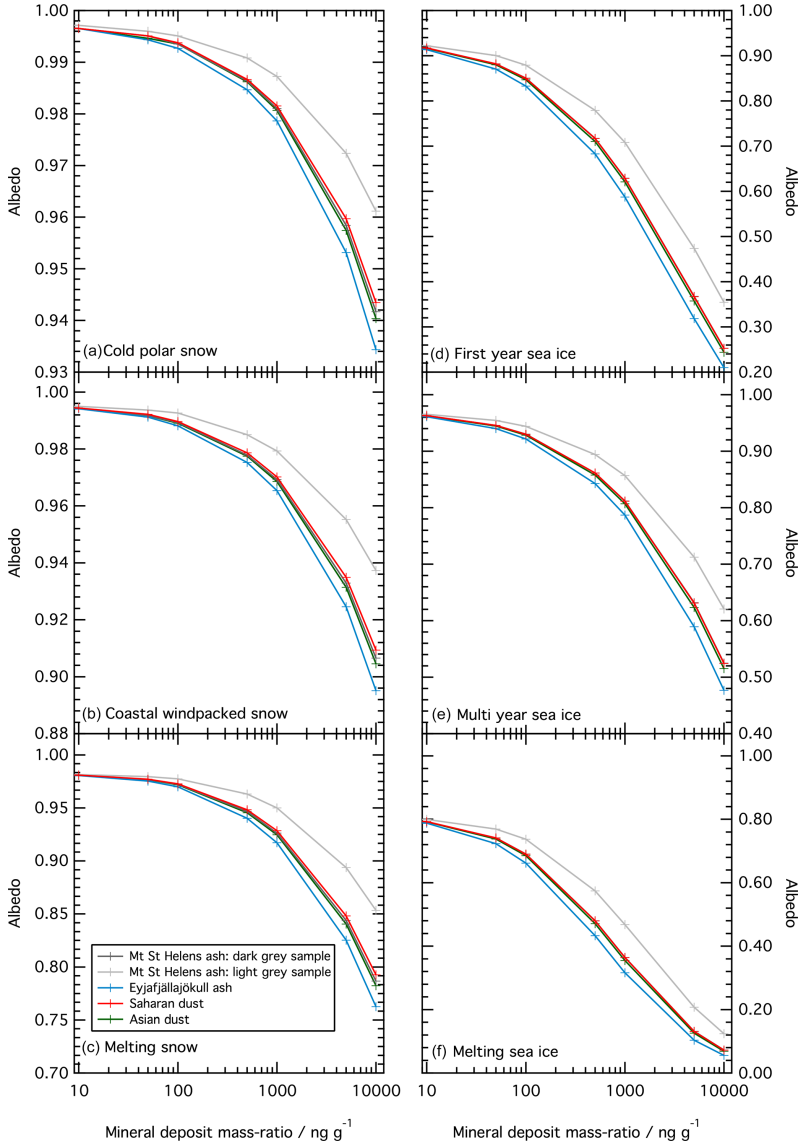

Figure 5. Albedo of three semi-infinite snow and sea ice types with increasing mineral aerosol deposits mass ratio at 450 nm. The *y* axis has different scales in each section to cover the large range of values.

also being representative of the range of mineral aerosol deposits (Figs. 1 and 2).

3.2 The effects of increasing mineral dust mass ratios in snow and sea ice on albedo

Figure 6 shows the change in albedo at 550 nm of an increasing mass ratio of the two most common types of mineral dust found in the Arctic for three different types of sea ice (first-year, multi-year and melting sea ice) and snow (cold polar, coastal windpacked and melting snow) relative to a clean medium. The results presented here, as well as for Figs. 6, 5 and 7 are for a wavelength of 550 nm, but are representative of the behaviour for a wavelength range between 400 and 600 nm. The change in albedo shown in Figs. 6 and 9 is calculated as the ratio between the albedo of snow or sea ice containing mineral aerosol deposits and albedo calculated with a snow or sea ice containing mineral aerosol deposits at a mass ratio of $1\,\mathrm{ng\,g^{-1}}$. Similarly to black carbon (Marks and King, 2014), mineral dust deposits have a larger impact on the albedo of sea ice than snow, with melting sea ice being the most sensitive medium. The relative change in albedo as a function of mineral dust is 87 % larger for melting sea ice than a cold polar snowpack for mass ratio of $10\,000\,\mathrm{ng\,g^{-1}}$ of mineral dust (Fig. 6). However, such mass ratios of dust are rare in polar regions (Lawrence and Neff, 2009). Such large mass ratios are included here to allow for a wide range of applications (i.e. study areas close to aerosol sources, astrobiology and general cases). A realistic loading is below

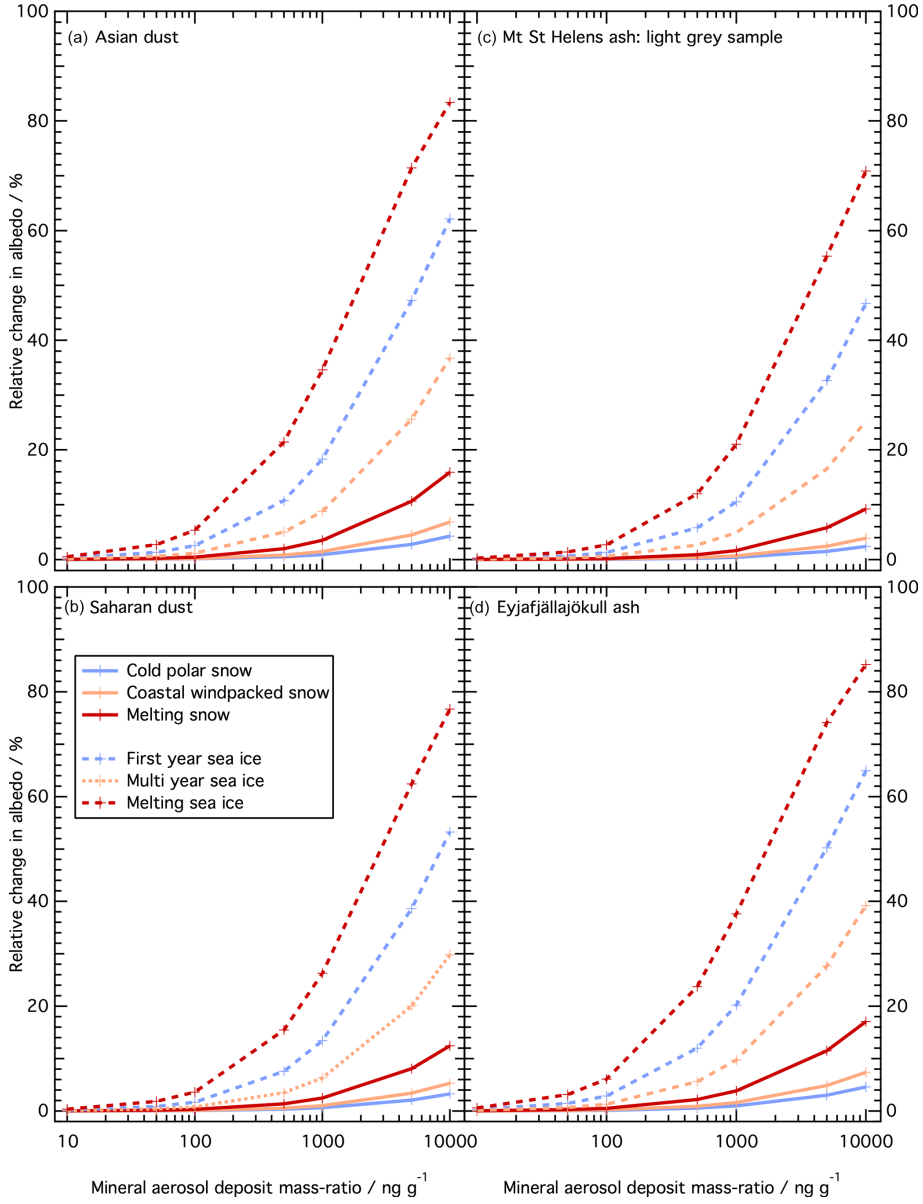

Figure 6. Relative change in albedo at a wavelength of 550 nm for an increasing mass ratio of **(a)** Asian mineral dust **(b)** Saharan mineral dust **(c)** Mt. St. Helens volcanic ash **(d)** Eyjafjällajökull volcanic ash relative to a mass ratio of 1 ng g^{-1} throughout three semi-infinite snow and sea ice types. The albedo for 1 ng g^{-1} of mineral aerosol deposits, valid for **(a)**, **(b)**, **(c)** and **(d)**, is 0.988 for cold polar snow, 0.981 for coastal windpacked snow, 0.953 for melting snow, 0.727 for first-year sea ice, 0.867 for multi-year sea ice and 0.494 for melting sea ice. The values presented for a wavelength of 550 nm are indicative of the same behaviour for wavelengths between 400 and 600 nm.

a mass ratio of 100 ng g^{-1} (Zdanowicz et al., 1998), where mineral aerosol deposits only change albedo by up to 0.03. The decrease of the albedo of melting sea ice with 100 ng g^{-1} of Asian dust relative to 1 ng g^{-1} is 5.35 % and only 0.12 % for cold polar snow. For smaller mass ratios, the effects of mineral aerosol deposits are negligible in snow and small in sea ice: 10 ng g^{-1} of Asian dust decreases the albedo of cold polar snow by 0.002 % and melting sea ice by 0.52 % relative to a mass ratio of 1 ng g^{-1}.

Figure 7 displays decreasing albedo with increasing mass loading of Asian mineral dust at a wavelength of 550 nm with realistic thicknesses of snow and sea ice (Table 1). The realistic thickness of snow and sea ice prevents the snow and sea ice types (except multi-year sea ice) from being optically thick. Using realistic values, the absorbing medium under the snowpack or sea ice affects the value of surface albedo. Table 1 highlights typical values for the different snow or sea ice types along with their *e*-folding depths. The snow and sea ice packs were considered to become optically thick at 3 *e*-

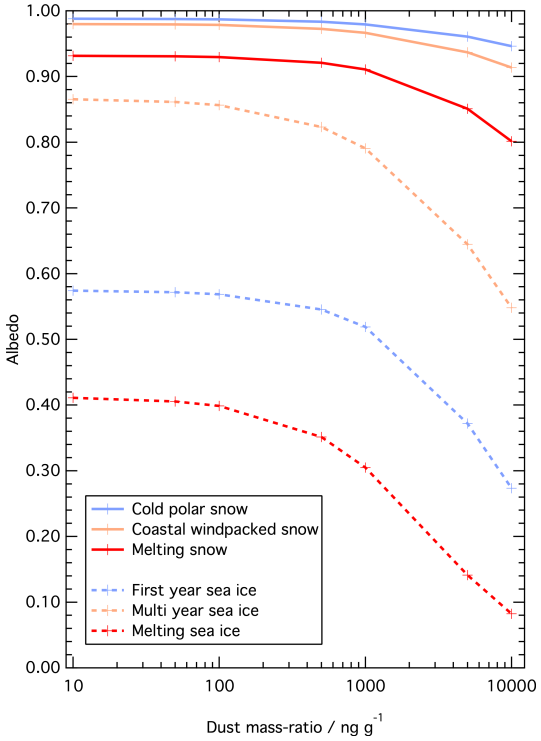

Figure 7. Albedo of three snow and sea ice types with increasing Asian dust mass ratio at 550 nm. Snow thickness: 40 cm, first-year sea ice: 80 cm, multi-year and melting sea ice: 250 cm.

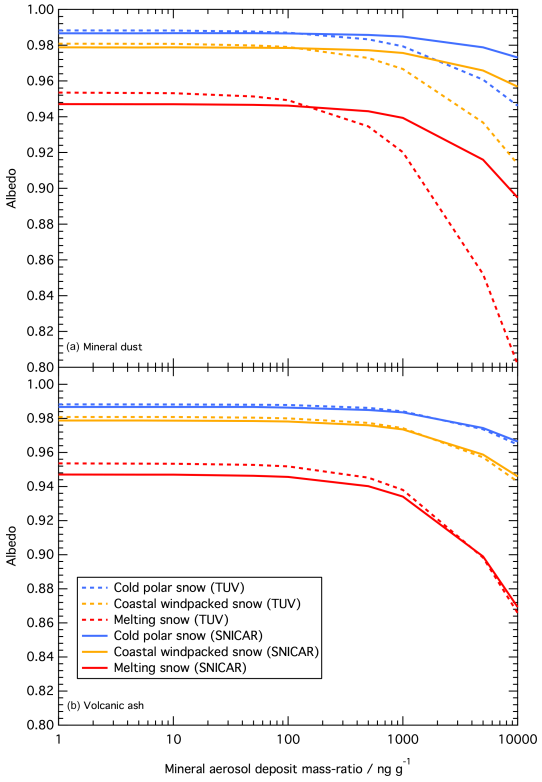

Figure 8. Comparison between the albedo of three semi-infinite snow types with an increasing mass ratio of mineral aerosol deposits computed with TUV-snow and SNICAR-online models. The dotted lines show albedo as a function of an increasing mass ratio of Asian dust **(a)** and a light coloured sample of Mt St Helens volcanic ash **(b)**. The solid lines show the output from the SNICAR-Online model (Flanner et al., 2007) using input parameters matching TUV.

folding depths, where over 95 % of incident sunlight is attenuated (France et al., 2011b). The decrease in albedo between a clean snow or sea ice and a snow or sea ice containing the same loading of Asian dust is smaller for realistic depths than for semi-infinite packs. With a concentration of 100 ng g^{-1} of Asian dust, the variation is smaller by a factor of ~ 0.97 for a realistic thickness than a semi-infinite cold polar snowpack, ~ 1.18 for coastal wind packed snow, ~ 1.91 for melting snow, ~ 3.05 for first-year sea ice, ~ 1.02 for multi-year sea ice and ~ 1.97 for melting sea ice. The strong absorbing layer under the snow or sea ice (albedo of 0.1) and a thickness smaller than the minimal optical thickness for the realistic snow and sea ice layers explain a reduction in albedo and smaller variations due to mineral aerosol deposits. Figure 7 also highlights the difference in albedo decrease between realistic snow and sea ice with the same mass ratio and category of mineral aerosol deposit. Within the snow, reduction in albedo is greater for melting snow, where 1000 ng g^{-1} of mineral aerosol deposits causes a 2.25 % decrease relative to a clean snow pack, than for cold polar snow, where the same loading causes a 0.89 % decrease. Moreover, warmer sea ice is more sensitive than cold first-year sea ice, as a mass ratio of 1000 ng g^{-1} of mineral aerosol deposits causes a 26.05 % reduction in albedo relative to clean ice for melting sea ice and 9.71 % for first-year sea ice. The results presented in this section suggest that the type of snow or sea ice are more important to consider than the type of mineral aerosol deposits when studying the impact of atmospheric mineral aerosol deposition on the albedo of snow and sea ice.

When comparing the results from the modelling in this study with the output from SNICAR-online (Flanner et al., 2007), a very good agreement for the albedo of an increasing mass ratio of volcanic ash can be observed (Fig. 8). The mean difference between the models (350 to 800 nm) is 0.0013 for cold polar snow, 0.0019 for coastal wind packed snow and 0.0050 for melting snow. With mineral dust, the models present a good agreement until 100 ng g^{-1}. For larger mass ratios, TUV-snow predicts a significantly lower albedo than SNICAR-online. The mean difference between the models when comparing mineral dusts is 0.0065 for cold polar snow, 0.010 for coastal wind packed snow and 0.023 for melting snow.

3.3 The effect of mineral dust layers in snow and sea ice

Owing to the episodic nature of dust storms and volcanic eruptions, mineral aerosol deposits can occur in snow and sea

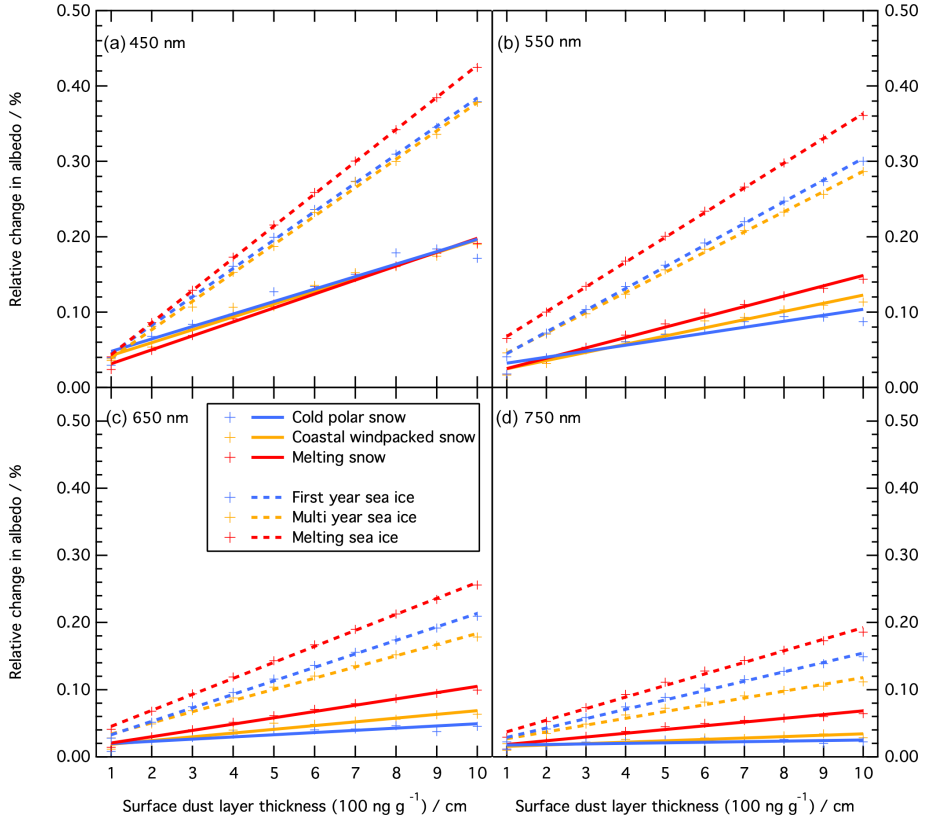

Figure 9. Relative change in albedo for an increasing surface layer of 100 ng g^{-1} of mineral dust between 1cm and 10 cm at 450 **(a)**, 550 **(b)**, 650 **(c)** and 750 nm **(d)**. The albedo without a surface layer is 0.996 at 450 nm, 0.988 at 550 nm, 0.973 at 650 nm and 0.950 at 750 nm for cold polar snow, 0.989 at 450 nm, 0.980 at 550 nm, 0.957 at 650 nm and 0.920 at 750 nm for coastal windpacked snow, 0.943 at 450 nm, 0.932 at 550 nm, 0.892 at 650 nm and 0.815 at 750 nm for melting snow, 0.611 at 450 nm, 0.575 at 550 nm, 0.452 at 650 nm and 0.267 at 750 nm for first-year sea ice, 0.950 at 450 nm, 0.866 at 550 nm, 0.721 at 650 nm and 0.542 at 750 nm for multi-year sea ice and 0.505 at 450 nm, 0.412 at 550 nm, 0.215 at 650 nm and 0.079 at 750 nm for melting sea ice.

ice as layers resulting from these events. The previous calculations were repeated, confining the mineral aerosol deposits to a surface layer with a thickness varying from 1 to 10 cm, then to a series of five layers of 1 cm with a spacing varying from 1 to 8 cm. Figure 9 demonstrates the relative change in albedo for an increasing mass ratio of Asian dust in an increasing surface layer in snow and sea ice. The change in albedo is small: 10 cm of 100 ng g^{-1} of dust on melting sea ice induces a change of 0.47 % at 450 nm, 0.36 % at 550 nm, 0.26 % at 650 nm and 0.19 % at 750 nm relative to a clean sea ice. Although the mass ratio of mineral dust observed in the Arctic is much larger than black carbon, the impact of the former on snow and sea ice is less important. Marks and King (2014) show that a surface layer of 5 cm of evenly distributed black carbon with a mass ratio of 100 ng g^{-1} causes a reduction of albedo of 1.3 % at 450 nm for first-year sea ice. The same layer, containing 100 ng g^{-1} of Asian dust only reduces albedo by 0.21 % at 450 nm (Fig. 9).

Figure 10 shows the effect of multiple layers evenly buried in a snow pack. Five layers of 1 cm containing 800 ng g^{-1} of Asian dust were placed in different 40 cm thick snow packs (polar, coastal wind packed and melting snow). The distance between the layers was increased evenly from 1 to 8 cm. Surface albedo was compared with a single 1 cm surface layer containing 800 ng g^{-1} of Asian dust and a clean snow pack. Figure 10 shows that multiple layers of mineral dust play an important part in the reduction of albedo, even when placed wide apart in the snowpack. Indeed, 1 cm layers containing mineral dust placed 8 cm apart continue to reduce albedo without the overlying snow reducing the contribution to zero. When comparing the results from Figs. 10 and 7, the difference in albedo between a uniform 40 cm snowpack containing 100 ng g^{-1} of Asian dust and the same mass of dust concentrated into five layers of 800 ng g^{-1} with a 1 cm interval is small: 0.0025 for polar snow and 0.0031 for coastal wind packed and melting snow at 550 nm. A snowpack containing multiple layers of more concentrated dust with a small spacing is thus likely to cause a similar reduction in albedo at shorter wavelengths than a snowpack where the dust is uniformly distributed.

As seen in the previous results, the effects of mineral dust are more important at shorter wavelengths than in the near

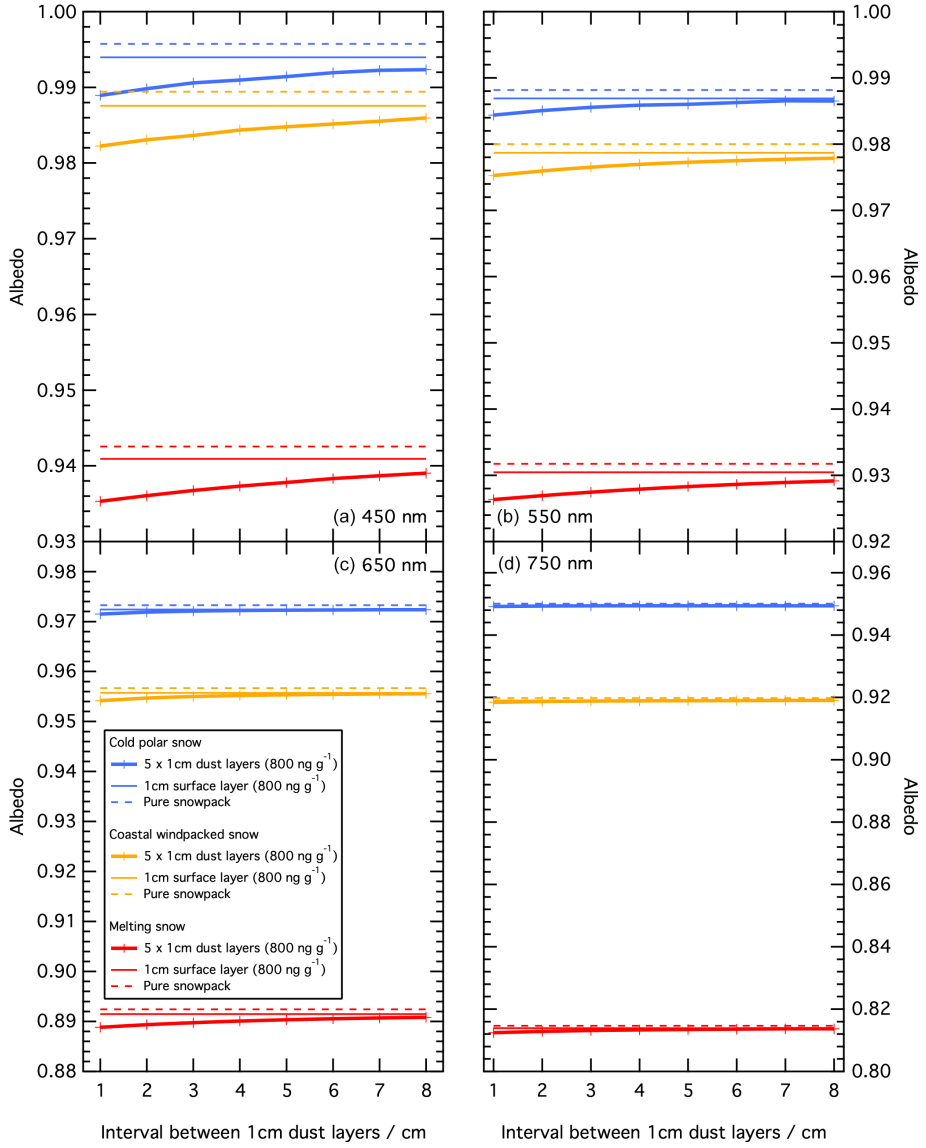

Figure 10. Albedo of three snow types (40 cm thick) containing five layers of 800 ng g^{-1} dust with varying intervals from 1 to 8 cm. The dotted line represents a pure snowpack containing a dust mass ratio of 1 ng g^{-1} of Asian dust. The thin line represents a pure snowpack with a 1 cm thick surface layer containing 800 ng g^{-1} of Asian dust. The thick line and markers represent a pure snowpack with 5 layers each containing 800 ng g^{-1} of Asian dust. The x axis shows the spacing between the 5 layers, varying between 1 and 8 cm.

infrared. At 550 nm, five layers at 1 cm interval containing 800 ng g^{-1} of mineral dust in cold polar snow cause a reduction in albedo of 0.68 % relative to a clean snow pack against only 0.10 % at 750 nm.

4 Discussion

The following discussion provides explanations of the results presented in Sect. 3 and a discussion on the limitations of this study.

4.1 Model uncertainties

4.1.1 Mie calculation

The composition of light-absorbing impurities in polar snow and sea ice has been well characterised (e.g. Flanner et al., 2012; Kumai, 1977; Thompson, 1977; Warren, 1982; Zdanowicz et al., 1998). However, values of the optical properties of dust and volcanic ash aerosols remain scarce. Work has been carried out to measure the phase function (e.g. Dubovik et al., 2002a) scattering matrices (Muñoz, 2004) and brightness temperature (Newman et al., 2012) of mineral aerosols, but, to the knowledge of the authors of this

paper, comprehensive results of wavelength-dependant complex refractive index measurements other than the data presented in this paper are lacking. When presented, refractive index data generally refer to mineral equivalents or weighted combinations of mineral values (Flanner et al., 2007; Derimian et al., 2012). Consequently, the study was limited to a reduced number of sources when choosing appropriate mineral aerosol optical properties presented here as model input parameters. However, variation between the type of mineral aerosol deposits has a limited impact on albedo relative to the effect of variation in the type of snow and sea ice, as discussed in Sect. 4.2. An array of mineral dusts and ashes was selected from plausible geographical sources contributing to the Arctic at present (Pacyna and Ottar, 1989; Zdanowicz et al., 1998; Bory, 2003; VanCuren et al., 2012). More importantly, the selection covers a range of complex refractive indices that can be applied to different study areas. The absorption cross-sections of the selection of mineral aerosols used in this study vary by a factor of ~ 2, allowing the model to be adapted to different areas affected by different types of dust.

In order to calculate the absorption spectrum of the mineral aerosol deposits, Mie scattering theory was used, assuming that the particles were spheres. Dust particles are known to be non-spherical, thus affecting differently the light scattering properties (Mishchenko et al., 1995, 1999; Dubovik et al., 2002b). Studies have focused on non-spherical particles in Mie theory (e.g. Purcell and Pennypacker, 1973), but due to the complexity of the interaction of light with multiple shapes, its modelling is very challenging (Nousiainen, 2009), and approximations have to be made. However, it is possible to calculate a relative change in absorption cross-section if a spherical Mie scattering particle is morphed into a needle or a disk. Bohren and Huffman (1983) proposed three equations for extreme forms of ellipsoids (spheres, needles and disks) allowing for the representation of the shapes found in mineral aerosols. Needles may correspond to glass shards found in volcanic ash (Johnson et al., 2012), and dust particles take on a variety of shapes amongst which flat disks can be observed (Mishra and Tripathi, 2008). At 550 nm the absorption cross-section for the volcanic ash may increase by a factor of ~ 1.20 for needles and ~ 1.53 for disks. The absorption cross-section for the dusts may increase by a factor of ~ 1.21 for needles and ~ 1.56 for disks. Whilst the shape of needles, disks and spheres is probably too limited to describe mineral particles, consideration of the particle morphology allows the magnitude of the effect of morphology to be estimated. The calculation is dependant on the refractive index of particles but the change in shape would be expected to cause a larger change to the absorption cross-section than the small difference in refractive index between the particles. The effect being multiplicative, the percentage of change in values can be applied to the mass ratio values in the relative change in albedo (see Figs. 6 and 7) to correct for shape effects. The variations related to particle shape were not considered in this study, but a typical uncertainty is a factor of ~ 1.5.

Whilst calculating the absorption cross section of mineral aerosol deposits using Mie theory, assumptions had to be made to include the impurities in the snow or sea ice. The particles can be considered either in or on the snow grains constituting the snowpack, and in sea ice, the particles can either be located in the ice or in the brine (Chýlek et al., 1983). The refractive index of air was used as a surrounding medium for particles in snow, considering that the impurities are external to the snow. In the case of sea ice, the values of pure ice from Warren and Brandt (2008) were used. The distribution of mineral contaminants in sea ice varies with depth and temperature, making it difficult to characterise their surrounding medium. After comparing cross-section absorption values of dust in brine (Maykut and Light, 1995) and in pure ice, the difference was considered to be negligible, with a relative change of 0.1 % between the two.

4.1.2 Snowpack or sea ice thickness

When modelling the albedo of semi-infinite and realistic thicknesses of snow and sea ice, the mineral dust was assumed to be uniformly distributed throughout the snow and sea ice. Such an assumption does not account for the layering effect observed in field measurements, but represents a mean value, easily applicable to a vast spatial extent. Layering effects were studied in Sect. 3.3 by looking at a surface layer and multiple buried layers. Although the configurations used here do not cover all the possibilities found in the field, this study presents an overview of an effect previously unquantified and can be adapted to particular scenarios.

Snow or sea ice thickness is an essential parameter in the calculation of albedo. It is also difficult to quantify, due to temporal and spatial heterogeneity. Sea ice has varying surface conditions, associated with depths ranging from 0 to over 10 m at pressure ridges (Perovich, 1996). A detailed study would require individual cases with different layers of sea ice and associated thicknesses. Where snow is typically sufficiently optically thick to produce general results, this is not the case for sea ice. Therefore, a range of sea ice types (first-year sea ice, multi-year sea ice and melting sea ice) and their associated depths was produced in this study. To calculate the relative change in albedo with an increasing mass ratio of mineral aerosol deposits (Fig. 6) and the effects of different types of mineral dusts and volcanic ashes (Fig. 4), thickness values large enough to guarantee a semi-infinite medium were used, allowing for the fair comparison of the effects of mineral aerosol deposits on the albedo of each type of snow and sea ice. When accounting for realistic thicknesses in Fig. 7, typical depths found in the literature were picked. The selection of depths used in this study are considered to be representative and the results can be calculated for any given thickness using the method presented in Sect. 2.

The modelling presented here has several limitations. In this study, the combination of different types of absorbing impurities that can be found in the Arctic, such as soot, HULIS, or black carbon (Marks and King, 2013; Warren and Clarke, 1990) was not considered. However, Marks and King (2014) have modelled the effects of black carbon in similar types of snow and sea ice to the ones used here and the effects of soot have been considered by Warren and Clarke (1990). Organic debris and algae, that have an effect on albedo (Grenfell, 1991) and may have been observed in field data (France et al., 2012), were not examined in this study. Indeed, light-absorbing impurities other than the mineral aerosol deposits described in Sect. 2.2 were not considered. In the case of studies considering multiple light-absorbing impurities in the snow or sea ice, France et al. (2012) demonstrated how to separate the effects of different light-absorbing impurities from black carbon for snow on sea ice.

4.1.3 Asymmetry parameter

The asymmetry parameter, g, was one of the parameters used to describe the snow and sea ice. A fixed value of 0.95 for sea ice and 0.89 for snow were determined, based on the values presented by France et al. (2012) and Marks and King (2013). In the two papers, g was held constant and σ_{scatt} and σ_{abs}^{+} varied, based on the methods of Lee Taylor and Madronich (2002). Libois et al. (2014) advocate the use of a value of $g = 0.86$ when modelling snow. To gauge the effects of the value of g on albedo, the scattering and absorption coefficients of the cold polar snow and the melting snow were recalculated from albedo and e-folding depth data, using the optical properties in Table 1. The calculations for the effects of Saharan dust were then repeated with the value of g recommended by Libois et al. (2014). The difference in albedo between $g = 0.89$ and $g = 0.86$ was of 0.006 % for a cold polar snowpack containing $10\,\text{ng}\,\text{g}^{-1}$ of Saharan dust, 0.009 % for $100\,\text{ng}\,\text{g}^{-1}$ and 0.18 % for $10\,000\,\text{ng}\,\text{g}^{-1}$ and 0.01 % for a melting snowpack containing $10\,\text{ng}\,\text{g}^{-1}$ of Saharan dust, 0.02 % for $100\,\text{ng}\,\text{g}^{-1}$ and 0.93 % for $10\,000\,\text{ng}\,\text{g}^{-1}$. Therefore, the results presented in this study have been produced without updating the asymmetry parameter g.

4.2 Effect of mineral aerosol deposits on snow and sea ice

Much larger mass ratios of mineral aerosol deposits are necessary to induce a change in albedo, in comparison with black carbon or soot. In a similar modelling study, Marks and King (2014) found that for a wavelength of 550 nm, $10\,\text{ng}\,\text{g}^{-1}$ of black carbon evenly distributed throughout semi-infinite sea ice causes a 22.9 % change in albedo relative to a clean medium for first-year sea ice, 11.2 % for multi-year sea ice and 37.6 % for melting sea ice. To achieve the same change, a mass ratio between 1083 and $1197\,\text{ng}\,\text{g}^{-1}$ of Asian dust would be necessary. However, larger mass ratios of dust are found in polar snow and sea ice, with seasonal deposition events (Zdanowicz et al., 1998).

The calculations of the albedo of snow and sea ice in relation to different types of mineral aerosol deposits commonly found in the Arctic enabled the comparison between types of contaminants and between the different snow and sea ice types. The change in albedo induced by different types of snow or sea ice is greater than the type of mineral. The results obtained here show that snow and sea ice with a smaller scattering cross-section are more sensitive to the effects of mineral aerosol deposits on the albedo, confirming the work of Marks and King (2014), who quantified the phenomenon for the same snow and sea ice types.

The wavelength-dependant effects of mineral aerosol deposits on albedo are similar to black carbon. The results of this study present a good agreement with the work of Warren and Wiscombe (1980). Indeed, the absorbing aerosol deposits mainly affect shortwave radiation. In the infrared, mineral aerosol deposits barely influence the albedo of snow and sea ice, as described by Warren and Wiscombe (1980) and Carmagnola et al. (2013). The effect of mineral aerosol deposits becoming smaller at larger wavelengths can be explained by the increasing absorption by the ice that exceeds absorption by mineral aerosol deposits.

4.3 Comparison with SNICAR-online

The results of this modelling study were compared with the output of the SNICAR-online model. The two models are in agreement when the same mineral aerosol deposits in the snow are used. The volcanic ash in the model from Flanner et al. (2007) was derived from measurements of Mt. St. Helens eruption (Patterson, 1981), corresponding to the light grey sample of Mt. St. Helens ash used in this study. The difference in the results for mineral dust can be explained by the use of a different type of dust as input. SNICAR-online uses a combination of indices of refraction of quartz, limestone, montmorillonite, illite and hematite (Flanner et al., 2007), whereas the work presented here uses the refractive indices of real dust sources, which are more representative of the aerosols present in the atmosphere. Nevertheless, the difference in albedo for high loadings of different dusts shows the importance of the mineral aerosol type at extreme loadings. The comparison between the two models for other types of mineral aerosol deposits, sea ice or layers was not possible, as the features are not present in SNICAR-online.

In Fig. 9, the relative change in albedo with an increasing surface layer of mineral dust can be fitted with a linear regression. However, the relative change in albedo for media containing a uniform loading throughout is not linear. For small changes in albedo, the relationship between fractional change in albedo and dust mass ratio is approximately linear. Although the loading is important in the surface layer, the total amount of mineral aerosol deposit is small compared to

a snow or ice pack with an even loading of mineral aerosol deposits.

The effect of dust layers varies significantly depending on their vertical location and distribution of the dust layers. An increasing surface layer thickness only causes a small change, as seen in Fig. 9. At visible wavelengths, the effect of multiple layers of dust distributed through the snowpack has a significant effect on the reduction of albedo. A 1 cm thick layer containing the same mass ratio as the individual buried layers was placed on the snow surface (Fig. 10) to compare with the role of the buried layers. Even when spaced out with 8 cm intervals, the buried layers caused a 0.0034 reduction in albedo at 450 nm for cold polar snow where a 1 cm surface layer caused a change in albedo of 0.0017. For comparison, the same mass evenly spread out through the snowpack causes a decrease of 0.0012 in albedo compared to a clean snowpack. Dust layers within snowpacks are typically greater than 8 cm (e.g. Zdanowicz et al., 1998; Osada et al., 2004; Dong et al., 2013) and inspection of Fig. 10 shows that as the distance between the layers increases, the difference between the albedo of the layered snowpack and the snowpack containing a single surface layer becomes small. Therefore as a first approximation, layer thicknesses significantly greater than 8 cm may be neglected.

5 Conclusions

The response of the albedo of snow and sea ice to mineral aerosol deposits is more sensitive to the type of snow or sea ice than to the properties of the mineral aerosol deposits themselves. Radiative-transfer calculations show that the albedo of melting sea ice is more responsive to mineral aerosol deposits than snow or first/multi-year sea ice. However, larger mass ratios of mineral aerosol deposits than what is found in nature are needed to induce a significant change in albedo, even for the more responsive melting sea ice. These higher mass ratios are more likely to be deposited by storm events on snowpacks thus forming alternating layers of polluted and pure snow. The thickness of a surface layer has surprisingly little effect on albedo, whereas multiple layers buried in snow have a larger impact than a uniform mixing throughout the snowpack. Amongst the different snow and sea ice types investigated, a melting medium is more affected by the radiative forcing of mineral aerosol deposits. The time of year associated with these snow and sea ice cover implies that solar radiation is at its strongest, creating positive feedback and accelerating the melting process further.

So far, few studies have focussed on the impact of mineral aerosol deposits, giving more importance to black carbon and soot. This study demonstrates that the effects of natural pollutants need to be taken into account when investigating albedo reduction in the Arctic. Therefore, the community studying global climate change can use Fig. 6 as an input in general circulation models with very little computational effort, further reducing uncertainties.

Acknowledgements. MDK and MLL thank NERC for support under Grant NE/K000770X/1 and NERC FSF (555.0608).

Edited by: J. Huang

References

Aoki, T., Aoki, T., Fukabori, M., Tachibana, Y., Zaizen, Y., Nishio, F., and Oishi, T.: Spectral albedo observation on the snow field at Barrow, Alaska, Polar Meteorol. Glaciol., 12, 1–9, 1998.

Balkanski, Y., Schulz, M., Claquin, T., and Guibert, S.: Reevaluation of Mineral aerosol radiative forcings suggests a better agreement with satellite and AERONET data, Atmos. Chem. Phys., 7, 81–95, doi:10.5194/acp-7-81-2007, 2007.

Barry, R. G., Serreze, M. C., Maslanik, J. A., and Preller, R. H.: The Arctic Sea Ice-Climate System: Observations and modeling, Rev. Geophys., 31, 397–422, 1993.

Bohren, C. F. and Huffman, D. R.: Absorption and Scattering of Light by Small Particles, John Wiley & Sons, Weinheim, Germany, 1983.

Bory, A. J. M.: Two distinct seasonal Asian source regions for mineral dust deposited in Greenland (NorthGRIP), Geophys. Res. Lett., 30, 1167, doi:10.1029/2002GL016446, 2003.

Bourke, R. H. and Garrett, R. P.: Sea ice thickness distribution in the Arctic Ocean, Cold Reg. Sci. Technol., 13, 259–280, 1987.

Buckley, R. G. and Trodahl, H. J.: Thermally driven changes in the optical properties of sea ice, Cold Reg. Sci. Technol., 14, 201–204, 1987.

Carmagnola, C. M., Domine, F., Dumont, M., Wright, P., Strellis, B., Bergin, M., Dibb, J., Picard, G., Libois, Q., Arnaud, L., and Morin, S.: Snow spectral albedo at Summit, Greenland: measurements and numerical simulations based on physical and chemical properties of the snowpack, The Cryosphere, 7, 1139–1160, doi:10.5194/tc-7-1139-2013, 2013.

Chýlek, P., Ramaswamy, V., and Srivastava, V.: Albedo of soot-contaminated snow, J. Geophys. Res.-Atmos., 88, 10837–10843, 1983.

Clarke, A. D. and Noone, K. J.: Soot in the Arctic snowpack: A cause for perturbations in radiative transfer, Atmos. Environ., 19, 2045–2053, 1985.

Conway, H., Gades, A., and Raymond, C. F.: Albedo of dirty snow during conditions of melt, Water Resour. Res., 32, 1713–1718, 1996.

Curry, J. A., Schramm, J. L., and Ebert, E. E.: Sea Ice-Albedo Climate Feedback Mechanism, J. Climate, 8, 240–247, 1995.

Dang, C., Brandt, R. E., and Warren, S. G.: Parameterizations for narrowband and broadband albedo of pure snow and snow containing mineral dust and black carbon, J. Geophys. Res.-Atmos., 120, 5446–5468, doi:10.1002/2014JD022646, 2015.

Derimian, Y., Dubovik, O., Tanre, D., Goloub, P., Lapyonok, T., and Mortier, A.: Optical properties and radiative forcing of the Eyjafjallajökull volcanic ash layer observed over Lille, France, in 2010, J. Geophys. Res.-Atmos., 117, D00U25, doi:10.1029/2011JD016815, 2012.

Doherty, S. J., Warren, S. G., Grenfell, T. C., Clarke, A. D., and Brandt, R. E.: Light-absorbing impurities in Arctic snow, Atmos. Chem. Phys., 10, 11647–11680, doi:10.5194/acp-10-11647-2010, 2010.

Dong, Z., Li, Z., Wang, W., Li, K., and Zhou, P.: Characteristics of atmospheric dust deposition in snow on Glacier No. 4, Mt Bogeda, China, Environ. Earth Sci., 70, 1423–1433, doi:10.1007/s12665-013-2228-z, 2013.

Dong, Z., Qin, D., Kang, S., Ren, J., Chen, J., Cui, X., Du, Z., and Qin, X.: Physicochemical characteristics and sources of atmospheric dust deposition in snow packs on the glaciers of western Qilian Mountains, China, Tellus B, 66, 20956, doi:10.3402/tellusb.v66.20956, 2014.

Dubovik, O., Holben, B., Eck, T. F., Smirnov, A., Kaufman, Y. J., King, M. D., Tanré, D., and Slutsker, I.: Variability of absorption and optical properties of key aerosol types observed in worldwide locations, J. Atmos. Sci., 59, 590–608, doi:10.1175/1520-0469(2002)059<0590:VOAAOP>2.0.CO;2, 2002a.

Dubovik, O., Holben, B., Lapyonok, T., Sinyuk, A., Mishchenko, M., Yang, P., and Slutsker, I.: Non-spherical aerosol retrieval method employing light scattering by spheroids, Geophys. Res. Lett., 29, 54-1–54-4, doi:10.1029/2001GL014506, 2002b.

Fischer, H., Siggaard-Andersen, M.-L., Ruth, U., Röthlisberger, R., and Wolff, E.: Glacial/interglacial changes in mineral dust and sea-salt records in polar ice cores: Sources, transport, and deposition, Rev. Geophys., 45, RG1002, doi:10.1029/2005RG000192, 2007.

Flanner, M. G., Zender, C. S., Randerson, J. T., and Rasch, P. J.: Present-day climate forcing and response from black carbon in snow, J. Geophys. Res.-Atmos., 112, D11202, doi:10.1029/2006JD008003, 2007.

Flanner, M. G., Zender, C. S., Hess, P. G., Mahowald, N. M., Painter, T. H., Ramanathan, V., and Rasch, P. J.: Springtime warming and reduced snow cover from carbonaceous particles, Atmos. Chem. Phys., 9, 2481–2497, doi:10.5194/acp-9-2481-2009, 2009.

Flanner, M. G., Liu, X., Zhou, C., Penner, J. E., and Jiao, C.: Enhanced solar energy absorption by internally-mixed black carbon in snow grains, Atmos. Chem. Phys., 12, 4699–4721, doi:10.5194/acp-12-4699-2012, 2012.

France, J. L., King, M. D., Frey, M. M., Erbland, J., Picard, G., Preunkert, S., MacArthur, A., and Savarino, J.: Snow optical properties at Dome C (Concordia), Antarctica; implications for snow emissions and snow chemistry of reactive nitrogen, Atmos. Chem. Phys., 11, 9787–9801, doi:10.5194/acp-11-9787-2011, 2011a.

France, J. L., King, M., Lee-Taylor, J., Beine, H. J., Ianniello, A., Domine, F., and MacArthur, A.: Calculations of in-snow NO2 and OH radical photochemical production and photolysis rates: A field and radiative-transfer study of the optical properties of Arctic (Ny-Alesund, Svalbard) snow, J. Geophys. Res., 116, F04013, doi:10.1029/2011JF002019, 2011b.

France, J. L., Reay, H. J., King, M. D., Voisin, D., Jacobi, H. W., Domine, F., Beine, H., Anastasio, C., MacArthur, A., and Lee-Taylor, J.: Hydroxyl radical and NOx production rates, black carbon concentrations and light-absorbing impurities in snow from field measurements of light penetration and nadir reflectivity of onshore and offshore coastal Alaskan snow, J. Geophys. Res.-Atmos., 117, D00R12, doi:10.1029/2011JD016639, 2012.

Fratini, G., Ciccioli, P., Febo, A., Forgione, A., and Valentini, R.: Size-segregated fluxes of mineral dust from a desert area of northern China by eddy covariance, Atmos. Chem. Phys., 7, 2839–2854, doi:10.5194/acp-7-2839-2007, 2007.

Ginoux, P., Garbuzov, D., and Hsu, N. C.: Identification of anthropogenic and natural dust sources using Moderate Resolution Imaging Spectroradiometer (MODIS) Deep Blue level 2 data, J. Geophys. Res.-Atmos., 115, D05204, doi:10.1029/2009JD012398, 2010.

Grenfell, T. C.: A radiative transfer model for sea ice with vertical structure variations, J. Geophys. Res.-Atmos., 96, 16991–17001, 1991.

Grenfell, T. C. and Makyut, G. A.: The optical properties of ice and snow in the Arctic Basin, J. Glaciol., 18, 445–463, 1977.

Grenfell, T. C. and Perovich, D. K.: Spectral albedos of sea ice and incident solar irradiance in the southern Beaufort Sea, J. Geophys. Res.-Atmos., 89, 3573–3580, 1984.

Grenfell, T. C., Light, B., and Sturm, M.: Spatial distribution and radiative effects of soot in the snow and sea ice during the SHEBA experiment, J. Geophys. Res.-Atmos., 107, SHE 7-1–SHE 7-7, doi:10.1029/2000JC000414, 2002.

Hanesiak, J. M., Barber, D. G., De Abreu, R. A., and Yackel, J. J.: Local and regional albedo observations of arctic first-year sea ice during melt ponding, J. Geophys. Res.-Atmos., 106, 1005–1016, 2001.

Hess, M., Koepke, P., and Schult, I.: Optical Properties of Aerosols and Clouds: The Software Package OPAC, B. Am. Meteorol. Soc., 79, 831–844, 1998.

Huang, J., Fu, Q., Zhang, W., Wang, X., Zhang, R., Ye, H., and Warren, S. G.: Dust and Black Carbon in Seasonal Snow Across Northern China, B. Am. Meteorol. Soc., 92, 175–181, doi:10.1175/2010BAMS3064.1, 2011.

Jacobson, M. Z.: Climate response of fossil fuel and biofuel soot, accounting for soot's feedback to snow and sea ice albedo and emissivity, J. Geophys. Res.-Atmos., 109, D21201, doi:10.1029/2004JD004945, 2004.

Johnson, B., Turnbull, K., Brown, P., Burgess, R., Dorsey, J., Baran, A. J., Webster, H., Haywood, J., Cotton, R., Ulanowski, Z., Hesse, E., Woolley, A., and Rosenberg, P.: In situ observations of volcanic ash clouds from the FAAM aircraft during the eruption of Eyjafjallajökull in 2010, J. Geophys. Res., 117, D00U24, doi:10.1029/2011JD016760, 2012.

Koerner, R. M.: Distribution of microparticles in a 299-m core through the Devon Island ice cap, Northwest Territories, Canada, Int. Assoc. Hydrol. Sci., 118, 371–376, 1977.

Kohler, J., Brandt, O., Johansson, M., and Callaghan, T.: A long-term Arctic snow depth record from Abisko, northern Sweden, 1913–2004, Polar Res., 25, 91–113, 2006.

Kumai, M.: Electron microscope analysis of aerosols in snow and deep ice cores from Greenland, Isotopes and Impurities in Snow and Ice, IAHS Publ., 118, 341–349, 1977.

Langleben, M. P.: Albedo and degree of puddling of a melting cover of sea ice, J. Glaciol., 8, 407–412, 1969.

Langleben, M. P.: Albedo Of Melting Sea Ice in the Southern Beaufort Sea, J. Glaciol., 10, 101–104, 1971.

Laven, P.: MiePlot: a computer program for scattering of light from a sphere using Mie theory & the Debye series, PhilipLaven. com, 10, 2006.

Lawrence, C. R. and Neff, J. C.: The contemporary physical and chemical flux of aeolian dust: A synthesis of direct measurements of dust deposition, Chem. Geol., 267, 46–63, 2009.

Laxon, S., Peacock, N., and Smith, D.: High interannual variability of sea ice thickness in the Arctic region, Nature, 425, 947–950, 2003.

Lee Taylor, J. and Madronich, S.: Calculation of actinic fluxes with a coupled atmosphere–snow radiative transfer model, J. Geophys. Res.-Atmos., 107, ACH 22–1–ACH 22–10, 2002.

Libois, Q., Picard, G., Dumont, M., Arnaud, L., Sergent, C., Pougatch, E., Sudul, M., and Vial, D.: Experimental determination of the absorption enhancement parameter of snow, J. Glaciol., 60, 714–724, 2014.

Light, B., Eicken, H., Maykut, G. A., and Grenfell, T. C.: The effect of included participates on the spectral albedo of sea ice, J. Geophys. Res.-Atmos., 103, 27739–27752, 1998.

Marks, A. A. and King, M. D.: The effects of additional black carbon on the albedo of Arctic sea ice: variation with sea ice type and snow cover, The Cryosphere, 7, 1193–1204, doi:10.5194/tc-7-1193-2013, 2013.

Marks, A. A. and King, M. D.: The effect of snow/sea ice type on the response of albedo and light penetration depth (*e*-folding depth) to increasing black carbon, The Cryosphere, 8, 1625–1638, doi:10.5194/tc-8-1625-2014, 2014.

Maykut, G. A. and Light, B.: Refractive-index measurements in freezing sea-ice and sodium chloride brines, Appl. Optics, 34, 950–961, 1995.

Mishchenko, M. I., Lacis, A. A., Carlson, B. E., and Travis, L. D.: Nonsphericity of dust-like tropospheric aerosols: Implications for aerosol remote sensing and climate modeling, Geophys. Res. Lett., 22, 1077–1080, 1995.

Mishchenko, M. I., Hovenier, J. W., and Travis, L. D.: Light Scattering by Nonspherical Particles, Theory, Measurements, and Applications, Academic Press, San Diego, USA, 1999.

Mishra, S. K. and Tripathi, S. N.: Modeling optical properties of mineral dust over the Indian Desert, J. Geophys. Res.-Atmos., 113, D23201, doi:10.1029/2008JD010048, 2008.

Muñoz, O.: Scattering matrices of volcanic ash particles of Mount St. Helens, Redoubt, and Mount Spurr Volcanoes, J. Geophys. Res., 109, D16201, doi:10.1029/2004JD004684, 2004.

Newman, S. M., Clarisse, L., Hurtmans, D., Marenco, F., Johnson, B., Turnbull, K., Havemann, S., Baran, A. J., O'Sullivan, D., and Haywood, J.: A case study of observations of volcanic ash from the Eyjafjallajökull eruption: 2. Airborne and satellite radiative measurements, J. Geophys. Res., 117, D00U13, doi:10.1029/2011JD016780, 2012.

Nousiainen, T.: Optical modeling of mineral dust particles: A review, J. Quant. Spectr. Ra., 110, 1261–1279, 2009.

Osada, K., Iida, H., Kido, M., Matsunaga, K., and Iwasaka, Y.: Mineral dust layers in snow at Mount Tateyama, Central Japan: formation processes and characteristics, Tellus B, 56, 382–392, doi:10.1111/j.1600-0889.2004.00108.x, 2004.

Pacyna, J. M. and Ottar, B.: Origin of natural constituents in the Arctic aerosol, Atmos. Environ., 23, 809–815, 1989.

Painter, T. H., Skiles, S., Deems, J. S., and Bryant, A. C.: Dust radiative forcing in snow of the Upper Colorado River Basin: 1. A 6 year record of energy balance, radiation, and dust concentrations, Water Resour. Res., 48, W07521, doi:10.1029/2012WR011985, 2012.

Painter, T. H., Barrett, A. P., Landry, C. C., Neff, J. C., Cassidy, M. P., Lawrence, C. R., McBride, K. E., and Farmer, G. L.: Impact of disturbed desert soils on duration of mountain snow cover, Geophys. Res. Lett., 34, L12502, doi:10.1029/2007GL030284, 2007.

Patterson, E. M.: Measurements of the Imaginary Part of the Refractive Index Between 300 and 700 Nanometers for Mount St. Helens Ash, Science, 211, 836–838, 1981.

Patterson, E. M. and Gillette, D. A.: Complex index of refraction between 300 and 700 nm for Saharan aerosols, J. Geophys. Res., 82, 3153–3160, 1977.

Perovich, D. K.: The Optical Properties of Sea Ice, Monograph 96-1, US Cold Reg. Res. and Eng. Lab., Philadelphia, USA, 1996.

Perovich, D. K., Maykut, G. A., and Grenfell, T. C.: Optical Properties Of Ice And Snow In The Polar Oceans. I: Observations, 1986 Technical Symposium Southeast, 7 August 1986, Orlando, USA, 0637, 232–241, 1986.

Perovich, D. K., Roesler, C. S., and Pegau, W. S.: Variability in Arctic sea ice optical properties, J. Geophys. Res.-Oceans, 103, 1193–1208, 1998.

Prospero, J. M., Ginoux, P., Torres, O., Nicholson, S. E., and Gill, T. E.: Environmental characterization of global sources of atmospheric soil dust identified with the Nimbus 7 Total Ozone Mapping Spectrometer (TOMS) absorbing aerosol product, Rev. Geophys., 40, 2-1–2-31, 2002.

Purcell, E. M. and Pennypacker, C. R.: Scattering and absorption of light by nonspherical dielectric grains, Astrophys. J., 186, 705–714, 1973.

Ram, M. and Gayley, R. I.: Long-range transport of volcanic ash to the Greeland ice sheet, Nature, 349, 401–404, 1991.

Reay, H. J., France, J. L., and King, M. D.: Decreased albedo, e-folding depth and photolytic OH radical and NO_2 production with increasing black carbon content in Arctic snow, J. Geophys. Res.-Atmos., 117, D00R20, doi:10.1029/2011JD016630, 2012.

Sarna-Wojcicki, A. M., Shipley, S., Waitt Jr., R. B., and Dzurisin, D.: Areal distribution, thickness, mass, volume, and grain size of air-fall ash from the six major eruptions of 1980, U.S. Geol. Surv. Prof. Pap., 1250, 577–600, 1981.

Schwikowski, M., Seibert, P., Baltensperger, U., and Gaggeler, H. W.: A study of an outstanding Saharan dust event at the high-alpine site Jungfraujoch, Switzerland, Atmos. Environ., 29, 1829–1842, 1995.

Serreze, M. C. and Barry, R. G.: The Arctic Climate System, Cambridge Atmospheric and Space Science Series Publisher Cambridge University Press, Cambridge, UK, ISBN 0521116007, 9780521116008, 404 pp., 2005.

Shaw, G. E.: Microparticle size spectrum of Arctic haze, Geophys. Res. Lett., 11, 409–412, 1984.

Sokolik, I. and Toon, O. B.: Modeling the radiative characteristics of airborne mineral aerosols at infrared wavelenghts, J. Geophys. Res., 103, 8813–8826, 2007.

Sokolik, I., Andronova, A., and Johnson, T. C.: Complex refractive index of atmospheric dust aerosols, Atmos. Environ. Part A General Topics, 27, 2495–2502, 1993.

Stamnes, K., Tsay, S.-C., Wiscombe, W., and Jayaweera, K.: Numerically stable algorithm for discrete-ordinate-method radiative transfer in multiple scattering and emitting layered media, Appl. Optics, 27, 2502–2509, 1988.

Stone, R. S., Key, J. R., and Dutton, E. G.: Properties and decay of stratospheric aerosols in the Arctic following the 1991 eruptions of Mount Pinatubo, Geophys. Res. Lett., 20, 2359–2362, 1993.

Tegen, I. and Fung, I.: Modeling of mineral dust in the atmosphere: Sources, transport, and optical thickness, J. Geophys. Res.-Atmos., 99, 22897–22914, 1994.

Thompson, L.: Variations in microparticle concentration, size distribution and elemental composition found in Camp Century, Greenland, and Byrd station, Antarctica, deep ice cores, in: Proceedings of symposium on isotopes and impurities in snow and ice, International Association of Hydrological Sciences, Commission of snow and ice, I.U.G.G., XVI, General Assembly, Grenoble, France, August–September 1975, Washington DC, USA, 351–363, 1977.

Thorsteinsson, T., Johannsson, T., Stohl, A., and Kristiansen, N. I.: High levels of particulate matter in Iceland due to direct ash emissions by the Eyjafjallajokull eruption and resuspension of deposited ash, J. Geophys. Res.-Solid Earth, 117, B00C05, doi:10.1029/2011JB008756, 2012.

Toon, O. B., McKay, C. P., Ackerman, T. P., and Santhanam, K.: Rapid calculation of radiative heating rates and photodissociation rates in inhomogeneous multiple scattering atmospheres, J. Geophys. Res.-Atmos., 94, 16287–16301, 1989.

Turnbull, K., Johnson, B., Marenco, F., Haywood, J., Minikin, A., Weinzierl, B., Schlager, H., Schumann, U., Leadbetter, S., and Woolley, A.: A case study of observations of volcanic ash from the Eyjafjallajökull eruption: 1. In situ airborne observations, J. Geophys. Res., 117, D00U12, doi:10.1029/2011JD016688, 2012.

VanCuren, R. A., Cahill, T., Burkhart, J., Barnes, D., Zhao, Y., Perry, K., Cliff, S., and McConnell, J.: Aerosols and their sources at Summit Greenland – First results of continuous size- and time-resolved sampling, Atmos. Environ., 52, 82–97, 2012.

Wang, X., Doherty, S. J., and Huang, J.: Black carbon and other light-absorbing impurities in snow across Northern China, J. Geophys. Res.-Atmos., 118, 1471–1492, doi:10.1029/2012JD018291, 2013.

Warren, S. G.: Optical properties of snow, Rev. Geophys., 20, 67–89, 1982.

Warren, S. G.: Impurities in snow: effects on albedo and snow melt (Review), Ann. Glaciol., 5, 177–179, 1984.

Warren, S. G. and Brandt, R. E.: Optical constants of ice from the ultraviolet to the microwave: A revised compilation, J. Geophys. Res.-Atmos., 113, D14220, doi:10.1029/2007JD009744, 2008.

Warren, S. G. and Clarke, A. D.: Soot in the atmosphere and snow surface of Antarctica, J. Geophys. Res.-Atmos., 95, 1811–1816, 1990.

Warren, S. G. and Wiscombe, W. J.: A Model for the Spectral Albedo of Snow. II: Snow Containing Atmospheric Aerosols, J. Atmos. Sci., 37, 2734–2745, 1980.

Warren, S. G., Rigor, I. G., and Untersteiner, N.: Snow depth on Arctic sea ice, J. Climate, 12, 1814–1828, 1999.

Weeks, W.: On Sea Ice, University of Alaska Press, Fairbanks, Alaska, USA, 2010.

Westphal, D. L., Toon, O. B., and Carlson, T. N.: A two-dimensional numerical investigation of the dynamics and microphysics of Saharan dust storms, J. Geophys. Res.-Atmos., 92, 3027–3049, 1987.

Wiscombe, W. J. and Warren, S. G.: A Model for the Spectral Albedo of Snow. I: Pure Snow, J. Atmos. Sci., 37, 2712–2733, 1980.

Woo, M.-K. and Dubreuil, M.-A.: Empirical relationship between dust content and Arctic snow albedo, Cold Reg. Sci. Technol., 10, 125–132, 1985.

Yasunari, T. J., Lau, K. M., Mahanama, S., and Colarco, P. R.: The GOddard SnoW Impurity Module (GOSWIM) for the NASA GEOS-5 Earth System Model: Preliminary Comparisons with Observations in Sapporo, Japan, SOLA, 2014.

Ye, H., Zhang, R., Shi, J., Huang, J., Warren, S. G., and Fu, Q.: Black carbon in seasonal snow across northern Xinjiang in northwestern China, Environ. Res. Lett., 7, 044002, doi:10.1088/1748-9326/7/4/044002, 2012.

Young, C. L., Sokolik, I. N., and Dufek, J.: Regional radiative impact of volcanic aerosol from the 2009 eruption of Mt. Redoubt, Atmos. Chem. Phys., 12, 3699–3715, doi:10.5194/acp-12-3699-2012, 2012.

Zdanowicz, C. M., Zielinski, G. A., and Wake, C. P.: Characteristics of modern atmospheric dust deposition in snow on the Penny Ice Cap, Baffin Island, Arctic Canada, Tellus B, 50, 506–520, 1998.

Zhang, R., Hegg, D. A., Huang, J., and Fu, Q.: Source attribution of insoluble light-absorbing particles in seasonal snow across northern China, Atmos. Chem. Phys., 13, 6091–6099, doi:10.5194/acp-13-6091-2013, 2013.

Zhao, C., Hu, Z., Qian, Y., Ruby Leung, L., Huang, J., Huang, M., Jin, J., Flanner, M. G., Zhang, R., Wang, H., Yan, H., Lu, Z., and Streets, D. G.: Simulating black carbon and dust and their radiative forcing in seasonal snow: a case study over North China with field campaign measurements, Atmos. Chem. Phys., 14, 11475–11491, doi:10.5194/acp-14-11475-2014, 2014.

Zielinski, G. A., Mayewski, P. A., Meeker, L. D., Grönvold, K., Germani, M. S., Whitlow, S., Twickler, M. S., and Taylor, K.: Volcanic aerosol records and tephrochronology of the Summit, Greenland, ice cores, J. Geophys. Res.-Oceans, 102, 26625–26640, 1997.

Chapter 4

Optical properties of laboratory grown sea ice doped with light absorbing impurities (black carbon)

Citation:
Marks, A., Lamare, M. L., & King, M. D. (2017). Optical properties of laboratory grown sea ice doped with light absorbing impurities (black carbon). The Cryosphere Discussions. In review: accepted for publication.

Author contributions:
Lamare, M. did the integrating sandwich spectrometer experiments, acquired the SEM images, calculated the size distribution for the black carbon particles, and wrote section 2.3.2.

Marks, A. did the reflectance and *e*-folding depth measurements in the sea ice laboratory, performed the radiative-transfer calculations, and was the main author of the paper.

King, M.D. oversaw the study, and proof-read the paper.

Optical properties of sea ice doped with black carbon- An experimental and radiative-transfer modelling comparison

Amelia A. Marks[1], Maxim L. Lamare[1], and Martin D. King[1]

[1]Department of Earth Sciences, Royal Holloway University of London, Egham, Surrey, TW20 0EX, UK.

Correspondence to: Martin King (M.King@rhul.ac.uk)

Abstract.

Radiative-transfer calculations of the light reflectivity and extinction coefficient in laboratory generated sea ice doped with and without black carbon demonstrate that the radiative transfer model TUV-snow can be used to predict the light reflectance and extinction coefficient as a function of wavelength. The sea ice is representative of first year sea ice containing typical amounts of black carbon and other light absorbing impurities. The experiments give confidence in the application of the model to predict albedo of other sea ice fabrics.

Sea ices, ∼30 cm thick, were generated in the Royal Holloway Sea Ice Simulator (∼2000 L tanks) with scattering cross-sections measured between 0.012 and 0.032 m^2 kg^{-1} for four ices. Sea ices were generated with and without ∼5 cm upper layers containing particulate black carbon. Nadir reflectances between 0.60 and 0.78 where measured along with extinction coefficients of 0.1 to 0.03 cm^{-1} (*e*-folding depths of 10–30 cm) at a wavelength of 500 nm. Values were measured between light wavelengths of 350 and 650 nm. The sea ices generated in the Royal Holloway Sea Ice Simulator were found to be representative of natural sea ices.

Particulate black carbon at mass ratios of ∼75, ∼150 and ∼300 ng g^{-1} in a 5 cm ice layer lowers the albedo to 97%, 90%, and 79% of the reflectivity of an undoped "clean" sea ice (at a wavelength of 500 nm).

1 Introduction

Rapid decline of sea ice in the Arctic is often seen as a bellwether for modern day climate change (e.g. IPCC (2013)). Model predictions of future sea ice extent have a large degree of uncertainty (e.g. IPCC (2013)). Accurate representation and recreation of the optical and physical properties of sea ice is essential to develop accurate models of sea ice. The Royal Holloway (RHUL) Sea Ice Simulator facility aims to create a realistic sea ice within a controlled environment with the ability to monitor both the physical (temperature, salinity and density) and optical (nadir reflectivity and extinction coefficient) properties of the sea ice. The results from which can be used to evaluate sea ice models.

The following study presents the first data from the RHUL sea ice simulator used to validate the Tropospheric ultraviolet and visible (TUV)-snow radiative-transfer model for use with sea ice. The TUV-snow model is a coupled atmosphere-snow radiative-transfer model, described in detail by Lee-Taylor and Madronich (2002). The model has been used multiple times for investigations of radiative-transfer in snow (e.g. King et al. (2005), France et al. (2011), France et al. (2012), Reay et al.

(2012)) and has also been adapted for use with sea ice (e.g. King et al. (2005), Marks and King (2013), Marks and King (2014) and Lamare et al. (2016)). The model has previously been experimentally validated for photochemistry in snow by Phillips and Simpson (2005) but it has not been experimentally validated for sea ice.

The TUV-snow model will be evaluated by comparing measured optical properties (reflectance and extinction coefficient) of sea ice grown in a laboratory to TUV-snow model radiative-transfer calculations for a sea ice with the same properties. Secondly, the model will be evaluated by comparing measured nadir reflectance with light absorbing impurities in the laboratory sea ice to radiative-transfer calculations with the same light absorbing impurities in the sea ice, namely black carbon and algae.

Sea ice typically contains impurities such as black carbon, sediment and algae (e.g.Perovich (1996)). Black carbon is an efficient absorber of solar radiation (e.g. Mitchell (1957); Highwood and Kinnersley (2006); Hansen and Nazarenko (2004); Jacobson (2001); Ramanathan and Carmichael (2008); Bond et al. (2013)) and its deposition onto, or incorporation into, sea ice has been shown through modelling calculations to decrease the surface reflectance of the sea ice, increasing melt rates (e.g. Grenfell et al. (2002); Jacobson (2004); Light et al. (1998); Ledley and Thompson (1986); Goldenson et al. (2012); Holland et al. (2012); Marks and King (2013, 2014)). To evaluate the TUV-snow model with black carbon, a commercial black carbon is added to a 5 cm surface layer of 30–50 cm thick sea ice created in the laboratory in mass-ratios of 0, 75, 150 and 300 ng g^{-1} and the nadir reflectance of sea ice measured. The experimental reflectivity is compared to a calculated reflectivity using the TUV-snow model, for the same black carbon mass-ratios. The work presented here will demonstrate that radiative-transfer modelling with TUV-snow model (Lee-Taylor and Madronich, 2002) can reproduce laboratory grown ices with differing fabrics with a range of mass-ratios of light absorbing impurities. Such a validation will give confidence to others in the calculations of TUV-snow for other sea ice types and other light absorbing impurities.

Previous research on the effects of black carbon on sea ice optical properties have used radiative-transfer calculations and global climate model simulations. To the authors' knowledge there are no laboratory or field studies examining the effects of added black carbon on reducing sea ice reflectance. A related study by Hadley and Kirchstetter (2012) carried out successful laboratory experiments on artificial snow investigating the effects of black carbon on snow reflectance. The results from Hadley and Kirchstetter (2012) were used to validate the Snow, Ice and Aerosol radiation (SNICAR) model (Flanner et al., 2007) used in the 2013 IPCC report (IPCC, 2013). Similarly, Brandt et al. (2011) investigated the effect of black carbon on albedo of artificial snowpacks using snowmaking machines, showing a good match between measured values and albedos calculated from radiative-transfer modelling. Peltoniemi et al. (2015) measured the effect on snow bi-directional reflectance owing to additions of chimney soot, volcanic sand, and glaciogenic silt, demonstrating how snow metamorphism caused by the addition of these particles subsequently impacted on the albedo.

The study presented here includes the first experiments with the Royal Holloway Sea Ice Simulator, the first experiments to evaluate the TUV-snow radiative-transfer model for calculations of extinction coefficient and reflectivity of undoped sea ice, the first experimental results to demonstrate the change in reflectance owing to light absorbing impurities in sea ice and finally the first experiments to evaluate the accuracy of the TUV-snow model for reflectivity calculations for light absorbing impurities in sea ice.

Throughout the paper the term "experimental" refers to experiments with laboratory grown sea ice using the sea ice simulator described in section 2.1, with results being referred to as "measured" values. The term "modelled" refers to calculations from the TUV-snow radiative-transfer model, the results from which are referred to as "calculated" values.

2 Experimental method

The following sections will describe the design of the sea ice simulator (section 2.1), the characterisation of both the optical and physical properties of the laboratory ice (section 2.2) and the creation of sea ice doped with black carbon particles (section 2.3).

2.1 Sea ice simulator design

The sea ice simulator is designed to replicate a Polar sea ice growth environment under UV and visible wavelengths of solar radiation. Previous experiments with sea ice simulators have been carried out by, for example, Light et al. (2015); Buist et al. (2011); Papadimitriou et al. (2003); Haas et al. (1999); Polach et al. (2013); Hare et al. (2013); Grenfell and Perovich (1981). The set up of the simulator is shown in figure 1. The simulator is housed in a refrigerated shipping container (11.95 m length $\times$ 2.56 m high $\times$ 2.29 m width) which can be temperature controlled from –25°C to 25° C. The air temperature within the container varies by $\pm$1°C although thermocouples monitoring temperature at the ice surface show better temperature stability whilst the temperature variation measured within the ice is less than the precision of the probes ($\pm$ 0.2°C). Every 12 hours the chiller removes ice build-up on the cooling plant and air temperature rises briefly by $\sim$6°C. Inside the container sea ice is formed in a 2000 L polyethylene cylindrical white plastic tank (1.32 m high $\times$ 1.39 m diameter) placed on insulated pallets. Following the approach of Perovich and Grenfell (1981) a cylindrical design is utilised for the tank to help avoid mechanical stress at particular locations. A 1 cm insulating layer of black neoprene also surrounds the tank sides. A metal Unistrut frame surrounds the tank to further improve structural integrity. Black wooden boards, painted with mould resistant paint, are fixed around the Unistrut structure with 3 cm thick polystyrene insulation fitting between the wooden boards and the tank.

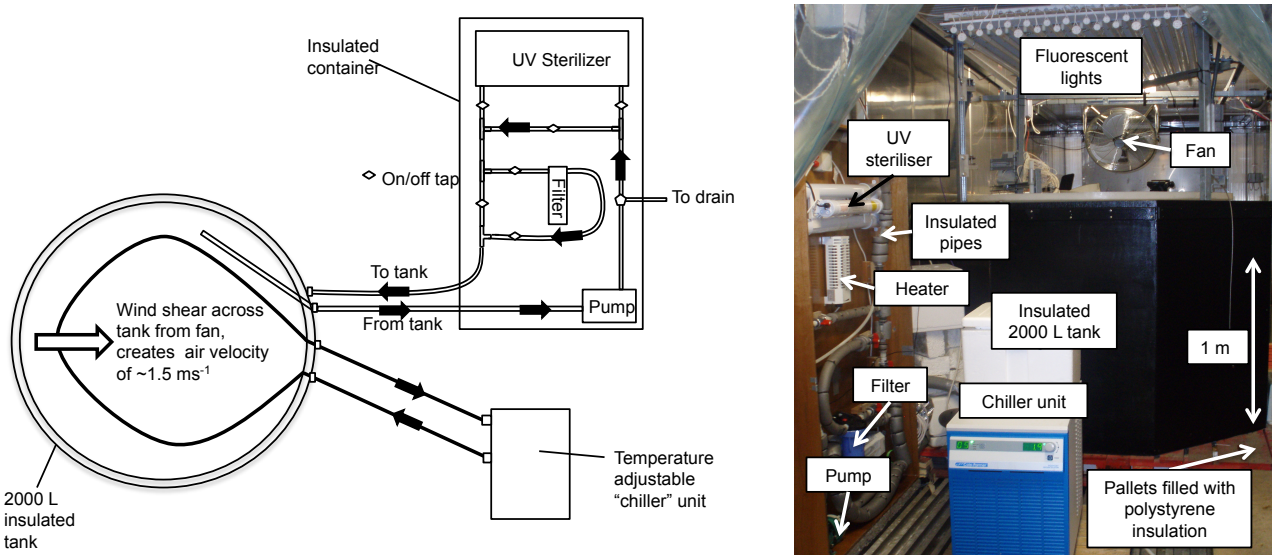

Figure 1. Plan of the sea ice simulator showing the 2000 L cylindrical tank (1.32 m high $\times$ 1.39 m diameter) in plan view and water conditioning unit in horizontal view and annotated photo of the facility. A closed pipe runs around the base of the tank connected to a heater unit circulating a water and glycol mixture gently warming the base of the tank. Water is circulated around the tank by a pump in an insulated container and also passed through a UV steriliser and particulate filter. Note the diffusing hood and insulation have been stripped away for clarity in the photo.

The tank is filled with a solution of Tropic Marine (Atkinson and Bingman, 1997) giving water with a salinity of 32 PSU, representing Arctic ocean salinity (Boyer et al., 2013). Tropic Marine is a synthetic sea salt mixture for aquaculture containing over 70 chemical elements in typical natural concentrations representative of the ocean with the notable exception of nitrate and phosphate, to inhibit algae growth. Atkinson and Bingman (1997) show the concentrations of major cations and anions of Tropic Marine are within 10% of seawater. Previous sea ice simulators use either sodium chloride or synthetic sea salt mixtures similar to Tropic Marine (e.g. Krembs et al. (2001), Mock et al. (2002), Papadimitriou et al. (2003) and Hare et al. (2013)).

To create circulation within the tank, ensuring temperature and salinity stratification does not occur, an Iwaki MD-10 pump circulates water at $\sim$10 L min^{-1} at the base of the tank, as shown in figure 1. The circulated water is also pumped through a 10 μm filter to remove any particulate impurities and a UV steriliser to prevent algae growth.

Sea ice grows from surface cooling of a salt water body (Weeks, 2010). To ensure even and realistic ice growth in the tank (from the surface, downwards) a closed pipe is run around the bottom of the tank, connected to a heater unit. The heater unit contains a solution of water and pure ethylene glycol (in a 1:1 ratio) which is pumped around the pipe at a constant temperature (0°C), to warm the base of the tank and preventing freezing. Figure 2 demonstrates that the temperature of the water beneath the sea ice is not thermally stratified, ice temperature decreases linearly through the ice with depth and the ice surface temperature is at a constant -15°C.

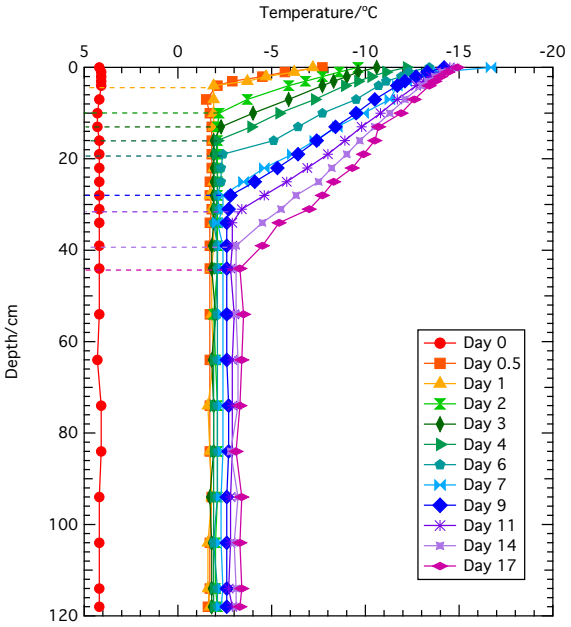

Figure 2. Temperature profiles through ice during ice growth. The top section, showing a linear increase in temperature, shows measurements from the ice, while the bottom section, with a constant temperature, shows measurements from the under-ice seawater, demonstrating the water is not thermally stratified.

Illumination, during optical measurements only, and replicating shortwave solar wavelengths over 350–650 nm is provided with a set of twenty Daystar daylight simulation fluorescent tubes and five sun-bed ultraviolet tube lights (peak illumination wavelength ∼350 nm, 40 nm FWHM). Measurements of reflectance of the sea ice is a relative measurement, (i.e. the quotient of reflected radiance of sea ice to reflected radiance from a reflectance standard) thus the intensity-spectrum of the lamp does not have to match the solar spectrum. The lights are evenly distributed directly above the tank to provide a diffuse illumination source. The light is further diffused by opaque white boards placed around the edges of the tank. Diffuse lighting was used to simplify the measurement of extinction coefficient and provide a useful reflectance product. The radiance, as a function of azimuth and zenith angle within the experiment was checked with a fibre optic probe and a broadband visible wavelength measurement and found to vary by 5-10%. The short term variability of the lamps was less than 0.1% (after an initial warm-up) on the timescale of the measurement of reflectivity or *e*-folding depth. Note that both the value of nadir reflectance (relative to a Spectralon panel) and light penetration depth are not dependent on the illumination irradiance providing the irradiance does not change during the measurement. Figure 3 shows the change in ice nadir reflectance during ice growth and the day-to-day reflectance stability of the optically thick ice.

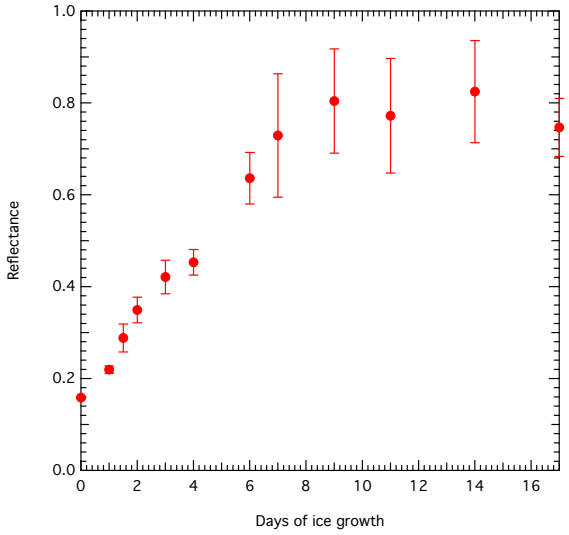

Figure 3. Reflectance of sea ice during ice growth and the day-to-day reflectance stability of the potentially optically thick ice (day 10 onwards).

2.2 Creation and characterisation of sea ice

To create sea ice an air temperature inside the container of $\sim -15°$C is maintained. Cold air is circulated within the container with fans. An additional air fan, attached to the ceiling, blows cold, ambient air at the water surface (110 m^3 min^{-1}) increasing the heat flux from the ice surface, quickening ice formation and assisting the production of columnar ice (Weeks, 2010).

Sea ice is grown in the simulator for $\sim$17 days producing ice with a thickness of $\sim$30 cm. Temperature depth profiles and nadir reflectance of the ice were measured daily during growth (described in sections 2.2.2 and 2.2.5 respectively). The extinction coefficient is measured at the end of the experiment as it destroys the homogeneity of the ice (described in section 2.2.6).

2.2.1 Characterisation of sea ice physical properties

2.2.2 Temperature profiles

Temperature profiles through the sea ice are recorded daily during ice growth to give an indication of sea ice thickness and ensure that temperature stratification does not occur within the underlying seawater. The temperature is recorded via a series of thermocouples, as used by Rabus and Echelmeyer (2002); Johnston and Timco (2002); Nomurai et al. (2006). Calibrated type T thermocouples are inserted into a thin plastic sleeve and then a white polypropylene pole at regular depths (every 2 cm) into the water and then frozen in place during ice formation. The precision on all the thermocouples at –15°C was measured as

± 0.2°C. Temperature of sea ice decreases from the surface to the base; ice thickness can be determined from the point where the temperature becomes constant with depth which can be assumed to be seawater, as shown in figure 2.

2.2.3 Determining sea ice properties by ice coring

Cores of the ice are taken to determine sea ice properties at the conclusion of the optical experiments (section 2.2.4). The corer design was based on a CRREL report by Rand and Mellor (1985). Cores are photographed, divided into ∼5 cm sections and their dimensions and mass measured to derive density. Salinity is measured after melting using a Fisher Scientific seawater refractometer (cross-calibrated with an accurate ion conduction probe).

2.2.4 Characterisation of sea ice optical properties

2.2.5 Measuring reflectance

The nadir reflectance of the sea ice is measured daily during ice growth until the value became constant (taking between 6 and 12 days). Reflectance becomes constant once a sufficient ice thickness is reached that the increasing ice thickness does not change the measured reflectivity. Upwelling radiance from the ice is measured via an optical lens connected to a 400 μm xsr fibre optic coupled to an Ocean Optics USB 2000+ spectrometer (wavelength range: 200-850 nm, resolution: 1.5 nm FWHM, signal:noise 250:1). The optical lens is situated ∼40 cm above the sea ice surface at nadir with a view footprint covering a circular area ∼315 cm^2. The footprint is an order of magnitude larger than any surface feature on the sea ice.

To convert ice surface radiance measurements to reflectance the radiance of light from the sea ice surface measured at nadir is ratioed to the radiance from a reference Lambertian reflector at nadir (a Spectralon panel) measured in the same location but raised 5 mm above the ice surface and under identical illumination as the sea ice.

During a reflectivity measurement a 30 cm × 30 cm Spectralon panel is added to the diffuse lighting environment above the sea ice. The addition of this panel increases the radiance, L, within the diffuse lighting environment. A very conservative estimate of the effect on the measurement of the reflectivity can be calculated by analogy to an integrating sphere. The Spectralon panel represents 0.66% of the area of the diffuse lighting environment, which is approximately a cube made up of white panels and sea ice (i.e. 6 × 1.5 m × 1.5 m = 13.5 m^2). Treating the diffuse lighting environment above the sea ice as a crude integrating sphere and considering fractional change in radiance, $\frac{\delta L}{L}$, after Ball et al. (2013) who suggest $\frac{\delta L}{L} \approx \frac{A_{panel}}{A_{environment}\rho}$. Where A_{panel} is the area of the Spectralon panel, $A_{environment}$ is the area of the diffusing "cube" and ρ is the overall reflectivity of the diffusing cube. A very crude analysis assumes reflectivity of the panel is 1 and the part fraction of the hypothetical integrating sphere is 0. In the limit of a reflective environment $\frac{\delta L}{L} \to \frac{A_{panel}}{A_{environment}\rho} \sim 0.67\%$. Thus the overestimation of the radiance (∼0.67%) is significantly less than the uncertainty displayed on the measurement of nadir reflectivity displayed in figure 3 and figure 7.

2.2.6 Measuring extinction coefficient

At the completion of the experiment the extinction coefficient and *e*-folding depth are measured. The *e*-folding depth is the distance over which light intensity reduces to $\frac{1}{e}$ of its initial value and is the reciprocal of the extinction coefficient. The *e*-folding depth is reported in addition to the extinction coefficient. The sea ice *e*-folding depth and extinction coefficient is measured by drilling a single hole gradually through the ice in ∼5 cm increments with a sharp drill. At each depth drilled the same fibre optic is inserted into the hole and the light intensity (upwelling radiance) measured via an Ocean Optics spectrometer. In an optically thick sea ice the measurement of either up or downwelling light for e-folding depth is not important as has been shown by France and King (2012). The hole is a tight fit around the fibre but a thin, light diffusing disk, of white PTFE is also placed around the fibre at the ice surface to minimise any stray light entering the hole without altering the light field near the hole.

Simultaneously to the light intensity in the hole being measured (I_{raw}) the light intensity of another fibre optic inside a diffusing PTFE container at the ice surface was measured (I_{ref}) to account for any change in the intensity of the fluorescent lights. The relative light intensity, I_z , at depth, z, is then calculated using equation 1.

$$I_z = \frac{I_{raw(z)}}{I_{ref}} \tag{1}$$

The *e*-folding depth, ϵ, is calculated using equation 2, where I_z is the relative intensity at a depth, z, and $I_{z'}$ is intensity at the shallowest depth, z'. From the measured light intensity the *e*-folding depth is calculated by fitting an exponential curve through I_z versus z data.

$$\frac{I_z}{I_{z'}} = e^{-\left(\frac{(z-z')}{\epsilon}\right)} \tag{2}$$

The extinction coefficient, *k*, is than calculated as the reciprocal of the *e*-folding depth.

Measurements used to calculate the *e*-folding depth are only conducted in the middle of the ice as the irradiance profile changes rapidly at the air-ice and ice-water boundary (a good example shown in King et al. (2005)). The calculation of an *e*-folding depth from the modelled downwelling irradiance was calculated from similar depths as the experimental ice. The modelled ice had the same thickness and underlying tank radiance field as the experiment. The extinction coefficient and *e*-folding depth measured in the work presented here are asymptotic (reaches a constant value as shown in King et al. (2005)) as the light field to the sea ice is diffuse and thus there are no near surface effects as found frequently in fieldwork (e.g. Reay et al. (2012) and references therein).

2.3 Creation of black carbon doped sea ice

Once the sea ice has grown to ∼30 cm thick (∼3 weeks of ice growth) 75 L (equivalent to a ∼5 cm layer) of chilled seawater doped with a known concentration of black carbon (described in section 2.3.1) is added to the surface and frozen in place forming a 5 cm black carbon bearing ice layer. Black carbon is placed within a 5 cm surface layer of the artificial ice to replicate black carbon entrainment into sea ice following melting of overlying snow as described by Grenfell et al. (2002) and

Doherty et al. (2010). The new 5 cm layer of black carbon bearing seawater is left to freeze for three days and the reflectivity of the new sea ice surface then measured daily over a week. The sea ice is then cored and density and salinity measured down the core to record the physical ice structure before and after the black carbon bearing layer is added.

At completion of the experiment the ice is melted and water is purified by filtration through a 1 μm Purtex filter to remove black carbon particulates. If any black carbon particulates were to remain the concentration would be negligible as it would be diluted by 2000 L of sea water (a dilution factor of $\sim$30). The whole process is repeated with other black carbon concentrations in the 5 cm layer giving a total of four mass loadings; $\sim$75 ng g^{-1}, $\sim$150 ng g^{-1} and $\sim$300 ng g^{-1} and a blank run with 0 ng g^{-1} of black carbon. The sea ice was melted and the resulting seawater was treated with aqueous hypochlorous acid (HOCl) and filtered between experimental runs to remove any algae that may have grown. No algae was visible to the naked eye.

2.3.1 Creating atmospherically representative black carbon

To create the aqueous black carbon solutions a method from Clarke (1982) is adapted. The black carbon used, Monarch 120, is produced by Cabot Corporation to replace the discontinued Monarch 71 used by Grenfell et al. (2011). Approximately 1 g of the black carbon is added to a solution of 800 ml of pure water and 200 ml isopropanol (isopropanol aids dispersal of the black carbon in the concentrated solution) (Clarke, 1982). The solution is then placed in an ultrasonic bath for 2 hours to ensure the black carbon is fully dispersed and to break up conglomerated lumps. The solution is then suction filtered through 2 μm Nuclepore membrane filters followed by 0.8 μm Nuclepore filter to remove larger particles and ensure the final solution is representative of atmospheric black carbon i.e. particle diameter $<$0.8 μm (Clarke, 1982). The mass loading of black carbon in the solution is determined gravimetrically (i.e. by evaporating and weighing a portion of the black carbon solution). Two black carbon solutions were used with mass loadings of 46 $\pm$ 11 μg g^{-1} and 11 $\pm$ 1.5 μg g^{-1}. The uncertainties are the standard deviation of three repeated gravimetric determinations. Known amounts of solutions 1 and 2 are mixed with 75 L of artificial seawater to give overall black carbon mass-ratios detailed in table 1. The mass-ratios of black carbon are approximately 0, 75, 150 and 300 ng g^{-1}, these approximate values will be subsequently used in the text whilst precise values are reported in table 1.

2.3.2 Characterisation of black carbon optical properties

The mass absorption cross-section of the black carbon used in the present study is estimated using an integrating sandwich spectrometer, described by Grenfell et al. (2011), based on Clarke (1982). The integrating sandwich spectrometer measures the absorption spectrum of particulate matter on filter samples in a diffuse radiance environment. Absorption spectra of multiple filters containing black carbon loadings are converted to a mass absorption cross-section. A mass absorption cross-section of 2.1 m^{2}g^{-1}, (λ = 610 nm) is estimated for the black carbon placed in the artificial sea ice. The values are a factor of 3 smaller than the black carbon mass absorption cross-section of 6.57 m^{2}g^{-1}, for a wavelength of 610 nm, (Flanner et al., 2007) typically used in radiative-transfer calculations, but are similar to values used by Dang et al. (2015) owing to the size of the black carbon particles used.

Table 1. Optical and physical properties of sea ice for each run including the mass-ratio of black carbon added to the top layer of ice, density of ice and scattering cross-section (σ_{scatt}) of both the top and bottom layers of the ice. The uncertainty in sea ice density is 1 standard deviation of the average of measurements taken from the core profile. Uncertainty is not provided for the density of the top layer as this is the average of only two measurements, although the uncertainty is likely to be similar to that of the lower layer. The mass ratio of black carbon added to the surface layer is also shown. The uncertainty in the black carbon mass-ratio is the uncertainty in the gravimetric method used for determining the mass-ratio, as described on section 2.3.1.

Run number	**Black carbon mass-ratio added /ng g^{-1}**	**Density of bottom (undoped) layer/ g cm^{-3}**	**Density of top (doped) layer layer/ g cm^{-3}**	**σ_{scatt} bottom layer /m^2 kg^{-1}**	**σ_{scatt} top BC layer /m^2 kg^{-1}**
1	0	0.91±0.084	0.92	0.315±0.040	0.05
2	77±18	0.91±0.059	0.91	0.235±0.041	0.05
3	153±37	0.92±0.044	1.00	0.115±0.004	0.35
4	305±62	0.95±0.050	0.93	0.126±0.016	0.2

Six known aliquots of the filtered black carbon solution described in section 2.3.1 were filtered through 0.4 μm Nuclepore filters, providing filter loadings of 10.18, 15.12, 20.15, 25.19, 50.38 and 100.77 μg cm^{-2}. The absorbance spectra of the filters (figure 4a) is calculated using equation 3:

$$A(\lambda) = -ln\frac{I(\lambda)}{I_0(\lambda)} \tag{3}$$

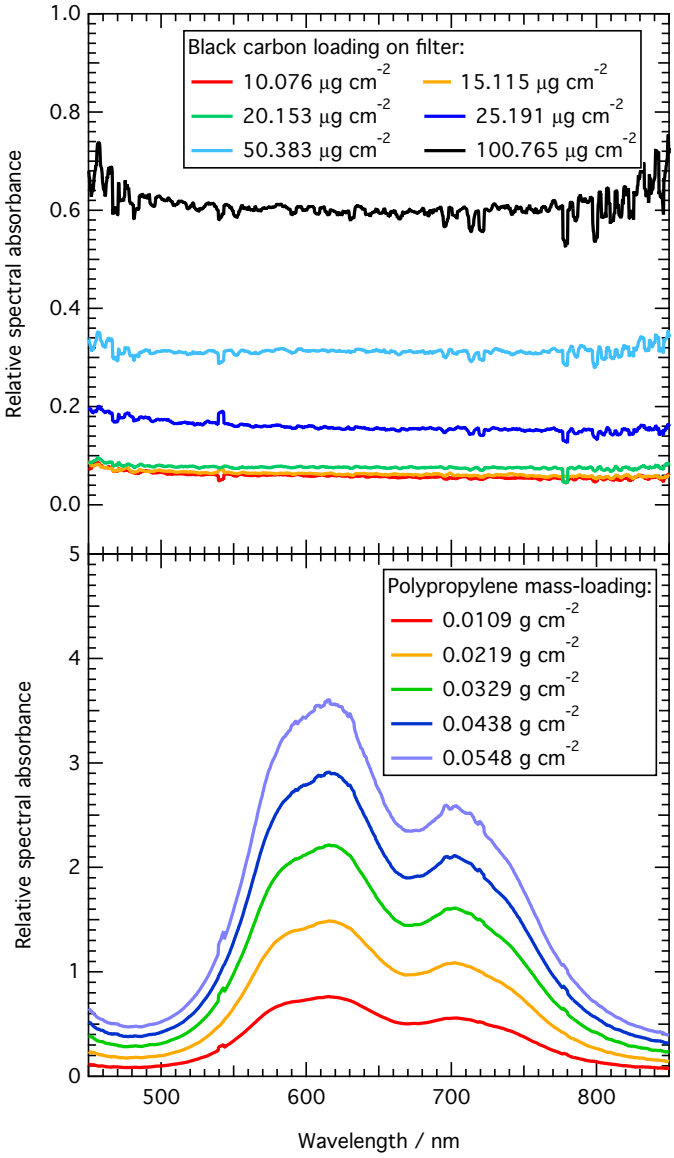

Figure 4. a (top)) Relative spectral absorbance of black carbon versus wavelength for various loadings of black carbon on the filter. b (bottom)) Relative spectral absorbance versus wavelength for different mass loadings of polypropylene.

Where I is the intensity measured with the loaded filter in the integrating sandwich spectrometer, and I_0 is the intensity measured when a blank 0.4 μm Nuclepore filter, which is measured following the same procedure as the loaded filter. To calibrate the integrating sandwich spectrometer, a set of translucent standard plastic sheets (light blue polypropylene, 100 μm) with measurable mass absorption coefficients are used. The sheets are placed on a 0.4 μm Nuclepore filter and measured in the

integrating sandwich spectrometer using the same method as the black carbon filters. Multiple sheets of the polypropylene are stacked, providing loadings of 0.011, 0.0219, 0.0329, 0.0439 and 0.0548 g cm^{-2} (figure 4b)

Grenfell et al. (2011) showed that for small amounts of black carbon the mass loading is directly proportional to the absorbance measured by the integrating sandwich spectrometer. In this study, we considered the linear sensitivity between the black carbon mass loading and the black carbon absorbance with the ratio between black carbon and polypropylene and we equate the ratio of sensitivities to the ratio of the mass absorption cross-section. Therefore, the mass absorption cross-section of the black carbon is expressed in equation 4:

$$\sigma_{BC} = \sigma_{\rho l} \frac{\alpha_{\rho l}}{\beta_{bc}} \tag{4}$$

where $\alpha_{\rho l}$ is the slope of the linear regression between the mass loading of the polypropylene calibration sheets and the relative absorbance of the polypropylene measured in the integrating sandwich spectrometer, β_{bc} is the slope of the linear regression between the mass loading of the black carbon filters and the relative absorbance of the black carbon measured in the integrating sandwich spectrometer and $\sigma_{\rho l}$ is the mass absorption cross-section of the polypropylene, given by the Beer-Lambert law.

The mass absorption coefficients of the polypropylene sheets are measured with a standard spectrometer using Beer-Lambert law. The measured mass absorption coefficient is 229.23$\pm$0.02 $cm^2 g^{-1}$ (λ = 610 nm).

To visually investigate the size and shape of the black carbon particles used in the experiment, scanning electron microscopy (SEM) is employed. Approximately 6 mm wide squares of the 0.4 μm filters containing black carbon particles were cut and glued on standard 12.7 mm diameter SEM stubs using double-faced carbon tabs. The samples were gold coated using a Polaron E5100 Series II Cool Sputter Coater for 3 minutes in air, creating a 45 nm thick coating. SEM images were generated on a Hitachi S3000N scanning electron microscope. The images were obtained at a magnification of $\times 4000$ at a working distance of 12.5 mm, with an acceleration energy of 20 kV and a beam current of 85000 nA. Figure 5 shows a SEM image of black carbon particles on a 0.4 μm Nuclepore filter. The SEM images are analysed using the ImageJ image analysis software (Abramoff et al., 2004), to determine the size distribution and the circularity of the black carbon particles. The circularity of the particles is determined by the shape factor Heilbronner and Barrett (2013), calculated using equation 5:

$$SF = \frac{4\pi A}{P^2} \tag{5}$$

Where A is the area of the shape and P, the perimeter of the shape. The shape factor represents the deviation of the perimeter of a particle from a circle of the same area. Values of the shape factor vary between 0, representing an elongated shape and 1, describing a circle. The average shape factor of the particles shown in figure 5 is 0.842, indicating a rough spherical shape. Assuming a spherical nature of the particles, the diameter is calculated as the maximum Feret diameter. The average diameter of the particles shown in figure 5 is 0.461$\pm$ 0.331 (2σ) μm.

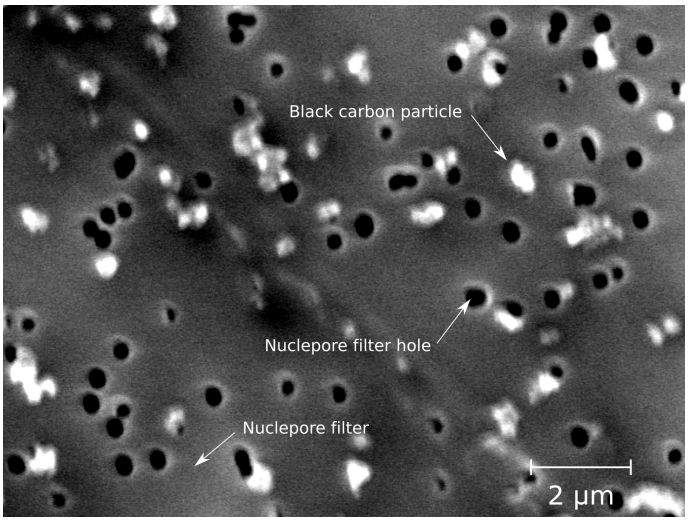

Figure 5. Scanning electron microscope image of gold coated black carbon particles (white) at a magnification of $\times 4000$, showing a roughly spherical shape of the particles and an average particle diameter of 0.461 ± 0.331 μm. Note the image also shows the Nuclepore filter holes at 0.4 μm diameter

The mass absorption coefficients of the black carbon is also estimated by a Mie light scattering calculation using the SEM data. Mie calculations are performed using size data from the SEM to provide a check of the value for black carbon absorption-cross section for the radiative-transfer calculations. For the Mie calculations the black carbon diameter of 0.461 μm is used with a density of 1.8 g cm^{-3} and a commonly used refractive index of 1.8 – 0.5 (Clarke and Noone, 1985), giving an absorption cross section at a wavelength of 550 nm of 2.78 m^{2}g^{-1}.

In the work presented here a absorption cross-section value of 2.5 m^{2}g^{-1} will be used for radiative-transfer calculations, as this is between the values from the Mie calculations and from the integrating sandwich spectrometer.

3 TUV-snow radiative-transfer calculations

Calculations using the TUV-snow radiative transfer model (described in section 3.1) are undertaken to simulate optical and physical properties measured of the sea ice. For undoped ice reflectance and extinction coefficient/*e*-folding depth are calculated (section 3.2) while for sea ice with black carbon the model is used to calculate only reflectance (section 3.3).

3.1 The TUV-snow radiative-transfer model

The TUV-snow model is a coupled atmosphere-snow-sea ice radiative-transfer model using the DISORT code (Stamnes et al., 1988) and is described in detail by Lee-Taylor and Madronich (2002). The model parameterises sea ice optical properties using only an asymmetry factor, g, a wavelength independent scattering cross-section, σ_{scatt}, a wavelength dependant absorption cross-section, σ^{+}_{abs}, and sea ice density and thickness.

3.2 Calculations of undoped ice reflectance and extinction coefficient/*e*-folding depth

The reflectance and extinction coefficient/*e*-folding depth of the undoped sea ice are calculated through radiative-transfer calculations using the TUV-snow model with derived scattering and absorption cross sections for the ice. To derive these values, values of scattering and absorption cross section are varied until they reproduce the experimentally measured reflectivity and *e*-folding depth data for the sea ice as detailed in King et al. (2005); France et al. (2011, 2012); Marks and King (2014). Ice density and thickness are measured from ice cored at the end of an experiment. The density of the ice is detailed in table 1. The ice is modelled with a 30 cm thick bottom layer subdivided into 45 sub-layers with each sub-layer representing 1 cm apart from the bottom and top 5 sub-layers which are 1 mm thick. The asymmetry factor for the ice is fixed at 0.95, based on a value suggested by Mobley et al. (1998) for a bubble rich ice, which is observed in ice cores taken from the tank.

All calculations are undertaken between wavelengths 350–650 nm, using eight-streams in DISORT. The wavelength dependant, nadir reflectance of the water filled tank is measured and included in the model as the under ice reflectance, the measurements are included in the supplementary information. The model illuminates the ice with diffuse light.

Reflectivity is calculated as the ratio of upwelling, Irr_{up}, to downwelling Irr_{down}, irradiance at the surface of the sea ice, $\left(\frac{Irr_{up}}{Irr_{down}}\right)$. The *e*-folding depth is calculated using equation 2, and the irradiances calculated at depths of 5, 10, 15 and 20 cm in the sea ice with reference irradiance at a depth of 5 cm (to reproduce experimentally derived *e*-folding depths). The extinction coefficient is calculated as the reciprocal of the value of *e*-folding depth.

3.3 Calculating surface reflectance of ice with a black carbon doped layer

The radiative transfer modelling was repeated for the black carbon doped sea ices. For these radiative transfer calculations parameters are kept the same as the undoped ice calculations, although the ice is modelled as two layers; a 30 cm thick undoped bottom layer and a 5 cm upper, black carbon bearing, layer. These principal layers are subdivided into 45 sub-layers for the bottom layer and 14 sub-layers in the top layer, with each sub-layer being 1 cm thick, apart from 0.5 cm either side of a boundary (air-ice, undoped ice-doped ice and ice-water), where sub-layers are 1 mm.

The absorption cross-section of the top layer was the same as the bottom undoped layer plus additional absorption for any black carbon present (0, 75, 150 and 300 ng g^{-1}), where the absorption cross-section of the black carbon is 2.5 $m^2 g^{-1}$ (see section 2.3.2). The scattering cross-section of the top layer was derived by a trial and error method to obtain the best fit (judged by eye) between modelled and measured values of reflectance and *e*-folding depth as described in section 4.3. Densities of the top layers are shown in table 1.

4 Results

4.1 Physical properties of sea ice and growth rates

Salinity, density and temperature depth profiles of all ice cores are given in the supplementary information. A typical salinity and temperature profile is given in figure 6. The average density for the top and bottom layer for each black carbon loading is shown in table 1.

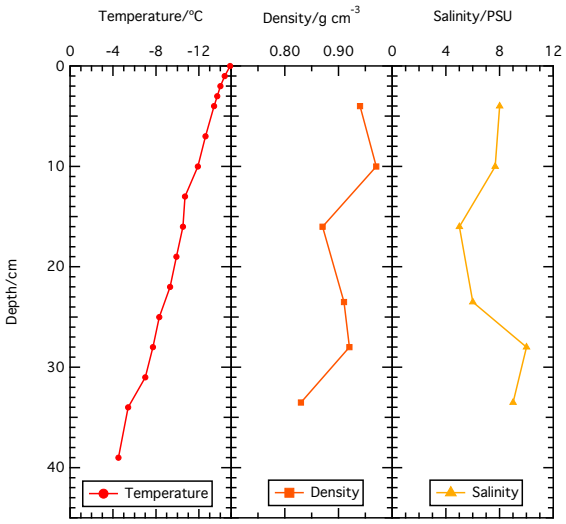

Figure 6. Example temperature, salinity and density data for an ice core from run 2 before the black carbon bearing layer was added.

Ice growth rates were similar for all runs with the ice growing at approximately 1.8 cm per day. For all runs the growth rate gradually declined as ice growth progressed. The time taken for reflectance of the ice to become a constant value became longer, taking 5 days for run 1, 7 days for run 2, 11 days for run 3 and 13 days for run 4 owing to an issue with the maintenance of the refrigerator plant which reduced its heat flux from the simulator but not its maintained temperature. The sea ice produced for each run had a slightly different fabric and subsequently produced less scattering sea ice as shown by the value of σ_{scatt} in table 1.

4.2 Measured and modelled reflectivity and extinction coefficient/e-folding depth of undoped sea ice

4.2.1 Experimental measurements and calculations of reflectance and extinction coefficient/e-folding depth for undoped ice

The measured nadir reflectance of the undoped ice layer, is shown in figure 7 for the four runs. Each run represents an experiment with new sea ice growth before the black carbon bearing layer is added. The reflectance is wavelength dependent peaking

at values around 500 nm, as would be expected for sea ice (e.g. Grenfell and Maykut (1977)). Measurements of reflectance shown in figure 7 are the average of 5 days of reflectance measurements taken when ice reflectance had become constant. The reflectance of the undoped sea ice decreases from run 1 to run 4 which is attributable to the slightly different ice fabrics in each run and the fact that the ice thickness is not optically thick.

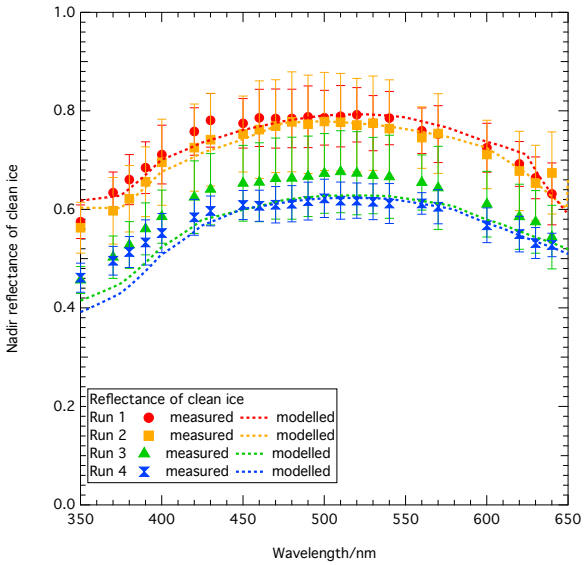

Figure 7. Measured sea ice surface reflectance versus wavelength (solid shapes) and modelled sea ice reflectance versus wavelength (dashed lines) for sea ice with no added black carbon

The extinction coefficient and *e*-folding depth of the undoped ice, figure 8, are also wavelength dependent with the largest values of *e*-folding depth observed around 550 nm for all runs again representing a natural sea ice (e.g. Grenfell and Maykut (1977)). The *e*-folding depths increase with run number which is again attributable to the different ice fabrics created. The increased *e*-folding depth can be attributed to a less light scattering sea ice matrix.

Figures 7 and 8 also contain the modelled reflectivity and extinction coefficient/*e*-folding depth fitted to the experimental data. With the exception of the UV nadir reflectivity of run 3 and 4 the modelled fits are well within uncertainty of the measurement.

It should be noted it is more difficult to find a pair of values for scattering and absorption cross-sections (σ_{scatt} and σ^{+}_{abs}) for each wavelength that produce a good reproduction of the experimental reflectivity *and* *e*-folding depth, rather than reflectivity alone, as the system described here is significantly more constrained in the number of degrees of freedom. Thus measuring reflectivity and *e*-folding depth gives the reader more confidence in the values of σ_{scatt} and σ^{+}_{abs}.

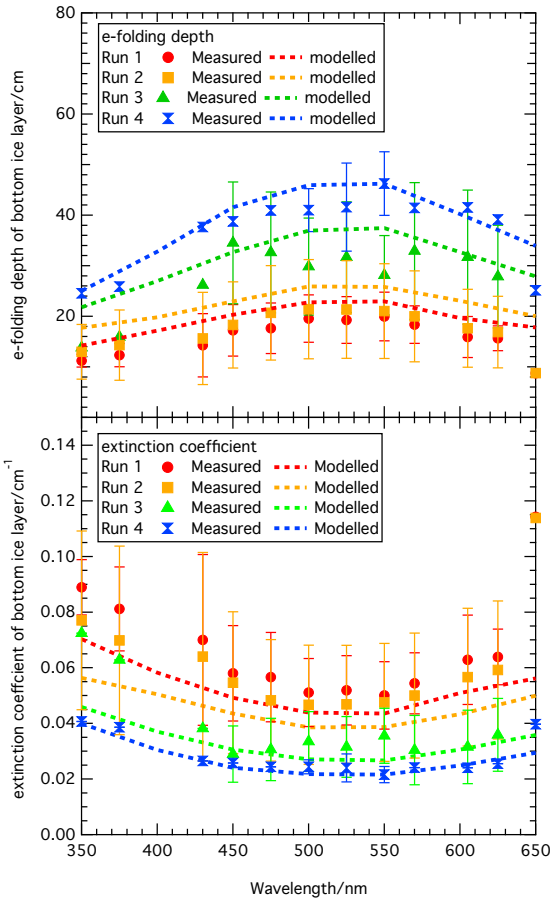

Figure 8. a (top)) Measured sea ice *e*-folding depth versus wavelength (solid shapes) and modelled sea ice *e*-folding depth versus wavelength (dashed lines) for sea ice with no added black carbon. b (bottom)) Measured sea ice extinction coefficient versus wavelength (solid shapes) and modelled sea ice extinction coefficient versus wavelength (dashed lines).

4.2.2 Derived absorption and scattering cross-sections from experimental data for undoped ice

The calculated values of the absorption cross-section of impurities in the undoped ice used in the radiative transfer calculations are shown in figure 9. The shape of the derived absorption cross-section for each run is similar, decreasing slightly with increased run number. Ideally the absorption should be zero for undoped ice (no impurities). Absorption cross-sections of Saharan dust from Lamare et al. (2016) and chlorophyll in algae from Bricaud et al. (2004) and Mundy et al. (2011) are shown in figure 9 for comparison to the sea ice impurity absorption cross-section. A characteristic signal of chlorophyll in algae is present. It should be noted that the algae was unintentional, not observed by the naked eye and resisted several cycles of disinfection. It is testament to the sensitivity of the technique for deriving absorption and scattering cross-sections that the absorption cross-section of the algae can be calculated.

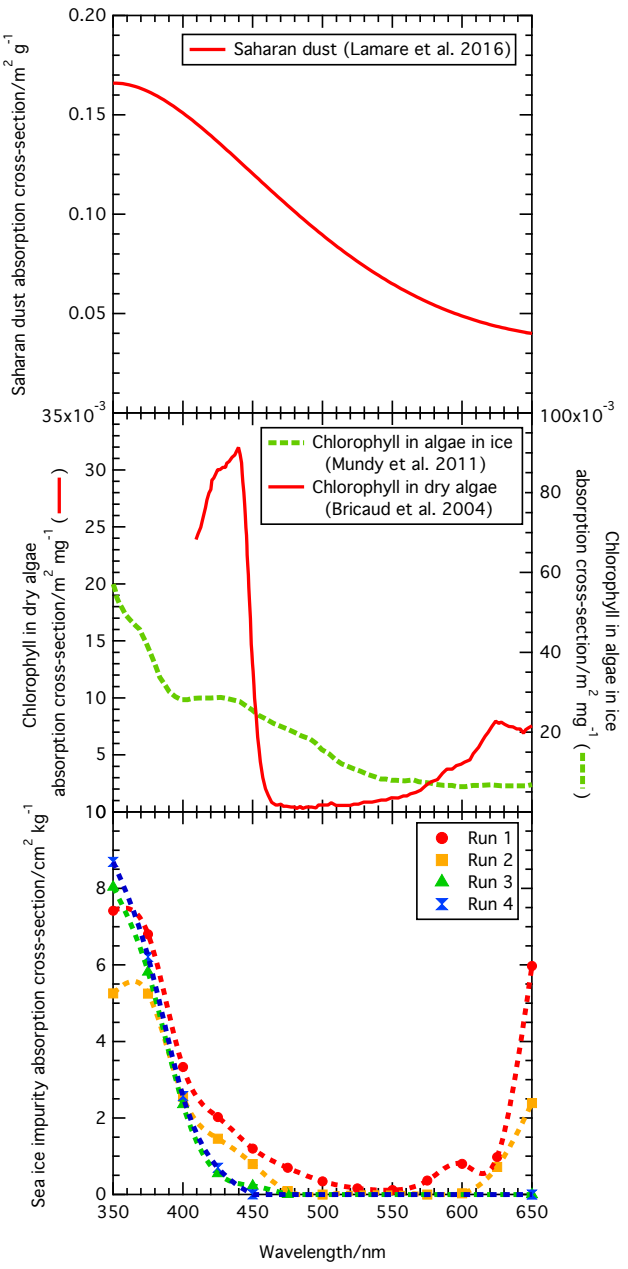

Figure 9. A (top)) Absorption cross-section of Saharan dust taken from Lamare et al. (2016). B (middle)) Absorption cross-sections of chlorophyll. Chlorophyll in ice (dashed line) taken from Mundy et al. (2011) is per mg of algae determined by fluorescence. Chlorophyll (solid line) is taken from Bricaud et al. (2004) is per mg of dry weight cells. C (bottom)) Wavelength dependent absorption cross-section derived from reflectance and *e*-folding depth data from runs 1 to 4 for the undoped ice. A smooth line is added to guide the eye. Values for run 4 are too small to plot clearly at longer wavelengths. Error bars show the possible variation in absorption cross-section obtained from different fits of the original reflectance and *e*-folding depth data.

The modelled scattering coefficient used in the radiative-transfer calculations is wavelength independent and reported in table 1.

4.3 Surface reflectivity of black carbon doped sea ice

The reflectance of the sea ice with an extra 5 cm black carbon bearing ice layer decreases at all wavelengths as the black carbon mass-ratio increases; as shown in figure 10. At a wavelength of 500 nm, reflectance decreases to 97% of the reflectance of undoped ice (Run 1) for an addition of seawater with a mass ratio of black carbon of 75 ng g^{-1}, to 90% for an addition with a mass-ratio of 150 ng g^{-1} compared to undoped ice and to 79% for an addition with a mass ratio of 300 ng g^{-1} compared to reflectivity of undoped ice.

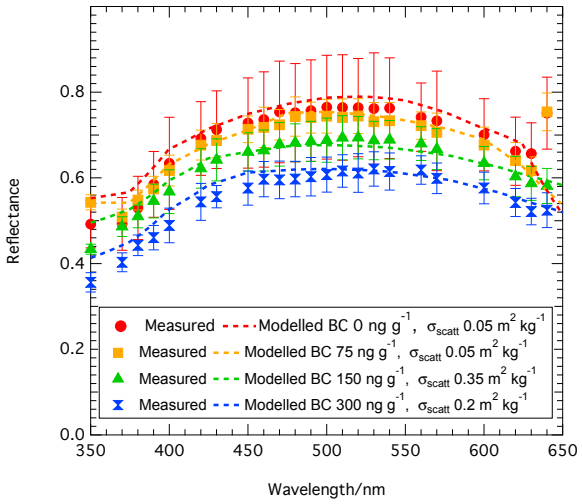

Figure 10. Comparison between measured (solid shapes) and calculated (dashed lines) reflectance of laboratory sea ice surface with black carbon in a 5 cm surface layer in varying mass ratios. The figure shows the best fit possible by altering scattering cross-section of the upper black carbon bearing layer (values shown on plot).

The extinction coefficient/*e*-folding depth of the ice after the black carbon layer was added was not measured as the total ice could no longer be considered a homogeneous medium and the 5 cm doped layer was too thin to measure the extinction coefficient in this layer alone.

The best fit obtained between the measured and calculated reflectance values from varying the scattering cross-section of the upper sea ice layer between realistic values is shown in figure 10. These values of the scattering cross-section are shown in figure 10, varying from 0.05 m^2 kg^{-1} to 0.35 m^2 kg^{-1}. The fit between the measured and calculated reflectance is well within uncertainty limits for all runs demonstrating the TUV-snow model can reproduce experimental reflectance for sea ice doped with black carbon, even with varying fabrics of sea ice.

5 Discussion

In the discussion section possible sources of uncertainty in the experimental measurements compared to the calculated values will be discussed as well as the realism of the laboratory sea ice and potential limitations of the sea ice simulator.

5.1 Sources of uncertainty in the experimental measurements compared to the calculated values

The comparison between experimentally measured and calculated values reported here are presented under the assumption that the experimental conditions are accurately replicated by the TUV-snow radiative-transfer model. Potential sources for uncertainty in comparing experimentally measured values to calculated values include: aggregation of black carbon particles; mobilisation of black carbon from the top layer of sea ice into the underlying ice and sea water; the value of the asymmetry parameter used in the radiative transfer modelling; uncertainty in the derived scattering and absorption cross-sections of the experimental sea ice and uncertainty in the mass ratio of black carbon added to the laboratory sea ice. The possible contribution of each of these factors is subsequently reviewed.

5.1.1 Aggregation of particles

The effect of aggregation of black carbon particles decreases the absorption cross-section in two ways. Assuming two black carbon particles aggregate to form a new spherical black carbon particle, the newly formed particle would have twice the volume and the radius would be a factor of $\sqrt[3]{2}$ larger. Mie calculations show that the absorption cross-section would decrease and the mass-absorption cross-section would decrease and flatten according to Dang et al. (2015). Secondly aggregation would reduce the number density of black carbon particles further reducing the absorption of light within the ice. However, the good agreement shown between measured and calculated reflectance for the black carbon doped ice suggests aggregation is not occurring within the ice.

5.1.2 Black carbon mobilisation

The radiative-transfer model assumes the black carbon is distributed evenly within the black carbon doped layer, however the experimental ice may not have had an even distribution. Sea ice forms brine pockets and brine channels on freezing (e.g. Weeks (2010)). As the extra layer of seawater freezes brine will drain downwards into the layer of ice below and also be expelled onto the surface. Eicken (2003) suggest that impurities in seawater are trapped in the brine inclusions as sea ice grows. If black carbon is situated in brine inclusions then some of it may drain into the underlying layer of sea ice and eventually into the underlying seawater as described by Eicken (2003). Doherty et al. (2010), who measured black carbon mass-ratios in sea ice in the Arctic, showed that black carbon is concentrated at the surface of the sea ice but also found in smaller concentrations throughout the ice, supporting the idea that black carbon deposited onto the surface of sea ice can be mobilised through the ice. If there was a reduced black carbon mass ratio in the upper layer then surface reflectance would increase (e.g. Marks and King (2013)).

5.1.3 Asymmetry parameter

A value of the asymmetry parameter, g, of 0.95 was used based on the work of Mobley et al. (1998). However Mobley et al. (1998) demonstrate that g may vary between 0.94 and 0.99. Figure 11 shows the effect on the determination of the absorption cross-section, σ_{abs} owing to absorption by impurities and the ice scattering cross-section at 400 nm for changing the value of g within possible values for sea ice; 0.94–0.99 (Mobley et al., 1998).

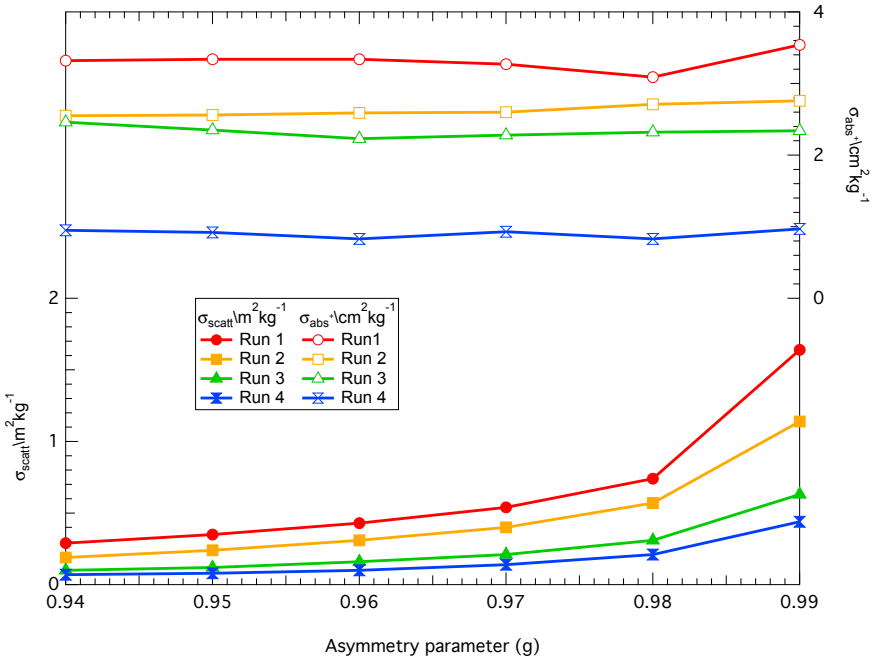

Figure 11. Variation in absorption cross-section, σ^{+}_{abs}, (cm^2 kg^{-1}) (upper, non-filled markers) and scattering cross-section, σ_{scatt}, (m^2 kg^{-1}) (lower, filled symbols) owing to variation in the asymmetry parameter at 400 nm. Note the scatter in the values of σ^{+}_{abs} is due to the fitting process used.

The change in the g value has very little effect on the values of absorption cross-section, as also noted by Libois et al. (2013), with variation in g between 0.94 to 0.99 having only a factor of 0.092 effect on the absorption cross-section, demonstrating the model is insensitive to the value of g for determining light absorbing impurities.

In the case of scattering cross-section, the effect of changing g from 0.94 to 0.99 at 400 nm has a much larger effect on the scattering cross-section, with a larger g value giving a larger scattering cross-section i.e. the similarity principle. An increase in the scattering cross-section would change the shape of the reflectance-wavelength curve as well as the values of reflectance, as absorbing impurities have less effect in a sea ice with a large scattering cross-section compared to a small one, as described in Marks and King (2014).

5.1.4 Uncertainty in derived scattering and absorption cross-section and black carbon mass ratio

The determination of the cross-section for light scattering and absorption, described in section 4.2.2, depends on varying their values to reproduce the measured values of the *e*-folding depth and the nadir reflectivity within the experimental uncertainties of measured values of the *e*-folding depth and the nadir reflectivity, all as a function of wavelength. The latter assists in constraining the determination of the values of the cross-section for absorption and scattering. The propagated uncertainty in the determined values of the cross-sections for light scattering and absorption from uncertainties in either the value of the *e*-folding depth or nadir reflectivity in isolation have not been calculated as our method fits both *e*-folding depth and reflectivity. Considering the experimental uncertainty in *e*-folding depth and nadir reflectivity gives a more representative uncertainty of the process. The uncertainty in the reflectance and *e*-folding depth measurement data of the undoped ice is shown in figures 7 and 8. Table 1 gives an indication of the uncertainty in the derived scattering cross-section which is estimated by varying the values of σ_{scatt} and σ_{abs} and still obtaining a good fit (by eye) to the experimental data within the uncertainties of the measured *e*-folding depth and nadir reflectivity.

5.2 Realism of artificial sea ice

The sea ice simulator is designed to replicate natural sea ice growth in a controlled environment. Section 5.2 will review how the measured physical and optical parameters of the sea ice compare to field measurements of sea ice to ascertain how the laboratory sea ice compares to natural ice. Although the simulator creates a realistic sea ice environment, as with all simulators, there are limitations in the degree to which a "natural" sea ice environment can be created. Limitations in the following metrics were noted; light intensity, uneven ice growth, hyper-saline seawater, surface brine expulsion and reflectance measurements.

Temperature profiles from the laboratory sea ice show a linear increase in temperature from the surface to the ice base, this has been commonly reported (e.g. Eicken (2003); Perovich et al. (1998b)). Eicken (2003) also suggest that at typical winter temperatures ice would take $\sim$1 month to form 50 cm, this is a similar growth rate to that observed for the laboratory grown sea ice where it took approximately three weeks to grow 30 cm of ice.

Typical sea ice densities are reviewed by Timco and Frederking (1996) reporting first year sea ice densities in the range 0.84 to 0.94 g cm^{-3}, the density of sea ice created in the simulator ranged from 0.85 to 0.95 g cm^{-3}, thus being in the range of natural ice. Perovich et al. (1998b) measured density profiles through Arctic first year sea ice showing no clear variation with depth which is also observed in the laboratory sea ice.

Plots of salinity versus depth from ice cores from the sea ice simulator show the distinctive "C" shape with a higher salinity seen at the base and top of the cores, see figure 6. Malgrem et al. (1927) studied salinity of first-year ice also showing a characteristic "C" shape to the sea ice salinity profile. The shape of the salinity profile, explained by Eicken (2003), is due to a combination of salt segregation, gravity drainage and brine expulsion on the surface of the ice. Initially as sea ice in the simulator grows the seawater below the ice increases in salinity and similarly to natural sea ice the seawater below the ice is commonly hyper-saline. As the simulator continues to generate thicker sea ice there is an increase in the salinity of the brine beneath the sea ice which may eventually retard the growth and the water may become unrealistically saline if the experiment

were allowed to continue. In the experiment discussed here this is not a major problem for the experiments as the experiments were performed with ice thicknesses of 30 cm.

The typical structure of a first year sea ice is described by Eicken (2003) showing a granular surface layer, overlying columnar ice with granular/platelet ice at the ice-water boundary. The structure described by Eicken (2003) is the same as that observed in ice cores of the laboratory grown ice. The surface of the laboratory grown ice has a clear granular texture, and at the base there is a slushy platelet layer with columnar ice in between.

Although the sides of the tank are insulated ice growth across the tank is not quite uniform with slightly thicker ice ($\sim$5 cm) around the edges of the tank towards the end of an experiment ($\sim$3 cm from the sides) and around the polypropylene pole which the thermocouples were inserted into. Unfortunately the thicker ice areas could not be rectified but are unimportant as reflectance measurements were taken in the same place, away from the sides of the tank. All measurements of the extinction coefficient/*e*-folding depth were made more than three *e*-folding depths from the sides of the tank so that any extra ice growth at the edges of the tank would have no impact on the measurements.

Typical extinction coefficients of sea ice at around 500 nm are around $\sim$0.03 cm^{-1} (Grenfell and Maykut, 1977). Calculated extinction coefficients for the laboratory grown ice range from 0.1–0.03 cm^{-1}.

Overall the sea ice simulator creates a realistic sea ice, recreating typical growth rates, salinity and temperature profiles, reflectance and extinction coefficients of a first year sea ice.

6 Conclusions

The study has shown that the TUV-snow radiative transfer model can reproduce reflectivity of undoped and black carbon doped sea ice with different sea ice fabrics and thus the model can be used with confidence. Black carbon in laboratory sea ice has been shown to reduce the reflectivity of the ice to 97%, 90%, and 79% of the clean ice reflectivity at a wavelength of 500 nm for mass ratios of 75, 150 and 300 ng g^{-1} of black carbon respectively in the top 5 cm layer of the laboratory sea ice, which is in agreement with radiative-transfer calculations. To reproduce the reflectivity using the TUV-snow model measured reflectivity and *e*-folding depth data from laboratory sea ice is used to derive scattering and absorption cross-sections of the ice using the TUV-snow model. The derived scattering cross-section values are typical of sea ice (e.g. Grenfell and Maykut (1977), Timco and Frederking (1996) and Perovich (1996), while the derived absorption cross-sections show the presence of other absorbing impurities in the undoped ice, which matches the absorption spectra of algae.

Acknowledgements. M. Lamare wishes to thank NERC for support from NE/K00770X/1. M. D. King acknowledges support from RHUL for construction of the sea ice simulator with money from JIF funds. All authors thank the Cabot Corporation for the Monarch 120.

References

Abramoff, M., Magalhaes, P., and Ram, S.: Image Processing with ImageJ, Biophotonics International, 11, 36–42, 2004.

Atkinson, M. and Bingman, C.: Elemental composition of commercial seasalts, Journal of Aquariculture and Aquatic Sciences, 8, 39, 1997.

Ball, C., Levick, A., Woolliams, E., Green, P., Dury, M., Winkler, R., Deadman, A., Fox, N., and King, M.: Effect of polytetrafluoroethylene (PTFE) phase transition at 19 °C on the use of Spectralon as a reference standard for reflectance, Applied Optics, 52, 4806–4812, 2013.

Bond, T., Doherty, S., Fahey, D., Forster, P., Berntsen, T., DeAngelo, B., Flanner, M., Ghan, S., Kärcher, B., and Koch, D.: Bounding the role of black carbon in the climate system: A scientific assessment, Journal of Geophysical Research: Atmospheres, 118, 5380–5552, 2013.

Boyer, T., Antonov, J., Baranova, O., Coleman, C., Garcia, H., Grodsky, A., Johnson, D., Locarnini, R., Mishonov, A., O'Brien, T., Paver, C., Reagan, J., Seidov, D., Smolyar, I., and Zweng, M.: World Ocean Database 2013, Tech. Rep. NOAA Atlas NESDIS 72, National Oceanic and Atmospheric Administration, 2013.

Brandt, R. E., Warren, S. G., and Clarke, A. D.: A controlled snowmaking experiment testing the relation between black carbon content and reduction of snow albedo, Journal of Geophysical Research: Atmospheres, 116, 2011.

Bricaud, A., Claustre, H., Ras, J., and Oubelkheir, K.: Natural variability of phytoplanktonic absorption in oceanic waters: Influence of the size structure of algal populations, Journal of Geophysical Research, 109, 2004.

Buist, I., Potter, S., Nedwed, T., and Mullin, J.: Herding surfactants to contract and thicken oil spills in pack ice for in situ burning, Cold regions science and technology, 2011.

Clarke, A.: Integrating sandwich: a new method of measurement of the light absorption coefficient for atmospheric particles, Applied Optics, 21, 1982.

Clarke, A. and Noone, K.: Soot in the Arctic snowpack: A cause for perturbations in radiative transfer, Atmospheric Environment (1967), 19, 2045–2053, 1985.

Dang, C., Brandt, R. E., and Warren, S. G.: Parameterizations for narrowband and broadband albedo of pure snow and snow containing mineral dust and black carbon., Journal of Geophysical Research: Atmospheres, 120, 5446–5468, 2015.

Doherty, S., Warren, S., Grenfell, T., Clarke, A., and Brandt, R.: Light-absorbing impurities in Arctic snow, Atmospheric Chemistry and Physics, 10, 18 807–18 878, 2010.

Eicken, H.: Sea ice-an introduction to its physics, biology, chemistry and geology, chap. From the microscopic, to the macroscopic, to the regional scale: growth, microstructure and properties of sea ice, Blackwell Science, London, 2003.

Flanner, M., Zender, C., Randerson, J., and Rasch, P.: Present-day climate forcing and response from black carbon in snow, Journal of Geophysical Research, 112, 2007.

France, J. and King, M.: The effect of measurement geometry on recording solar radiation attenuation in snowpack (e-folding depth) using fibre-optic probes, Journal of Glaciology, 58, 2012.

France, J., King, M., Frey, M., Erbland, J., Picard, G., Preunkert, S., MacArthur, A., and Savarino, J.: Snow optical properties at Dome C (Concordia), Antarctica; implications for snow emissions and snow chemistry of reactive nitrogen, Atmospheric Chemistry and Physics, 11, 9787–9801, 2011.

France, J., Reay, H., King, M., Voison, D., Jacobi, H., Domine, F., Beine, H., Anastasio, C., MacArthur, A., and Lee-Taylor, J.: Hydroxyl Radical and NO_x producion rates, black carbon concentrations and light-absorbing impurities in the snow from field measurements of light penetration and nadir reflectivity of on-shore and off-shore coastal Alaskan snow, Journal of Geophysical Research, 117, 2012.

Goldenson, N., Doherty, S., Bitz, C., and Holland, M.: Arctic climate response to forcing from light-absorbing particles in snow and sea ice in CESM, Atmospheric Chemistry and Physics, 12, 7903–7920, 2012.

Grenfell, T. and Maykut, G.: The optical properties of ice and snow in the Arctic Basin, Journal of Glaciology, 18, 1977.

Grenfell, T. and Perovich, D.: Radiation absorption coefficients of polycrystalline ice from 400–1400 nm, Journal of Geophysical Research, 86, 7447–7450, 1981.

Grenfell, T., Light, B., and Sturm, M.: Spatial distribution and radiative effects of soot in the snow and sea ice during the SHEBA experiment: The surface heat budget of Arctic ocen (SHEBA), Journal of Geophysical Research, 107, 2002.

Grenfell, T., Doherty, S., Clarke, A., and Warren, S.: Light absorption from particulate impurities in snow and ice determined by spectrophotometric analysis of filters, Applied Optics, 50, 2037–2048, 2011.

Haas, C., Cottier, F., Smedsrud, L., and Thomas, D.: Multidisciplinary ice tank study shedding new light on sea ice growth processes, EOS, Transactions, 80, 507–513, 1999.

Hadley, O. and Kirchstetter, T.: Black carbon reduction of snow albedo, Nature Climate Change, 2, 437–440, 2012.

Hansen, J. and Nazarenko, L.: Soot climate forcing via snow and ice albedos, Proceedings of the National Academy of Sciences of the United States of America, 101, 423, 2004.

Hare, A., Wang, F., Barber, D., Geilfus, N., and Galley, R.: pH evolution in sea ice grown at an outdoor experimental facility, Marine Chemistry, 2013.

Heilbronner, R. and Barrett, S.: Image analysis in Earth Sciences: microstructures and textures of earth materials, Springer Science and Business Media, 129, 2013.

Highwood, E. and Kinnersley, R.: When smoke gets in our eyes: The multiple impacts of atmospheric black carbon on climate, air quality and health, Environment international, 32, 560–566, 2006.

Holland, M., Bailey, D., Breigleb, B., Light, B., and Hunke, E.: Improved sea ice short wave radiation physics in CCSM4: The impact of melt ponds and aerosols on Arctic sea ice, Journal of Climate, 25, 1413–1430, 2012.

IPCC: IPCC Working Group 1 Fifth Assessment Report Summary for Policy Makers - Climate Change 2013: The Physical Science Basis., Tech. rep., IPCC, 2013.

Jacobson, M.: Strong radiative heating due to the mixing state of black carbon in atmospheric aerosols, Nature, 409, 695–697, 2001.

Jacobson, M.: Climate response of fossil fuel and biofuel soot, accounting for soot's feedback to snow and sea ice albedo and emissivity, Journal of Geophysical Research, 109, 2004.

Johnston, M. and Timco, G.: Temperature Changes in First Year Arctic Sea Ice During the Decay Process., in: Proceedings of the 16th IAHR International Symposium on Ice, vol. 2, pp. 194–202, 2002.

King, M., France, J., Fisher, F., and Beine, H.: Measurement and modelling of UV radiation penetration and photolysis rates of nitrate and hydrogen peroxide in Antarctic sea ice: An estimate of the production rate of hydroxyl radicals in first-year sea ice, Journal of Photochemistry and Photobiology A: Chemistry, 176, 39–49, 2005.

Krembs, C., Mock, T., and Gradinger, R.: A mesocosm study of physical-biological interactions in artificial sea ice: effects of brine channel surface evolution and brine movement on algal biomass, Polar Biology, 24, 356–364, 2001.

Lamare, M. L., Lee-Taylor, J., and King, M. D.: The impact of atmospheric mineral aerosol deposition on the albedo of snow and sea ice-are snow and sea ice optical properties more important than mineral aerosol optical properties?, Atmospheric Chemistry and Physics, 16, 843–860, 2016.

Ledley, T. and Thompson, S.: Potential effect of nuclear war smokefall on sea ice, Climatic Change, 8, 155–171, 1986.

Lee-Taylor, J. and Madronich, S.: Calculation of actinic fluxes with a coupled atmosphere-snow radiative transfer model, Journal of Geophysical Research, 107, 2002.

Libois, Q., Picard, G., France, J., Arnaud, L., Dumont, M., Carmagnola, C., and King, M. D.: Influence of grain shape on light penetration in snow, The Cryosphere, 7, 1803–1818, 2013.

Light, B., Eicken, H., Maykut, G., and Grenfell, T.: The effect of included particulates on the spectral albedo of sea ice, Journal of Geophysical Research, 103, 27 739–27 752, 1998.

Light, B., Carns, R., and Warren, S.: "Albedo dome": A method for measuring spectral flux-reflectance in a laboratory for media with long optical paths, Applied Optics, 54, 2015.

Malgrem, F., Institutt, G., Forskningsfond, S., and Fond, N.: The Norwegian Polar Expedition 'Maud,' 1918–1925:Scientific Results, vol. 1, chap. On the properties of sea-ice, pp. 1–67, Gofys. Inst., Bergen, Norway, 1927.

Marks, A. and King, M.: The effects of additional black carbon on the albedo of Arctic sea ice: variation with sea ice type and snow cover, The Cryosphere, 7, 1193–1204, 2013.

Marks, A. and King, M.: The effect of snow/sea ice type on the response of albedo and light penetration depth (e-folding depth) to increasing black carbon, The Cryosphere, 8, 1023–1056, 2014.

Mitchell, J.: Visual range in the polar regions with particular reference to the Alaskan Arctic, Journal of Atmospheric and Terrestrial Physics Special Supplement, pp. 195–211, 1957.

Mobley, C., Cota, G., Grenfell, T., Maffione, R., Pegau, W., and Perovich, D.: Modeling light propagation in sea ice, Geoscience and Remote Sensing, IEEE Transactions on, 36, 1743–1749, 1998.

Mock, T., Dieckmann, G., Haas, C., Krell, A., Tison, J., Belem, A., Papadimitriou, S., and Thomas, D.: Micro-optodes in sea ice: a new approach to investigate oxygen dynamics during sea ice formation, Aquatic Microbial Ecology, 2002.

Mundy, C., Gosselin, M., Ehn, J., Belzile, C., Poulin, M., Alou, E., Roy, S., Hop, H., Lessard, S., Papakyriakau, T., Barber, D., and Stewart, J.: Characteristics of two distinct high-light acclimated algal communities during advanced stages of sea ice melt, Polar Biology, 34, 1869–1886, 2011.

Nomurai, D., Yoshikawa-Inoue, H., and Toyota, T.: The effect of sea-ice growth on air–sea CO_2 flux in a tank experiment, Tellus B, 58, 2006.

Papadimitriou, S., Kennedy, H., Kattner, G., Dieckmann, G., and Thomas, D.: Experimental evidence for carbonate precipitation and CO_2 degassing during sea ice formation, Geochemica et Cosmochimica Acta, 68, 1749–1761, 2003.

Peltoniemi, J., Gritsevich, M., Hakala, T., Dagsson-Waldhauserová, P., Arnalds, Ó., Anttila, K., Hannula, H., Kivekäs, N., Lihavainen, H., Meinander, O., Svensson, J., Virkkula, A., and De Leeuw, G.: Soot on Snow experiment: bidirectional reflectance factor measurements of contaminated snow, The Cryosphere, 9, 2323–2337, 2015.

Perovich, D.: The Optical Properties of Sea Ice., US Army Corps of Engineers: Cold Regions Research and Engineering Laboratory, 96, 1996.

Perovich, D. and Grenfell, T.: Laboratory studies of the optical properties of young sea ice, Journal of Glaciology, 27, 1981.

Perovich, D., Roesler, C., and Pegau, W.: Variability in Arctic sea ice optical properties, Journal of Geophysical Research, 103, 1193–1208, 1998b.

Phillips, G. and Simpson, W.: Verification of snowpack radiation transfer models using actinometry, Journal of Geophysical Research, 110, 2005.

Polach, R., Ehlers, S., and Kujala, P.: Model-Scale Ice-Part A: Experiments, Cold regions science and technology, 94, 74–81, 2013.

Rabus, B. and Echelmeyer, K.: Increase of 10 m ice temperature: climate warming or glacier thinning?, Journal of Glaciology, 48, 2002.

Ramanathan, V. and Carmichael, G.: Global and regional climate changes due to black carbon, Nature Geoscience, 1, 221–227, 2008.

Rand, J. and Mellor, M.: Ice-coring augers for shallow depth sampling, Tech. Rep. 85-21, CRREL, Washington, 1985.

Reay, H., France, J., and King, M.: Decreased albedo, efolding depth and photolytic OH radical and NO_2 production with increasing black carbon content in Arctic snow., Journal of Geophysical Research, 117, 2012.

Stamnes, K., Tsay, S., Jayaweera, K., and Wiscombe, W.: Numerically stable algorithm for discrete-ordinate-method radiative transfer in multiple scattering and emitting layered media, Applied Optics, 27, 2502–2509, 1988.

Timco, G. and Frederking, R.: A review of sea ice density, Cold regions science and technology, 24, 1–6, 1996.

Weeks, W.: On sea ice, chap. Snow, pp. 417–433, University of Alaska Press, 2010.

Chapter 5

Extreme low light requirement for algae growth underneath sea ice: A case study from Station Nord, NE Greenland

Citation:
Hancke, K., Lund-Hansen, L. C., **Lamare, M. L.**, King, M. D., Andersen, P., & Sorrell, B. K. (2017). Extreme low light requirement for algae growth underneath sea ice: A case study from Station Nord, NE Greenland. Submitted to: JGR Oceans.

Author contributions:
Lamare, M. performed the radiative-transfer calculations, participated in the theoretical discussions about the optical properties of snow and sea ice, and wrote section 2.5.

Hancke, K., Lund-Hansen, L. C., Andersen, P., and Sorrell, B. K. aqcuired the data in the field.

Hancke, K., Lund-Hansen, and Sorrell, B. K. piloted the study.

Hancke, K. processed the field data and was the main author of the paper.

King, M.D. oversaw the modelling part of the study and wrote section 3.6.

Running head: Minimum light requirement for ice algae

Extreme low light requirement for algae growth underneath sea ice: A case study from Station Nord, NE Greenland

Kasper Hancke[1,2]†, Lars C. Lund-Hansen[1,3], Maxim L. Lamare[4], Stine Højlund Pedersen[3,5], Martin D. King[4], Per Andersen[6], and Brian K. Sorrell[1]

[1]Aarhus University, Department of Bioscience, Aquatic Biology, Ole Worms Allé 1, 8000 Aarhus C, Denmark.

[2] Norwegian Institute for Water Research (NIVA), Research Centre for Coast and Ocean, Gaustadalléen 21, NO-0349 Oslo, Norway.

[3] Aarhus University, Department of Bioscience, Arctic Research Centre, Ny Munkegade 116, 8000 Aarhus C, Denmark.

[4] Royal Holloway University of London, Department of Earth Sciences, Egham, Surrey, TW20 0EX, UK.

[5] Department of Biological Sciences, University of Alaska Anchorage, 3151 Alumni Loop, Anchorage, Alaska 99501, USA.

[6] NIRAS, Ceres Allé 3, 8000 Aarhus C

Corresponding author: Kasper Hancke (kasper.hancke@niva.no)

†Current address: Norwegian Institute for Water Research (NIVA), Research Centre for Coast and Ocean, Gaustadalléen 21, NO-0349 Oslo, Norway.

Key Points:

- Extreme low light requirement for algae growth
- Unique measurements of under-ice algae growth under ~2 m of snow and sea ice
- Change in snow optical properties allow algae growth via temperature-driven snow metamorphosis

Abstract (<250 words)

Microalgae colonizing the underside of sea ice in spring are a key component of the Arctic foodweb as they drive early primary production, and transport carbon from the atmosphere to the ocean interior. Onset of the ice algae spring bloom is typically limited by light availability, and consensus is that a few decimeters of snow is enough to prevent sufficient solar radiation to reach underneath the sea ice. We challenged this consensus and investigated the onset of spring bloom and the light requirement of algae growth underneath sea ice, and the importance of snow optical properties for light penetration. Colonization by ice algae began in May under >1 m of first-year sea ice with ~1 m thick snow cover on top, in NE Greenland. The initial growth of ice algae began at extremely low irradiance (<0.17 μmol photons m^{-2} s^{-1}) and was documented as an increase in Chlorophyll *a* (chl *a*), an increase in algal cell number, and a viable phototrophic activity (quantum yield). Snow thickness changed little during May (from 110 to 91 cm), however the snow temperature increase steadily, as observed from high frequency temperature profiles. We propose that changes in snow optical properties, caused by temperature-driven snow metamorphosis, was the primary driver allowing for sufficient light to penetrate through the thick snow and initiate algae growth below the sea ice. This was supported by radiative transfer modelling of light attenuation. Implications are a possible earlier productivity by ice algae in Arctic sea ice than recognized today.

Introduction

Recently, a dynamic and viable ecosystem has been discovered in Arctic sea waters during the polar night, suggesting that even very low light conditions can enable the onset of biological activity and possibly 'spring awakening' of the Arctic marine food web [*Berge et al.*, 2015a; *Berge et al.*, 2015b]. In addition, extreme low light conditions have been measured in polar waters during the polar night, demonstrating biological responses to solar radiation levels well below what has previously been assumed significant [*Cohen et al.*, 2015].

Ice algae are a substantial contributor to the Arctic primary production creating the food source for ice-associated zooplankton and amphipods [*Kevin R. Arrigo*, 2014; *Soreide et al.*, 2010], both of which are key contributors to the Arctic food web. For instance, it has been shown that the timing of the ice algae bloom has implications for the food availability and quality for ice-associated zooplankton, and for the success rate of zooplankton hatching [*Leu et al.*, 2011; *Leu et al.*, 2010]. Moreover, ice algae play a significant role for the Arctic carbon cycle and sequestration, and are important as a carbon export pathway from surface waters to the deep ocean [*Assmy et al.*, 2013; *Fernandez-Mendez et al.*, 2014].

Ice algae are typically abundant when there is sufficient irradiance underneath the sea ice for photosynthesis and growth, and their biomass can be considerable, compared to phytoplankton in Arctic coastal and ocean ecosystems [*Leu et al.*, 2015, and references herein]. However, little is known about the early timing of ice algae blooms, and especially the threshold irradiances required to trigger early ice algae colonization and growth, and how well ice algae are acclimated to very low light levels.

Light availability underneath sea ice is regulated by radiative transfer of solar radiation through the ice and overlying snow cover [*Gosselin et al.*, 1990; *Marks and King*, 2014; *Thomas and Dieckmann*, 2009]. Despite an often thicker layer of ice than snow, snow thickness is most important in regulating the availability of light for ice algae, because of its much higher light scattering properties and albedo.

Scattering properties of snow is regulated by its density and grain size, which again is affected by snow temperature via metamorphism of snow [*Marks and King*, 2014]. On sea ice, temperature gradients within the snowpack is typical creating a vapor pressure gradient from the relative warm bottom upwards to the colder layers interfacing the air. Such vapor

gradients lead to an increase in snow grain size and a decrease in the optical scattering cross-section of the snow, again leading to a decrease in the light attenuation [*Lamare et al.*, 2016; *Libois et al.*, 2013]. It has been suggested that ~40 cm of snow cover is enough to prevent algae growth [*Campbell et al.*, 2014; *Mundy et al.*, 2007].Until recently, is has been anticipated that below such snow covers, little biological activity is occurring due to the absent of light.

In this study, we provide evidence of an onset of ice algae growth at very low light conditions, below ~1 m of snow on top of 1m of sea ice. Further, we provide modelled data of the photon flux penetrating a thick snow cover and under lying sea ice, and argue that optical properties of snow are regulating the light availability underneath sea ice early in the spring. Here we aimed to study the light requirement for ice algae growth, and to quantify the minimum photon flux needed to support net growth of ice algae and initiate the spring colonization. Further, we test the hypothesis that optical properties of snow impact the light availability underneath sea ice. Implications are that Arctic sea ice algae may bloom much earlier than often anticipated with consequences for the Arctic primary production carbon flux.

2 Materials and Methods

2.1 Site description and sample collection

This study provides the first sea ice algae data from the Wandel Sea near the newly established Villum Research Station (VRS), located at the Danish military base “Station Nord” in far North East Greenland (Figure 1). Data were collected between 16 April and 24 May 2015 as part of the large international Arctic Science Partnership research campaign, and coordinated by the Arctic Research Center, Aarhus University, Denmark.

Data were collected at a main station (termed 1C) approximately every third day, and along a ~20km transect (1A to 1E) stretching NW from the shoreline of the research station. The inner part of the Wandel Sea is relatively shallow stretching from the shoreline to the shelf drop, with water depth of <200m. Water depths at the investigated stations are listed in Table 1. The Wandel Sea meets a complex of large fjords to the south west consisting of Danmarks Fjord, Hagens Fjord and Independence Fjord, while bordering the Arctic Ocean at the

Northeast [*Dmitrenko et al.*, 2016]. Sea ice completely covers the fjord complex during winter, in part by First-Year (FYI) and in part by Multi-year (MYI) sea ice; where FYI typically dominates along the shores and MYI the interior of the basin. This study includes only land-fast first-year sea ice samples.

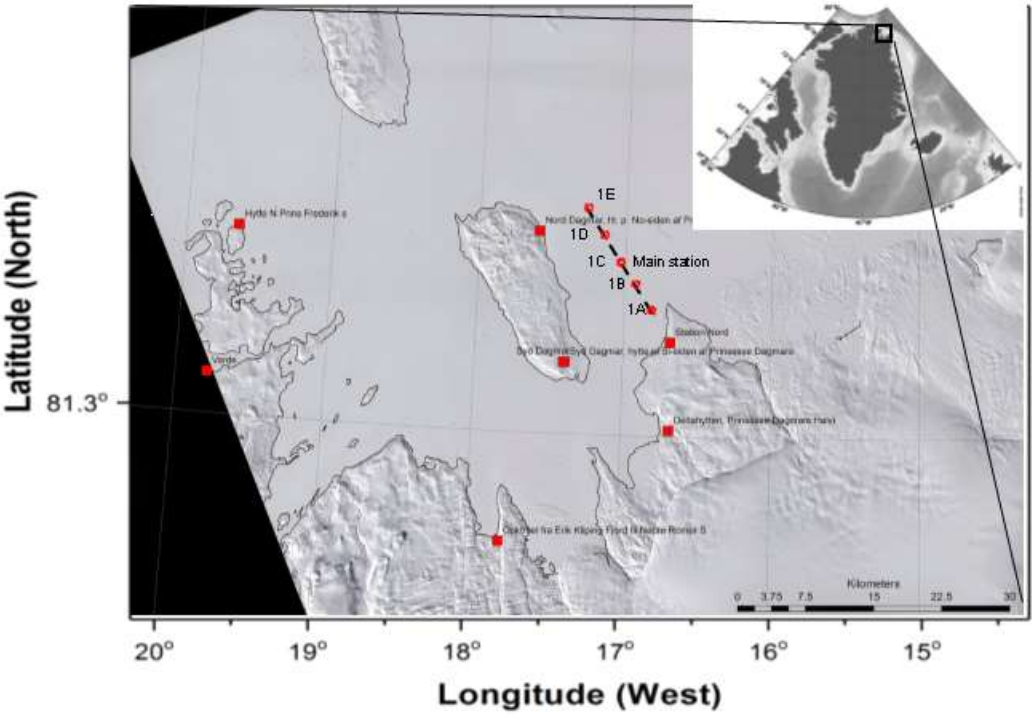

Figure 1: Map of sampling area, including the 5 sampling stations (1A to 1E) located across a transect stretching ~20 km to the north west from the shore line outside the Villum Research Station and Station Nord, a Danish military station. The map is based on a MODIS AQUA (NASA) image from 25 April 2015, downloaded from www.dmi.dk.

The thickness of snow cover was measured with a manual snow-depth probe at each sea-ice coring site. Snow-depth observations were also collected in the greater surrounding area of site 1C in a right-triangle transect (~700 m in total length). In addition, the snow-cover thickness was estimated automatically using a sonic ranging sensor (Campbell Scientific SR50A) on a land-based monitoring station 2 km from the Villum Research Station. Observations of the physical properties of the snowpack was collected in snow pits dug at 1C on 5 May and 16 May including snow temperature (handheld digital thermometer), snow density (Snow-Hydro 100cc density cutter), and snow grain size, i.e., the longest dimension of the crystal (snowmetrics.com crystal card and magnifier).

Sea ice cores were collected using a Mark II Coring system with a diameter of 9 cm (Kovacs Enterprises), after removal of snow from the sea ice. A minimum of three cores were collected at each site, of which the lower 5 cm was sectioned for further analyses (e.g. chlorophyll, cell number, and nutrients). In the laboratory ice samples were melted slowly in the dark, diluted 1:1 with Whatman GF/F filtered sea water, sampled immediately under the sea ice. Samples of Under-Ice Water (UIW) were collected from 1m beneath the sea ice using a small handheld water sampler (temperature and salinity are shown in Table 1).

A perturbation experiment clearing the snow cover (2x2m) on the sea ice was carried out at the main station (1C), initiated on 24 April. Owing to strong winds and precipitation, snow had to be repeatedly removed from the manipulated site on 1 May and 6 May. Samples of sea ice and sea water were collected from the snow-cleared site in a similar matter to the undisturbed stations.

Table 1: Station position, ice type, thickness of ice and snow and water physics.

Station	Lat.	Long.	Ice type	Ice thickness *	Snow thickness **	Snow thickness from transect ***	UIW		water depth
#	N	W	#	cm	cm	cm	temp oC	sal PSU	m
1A	81.623	16.807	FYI	115	98.9 ± 5.3		-1.1	19.5	20
1B	81.652	16.896	FYI	118	91.6 ± 3.1		-1.2	19.5	58
1C	81.673	16.969	FYI	110	95.0 ± 4.4	95.4 ± 7.0 (5 May) 94.1 ± 10.3 (16 May)	-1.2	19.4	73
1D	81.696	17.043	FYI	114	99.2 ± 3.1		-1.1	19.3	75
1E	81.72	17.115	FYI	145	98.7 ± 3.4		-1.1	19.3	87

* n = 3, ** n = 10, *** n= 198

2.2 Optical measurements

Incident downwelling and upwelling Photosynthetically Active Radiation (PAR) above the snowpack and under-ice PAR were measured continuously at the main station (1C) during the campaign, using flat cosine-corrected PAR sensors (LiCor 191 above and LiCor 192 below) connected to a Campbell CR10X data logger. The under-ice sensor was positioned through a 9 cm diameter core hole penetrating both the snow pack and sea ice. The sensor

was positioned 3 cm below the underside of the sea ice 15 cm away from the core hole. After positioning the sensor, the drill hole was carefully filled with the drill core and packed with snow. The instruments were undisturbed during the field campaign. Also, down- and upwelling solar (global) radiation (CNR4 Net Radiometer, Kipp & Zonen) was measured at the Villum Research Station using an automatic weather station (established by Asiaq, Greenland Survey on behalf of the Department of Environmental Science/Danish Centre for Environment and Energy [DCE], and operated by Aarhus University).

Albedo of the snow pack was calculated as the ratio of upwelling PAR to downwelling PAR. The detection limit of the PAR sensors was 0.15 µmol photons m^{-2} s^{-1}.

Vertical profiles of downwelling spectral irradiance [$E_d(\lambda)$] were measured through the snow pack after digging a snow-pit allowing for a vertical positioning of a spectral irradiance sensor [*France and King*, 2012]. Profiling was conducted in the snow to the south of the pit hole around solar noon, after characterizing the physical properties of the snow. The vertical resolution of the profiles was 5 to 20 cm, and measurements started from the snow-ice interface working upwards. Spectral irradiance was measured from 320 to 950 nm, with a 3.3nm spectral resolution using a spectroradiometer (RAMSES ACC-VIS, TriOS, Germany). Also, under-ice spectral irradiance was measured using the RAMSES sensor at 5 cm below the ice-water interface 50 cm laterally from the core hole, positioned using a folding L-shaped metal 'arm' reaching underneath the ice. During profiling, the surface incident PAR was measured simultaneously using a small cosine-corrected quantum sensor (MQS-B, logged on a ULM-500 data logger, Walz, Germany). Only irradiance-depth profiles measured during stable surface irradiance (+/– 5%) were collected. The RAMSES spectral irradiance sensor was freshly factory-calibrated for the campaign, and acted as the campaign standard for all the PAR sensors which were calibrated against this. Unfortunately, the RAMSES sensor filled with seawater after the measurements on May 7th, and failed thereafter.

Diffuse vertical attenuation coefficients were calculated wavelength specifically ($K_d(\lambda)$, m^{-1}) accordingly [*Kirk*, 1994]:

$$K_{d(\lambda)} = \frac{\ln\left(E_{dz1(\lambda)}/E_{dz2(\lambda)}\right)}{z2-z1} \qquad (1)$$

where $E_{dz1(\lambda)}$ and $E_{dz2(\lambda)}$ represent downwelling irradiance at two different depths (z) in the snow/ice column, respectively.

178

179 **2.3 Photosynthetic measurements**

180 Photosynthetic activity of the sea ice algae were measured using a Walz PhytoPAM variable
181 fluorometer (System I, Walz, Effeltrich, Germany,[*Schreiber et al.*, 1986]), equipped with a
182 highly sensitive Photomultiplier-Detector (PM-101P, Walz). Algae on ice crystals from the
183 lower 1cm of collected cores were transferred immediately after sampling to a standard
184 plastic cuvette (with 4 clear sides), then heated just enough for the ice crystals to melt in the
185 palm of a hand (wearing disposable powder-free vinyl gloves). Instantly when the sample
186 became liquid it was placed inside the PAM incubation chamber and acclimated in the dark
187 (3 min). For purpose of PAM measurements, a tent camp was established on the ice at the
188 main station (1C) ensuring minimum transportation, rapid sample handling, and a shaded
189 working environment with an air temperature at ~0^{o}C. The maximum quantum yield of
190 charge separation (Φ_{max}) was calculated from the dark-acclimated fluorescence (F_o) and the
191 maximum fluorescence (F_m) after a saturation light pulse, as $(F_m - F_o) / F_m$ [*Genty et al.*,
192 1989]. F_o and F_m measures were corrected for background fluorescence using a 'blank'
193 obtained by 0.2 µm filtering of a sub-sample to the original sample. For details on the
194 measuring protocol see [*Hancke et al.*, 2015].

195 **2.4 Laboratory analyses**

196 The Chlorophyll *a* (Chl *a*) concentration (mg m^{-3}) in ice cores was measured from the sea-
197 water-diluted samples filtered onto GF/F glass fiber filters (Whatman) extracted in 5 mL 96%
198 ethanol during 24h (dark, 4°C). The concentration was determined in triplicate using a pre-
199 calibrated fluorometer (Turner Designs TD-700) [*Lorenzen*, 1966; *lund-Hansen et al.*, 2016].
200 The same procedure was used for Chl *a* measurements of the UIW, except that these were not
201 diluted prior to filtering.

202 Dominating algae groups were identified from light-microscopy analyses using a Palmer
203 Maloney chamber, on samples collected from FYI cores and from UIW preserved in LUGOL
204 (neutral, 1% final solution).

205 Concentration of [NO_3^-] and [NO_2^-], collectively termed [NO_3^-], was determined as NO on a
206 NOx analyzer (Model 42C, Thermo Environmental Instruments Inc.) after reduction to NO in
207 hot Vanadium Chloride [*Braman and Hendrix*, 1989]. Concentrations of [PO_4^{3-}] and [NH_4^+]

208 were determined by standard colorimetric methods [*Grasshoff et al.*, 1999] on a Shimadzu
209 UV-1800 spectrophotometer.

210

211 **2.5 Modelling**

212 Numerical radiative-transfer calculations of downwelling PAR throughout the snow and sea
213 ice were undertaken using the Tropospheric Ultraviolet and Visible Radiation Model (TUV-
214 snow) [*Lee-Taylor and Madronich*, 2002]. The TUV-snow model is a coupled atmosphere /
215 snow or sea ice model that uses the DISORT code [*Stamnes et al.*, 1988] and is described
216 fully in [*Lee-Taylor and Madronich*, 2002].

217

218 To model the field observations of PAR at station 1C, a layer of snow was modelled on a
219 first-year sea ice layer, with an underlying optically thick layer representing the seawater
220 under the sea ice. The layers of snow and sea ice were further split into multiple layers with
221 all the same optical properties for the snow and sea ice respectively. Two modelling
222 approaches were adopted. In the first scenario, the snow was consecutively given the optical
223 properties of three snow types previously characterized by the authors [*Lamare et al.*, 2016;
224 *Marks and King*, 2014]: cold polar snow, coastal windpacked snow and melting snow. A 1m
225 thick cover of snow, representing the average thickness of the snowpack at station 1C, was
226 defined on a 1m thick sea ice. In the second scenario, the sea ice optical properties remained
227 the same but the thickness of the snowpack was set to 91 and 110 cm respectively, to fit the
228 observations. The value of the light scattering cross-section of the snowpack, σ_{scatt}, was
229 varied over a wide range to represent snow metamorphism. The value of σ_{scatt} is inversely
230 proportional to the snow grain size [*Libois et al.*, 2013], and metamorphism of the snow tends
231 to increase the snow grain size [*Warren*, 1982] and thereby decrease the value of σ_{scatt}.

232

233 The light scattering and absorption in each sea ice and snow simulation are constrained in the
234 model by an asymmetry factor, *e.g*, a wavelength independent scattering cross section, σ_{scatt},
235 a wavelength dependent absorption cross section, σ_{abs}^{+}, and the sea ice/snow density and
236 thickness [*Lamare et al.*, 2016; *Lee-Taylor and Madronich*, 2002]. A first year sea ice layer
237 was modelled with a mass density of 800 kg m^{-3}, a scattering cross-section of 0.15 m^2 kg^{-1}
238 and a fixed asymmetry parameter *g* of 0.98, based on field values parametrized in *Marks and*
239 *King* [2014]. A density of 400 kg m^{-3} and a fixed asymmetry parameter *g* of 0.89 were used

240 to model the covering snow layer. The value of the scattering cross-section of the snow was
241 set to 1.25 m^2 kg^{-1} for melting snow, 7.50 m^2 kg^{-1} for coastal windpacked snow and 20.0 m^2
242 kg^{-1} for melting snow [*Lamare et al.*, 2016; *Marks and King*, 2014]. The scattering cross-
243 section was then varied between 1 m^2 kg^{-1} and 25 m^2 kg^{-1}, in 5 m^2 kg^{-1} steps for the second
244 modelling experiment.
245 The wavelength dependent absorption cross-section of ice was obtained from [*Warren and*
246 *Brandt*, 2008] for the snow and sea ice. A mass-ratio of 1 ng g^{-1} of black carbon was added to
247 the sea ice and snow, as small quantities of black carbon are likely to be found in snow and
248 sea ice in polar regions [e.g. *Doherty et al.*, 2010]. To represent the seawater under the sea
249 ice, a fixed wavelength independent albedo of 0.1 was used. The atmospheric parameters
250 used in the model are the same to that described in detail in [*Lamare et al.*, 2016].
251
252 The downwelling PAR throughout the snow and sea ice column was calculated as:
253
254 $$PAR = \int_{\lambda=400nm}^{\lambda=700nm} I(\lambda) d\lambda, \qquad (2)$$
255
256 with ***I(λ)***, the downwelling monochromatic irradiance and ***λ***, the wavelength. The snow and
257 sea ice were subdivided into 1 cm thick layers, apart from the 10 layers between atmosphere
258 and snow, snow and ice, and ice and seawater, which were 1 mm thick. The downwelling
259 PAR was calculated for each layer throughout the snow and sea ice.
260
261
262

3 Results and Discussion

3.1 Initiation of ice algae growth under extremely low light conditions

Here we document the initial phase of ice algae growth underneath thick landfast sea ice in Arctic NE Greenland, and provide evidence that ice algae spring growth may initiate at irradiance of <0.17 µmol photons m^{-2} s^{-1}, much lower than previously anticipated. We also present data to support the hypothesis that a change in optical properties of snow can lead to increased irradiance availability underneath sea ice from decreasing the optical scattering cross-section, using a radiative transfer model.

During the campaign period through April to June the Wandel Sea was permanently covered by ~1m of snow and >1m of sea ice (Table 1, Figure 2). Until early June snow thickness only decreased marginally, and air temperature was well below 0°C (average for April was –19.2°C, for May –13.2°C, and for June +1.2°C, Figure 2b).

During this period, incident solar radiation increased by ~4 fold, as the noon incident PAR increased from ~300 to ~1200 µmol photons m^{-2} s^{-1} (corresponding to 13 and 69 mol photons m^{-2} d^{-1}, Figure 2a). Driving this, the solar elevation angle increased from 13 to 30 degrees (a solar zenith angle change of 77º to 60º), from early April to late May.

The albedo in the PAR range was nearly unchanged during this same period of time (average ~0.9, Figure 2c). The under-ice irradiance was below the detection limit of the installed PAR sensor on the monitoring station C (0.15 µmol photons m^{-2} s^{-1}) until May 21th, and did not exceed 0.2 µmol m^{-2} s^{-1} until June 16 (Figure 2c). On May 7th, a PAR intensity of 0.17 µmol m^{-2} s^{-1} was measured underneath the sea ice after an intrusive spectral irradiance sensor (TriOS) was sent through a drill hole (see below).

The first signal of under-ice Chl was detected on May 5 (0.001 mg m^{-2}) when the concentration was significantly different from zero, despite a nearly unchanged thickness in snow and sea ice cover the preceding month (Figure 2c). Following this, we interpreted the increasing Chl *a* concentration as robust evidence of algae net growth and the very first stage of an ice algae bloom and colonization. This was a surprising result, as light availability underneath the ice cover was still extremely low, and the photon flux reaching the under-ice environment was efficiently hampered by the thick snow and ice cover.

It seems likely, that the lowest documented light intensity (0.17 μmol photons m^{-2} s^{-1}) observed indeed supported net growth of algae, and thus is confirmed as exceeding the compensation irradiance of an ice algae community. Irradiance intensities above the compensation point [i.e. the irradiance at which gross primary production equals community respiration] marks the initial start of an algae bloom [*Marra*, 2004]. To our knowledge, the lowest estimate of ice algae compensation irradiance is reported at 0.36 μmol photons m^{-2} s^{-1} [*Mock and Gradinger*, 2000], however this finding has later been questioned due to possibly effects of scattering in the ice [*Ehn and Mundy*, 2013]. In general, ice algae have been reported as some of the most extreme low-light adapted phototrophic species but in situ measurements are rare due to experimental and logistical challenges [*Thomas and Dieckmann*, 2009]. Commonly, values in the range of 2 to 9 μmol m^{-2} s^{-1} are considered compensation irradiances for ice algae [*Gosselin et al.*, 1986; *Horner and Schrader*, 1982; *Leu et al.*, 2010], but in extreme low light environments in the Antarctic, benthic microalgae have been reported photosynthetically active at less than 1 μmol photons m^{-2} s^{-1} [*Robinson et al.*, 1995]. In the deep, extreme low-light adapted red macro algae have demonstrated a minimum light requirements of 1.5 μmol photons m^{-2} s^{-1} [Pritchard et al., 2013]. Thus, we here suggest a new minimum light requirement for ice algae net growth.

In regions with less snow, ice algae colonization typically begins earlier in the season under Arctic landfast sea ice depending on latitude, as reviewed by *Leu et al.* [2015] and references therein. Field data from Resolute Bay (Arctic Canada) show a consistent relationship between development of ice algae chl *a* concentrations and the thickness of the snow pack. In years with <10cm of snow, ice algae colonization began in the middle of March, in the beginning of April if snow cover was between 10 cm and 20 cm, and in the middle of April at snow depths >20 cm (data compiled from multiple studies from 1985 to 2011 [*Leu et al.*, 2015]). A snow thickness less than 40 cm has been suggested as a required threshold for algae growth to occur [*Campbell et al.*, 2015; *Mundy et al.*, 2007], and most ice algae studies have been conducted with conditions of only a few centimeters of snow on the sea [e.g. *Hawes et al.*, 2012; *Leu et al.*, 2010; *Mundy et al.*, 2007]. To our knowledge, there are no previous scientific reports of ice algae abundance or thickness of snow from further north in East Greenland than Young Sound (74.3 °N). However, the region is known for extensive winter precipitation compared to typical High Arctic regions, partially explained by the presence of the Northeast Water (NEW) Polynya of the east coast [*Day et al.*, 2013; *Krabill et al.*, 2000].

The Danish military Sirius dog sled patrol reports that >1m of snow is not unusual for the region around Villum Research Station (*personal communication*).

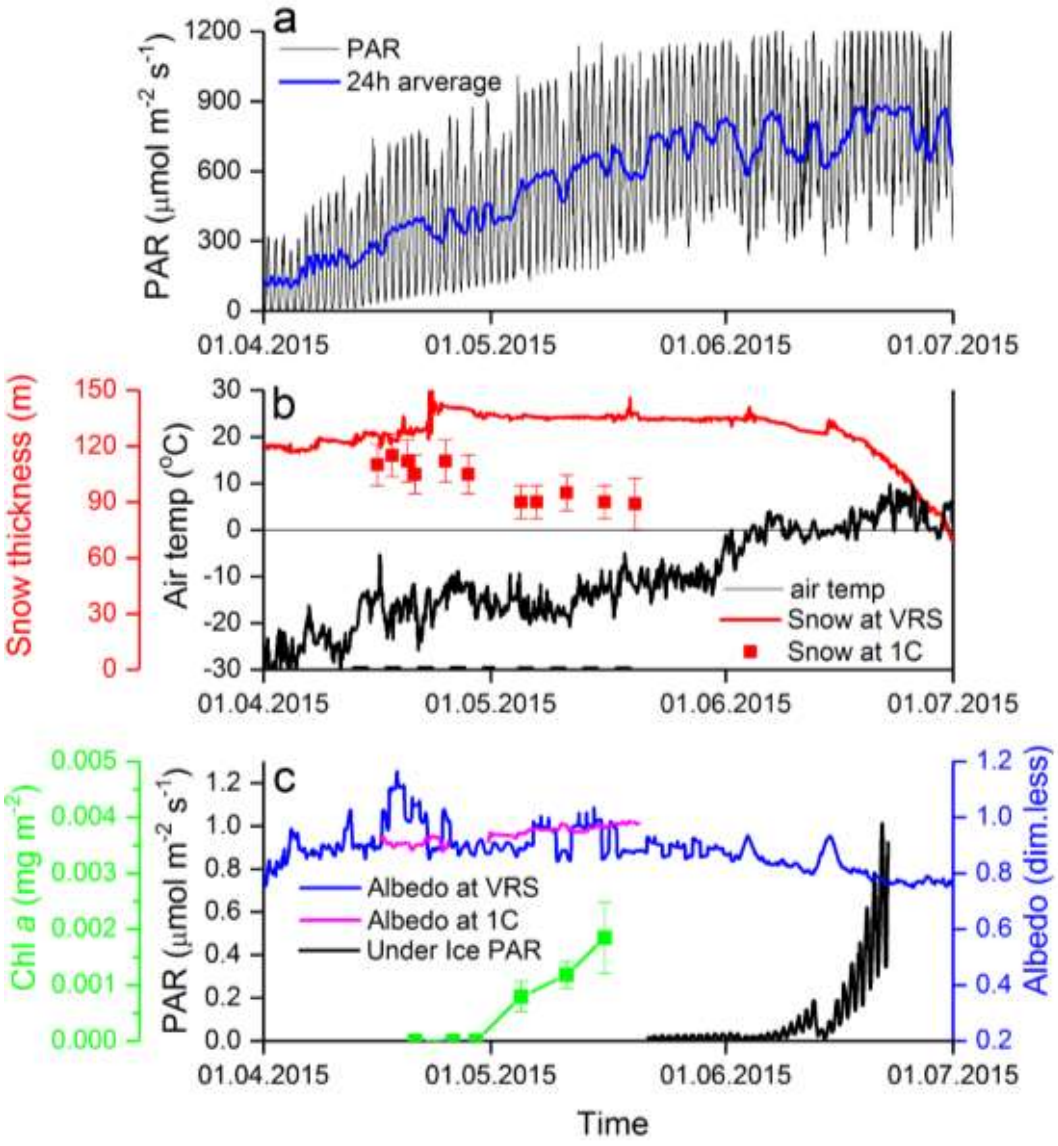

Figure 2: (a) Surface incident PAR (sampled every 30min, 24h running average in blue); (b) snow thickness at the Villum Research station (VRS, red line) and at station 1C (red squares), and air temperature (black line); and (c) surface albedo at the VRS (blue line) and at station 1C (magenta line), under ice PAR (black), and under-ice Chl a (green). Data at the Villum Research Station were collected on land.

To verify that the observation of the early abundance of ice algae Chl *a* (Figure 2c) was not only a sparse trace at the monitoring station 1C, we sampled ice cores and under-ice-water (UIW) from 5 stations across a 20 km transect on May 11th and 14th (Figure 1, 3a). The ice cores showed consistent concentrations of Chl *a* in the lower 3 cm between 0.001 and 0.002 mg m^{-2} along the transect, significantly different from zero ($p < 0.05$, Figure 3b). This documented that the trend of the time series data at station 1C was an accurate characterization of the trend in the region rather than a local phenomenon. The relatively large error bars in the figure shall be interpreted in respect of the very low concentration of Chl *a*. Like Chl *a* in ice cores, Chl *a* concentrations in the under-ice-water (UIW) also showed initial growth and increased from below detection to 0.01 mg m^{-3} as a function of time towards May 16th (Figure 3c). These observations were also supported by findings across the 20 km transect showing similar concentrations of Chl *a* in the UIW (0.005-0.01 mg m^{-3}, Figure 3d). Cell abundance obtained from Lugol fixed samples further verified the presence of algae cells and the temporal development in sea ice and under-ice water samples (Figure 3a, c). Dominating algae species in the lower 3 cm of the sea ice are given in Table 2.

Table 2: Dominating algae groups and inorganic nutrient concentrations in the brine of the lower 3 cm of the first-year old sea ice (FYI), and in the under ice water (UIW). All sampled at Station 1C.

	Dominating algae groups * (%)			Nutrients, FYI (µmol L^{-1})				Nutrients, UIW (µmol L^{-1})			
	Flagellates	Dinoflagellates	Diatoms	$N0_2+NO_3$ **	NH_3 **	PO_4 **	Si	$N0_2+NO_3$	NH_3	PO_4	Si
29 Apr	-	-	-	0.65	5.3	0.1	2.4	0.9	0.4	0.4	2.3
5 May	99.6[a]	-	[b]	-	-	-	-	-	-	-	-
7 May	91	1.3[a]	7.7[c]	0.3±0.1	1.1±0.2	0.1±0.03	-	-	-	-	-
11 May	-	-	-	0.7±0.17	3.0±0.4	0.1±0.05	0.4	1.2	0.9	0.3	2.3
16 May	99.7	0.15[d]	0.15[c]	1.6	7.8	0.5	0.5	1.3	0.6	0.4	2.6

[*] Unidentified pico-algae were dominating (>70% cell abundance) in all FYI samples. Here the remaining groups in percent of total minus pico-algae
[**] (n=3)
a) Unidentified (excl. bacteria)
b) Traces of *Thalassiosira sp.*
c) *Nitzschia closterium, N. longissima, Skeletonema costatum,* and unidentified
d) *Prorocentrum spp, Protoperidinium spp.*

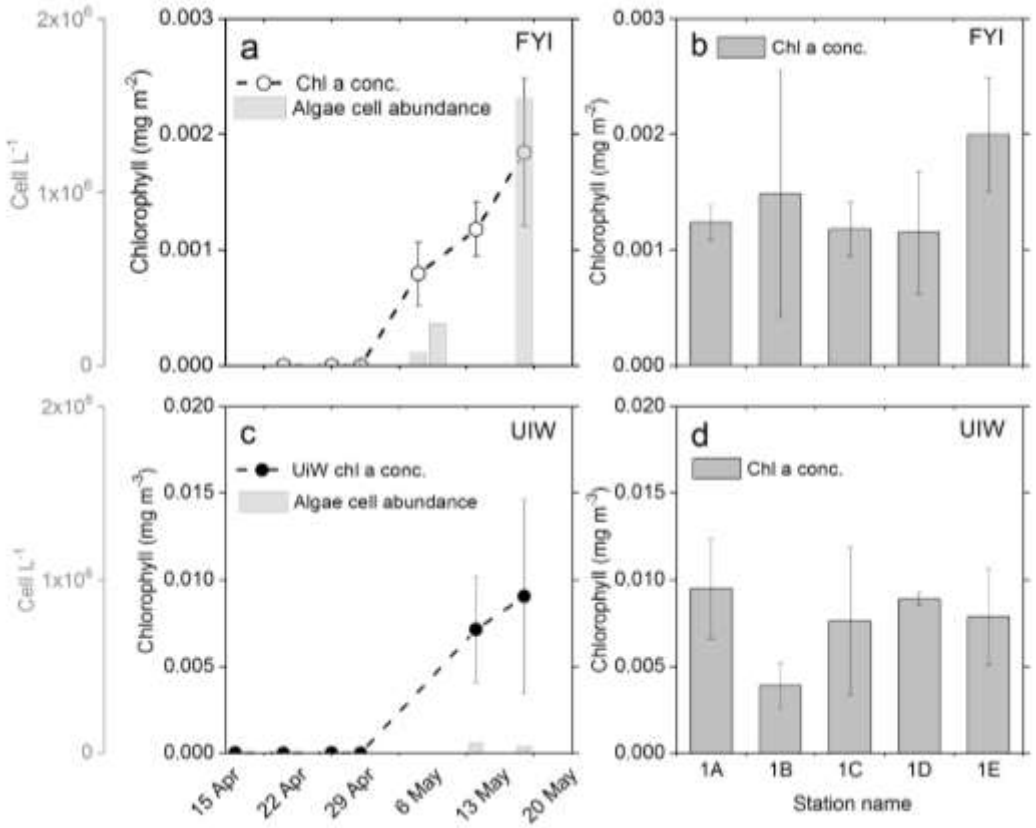

Figure 3: Chl *a* in first year ice (FYI) and in sea water underneath the ice (UIW): (a) Chl *a* and algae cell abundance in FYI as a function of time (Chl *a* data from Figure 2c), and (b) Chl *a* concentration at 5 stations across a ~20 km long transect from station A to E on 11 May (Station E was sampled on 14 May, n=3). c) Chl *a* and algae cell abundance in under-ice-water (UIW) as a function of time and d) across the transects (n=3).

The concentrations of Chl *a* presented here are extremely low compared to previous published values. In East and West Greenland, sympagic Chl *a* concentrations typically reach a seasonal maximum around 1 mg m^{-2} [*Glud et al.*, 2007; *Hawes et al.*, 2012; *Mikkelsen et al.*, 2008; *Rysgaard et al.*, 2001]. This is, however, low in a Pan-Arctic perspective, which typical shows seasonal peak concentrations near 20 mg m^{-2} [*Leu et al.*, 2015, and references herein; *Rysgaard and Glud*, 2007]. In the Canadian Arctic, seasonal peak values of >100 mg m^{-2} have occasionally been reported [e.g. *Cota and Horne*, 1989].

371 It should be emphasized that it is highly unlikely that the chlorophyll signal identified in this
372 study could be due to advection from an open water source, given the great distance (> 100
373 km) to the nearest open water (NEW polynya) and absence of ridges or cracks in the FYI (as
374 observed from satellite data and ground observations). An oceanographic survey of the region
375 during the same campaign reports of relatively fresh water immediately below the ice
376 (salinity of 16-21 at 1–5 m), with no trace of imported water masses [*Dmitrenko et al.*, 2016].
377 The fresh water assumedly origins from previous summer snow/ice melt water and freshwater
378 from a nearby glacial runoff.

379 Inorganic nutrients from the ice and under-ice water showed sufficient concentrations to
380 support algae growth and there are no reasons to suspect nutrient concentrations to be
381 limiting (Table 2). These values corresponded to inorganic nutrient concentrations observed
382 elsewhere in East Greenland, e.g. Young Sound [*Rysgaard et al.*, 2001], but are lower than
383 typically found elsewhere in sea ice and under-ice water around Svalbard [*Leu et al.*, 2010],
384 and in the Canadian Arctic [*Alou-Font et al.*, 2013; *Mundy et al.*, 2007].

385

386 **3.2 Light attenuation and requirement for growth**

387 Visible light attenuation in the snowpack was exponential in the bulk snow, giving e-folding
388 depths of ~16 cm (K_d ~6 m^{-1}, Figure 4a, b). These findings are comparable to values found in
389 Barrow, Alaska [*France et al.*, 2012], and Ny-Ålesund, Svalbard [*France et al.*, 2011].
390 Visible light attenuation in the near surface region of the snowpack depends on solar zenith
391 angle and sky conditions [*Simpson et al.*, 2002; *Warren*, 1982], and corresponding values of
392 K_d are effectively phonological of the measurements.

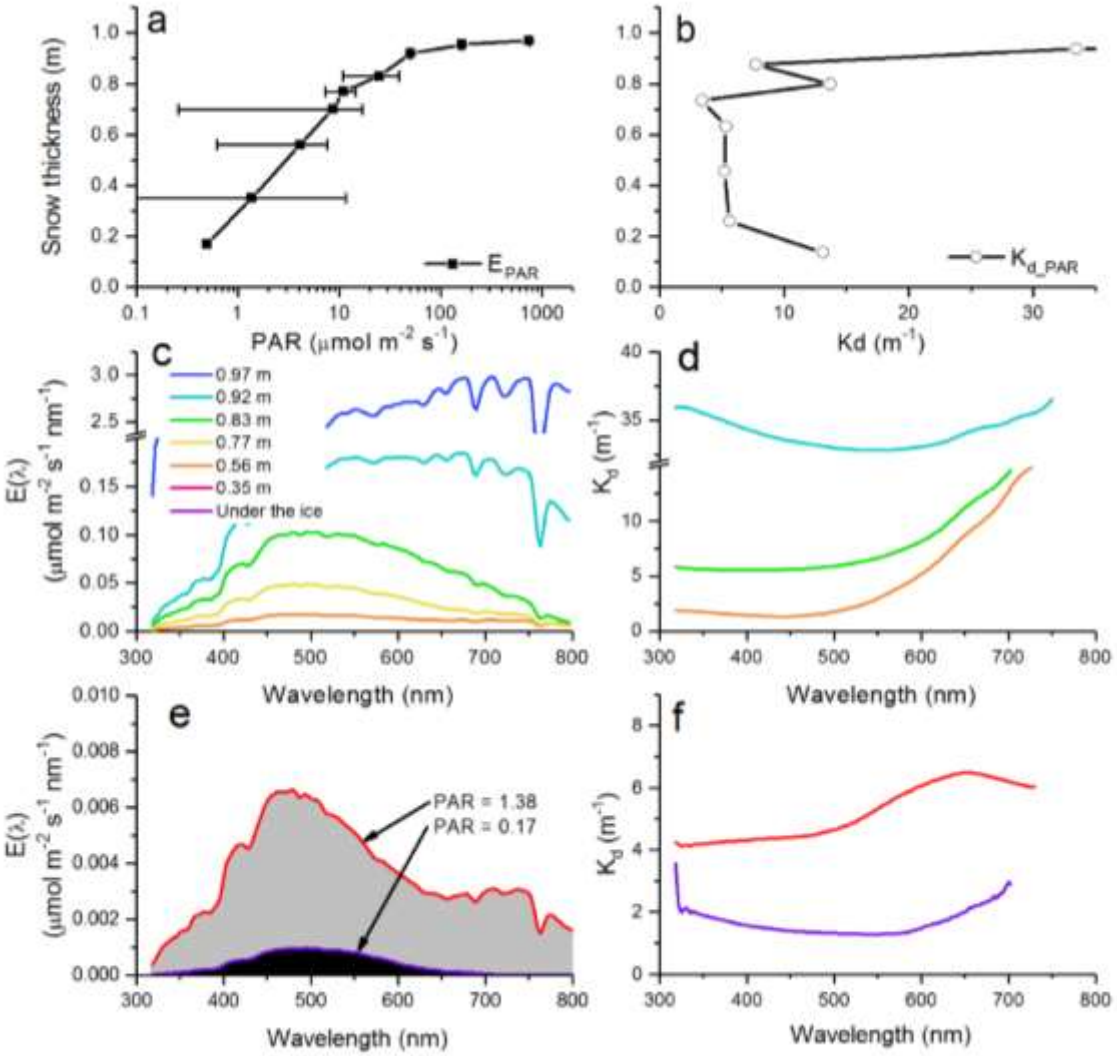

Fig 4: Measured spectral irradiance through the snow cover and under sea ice and the corresponding attenuation coefficients (K_d). (a) Profile of PAR (error bars are C.V); (b) profile of $K_{d,PAR}$; (c) E(λ) at different depth in the snow cover (see figure legend) and (d) correspond $K_{d(\lambda)}$(data represent lower depth). (e) E(λ) under the sea ice (purple) and 0.35m above in the snow (lowest good measure) and (f) correspond $K_{d(\lambda)}$. Data are from station 1C, collected on May 7th at noon with a surface PAR of 750 µmol photons m^{-2} s^{-1}.

On 7 May, the surface PAR was 750 µmol photons m^{-2} s^{-1} during light attenuation measurements, the corresponding downwelling irradiance at the ice-snow interface was <1

404 µmol photons m^{-2} s^{-1} (Figure 4a), and the under-ice PAR was 0.17 µmol photons m^{-2} s^{-1}.
405 This corresponded to a transmission through the snow and ice layers of 0.023%, which is
406 considerably lower than previously recorded in the presence of ice algae. Typical low
407 recordings include a minimum transmittance recorded in Ripfjorden, Svalbard of ~0.5% in
408 April [Leu et al., 2010], and a PAR transmittance of 1.1 to 3.2% during the spring bloom in
409 the Canadian Arctic [Campbell et al., 2016]. In the Arctic Ocean PAR transmittance of <1%
410 has been recorded under 'thick ice' in spring [*Assmy et al.*, 2017], while on average 9 ± 3%
411 was recorded across 25 stations during summer in 2012 [Lund-Hansen et al., 2015]. These all
412 reports of algae growth under considerably more light underneath the ice than observed here.

413 In the snowpack, the downwelling attenuation coefficients (K_d) were between 5 and 15 m^{-1}
414 (Figure 4b, e-folding depths of 20-67 cm) and consistent with previous recording from the
415 Arctic region, [*France et al.*, 2011; *France et al.*, 2012]. Spectral irradiance available at
416 different depth throughout the snow pack were measured for each density layer (Figure 4c),
417 and show presence of light across the ultra-violet (UV, 3-400nm), PAR (4-700nm), and
418 infrared regions (IR, 7-800nm) of the spectrum. Light attenuation was lowest in the UV and
419 blue-green part of the PAR spectrum (<500nm) with increasing attenuation in the yellow-red
420 part (>575 nm) and throughout the IR. The observed spectral shape of the attenuation was in
421 agreement with previous observations of the optical properties of snow [*France et al.*, 2012;
422 *Warren*, 1982; *Warren and Brandt*, 2008]. The spectral light availability below the sea ice
423 was mostly restricted to the PAR region due to the strong attenuation of UV and IR light
424 (Figure 4e, f). In the present study it was not possible to obtain irradiance attenuation
425 measurements through the ice, neither did we succeed in measuring downwelling spectral
426 irradiance closer to the snow-ice interface than 35cm (for practical reasons). Spectral vertical
427 attenuation was markedly lower in the ice than in the snow (Figure 4f). However, note that
428 the integrated measure of the light attenuation across the 1m thick sea ice includes 35cm of
429 snow on top. It should also be noted that the measured irradiance in the snow represents
430 downwelling irradiance only and thus underestimates the light availability for phototrophic
431 and photochemical reactions as it does not account for the upwelling irradiance. In highly
432 scattering media as snow, upwelling irradiance can account for up to almost half of the
433 available light scalar irradiance [*Lee-Taylor and Madronich*, 2002]. However, for the under-
434 ice light region over clear water, upwelling irradiance accounts to only a very minor fraction,
435 thus downwelling irradiance is well representing the light availability immediately below the
436 ice. Inherently, light measurement beneath sea ice with algae underestimates the light

availability to algae communities by the absorption of the algae themselves then passing downward. This hinders empirically accurate measures of light availability to ice-associated algae communities. However, in this case Chl *a* concentrations were extremely low and we consider this effect neglectable. More importantly, the light availability to ice algae photosynthesis at the water ice interface has been suggested to be severely underestimated from under ice measured of downwelling irradiance, due to strong scattering of light in the skeleton layer of ice forming and hosting algae communities in the under ice environment ([*Ehn and Mundy*, 2013]. This theoretical assessment has not been documented empirically but the authors recognize the potential effect. On the contrary, the invasive light measurements obtained with the TriOs sensor likely overestimated the under-ice irradiance, as snow was removed and a hole drilled through the snow and ice to position the instrument under the sea ice. This may explain the discrepancy that the PAR sensor positioned under the ice at the monitoring station did not detect any irradiance prior to May 21 (sensitivity of 0.15 μmol photons m^{-2} s^{-1}).

3.3 Verification of a viable and photosynthetically active ice algae community

To verify that the observed algae community beneath the sea ice was viable and photosynthetically active we performed a perturbation experiment and cleared the snow cover (2x2m). This showed a pronounced effect on the Chl a concentration in the sea ice at the ice-water interface (Figure 5). Removal of the snow allowed light to access the sea ice unattenuated and was only attenuated by the sea ice itself. This lead to a multi-fold increase in the Chl a concentration that increased steadily from when the experiment was initiated on April 24th. By May 16th the Chl a concentration had increased by 36 times relative to the untreated site. Two conclusion were drawn from the experiment. First, that viable and active ice algae were present beneath the sea ice, and secondly, that the algae community was limited by light, not nutrient. Similar effects of snow clearing experiments have previously been observed [*Campbell et al.*, 2015; *Lund-Hansen et al.*, 2014].

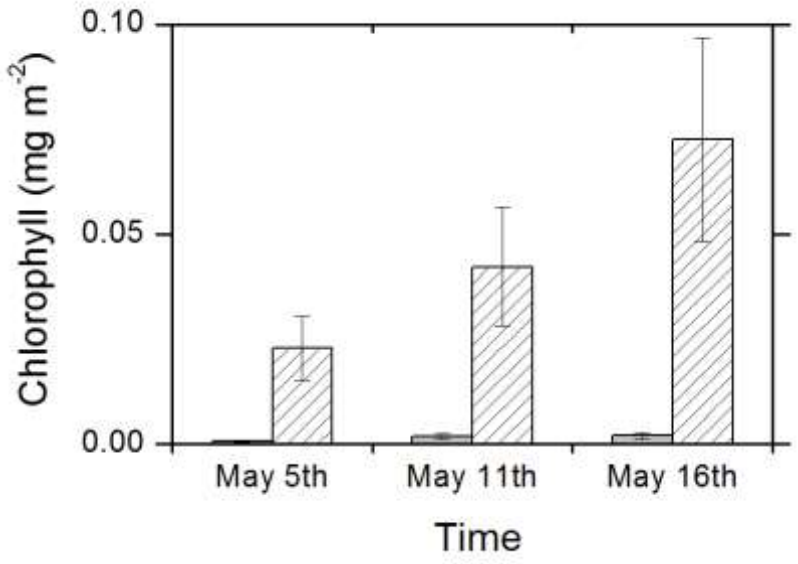

464

465 Figure 5: Effect on Chl *a* of snow-removal experiment in first-year sea ice. Dashed bars
466 represent samples collected where the ~1m thick snow was removed from the sea ice forming
467 a ~4m^2 pit. Grey bars are Chl *a* sampled the same days at the main site (1C). Snow was
468 initially removed on April 24. The result demonstrates the potential for ice algae to grow and
469 bloom in absence of snow, which restrict the solar radiation from penetrating through the sea
470 ice.

471

472 PAM fluorescence measurements were used to verified if microalgae collected from the ice
473 and UIW were viable and photosynthetically active. Measurements supported viable algae
474 from the bottom of the sea ice showing a maximum quantum yield of 0.31 ± 0.031
475 (dimension less, Figure 6). This is a strong argument that supports that the ice algae were
476 actively growing under the ambient light conditions. Values are within, however in the lower
477 end of the range of previous published photosynthetic quantum yields in ice algae [*Hawes et*
478 *al.*, 2012; *Robinson et al.*, 1997; *Rysgaard et al.*, 2001]. At patches, there snow were removed
479 the maximum quantum yield was 0.017 ± 0.011, and in UIW it was 0.13 ± 0.013. These
480 values are low compared to optimum values for diatoms in laboratory suspensions and mixed
481 pelagic populations (0.6-0.8, [*Hancke et al.*, 2015; *Hancke et al.*, 2008]). Where snow was
482 removed the maximum quantum yield was not significantly different from zero. The low
483 quantum yields should be interpreted in context of an extremely low biomass (at detection
484 limit of the instrument), harsh sampling conditions (>20^{o}C different between in situ and ex

485 situ) and high irradiance at the top of the sea ice (>700 µmol m^{-2} s^{-1}) which cannot be
486 excluded as having a shocking effect on the fragile ice algae during sampling, even when
487 great care was taken to prevent stress (e.g. shading of ice cores immediately after sampling,
488 transport time of less than 5 min, and controlled temperature conditions). Nevertheless, do
489 the quantum yields compare well with findings by Hawes et al. [2012] that found values of
490 ~0.1 for ice algae at the initial stage of colonization, with a subsequent increase to ~0.5 when
491 the algae bloom had established.

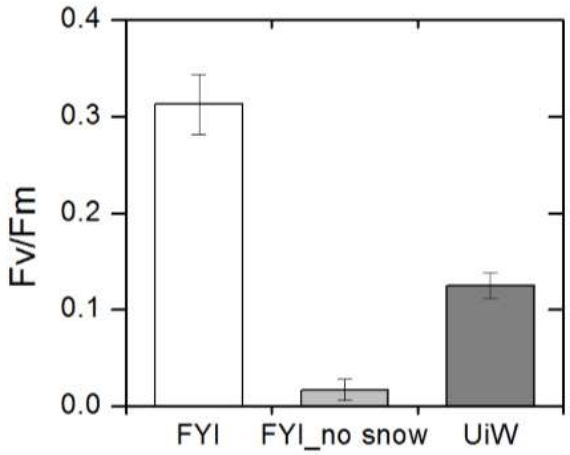

492

493 Figure 6: Maximum photosynthetic quantum yield (Φ_{PSII_max}) in dark-acclimated ice algae
494 from First-Year Ice (FYI), from FYI with no snow cover, and in Under Ice Water (UIW).
495 Data were measured with a portable PAM fluorometer (PhytoPAM, Walz) within minutes
496 after sampling of the ice cores, shaded from ambient light and temperature in a small tent.
497 Samples are from Station 1C, 16 May around solar noon.

498

499 **3.5 Snow metamorphosis driven by temperature gradients**

500 Temperature profiles through the snow and ice pack was measured continuously every hour
501 from 5 May until end of June. Snow temperature showed a pronounced diel variation with
502 minimum temperatures during night time and a maximum around noon (Figure 7). Most
503 pronounced were the diel variation a few cm below the snow-air interface, showing the net
504 result of air temperature and solar radiation heating of the surface snowpack. The depth in the
505 snow at which temperature was constant through the day was getting closer to the snow-ice

506 interface with progression of the season, from ~50 cm on 8 May, ~35 cm on 15 May, to ~20
507 cm on 19 May (Figure 7). This demonstrates a decrease in the insolation properties and
508 increased wetting of the snowpack. There was no temperature gradient in the ice from the
509 snow-ice to the ice-water interface during the entire measurement campaign, and the ice
510 temperature was constant at –1.2 ^{o}C. The isotherm sea ice was confirmed from manual
511 measurements of segments immediately after ice coring on several occasions (data not
512 shown). The efficient insolation properties of the overlaying snow ensured these stable
513 physical conditions in the ice, and minimum freezing and thawing of the ice at the ice-water
514 interface, during May.

515 The profiles overall demonstrated a strong temperature gradient showing an increase in
516 temperature in direction from the top of the snow towards the snow-ice interface (Figure 7).
517 This temperature gradient was confirmed from manually recordings in snow pits on 7 and 16
518 May (data not shown). Such conditions are optimal for snow metamorphism, i.e., a
519 restructuring and reshaping of the snow crystal/grain in snowpacks [*Colbeck*, 1982].
520 Temperature gradient in snow generates a vapor pressure gradient, which produce a flux of
521 vapor molecules upwards to the relatively colder layers on the top. When water vapor
522 condensate on the above-lying snow crystals, it stimulates crystal growth and increase in
523 snow grain size and decrease in snow density [*LaChapelle*, 1969]. This effect is particularly
524 strong when temperature gradients are larger than 1 ^{o}C per 10 cm of snow, as observed here
525 during beginning of May (Figure 7). Field data from the snow pits confirmed an increase in
526 grain size and decrease in snow density showing a 14% increase in overall grain size and a
527 25% decrease in bulk snow density (from 325.6 ± 91.4 kg m^{-1} to 244.8 ± 97.3 kg m^{-1})
528 between 7 and 16 May (10 days). Such an increase in grain size would lead to a decrease in
529 the optical scattering cross-section and a concurrent decrease in the diffusive light attenuation
530 properties of the snow [Lamare et al., 2016; Libois et al., 2013]. Thus, we introduced a
531 radiative transfer model to assess if this change in the scattering cross-section of the snow can
532 explain an apparent increase in the under ice light climate and supply an ice algae community
533 with a sufficient photon flux to growth.

534

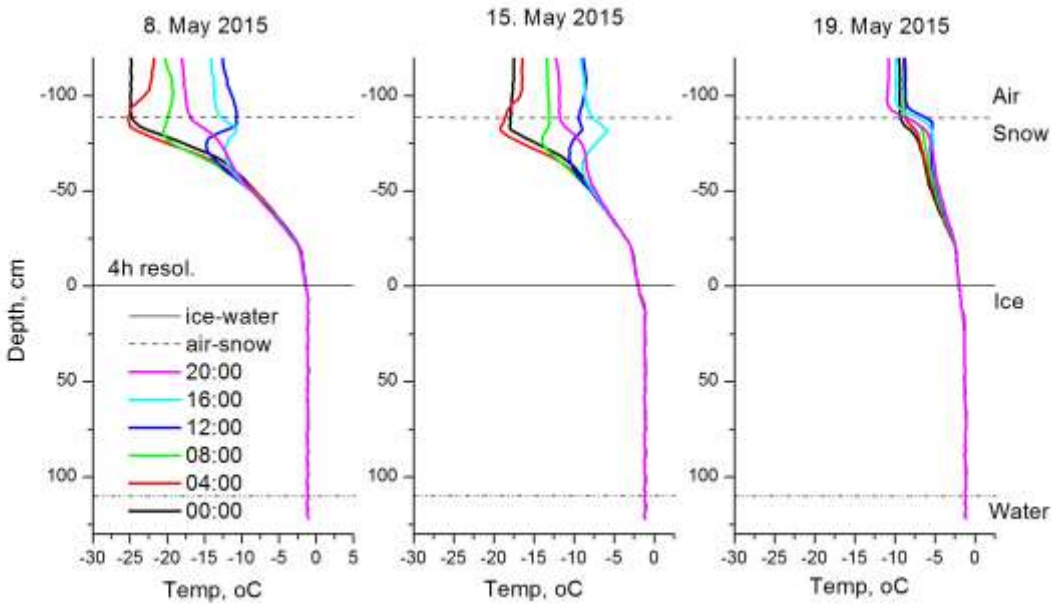

Figure 7: Temperature profiles in cross section through the snow and sea ice, showing air temperatures at the top and sea water temperature at the bottom. Profiles representing every 4 hours at three selected days illustrating how the snow pack is warming through May. The figure illustrates how solar heating is progressing increasing the snow temperature deeper in the snow pack over time, changing the temperature gradient within the snowpack. Y-axe refers to water depth in cm, negative numbers being above the ice-snow interface.

3.6 Radiative transfer modelling

A radiative-transfer model, TUV-snow, was used to compute the downwelling PAR through a combined snow and sea ice to analyze if changing snow conditions could explain the empirical observations. Specifically, if a change in the optical properties of the snowpack by metamorphism could increase the PAR at the bottom of the ice, as previously suggested by *Mundy et al.* [2005]. Figure 8 shows how the amount of PAR within snow and sea ice decreases with depth relative to a surface PAR (plot in relative units). The figure particularly demonstrates that the snowpack is the most attenuating medium compared to the sea ice, and demonstrates how the amount of the light reaching the bottom of the sea ice is dependent on the type of snowpack. Three characteristic snowpacks are shown; i.e. Cold Polar snow, Coastal Windpacked snow, and Melting snow [*Lamare et al.*, 2016]. The figure also

555 demonstrates that the difference between the snowpacks can achieve appreciable differences
556 in PAR reaching the snow ice interface (y = 1.0) and the bottom of the sea ice (y = 0). PAR
557 at the bottom of the sea ice varies by at least an order of magnitude, just by considering
558 reasonable changes in the snowpack optical properties.

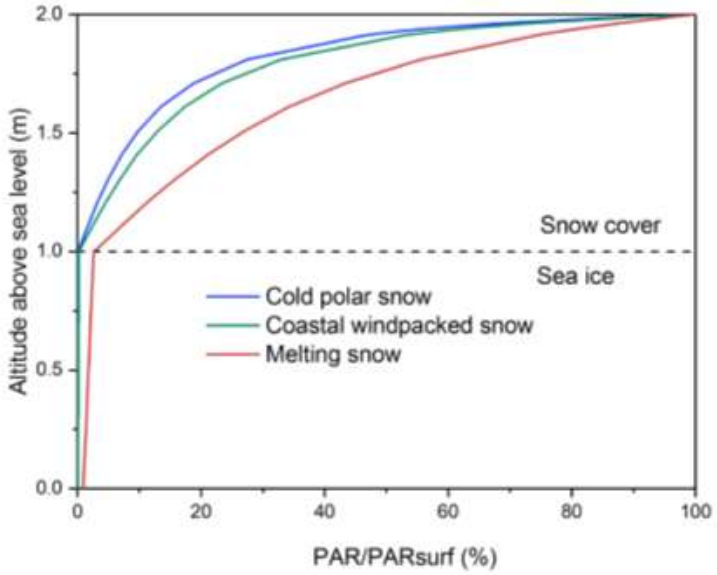

559

560 Figure 8: Modelled downwelling irradiance (PAR) through the snow and ice (1 + 1 m) with
561 three different snow types. The plot shows the importance of snow optical properties on the
562 light penetration to the underside of the sea ice, where Cold Polar, Coastal windpacked, and
563 Melting snow gave irradiance of 0.235, 0.645, and 7.067 µmol photons m^{-2} s^{-1}, respectively.

564 The amount of light scattering within the snowpack can be assessed by the metric of the light
565 scattering length of the snowpack, equal to the reciprocal product of the light scattering cross-
566 section and the snowpack density. Thus, as the light scattering cross-section increases the
567 scattering length of the snowpack decreases. Figure 9 demonstrates that changing the
568 properties of the snowpack and thus changing the light scattering length drastically changes
569 the amount of PAR reaching the bottom of the sea ice. The PAR at the sea ice bottom
570 increases as the light scattering length increases (and scattering cross-section decreases). In
571 physical terms as the season progresses snow metamorphoses increase, with a subsequent
572 increase in grain size, and decrease in the scattering length and scattering cross-section,
573 facilitating an increased PAR flux to the bottom of the sea ice.

574 The vertical dashed lines on figure 9 represent three characteristic snow packs, (cold polar,
575 coastal windpack and melting snow). These characteristic snowpacks are based on extensive
576 combined field and modelling work with the radiative-transfer model described here
577 exploring the penetration depth (the e-folding depth) of light in many different snowpacks
578 [*Beine et al.*, 2012; *France and King*, 2012; *France et al.*, 2011; *France et al.*, 2012; *Marks*
579 *and King*, 2014]. The e-folding depth is the distance over which initial light irradiance within
580 the snowpack decreases to 1/e of its initial value (~37%). Other field studies have also
581 demonstrated the changing snow conditions results in different snow e-folding depths
582 [*Galbavy et al.*, 2007; *Libois et al.*, 2014; *Warren*, 1982].

583 Cold polar snowpacks have large values of scattering cross-sections and relative short light
584 penetration depths, whilst melting snow has small values of the scattering cross-section and
585 large light penetration depths. Each characteristic snowpack has almost one order of
586 magnitude different value of PAR at the base of the sea ice. Thus, the radiative-transfer
587 modelling demonstrated that it is entirely plausible that the increase in PAR at the base of sea
588 ice increased due to a change in the snow optical properties.

589

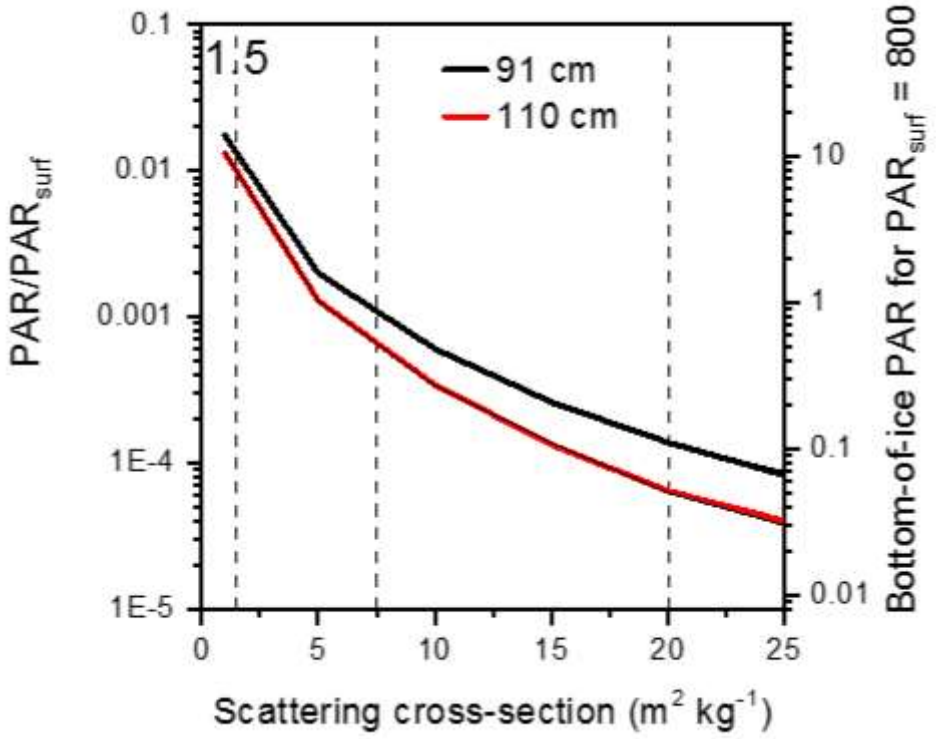

Figure 9 (could be joint with fig 8): Effect of the optical scattering cross-section of snow on the transmittance properties and the light availability beneath the sea ice (relative PAR) at snow thickness of 91 and 110 cm, respectively.

We speculate that implications of the low light requirement for algae growth are a possible earlier productivity by ice algae in Arctic sea ice than is recognized today, with consequences for modelling of Arctic carbon budgets [*Vancoppenolle et al.*, 2013]. This is in agreement with resent observations documenting that phytoplankton blooms underneath sea ice apparently is becoming more abundant [*K. R. Arrigo et al.*, 2012; *Mundy et al.*, 2014] even with the presence of snow cover on the ice [*Assmy et al.*, 2017].

5 Conclusions

In this study we have clearly documented the very initial phase of ice algae spring growth beginning under extremely low light conditions (PAR <0.15 µmol photons m^{-2} s^{-1}). This occurred below >1 m thick sea ice covered with ~1m of windpacked snow in landfast FYI at NE Greenland. This supports earlier observations that ice algae only require very little light to support growth and initiate a colonization. More importantly, it supports the principle that

primary production beneath snow covered FYI can occur widely in the Arctic and may have a high potential to contribute strongly to the overall primary production of the Arctic ocean. Using numerical modelling and empirical data we have demonstrated that a change in the optical properties of snow can change the available light underneath the ice by an order of magnitude, and that snow optical properties can be just as important as the thickness of the snow cover. This have implications for the minimum requirement for photosynthetic activity and ice algae growth in the wider Arctic. The general thinning of the snow thickness and the sea ice in the Arctic will likely stimulate an increase in ice algae biomass and productivity, and possibly will the spring bloom initiate even earlier than forecasted today, with possible implications for light absorption and Arctic primary production.

Acknowledgments, Samples, and Data

We thank the Department of Environmental Science, Aarhus University for providing logistics at Villum Research Station (VRS) in North Greenland, and for access to the monitoring data of solar radiation and snow depth. We also gratefully acknowledge the contributions from Arctic Research Centre (ARC), Aarhus University in supporting the field campaign. This work is a contribution to the Arctic Science Partnership (ASP) asp-net.org. We are very grateful for highly qualified assistance in the field at VRS, particularly Bjarki Friis, Ivali Lennert, Kunuk Lennert, and Jesper Hoffman, and the research teams at VRS. We owe the staff at the ‘Station Nord’ Danish military unit a grateful thank you for assistance with scientific sampling and maintenance of equipment. Financial support is acknowledged to KH, LCLH, and BKS from the Danish Council for Independent Research (Project DFF – 1323-00335: Sea ice ecosystems: Ecological effects of a thinning snow cover) and Carlsberg Foundation Project CF14-0888. MDK and MLL thank NERC for support via grant NE/K00077OX/1.

References

Alou-Font, E., C. J. Mundy, S. Roy, M. Gosselin, and S. Agusti (2013), Snow cover affects ice algal pigment composition in the coastal Arctic Ocean during spring, *Marine Ecology Progress Series*, *474*, 89-+, doi:10.3354/meps10107.

Arrigo, K. R. (2014), Sea Ice Ecosystems, *Annu Rev Mar Sci*, *6*, 439-467, doi:10.1146/annurev-marine-010213-135103.

Arrigo, K. R., et al. (2012), Massive Phytoplankton Blooms Under Arctic Sea Ice, *Science*, *336*(6087), 1408-1408, doi:10.1126/science.1215065.

Assmy, P., et al. (2013), Floating Ice-Algal Aggregates below Melting Arctic Sea Ice, *Plos One*, *8*(10), doi:ARTN e76599 10.1371/journal.pone.0076599.

Assmy, P., et al. (2017), Leads in Arctic pack ice enable early phytoplankton blooms below snow-covered sea ice, *Sci Rep-Uk*, *7*, doi:ARTN 40850 10.1038/srep40850.

Beine, H., C. Anastasio, F. Domine, T. Douglas, M. Barret, J. France, M. King, S. Hall, and K. Ullmann (2012), Soluble chromophores in marine snow, seawater, sea ice and frost flowers near Barrow, Alaska, *J Geophys Res-Atmos*, *117*, doi:10.1029/2011jd016650.

Berge, J., et al. (2015a), Unexpected Levels of Biological Activity during the Polar Night Offer New Perspectives on a Warming Arctic, *Curr Biol*, *25*(19), 2555-2561, doi:10.1016/j.cub.2015.08.024.

Berge, J., et al. (2015b), In the dark: A review of ecosystem processes during the Arctic polar night, *Progress in Oceanography*, *139*, 258-271, doi:10.1016/j.pocean.2015.08.005.

Braman, R. S., and S. A. Hendrix (1989), Nanogram Nitrite and Nitrate Determination in Environmental and Biological-Materials by Vanadium(Iii) Reduction with Chemi-Luminescence Detection, *Analytical Chemistry*, *61*(24), 2715-2718, doi:Doi 10.1021/Ac00199a007.

Campbell, K., C. J. Mundy, D. G. Barber, and M. Gosselin (2014), Remote Estimates of Ice Algae Biomass and Their Response to Environmental Conditions during Spring Melt, *Arctic*, *67*(3), 375-387.

Campbell, K., C. J. Mundy, D. G. Barber, and M. Gosselin (2015), Characterizing the sea ice algae chlorophyll a-snow depth relationship over Arctic spring melt using transmitted irradiance, *Journal of Marine Systems*, *147*, 76-84, doi:10.1016/j.jmarsys.2014.01.008.

Campbell, K., C. J. Mundy, J. C. Landy, A. Delaforge, C. Michel, and S. Rysgaard (2016), Community dynamics of bottom-ice algae in Dease Strait of the Canadian Arctic, *Progress in Oceanography*, *149*, 27-39, doi:10.1016/j.pocean.2016.10.005.

Cohen, J. H., et al. (2015), Is Ambient Light during the High Arctic Polar Night Sufficient to Act as a Visual Cue for Zooplankton?, *Plos One*, *10*(6), doi:ARTN e0126247 10.1371/journal.pone.0126247.

Colbeck, S. C. (1982), An overview of seasonal snow metamorphism, *Rev. Geophys. Space Phys.*, *20*, 45-61.

Cota, G. F., and E. P. W. Horne (1989), Physical Control of Arctic Ice Algal Production, *Marine Ecology Progress Series*, *52*(2), 111-121, doi:DOI 10.3354/meps052111.

Day, J. J., J. L. Bamber, and P. J. Valdes (2013), The Greenland Ice Sheet's surface mass balance in a seasonally sea ice-free Arctic, *J Geophys Res-Earth*, *118*(3), 1533-1544, doi:10.1002/jgrf.20112.

Dmitrenko, I. A., S. A. Kirillov, B. Rudels, D. G. Babb, L. T. Pedersen, S. Rysgaard, Y. Kristoffersen, and D. G. Barber (2016), First oceanographic observations on the Wandel Sea shelf in Northeast Greenland: Tracing the Arctic Ocean outflow through the western Fram Strait, *EGU General Assembly Conference Abstracts*, *18*, 1006.

Doherty, S. J., S. G. Warren, T. C. Grenfell, A. D. Clarke, and R. E. Brandt (2010), Light-absorbing impurities in Arctic snow, *Atmos Chem Phys*, *10*(23), 11647-11680, doi:10.5194/acp-10-11647-2010.

Ehn, J. K., and C. J. Mundy (2013), Assessment of light absorption within highly scattering bottom sea ice from under-ice light measurements: Implications for Arctic ice algae primary production, *Limnology and Oceanography*, *58*(3), 893-902, doi:10.4319/lo.2013.58.3.0893.

Fernandez-Mendez, M., F. Wenzhofer, I. Peeken, H. L. Sorensen, R. N. Glud, and A. Boetius (2014), Composition, Buoyancy Regulation and Fate of Ice Algal Aggregates in the Central Arctic Ocean, *Plos One*, *9*(9), doi:ARTN e107452 10.1371/journal.pone.0107452.

France, J. L., and M. D. King (2012), The effect of measurement geometry on recording solar radiation attenuation in snowpack (e-folding depth) using fibre-optic probes, *Journal of Glaciology*, *58*(208), 417-418, doi:10.3189/2012JoG11J227.

France, J. L., M. D. King, J. Lee-Taylor, H. J. Beine, A. Ianniello, F. Domine, and A. MacArthur (2011), Calculations of in-snow NO2 and OH radical photochemical production and photolysis rates: A field and radiative-transfer study of the optical properties of Arctic (Ny-Alesund, Svalbard) snow, *J Geophys Res-Earth*, *116*, doi:Artn F04013 10.1029/2011jf002019.

France, J. L., H. J. Reay, M. D. King, D. Voisin, H. W. Jacobi, F. Domine, H. Beine, C. Anastasio, A. MacArthur, and J. Lee-Taylor (2012), Hydroxyl radical and NOx production rates, black carbon concentrations and light-absorbing impurities in snow from field measurements of light penetration and nadir reflectivity of onshore and offshore coastal Alaskan snow, *J Geophys Res-Atmos*, *117*, doi:Artn D00r12 10.1029/2011jd016639.

Galbavy, E. S., C. Anastasio, B. L. Lefer, and S. R. Hall (2007), Light penetration in the snowpack at Summit, Greenland. Part 1. Nitrite and hydrogen peroxide photolysis, *Atmos. Environ.*, *41*, 5077–5090, doi:10.1016/j.atmosenv.2006.04.072.

Genty, B., J. M. Briantais, and N. R. Baker (1989), The Relationship between the Quantum Yield of Photosynthetic Electron-Transport and Quenching of Chlorophyll Fluorescence, *Biochimica Et Biophysica Acta*, *990*(1), 87-92.

Glud, R. N., S. Rysgaard, M. Kühl, and J. W. Hansen (2007), The sea-ice in Young sound: Implications for carbon cycling, in *Carbon cycling in Arctic marine ecosystems: Case study Young Sound*, edited by S. Rysgaard and R. N. Glud, pp. 62-85, Meddr Greenland, Bioscience Special Issue.

Gosselin, M., L. Legendre, J. C. Therriault, and S. Demers (1990), Light and Nutrient Limitation of Sea-Ice Microalgae (Hudson-Bay, Canadian Arctic), *Journal of Phycology*, *26*(2), 220-232, doi:DOI 10.1111/j.0022-3646.1990.00220.x.

Gosselin, M., L. Legendre, J. C. Therriault, S. Demers, and M. Rochet (1986), Physical Control of the Horizontal Patchiness of Sea-Ice Microalgae, *Marine Ecology Progress Series*, *29*(3), 289-298, doi:DOI 10.3354/meps029289.

Grasshoff, K., M. Ehrhardt, and K. Kremling (1999), *Methods of Seawater Analysis*, third ed., 600 pp., Verlag Chemie GmbH, Weinheim.

Hancke, K., T. Dalsgaard, M. K. Sejr, S. Markager, and R. N. Glud (2015), Phytoplankton Productivity in an Arctic Fjord (West Greenland): Estimating Electron Requirements for Carbon Fixation and Oxygen Production, *Plos One*, *10*(7), doi:ARTN e0133275 10.1371/journal.pone.0133275.

Hancke, K., T. B. Hancke, L. M. Olsen, G. Johnsen, and R. N. Glud (2008), Temperature effects on microalgal photosynthesis-light responses measured by O_2 production, pulse-amplitude-modulated fluorescence, and ^{14}C assimilation, *Journal of Phycology*, *44*(2), 501-514, doi:10.1111/j.1529-8817.2008.00487.x.

Hawes, I., L. C. Lund-Hansen, B. K. Sorrell, M. H. Nielsen, R. Borzak, and I. Buss (2012), Photobiology of sea ice algae during initial spring growth in Kangerlussuaq, West Greenland: insights from imaging variable chlorophyll fluorescence of ice cores, *Photosynthesis Research*, *112*(2), 103-115, doi:10.1007/s11120-012-9736-7.

Horner, R., and G. C. Schrader (1982), RELATIVE CONTRIBUTIONS OF ICE ALGAE, PHYTOPLANKTON, AND BENTHIC MICROALGAE TO PRIMARY PRODUCTION IN NEARSHORE REGIONS OF THE BEAUFORT SEA, *Arctic*, *35*(4), 485-503.

Kirk, J. T. O. (1994), *Light and Photosynthesis in Aquatic Ecosystems*, 2. edition ed., Cambridge University Press, Bristol.

Krabill, W., W. Abdalati, E. Frederick, S. Manizade, C. Martin, J. Sonntag, R. Swift, R. Thomas, W. Wright, and J. Yungel (2000), Greenland ice sheet: High-elevation balance and peripheral thinning, *Science*, *289*(5478), 428-430, doi:DOI 10.1126/science.289.5478.428.

LaChapelle, E. R. (1969), *Field guide to snow crystals*, University of Washington Press, 101 p.

Lamare, M. L., J. Lee-Taylor, and M. D. King (2016), The impact of atmospheric mineral aerosol deposition on the albedo of snow & sea ice: are snow and sea ice optical properties more important than mineral aerosol optical properties?, *Atmos Chem Phys*, *16*(2), 843-860, doi:10.5194/acp-16-843-2016.

Lee-Taylor, J., and S. Madronich (2002), Calculation of actinic fluxes with a coupled atmosphere-snow radiative transfer model, *J Geophys Res-Atmos*, *107*(D24), doi:Artn 4796 10.1029/2002jd002084.

Leu, E., C. J. Mundy, P. Assmy, K. Campbell, T. M. Gabrielsen, M. Gosselin, T. Juul-Pedersen, and R. Gradinger (2015), Arctic spring awakening - Steering principles behind the phenology of vernal ice algal blooms, *Progress in Oceanography*, *139*, 151-170, doi:10.1016/j.pocean.2015.07.012.

Leu, E., J. E. Soreide, D. O. Hessen, S. Falk-Petersen, and J. Berge (2011), Consequences of changing sea-ice cover for primary and secondary producers in the European Arctic shelf seas: Timing, quantity, and quality, *Progress in Oceanography*, *90*(1-4), 18-32, doi:10.1016/j.pocean.2011.02.004.

Leu, E., J. Wiktor, J. E. Soreide, J. Berge, and S. Falk-Petersen (2010), Increased irradiance reduces food quality of sea ice algae, *Marine Ecology Progress Series*, *411*, 49-60, doi:10.3354/meps08647.

Libois, Q., G. Picard, L. Arnaud, S. Morin, and E. Brun (2014), Modeling the impact of snow drift on the decameter-scale variability of snow properties on the Antarctic Plateau, *journal of geophysical Research: Atmospheres*, *119*(20), 11662-11681, doi:10.1002/2014JD022361.

Libois, Q., G. Picard, J. L. France, L. Arnaud, M. Dumont, C. M. Carmagnola, and M. D. King (2013), Influence of grain shape on light penetration in snow, *Cryosphere*, *7*(6), 1803-1818, doi:10.5194/tc-7-1803-2013.

Lorenzen, C. J. (1966), A method for the continuous measurement of in vivo chlorophyll concentration *Deep-Sea Research Part a-Oceanographic Research Papers*, *13*, 223-227.

lund-Hansen, L. C., I. Hawes, M. H. Nielsen, and B. K. Sorrell (2016), Is colonization of sea ice by diatoms facilitated by increased surface roughness in growing ice crystals? , *Polar Biology* doi:10.1007/s00300-016-1981-3.

Lund-Hansen, L. C., I. Hawes, B. K. Sorrell, and M. H. Nielsen (2014), Removal of snow cover inhibits spring growth of Arctic ice algae through physiological and behavioral effects, *Polar Biology*, *37*(4), 471-481, doi:DOI 10.1007/s00300-013-1444-z.

Lund-Hansen, L. C., S. Markager, K. Hancke, T. Stratmann, S. Rysgaard, H. Ramiov, and B. K. Sorrell (2015), Effects of sea-ice light attenuation and CDOM absorption in the water below the Eurasian sector of central Arctic Ocean (> 88 degrees N), *Polar Research*, *34*, doi:ARTN 23978

10.3402/polar.v34.23978.
Marks, A. A., and M. D. King (2014), The effect of snow/sea ice type on the response of albedo and light penetration depth (e-folding depth) to increasing black carbon, *Cryosphere*, *8*(5), 1625-1638, doi:10.5194/tc-8-1625-2014.
Marra, J. (2004), The compensation irradiance for phytoplankton in nature, *Geophysical Research Letters*, *31*(6), doi:Artn L06305
Doi 10.1029/2003gl018881.
Mikkelsen, D. M., S. Rysgaard, and R. N. Glud (2008), Microalgal composition and primary production in Arctic sea ice: a seasonal study from Kobbeijord (Kangerluarsunnguaq), West Greenland, *Marine Ecology-Progress Series*, *368*, 65-74, doi:10.3354/meps07627.
Mock, T., and R. Gradinger (2000), Changes in photosynthetic carbon allocation in algal assemblages of Arctic sea ice with decreasing nutrient concentrations and irradiance, *Marine Ecology-Progress Series*, *202*, 1-11.
Mundy, C. J., D. G. Barber, and C. Michel (2005), Variability of snow and ice thermal, physical and optical properties pertinent to sea ice algae biomass during spring, *Journal of Marine Systems*, *58*(3-4), 107-120, doi:10.1016/j.jmarsys.2005.07.003.
Mundy, C. J., J. K. Ehn, D. G. Barber, and C. Michel (2007), Influence of snow cover and algae on the spectral dependence of transmitted irradiance through Arctic landfast first-year sea ice, *Journal of Geophysical Research-Oceans*, *112*(C3), doi:Artn C03007
10.1029/2006jc003683.
Mundy, C. J., M. Gosselin, Y. Gratton, K. Brown, V. Galindo, K. Campbell, M. Levasseur, D. Barber, T. Papakyriakou, and S. Belanger (2014), Role of environmental factors on phytoplankton bloom initiation under landfast sea ice in Resolute Passage, Canada, *Marine Ecology Progress Series*, *497*, 39-+, doi:10.3354/meps10587.
Pritchard, D. W., C. L. Hurd, J. Beardall, and C. D. Hepburn (2013), Survival in Low Light: Photosynthesis and Growth of a Red Alga in Relation to Measured in Situ Irradiance, *Journal of Phycology*, *49*(5), 867-879, doi:10.1111/jpy.12093.
Robinson, D. H., K. R. Arrigo, R. Iturriaga, and C. W. Sullivan (1995), Microalgal Light-Harvesting in Extreme Low-Light Environments in Mcmurdo Sound, Antarctica, *Journal of Phycology*, *31*(4), 508-520, doi:DOI 10.1111/j.1529-8817.1995.tb02544.x.
Robinson, D. H., Z. Kolber, and C. W. Sullivan (1997), Photophysiology and photoacclimation in surface sea ice algae from McMurdo Sound, Antarctica, *Marine Ecology Progress Series*, *147*(1-3), 243-256, doi:10.3354/meps147243.
Rysgaard, S., and R. N. Glud (2007), Carbon cycling and climate change: predictions for a High Arctic marine ecosystem (Young Sound, NE Greenland), *Meddelelser om Gronland Bioscience*, *58*, 205-214.
Rysgaard, S., M. Kuhl, R. N. Glud, and J. W. Hansen (2001), Biomass, production and horizontal patchiness of sea ice algae in a high-Arctic fjord (Young Sound, NE Greenland), *Marine Ecology-Progress Series*, *223*, 15-26.
Schreiber, U., U. Schliwa, and W. Bilger (1986), Continuous Recording of Photochemical and Nonphotochemical Chlorophyll Fluorescence Quenching with a New Type of Modulation Fluorometer, *Photosynthesis Research*, *10*(1-2), 51-62.
Simpson, W. R., M. D. King, H. J. Beine, R. E. Honrath, and X. L. Zhou (2002), Radiation-transfer modeling of snow-pack photochemical processes during ALERT 2000, *Atmospheric Environment*, *36*(15-16), 2663-2670, doi:Pii S1352-2310(02)00124-3
Doi 10.1016/S1352-2310(02)00124-3.
Soreide, J. E., E. Leu, J. Berge, M. Graeve, and S. Falk-Petersen (2010), Timing of blooms, algal food quality and Calanus glacialis reproduction and growth in a changing Arctic, *Global Change Biology*, *16*(11), 3154-3163, doi:10.1111/j.1365-2486.2010.02175.x.

831 Stamnes, K., S. C. Tsay, W. Wiscombe, and K. Jayaweera (1988), Numerically Stable
832 Algorithm for Discrete-Ordinate-Method Radiative-Transfer in Multiple-Scattering and
833 Emitting Layered Media, *Applied Optics*, *27*(12), 2502-2509.
834 Thomas, D. N., and G. S. Dieckmann (2009), *Sea Ice*, Wiley-Blackwell.
835 Vancoppenolle, M., L. Bopp, G. Madec, J. Dunne, T. Ilyina, P. R. Halloran, and N. Steiner
836 (2013), Future Arctic Ocean primary productivity from CMIP5 simulations: Uncertain
837 outcome, but consistent mechanisms, *Global Biogeochemical Cycles*, *27*(3), 605-619,
838 doi:10.1002/gbc.20055.
839 Warren, S. G. (1982), Optical-Properties of Snow, *Rev Geophys*, *20*(1), 67-89, doi:DOI
840 10.1029/RG020i001p00067.
841 Warren, S. G., and R. E. Brandt (2008), Optical constants of ice from the ultraviolet to the
842 microwave: A revised compilation, *J Geophys Res-Atmos*, *113*(D14), doi:Artn D14220
843 10.1029/2007jd009744.

844

845

Chapter 6

The effects of surface roughness on the spectral (300 – 1400 nm) bidirectional reflectance distribution function (BRDF) of sea ice

Citation:
Lamare, M. L., Hedley, J., & King, M. D. (2017). The effects of surface roughness on the spectral (300–1400 nm) bidirectional reflectance distribution function (BRDF) of sea ice. In preparation for: The Cryosphere.

Author contributions:
Lamare, M. performed the radiative-transfer calculations, did the data analysis, prepared the results and wrote the paper.

Hedley, J. designed the radiative-transfer model, implemented the roughness model and the underlying BRDF function for this study, and proof-read the paper.

King, M.D. conceived and oversaw the study, and proof-read the paper.

The effects of surface roughness on the spectral (300 – 1400 nm) bidirectional reflectance distribution function (BRDF) of sea ice

Maxim L. Lamare[1], John Hedley[2], and Martin D. King[1]

[1]Department of Earth Sciences, Royal Holloway University of London, Egham, Surrey, TW20 0EX, UK
[2]Environmental Computer Science Ltd., Hammet Square, Tiverton, Devon, EX16 6LR

Correspondence to: M.D. King (m.king@rhul.ac.uk)

Abstract. The Bidirectional Reflectance Distribution Function (BRDF) has been calculated for three types of bare sea ice for varying surface roughness (σ = 0.1 – 10 cm) and ice thicknesses (50 – 2000 cm) over an incident solar irradiance wavelength range of 300 – 1400 nm. The comprehensive study of the BRDF of sea ice presented here is paramount for interpreting sea ice measurements from satellite imagery and inter-calibrating spaceborne sensors that derive albedo from multiple multi-angular measurements. The calculations performed by a radiative transfer code (PlanarRad) show that the BRDF of sea ice is sensitive to realistic values of surface roughness. The results presented here show that surface roughness cannot be considered independently of sea ice thickness, solar zenith angle and wavelength. A typical BRDF of sea ice has a quasi-isotropic reflectance over the hemisphere, associated with a strong forward scattering peak of light. Surface roughness is crucial for the location, size and intensity of the forward scattering peak. The BRDF calculations presented in this study form the first set of complete BRDF values for bare sea ice with a wide range of configurations.

1 Introduction

Knowledge of the surface albedo of sea ice and its temporal variability is essential to understand the energy budget of polar regions, that strongly affects the Earth's climate system (e.g. Curry et al., 1995; Qu and Hall, 2005; Flanner et al., 2011). Sensors aboard Earth Observing satellites allow the synoptic observation of expansive areas with regular repeat coverage, providing an ideal tool for the monitoring of albedo at high latitudes. However, the scattering of light from the surface of sea ice is not isotropic (e.g. Buckley and Trodahl, 1987) and therefore calculations of spectral albedo rely on the knowledge of viewing and illumination angles. Most satellite sensors are only able to measure reflected energy over a small number of viewing angles and spectral bands. Indeed, only a limited number of satellite systems currently provide near-simultaneous multi-angular measurements (Gatebe and King, 2016) and satellite sensors commonly used to derive surface albedo such as MODIS (Moderate Resolution Imaging Spectroradiometer), are constrained to collecting multi-angular measurements over several orbits. Therefore prior knowledge of the angular distribution of the reflected radiation of sea ice is necessary to accurately derive surface albedo form satellite observations using inversion models, and provide climate models with reliable inputs. The Bidirectional Reflectance Distribution Function (BRDF) is a directional description of albedo, describing the relationship between illumination and viewing angles (Nicodemus et al., 1977). The retrieval of satellite albedo products made using BRDF inversions rely

on the use of accurate BRDF models which is constrained by quality input observations (Schaaf et al., 2002). Previous studies have characterised BRDF of snow, either with field measurements of the Hemispherical Directional Reflectance Function (HDRF) as an approximation of BRDF (e.g. Middleton and Mungall, 1952; Dirmhirn and Eaton, 1975; Dozier et al., 1988; Leroux et al., 1998; Aoki et al., 2000; Painter and Dozier, 2004; Peltoniemi et al., 2005; Bourgeois et al., 2006; Hudson et al., 2006; Dumont et al., 2010; Ball et al., 2015; Marks et al., 2015; Peltoniemi et al., 2015) or by modelling BRDF or the Bidirectional Reflection Factor (BRF) as an approximation of BRDF (e.g. Leroux et al., 1999; Mishchenko et al., 1999; Dumont et al., 2010; Heygster et al., 2012; Kokhanovsky and Breon, 2012; Xiong and Shi, 2014). The BRDF of snow covered sea ice has also been measured or modelled (e.g. Arnold et al., 2002; Li and Zhou, 2004), but the characterisation of the BRDF of bare sea ice in the literature remains scarce. Jin and Simpson (1999) calculated the Anisotropy Reflectance Factor (ARF) for bare sea ice, representing the "departure of the reflected radiation field from an isotropic distribution", that takes in account backscattering radiance, upwelling flux, BRDF and albedo, using a radiative-transfer model. Jin and Simpson (1999) showed that sea ice has a larger reflectance in the forward observation direction and presents a high sensitivity to solar elevation and surface roughness. However the study was limited to 2 spectral bands at 580 – 680 nm and 725 – 1000 nm and a single type of multi-year sea ice with parameters obtained from Weeks and Ackley (1994). Schlosser (1988) measured the angular reflected radiance of laboratory grown sea ice for varying ice thicknesses between 6 mm and 11 cm, showing a strong dependance of BRDF on ice thickness and structure. Arnold et al. (2002) and Gatebe and King (2016) described airborne BRDF measurements acquired for a variety of natural surfaces over 13 bands from 502 nm to 2289 nm, including polar snow and sea ice. The BRDF of snow-covered sea ice, melt-season sea ice and snow-covered tundra were reported for a limited number of solar zenith angles, showing quasi-isotropic reflectance outside an enhanced forward scattering peak. Stamnes et al. (2011) modelled the BRDF of snow covered and bare sea ice, using a coupled atmosphere-snow-ice-ocean radiative-transfer model. Using sea ice inherent optical properties (IOPs), Stamnes et al. (2011) computed the BRDF for a range of sea ice types between 300 and 4000 nm. The theoretical computations relied on a smooth interface between the media however, and to represent surface roughness, the authors used a fixed 10° Gaussian beam, that did not take in account varying surface roughness effects which have been shown to significantly affect BRDF (Jin and Simpson, 1999).

Owing to its complex nature, the optical and physical properties of sea ice vary spatially and temporally, altering the solar radiation reflected from the surface (Perovich, 1996). Previous studies have demonstrated a strong dependence of albedo on the type of sea ice (e.g. Perovich et al., 2002). Light reflection and transmission are sensitive to changes in the thickness of the sea ice (Perovich, 1996), and surface roughness has been shown to significantly affect the angular pattern of reflectance at larger viewing angles for snow (Warren et al., 1998; Ball et al., 2015) and sea ice (Jin and Simpson, 1999). Yet, to the authors' knowledge, no modelling studies comprehensively characterising the BRDF of bare sea ice have been carried out previously. Thus, a systematic study of the dependance of the BRDF of multiple types of bare sea ice to changing surface roughness conditions and varying thickness is required.

In this work, the radiative-transfer model PlanarRad (Hedley, 2008, 2015) was used to model the BRDF of three different types of sea ice from 300 to 1400 nm with varying thicknesses as a function of surface roughness in two steps. Firstly, the BRDF of three different types of sea ice with a thickness large enough to be optically deep was modelled with an increasing surface

roughness. Secondly, the calculations performed in the first step were repeated, the optically deep thicknesses having been replaced with fixed thicknesses of 50 cm and 100 cm for each type of sea ice.

2 Methods

The description of the method is divided into three sections: the calculations of BRDF and BRF are presented, the model is described, and the modelling experiment is outlined.

2.1 Definitions

BRDF is commonly used to represent the reflective properties of a surface by describing the angular distribution of the scattering of light from the surface (Nicodemus et al., 1977). The spectral BRDF describes the relationship between the irradiance incident from a given direction relative to its contribution to the reflected radiance in another direction (Nicodemus et al., 1977), which can be expressed mathematically by:

$$BRDF(\lambda) = fr(\theta_i, \phi_i; \theta_r, \phi_r; \lambda) = \frac{dL_r(\theta_i, \phi_i; \theta_r, \phi_r; \lambda)}{dE_i(\theta_i, \phi_i; \lambda)}, \tag{1}$$

where θ and ϕ are the zenith and azimuth angles respectively in a spherical coordinate system, λ is the wavelength of light, L is radiance, E is irradiance, *i* refers to incident directions and *r* to reflected directions (Nicodemus et al., 1977; Schaepman-Strub et al., 2006). The angles used to define BRDF are shown in Figure 1a. BRDF requires the irradiance to be in the form of a collimated beam and the radiance to be measured with an infinitesimal solid angle. Thus, BRDF cannot be measured directly (Schaepman-Strub et al., 2006). In order to facilitate comparison with the literature and field studies, the BRDF computed in this study was converted to the unitless Bidirectional Reflectance Factor (BRF). BRF is defined by the ratio of the reflected radiant flux, $d\Phi_r$ from a surface area to the reflected radiant flux, $d\Phi_r^{lamb}$ from an idea Lambertian reflector under identical viewing angles and single direction illumination (Schaepman-Strub et al., 2006). Therefore, BRF is expressed as:

$$BRF(\lambda) = \frac{d\Phi_r(\theta_i, \phi_i; \theta_r, \phi_r; \lambda)}{d\Phi_r^{lamb}(\theta_i, \phi_i; \lambda)} \tag{2}$$

The BRDF of an ideal Lambertian reflector is $\frac{1}{\pi}$ (Nicodemus et al., 1977; Schaepman-Strub et al., 2006). Hence, the BRDF calculated by PlanarRad may be converted to BRF by multiplying by π.

2.2 Model description

The calculations of the BRDF of sea ice were performed using PlanarRad (Hedley, 2015), a radiative-transfer model that computes the radiance distributions and derived quantities for homogeneous scattering and absorbing media (Hedley, 2008). The model is an open-source implementation of the invariant imbedded numerical integration technique for radiative-transfer, based on the algorithm described by Mobley (1994). PlanarRad has previously been used for reflectance computations in marine environments (Lim et al., 2009; Hedley et al., 2012) and is functionally similar to the commercial software Hydrolight (Mobley, 1989).

In PlanarRad, radiance is calculated as the average radiance over finite solid angles, defined by a discretisation of the surface of a sphere divided into two hemispheres (Figure 1b). The lower hemisphere corresponds to the upwelling radiance (exiting the surface), whereas the upper hemisphere corresponds to the downwelling direct sky radiance. The discretisation is determined by bounding lines of constant zenith (θ) and azimuth (ϕ) angle, forming quadrangular regions, commonly called "quads". The two hemispheres are divided into 9 by 24 segments each, forming a total of 432 quads over the whole sphere. The directionally averaged radiance is computed by PlanarRad within each quad. The input irradiance is set to a single quad with a fixed azimuth, ϕ_i and a variable zenith, θ_i, the model being rotationally invariant. For the rough surface constructed from randomly oriented surfaces used in this study, only the relative azimuth angle between ϕ_i and ϕ_r is required. The incident irradiance was fixed at a constant value for the purpose of this study. The azimuth angles corresponding to the quad centres are located every 15° from $\phi = 0^\circ$ to $\phi = 345^\circ$and the zenith angles corresponding to the quad centres are located at $\theta = 0, 10, 20, 30, 40, 50, 60, 70, 80$ and 87.5°. Out of convention, the incident azimuth angle, ϕ_i was set to 180°, the quarter-sphere from 270 to 90° azimuth representing the forward scattering of light and the quarter-sphere from 90 to 270° azimuth representing the backward scattering. Thus, the solar principal plane is defined as $\phi = 180 - 0^\circ$. Figure 2 shows a typical 2D polar plot of a PlanarRad output for optically deep (as described in Sect. 2.3) first-year sea ice, with a solar zenith angle, $\theta_i = 60^\circ$ and a roughness parameter of $\sigma = 0.01$ m (described below).

The absorption coefficient, a, attenuation coefficient, α, scattering phase function, complex refractive index of sea ice, complex refractive index outside the sea ice, surface roughness and thickness of the sea ice were used in the radiative-transfer calculations. The parameters are presented in Sect. 2.3. The calculations presented here assume that no atmosphere is present and that the sea ice is floating on an optically thick body of sea water that has a wavelength independent diffuse reflectance of 0.1.

A roughness parameter effecting the statistical distribution of surface slope was implemented in a similar way to that described in Mobley (1994). The roughness parameter, σ, describes the standard deviation of the height relative to the horizontal distance, and is therefore unitless. For example, if $\sigma = 1$, the slope between points located 1 mm apart has a standard deviation of 1 mm. Because the system is considered spatially consistent, the overall BRDF and the effect of σ is scale invariant. The surface was modelled as a grid of equilateral triangles and the height of the vertices was set randomly using σ. The procedure is the same as the one applied to water surfaces in Mobley (1994), except there σ is derived from windspeed and the triangles are not equilateral to account for directional dependancy of water waves. The light transfer across the realised surfaces was modelled using Monte Carlo ray tracing, over the discretised sphere described previously. In the work presented here, 5 modelled surfaces were generated with an elevation standard deviation, σ = 0.001, 0.005, 0.01, 0.05 and 0.1 (Figure 3). The surfaces were generated using 10 rays per quad (4320 rays in total) with results averaged over 2000 surfaces. The roughness model being scale invariant, and the relative amplitude defined as 1 meter, the scale height of the roughness is 0.1, 0.5, 1, 5 and 10 cm.

2.3 Calculation of the BRF of 3 types of sea ice with different roughness parameters

The BRF of three types of sea ice were modelled: first-year ice, multi-year ice and melting ice. The selected optical and physical parameters were based on field studies and cover a wide range of observed values. A base amount of black carbon was added to the model to be more representative of natural sea ice, as small quantities of black carbon deposited from the atmosphere in

polar regions (e.g Doherty et al., 2010) are likely to be found in sea ice. The mass absorption coefficient of black carbon was calculated using Mie theory, using refractive indices from Chang and Charalampopoulos (1990), and following the method described by Flanner et al. (2007). A mass-ratio of 1 ng g^{-1} of black carbon was added to the sea ice, by combining the mass absorption coefficients of sea ice and black carbon. The attenuation coefficient of sea ice was calculated using the scattering cross-sections and densities described by Lamare et al. (2016) and Marks and King (2014), as:

$$\alpha(\lambda) = a(\lambda) + s(\lambda); \quad s(\lambda) = \phi_s \sigma_s, \tag{3}$$

where α is the attenuation coefficient of sea ice, a is the absorption coefficient of sea ice with an added mass-ratio of 1 ng g^{-1} of black carbon, s is the scattering coefficient of sea ice, ϕ_s is the scattering cross-section and σ_s is the density. According to Light et al. (2004), the fractional volume of ice is larger than the fractional volume of brine, and the absorption coefficient of ice is similar to the absorption coefficient of brine, hence the absorption coefficient of sea ice is equivalent to pure ice. Therefore, the refractive index of pure ice (Warren and Brandt, 2008) was used for sea ice and a refractive index value of 1.0 was used above sea ice. To describe the directionality of the scattering of the sea ice, the Henyey-Greenstein phase function (Henyey and Greenstein, 1941) was used, with a fixed, wavelength independent asymmetry factor g of 0.98 (Lamare et al., 2016). In this work, the asymmetry parameter, g, and the attenuation coefficient, a were held constant, and the scattering coefficient, s was varied to simulate different sea ice configurations, according to the methods outlined in Lee-Taylor and Madronich (2002). The optical and physical parameters of the selected sea ice types are summarised in Table 1.

The BRDF of the three different types of sea ice were subjected to solar radiation with a wavelength from 300 to 1400 nm with a 100 nm interval, as a function of surface roughness and thickness. The solar zenith angle was varied in 10 steps corresponding to the centre of the quads, from $\theta_i = 0^\circ$ to $\theta_i = 87.5^\circ$, and the surface roughness parameterisations described in section 2.2 were used, providing a wide range of configurations.

In some of the experiments described here, the sea ice was defined as optically deep, to allow for a direct comparison between the different types of ice and with studies present in the literature. An optically deep sea ice as defined in this study is a sea ice with a thickness for which the underlying medium (i.e. seawater) does not affect the surface reflectance. The sea ice was considered to be optically deep between 3 to 5 *e*-folding depths, where over 95% of the incident light is attenuated (France et al., 2011). An optically deep thickness of 1.85 m for first-year sea ice, 3.75 m for multi-year sea ice and 20 m for melting sea ice were picked, based on values compiled by Lamare et al. (2016). In a second step, sea ice thicknesses of 50 cm and 100 cm were selected for the three different types of sea ice. The two thicknesses were chosen to examine and inter-compare the effect of the sea ice thickness and roughness on the BRDF of different sea ice types rather than model representative values. Nevertheless, the model can produce results for a range of thicknesses, from the centimetre scale to optically deep thicknesses.

3 Results

The results are presented in two sections: the nadir BRF of three types of sea ice is examined for different thicknesses and roughnesses, and the effects of roughness on the forward scattering peak are presented, secondly the BRF of three differ-

ent types of sea ice with increasing surface roughness is shown as a function of thickness, solar zenith angle and spectrum wavelength.

3.1 Nadir BRF of sea ice and forward scattering peak

The nadir BRF of the three types of sea ice was computed with varying thicknesses from 300 nm to 1400 nm and for a fixed solar zenith angle of $\theta_i = 60°$. In a second step, the forward principal plane of optically deep first year sea ice was plotted as a function of solar zenith angle for a range of surface roughness values.

3.1.1 Nadir BRF of sea ice for varying sea ice thicknesses and surface roughness

The nadir BRF of first-year sea ice, multi-year sea ice and melting sea ice with thicknesses 50 cm, 100 cm and the optically deep thicknesses are shown in Figure 4. The plotted data were obtained from the nadir quad of PlanarRad, with a surface roughness of $\sigma = 0.01$ m, and a solar zenith angle $\theta_i = 60°$. For the three types of sea ice, the BRF is strongly wavelength dependent due to the large absorption in the ice dominating the signal beyond 700 nm, and significantly lowering the BRF. Although the different types of sea ice have a similar pattern with wavelength, the BRF increases by 29.5% from first-year sea ice to multi-year sea ice at 400 nm and up to 630.7% at 1100 nm, 31.5% from melting sea ice to multi-year sea ice at 400 nm and a maximum of 97.7% at 900 nm, and 11.3% from melting sea ice to first-year sea ice at 400 nm and up to 86.2% at 800 nm. The effect of the thickness of the sea ice on the BRF varies according to the type of sea ice. The BRF decreases by 20.6% when going from an optically deep first-year sea ice to a 100 cm thick first-year sea ice and 47.4% from optically deep to 50 cm. For multi-year ice the decrease in BRF is 3% from optically deep to 100 cm and 12.8% from an optically deep thickness to 50 cm. Melting sea ice shows the largest change in BRF relative to thickness with a decrease in BRF of 72.9% between an optically deep thickness and 100 cm and 83.6% between an optically deep thickness and 50 cm. Melting sea ice is more translucent than first-year or multi-year sea ice, therefore more light penetrates the sea ice deeper and is absorbed by the underlying seawater, explaining the larger reduction in BRF at nadir. On the contrary, with more scattering sea ice types, less light penetrates the ice and the absorption by the seawater under the ice is less.

3.1.2 The effects of roughness on the quasi-isotropic part of the BRF

Figure 6 shows the BRF of semi-infinite first-year sea ice, multi-year sea ice and melting sea ice along the orthogonal plane, with a solar zenith angle of $\theta_i = 60°$, at 500 nm. The BRF is plotted for surface roughnesses of $\sigma = 0.001$ m and $\sigma = 0.1$ m. The orthogonal plane corresponds to the quads located along the viewing azimuth angles $\phi_r = 270°$ (negative zenith angles) and $\phi_r = 90°$, forming a cross-section of the polar plot. For clarity, only the two extreme values on the roughness scale were plotted here. An increasing surface roughness value has little effect on the BRF along the orthogonal plane for zenith angles below $\theta_r = 70°$. Values of the BRF are larger for the smaller surface roughness, but the increase in BRF is less than 0.01 for the three types of sea ice. Furthermore, for each surface roughness value, the BRF varies by less than 0.1 across the orthogonal plane, with a slightly lower value for the nadir quad. Values of the BRF are larger for the smaller surface roughness, but the

increase in BRF is less than 0.01 for the three types of sea ice. For viewing zenith angles close to the horizon ($\theta_r > 70°$), the impact of surface roughness is more important than over the other quads. For the quad centered over $\theta_r = 80°$, the BRF of sea ice with a surface roughness of $\sigma = 0.1$ compared to a surface roughness of $\sigma = 0.001$ is approximately 24% higher for all sea ice types, and 140% higher for the quad centered over $\theta_r = 87.5°$.

To assess the effects of surface roughness on the entire quasi-isotropic part of the BRF, the BRF of the three types of sea ice with a solar zenith angle of $\theta_i = 60°$ at 500 nm, was plotted in figure 7, after having removed the forward scattering maxima. The dots in the scatter plot represent quads located between viewing azimuth angles $\phi_r = 315°$ and $\phi_r = 45°$, for all viewing zenith angles. The values for a surface roughness of $\sigma = 0.001$ are shown on the x-axis and the values for a surface roughness of $\sigma = 0.1$ are shown on the y-axis. The figure shows that most of the quad values are located along the identity (x=y) line. Two separate groups of quads distinguish themselves from a larger cloud of points: the group of points with lower values corresponds to the quads centered over a viewing zenith angle $\theta_r = 87.5°$, and the group of points with intermediate values represents points located over $\theta_i = 80°$. The higher values for a surface roughness $\sigma = 0.001$ of the quads at higher viewing zenith angles are in agreement with figure 6, where the outer quads exhibit lower values for smaller amounts of surface roughness. The values distributed along the identity line, show slightly higher BRF values for an increasing surface roughness, however the values are similar, with very small differences between the different surface roughnesses.

3.1.3 The effects of roughness on the forward scattering peak of the BRF

To investigate the influence of surface roughness on the location of the dominant directional scattering of light, hereafter referred to as forward scattering peak, the BRF along the solar principal plane is presented. Knowledge of the intensity and size of the forward scattering peak is essential to reliably calculate the energy budget of the sea ice, and correct for the fluctuations in temporal remote sensing data (e.g. Leroy and Roujean, 1994; Li et al., 1996). Figure 5 shows the effects of surface roughness on the forward scattering peak of the BRF of optically deep first-year sea ice with a solar zenith angle, $\theta_i = 60°$. The results are also representative of multi-year and melting sea ice. Figure 5a displays the intensity, shape and position of the BRF peak on the forward solar principal plane ($\phi_r = 0°$). As the surface roughness increases, a spreading of the BRF peak is observed. Indeed, the peak remains specular for the smaller surface roughnesses ($\sigma = 0.001$ m to $\sigma = 0.01$ m), whereas for larger surface roughness features (above $\sigma = 0.05$ m), the peak spreads out over multiple quads with a lower intensity than for smaller roughness features, and the highest value is displaced further out on the solar principal plane. Figure 5b shows the effect of surface roughness on the position of the BRF peak on the solar principal plane under different illumination conditions ($\theta_i = 0$ to $87.5°$). For the smaller roughness features ($\sigma = 0.001$ m to $\sigma = 0.01$ m), the position of the peak on the solar principal plane is specular and therefore matches the solar zenith angle. A roughness of $\sigma = 0.05$ m affects the position of the BRF peak at low sun angles ($\theta_i = 60$ to $87.5°$), moving the peak to a lower position on the hemisphere and therefore to a higher viewing zenith angle. For a solar zenith angle $\theta_i = 60°$, the viewing zenith angle is $\theta_r = 70°$, for $\theta_i = 70°$, $\theta_r = 80°$ and for $\theta_i = 80°$ and $87.5°$, $\theta_r = 87.5°$. With a surface roughness of $\sigma = 0.1$ m, the forward scattering peak is located at higher viewing zenith

angles than the solar zenith angles, except for $\theta_i = 10$ and 20°, where the angle of the forward scattering peak equals the angle of incident illumination.

3.2 The BRF of sea ice with varying surface roughness

The BRF of the three types of sea ice was computed for increasing surface roughness, varying thicknesses, solar zenith angles and wavelengths.

3.2.1 BRF and thickness

Figure 8 shows the BRF of first-year, multi-year and melting sea ice with a solar zenith angle, $\theta_i = 60^\circ$ and at a wavelength, $\lambda = 500$ nm. The BRF was modelled for three thicknesses as a function of surface roughness: 50 cm, 100 cm and an optically deep layer. The modelled BRF pattern is similar to snow (e.g. Dumont et al., 2010) and consistent with the literature for sea ice (e.g Arnold et al., 2002), showing a quasi-isotropic reflectance apart from a strong forward scattering peak. The surface roughness plays an essential role in the BRF of sea ice, by controlling the location and size of the forward scattering peak, as shown previously in Figure 5. Indeed, the peak is mostly specular and located in a single quad for a surface roughness of $\sigma = 0.001$ m and spreads out over multiple quads and moves lower on the hemisphere with a larger surface roughness. As a specific example, for first-year sea ice at $\lambda = 500$ nm and $\theta_i = 60^\circ$, the BRF of an optically deep layer with surface roughness of $\sigma = 0.001$ m is 0.543 at nadir. The forward scattering peak is spread over a single quad located at $\phi_r = 0^\circ$, $\theta_r = 60^\circ$, that has a BRF of 9.748. For the same configuration with surface roughness of $\sigma = 0.1$ m, the nadir has a BRF of 0.549 and the forward scattering peak is spread over 18 quads, located between $\phi_r = 345^\circ$ and $\phi_r = 15^\circ$, $\theta_r = 40^\circ$ and $\theta_r = 87.5^\circ$ with values between 0.776 and 5.089. Furthermore, the effects of thickness and surface roughness on the BRF of sea ice are inter-dependant. For smaller surface roughness parameters, an increase in the thickness of the sea ice mainly changes the intensity of the quasi-isotropic part of the BRF, affecting the forward scattering peak much less. For the first-year sea ice with the configuration described above and a roughness parameter of $\sigma = 0.001$ m, the BRF of the quad with the highest value in the specular peak increases by 2.42% from a 50 cm layer to an optically deep layer whereas the BRF at nadir increases by 45.57%. For larger surface roughnesses, a change in sea ice thickness affects the specular peak strongly, as well as the quasi-isotropic part of the BRF. The BRF of the first-year sea ice described previously with a surface roughness of $\sigma = 0.1$ m changes by 81.66% at nadir and between 3.27% and 69.07% in the forward scattering peak between a layer of 50 cm and an optically deep layer. Thus, the distribution and values of the BRF over the azimuth, ϕ and zenith, θ are sensitive to the thickness and the roughness.

3.2.2 BRF and solar zenith angle

Figure 9 shows the BRF of optically deep first-year, multi-year and melting sea ice at $\lambda = 500$ nm, with an increasing surface roughness for three solar zenith angles, $\theta_i = 50^\circ$, $\theta_i = 70^\circ$ and $\theta_i = 80^\circ$. The results for $\theta_i = 60^\circ$ can be found in Figure 8 for comparison. Low illumination angles (large solar zenith angles) are presented in this study, as they are representative of

conditions observable in polar regions. The location and intensity of the forward scattering peak are strongly influenced by the incident zenith angle, which effects are inter-dependant of surface roughness. For a small surface roughness of $\sigma = 0.001$ m, the highest value of the forward scattering peak is equal to the incident illumination angle over the range of solar zenith angles, however the intensity of peak increases with θ_i. For first-year sea ice, the peak BRF increases from 5.01 for $\theta_i = 50°$ to 28.92 for $\theta_i = 70°$ and to 143.16 for $\theta_i = 80°$. The forward scattering peak diffuses with larger solar zenith angles, from 1 quad at $\theta_i = 50°$ to 3 quads at $\theta_i = 80°$ for all three types of sea ice. With surface roughnesses of $\sigma = 0.005$ m and $\sigma = 0.01$ m, the forward scattering peak increases in intensity with increasing solar zenith angles, however the peak remains spread over a similar number of quads between $\theta_i = 50°$ and $\theta_i = 80°$. For larger surface roughnesses of $\sigma = 0.05$ m and $\sigma = 0.1$ m, although the intensity of the wide forward scattering peak increases with larger solar zenith angles, the intensity is lower than for small roughness parameters. For first-year sea ice with a surface roughness of $\sigma = 0.1$ m, the highest BRF value is 1.360 for $\theta_i = 50°$ and 54.271 for $\theta_i = 80°$. Moreover, the forward scattering peak is distributed over a larger number of quads for higher incident illumination angles. At large solar zenith angles, typical of polar latitudes, the isotropic part of the BRF remains similar with an increasing surface roughness, whilst the forward scattering peak diffuses and moves to larger viewing zenith angles than the incident illumination angles.

3.2.3 BRF and wavelength

The BRF of optically deep first-year sea ice, multi-year sea ice and melting sea ice with increasing surface roughness, for a solar zenith angle $\theta_i = 60°$ and for wavelengths of $\lambda =$ 400 nm, 800 nm and 1300 nm is shown in Figure 10. The results for $\lambda =$ 500 nm can be found in Figure 8 for direct comparison. As partly shown in Figure 4, the BRF of sea ice is strongly wavelength dependent. At nadir, the highest BRF values are found in the near ultra violet and visible wavelengths, decreasing rapidly between 500 and 900 nm. Beyond 900 nm for first-year and melting sea ice and 1000 nm for multi-year sea ice, the BRF tends to zero, owing to the absorption by the sea ice. However, the BRF does not decrease uniformly over the hemisphere with an increasing wavelength. The quasi-isotropic part of the hemisphere follows the same trend as the nadir, whereas the forward scattering peak conserves high BRF values, independently of the wavelength. The behaviour is valid for the entire range of roughness parameters. For optically deep first-year sea ice with a solar zenith angle, $\theta_i = 60°$, the nadir BRF decreases by 99.92% from 400 nm to 1300 nm for a surface roughness of $\sigma =$ 0.001 m, and by 99.90% for a surface roughness of $\sigma = 0.1$ m. However, the change within the forward scattering peak with wavelength differs for different amounts of surface roughness. The forward scattering peak located at $\phi_r = 0°, \theta_r = 60°$ for first-year sea ice with a surface roughness of $\sigma = 0.001$ m, decreases by 13.94%. For the same configuration with a surface roughness of $\sigma = 0.1$ m, the wider forward scattering peak decreases non-uniformly and reduces in size. Within the 18 quads of the forward scattering peak located between $\phi_r = 345°$ and $\phi_r = 15°$, $\theta_r = 40°$ and $\theta_r = 87.5°$, the highest BRF value ($\phi_r = 0°, \theta_r = 87.5°$) decreases by 14.92%, but the lowest BRF value ($\phi_r = 15°, \theta_r = 40°$) decreases by 83.05% between 400 and 1300 nm. The same behaviour is observable for multi-year and melting sea ice. For small roughnesses ($\sigma \leqslant 0.01$ m) the intensity of the forward scattering peak that does not change in size varies little with wavelength compared to the quasi-isotropic part of the BRF. For large roughnesses ($\sigma >$ 0.01 m) the forward scattering peak decreases strongly around the edges with wavelength, whereas the centre quads vary by a small amount

as with smaller roughnesses. Furthermore, the quasi-isotropic part of the BRF behaves in the same manner than for smaller surface roughnesses.

4 Discussion

In the following discussion, the results presented in Sect. 3 are explained and the limitations of the study are addressed.

4.1 The effects of surface roughness on the BRF of sea ice

As shown in Sect. 3, surface roughness plays a paramount role in the BRF of bare sea ice. Not only does surface roughness have an effect on the reflected radiance, particularly in the forward scattering peak, it also modifies the behaviour of the BRF with other controlling parameters such as thickness, solar zenith angle or wavelength. Surface roughness alone has a small effect on the quasi-lambertian part of the hemisphere, with the exception of high viewing zenith angles (close to the horizon), where rougher surfaces increase the BRF. Indeed, as light is scattered in multiple directions by a rougher surface, the amount of light scattered at grazing viewing angles is increased compared to a smooth surface. However, very high viewing zenith angles are of lesser interest for remote sensing community than the rest of the hemisphere as they present more noise (Lucht, 1998), and comparisons with field measurements have larger uncertainties at high viewing zenith angles (Picard et al., 2016). An increase in surface roughness has a limited effect on the rest of the hemisphere outside of the forward scattering peak, with a slight increase of BRF values as shown in figure 7. The modelling results show that for remote sensing purposes, if the forward scattering peak is avoided, the effects of surface roughness are negligible on the BRF of sea ice with varying optical properties. However, surface roughness strongly changes the specular forward scattering peak by diffusing it around the specular point and outwards to a larger zenith angle. Indeed, a smooth surface reflects the incident light specularly, whereas reflection from a roughened surface is composed of the specular reflection of the angled facets in multiple directions as well as a diffuse component from the multiple reflections among the facets (Torrance and Sparrow, 1967). A reduction in thickness of a sea ice layer with a small amount of surface roughness mainly decreases the BRF in the quasi-isotropic part, having little effect on the specular peak (Figure 8). Indeed, with a thinner sea ice layer, a number of the scattered photons are absorbed by the strongly absorbing underlying layer (reflectance of 0.1) instead of exiting the medium upwards. Most of the light scattered forwards exits the sea ice in the same manner as for an optically deep layer, explaining the smaller reduction in BRF for the forward scattering peak. When surface roughness is included, the forward scattering peak is more sensitive to a changing thickness. With an increasing solar zenith angle, the BRF with a smaller roughness parameter shows a decrease in intensity of the BRF over the whole hemisphere apart from the specular peak that increases and moves in a specular manner relative to the solar zenith angle. With a higher solar zenith angle (lower sun on the horizon), the photons travel less deep into the sea ice than for a lower solar zenith angle and go through fewer scattering events due to the shorter path length and the relative angle between the incident light path and the surface. Therefore, the light is less scattered in multiple directions (lower BRF over the hemisphere) and more light is scattered forwards (stronger specular peak). However increasing the surface roughness introduces more scattering events, as the light is reflected at different angles off the features. Less photons travel directly in

a specular manner, reducing the increase in the forward scattering peak with an increasing solar zenith angle, and the larger number of scattering events lead to a smaller reduction in the BRF of the remaining hemisphere. The BRF of sea ice is strongly wavelength dependent owing to the light scattering and absorption by the ice. At shorter wavelengths (300 – 900 nm), sea ice is highly scattering, whereas from 900 – 1400 nm the absorption by the ice dominates, with a nadir BRF close to zero (Figure 4). For a small amount of surface roughness, the BRF exhibits the same wavelength dependence over the hemisphere, bar the specular peak (Figure 10). Indeed, at longer wavelengths, the photons that are scattered in the sea ice are more likely to be absorbed than the photons quickly exiting the medium in a specular direction, creating a strong anisotropy. With increased surface roughness, a similar trend to the smaller surface roughness is observable, however the size of the forward scattering peak decreases with wavelength. The reduction may be caused by the absorption of photons at larger wavelengths that would otherwise have exited the ice in a forward direction after a low number of scattering events within the roughness features at lower wavelengths.

In the literature, a similar behaviour of the response of BRF to an increasing roughness was observed by Jin and Simpson (1999), when modelling the anisotropic reflectance factor of sea ice with three different roughnesses. Jin and Simpson (1999) also modelled the effects of a varying solar zenith angle on the anisotropic reflectance factor of sea ice for a fixed roughness, showing that the reflectance anisotropy is much larger for a solar zenith angle of 60° than for 45°. The effect of the solar zenith angle on the angular reflectance of sea ice was confirmed in the work presented here, additionally showing that surface roughness modulates the intensity and width of the forward scattering peak. Arnold et al. (2002) presented a airborne case measurement of BRF for melt-season ice with a solar zenith angle $\theta_i = 55°$. Their measurement of BRF shows no significant departure from uniformity across the hemisphere, apart from a forward scattering peak spread widely forward of the specular peak, suggesting large surface roughness. The BRF pattern, as well as the BRF reported in the principal plane for melt-season sea ice are in agreement with the modelled BRF presented here. However, the results from Arnold et al. (2002) are not directly comparable with the modelled BRF, as the irradiance for the BRF measured with the Cloud Absorption Radiometer instrument is composed of a direct and a diffuse component, whereas the illumination in the modelling conducted here is direct only.

4.2 Defining the roughness parameter

Sea ice roughness shows significant spatial variability, with vertical features ranging from the millimetre-scale to the meter-scale (e.g. Manninen, 1997; Peterson et al., 2008). The larger surface roughness features are generally caused by the deformation of the sea ice, forming rubble fields and pressure ridges that can reach 10 to 20 m in height (Tucker et al., 2013). At a smaller scale, brash ice, ridged blocks or frost flowers can create roughness with a standard deviation of a few millimetres to centimetres. As shown in the results (Sect. 3), surface roughness strongly influences the BRDF of sea ice. To cover a wide range of conditions, a selection of five surface roughness parameters, defined by the standard deviation of the height of the surface were picked, with a standard deviation of 1 mm to 10 cm. The range of surface roughness is in agreement with observations reported in the literature for small scale roughnesses (e.g. Tucker et al., 2013).

Random surface realisations were generated to calculate the surface roughness in the model, which is rotationally invariant. Therefore, Planarrad produces random a surface roughness, that has no specific structure or pattern. Specific shapes present in sea ice, such as pressure ridges could not be modelled.

4.3 Model limitations

As described in Sect. 2.2, Planarrad computes the BRDF over a hemisphere discretised into quads, and the calculated radiance leaving the surface is averaged over each quad. The input irradiance was set to a single quad in this study. Therefore the angular resolution of the model is limited to the quad size. Any differences in radiance within a single quad cannot be resolved, which results in a loss of definition for features smaller than the size of a single quad. Furthermore, in this configuration, the radiance for a quad containing the forward scattering maxima is lower than the radiance of a specular peak if it is smaller than a quad. Ideally the solid angle of the illumination source, as well as the solid angle of the quads should tend to zero. However, increasing the discretisation necessitates a considerable computational effort, which led the authors to the current choice of angular resolution representing a balance between resolution and computational resources.

The radiative-transfer equation was computed without an atmosphere, providing a surface BRDF product, whereas the radiance measured by satellite sensors at the Top-Of-Atmosphere (TOA) is a function of the properties of the surface and the atmospheric conditions at the time of the measurement. The purpose of the study was to characterise the intrinsic BRDF of sea ice as a function of roughness and thickness that can be incorporated in radiative transfer models by the community. Therefore, to obtain a direct comparison with remote sensing products that have not been corrected for atmospheric effects, the results of this study have to be propagated to the TOA using an additional radiative-transfer model (e.g. Kotchenova et al., 2008).

In this study, the sea ice was modelled as a single homogeneous slab with defined optical properties. The model does not presently allow for the study of multiple layers with different optical properties. However, PlanarRad allows the input of a BRDF as a lower boundary condition, therefore calculations for a layer of snow on the sea ice are possible. The work presented here focusses on a comprehensive characterisation of the BRDF of bare sea ice which lacks in the literature, and adding a layer of snow on the sea ice would have added too much complexity. Thus snow was not considered in this study. Nevertheless, calculations of a snow covered sea ice layer will be the subject of a forthcoming publication.

For the BRDF calculations described here, black carbon was assumed to be the only external absorber present in the ice. As described in Sect. 2.3, a base mass-ratio of 1 ng g^{-1} was added to the modelled sea ice. Although organic debris, algae, soot, HULIS or mineral dust have an effect of the radiative forcing of sea ice, other light-absorbing impurities other than black carbon were not examined in this study. Additionally, further investigation related to the effects of a varying mass-ratio of black carbon in sea ice is required.

5 Conclusions

This study provides a large dataset parameterising the BRDF of bare sea ice, accounting for varying surface roughnesses. The BRDF / BRF of three different types of sea ice was modelled, for a wavelength range of 300 – 1400 nm. The effects of surface

roughness were investigated as a function of thickness, solar zenith angle and wavelength. Radiative-transfer calculations show that surface roughness has a significant effect on the BRDF of sea ice, controlling the anisotropy through the forward scattering peak. Furthermore, the surface roughness is inter-dependent of other parameters that determine the BRDF pattern of sea ice, such as thickness, solar zenith angle and wavelength. As predicted by the model, the BRDF of sea ice exhibits a strong forward scattering peak surrounded by a quasi-isotropic response. For small amounts of surface roughness, a reduction in sea ice thickness decreases the quasi-isotropic part of the BRDF, affecting the forward scattering peak very little, the forward scattering peak changes consistently in a specular manner with a varying solar zenith angle while the intensity of the peak increases, and the forward scattering peak is much less wavelength dependant than the surrounding quasi-isotropic part of the hemisphere. For larger amounts of surface roughness, a decrease in thickness affects strongly the entire BRDF, including the forward scattering peak, the intensity of the forward scattering peak increases and moves to larger viewing zenith angles than the solar zenith angles as the latter increase but remains overall lower than for smaller amounts of surface roughness, and the size of forward scattering peak is strongly wavelength dependent. Because surface roughness is inter-dependent of other physical parameters, it is essential to account for roughness in the theoretical calculations of the radiation budget of sea ice.

This study provides a wide range of BRDF for sea ice that cover a diversity of conditions encountered in nature. The data generated here is expected to facilitate the development of more accurate radiative-transfer models used to derive albedo products by the remote sensing community, as well as reduce uncertainties in global climate models.

Author contributions. M. L. Lamare performed the modelling, including the data analysis and result preparation, and authored the paper. J. Hedley designed the model, wrote the roughness code, and edited the paper. M. D. King conceived and oversaw the study, and edited the paper.

Acknowledgements. The output data from this modelling study are stored on the open repository Zenodo, run by the CERN data centre, under a Creative Commons license. The data can be found at DOI xxx. MDK and MLL thank NERC for support under Grant NE/K000770X/1

References

Aoki, T., Aoki, T., Fukabori, M., Hachikubo, A., Tachibana, Y., and Nishio, F.: Effects of snow physical parameters on spectral albedo and bidirectional reflectance of snow surface, Journal of Geophysical Research: Atmospheres, 105, 10 219–10 236, doi:10.1029/1999JD901122, 2000.

Arnold, G. T., Tsay, S.-C., King, M. D., Li, J. Y., and Soulen, P. F.: Airborne spectral measurements of surface-atmosphere anisotropy for arctic sea ice and tundra, International Journal of Remote Sensing, 23, 3763–3781, doi:10.1080/01431160110117373, 2002.

Ball, C. P., Marks, A. A., Green, P. D., MacArthur, A., Maturilli, M., Fox, N. P., and King, M. D.: Hemispherical-Directional Reflectance (HDRF) of Windblown Snow-Covered Arctic Tundra at Large Solar Zenith Angles, IEEE Transactions on Geoscience and Remote Sensing, 53, 5377–5387, doi:10.1109/TGRS.2015.2421733, 2015.

Bourgeois, C. S., Calanca, P., and Ohmura, A.: A field study of the hemispherical directional reflectance factor and spectral albedo of dry snow, Journal of Geophysical Research: Atmospheres, 111, doi:10.1029/2006JD007296, d20108, 2006.

Buckley, R. G. and Trodahl, H. J.: Scattering and absorption of visible light by sea ice, Nature, 326, 867–869, doi:10.1038/326867a0, 1987.

Chang, H. and Charalampopoulos, T. T.: Determination of the Wavelength Dependence of Refractive Indices of Flame Soot, Proceedings of the Royal Society of London A: Mathematical, Physical and Engineering Sciences, 430, 577–591, doi:10.1098/rspa.1990.0107, http://rspa.royalsocietypublishing.org/content/430/1880/577, 1990.

Curry, J. A., Schramm, J. L., and Ebert, E. E.: Sea Ice-Albedo Climate Feedback Mechanism, Journal of Climate, 8, 240–247, doi:10.1175/1520-0442(1995)008<0240:SIACFM>2.0.CO;2, 1995.

Dirmhirn, I. and Eaton, F. D.: Some Characteristics of the Albedo of Snow, Journal of Applied Meteorology, 14, 375–379, doi:10.1175/1520-0450(1975)014<0375:SCOTAO>2.0.CO;2, 1975.

Doherty, S. J., Warren, S. G., Grenfell, T. C., Clarke, A. D., and Brandt, R. E.: Light-absorbing impurities in Arctic snow, Atmospheric Chemistry and Physics, 10, 11 647–11 680, doi:10.5194/acp-10-11647-2010, 2010.

Dozier, J., Davis, R. E., Chang, A. T. C., and Brown, K.: The Spectral Bidirectional Reflectance of Snow, in: Spectral Signatures of Objects in Remote Sensing, edited by Guyenne, T. D. and Hunt, J. J., vol. 287 of *ESA Special Publication*, p. 87, 1988.

Dumont, M., Brissaud, O., Picard, G., Schmitt, B., Gallet, J.-C., and Arnaud, Y.: High-accuracy measurements of snow Bidirectional Reflectance Distribution Function at visible and NIR wavelengths & comparison with modelling results, Atmospheric Chemistry and Physics, 10, 2507–2520, doi:10.5194/acp-10-2507-2010, 2010.

Flanner, M. G., Zender, C. S., Randerson, J. T., and Rasch, P. J.: Present-day climate forcing and response from black carbon in snow, Journal of Geophysical Research: Atmospheres, 112, doi:10.1029/2006JD008003, 2007.

Flanner, M. G., Shell, K. M., Barlage, M., Perovich, D. K., and Tschudi, M. A.: Radiative forcing and albedo feedback from the Northern Hemisphere cryosphere between 1979 and 2008, Nature Geoscience, 4, 151–155, doi:10.1038/ngeo1062, 2011.

France, J. L., King, M. D., Lee-Taylor, J., Beine, H. J., Ianniello, A., Domine, F., and MacArthur, A.: Calculations of in-snow NO2 and OH radical photochemical production and photolysis rates: A field and radiative-transfer study of the optical properties of Arctic (Ny-Ålesund, Svalbard) snow, Journal of Geophysical Research: Earth Surface, 116, doi:10.1029/2011JF002019, 2011.

Gatebe, C. K. and King, M. D.: Airborne spectral BRDF of various surface types (ocean, vegetation, snow, desert, wetlands, cloud decks, smoke layers) for remote sensing applications, Remote Sensing of Environment, 179, 131 – 148, doi:10.1016/j.rse.2016.03.029, 2016.

Hedley, J.: A three-dimensional radiative transfer model for shallow water environments, Opt. Express, 16, 21 887–21 902, doi:10.1364/OE.16.021887, 2008.

Hedley, J.: PlanaRad, http://www.planarrad.com, 2015.

Hedley, J. D., Roelfsema, C. M., Phinn, S. R., and Mumby, P. J.: Environmental and Sensor Limitations in Optical Remote Sensing of Coral Reefs: Implications for Monitoring and Sensor Design, Remote Sensing, 4, 271, doi:10.3390/rs4010271, 2012.

Henyey, L. G. and Greenstein, J. L.: Diffuse radiation in the Galaxy, Astrophysical Journal, 93, 70–83, doi:10.1086/144246, 1941.

Heygster, G., Alexandrov, V., Dybkjær, G., von Hoyningen-Huene, W., Girard-Ardhuin, F., Katsev, I. L., Kokhanovsky, A., Lavergne, T., Malinka, A. V., Melsheimer, C., Toudal Pedersen, L., Prikhach, A. S., Saldo, R., Tonboe, R., Wiebe, H., and Zege, E. P.: Remote sensing of sea ice: advances during the DAMOCLES project, The Cryosphere, 6, 1411–1434, doi:10.5194/tc-6-1411-2012, 2012.

Hudson, S. R., Warren, S. G., Brandt, R. E., Grenfell, T. C., and Six, D.: Spectral bidirectional reflectance of Antarctic snow: Measurements and parameterization, Journal of Geophysical Research: Atmospheres (1984–2012), 2006.

Jin, Z. and Simpson, J. J.: Bidirectional anisotropic reflectance of snow and sea ice in AVHRR Channel 1 and 2 spectral regions. I. Theoretical analysis, Geoscience and Remote Sensing, IEEE Transactions on, 1999.

Kokhanovsky, A. A. and Breon, F. M.: Validation of an Analytical Snow BRDF Model Using PARASOL Multi-Angular and Multispectral Observations, Geoscience and Remote Sensing Letters, IEEE, 2012.

Kotchenova, S. Y., Vermote, E. F., Levy, R., and Lyapustin, A.: Radiative transfer codes for atmospheric correction and aerosol retrieval: intercomparison study., Applied Optics, 47, 2215–2226, 2008.

Lamare, M. L., Lee-Taylor, J., and King, M. D.: The impact of atmospheric mineral aerosol deposition on the albedo of snow & sea ice: are snow and sea ice optical properties more important than mineral aerosol optical properties?, Atmospheric Chemistry and Physics, 2016.

Lee-Taylor, J. and Madronich, S.: Calculation of actinic fluxes with a coupled atmosphere–snow radiative transfer model, Journal of Geophysical Research: Atmospheres, 107, ACH 22–1–ACH 22–10, doi:10.1029/2002JD002084, 2002.

Leroux, C., Deuzé, J.-L., Goloub, P., Sergent, C., and Fily, M.: Ground measurements of the polarized bidirectional reflectance of snow in the near-infrared spectral domain: Comparisons with model results, Journal of Geophysical Research: Atmospheres (1984–2012), 1998.

Leroux, C., Lenoble, J., Brogniez, G., Hovenier, J. W., and de Haan, J. F.: A MODEL FOR THE BIDIRECTIONAL POLARIZED REFLECTANCE OF SNOW, Journal of Quantitative Spectroscopy & Radiative Transfer, 1999.

Leroy, M. and Roujean, J. L.: Sun and view angle corrections on reflectances derived from NOAA/AVHRR data, IEEE Transactions on Geoscience and Remote Sensing, 32, 684–697, doi:10.1109/36.297985, 1994.

Li, S. and Zhou, X.: Modelling and measuring the spectral bidirectional reflectance factor of snow-covered sea ice: an intercomparison study, Hydrological Processes, 2004.

Li, Z., Cihlar, J., Zheng, X., Moreau, L., and Ly, H.: The bidirectional effects of AVHRR measurements over boreal regions, IEEE Transactions on Geoscience and Remote Sensing, 34, 1308–1322, doi:10.1109/36.544556, 1996.

Light, B., Maykut, G. A., and Grenfell, T. C.: A temperature-dependent, structural-optical model of first-year sea ice, Journal of Geophysical Research: Oceans, 109, n/a–n/a, doi:10.1029/2003JC002164, c06013, 2004.

Lim, A., Hedley, J. D., LeDrew, E., Mumby, P. J., and Roelfsema, C.: The effects of ecologically determined spatial complexity on the classification accuracy of simulated coral reef images, Remote Sensing of Environment, 113, 965 – 978, doi:http://dx.doi.org/10.1016/j.rse.2009.01.011, 2009.

Lucht, W.: Expected retrieval accuracies of bidirectional reflectance and albedo from EOS-MODIS and MISR angular sampling, Journal of Geophysical Research: Atmospheres, 103, 8763–8778, 1998.

Manninen, A. T.: Surface roughness of Baltic sea ice, Journal of Geophysical Research: Oceans, 102, 1119–1139, doi:10.1029/96JC02991, http://dx.doi.org/10.1029/96JC02991, 1997.

Marks, A., Fragiacomo, C., MacArthur, A., Zibordi, G., Fox, N., and King, M. D.: Characterisation of the HDRF (as a proxy for BRDF) of snow surfaces at Dome C, Antarctica, for the inter-calibration and inter-comparison of satellite optical data, Remote Sensing of Environment, 2015.

Marks, A. A. and King, M. D.: The effect of snow/sea ice type on the response of albedo and light penetration depth (e-folding depth) to increasing black carbon, The Cryosphere, 2014.

Middleton, W. E. K. and Mungall, A. G.: The Luminous Directional Reflectance of Snow, J. Opt. Soc. Am., 1952.

Mishchenko, M. I., Dlugach, J. M., Yanovitskij, E. G., and Zakharova, N. T.: Bidirectional reflectance of flat, optically thick particulate layers: an efficient radiative transfer solution and applications to snow and soil surfaces, Journal of Quantitative Spectroscopy & Radiative Transfer, 1999.

Mobley, C. D.: A numerical model for the computation of radiance distributions in natural waters with wind-roughened surfaces, Limnology and Oceanography, 34, 1473–1483, doi:10.4319/lo.1989.34.8.1473, 1989.

Mobley, C. D.: Light and Water: Radiative Transfer in Natural Waters, Academic Press, 1994.

Nicodemus, F. E., Richmond, J. C., Hsia, J. J., Ginsberg, I. W., and Limperis, T.: Geometrical Considerations and Nomenclature for Reflectance, U.S. Nat. Bureau Standards, 1977.

Painter, T. H. and Dozier, J.: Measurements of the hemispherical-directional reflectance of snow at fine spectral and angular resolution, Journal of Geophysical Research: Atmospheres (1984–2012), 2004.

Peltoniemi, J. I., Kaasalainen, S., and Naranen, J.: Measurement of directional and spectral signatures of light reflectance by snow, Geoscience and Remote Sensing, IEEE Transactions on, 2005.

Peltoniemi, J. I., Gritsevich, M., Hakala, T., Dagsson-Waldhauserová, P., Arnalds, O., Anttila, K., Hannula, H.-R., Kivekäs, N., Lihavainen, H., Meinander, O., Svensson, J., Virkkula, A., and de Leeuw, G.: Soot on Snow experiment: bidirectional reflectance factor measurements of contaminated snow, The Cryosphere, 9, 2323–2337, doi:10.5194/tc-9-2323-2015, 2015.

Perovich, D. K.: The Optical Properties of Sea Ice., Monograph 96-1, U. S. Cold Reg. Res. and Eng. Lab., 1996.

Perovich, D. K., Grenfell, T. C., Light, B., and Hobbs, P. V.: Seasonal evolution of the albedo of multiyear Arctic sea ice, Journal of Geophysical Research: Oceans, 107, doi:10.1029/2000JC000438, 8044, 2002.

Peterson, I. K., Prinsenberg, S. J., and Holladay, J. S.: Observations of sea ice thickness, surface roughness and ice motion in Amundsen Gulf, Journal of Geophysical Research: Oceans, 113, n/a–n/a, doi:10.1029/2007JC004456, http://dx.doi.org/10.1029/2007JC004456, 2008.

Picard, G., Libois, Q., Arnaud, L., Verin, G., and Dumont, M.: Development and calibration of an automatic spectral albedometer to estimate near-surface snow SSA time series, The Cryosphere, 10, 1297–1316, doi:10.5194/tc-10-1297-2016, 2016.

Qu, X. and Hall, A.: Surface Contribution to Planetary Albedo Variability in Cryosphere Regions, Journal of climate . . . , 2005.

Schaaf, C. B., Gao, F., Strahler, A. H., Lucht, W., Li, X., Tsang, T., Strugnell, N. C., Zhang, X., Jin, Y., Muller, J.-P., Lewis, P., Barnsley, M., Hobson, P., Disney, M., Roberts, G., Dunderdale, M., Doll, C., d'Entremont, R. P., Hu, B., Liang, S., Privette, J. L., and Roy, D.: First operational BRDF, albedo nadir reflectance products from MODIS, Remote Sensing of Environment, 83, 135 – 148, doi:http://dx.doi.org/10.1016/S0034-4257(02)00091-3, 2002.

Schaepman-Strub, G., Schaepman, M. E., Painter, T. H., Dangel, S., and Martonchik, J. V.: Reflectance quantities in optical remote sensing—definitions and case studies, Remote Sensing of Environment, 2006.

Schlosser, E.: Optical studies of Antarctic sea ice, Cold Regions Science and Technology, 1988.

Stamnes, K., Hamre, B., Stamnes, J., Ryzhikov, G., Biryulina, M., Mahoney, R., Hauss, B., and Sei, A.: Modeling of radiation transport in coupled atmosphere-snow-ice-ocean systems, Journal of Quantitative Spectroscopy and Radiative Transfer, 112, 714 – 726, doi:http://dx.doi.org/10.1016/j.jqsrt.2010.06.006, 2011.

Torrance, K. E. and Sparrow, E. M.: Theory for Off-Specular Reflection From Roughened Surfaces*, J. Opt. Soc. Am., 57, 1105–1114, doi:10.1364/JOSA.57.001105, 1967.

Tucker, W. B., Perovich, D. K., Gow, A. J., Weeks, W. F., and Drinkwater, M. R.: Physical Properties of Sea Ice Relevant to Remote Sensing, pp. 9–28, American Geophysical Union, doi:10.1029/GM068p0009, http://dx.doi.org/10.1029/GM068p0009, 2013.

Warren, S. G. and Brandt, R. E.: Optical constants of ice from the ultraviolet to the microwave: A revised compilation, Journal of Geophysical Research: Atmospheres (1984–2012), 2008.

Warren, S. G., Brandt, R. E., and O'Rawe Hinton, P.: Effect of surface roughness on bidirectional reflectance of Antarctic snow, Journal of Geophysical Research: Planets, 103, 25 789–25 807, doi:10.1029/98JE01898, 1998.

Weeks, W. F. and Ackley, S. F.: Growth conditions and the structure and properties of sea ice, in: Physics of Ice Covered Seas: An Advanced Study Institute-Summer School, 1994.

Xiong, C. and Shi, J.: Simulating polarized light scattering in terrestrial snow based on bicontinuous random medium and Monte Carlo ray tracing, Journal of Quantitative Spectroscopy & Radiative Transfer, 2014.

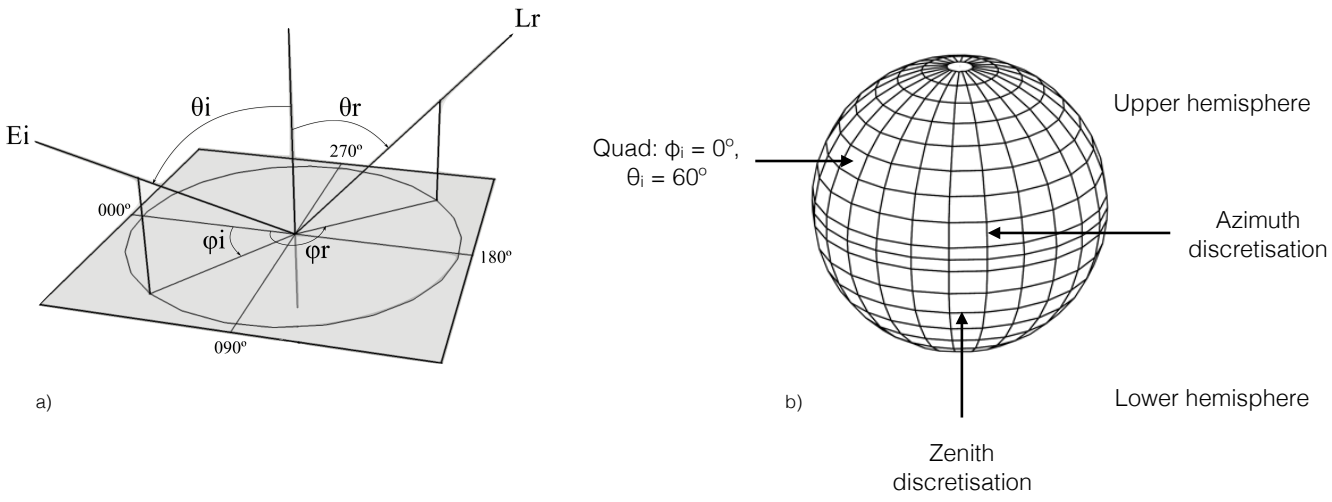

Figure 1. a) Diagram of the incident and viewing configuration defining BRDF. E_i is the irradiance from the azimuth angle ϕ_i and the zenith angle θ_i. L_r is the radiance in the azimuth angle ϕ_r and zenith angle θr. In this study, ϕ_i was fixed to 180°, the model being rotationally invariant. **b)** Diagram of the directional surface discretisation scheme used by PlanarRad to compute BRDF. Adapted from Hedley (2008).

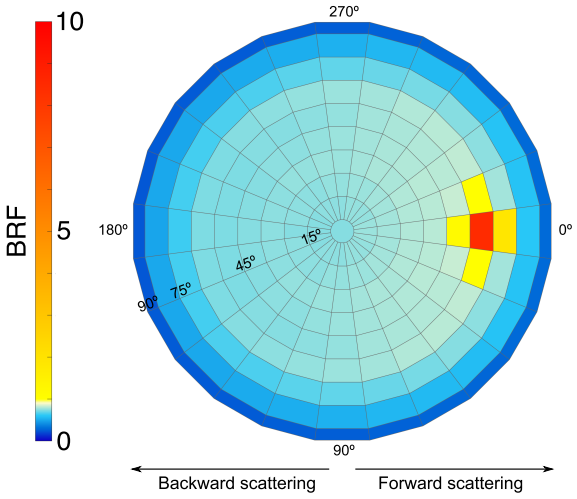

Figure 2. Polar plot of the BRF of optically deep first-year sea ice, with a solar zenith angle, $\theta = 60^\circ$ and a roughness parameter of $\sigma = 0.01$ m. The solar azimuth angle ϕ_i is located at 180°, consequently the left half of the hemisphere between $\phi = 90^\circ$ and $\phi = 270^\circ$ represents the backward scattering component and the right half of the hemisphere between $\phi = 270^\circ$ and $\phi = 90^\circ$ represents the forward scattering component. In this case, a strong specular forward scattering peak can be observed centred over the quad located at $\phi_r = 0^\circ$ and $\theta_r = 60^\circ$. A nonlinear colour bar was used to capture the large values around the scattering peak whilst showing the pattern in the quasi-isotropic part of the BRF.

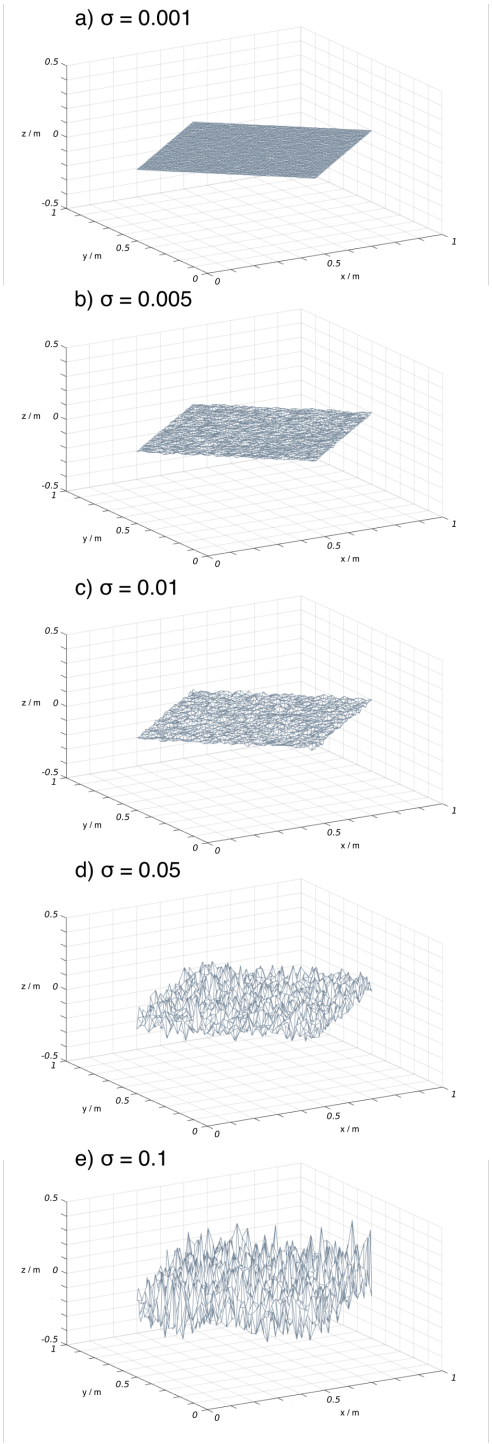

Figure 3. Visualisation of example random surface roughness input parameters, controlled by the standard deviation (σ) of the elevation of the surface. In this study, 5 surface roughnesses of **a)** $\sigma = 0.001$, **b)** $\sigma = 0.005$, **c)** $\sigma = 0.01$, **d)** $\sigma = 0.05$ and **e)** $\sigma = 0.1$ meters were generated.

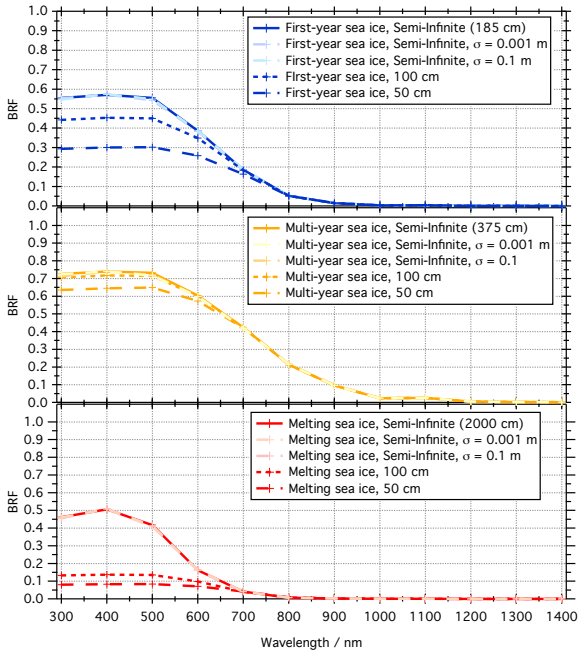

Figure 4. Nadir BRF for first-year, multi-year and melting sea ice, from 300 to 1400 nm in 100 nm steps with a solar zenith angle, $\theta = 60^{\circ}$ and a roughness parameter of $\sigma = 0.01$ m. The BRF of the different types of sea ice is plotted for an optically deep layer (185, 375 and 2000 cm), 100 cm and 50 cm. For each optically deep layer of sea ice, the nadir BRF is plotted for surface roughnesses of $\sigma = 0.001$ m and of $\sigma = 0.1$ m. The different sea ice parameters defined in this study are reported in Table 1

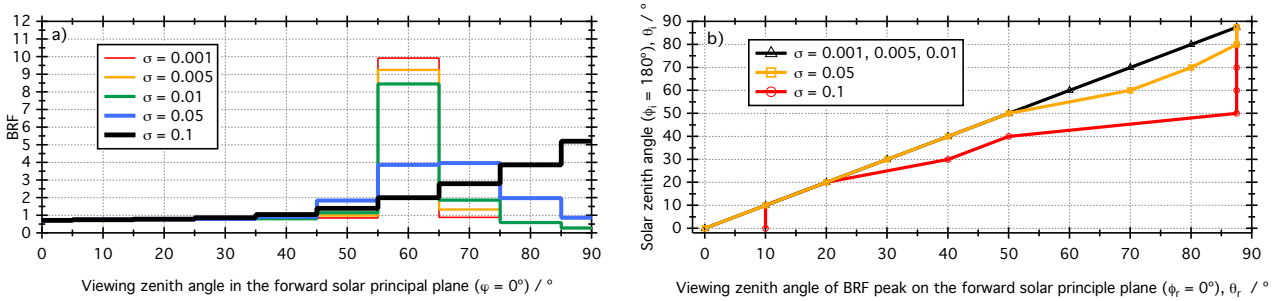

Figure 5. The effects of roughness on the forward scattering peak of the BRF. **(a)** BRF in the forward solar principle plane ($\phi_r = 0^{\circ}$) of optically deep first-year sea ice, modelled with a solar zenith angle $\theta_i = 60^{\circ}$ as a function of surface roughness. **(b)** Location of the BRF peak of optically deep first-year sea ice on the forward solar principle plane ($\phi_r = 0^{\circ}$) as a function of solar zenith angle, θ_i for different surface roughness parameters.

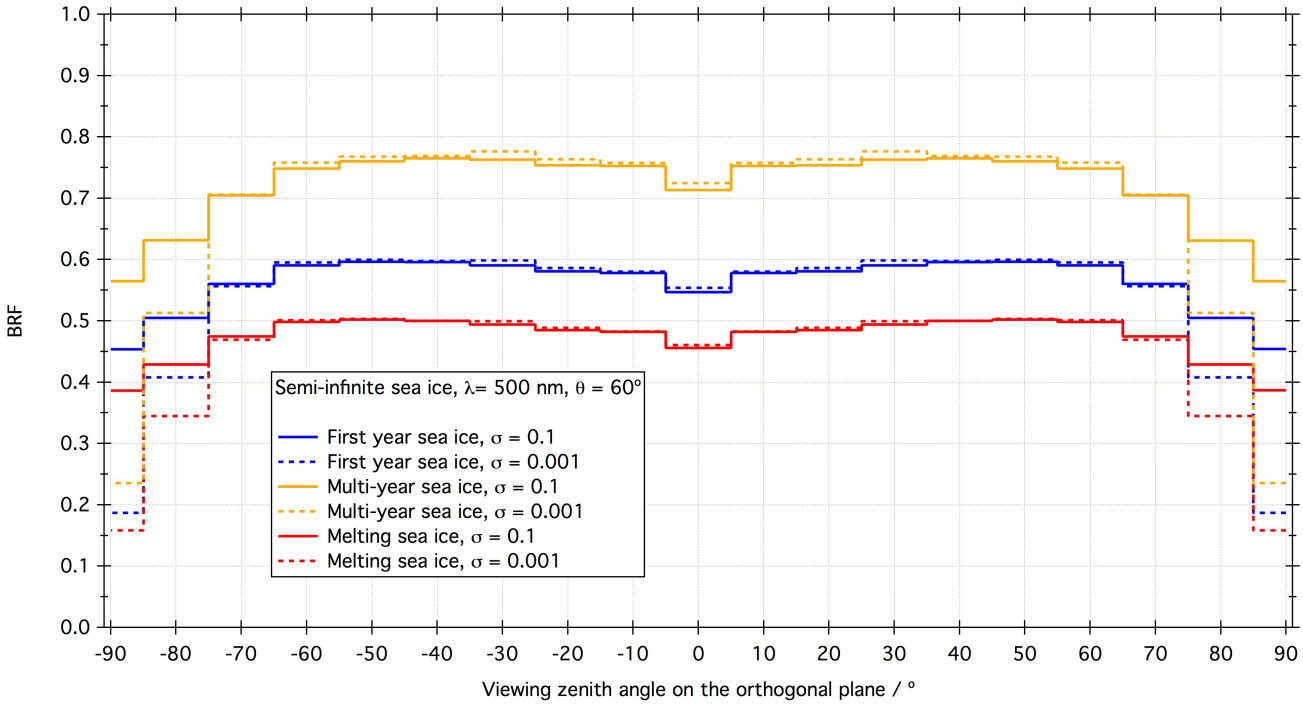

Figure 6. BRF of three semi-infinite sea ice types across the orthogonal plane (along the azimuth angles $\phi_r = 90°$ (negative zenith angles) and $\phi_r = 270°$ (positive zenith angles)) for surface roughnesses of $\sigma = 0.001$ and $\sigma = 0.1$, with a solar zenith angle $\theta_i = 60°$, at $\lambda = 500$ nm.

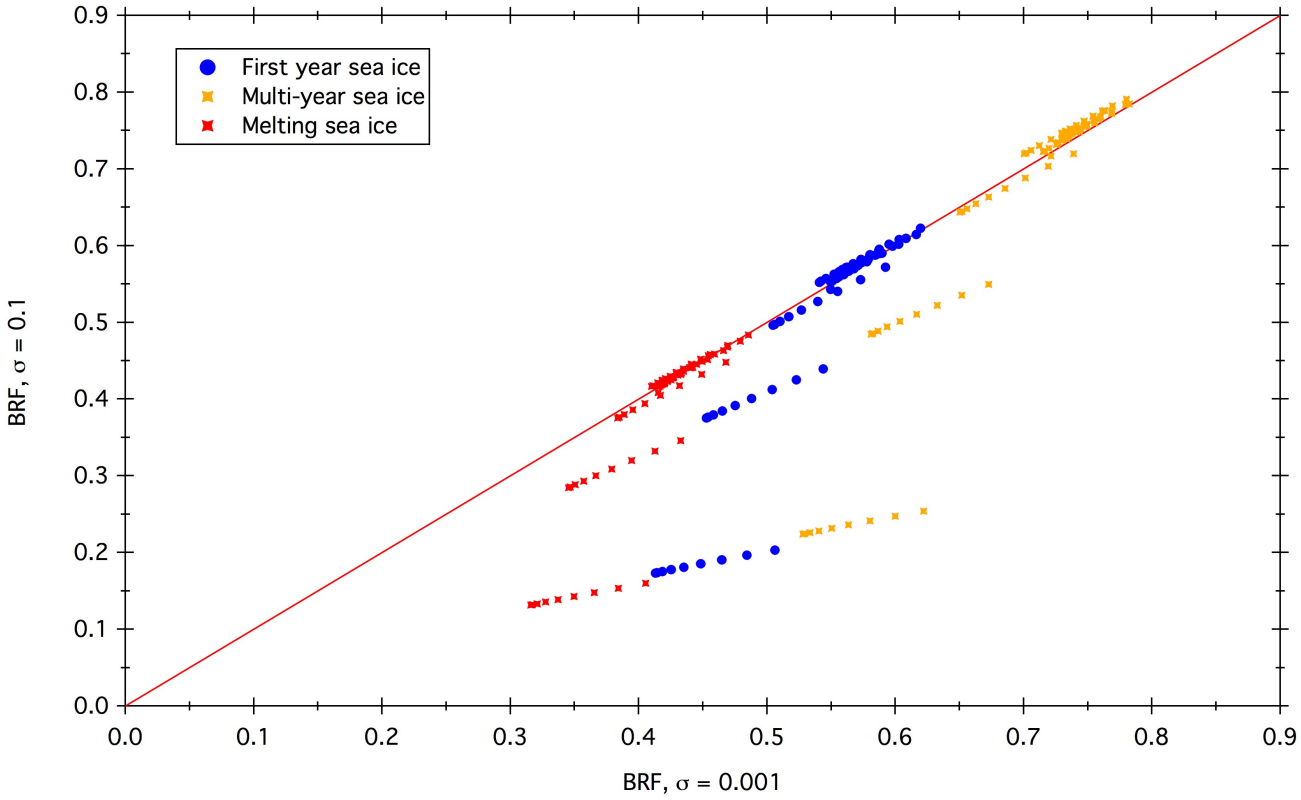

Figure 7. Scatter plot of BRF values for three sea ice types outside of the forward scattering peak (between $\phi_r = 315 - 45°$ and $\theta_r = 0° - 90°$). BRF values with a surface roughnesses value $\sigma = 0.001$ are represented on the x-axis, and $\sigma = 0.1$ on the y-axis. The red line represents x = y.

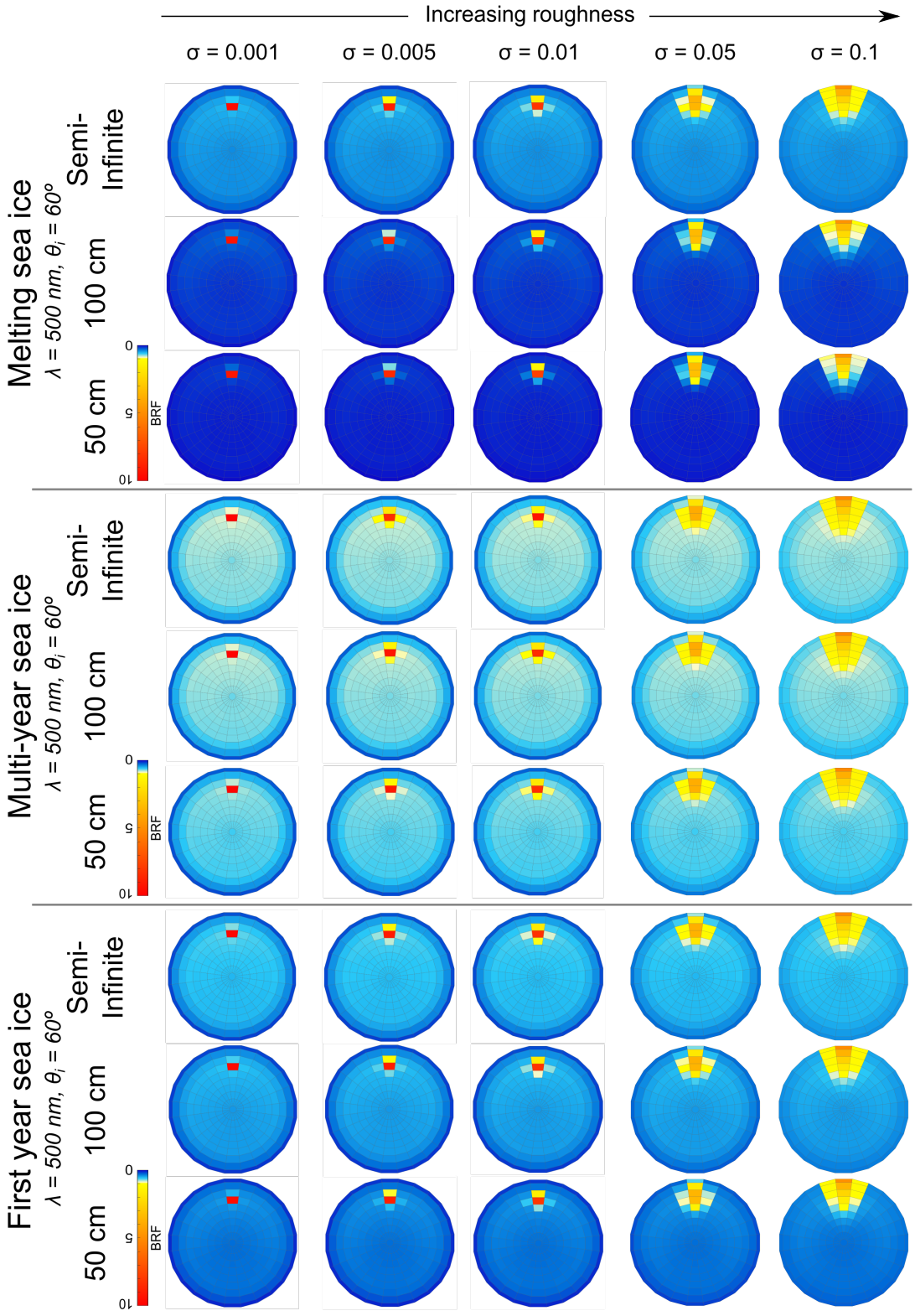

Figure 8. BRF of 50 cm, 100 cm and optically deep first-year sea ice, multi-year sea ice and melting sea ice with an increasing surface roughness.The incident angle is $\theta_i = 60^\circ$, and the results are reported for $\lambda = 500$ nm.

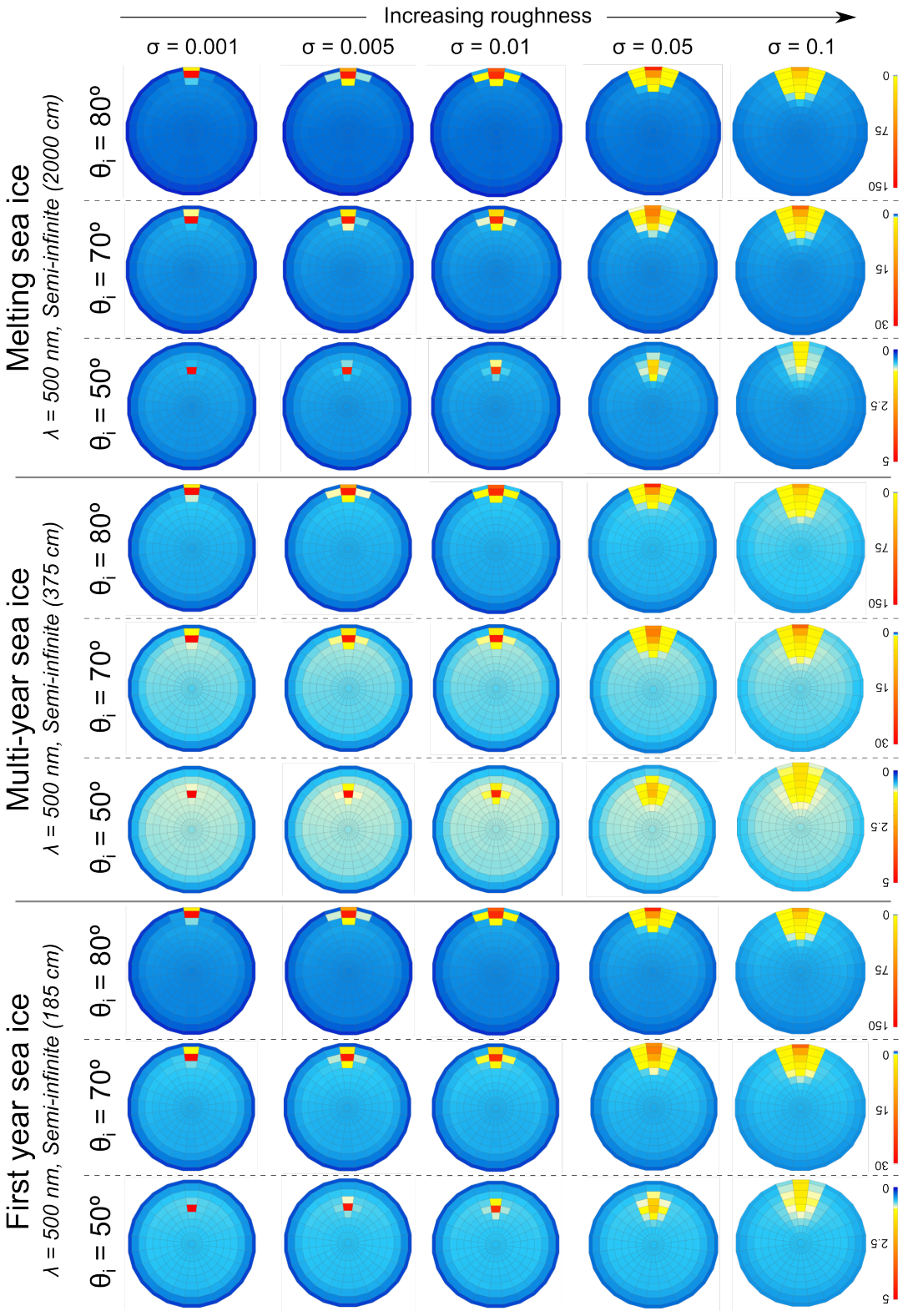

Figure 9. BRF of optically deep first-year sea ice, multi-year sea ice and melting sea ice with an increasing surface roughness at $\lambda = 500$ nm. The incident angles are $\theta_i = 50°$, $\theta_i = 70°$ and $\theta_i = 80°$. Note that the scale of the colour bar varies for the different illumination angles in order to visualise clearly the BRF pattern.

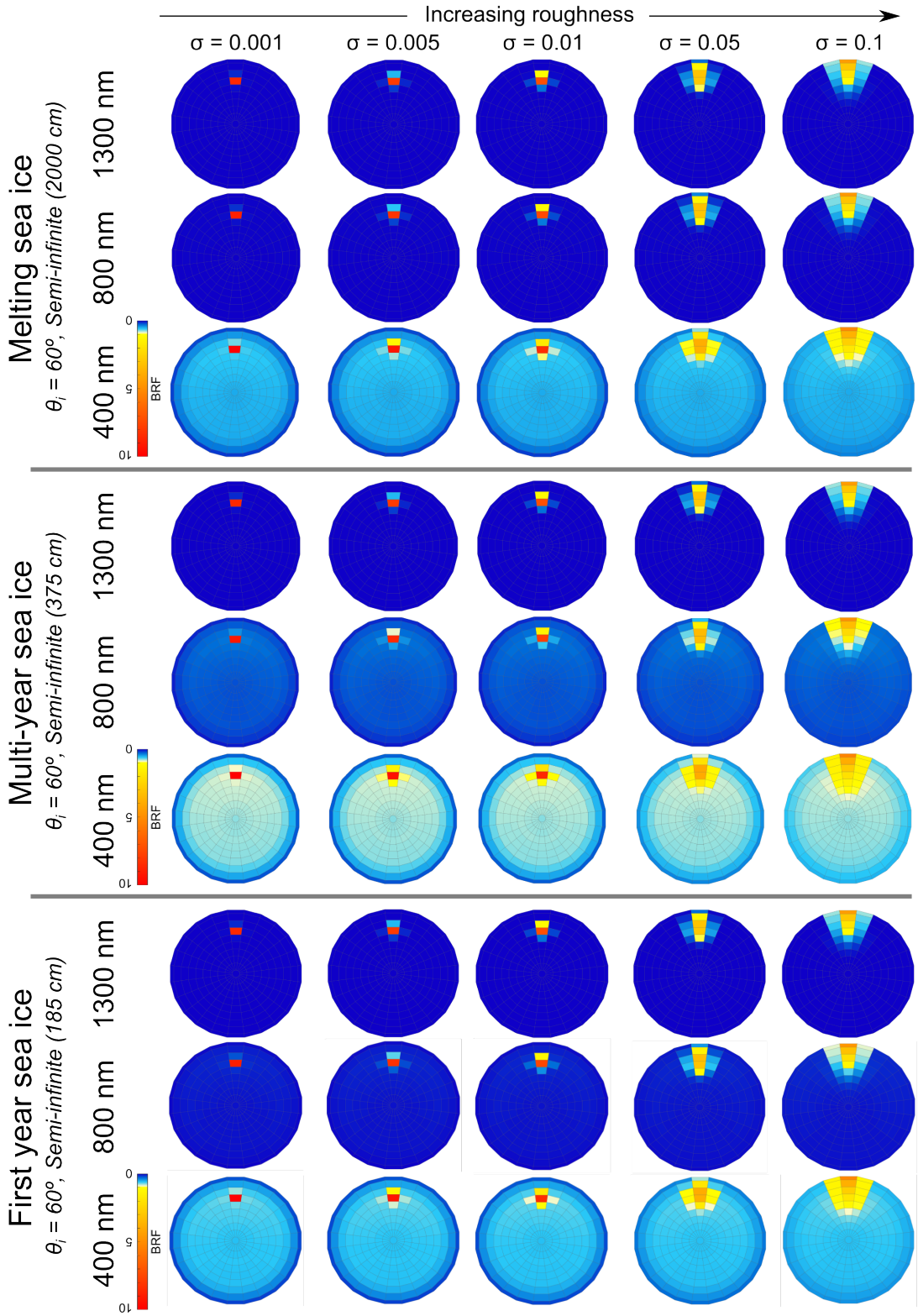

Figure 10. BRF of optically deep first-year sea ice, multi-year sea ice and melting sea ice with an increasing surface roughness for $\lambda = 400$, $\lambda = 800$ and $\lambda = 1300$. The incident angle is $\theta_i = 60°$.

Table 1. Sea ice parameters used as input parameters for the PlanarRad model, based on literature values and detailed in the work of Lamare et al. (2016).

Sea ice type	Sea ice density (kg m^{-3})	Sea ice scattering coefficient (m^{-1})	Sea ice asymmetry parameter g	optically deep thickness (cm)	Thickness modelled (cm)
First year sea ice	800	120	0.98	185	50, 100, 185
Multi-year sea ice	800	600	0.98	375	50, 100, 375
Melting sea ice	800	24	0.98	2000	50, 100, 2000

Chapter 7

The impact of light-absorbing particulates (black carbon and volcanic ash) on the bidirectional reflectance factor (BRF) of laboratory grown sea ice

Citation:
Lamare, M., Hedley, J., & King, M. D. (2017). The impact of light-absorbing particulates (black carbon and volcanic ash) on the bidirectional reflectance factor (BRF) of laboratory grown sea ice. In preparation for: JGR Atmospheres.

Author contributions:
Lamare, M. performed the experiments in the sea ice laboratory and in the optical laboratory, did the data analysis, prepared the results and wrote the paper.

Hedley, J. designed the radiative-transfer model, implemented the roughness model and the underlying BRDF function for this study, and proof-read the paper.

King, M.D. conceived and oversaw the study, and proof-read the paper.

The impact of light-absorbing particulates (black carbon and volcanic ash) on the bidirectional reflectance factor (BRF) of laboratory grown sea ice

M.L. Lamare[1], **J. Hedley**[2], **M.D. King**[1]

[1]Department of Earth Sciences, Royal Holloway University of London, Egham, Surrey, TW20 0EX, UK
[2]Environmental Computer Science Ltd., Hammet Square, Tiverton, Devon, EX16 6LR

Corresponding author: M.D. King, m.king@rhul.ac.uk

Abstract

Measurements of the BRDF of sea ice are essential to derive accurate albedo products from Earth Observation satellite products and normalise satellite images acquired at different viewing angles, owing to the anisotropy of the sea ice reflection. Impurities deposited in the sea ice from the atmosphere absorb solar radiation and strongly affect the radiative budget of sea ice. The effects of the light-absorbing impurities on the albedo of sea ice have been well characterised, but the angular response is lacking. Here, the bidirectional reflectance factor (BRF) of sea ice was measured in an artificial sea ice laboratory at the Royal Holloway university of London. Known quantities of black carbon and volcanic ash particles were placed in a 5 cm surface layer of sea ice and the BRF was measured. The measured properties of the sea ice were used to parameterise a radiative-transfer model. The model was used to calculate the optical properties (scattering coefficient) of the sea ice and characterise the angular effects of aerosols in sea ice on reflected radiation. The BRF of the artificial sea ice was shown to be more sensitive to the impurities at nadir and across the hemisphere than for the characteristic strong forward scattering peak. The pattern of the BRF of the sea ice across the hemisphere was shown to remain similar as the mass-loadings of black carbon were increased. The comparison between the modelled BRF and the measured BRF, showed that the radiative-transfer model can be used to derive the surface characteristics of sea ice from angular measurements.

1 Introduction

Knowledge of the bidirectional reflectance distribution function (BRDF) of sea ice is essential to quantify the radiation budget of polar regions using satellite remote sensing products. The solar radiation reflected from snow and sea ice surfaces is anisotropic [e.g. *Warren*, 1982; *Buckley and Trodahl*, 1987; *Schlosser*, 1988; *Hudson et al.*, 2006a] and strongly wavelength dependent [*Grenfell et al.*, 1994; *Perovich*, 1996]. Therefore, the characterisation of the BRDF of snow or sea ice is necessary to normalise the viewing angles of satellite observations in multi-temporal or multi-sensor studies, as the anisotropy of the reflected radiation from the observed surface may lead to errors in the interpretation of the satellite images [*Jin and Simpson*, 1999]. Furthermore, the BRDF is necessary to derive surface albedo, which is an important parameter for climate studies to quantify the energy balance of the surface of the Earth. In polar regions, variations of the high surface albedo of snow and sea ice have a significant impact on the global climate system through the ice-albedo feedback mechanism [e.g. *Curry et al.*, 1995; *Holland and Bitz*, 2003]. The negative trends in the sea ice extent in the Arctic over the last decades [e.g. *Serreze et al.*, 2007; *Kwok and Rothrock*, 2009; *Kay et al.*, 2011], leading to a transition towards a thinner sea ice cover [*Comiso*, 2006; *Stroeve et al.*, 2012] are simulated using general circulation models [e.g. *Meehl and Washington*, 1990; *Weatherly et al.*, 1998; *Overland and Wang*, 2013], which provide an understanding of the global climate system, and predictions of future trends of the extent of sea ice. Current general circulation models use the albedo of sea ice as a tuning parameter [*Curry et al.*, 2001] to represent the cryospheric processes in climate predictions, and rely on accurate satellite observations of the reflected solar radiation from different sea ice surfaces [*Dickinson et al.*, 1990]. Although a certain number of satellite remote sensing instruments [e.g. *Roujean et al.*, 1992; *Deschamps et al.*, 1994; *Diner et al.*, 1998; *Barnsley et al.*, 2004] provide multi-angular observations of the Earth's surface, the discrete number of viewing geometries and spectral bands over which data is acquired is insufficient to derive albedo accurately [*Cabot and Dedieu*, 1997]. Consequently, remote sensing albedo products are derived using radiative-transfer models based on a prior knowledge of the hyperspectral BRDF of the measured surface [*Lucht et al.*, 2000].

The angular distribution of reflected solar radiation above the surface of snow has been widely characterised through field measurements [e.g. *Middleton and Mungall*, 1952; *Steffen*, 1987; *Winther*, 1994; *Warren et al.*, 1998; *Abdou et al.*, 2001; *Painter*, 2004; *Peltoniemi et al.*, 2005; *Bourgeois et al.*, 2006; *Hudson et al.*, 2006a; *Ball et al.*, 2015; *Marks et al.*, 2015], modelling studies [e.g. *Leroux et al.*, 1999; *Mishchenko et al.*, 1999; *Nolin and Liang*, 2000; *Kokhanovsky and Zege*, 2004], or a combination of both [e.g. *Sergent et al.*, 1998; *Aoki et al.*, 2000; *Tanikawa et al.*, 2002; *Kokhanovsky and Breon*, 2012]. The BDRF of snow is strongly influenced by the physical structure of the medium,

such as grain size [*Aoki et al.*, 2000], snow type [*Peltoniemi et al.*, 2005], thickness [*Nolin et al.*, 1990], and surface roughness [*Warren et al.*, 1998]. Light-absorbing impurities deposited from the atmosphere have been shown to strongly influence the radiative forcing in snow [e.g. *Flanner et al.*, 2007; *Lamare et al.*, 2016], leading to accelerated melt [e.g. *Painter et al.*, 2007; *Doherty et al.*, 2013], particularly over ultra-violet and visible wavelengths, where the snow is highly scattering and weakly absorbing. Studies reporting the dependence of the viewing angle on contaminants in snow are scarce. *Peltoniemi et al.* [2015] measured the bidirectional reflectance factor (BRF) of snow using a field goniometer, before and after artificially depositing controlled amounts of chimney soot, volcanic sand and glaciogenic silt to investigate quantify the effects of light-absorbing particles on the BRF of snow. The experiments showed that as the particles absorbed solar radiation and sank into the snowpack, the BRF of the snow at nadir was significantly reduced compared to larger viewing angles.

Studies of the angular reflectance of sea ice are not as widely available as for snow. *Schlosser* [1988] measured the BRF of laboratory grown sea ice, showing a strong forward scattering specular peak, diminishing with sea ice thickness. The BRDF or BRF of sea ice were modelled with a radiative-transfer model based on the discrete ordinates method [*Stamnes et al.*, 2011], and using an optical model based on simple analytical formulas [*Malinka et al.*, 2016]. The modelling of the BRDF of the sea ice by *Stamnes et al.* [2011] showed a strong specular scattering peak for bare ice, that was reduced as the thickness of an overlying layer of snow was increased. The reflectances generated from the BRDF were in agreement with modelled and observed data from the literature. However, *Stamnes et al.* [2011] did not account for surface roughness in the study. *Perovich* [1998] measured the angular reflectance of multiple sea ice surfaces, showing the dependence of reflectance with viewing zenith angle. *Perovich* [1998] isolated the effects of surface roughness by artificially placing pieces of ice on the surface of a smooth ice layer. Higher values of reflectance were found close to the specular reflection point for smooth sea ice than for rough sea ice. *Jin and Simpson* [1999] modelled the bidirectional reflectance anisotropy of sea ice, highlighting the importance of surface roughness and solar elevation on the anisotropy of the reflected radiation. Smooth surfaces exhibit a narrow reflecting peak around the horizontal specular reflecting point, whereas for rough surfaces, the values of the specular reflection maxima are diminished and the size of the scattering peak is larger. The anisotropy of sea ice is shown to increase as a function of solar zenith angle. *Nolin et al.* [2002] showed that the angular spectral signatures of sea ice measured using satellite imagery could be used to derive surface roughness and sea ice types. *Lamare et al.* [2017a] present a comprehensive radiative-transfer study of the BRDF of sea ice for a range of thicknesses, sea ice types and surface roughnesses, providing the remote sensing community with a parameterisation for sea ice. Results show that for the typically high solar zenith angles occurring in polar regions, the strong reflecting peak above 45° viewing zenith angle is less wavelength-dependent than the surrounding quasi-isotropic part of the hemisphere. Furthermore, the roughness of the sea ice was shown to affect the scattering peak, confirming the results of *Jin and Simpson* [1999]. However, *Lamare et al.* [2017a] show that the surface roughness cannot be considered independently from the physical parameters of the sea ice, as changes in the properties of the sea ice affect the scattering peak differently to the surrounding hemisphere. Although the effects of impurities on the albedo of sea ice have been quantified [e.g. *Hansen and Nazarenko*, 2004; *Jacobson*, 2004; *Ramanathan and Carmichael*, 2008; *Marks and King*, 2013; *Lamare et al.*, 2016], to the knowledge of the authors no studies investigating the angular dependance of light-absorbing particulates on the BRDF of sea ice are available in the literature. The model proposed by *Stamnes et al.* [2011] computes the BRDF of sea ice, based on the inherent optical properties of the medium, including impurities. However, the effects of the impurities were only reported for flux reflectances derived from the BRDF. *Lamare et al.* [2017b] reported measurements of bare sea ice grown in an outdoor artificial facility. The authors calculated the mass-ratio of black carbon and algae present in the sea ice by fitting the observational data with a radiative-transfer model. Therefore, a study presenting the effect of impurities on the angular distribution of the BRDF is required.

In this paper, the impact of black carbon and mineral aerosol deposits on the BRDF of sea ice was investigated using a combination of laboratory measurements and radiative-transfer modelling.

To quantify the effects of the deposited particulates on the BRDF of sea ice, the study presented here was divided into two steps. 1) The bidirectional reflectance factor (BRF) of clean sea ice grown in a laboratory was measured as an approximation of BRDF, using a specifically designed Gonio-Spectrometer. Known quantities of light-absorbing impurities were added to a 5 cm thick surface layer above the clean sea ice, and the BRF of the poisoned sea ice was measured. 2) A radiative-transfer model was used to compute the BRF of the artificial sea ice, based on the amounts of impurities added to the sea ice, as well as the physical properties of the sea ice measured in the laboratory, used as tuning parameters. The measurements performed in the laboratory were compared with the results from the radiative-transfer model, which allowed us to isolate the radiative effects of black carbon and mineral aerosol deposits from the variability of the physical parameters of the sea ice.

The purpose of this work was to quantify the effects of black carbon and mineral aerosol deposits on the BDRF of sea ice in order to correct multi-angular satellite retrievals of sea ice and provide an improved parameterisation for albedo products. To this end, light-absorbing impurities were placed in a surface layer of artificial sea ice, that was added to a layer of clean sea ice, and the BRDF was measured before and after, using a laboratory Gonio-Spectrometer. The artificial sea ice facility provided an instrumented and controlled environment in which the sea ice was grown, allowing the deposition of know quantities of impurities in the sea ice. Firstly, commercially available black carbon simulating carboneous particulates atmospherically transported to polar regions was filtered for the particle size to be representative of naturally deposited black carbon in sea ice. Mass-ratios of 34.31, 68.60 and 205.90 ng g^{-1} of black carbon were added to the sea ice. Secondly, a sample of volcanic ash from the Eyjafjallajökull 2010 eruption was used as a proxy for mineral aerosol deposits. *Lamare et al.* [2016] showed that the effects of mineral aerosol deposits on albedo depended more on the type of snow or sea ice than on the type of mineral impurity. Therefore, the volcanic ash used in the present work was considered to be representative of a range of mineral aerosol deposits. Mass-ratios of 550.00, 2202.67 and 5506.67 ng g^{-1} of volcanic ash were placed in the top layer of sea ice. To evaluate the impact of the impurities on the BRDF of sea ice, the laboratory measurements were compared to the output of a radiative-transfer model, serving as a validation tool for the model.

2 Methods

In the following methodology sections, the terminology used to describe angular reflectance quantities is defined, the artificial sea ice laboratory and the instrumental setup are presented, the preparation of the impurities placed in the sea ice is described, and the radiative-transfer modelling approach is detailed.

2.1 Definitions

The BRDF describes the quantities and angular directions of a parallel incident beam from a direction in the hemisphere scattered from a surface to an other direction in the hemisphere [*Nicodemus et al.*, 1977], providing information on the anisotropy of the radiation reflected from the surface. The spectral BRDF depends on the irradiance and radiance azimuth and zenith angles respectively, and therefore can be expressed as [*Schaepman-Strub et al.*, 2006]:

$$BRDF(\theta_i, \phi_i, \theta_r, \phi_r; \lambda) = \frac{L_r(\theta_i, \phi_i, \theta_r, \phi_r; \lambda)}{E_i(\theta_i, \phi_i; \lambda)}, \tag{1}$$

where L_r is the radiance with an azimuth angle ϕ_r and a zenith angle θ_r, E_i is the irradiance from the azimuth angle ϕ_i and the zenith angle ϕ_i, and λ is the wavelength.
Although BRDF measurements have been reported in the literature, the terminology employed was erroneous [*Schaepman-Strub et al.*, 2006], as the BRDF is defined by a ratio of infinitesimals [*Nicodemus et al.*, 1977], and cannot be measured directly.
The BRF, which also describes the anisotropy of the reflected flux from a surface, is defined as the

ratio of radiance reflected by a surface to the radiance reflected in the same direction by a lossless Lambertian diffuser [*Schaepman-Strub et al.*, 2006]. The BRF can be given by:

$$BRF(\theta_i, \phi_i, \theta_r, \phi_r; \lambda) = \frac{L_r(\theta_i, \phi_i, \theta_r, \phi_r; \lambda)}{L_{id}(\theta_i, \phi_i, \theta_r, \phi_r; \lambda)} \tag{2}$$

with L_{id} the radiance from an ideal lossless Lambertian reference.
Owing to the Lambertian surface being isotropic, the BRF can be related to BRDF by multiplying the BRDF by π [*Schaepman-Strub et al.*, 2006]. The BRF requires the illumination flux to be direct and collimated, and the measurements to be acquired with an infinitely small field of view solid angle. In the case of laboratory measurements, if the illumination and the viewing angles are not infinitesimal, the quantity measured is referred to as the biconical reflectance factor. Therefore, to calculate the BRF from the measurements of the artificial sea ice in the laboratory, several assumptions were made. Firstly, the illumination provided by the laboratory lamps was considered to be perfectly collimated, and the tiny differences in illumination azimuth and zenith angles from the different parts of the lamp were ignored. Secondly, the measurements of the upwelling radiation reflected from the sea ice was averaged over the solid angle of the field of view of the signal collector on the instrument, causing a smoothing of the BRF for rapidly changing intensities. However, the small viewing angle of the signal collector is considered to measure an acceptable approximation of BRF [*Martonchik et al.*, 2000], and the biconical reflectance factor will be referred to as BRF henceforth.

In order to isolate the angular dependence of the radiance reflected from the sea ice from the spectral signature of the ice, and better compare the laboratory measurements, the anisotropy factor (ANIF) was calculated. The ANIF is presented here as the BRF normalised by the BRF at nadir, and is expressed as [*Sandmeier et al.*, 1998]:

$$ANIF(\theta_i, \phi_i, \theta_r, \phi_r; \lambda) = \frac{R(\theta_i, \phi_i, \theta_r, \phi_r; \lambda)}{R_0(\theta_i, \phi_i, \theta_r = 0, \phi_r; \lambda)}. \tag{3}$$

with R, the BRF and R_0 the BRF at nadir.

2.2 Sea ice simulator description

The BRF measurements of the laboratory grown sea ice were performed at the sea ice simulator at Royal Holloway University of London, Egham, UK. The sea ice simulator, which was first described by *Marks et al.* [2017b], consists of a white polyethylene cylindrical tank with dimensions of 132 cm (height) x 139 cm (diameter), and an operating volume of approximately 2 m^{-3}. The tank is filled with artificial seawater, which is replaced at the start of each experiment. The artificial seawater is formulated by dissolving Tropic Marine salt in fresh water, to replicate the chemical composition of natural seawater (*Atkinson and Bingman* [1997]). Tropic Marine is a synthetic salt that has a similar weighted combination of chemical elements to that found in natural seawater (*Marks et al.* [2017b]), except for nitrate and phosphate. Tropic Marine was shown to have an ion content within 10% of natural seawater (*Atkinson and Bingman* [1997]). The amount of Tropic Marine added to the water in the tank was adjusted to maintain an average salinity of 31 practical salinity units (PSU) at the start of each experiment. The circulation of the seawater is provided by a heated pumping system running in a loop at the bottom of the tank. The seawater at the bottom of the tank in circulated at a rate of 10 L min^{-1} through a UV steriliser to limit algae growth, followed by a series of 10 µm and 1 µm filters to remove impurities. The water is drawn into the closed loop from one side of the pool and pumped back out on the opposite side using a diffusing head to prevent the formation of circulation patterns. Furthermore, a solution of fresh water and glycol was heated to 4°C using a heating unit and circulated in a closed external circuit of pipes at the bottom of the tank to prevent the artificial seawater from freezing at the base of the tank.
The seawater tank is located in a climate controlled shipping container which can generate ambient temperatures between -25°C and +25°C through a compression refrigeration system. The cold temperatures are achieved by circulating cooled outdoor air around the inside of the container. For the purpose of the experiments described in this paper, a structure was placed over the sea ice tank to minimise the stray light reflections from the metallic walls of the shipping container. The structure is

composed of aluminium struts wrapped in matte black foil, a black coated plywood roof and blackout rubberised curtains suspended around the tank, masking the operators who can introduce artifacts in the radiance measurements (*Kimes et al.* [1983]). The artificial sea ice is generated starting from liquid water conditions and setting the ambient air temperature in the unit to -18°C. Over the cooling and defrosting cycles of the system, the indoor temperature oscillates between -17.5°C and -12°C. An additional cooling fan blowing air across the surface of the water, accelerates the ice growth process by convection, removing the heat from the tank. Over the course of the experiments, the sea ice was allowed to grow between 24 and 44 days for each clean ice experiment, attaining thicknesses of 22 to 46 cm. To monitor the growth of the sea ice and the temperature of the seawater below, a type-T thermocouple array was connected at varying intervals to a polypropylene tube, which was placed vertically in the seawater and frozen into place during the experiment. The thermocouples were placed with a spacing of 20×2, 4×4 and 6×10 cm to monitor the temperature throughout the depth of the tank with a higher resolution in the upper part. The temperature profile of the sea ice was recorded throughout the growth of the sea ice. The thickness of the sea ice was estimated from the discontinuity in the temperature profile, the temperature becoming linear as a function of depth for the seawater. The air temperature in the container was monitored using a an automated digital thermometer with a precision of ±0.5°C. Each experiment performed in the sea ice simulator was divided into 2 stages. In a first step the sea ice was generated from open water, and BRF measurements were performed (described in section 2.5). In a second step, a layer of sea ice containing a known dosage of atmospheric particulates (black carbon or volcanic ash) was grown on the existing sea ice cover. To do so, a sample of 75 L of the artificial seawater was removed from the tank at the start of the experiment and stored in sealed polypropylene containers. After the measurements of the clean sea ice, a known solution of particulates, described in section 2.3, was added to the 75 L of seawater and poured on the surface of the ice. The layer of contaminated water exposed to the cold ambient air temperature of the container froze over the course of 48h forming a 5 cm layer of polluted sea ice. BRF measurements of the new layer of sea ice were performed between 1 and 2 weeks after the solution was placed on the ice. At the end of each experiment, the ambient temperature in the container was raised to +10°C, causing the ice to melt over the course of a week. The seawater was left to circulate through the UV steriliser and the filters for an additional week, to remove the particulates of black carbon or volcanic ash previously trapped in the sea ice. The effect of the remaining unfiltered particles in the new sea ice was considered to be negligible, owing to the dilution in the large volume of seawater and the filtering action. The seawater in the tank was emptied every 2 to 3 experiments, the tank was cleaned with NaClO to remove algae contamination, and a new solution of seawater was made.

2.3 Preparation of the impurities in the sea ice

Black carbon and volcanic ash particles were used to represent different types of deposited atmospheric particles typically deposited in the Arctic [*Zdanowicz et al.*, 1998; *Koch and Hansen*, 2005a] for the BRF measurements in the laboratory.

A sample of Cabot Corporation Monarch 120 black carbon was used as a proxy for black carbon, and a suspension was prepared following the procedure described by *Marks et al.* [2017b]. The mass-loading of the black carbon suspension was calculated by weighing the precipitates of an evaporated sample of 1200 mL of the suspension in three glass beakers. The resulting mass-loading of the suspension used in the present study was 6.36±0.22 $\mu g g^{-1}$ (1σ). Known aliquots of the black carbon suspension were mixed with 75 L of seawater withdrawn from the tank at the start of each experiment. The mass-ratio of the black carbon placed in the superficial layer of sea ice over three different experiments was 34.31 ng g^{-1}, 68.6 ng g^{-1} and 205.9 ng g^{-1}.

The volcanic ash used as a proxy for mineral aerosol deposits in the experiment originated from the 2010 Eyjafjallajökull eruption. A sample of volcanic ash was collected on the south flank of the Eyjafjallajökull volcano in July 2010. The sample was collected from the ground, after having removed a 5 cm layer of superficial darkened ash, so that the sample was more representative of the freshly deposited material. Owing to the volcanic ash having been collected close to the eruption source, and thus being composed of coarse particles, the particle size of the sample was not repre-

sentative of long-distance transported particles. Therefore, the sample of volcanic ash was placed in a vibrating powder mill for 3 minutes at 1500 rpm, to reduce the particle size. Mineral dust particles deposited in snow have been shown to be typically 2–3 orders of magnitude larger than black carbon particles [*Flanner et al.*, 2007]. Hence the filtration methods used for the black carbon were not applied to the volcanic ash. A sample of the milled volcanic ash was added with a ratio of 1:50 to a solution of a ratio of 1:4 ultra pure water (> 18Ω) and isopropyl alcohol. The role of the isopropyl alcohol was to facilitate the dispersal of the ash particles. The suspension was left to stand for a duration of 48 hours, equivalent to the freezing time of the upper sea ice layer in the sea ice laboratory. The top part of the suspension was then extracted under vacuum, and diluted with a ratio of 1:4 ultra pure water. The method presented above was used to prevent the volcanic ash particles from precipitating to the bottom of the layer of doped sea ice in the laboratory. The particles were therefore considered to be distributed evenly with the sea ice layer. The mass-loading of 413 ±0.67 µg g^{-1} (1 σ) of the suspension of volcanic ash was determined gravimetrically, as for the black carbon. Three experiments were performed using the volcanic ash particles in the sea ice, with mass-ratios of 550 ng g^{-1}, 2202.67 ng g^{-1} and 5506.67 ng g^{-1}.

In order to accurately parameterise the impurities placed in the sea ice in the radiative-transfer model, a characterisation of the absorption properties of the black carbon and volcanic ash was necessary. The mass absorption cross-section (MAC) of the black carbon and volcanic ash were calculated using Mie theory, based on the complex refractive-index, the density and the size distribution of the particles. The MAC of the Monarch 120 black carbon was calculated by *Marks et al.* [2017b], and the results were used in the present study. The values reported by the authors, with a MAC of 2.97 $m^2 g^{-1}$ at 550 nm, were similar to the values of the MAC of black carbon reported for a similar particle size by *Dang et al.* [2015]. The computations of the MAC of the volcanic ash were performed with the same method as for black carbon. The size and shape of Eyjafjallajökull volcanic ash particles in the suspension were assessed using scanning electron microscopy (SEM). The shape factor (*Heilbronner and Barrett* [2013]) of the observed particles was calculated using the ImageJ image analysis software (*Abràmoff et al.* [2004]). The average shape factor was 0.855, indicative of a spherical type shape and the average maximum Feret diameter was 0.83 ±0.31 (1 σ). A density of 2300 kg m^{-3} was obtained from *Johnson et al.* [2012], the refractive index of long-distance particles from the Eyjafjallajökull eruption was estimated by *Derimian et al.* [2012]. The resulting MAC of the volcanic ash had a value of 0.11 $m^2 g^{-1}$ at 550 nm, similar to the values obtained by *Dang et al.* [2015] for mineral dust. Although the absorption of the volcanic dust is much lower than the black carbon, mineral aerosol deposits are found in much larger mass-ratios than black carbon [*Dang et al.*, 2015, and references therein], which was reflected in the mass-ratios used during the experiments.

2.4 Instrumentation

A custom laboratory goniometer, designed for the measurements at the sea ice simulator was used to perform the BRF measurements. The goniometer, shown in figure 1, consists of a 77 cm diameter steel ring placed on 8 adjustable polytetrafluoroethylene (PTFE) pads which can be adjusted individually in height to control the level and height of the ring. A rotating mat black anodised sheet of aluminium is placed on the inside of the steel ring to reduce the generation of diffuse illumination. A carriage connected to the base ring with a set of wheels supports the arm of the instrument. The carriage can be manually rotated 360° around the base ring with a positioning precision of ±0.1°. The azimuth angle of the carriage is determined using a digital angle reader connected to the carriage wheels with a set of mechanical low friction gears. The goniometer arm connected to the carriage is formed of 2 hollow aluminium square sections covered in black rubberised material, forming an L shape and supported by diagonal supporting strut. The arm is placed on a pivot attached to the carriage, which allows the arm to be rotated up to 90° to the left or right of the carriage, providing movement over the zenith angles. A mechanical clamp allows the arm to be locked into position at any angle indicated by an electronic angle reader with a positioning precision of ±0.1°. A signal collector holder is located at the end of the horizontal section of the goniometer's arm, which, when the arm is placed vertically (0° zenith angle), is located above the centre point of the ring at a height of 48 cm above the surface. A combination of the rotation of the carriage on the base ring and

the inclination of the arm allows the sensor to take readings over the entire hemisphere. The signal collector, consisting of a 8° field of view lens was connected to a spectroradiometer via an optical fibre. The field of view of the optic was selected to provide the smallest solid angle possible whilst providing a sufficiently strong signal for the spectroradiometer. The viewing footprint measured at nadir was 6.7 cm in diameter and the small field of view of the signal collector allowed measurements to be carried out up to 75° zenith angle without the base ring being present in the elongated footprint. The lens was aligned before each measurement by shining a 650 nm laser down the optical fibre and plotting the laser footprint on tracing paper placed at target level. The carriage was rotated and the lens position adjusted until the centre of the footprint varied less than 1.8 cm over all azimuth angles. Over the duration of the laboratory measurement campaign, two different spectroradiometers were used. For the black carbon measurements, acquisitions were carried out with an Ocean Optics USB2000+ spectrometer, and for the measurements of the volcanic ash in the sea ice, an ASD Field Spec Pro spectroradiometer was used. The Ocean Optics USB2000+ spectrometer operates over the wavelength range 179–877 nm with a 0.3 nm spectral interval. The ASD covers a larger spectral range, with measurements between 350 and 2500 nm, and a wavelength interval of 1 nm.

The surface of the artificial sea ice was illuminated using a bank of nine 400 W tungsten-halogen lamps, each outputting 9500 lumens. The lamps provide a sufficiently strong signal for the spectoradiometer over the wavelength spectrum 400–1000 nm. The lamps were placed in a 3 x 3 array on a wooden board, covering an area of 55.0 cm x 48.5 cm. The supporting board was fixed to an adjustable tripod, allowing the height and inclination of the lamps to be adjusted in order to illuminate the surface of the artificial sea ice homogeneously at a determined angle. For the purpose of this study the lamps were placed at a distance of 155 cm from the centre of the sea ice sampling area and an zenith illumination angle (solar zenith angle) of 60° was fixed throughout the experiments to be representative of illumination conditions typically found in the Arctic in summer. A laser alignment system allowed the illumination zenith angle at the centre of the sampling ring to be positioned with an precision of ±1°.The entire surface of the ice in the tank was illuminated to account for the contribution of multiple scattering within the sea ice.For the purpose of this study the variations in illumination over the viewing footprint were considered to be negligible and the irradiance was considered to be collimated. Prior to the experiments, the stability of the intensity of the light source was assessed by measuring the raw signal of a Spectralon panel over a period of 200 minutes. The lamps exhibited good stability with a maximum change of less than 1.5 % relative to the start of the measurement.

To convert the raw radiance measurements of sea ice to BRF (section 2.1, equation 2), measurements of a Spectralon reference panel were performed directly after each angular sea ice radiance acquisition, under the same illumination conditions. A 20×20 cm Spectralon panel was used as an approximation of a lossless Lambertian reflector. The panel was attached to a supporting frame with three adjustable feet offset from the centre of the measuring area, limiting the disruption of the sea ice surface and allowing to adjust the levelling of the standard. Reference measurements of the panel were performed at the nadir viewing angle only, based on the assumption that the panel was Lambertian. The illumination angle being fixed throughout the experiments, the radiance of a perfectly Lambertian reference would be equal for all the viewing angles. Owing to the Spectralon panel not being perfectly lossless, a calibration over the wavelength range 400–1000 nm was carried out at the National Physical Laboratory, UK, using the National Reference Reflectometer (*Williams* [1999]). A reflectance correction factor was calculated for an illumination angle of 60°, which matches the illumination angle of the BRF measurements in the sea ice simulator. Because the correction factor varied by less than 0.5% over the wavelength range, a spectrally averaged value of 0.88 was used for the measurements presented in this study.

2.5 Measurements

Over the course of the experiment campaign at the sea ice simulator, a total of 12 BRF acquisitions were obtained. A summary of the experiments carried out can be found in table 1. After

the sea ice was formed, the laboratory goniometer was placed on the surface of the clean sea ice in the centre of the tank. The lamps and spectroradiometer were set up and left to warm up for a period of 1h before the start of the measurements, to enable the stabilisation of the power supplies. After the goniometer was geometrically calibrated, measurements of the BRF were performed at discrete points over the hemisphere. Measurements were acquired over approximately 75 viewing angle for each experiment, covering the hemisphere. Previous work has shown that the BRF of sea ice is quasi-isotropic with a strong forward scattering peak [*Jin and Simpson*, 1999]. To capture the extent and shape of the forward scattering peak, the measurement points were heavily weighted towards the forward scattering part of the hemisphere, around the solar principal plane. Owing to shading from the goniometer's arm, measurements between 180 ° in azimuth (equal to the illumination azimuth angle) and 270 ° were not achievable. The distribution of the measurement viewing angles across the hemisphere is shown in figure 2. An average full BRF measurement was performed over a duration of approximately 4h. After the measurements of the clean ice were performed, the instruments were removed from the surface of the sea ice, and the 75 L of seawater containing a suspension of impurities previously described were poured onto the surface of the sea ice. The seawater froze over the course of 48 hours, forming a 5 cm layer of doped sea ice on the surface of the clean ice. The new layer was left to consolidate over the duration of a week, and the BRF of the new surface layer of sea ice was measured. Once the measurements of the doped sea ice layer were performed, a sea ice core was taken from the centre of the tank, using a 3 cm diameter ice core auger. The ice core was sectioned at 2 to 5 cm intervals immediately after the coring, and placed in sealed PTFE containers. The ice core sections were left to melt at room temperature, and the bulk salinity was measured using a seawater refractometer.

2.6 Radiative-transfer modelling

The BRF of the sea ice measured in the laboratory was simulated using the PlanarRad radiative-transfer model. PlanarRad [*Hedley*, 2008], which uses the invariant imbedded method to solve the radiative-transfer equation, is the open source implementation of the Hydrolight model [*Mobley*, 1989] that computes directional radiance quantities for a homogeneous slab of media. The computation of the downwelling and upwelling radiances over the hemisphere is discretised into quadrilateral regions, hereupon referred to as "quads". Two hemispheres (one for the downwelling and one for the upwelling radiance) are divided into 217 quads each, with each quad covering 15° in azimuth and 10° in zenith, except for the quad located between 85° and 90° and the polar cap. The radiance quantities are averaged over each quad across the hemisphere. A description and representation of the discretisation into quads is found in *Mobley* [1994]. PlanarRad has previously been used to model the BRDF of different types of sea ice, with varying amounts of surface roughness [*Lamare et al.*, 2017a]. The calculations presented in this work allowed to examine the effects of the black carbon and volcanic ash deposited in the sea ice independently from the physical parameters of the sea ice, that varied during the experiments.

The parameters used as inputs to perform model calculations included the wavelength range, the illumination azimuth and zenith angles, the thickness of the sea ice, the reflectance of the underlying seawater and tank, the surface roughness, the phase function of the sea ice, the absorption coefficient of ice and impurities, and the attenuation coefficient of the sea ice. The parameters were divided into two groups: the fixed parameters obtained from empirical measurements or the literature, and parameters that were varied to reproduce the experimentally measured sea ice.
A wavelength range of the data presented in this paper was set to 400–850 nm, for the computations of black carbon in sea ice and 450–1000 nm for the volcanic ash. The wavelength ranges were chosen to match the instrument outputs in the laboratory, which were limited by the output of the illumination source. An interval of 50 nm was chosen as a compromise between computational effort and resolution. However, the input files provided in the data repository (DOI:xx) allow users to perform calculations for individual wavelength numbers in the range.
The illumination was fixed to a single quad centred over a zenith angle of 60 ° and an azimuth angle of 180 ° to match the illumination zenith angle in the laboratory. The model is rotationally invariant with the output being relative to the illumination azimuth angle, therefore an azimuth angle of 180 °

was chosen arbitrarily.
The thickness of the sea ice was calculated from the temperature profile measurements described in section 2.2. For the modelling of the clean sea ice, the lower boundary was set as the diffuse lambertian reflectance of the seawater and tank. The reflectance measurements of the seawater and the bottom of the tank were obtained from *Marks et al.* [2017b], who measured the nadir reflectance of the sea ice tank full of seawater in a diffuse illumination environment. When the layer of doped sea ice was placed on the surface of the clean sea ice, the lower boundary of the model was input as the full BRF of the clean sea ice layer with the underlying seawater and tank reflectance.
The phase function of the sea ice was calculated using the Heyey-Greenstein (HG) phase function [*Henyey and Greenstein*, 1941]. The HG phase function describes the directionality of the scattering within the sea ice, which is controlled by the asymmetry parameter, g. The asymmetry parameter was fixed to a wavelength independent value of 0.98 [*Marks and King*, 2014; *Lamare et al.*, 2016] during this study. The asymmetry parameter has been shown to be insensitive to particle shape over the visible spectrum of light *Grenfell and Warren* [1999], and was fixed for wavelengths < 1000 nm, as suggested by *Lee-Taylor and Madronich* [2002] for snow.
The surface roughness parameter, which was varied to fit the observations, was implemented in the model based on Monte Carlo statistical modelling described by [*Mobley*, 1994]. To generate rough surfaces, a surface of equilateral triangles is constructed, with the nodes of the triangles having a mean elevation of 0. The standard deviation of the elevation of the nodes, σ, controlling the random distributed elevations is used to described the roughness amount. The roughness parameter is scale invariant, as the distance between the nodes is fixed and the standard deviation of the height is relative to the horizontal distance. Once the surface is mathematically constructed a ray tracing simulation [*Mobley*, 1994] is applied to the surface, and path of the rays interacting with the surface are calculated. The resulting ratio of reflected radiance to irradiance is averaged over 2000 random surfaces, creating a statistical representative value for the surface. A refractive index of 1 was used above the surface for air, and the refractive index of ice [*Warren and Brandt*, 2008] was used for the sea ice. The surface roughness in this study was varied between $\sigma = 0.01$ and $\sigma = 0.2$, which, in the case of surface features located 5 cm apart, would be equivalent to a standard deviation of the height of the nodes equal to 0.5 mm and 1 cm respectively. The attenuation coefficient of the sea ice was calculated as the sum of the absorption coefficient of the sea ice and impurities, and the scattering coefficient of ice as:

$$\alpha(\lambda) = a_{ice}(\lambda) + a_{imp}(\lambda) + s, \tag{4}$$

with $a_{ice}(\lambda)$ the wavelength dependent absorption coefficient of ice, $a_{imp}(\lambda)$, the combined absorption coefficient of the impurities in the sea ice, and s, the wavelength independent scattering coefficient of the sea ice. The absorption coefficient of pure ice was obtained from *Warren and Brandt* [2008], and considered representative of sea ice, as described by *Light et al.* [2004]. The impurities in the sea ice were considered to be absorbing only, and the scattering from the impurities was disregarded. To model the clean ice in the sea ice tank, small quantities of black carbon were added to the ice. The absorption coefficient of the black carbon, representing contamination from the outdoor air circulating into the laboratory, was calculated using the mass absorption cross-section of black carbon with a particle diameter of 0.13 µm found in *Dang et al.* [2015]. To model the black carbon and volcanic ash placed in the surface layer of the sea ice, the absorption coefficient of the artificial black carbon and volcanic ash were used, calculated from the mass absorption cross-sections presented in section 2.3. The mass-ratio of the impurities in the sea ice, and therefore the absorption coefficient was varied to obtain the values from the measured data. The scattering coefficient of the sea ice was tuned to derived the value of the sea ice for each experiment, as small differences in the temperatures during the growth of the sea ice generated different fabrics.

For each experiment, the radiative-transfer modelling was performed in two stages. First, the clean sea ice layer was reproduced in the model, based on the parameters described above. Small amounts of black carbon, the scattering coefficient of the sea ice and the surface roughness were varied to obtain the best fit (described below) between the model and the measurements. In a second step, the calculations using PlanarRad were repeated to reproduce the BRF measurements of the sea ice with a doped surface layer. The model was split into two layers: a bottom layer of sea ice with the

same properties as the clean layer, and a top layer with a thickness of 5 cm, containing an additional known mass-ratio of the impurities placed in the sea ice (described in section 2.3). The lower layer was computed as the full BRF of the clean ice, using the best-fit parameters obtained in the first model run, with the thickness of the sea ice measured during the second part of the experiment minus the 5 cm surface layer to account for growth between the two experiments. The BRF was computed with a varying solar zenith angle over the ten zenith angle quads (9 quads + polar cap), and compiled into a single lower input parameter, used as a lower boundary condition in the model.

In order to obtain modelling results that best explain the parameters of the sea ice observed in the laboratory, the combination of the input parameters was varying in multiples steps. A first fit between the modelled and the measured data was assessed visually for the nadir BRF, using realistic values for the scattering coefficient and the black carbon absorption coefficient. Once the combination of parameters produced an approximate fit, the parameters were varied within a narrowed range of values and the goodness of fit was quantitively evaluated. For each model run with varying parameters, a reduced χ^2 test was performed for the nadir data. The reduced χ^2 test is expressed as:

$$\chi^2 = \sum_i \frac{(O_i - C_i)^2}{\sigma_i^2}, \tag{5}$$

with O_i the measured BRF values for the wavelength i, C_i the modelled BRF, and σ_i the standard deviation of the measured nadir BRF. The reduced χ^2 test, allowed different parameter combinations to be compared, and the combination yielding the lowest value was considered to be the best fit. After the best fit was obtained for the nadir BRF, the values between the modelled BRF and the measured BRF were compared across the hemisphere. In order to be able to compare the quad-averaged modelled BRF and the measured BRF sampled at discrete points over the hemisphere, the measured BRF values were interpolated based on a natural neighbour triangulation method [*Okabe et al.*, 1992] and averaged over the same discretisation of the hemisphere as PlanarRad. The surface roughness, which has been shown to strongly affect the BRF distribution of sea ice [*Lamare et al.*, 2017a] was varied, and the angular distribution was assessed visually. When the surface roughness parameter that provided the best fit of the BRF was found, the combination of parameters was iteratively assessed using the reduced χ^2 test at nadir.

3 Results

The results are presented in three sections: the measurements of the artificial sea ice in the laboratory are presented, the radiative-transfer model outputs are compared to the experimental data, and the modelled effects of impurities on the BRF of sea ice are shown.

3.1 Measured BRF of artificial sea ice

The average nadir spectral BRF of the clean sea ice measured in the laboratory is presented in figure 3 for each experiment. Each experiment was conducted from open seawater, and therefore represents a new sea ice. The nadir BRF spectra of the sea ice have the largest values at shorter wavelengths , with a maximum value between 400 and 550 nm, and decrease at longer wavelengths. A secondary maxima is observed between 840 and 850 nm. The spectral dependence of the nadir BRF observed in the laboratory is similar to natural sea ice [*Gerland et al.*, 1999], with a decreasing BRF owing to the increased absorption of the ice at higher wavelengths. Over the different experiments, the thickness of the sea ice grown in the laboratory was not constant, owing to differences in the temperature of the laboratory and the number of days the ice was grown. In figure 3, the nadir BRF spectra are not linear as a function of sea ice thickness, suggesting different ice optical properties for the different experiments. Owing to the differences in the fabric of the sea ice, the measurements were not directly comparable, requiring the modelling of the sea ice to characterise the optical properties of the sea ice, and separate the effects of impurities in the sea ice from the differences in thickness and structure.Furthermore, larger changes are observed between 400 and 800 nm, whereas the nadir BRF spectra remain within the uncertainties above 800 nm, except for the exper-

iment 6, where the clean ice nadir is larger by a factor of 1.5 than the average of the other experiments.

Figure 4 shows the polar plots for the BRF of a clean sea ice layer with a thickness of 33.5 cm (experiment 1) at 500, 600, 700, and 800 nm. The figure shows the angular pattern of the BRF. The BRF of the sea ice is homogenous across a large part of the hemisphere, with the exception of a forward scattering peak located between viewing zenith angles of 60 and 75 °, and is symmetrically distributed across the solar principle plane between azimuth angles of 345 and 15 °. Similarly to the forward scattering peak, the BRF is almost symmetrical along the solar principle plane across the entire hemisphere. The values of BRF outside of the forward scattering peak decrease consistently with the nadir BRF as the wavelength increases. The values of the BRF for the forward scattering also decrease as a function of wavelength, to a lesser extent than at nadir however. Indeed, the nadir BRF decreases by 240% at nadir, whereas the maxima in the hemisphere decreases by 20 % over the wavelength range 500–800 nm. A similar trend was observed for the HDRF of bare young sea ice measured in an outdoor sea ice laboratory [*Lamare et al.*, 2017b]. The difference in wavelength dependance between the quasi-isotropic part of the hemisphere and the forward scattering peak observed for the experiment 1 is representative for all the experiments presented in the present study.

The anisotropy of the BRF was compared for the 6 different clean sea ice experiments. The ANIF of the clean sea ice for each experiment is shown in figure 5, for a wavelength of 550 nm. Owing to the differences in the nadir values of BRF between the experiments, the ANIF was used to intercompare the different sea ice types, whilst removing the spectral differences. The anisotropy of the sea ice is distributed in a similar pattern across the different experiments. However, the intensity and the size of the forward scattering peak on the hemisphere varied between the measurements. The intensity of the forward scattering peak was a factor of 7.98 higher than nadir for the sea ice grown during the experiment 2 and 4.8 during the experiment 3. A noticeable difference is observed between the anisotropy of the sea ice measured during experiment n 6 and the anisotropy of the sea ice measured during the other experiments. The nadir BRF of the sea ice during experiment 6, shown in figure 3 is equally higher than for the other experiments. Excessive surface roughness as well as significant slush were observed during the experiment, due to a functioning issue with the refrigeration system. Therefore, the clean ice layer was only fitted at nadir when compared to the modelling results.

Figure 6 presents the anisotropy factor for each experiment after the surface layer bearing impurities was formed on the top of the clean sea ice. The results are not directly comparable to each other or to the clean sea ice measurements owing to differences in the sea ice fabric and surface roughness. However the figure underlines general trends, which may be indicative of the impurities in the sea ice, and which are confirmed by the radiative-transfer modelling. Figure 6 shows that intensity of the anisotropy of the doped sea ice is generally lower in the forward scattering peak for the doped sea ice than for the clean sea ice. The black carbon experiments exhibit a similar pattern in anisotropy compared to the clean sea ice, whereas for the larger mass-ratios of volcanic ash (figure 5 e and f; and figure 6 e and f) the forward scattering peak appears wider across the forward scattering part of the hemisphere. However, there is no significant difference in the intensity of the ANIF for a lower mass-ratio of volcanic ash.

The uncertainties of the measurements performed in the sea ice laboratory are assessed in figures 7, 8, and 9. Based on the assumption that the BRF of sea ice is symmetrical along the solar principal plane as it has been for snow [e.g. *Hudson et al.*, 2006b; *Dumont et al.*, 2010], and as predicted by the theory used in the radiative-transfer modelling, the differences in the measured BRF for symmetrical points on each side of the solar principal plane are considered to be due to uncertainties linked to the measurements or to surface roughness. Indeed, the sea ice modelled with the radiative-transfer code Planarrad to fit the measurements is computed with randomly orientated surface roughness, maintaining symmetry on each side of the solar principal plane. However, the surface roughness elements present in the artificial sea ice may have a dominant orientation, causing asymmetry across the principal plane, and therefore introducing discrepancies between the modelled

and the measured BRF.

Figure 7 shows BRF values for symmetrical points on each side the solar principal plane at 4 different wavelengths for the BRF measured during the experiment 1 for clean sea ice and doped sea ice. A linear fit was applied to the measurement pairs for each wavelength and the coefficient of determination, r^2 was calculated. Figure 7a (clean sea ice) shows a similar r^2 value for the 4 different wavelengths, indicating the absence of a wavelength-dependent effect in the BRF measurements. Furthermore, the r^2 value is high for the clean sea ice measurement, with values between 0.96 and 0.979, indicating a good agreement between the two halves of the hemisphere. The r^2 values for the BRF of doped sea ice measured at 4 wavelengths, shown in figure 7b is lower than for clean ice with r^2 values between 0.818 and 0.835. Nevertheless, the r^2 values are similar over the wavelength range presented, confirming once again the absence of wavelength-dependent effects.

The measured BRF values for symmetrical points on each side of the solar principal plane for each experiment are shown in figure 8 for a wavelength $\lambda = 550$ nm. For each experiment the values measured for the clean sea ice and the doped layer are presented. Overall, the two halves of the hemisphere are in good agreement, with the lowest r^2 value being 0.807 for the experiment 1 with doped sea ice, and the highest r^2 value being 0.986 for the experiment 2 with clean ice. A majority of the measurement points are located close to the identity line, and the largest mismatches between symmetrical points are for the larger BRF values, indicating larger uncertainties around the forward scattering peak, as shown below. In most cases, the linear fit of the BRF measurements is close to the identity line, and the deviations from this line can be used as an indicator of the uncertainties of the BRF measurements.

To better assess the spatial variability of the measurements across the hemisphere, the averaged symmetrical points on each side of the solar principal plane are shown in figure 9, as well as the ± 1 standard deviation. The data are represented as polar plots for each experiment with clean and doped sea ice, with the upper part of the hemisphere of the polar plot showing the standard deviation of the mean plotted in the lower half of the hemisphere. Confirming the results of figure 8, the main differences between the two halves of the hemisphere are mainly located towards the forward scattering peak. The higher standard deviations of the forward scattering peak may be explained by the rapid change in intensity around the forward scattering peak, which are exacerbated by small errors in the pointing accuracy of the laboratory goniometer, thus generating larger errors than for the quasi-isotropic part of the hemisphere. Moreover *Lamare et al.* [2017a] have shown that the effects of surface roughness are insignificant in the quasi-lambertian part of the hemisphere. Therefore, in the case of oriented surface roughness, the effects would only be present in the forward scattering peak. The polar plot of the standard deviation also highlights a number of spatial variations caused by the interpolation of the measured points across the hemisphere, clearly distinguishable as circular shapes outside the forward scattering peak. The level of confidence in the measurements, particularly when performing a comparison with the modelled quantities, can be assessed using figure 9, which highlights experiments with larger uncertainties (for example experiment 1b with a doped layer and experiment 5a with clean sea ice).

Owing to the variability in the measurements of the sea ice discussed above, the measurements of the artificial sea ice doped with impurities alone are not sufficient to characterise the effects of the particulates on the BRF of sea ice. To elucidate the effects of the impurities over the variations in the clean sea ice structure requires modelling. Therefore, radiative-transfer modelling was employed to reproduce the measurements, based on the physical properties of the sea ice, to: 1) determine the optical properties of the sea ice grown in the laboratory, and 2) investigate the effects of black carbon and mineral aerosol deposits on the angular distribution of the reflected radiance of sea ice.

3.2 Comparison with modelling results

In order to reproduce the BRF of the observed sea ice, values of the sea ice scattering coefficient and the absorption cross-section of black carbon were varied until a close visual fit was observed. Once a close fit was obtained, the reduced χ^2 was calculated for varying parameters in small increments, until the lowest value was found. The results presented in the following section were considered to be the best-fit for the measurements. For each measurement, the nadir BRF, the BRF across the solar principle plane and the BRF across the hemisphere are presented and compared to the model results for the clean sea ice layer and the doped layer. A summary of the optical properties of the sea ice and the impurity mass-ratios are shown in table 1.

For all the experiments, the BRF of the clean sea ice at nadir shows a good agreement between the measured and the modelled data across the wavelength range, except at wavelengths between 800 and 850 nm where for higher wavelengths, the model consistently underestimates the BRF (figures 10a, 11a, 12a, 13a, and 14a). All the calculations of the BRF at nadir below 800 nm, lie within the uncertainty limits of the measurements, except for the clean ice measurements shown in figure 12, where the model over-estimates the BRF at 550 and 600 nm. The values of the scattering coefficient, shown in table 1 varied between 200 and 380 m^{-1} which is equivalent to a scattering cross-section of 0.22 to 0.41 m^2 kg^{-1}. A comparison between the measured and modelled nadir BRF for experiment 6 is shown in figure 14. As described in section 2, technical difficulties with the refrigeration system entrained a different ice fabric during the measurements of the clean sea ice. To model the rough surface with a visually whiter soft surface, a scattering coefficient of 600 m^{-1} was necessary. Therefore, the reproduced BRF of the sea ice was not used as a lower boundary condition for the doped layer, as it was not representative of the ice during the second part of the experiment. Instead, the lower boundary was fitted iteratively, with a higher uncertainty in the results for experiment 6. The scattering cross-section values are similar to the values calculated by *Marks et al.* [2017b], using a different radiative-transfer model. Small amounts of black carbon were added to the model to account for particles being transported on the surface of the sea ice by the air pulled through the cooling system from outside of the sea ice laboratory. A mass-ratio of 30 ng g^{-1} of black carbon was found necessary to reproduce the measurements of the clean sea ice across the experiments, except for the sea ice measured during experiment 5, where the best fit was explained by 10 ng g^{-1} of black carbon.
The nadir BRF of the sea ice with a 5 cm surface layer of doped sea ice containing 68.6 ng g^{-1} of black carbon and 2202.6 ng g^{-1} of volcanic ash are shown in figure 10a and 13a respectively. For the sea ice with a doped surface layer, the model calculations were performed with a mass-ratio of 68 ng g^{-1} of black carbon and 2202.6 ng g^{-1} of volcanic ash. The modelled BRF of the clean ice layer fitting the clean ice before the surface layer was added as a lower boundary condition. The scattering coefficient of the 5 cm surface layer sea ice was then varied to fit the measurements. The model calculations provide a good fit of the measured spectra for the volcanic ash, with BRF values below the uncertainty limits of the measurements at 850 nm only. The modelled BRF of the layer of black carbon on the sea ice however, underestimates the measurements at 850 nm and over-estimates the BRF at 400 and 450 nm. In both cases, the surface layer of sea ice was shown to be more scattering than the clean sea ice, with a calculated scattering coefficient of 600 m^{-1} versus 330 m^{-1} for the clean ice in experiment 1, and 380 m^{-1} for the clean ice in experiment 5. The sea ice core taken after the measurements with a doped surface layer revealed a 5 cm top section of granular sea ice, that was less translucent, thus more scattering than the columnar sea ice observed below, confirming the model calculations.

The BRF plotted along the solar principal plane in figures 10b, 11b, 12b, 13b, and 14b, at a wavelength of 550 nm highlights a strong scattering peak in the forward direction for the higher viewing zenith angles. The modelled BRF is in good agreement with the measurements across the quasi-lambertian part of the solar principle plane. However, the model consistently over-estimates the BRF values in the forward scattering peak. Although the BRF of the clean sea ice is accurately reproduced by the model for the experiment 5, shown in figure 13, and the BRF values for viewing

zenith angles between -70 and 40° are similar for the both the model output and the measurements, the BRF of the forward scattering peak for the sea ice with a surface layer containing a mass-ratio of 2202.6 ng g^{-1} of volcanic ash is not well reproduced by the model. The modelling results are approximately a factor of 2 larger than the measurements. The discrepancy between the model and the measurements is highlighted in figure 13c, where the measured forward scattering peak is lower in intensity and diffused compared to the model. The BRF of the modelled layer of sea ice containing 68.6 ng g^{-1} of black carbon, provides a better fit of the observed data, with the quad located over a viewing zenith angle of 70° being 25 % higher than the observation.

The BRF pattern across the hemisphere is presented for each experiment in figures 10c, 11c, 12c, 13c, and 14c. The modelled BRF is shown over the entire hemisphere, whereas the number of BRF acquisitions in the lab were limited, as discussed in section 2.4 and 2.5. The outline of the measured BRF was placed on the modelled BRF polar plots to facilitate comparisons. Overall, the BRF pattern for sea ice is characterised by a quasi-lambertian response across the hemisphere and a forward scattering peak, as described previously. For all the modelling results presented in this study, a surface roughness of $\sigma = 0.1$ was used to describe the sea ice surface roughness. As shown by [*Lamare et al.*, 2017a], the surface roughness is a determining parameter in the width and position of the forward scattering peak of the BRF of sea ice.

3.3 Effects of black carbon and mineral aerosol deposits on the BRF of sea ice

To investigate the effects of black carbon and mineral aerosol deposits on the BRF of sea ice, the individual effects were considered separately from the other parameters affecting the BRF. To do so, the properties of the sea ice were fixed in the model, and the mass-ratios of black carbon and volcanic ash were varied.
Figure 15 presents the calculated values of BRF for a 50 cm sea ice layer, with an underlying diffuse reflectance of 0.1 (representing optically thick seawater), and a scattering coefficient of 300 m^{-1}. The black carbon absorption coefficient calculated for the particles placed in the artificial sea ice with Mie theory was used. The absorption coefficient of the black carbon is almost flat across the visible wavelength spectrum, and therefore the spectral dependence of the reduction in the BRF of sea ice with an increasing mass-loading of black carbon is governed by the absorption of the sea ice. The BRF computations using PlanarRad show that the absorption by black carbon in the sea ice is wavelength dependent, reducing the BRF at shorter wavelengths (where the signal is dominated by the sea ice scattering) more than at larger wavelengths (where the ice absorption dominates the signal). In the case of black carbon with an absorption cross-section of 2.97 m^2g^{-1} at 550 nm, 10 ng g^{-1} of black carbon evenly distributed in the sea ice reduce the BRF of a 50 cm thick multi-year sea ice by 4 % at 500 nm and 2.5 % at 800 nm. A mass-ratio of 50 ng g^{-1} of black carbon reduces the BRF by 18% at 500 nm and 11% at 800 nm. Mass-ratios above 100 ng g^{-1} are rarely found in the arctic, however mass-ratios up to 5000 ng g^{-1} are presented for completeness.
As shown in figure 16, the nadir BRF of sea ice is less sensitive to volcanic ash mass-loadings, as it has previously been shown in the literature [*Lamare et al.*, 2016]. The spectral shape of the absorption coefficient of the volcanic ash particles is more pronounced than the black carbon, with an enhanced absorption at shorter wavelengths. Therefore, even at larger mass-loadings, the nadir BRF of sea ice is negligeably reduced beyond 800 nm, compared to shorter wavelengths. In comparison to the black carbon, 10 ng g^{-1} of volcanic ash in the sea ice reduce the BRF of a 50 cm thick multi-year sea ice by 0.13 % at 500 nm and 0% at 800 nm. A mass-ratio of 500 ng g^{-1} of volcanic ash, which may be found after a punctual deposition event, reduces the BRF by 12% at 500 nm and 0.91% at 800 nm.

In figure 17, polar plots of the BRF of the sea ice described above, with varying mass-ratios of black carbon and volcanic ash are presented. The change in the nadir BRF for increasing amounts of impurities, shown in figures 15 and 16 is representative of the change in the BRF across the quasi-lambertian part of the hemisphere. However, the reduction in BRF for the forward scattering peak is lesser, with an increase in the anisotropy for higher mass-loadings of particulates. In contrast

to the measurements of the BRF of the artificial sea ice, the increase in mass-loading of impurities does not affect the shape of the forward scattering peak, which remains spread over the same number of quads regardless of the mass loading.

4 Discussion

In the following section the effects of impurities on the BRF of sea ice are discussed, and the limitations of the study are assessed.

4.1 The effect of impurities on the BRF of sea ice

4.1.1 Black carbon

The effects of black carbon aerosol deposits on the nadir reflectance of sea ice have been well characterised, showing a strong reduction in reflectance across the visible wavelengths as the black carbon mass-loading increases. The light absorption by the black carbon is more pronounced in the visible than the infrared wavelengths owing to the strong absorption of sea ice in the infrared. The results presented in this paper show a similar trend in the BRF at nadir. However, the reduction in BRF induced by the black carbon in the sea ice is not homogenous across the viewing angles in the hemisphere. The directional dependence of the BRF of sea ice to black carbon is much larger outside of the forward scattering peak than for the forward scattering peak.

In order to reproduce the BRF of the clean sea ice with the radiative-transfer model, small quantities of black carbon in the sea ice were necessary. The model calculations estimated between 10 and 30 ng g^{-1} of black carbon to be present in the clean sea ice. The authors consider the mass-loading to be realistic, as the sea ice laboratory is located near a car parking area, close to an international airport and major traffic routes.

The Monarch 120 black carbon sample used in the laboratory to mimic atmospherically deposited black carbon, is a gas soot produced by the combustion of hydrocarbons [*Muckenhuber and Grothe*, 2006]. Monarch 120 has previously been used in laboratory studies as an experimental analog for atmospheric black carbon / soot to inter-compare methods for the measurement of black carbon [*Hitzenberger et al.*, 1999; *Sadezky et al.*, 2005], and to study the radiative effects of black carbon / soot in snow or sea ice [*Brandt et al.*, 2011; *Zender et al.*, 2009; *Marks et al.*, 2017b]. The commercial soot was used as an equivalent of the discontinued Monarch 71 from Cabot Corporation, for which the optical properties were characterised [*Clarke et al.*, 1967; *Clarke and Noone*, 1985], and used by *Grenfell et al.* [2011] to calibrate integrating-sandwich spectrophotometer measurements of impurities in snow and ice. In this study, the mass absorption coefficient of Monarch 120 was considered to be within the range of black carbon values typically found in Arctic sea ice or snow. The calculated MAC value of the samples used was found to be similar to the values of the MAC of black carbon reported by *Dang et al.* [2015], as described in section 2.3. However, the black carbon deposits found in Arctic snow and sea ice originate from numerous sources and vary in composition. The black carbon deposited on the snow or sea ice surface is removed from the atmosphere by dry or wet deposition, the latter being the dominant process in the Arctic, totaling over 90% of the overall deposition [*Dou and Xiao*, 2016]. The deposited carbonaceous aerosols vary in provenance and therefore are made up of short range and long range transported particles. Today, uncertainties still remain on the exact provenance of the black carbon deposited in the Arctic. Early studies designated anthropogenic sources as the main contributor to black carbon transport to high latitudes, but later biomass burning was identified to be a significant contribution [*Hegg et al.*, 2009]. Based on the Goddart general circulation model, *Koch and Hansen* [2005b] suggested that 20% of the Arctic soot found in the Arctic is from industrial and biofuel emissions from south Asia. However, *Shindell et al.* [2008] showed that the aerosols found at surface level in the Arctic are mainly from European emissions, whereas East Asian emissions are found higher in altitude. *Stohl et al.* [2007] showed that high concentrations of carbonaceous material, which was shown to be a combination of elemental carbon and organic carbon, were found in the European Arctic, following emissions

from agricultural fires in the Baltic countries in 2006. Indeed, fires, including agricultural fires or forest fires have been shown to be a major source of black carbon [*Lavoue et al.*, 2000; *Paris et al.*, 2009] present in the Arctic, which has a strong radiative impact on the climate through deposition on snow [*Flanner et al.*, 2007; *Paris et al.*, 2009]. A modelling study of particule trajectories in the atmosphere proposed by *Stohl* [2006], indicates that fire may be the primary source of black carbon transport to the Arctic in the summer. *Popovicheva et al.* [2017] argue that approximately 50% of the black carbon found north of 60°N originates from flaring of gas associated with oil production. Black carbon quantities measured in studies often refer to black carbon as a generic term black carbon equivalent matter, owing to the differences in the size distribution, shape, coating and therefore the optical properties of the particles, which depend on the source and the distance from it. As they are first emitted, carbonaceous particles are formed of agglomerates of primary spherules [*Bond and Bergstrom*, 2006]. As the particles age or are wetted, the particles collapse to form aggregates [*Bond and Bergstrom*, 2006, and references therein] which changes the absorption and scattering values of the particles. Owing to the variability in size and optical properties of black carbon found in the atmosphere, *Bond and Bergstrom* [2006] suggest that the mass absorption coefficient of black carbon may vary by a factor of 4. The value of the mass absorption coefficient of the Monarch 120 used in the present study was 2.78 m^2g^-1 at a wavelength λ = 550 nm, which is approximately a factor 2.5 lower than the value of 7.5 m^2g^{-1} recommended by *Bond and Bergstrom* [2006] and *Flanner et al.* [2007]. However, the values of the mass absorption coefficient of black carbon in global models range from 2.3 to 18 m^2g^{-1} [*Bond et al.*, 2013, and references therein], meaning that the experimental black carbon used in this study is on the lower end of the the range used by the modelling community. Although the mass absorption coefficient of the black carbon used in the laboratory was lower than typical values found in the Arctic, the experimental black carbon allowed to validate the radiative-transfer calculations, and provide insight on the effects of black carbon on the BRF of sea ice. For more specific applications, such as fitting field observations or parameterising general circulation models, the authors recommend running the model with black carbon values adapted to each situation.

4.1.2 Volcanic ash / mineral aerosols

The modelling results of the effects of volcanic ash on the BRF of sea ice highlight the difference in the spectral response in comparison to black carbon at nadir. The volcanic ash exhibits an enhanced absorption at shorter wavelengths, and is less absorbing at larger wavelengths. Indeed, for mass-ratios between 1 and 1000 ng g^{-1}, the decrease in the BRF of doped sea ice is less than 0.03 above 650 nm, whereas at 450 nm, the reduction in BRF reaches 0.1. The characteristic signal from the absorption cross-section of minearal dust is clearly visible in figure 16 [*Lamare et al.*, 2016], contrasting with the flat response of black carbon. However, the modelled BRF of the entire hemisphere for sea ice containing black carbon or volcanic ash (figure 17) have a similar distribution across the hemisphere. The anisotropy of the BRF in response to mass-loadings of black carbon and mass-loadings of volcanic ash is similar, although for sea ice doped with volcanic ash, a mass-ratio of a factor of 10 higher is necessary to obtain similar BRF values to sea ice doped with black carbon. On the other hand, the measurements of the BRF of the laboratory sea ice doped with volcanic ash deposits in the surface layer suggest that the forward scattering peak is subdued and spread out in comparison to the BRF of clean sea ice and sea ice doped with black carbon. The observed discrepancy between the measurements and the modelling may be explained by a change in the fabric of the sea ice between experiments owing to the change in environmental conditions caused by a reduced heat flux from the refrigerator plant [*Marks et al.*, 2017b]. This explanation is supported by figure 5, which shows a weaker forward scattering maxima for the clean sea ice in experiment 6.

The sample of volcanic ash collected close to the Eyjafjallajökull volcano in Iceland was ground in a vibrating mill to achieve a typical aerosol size distribution of long-range transported ash, and an average particle diameter of 0.83 µm was obtained for the samples used in this study. The value is representative of fine particles found in long-range transported aerosols, and fits within the values measured in the literature across polar sites, inventoried by *Zdanowicz et al.* [1998]. However, the mean particle size used in the laboratory was approximately a factor of two smaller than dust samples measured on the Penny Ice Cap by *Zdanowicz et al.* [1998], which may be explained by

rapid transport of Saharan dust despite the distance, and highlighting the variability of mineral aerosol deposit sizes found in the Arctic. Obtaining representative values of the optical properties of volcanic ash is particularly difficult, as the variability in the size distribution of the particles and the mineral composition lead to a wide range of optical properties. Indeed, measurements of volcanic ash particles from the Eyjafjallajökull eruption in 2010 found in the literature show an important variability in the size distribution and optical properties of the ash: *Johnson et al.* [2012] measured aerosols approximately 1200 km from the source from the FAAM aircraft, with particles distributed around 0.1–0.6 µm and 0.6–35µm and extinction coefficient values of 0.45–1.06 m^2g^{-1} at 550 nm; *Turnbull et al.* [2012] performed measurements over the southern North Sea, showing a wide range of ash concentrations with diameters distributed around 0.2 µm for the fine mode and 4 µm for the coarse mode, and extinction coefficients between 0.6 and 0.8 m^2g^{-1} at 550 nm. *Newman et al.* [2012], based on the measurements performed by *Turnbull et al.* [2012] calculated a mass absorption coefficient of 0.035 m^2g^{-1} at 550 nm for Eyjafjallajökull ash, which is approximately three times less absorbing than the volcanic ash prepared in the laboratory presented in this study, that has a mass absorption coefficient of 0.11 m^2g^{-1} at 550 nm. Furthermore, as detailed in *Lamare et al.* [2016] the shape of the mineral particles has an effect on the absorption and scattering properties of the particles, impacting the response of the scattered light from the doped sea ice. However, the modelling study performed by *Newman et al.* [2012] showed that for Eyjafjallajökull ash, the optical properties are not particularly sensitive to assumptions of irregular or spherical particles. Although the variability of the volcanic ash optical properties is important, the mass absorption coefficient values of the samples used in this study are considered to be within the range of values of mineral aerosols deposited in the Arctic, and are in agreement with the values suggested by *Dang et al.* [2015]. Furthermore, as shown in *Lamare et al.* [2016] the change in the values of absorption cross-section of the mineral aerosol deposits only has little effect on the albedo for most sea ice types, with the differences in the optical properties of the sea ice types introducing larger changes than the differences in the optical properties of the mineral ash / dust. Thus, the Eyjafjallajökull ash sample was considered to be an acceptable proxy for mineral aerosol deposits. Nevertheless, as suggested for black carbon, the radiative-transfer model can be run with different mass absorption coefficient values, and therefore the authors recommend the input of specific mineral aerosol mass absorption coefficient data for specific applications of the model.

4.2 Model uncertainties

The calculations of the absorption of the impurities in the sea ice was based on Mie calculations. The size distributions of the black carbon and volcanic ash were obtained by observing trapped particles on a filter in an SEM. The Mie calculations relied on the assumption that the particles were spheres. The results have show a better agreement between the model and the measurements for the black carbon particle than for the volcanic ash. Although, the volcanic ash particles were determined to be spherical-like from the SEM image analysis, the discrepancy between the shape of the forward scattering peak in the model and the measurements for the experiments with a mass-loading of volcanic ash suggests that the particle shape affects the forward scattering peak. However, although the absorption cross-section may be adjusted for basic shapes [*Bohren and Huffman*, 1983], previous studies have shown that the non sphericity of particles is complex to model [*Nousiainen*, 2009].

The black carbon modelled in the sea ice to obtain a fit of the clean sea ice measurements was assumed to be evenly distributed throughout the sea ice. Owing to the air circulation, it is more likely that the particles were deposited on the surface of the sea ice. However, *Lamare et al.* [2016] have shown that layer of impurities in the sea ice have a similar effect on the albedo of snow than if the impurities are evenly distributed throughout the pack. Here, a similar assumption was made. Furthermore, *Marks et al.* [2017b] discuss the possibility of the black carbon particle being transported throughout the sea ice layer, via the brine channels, which mitigates further the effects of the layering of the black carbon.

During the experiments, roughness features were observed on the surface of the sea ice. The surface roughness was modelled in PlanarRad, based on a random mathematical surface realisation. The surface roughness is used as a tuning parameter in the model to fit the observations, controlling the intensity and width of the forward scattering peak in the hemisphere. A quantitative assessment of the surface roughness during the measurements was not performed. Therefore, the determination of the role of the surface roughness versus the volcanic ash on the diffusion of the forward scattering peak of the BRF for volcanic ash loadings observed during the measurements is complex. Further investigations of volcanic ash particles in sea ice grown with a smooth surface are recommended.

To enable the comparison between the measurements of the BRF across the hemisphere and the modelling results, the BRF was averaged over the model quad discretisation of the hemisphere. The interpolated measurements over discrete points on the hemisphere underline rapid changes in intensities around the forward scattering peak. By averaging over quadrilateral regions of $10 \times 15°$, a loss in the definition of the forward scattering peak is observed. Furthermore, the discrete measurement points across the hemisphere were interpolated, then quad averaged. The averaging of the interpolated data may introduce errors, particularly for quad which have a limited number of measurement points. Although, the model is able to characterise the overall pattern of the angular distribution of reflectance, a better resolution would provide more accurate data at higher zenith angles. However, for the part of the hemisphere outside the forward scattering peak direction, the lack of resolution of the model is not critical, owing to the simile-lambertian response of the sea ice. Furthermore, the discretisation was constrained by the computational resources available during this study, and the resolution can be adjusted in the model parameter files.

When fitting the observed BRF of the sea ice using the radiative-transfer model, the thickness of the sea ice was used as a constraining parameter. The thickness of the sea ice was determined using a thermocouple array attached to a PTFE rod placed in the sea ice tank, by observing the discontinuity of the temperature profile. Owing to the size of the sea ice tank, measurements of the sea ice coring were not possible, as the core hole would have affected the multiple scattering within the sea ice, which in turn would have affected the BRF measurements. The thermocouples were placed every 4 cm in the upper part of the tank, which was a compromise between the interval and the coverage over the depth of the tank. Furthermore, the thermocouple rod may have introduced small errors in the measurements, with ice growth on the rod. However, the profiles were compared to the lengths of the ice cores drilled after each experiment, and the temperature profiles were found to be consistent with the sea ice thickness in the centre of the tank. Small changes in the thickness of the sea ice which may have occurred, affect the spectral BRF in a similar manner to a changing scattering coefficient. The effect of small changes in thickness on the scattering coefficient of the ice will be investigated in the future.

5 Conclusions

The measurements of the BRF of artificial sea ice doped with black carbon and volcanic ash were performed in a sea ice laboratory, using a goniometer. The sea ice exhibited similar characteristics to natural sea ice, with a strong forward scattering maxima, located around the solar principle plane at viewing zenith angles similar to the illumination zenith angles. The optical properties of the sea ice were calculated by comparing the results from a radiative-transfer model to the measurements. The model study used the physical properties of the sea ice, combined with knowledge of the optical properties of the black carbon and volcanic ash particles to perform the BRF calculations. The scattering coefficients derived were in agreement with previous laboratory measurements [*Marks et al.*, 2017b] and representative of multi-year sea ice. For all the comparisons, the model over-estimated the BRF in the forward scattering peak, with much larger absolute differences in the forward scattering peak than across the rest of the hemisphere. Furthermore, the model provides a better representation of the BRF of sea ice containing black carbon particles than the BRF of sea ice with volcanic ash deposits. The angular distribution of the errors between the modelled and measured BRF of the sea ice containing volcanic ash particles suggests that the assumption of spherical particles in the Mie

calculations for the volcanic ash do not hold true. Further work investigating the effects of shaped particles on the BRF of sea ice is necessary.
The results improve the radiative-transfer modelling of the directional reflectance of sea ice, by validating the modelling results with empirical measurements. The comparison between the laboratory measurements and the modelling showed that the radiative-transfer model may be used to derive the optical properties of sea ice. The model workflow allows for the combination with an independent atmospheric radiative-transfer model, providing a useful tool for the remote sensing community interested in sea ice.

Acknowledgments
MDK and MLL thank NERC for support under Grant NE/K000770X/1 and NERC FSF (555.0608). The authors wish to thank C. Manning for providing the volcanic ash samples used in this study.

References

Abdou, W. A., M. C. Helmlinger, J. E. Conel, C. J. Bruegge, S. H. Pilorz, J. V. Martonchik, and B. J. Gaitley (2001), Ground measurements of surface BRF and HDRF using PARABOLA III, *Journal of Geophysical . . .* , *106*(D11), 11,967–11,976.

Abràmoff, M. D., P. J. Magalhães, and S. J. Ram (2004), Image processing with imagej, *Biophotonics international*, *11*(7), 36–42.

Aoki, T., T. Aoki, M. Fukabori, A. Hachikubo, Y. Tachibana, and F. Nishio (2000), Effects of snow physical parameters on spectral albedo and bidirectional reflectance of snow surface, *Journal of Geophysical Research: Atmospheres*, *105*(D8), 10,219–10,236.

Atkinson, M. J., and C. Bingman (1997), Elemental composition of commercial seasalts, *J Aquaric Aquat Sci*.

Ball, C. P., A. A. Marks, P. D. Green, A. MacArthur, M. Maturilli, N. P. Fox, and M. D. King (2015), Hemispherical-Directional Reflectance (HDRF) of Windblown Snow-Covered Arctic Tundra at Large Solar Zenith Angles, *IEEE Transactions on Geoscience and Remote Sensing*, *53*(10), 5377–5387.

Barnsley, M. J., J. J. Settle, M. A. Cutter, D. R. Lobb, and F. Teston (2004), The proba/chris mission: a low-cost smallsat for hyperspectral multiangle observations of the earth surface and atmosphere, *IEEE Transactions on Geoscience and Remote Sensing*, *42*(7), 1512–1520, doi:10.1109/TGRS.2004.827260.

Bohren, C. F., and D. R. Huffman (1983), *Absorption and scattering of light by small particles*.

Bond, T. C., and R. W. Bergstrom (2006), Light absorption by carbonaceous particles: An investigative review, *Aerosol Science and Technology*, *40*(1), 27–67, doi:10.1080/02786820500421521.

Bond, T. C., S. J. Doherty, D. W. Fahey, P. M. Forster, T. Berntsen, B. J. DeAngelo, M. G. Flanner, S. Ghan, B. KÃd̄rcher, D. Koch, S. Kinne, Y. Kondo, P. K. Quinn, M. C. Sarofim, M. G. Schultz, M. Schulz, C. Venkataraman, H. Zhang, S. Zhang, N. Bellouin, S. K. Guttikunda, P. K. Hopke, M. Z. Jacobson, J. W. Kaiser, Z. Klimont, U. Lohmann, J. P. Schwarz, D. Shindell, T. Storelvmo, S. G. Warren, and C. S. Zender (2013), Bounding the role of black carbon in the climate system: A scientific assessment, *Journal of Geophysical Research: Atmospheres*, *118*(11), 5380–5552, doi:10.1002/jgrd.50171.

Bourgeois, C. S., P. Calanca, and A. Ohmura (2006), A field study of the hemispherical directional reflectance factor and spectral albedo of dry snow, *Journal of Geophysical Research: Oceans*, *111*(D20), D20,108.

Brandt, R. E., S. G. Warren, and A. D. Clarke (2011), A controlled snowmaking experiment testing the relation between black carbon content and reduction of snow albedo, *Journal of Geophysical Research: Atmospheres*, *116*(D8), n/a–n/a, doi:10.1029/2010JD015330, d08109.

Buckley, R. G., and H. J. Trodahl (1987), Scattering and absorption of visible light by sea ice, *Nature*, *326*(6116), 867–869.

Cabot, F., and G. Dedieu (1997), Surface albedo from space: Coupling bidirectional models and remotely sensed measurements, *Journal of Geophysical Research: Atmospheres*, *102*(D16), 19,645–

19,663, doi:10.1029/97JD00085.

Clarke, A. D., and K. J. Noone (1985), Soot in the arctic snowpack: a cause for perturbations in radiative transfer, *Atmospheric Environment (1967)*, *19*(12), 2045 – 2053, doi:http://dx.doi.org/10.1016/0004-6981(85)90113-1.

Clarke, A. D., K. J. Noone, J. Heintzenberg, S. G. Warren, and D. S. Covert (1967), Aerosol light absorption measurement techniques: Analysis and intercomparisons, *Atmospheric Environment (1967)*, *21*(6), 1455 – 1465, doi:http://dx.doi.org/10.1016/0004-6981(67)90093-5.

Comiso, J. C. (2006), Abrupt decline in the arctic winter sea ice cover, *Geophysical Research Letters*, *33*(18), n/a–n/a, doi:10.1029/2006GL027341, l18504.

Curry, J. A., J. L. Schramm, and E. E. Ebert (1995), Sea ice-albedo climate feedback mechanism, *Journal of Climate*, *8*(2), 240–247.

Curry, J. A., J. L. Schramm, D. K. Perovich, and J. O. Pinto (2001), Applications of sheba/fire data to evaluation of snow/ice albedo parameterizations, *Journal of Geophysical Research: Atmospheres*, *106*(D14), 15,345–15,355, doi:10.1029/2000JD900311.

Dang, C., R. E. Brandt, and S. G. Warren (2015), Parameterizations for narrowband and broadband albedo of pure snow and snow containing mineral dust and black carbon, *Journal of Geophysical Research Atmospheres*, *120*(11), 5446–5468, doi:10.1002/2014JD022646.

Derimian, Y., O. Dubovik, D. Tanre, P. Goloub, T. Lapyonok, and A. Mortier (2012), Optical properties and radiative forcing of the eyjafjallajökull volcanic ash layer observed over lille, france, in 2010, *Journal of Geophysical Research: Atmospheres*, *117*(D20).

Deschamps, P. Y., F. M. Breon, M. Leroy, A. Podaire, A. Bricaud, J. C. Buriez, and G. Seze (1994), The polder mission: instrument characteristics and scientific objectives, *IEEE Transactions on Geoscience and Remote Sensing*, *32*(3), 598–615, doi:10.1109/36.297978.

Dickinson, R. E., B. Pinty, and M. M. Verstraete (1990), Relating surface albedos in gcm to remotely sensed data, *Agricultural and Forest Meteorology*, *52*(1), 109–131, doi:http://dx.doi.org/10.1016/0168-1923(90)90103-D.

Diner, D. J., J. C. Beckert, T. H. Reilly, C. J. Bruegge, J. E. Conel, R. A. Kahn, J. V. Martonchik, T. P. Ackerman, R. Davies, S. A. W. Gerstl, H. R. Gordon, J. P. Muller, R. B. Myneni, P. J. Sellers, B. Pinty, and M. M. Verstraete (1998), Multi-angle imaging spectroradiometer (misr) instrument description and experiment overview, *IEEE Transactions on Geoscience and Remote Sensing*, *36*(4), 1072–1087, doi:10.1109/36.700992.

Doherty, S. J., T. Grenfell, S. Forsström, D. L. Hegg, R. E. Brandt, and S. G. Warren (2013), Observed vertical redistribution of black carbon and other insoluble light-absorbing particles in melting snow, *Journal of Geophysical Research Atmospheres*, *118*(11), 5553–5569, doi:10.1002/jgrd.50235.

Dou, T.-F., and C.-D. Xiao (2016), An overview of black carbon deposition and its radiative forcing over the arctic, *Advances in Climate Change Research*, *7*(3), 115 – 122, doi:http://dx.doi.org/10.1016/j.accre.2016.10.003, including special topic on atmospheric black carbon and its effects on cryosphere.

Dumont, M., O. Brissaud, G. Picard, B. Schmitt, J. C. Gallet, and Y. Arnaud (2010), High-accuracy measurements of snow Bidirectional Reflectance Distribution Function at visible and NIR wavelengths – comparison with modelling results, *Atmospheric Chemistry and Physics*, *10*(5), 2507–2520.

Flanner, M. G., C. S. Zender, J. T. Randerson, and P. J. Rasch (2007), Present-day climate forcing and response from black carbon in snow, *Journal of Geophysical Research Atmospheres*, *112*(11), D11,202, doi:10.1029/2006JD008003.

Gerland, S., J. G. Winther, J. B. ??rb??k, and B. V. Ivanov (1999), Physical properties, spectral reflectance and thickness development of first year fast ice in Kongsfjorden, Svalbard, *Polar Research*, *18*(2), 275–282, doi:10.1111/j.1751-8369.1999.tb00304.x.

Grenfell, T. C., and S. G. Warren (1999), Representation of a nonspherical ice particle by a collection of independent spheres for scattering and absorption of radiation, *Journal of Geophysical Research: Atmospheres*, *104*(D24), 31,697–31,709, doi:10.1029/1999JD900496.

Grenfell, T. C., S. G. Warren, and P. C. Mullen (1994), Reflection of solar radiation by the antarctic snow surface at ultraviolet, visible, and near-infrared wavelengths, *Journal of Geophysical Research: Atmospheres*, *99*(D9), 18,669–18,684, doi:10.1029/94JD01484.

Grenfell, T. C., S. J. Doherty, A. D. Clarke, and S. G. Warren (2011), Light absorption from particulate impurities in snow and ice determined by spectrophotometric analysis of filters, *Applied optics*, *50*(14), 2037–2048.

Hansen, J., and L. Nazarenko (2004), Soot climate forcing via snow and ice albedos., *Proceedings of the National Academy of Sciences of the United States of America*, *101*(2), 423–8, doi: 10.1073/pnas.2237157100.

Hedley, J. (2008), A three-dimensional radiative transfer model for shallow water environments., *Optics express*, *16*(26), 21,887–21,902, doi:10.1364/OE.16.021887.

Hegg, D. A., S. G. Warren, T. C. Grenfell, S. J. Doherty, T. V. Larson, and A. D. Clarke (2009), Source attribution of black carbon in arctic snow, *Environmental science & technology*, *43*(11), 4016–4021.

Heilbronner, R., and S. Barrett (2013), *Image analysis in earth sciences: microstructures and textures of earth materials*, vol. 129, Springer Science & Business Media.

Henyey, L. C., and J. L. Greenstein (1941), Diffuse radiation in the Galaxy, *The Astrophysical Journal*, *93*, 70, doi:10.1086/144246.

Hitzenberger, R., S. Jennings, S. Larson, A. Dillner, H. Cachier, Z. Galambos, A. Rouc, and T. Spain (1999), Intercomparison of measurement methods for black carbon aerosols, *Atmospheric Environment*, *33*(17), 2823 – 2833, doi:http://dx.doi.org/10.1016/S1352-2310(98)00360-4.

Holland, M. M., and C. M. Bitz (2003), Polar amplification of climate change in coupled models, *Climate Dynamics*, *21*(3), 221–232, doi:10.1007/s00382-003-0332-6.

Hudson, S. R., S. G. Warren, R. E. Brandt, T. C. Grenfell, and D. Six (2006a), Spectral bidirectional reflectance of antarctic snow: Measurements and parameterization, *Journal of Geophysical Research: Atmospheres*, *111*(D18).

Hudson, S. R., S. G. Warren, R. E. Brandt, T. C. Grenfell, and D. Six (2006b), Spectral bidirectional reflectance of antarctic snow: Measurements and parameterization, *Journal of Geophysical Research: Atmospheres*, *111*(D18), doi:10.1029/2006JD007290, d18106.

Jacobson, M. Z. (2004), Climate response of fossil fuel and biofuel soot, accounting for soot's feedback to snow and sea ice albedo and emissivity, *Journal of Geophysical Research D: Atmospheres*, *109*(21), n/a–n/a, doi:10.1029/2004JD004945.

Jin, Z., and J. J. Simpson (1999), Bidirectional anisotropic reflectance of snow and sea ice in AVHRR Channel 1 and 2 spectral regions. I. Theoretical analysis, *IEEE transactions on geoscience and ...*, *37*(1), 543–554.

Johnson, B., K. Turnbull, P. Brown, R. Burgess, J. Dorsey, A. J. Baran, H. Webster, J. Haywood, R. Cotton, Z. Ulanowski, et al. (2012), In situ observations of volcanic ash clouds from the faam aircraft during the eruption of eyjafjallajökull in 2010, *Journal of Geophysical Research: Atmospheres*, *117*(D20).

Kay, J. E., M. M. Holland, and A. Jahn (2011), Inter-annual to multi-decadal arctic sea ice extent trends in a warming world, *Geophysical Research Letters*, *38*(15), n/a–n/a, doi: 10.1029/2011GL048008, l15708.

Kimes, D. S., J. A. Kirchner, and W. W. Newcomb (1983), Spectral radiance errors in remote sensing ground studies due to nearby objects., *Applied optics*, *22*(1), 8–10.

Koch, D., and J. Hansen (2005a), Distant origins of Arctic black carbon: A Goddard Institute for Space Studies ModelE experiment, *Journal of Geophysical Research D: Atmospheres*, *110*(4), 1–14, doi:10.1029/2004JD005296.

Koch, D., and J. Hansen (2005b), Distant origins of arctic black carbon: A goddard institute for space studies modele experiment, *Journal of Geophysical Research: Atmospheres*, *110*(D4), n/a–n/a, doi:10.1029/2004JD005296, d04204.

Kokhanovsky, A. A., and F. M. Breon (2012), Validation of an Analytical Snow BRDF Model Using PARASOL Multi-Angular and Multispectral Observations, *IEEE Geoscience and Remote Sensing*, *9*(5), 928–932.

Kokhanovsky, A. A., and E. P. Zege (2004), Scattering optics of snow., *Applied optics*, *43*(7), 1589–1602.

Kwok, R., and D. A. Rothrock (2009), Decline in arctic sea ice thickness from submarine and icesat records: 1958–2008, *Geophysical Research Letters*, *36*(15), n/a–n/a, doi:10.1029/2009GL039035,

l15501.

Lamare, M. L., J. Lee-Taylor, and M. D. King (2016), The impact of atmospheric mineral aerosol deposition on the albedo of snow and sea ice: are snow and sea ice optical properties more important than mineral aerosol optical properties?, *Atmospheric Chemistry and Physics Discussions*, *16*(2), 843–860, doi:10.5194/acpd-15-23131-2015.

Lamare, M. L., J. Hedley, and M. D. King (2017a), The effects of surface roughness on the spectral (300–1400 nm) bidirectional reflectance distribution function (BRDF) of sea ice, in preparation for *The Cryosphere*.

Lamare, M. L., C. Greenwell, F. Wang, M. King, and N. Fox (2017b), Bidirectional reflectance measurements (HDRF) of thin first-year sea ice at large solar zenith angles, in preparation for *Scientific Reports*.

Lavoue, D., C. Liousse, H. Cachier, B. J. Stocks, and J. G. Goldammer (2000), Modeling of carbonaceous particles emitted by boreal and temperate wildfires at northern latitudes, *Journal of Geophysical Research: Atmospheres*, *105*(D22), 26,871–26,890, doi:10.1029/2000JD900180.

Lee-Taylor, J., and S. Madronich (2002), Calculation of actinic fluxes with a coupled atmosphere-snow radiative transfer model, *Journal of Geophysical Research Atmospheres*, *107*(24), 4796, doi:10.1029/2002JD002084.

Leroux, C., J. Lenoble, G. Brogniez, J. W. Hovenier, and J. F. DE HAAN (1999), A MODEL FOR THE BIDIRECTIONAL POLARIZED REFLECTANCE OF SNOW, *Journal of Quantitative Spectroscopy and Radiative Transfer*, *61*(3), 273–285.

Light, B., G. A. Maykut, and T. C. Grenfell (2004), A temperature-dependent, structural-optical model of first-year sea ice, *Journal of Geophysical Research : Oceans*, *109*(6), C06,013, doi:10.1029/2003JC002164.

Lucht, W., C. B. Schaaf, and A. H. Strahler (2000), An algorithm for the retrieval of albedo from space using semiempirical brdf models, *IEEE Transactions on Geoscience and Remote Sensing*, *38*(2), 977–998, doi:10.1109/36.841980.

Malinka, A., E. Zege, G. Heygster, and L. Istomina (2016), Reflective properties of white sea ice and snow, *The Cryosphere*, *10*, 2541–2557, doi:10.5194/tc-10-2541-2016.

Marks, A., C. Fragiacomo, A. MacArthur, G. Zibordi, N. Fox, and M. D. King (2015), Characterisation of the HDRF (as a proxy for BRDF) of snow surfaces at Dome C, Antarctica, for the inter-calibration and inter-comparison of satellite optical data, *Remote Sensing of . . .*, *158*, 407–416.

Marks, A., M. Lamare, and M. King (2017a), Optical properties of laboratory grown sea ice doped with light absorbing impurities (black carbon), *In preparation for The Cryosphere*.

Marks, A. A., and M. D. King (2013), The effects of additional black carbon on the albedo of Arctic sea ice: Variation with sea ice type and snow cover, *Cryosphere*, *7*(4), 1193–1204, doi:10.5194/tc-7-1193-2013.

Marks, A. A., and M. D. King (2014), The effect of snow/sea ice type on the response of albedo and light penetration depth (ie-folding depth) to increasing black carbon, *Cryosphere*, *8*(5), 1625–1638, doi:10.5194/tc-8-1625-2014.

Marks, A. A., M. L. Lamare, and M. D. King (2017b), Optical properties of laboratory grown sea ice doped with light absorbing impurities (black carbon), *The Cryosphere Discussions*, *2017*, 1–26, doi:10.5194/tc-2017-76.

Martonchik, J. V., C. J. Bruegge, and A. H. Strahler (2000), A review of reflectance nomenclature used in remote sensing, *Remote Sensing Reviews*, *19*(January 2015), 9–20, doi:10.1080/02757250009532407.

Meehl, G. A., and W. M. Washington (1990), Co2 climate sensitivity and snow-sea-ice albedo parameterization in an atmospheric gcm coupled to a mixed-layer ocean model, *Climatic Change*, *16*(3), 283–306, doi:10.1007/BF00144505.

Middleton, W. E. K., and A. G. Mungall (1952), The Luminous Directional Reflectance of Snow, *JOSA*, *42*(8), 572.

Mishchenko, M. I., J. M. Dlugach, E. G. Yanovitskij, and N. T. Zakharova (1999), Bidirectional reflectance of flat, optically thick particulate layers: an efficient radiative transfer solution and applications to snow and soil surfaces, . . . *and Radiative Transfer*, *63*(2-6), 409–432.

Mobley, C. D. (1989), A numerical model for the computation of radiance distributions in natural waters with wind-roughened surfaces, *Limnology and Oceanography*, *34*(8), 1473–1483, doi: 10.4319/lo.1989.34.8.1473.

Mobley, C. D. (1994), *Light and Water: Radiative Transfer in Natural Waters*, 592 pp., Acedemic Press.

Muckenhuber, H., and H. Grothe (2006), The heterogeneous reaction between soot and NO2 at elevated temperature, *Carbon*, *44*(3), 546–559, doi:10.1016/j.carbon.2005.08.003.

Newman, S. M., L. Clarisse, D. Hurtmans, F. Marenco, B. Johnson, K. Turnbull, S. Havemann, A. J. Baran, D. O'Sullivan, and J. Haywood (2012), A case study of observations of volcanic ash from the eyjafjallajÃűkull eruption: 2. airborne and satellite radiative measurements, *Journal of Geophysical Research: Atmospheres*, *117*(D20), n/a–n/a, doi:10.1029/2011JD016780, d00U13.

Nicodemus, F., J. Richmond, and J. Hsia (1977), Geometrical considerations and nomenclature for reflectance, *Science And Technology*, *60*(October), 1–52, doi:10.1109/LPT.2009.2020494.

Nolin, A. W., and S. Liang (2000), Progress in bidirectional reflectance modeling and applications for surface particulate media: Snow and soils, *Remote Sensing Reviews*, *18*(2-4), 307–342.

Nolin, A. W., J. Dozier, and R. E. Davis (1990), Bidirectional reflectance of optically-thin snow, in *10th Annual International Symposium on Geoscience and Remote Sensing*, pp. 1159–1159, doi:10.1109/IGARSS.1990.688702.

Nolin, A. W., F. M. Fetterer, and T. A. Scambos (2002), Surface roughness characterizations of sea ice and ice sheets: Case studies with MISR data, *IEEE Transactions on Geoscience and Remote Sensing*, *40*(7), 1605–1615, doi:10.1109/TGRS.2002.801581.

Nousiainen, T. (2009), Optical modeling of mineral dust particles: A review, *Journal of Quantitative Spectroscopy and Radiative Transfer*, *110*(14–16), 1261 – 1279, doi: http://dx.doi.org/10.1016/j.jqsrt.2009.03.002, {XI} Conference on Electromagnetic and Light Scattering by Non-Spherical Particles: 2008.

Okabe, A., B. N. Boots, K. Sugihara, and D. G. Kendall (1992), *Spatial tessellations : concepts and applications of Voronoi diagrams*, 671 pp., Wiley.

Overland, J. E., and M. Wang (2013), When will the summer arctic be nearly sea ice free?, *Geophysical Research Letters*, *40*(10), 2097–2101, doi:10.1002/grl.50316.

Painter, T. H. (2004), Measurements of the hemispherical-directional reflectance of snow at fine spectral and angular resolution, *Journal of Geophysical Research: Oceans*, *109*(D18), D18,115.

Painter, T. H., A. P. Barrett, C. C. Landry, J. C. Neff, M. P. Cassidy, C. R. Lawrence, K. E. McBride, and G. L. Farmer (2007), Impact of disturbed desert soils on duration of mountain snow cover, *Geophysical Research Letters*, *34*(12), L12,502, doi:10.1029/2007GL030284.

Paris, J.-D., A. Stohl, P. Nédélec, M. Y. Arshinov, M. V. Panchenko, V. P. Shmargunov, K. S. Law, B. D. Belan, and P. Ciais (2009), Wildfire smoke in the siberian arctic in summer: source characterization and plume evolution from airborne measurements, *Atmospheric Chemistry and Physics*, *9*(23), 9315–9327, doi:10.5194/acp-9-9315-2009.

Peltoniemi, J. I., S. Kaasalainen, J. Näränen, L. Matikainen, and J. Piironen (2005), Measurement of directional and spectral signatures of light reflectance by snow, *IEEE Transactions on Geoscience and Remote Sensing*, *43*(10), 2294–2304.

Peltoniemi, J. I., M. Gritsevich, T. Hakala, P. Dagsson-Waldhauserová, Arnalds, K. Anttila, H. R. Hannula, N. Kivekäs, H. Lihavainen, O. Meinander, J. Svensson, A. Virkkula, and G. De Leeuw (2015), Soot on Snow experiment: Bidirectional reflectance factor measurements of contaminated snow, *Cryosphere*, *9*(6), 2323–2337, doi:10.5194/tc-9-2323-2015.

Perovich, D. K. (1996), *The Optical Properties of Sea Ice.*, vol. 96–1, 24 pp., US Army Corps of Engineers CRREL.

Perovich, D. K. (1998), Observations of the polarization of light reflected from sea ice, *Journal of Geophysical Research*, *103*(C3), 5563, doi:10.1029/97JC01615.

Popovicheva, O. B., N. Evangeliou, K. Eleftheriadis, A. C. Kalogridis, N. Sitnikov, S. Eckhardt, and A. Stohl (2017), Black carbon sources constrained by observations in the russian high arctic, *Environmental Science & Technology*, *51*(7), 3871–3879.

Ramanathan, R., and G. Carmichael (2008), Global and regional climate changes due to black carbon, *Nature Geoscience*, *1*(4), 221 – 227, doi:10.1038/ngeo156.

Roujean, J. L., M. Leroy, A. Podaire, and P. Y. Deschamps (1992), Evidence of surface reflectance bidirectional effects from a noaa/ avhrr multi-temporal data set, *International Journal of Remote Sensing*, *13*(4), 685–698, doi:10.1080/01431169208904146.

Sadezky, A., H. Muckenhuber, H. Grothe, R. Niessner, and U. PÃűschl (2005), Raman microspectroscopy of soot and related carbonaceous materials: Spectral analysis and structural information, *Carbon*, *43*(8), 1731 – 1742, doi:http://dx.doi.org/10.1016/j.carbon.2005.02.018.

Sandmeier, S., C. Müller, B. Hosgood, and G. Andreoli (1998), Physical mechanisms in hyperspectral BRDF data of grass and watercress, *Remote Sensing of Environment*, *66*(2), 222–233, doi:10.1016/S0034-4257(98)00060-1.

Schaepman-Strub, G., M. E. Schaepman, T. H. Painter, S. Dangel, and J. V. Martonchik (2006), Reflectance quantities in optical remote sensing-definitions and case studies, *Remote Sensing of Environment*, *103*(1), 27–42, doi:10.1016/j.rse.2006.03.002.

Schlosser, E. (1988), Optical studies of antarctic sea ice, *Cold Regions Science and Technology*, *15*(3), 289–293, doi:http://dx.doi.org/10.1016/0165-232X(88)90075-4.

Sergent, C., C. Leroux, E. Pougatch, and F. Guirado (1998), Hemispherical-directional reflectance measurements of natural snow in the 0.9-1.45 μm spectral range: comparison with adding-doubling modelling, *Annals of Glaciology*, *26*(1), 59–65.

Serreze, M. C., M. M. Holland, and J. Stroeve (2007), Perspectives on the arctic's shrinking sea-ice cover, *Science*, *315*(5818), 1533.

Shindell, D. T., M. Chin, F. Dentener, R. M. Doherty, G. Faluvegi, A. M. Fiore, P. Hess, D. M. Koch, I. A. MacKenzie, M. G. Sanderson, M. G. Schultz, M. Schulz, D. S. Stevenson, H. Teich, C. Textor, O. Wild, D. J. Bergmann, I. Bey, H. Bian, C. Cuvelier, B. N. Duncan, G. Folberth, L. W. Horowitz, J. Jonson, J. W. Kaminski, E. Marmer, R. Park, K. J. Pringle, S. Schroeder, S. Szopa, T. Takemura, G. Zeng, T. J. Keating, and A. Zuber (2008), A multi-model assessment of pollution transport to the arctic, *Atmospheric Chemistry and Physics*, *8*(17), 5353–5372, doi:10.5194/acp-8-5353-2008.

Stamnes, K., B. Hamre, J. Stamnes, G. Ryzhikov, M. Biryulina, R. Mahoney, B. Hauss, and A. Sei (2011), Modeling of radiation transport in coupled atmosphere-snow-ice-ocean systems, *Journal of Quantitative Spectroscopy and Radiative Transfer*, *112*(4), 714–726, doi:10.1016/j.jqsrt.2010.06.006.

Steffen, K. (1987), Bidirectional reflectance of snow at 500–600 nm, . . . *Association of Hydrological Sciences–IAHS Publication*.

Stohl, A. (2006), Characteristics of atmospheric transport into the arctic troposphere, *Journal of Geophysical Research: Atmospheres*, *111*(D11), doi:10.1029/2005JD006888, d11306.

Stohl, A., T. Berg, J. F. Burkhart, A. M. FjÇ¡raa, C. Forster, A. Herber, Ø. Hov, C. Lunder, W. W. McMillan, S. Oltmans, M. Shiobara, D. Simpson, S. Solberg, K. Stebel, J. Ström, K. Tørseth, R. Treffeisen, K. Virkkunen, and K. E. Yttri (2007), Arctic smoke & record high air pollution levels in the european arctic due to agricultural fires in eastern europe in spring 2006, *Atmospheric Chemistry and Physics*, *7*(2), 511–534, doi:10.5194/acp-7-511-2007.

Stroeve, J. C., M. C. Serreze, M. M. Holland, J. E. Kay, J. Malanik, and A. P. Barrett (2012), The arctic's rapidly shrinking sea ice cover: a research synthesis, *Climatic Change*, *110*(3), 1005–1027, doi:10.1007/s10584-011-0101-1.

Tanikawa, T., T. Aoki, and F. Nishio (2002), Remote sensing of snow grain-size and impurities from Airborne Multispectral Scanner data using a snow bidirectional reflectance distribution function model, *Annals of Glaciology*, *34*(1), 74–80.

Turnbull, K., B. Johnson, F. Marenco, J. Haywood, A. Minikin, B. Weinzierl, H. Schlager, U. Schumann, S. Leadbetter, and A. Woolley (2012), A case study of observations of volcanic ash from the eyjafjallajÃűkull eruption: 1. in situ airborne observations, *Journal of Geophysical Research: Atmospheres*, *117*(D20), n/a–n/a, doi:10.1029/2011JD016688, d00U12.

Warren, S. G. (1982), Optical properties of snow, *Reviews of Geophysics*, *20*(1), 67–89, doi:10.1029/RG020i001p00067.

Warren, S. G., and R. E. Brandt (2008), Optical constants of ice from the ultraviolet to the microwave: A revised compilation, *Journal of Geophysical Research Atmospheres*, *113*(14), doi:10.1029/2007JD009744.

Warren, S. G., R. E. Brandt, and P. O'Rawe Hinton (1998), Effect of surface roughness on bidirectional reflectance of Antarctic snow, *Journal of Geophysical Research: Planets*, *103*(E11), 25,789–25,807.

Weatherly, J. W., B. P. Briegleb, W. G. Large, and J. A. Maslanik (1998), Sea ice and polar climate in the ncar csm, *Journal of Climate*, *11*(6), 1472–1486, doi:10.1175/1520-0442(1998)011<1472:SIAPCI>2.0.CO;2.

Williams, D. C. (1999), Establishment of absolute diffuse reflectance scales using the NPL Reference Reflectometer, *Analytica chimica acta*, *380*(2-3), 165–172.

Winther, J.-G. (1994), Spectral bi-directional reflectance of snow and glacier ice measured in Dronning Maud Land, Antarctica, *Annals of Glaciology*, *20*, 1–5.

Zdanowicz, C. M., G. A. Zielinski, and C. P. Wake (1998), Characteristics of modern atmospheric dust deposition in snow on the Penny Ice Cap, Baffin Island, Arctic Canada, *Tellus, Series B: Chemical and Physical Meteorology*, *50*(5), 506–520, doi:10.1034/j.1600-0889.1998.t01-1-00008.x.

Zender, C. S., J.-C. Gallet, F. Dominé, G. Picard, and M. G. Flanner (2009), Albedo reduction by black carbon in snow: Measurements and implications, *Geophysical Research Letter*.

Table 1. Recapitulation of the experiments performed in the sea ice laboratory, the physical properties of the sea ice, and the optical properties of the sea ice derived from the radiative-transfer calculations.

Experiment number	Type of impurity added to the upper layer of sea ice	Mass-ratio of the impurities in the top layer / ng g^{-1}	Thickness of the sea ice (Clean run/ Poisoned run) / cm	Scattering coefficient of the clean sea ice / m^{-1}	Mass-ratio of black carbon in the clean sea ice / ng g^{-1}
1	Black carbon	68.6	33.5 / 36	330	30
2	Black carbon	34.3	40 / 44	300	30
3	Black carbon	205.9	28 / 33	200	30
4	Volcanic ash	550	27.5 / 32	310	20
5	Volcanic ash	2202.6	35 / 46	380	10
6	Volcanic ash	5506.6	36 / 43.5	600	30

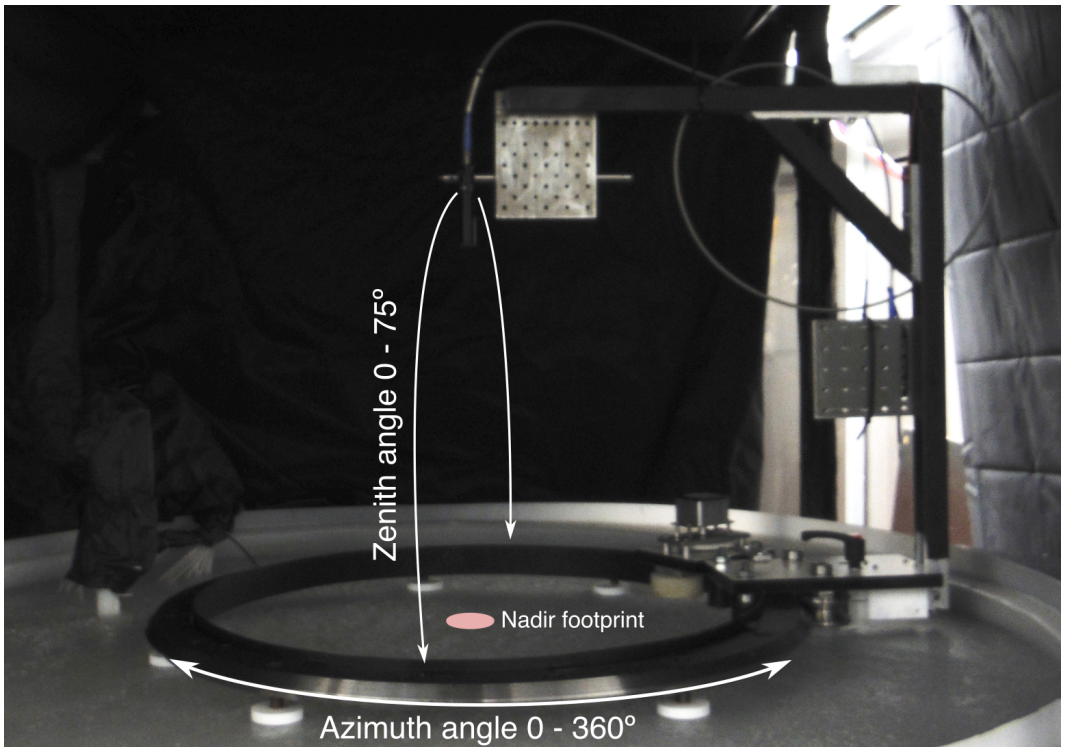

Figure 1. The laboratory goniometer on the surface of the artificial sea ice.

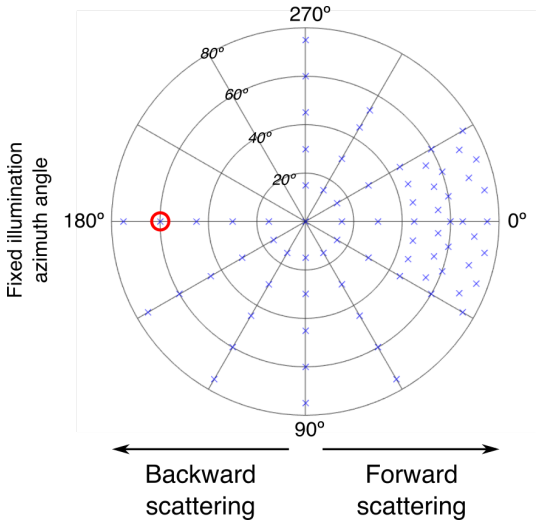

Figure 2. Polar plot of the typical acquisition angles of BRF over the hemisphere. The illumination azimuth angle was set to 180° out of convention. The red circle symbolises the fixed illumination angle (ϕ_i = 180°, θ_i = 60°) for the campaign. The left half of the polar plot represents light being scattered in a backward direction and the right part of the plot represents forward scattering.

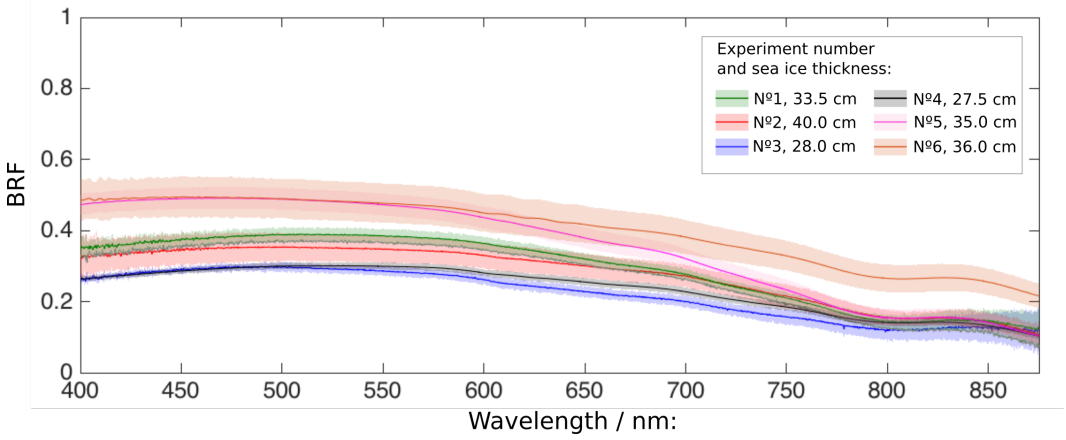

Figure 3. Nadir BRF of the clean sea ice measured in the laboratory with the goniometer. Experiments 1,2, and 3 were performed with the Ocean Optics spectrometer for the black carbon experiments, and experiments 4,5, and 6 with the ASD spectrometer for the volcanic ash experiments. The shaded areas represent $\pm 2\sigma$.

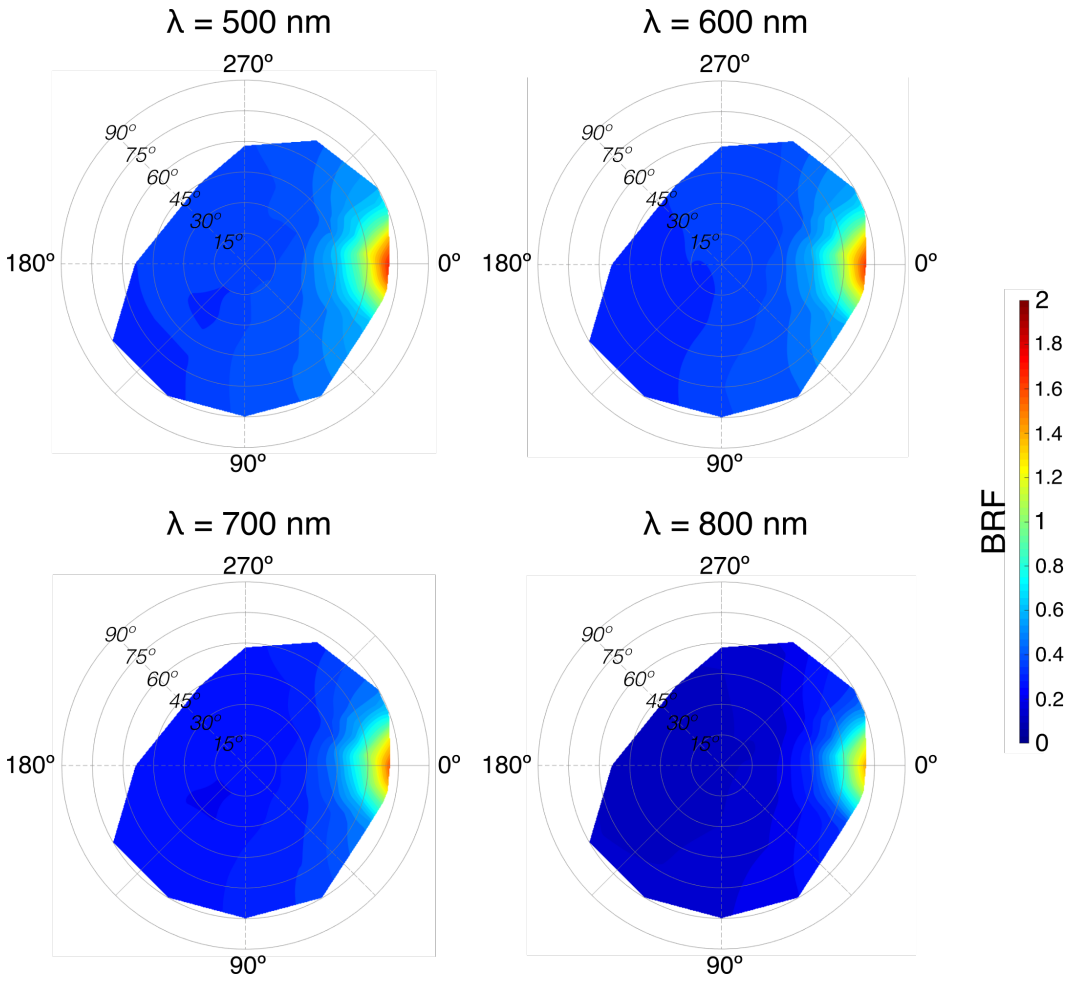

Figure 4. Measured BRF of clean sea ice in the laboratory for wavelengths 500, 600, 700 and 800 nm. The illumination angle was $\phi = 180°$, $\theta = 60°$.

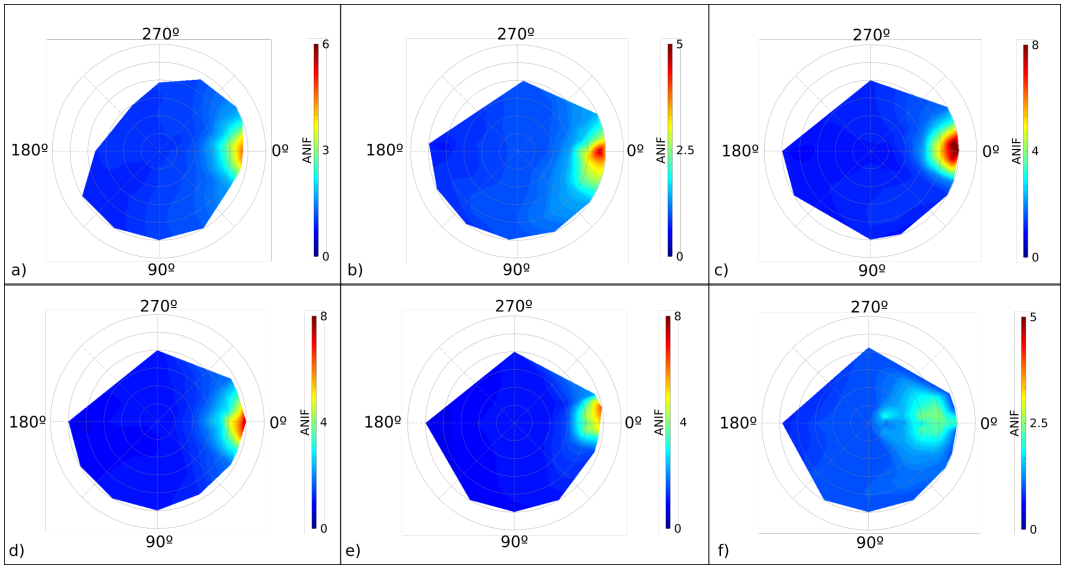

Figure 5. ANIF of the BRF of the clean sea ice measured (λ = 550 nm) in the laboratory during the different experiments, with varying sea ice thicknesses. a) Experiment 1, 33.5 cm, b) Experiment 2, 40.0 cm, c) Experiment 3, 28.0 cm, d) Experiment 4, 27.5 cm, e) Experiment 5, 35.0 cm, f) Experiment 6, 36.0 cm. Note that the colorbars have different scales for each ANIF.

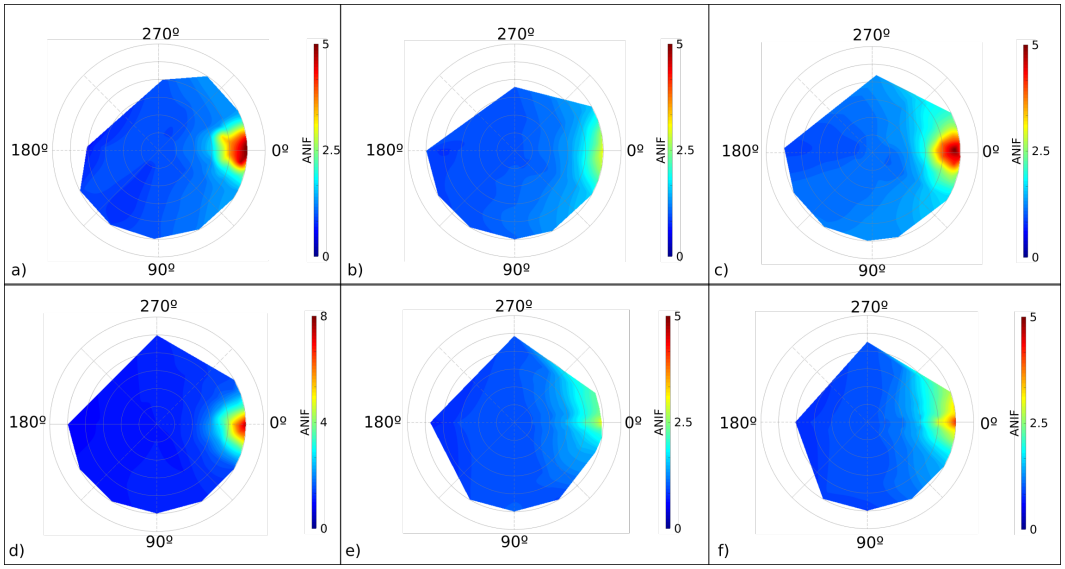

Figure 6. ANIF of the BRF of the sea ice with a surface layer doped with impurities measured in the laboratory during the different experiments, with varying thicknesses and mass-ratios of black carbon or volcanic ash. a) Experiment 1, 36.0 cm, 68.5 ng g^{-1} of black carbon, b) Experiment 2, 44.0 cm, 34.3 ng g^{-1} of black carbon, c) Experiment 3, 33.0 cm, 205.9 ng g^{-1} of black carbon, d) Experiment 5, 32.0 cm, 550 ng g^{-1} of volcanic ash, e) Experiment 5, 46.0 cm, 2202.6 ng g^{-1} of volcanic ash, f) Experiment 6, 43.5 cm, 5506.6 ng g^{-1} of volcanic ash. Note the different scale for subfigure d).

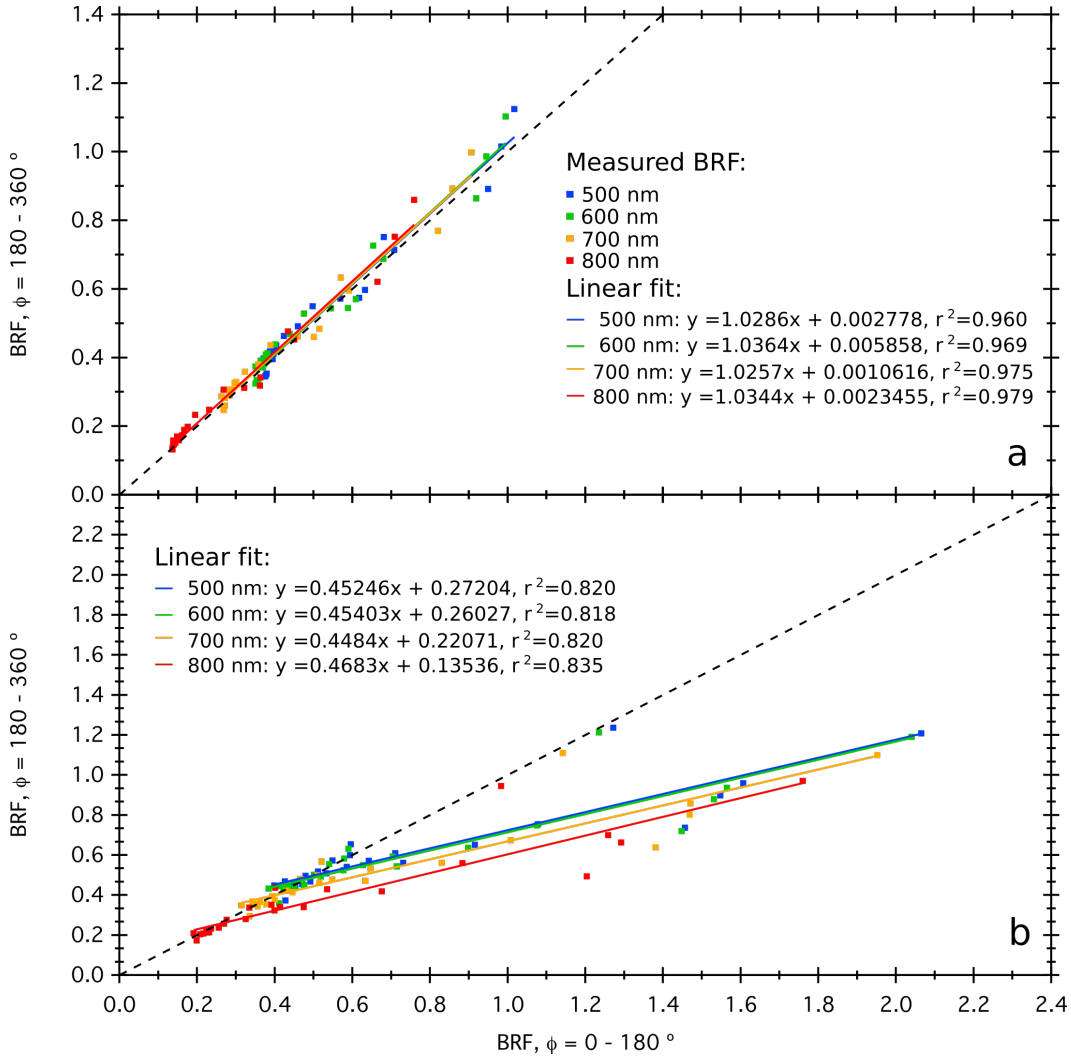

Figure 7. Scatter plot of measured BRF values for symmetrical points on each side of the solar principal plane at wavelengths 500, 600, 700, and 800 nm for a) experiment 1 with clean sea ice, b) experiment 1 with doped sea ice. A linear fit was performed for each dataset - the equations and r^2 values are indicated within the figure. The black dotted line represents x=y.

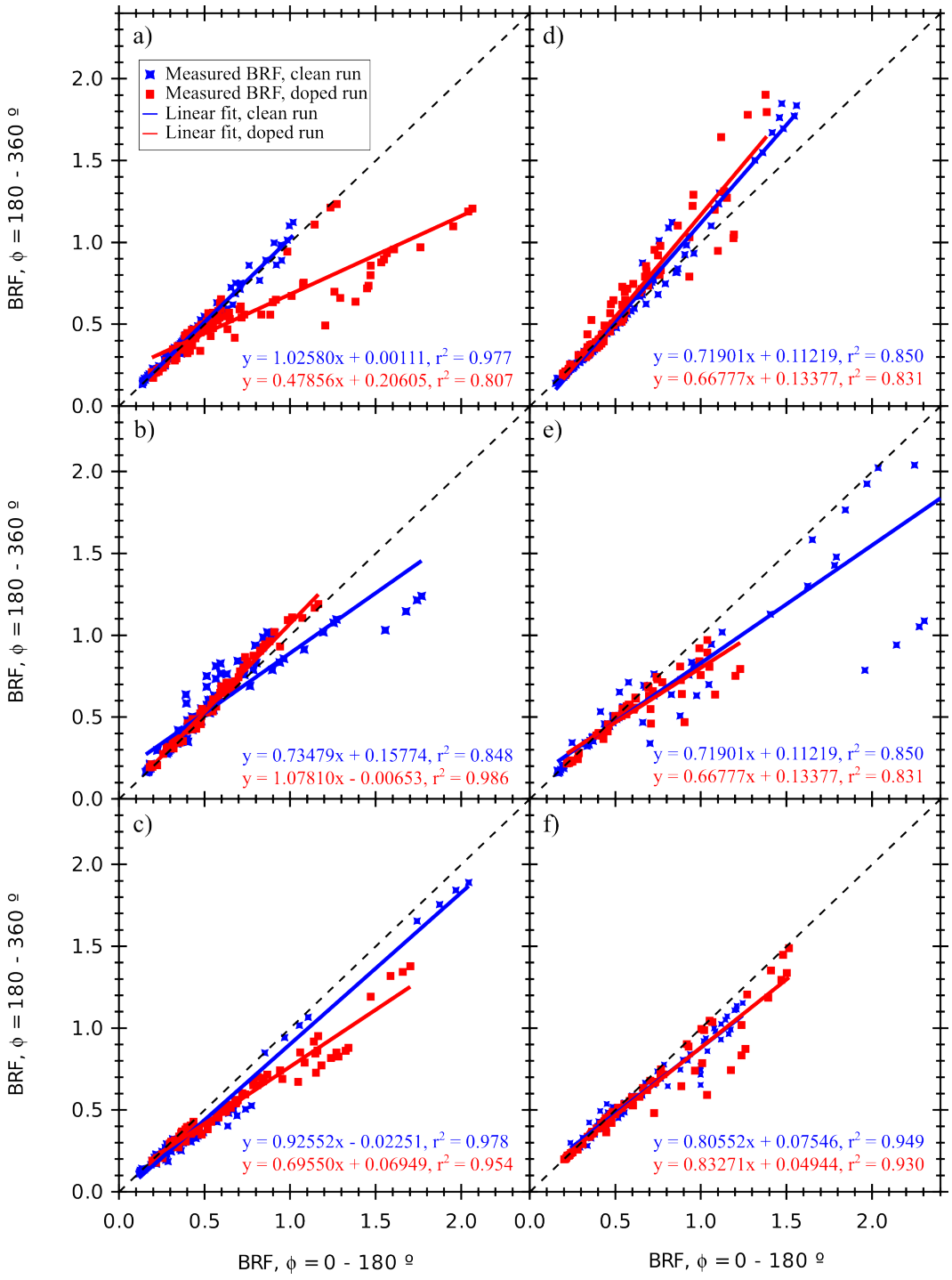

Figure 8. Scatter plot of measured BRF values for symmetrical points on each side of the solar principal plane at a wavelength λ = 550 nm for a) experiment 1, b) experiment 2, c) experiment 3, d) experiment 4, e) experiment 5, f) experiment 6. The blue dots represent measurements performed for a clean sea ice, and the red dots represent measurements performed for the doped sea ice. A linear fit was performed for each dataset - the equations and r^2 values are indicated within the figure. The black dotted line represents x=y.

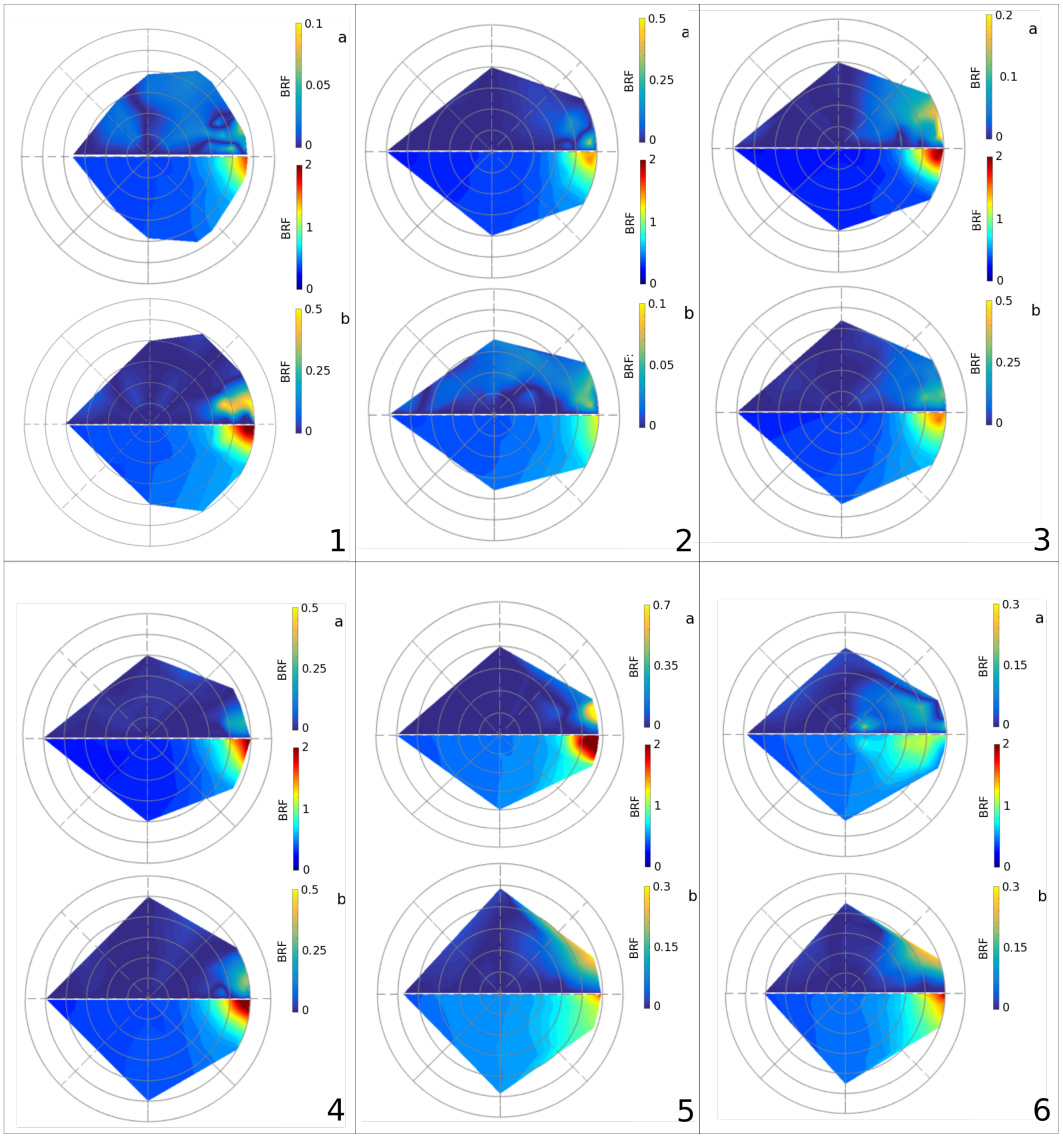

Figure 9. Mean BRF at λ = 550 nm of the measured artificial sea ice. The numbers in the figure indicate the number of the experiment, for a) clean sea ice, and b) sea ice with a doped layer. The bottom half of the polar plots represents the mean of the symmetrical points of the two half hemispheres along the solar principal plane. The top half of the polar plots represents the standard deviation of the mean.

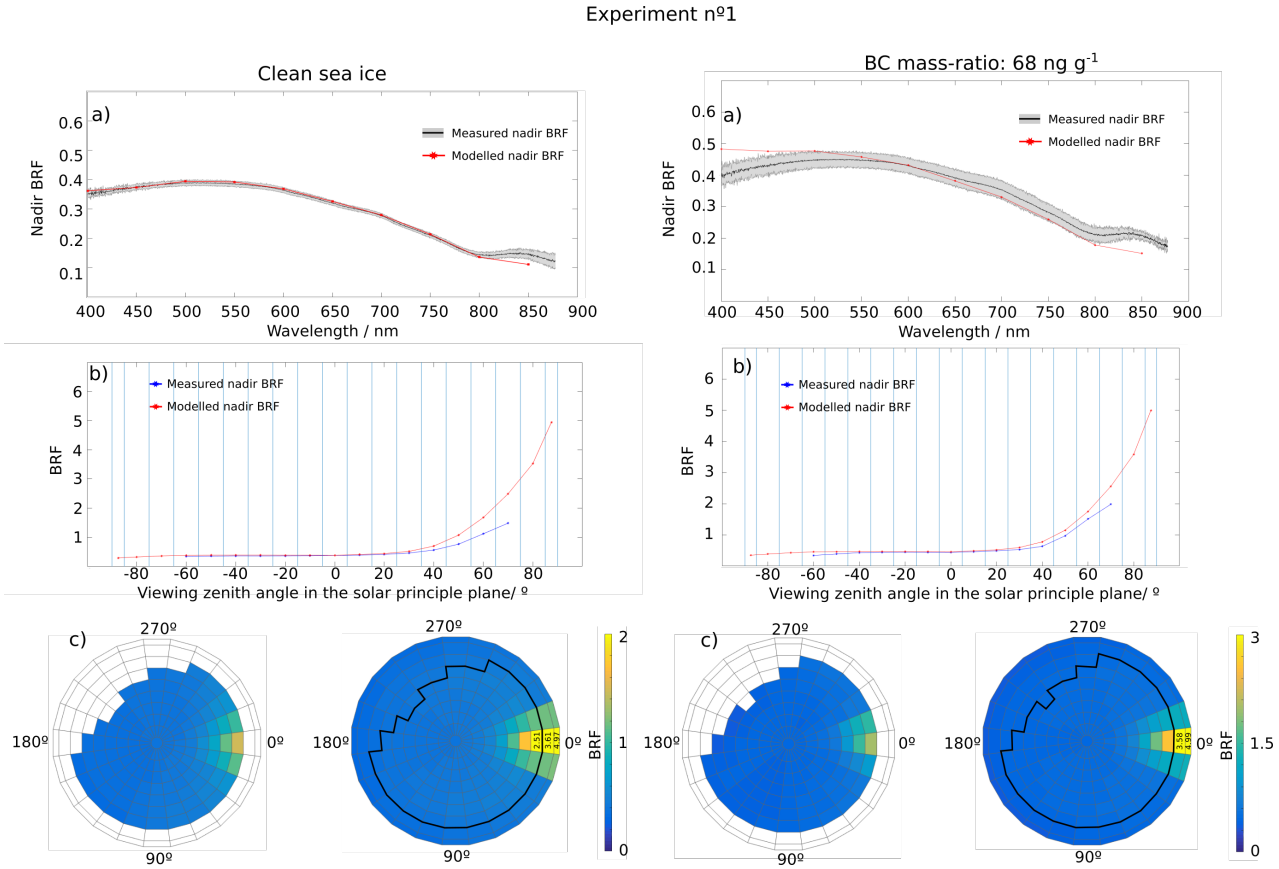

Figure 10. Comparison between the measured BRF and the modelled BRF for experiment n°1, where a surface layer containing 68.6 ng g^{-1} of black carbon was added. The clean sea ice was 33.5 cm thick, and the sea ice with a doped layer was 36.0 cm thick. a) Nadir BRF. The modelled BRF is shown as points at the calculated wavelengths, and a line was added to help the visualisation. The grey shaded area around the measured BRF spectra represents $\pm 2\sigma$. b) BRF across the solar principle plane plotted for a wavelength, λ = 550 nm: the negative numbers represent the backscattering part of the plane and the positive numbers, the forward scattering part of the plane. The vertical blue lines mark the zenith bounding lines of the quads over which the values were averaged. c) BRF across the hemisphere at a wavelength, λ = 550 nm, averaged for each quad. The BRF measurements (bottom left of each pane) are presented in the same format as the model output (bottom right of each panel) for ease of comparison. The outline of the measured quads is plotted on the model output to guide the eye. The values of the quads lying outside of the color scale range are indicated in black over each concerned quad.

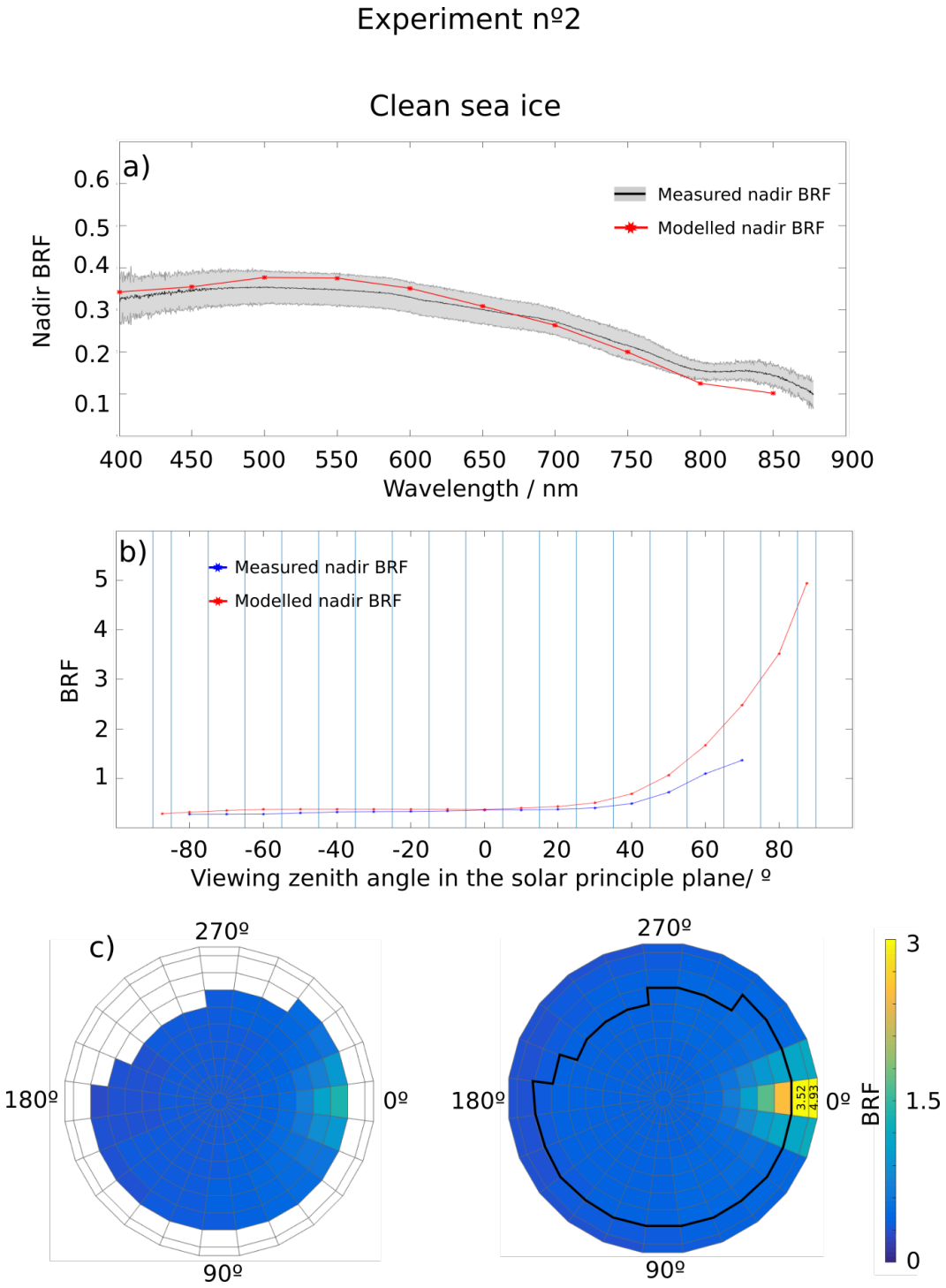

Figure 11. Comparison between the measured BRF and the modelled BRF for experiment n°2. The clean sea ice was 40.0 cm thick. See caption of figure 10 for more details.

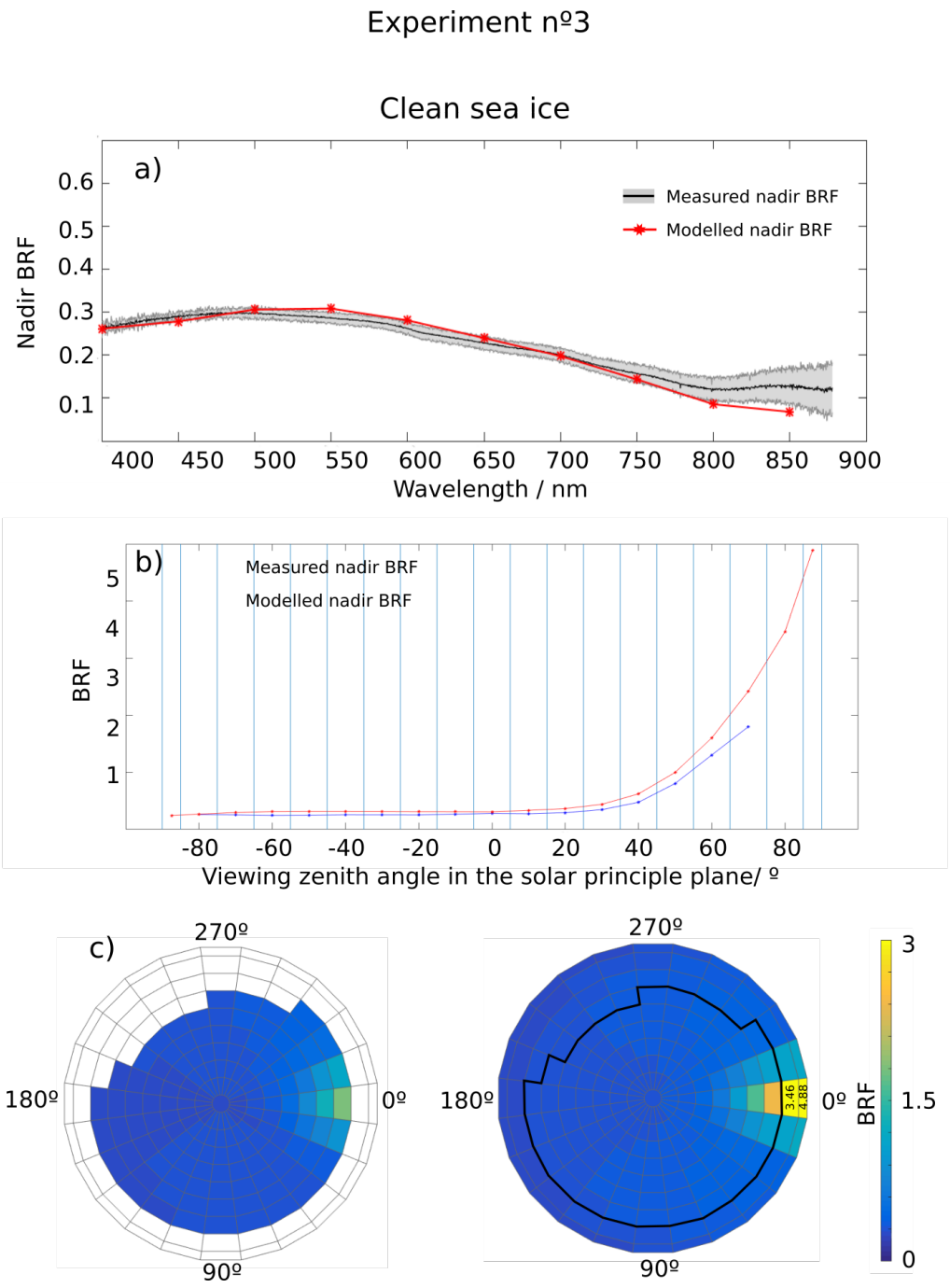

Figure 12. Comparison between the measured BRF and the modelled BRF for experiment n°3. The clean sea ice was 28.0 cm thick. See caption of figure 10 for more details.

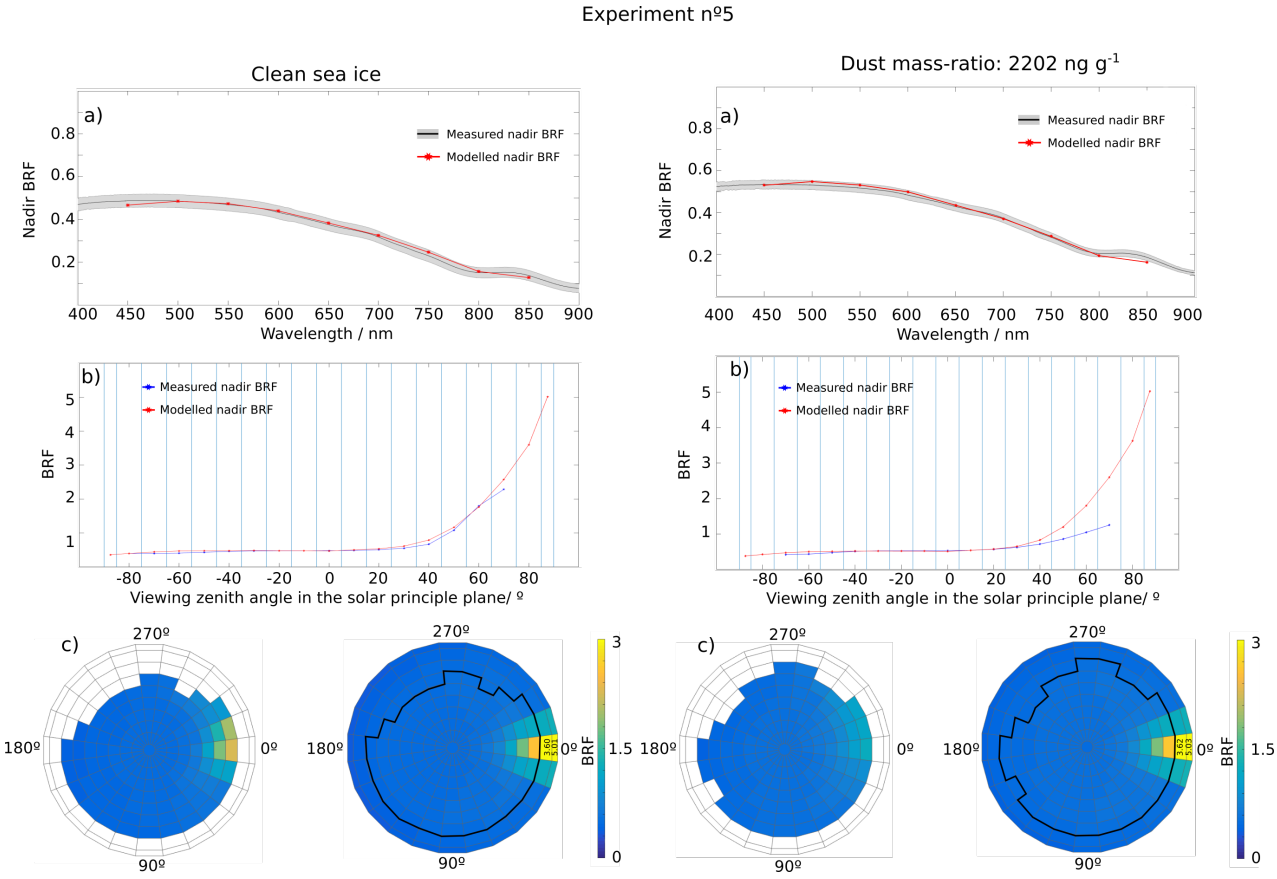

Figure 13. Comparison between the measured BRF and the modelled BRF for experiment n°5, where a surface layer containing 2202.6 ng g^{-1} of black carbon was added. The clean sea ice was 35.0 cm thick, and the sea ice with a doped layer was 46.0 cm thick. See caption of figure 10 for more details.

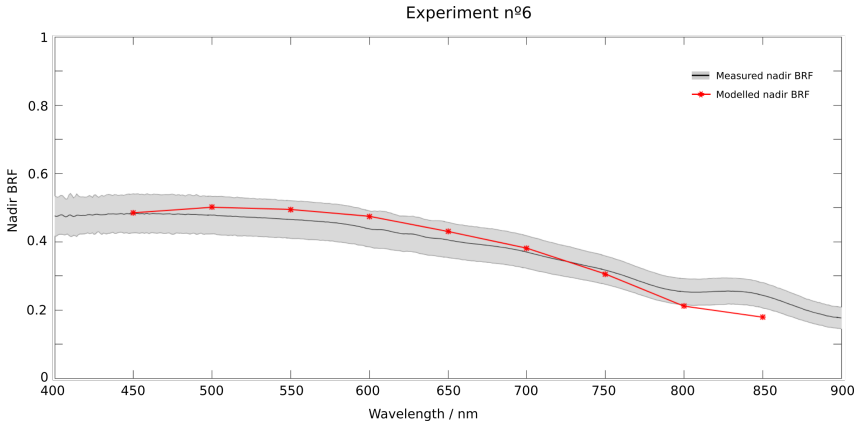

Figure 14. Comparison between between the measured nadir BRF and the modelled nadir BRF for experiment n°6. The clean sea ice was 36.0 cm thick. The BRF across the hemisphere was not modelled owing to the particularity of the layer during the measurements.

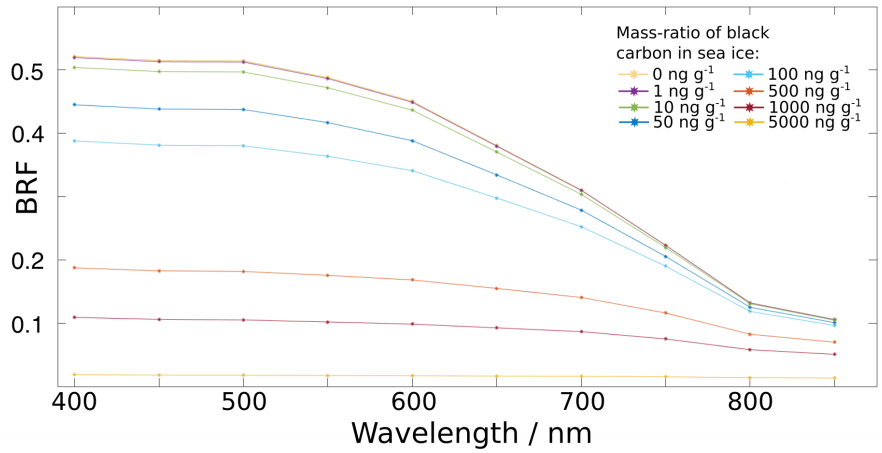

Figure 15. Nadir BRF of a clean sea ice layer with a varying mass-ratio of black carbon. The ice was modelled with a thickness of 50 cm, a underlying diffuse reflectance of 0.1, and a scattering coefficient of 300 m^{-1} for an illumination zenith angle of 60 ° and a wavelength range 400–850 nm. The mass-ratio of black carbon distributed throughout the sea ice was varied between 0 ng g^{-1} and 5000 ng g−1.

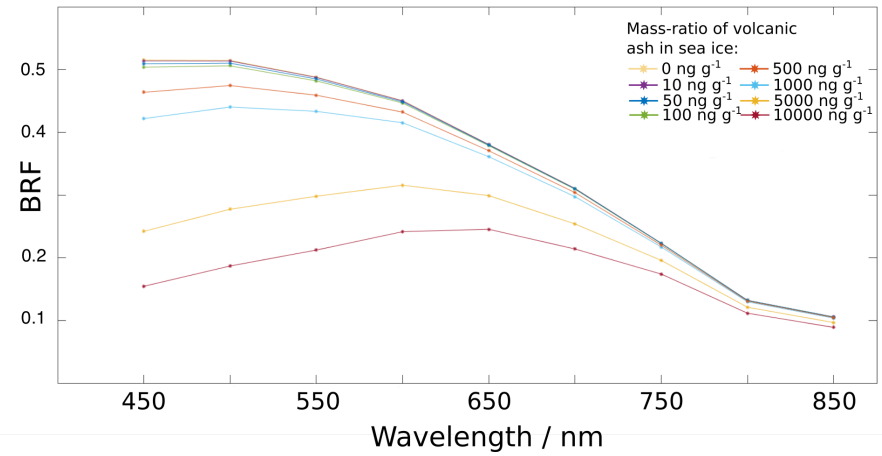

Figure 16. Nadir BRF of a clean sea ice layer with a varying mass-ratio of volcanic ash. The ice was modelled with a thickness of 50 cm, a underlying diffuse reflectance of 0.1, and a scattering coefficient of 300 m^{-1} for an illumination zenith angle of 60 ° and a wavelength range 400–850 nm. The mass-ratio of volcanic ash distributed throughout the sea ice was varied between 0 ng g^{-1} and 10000 ng g−1.

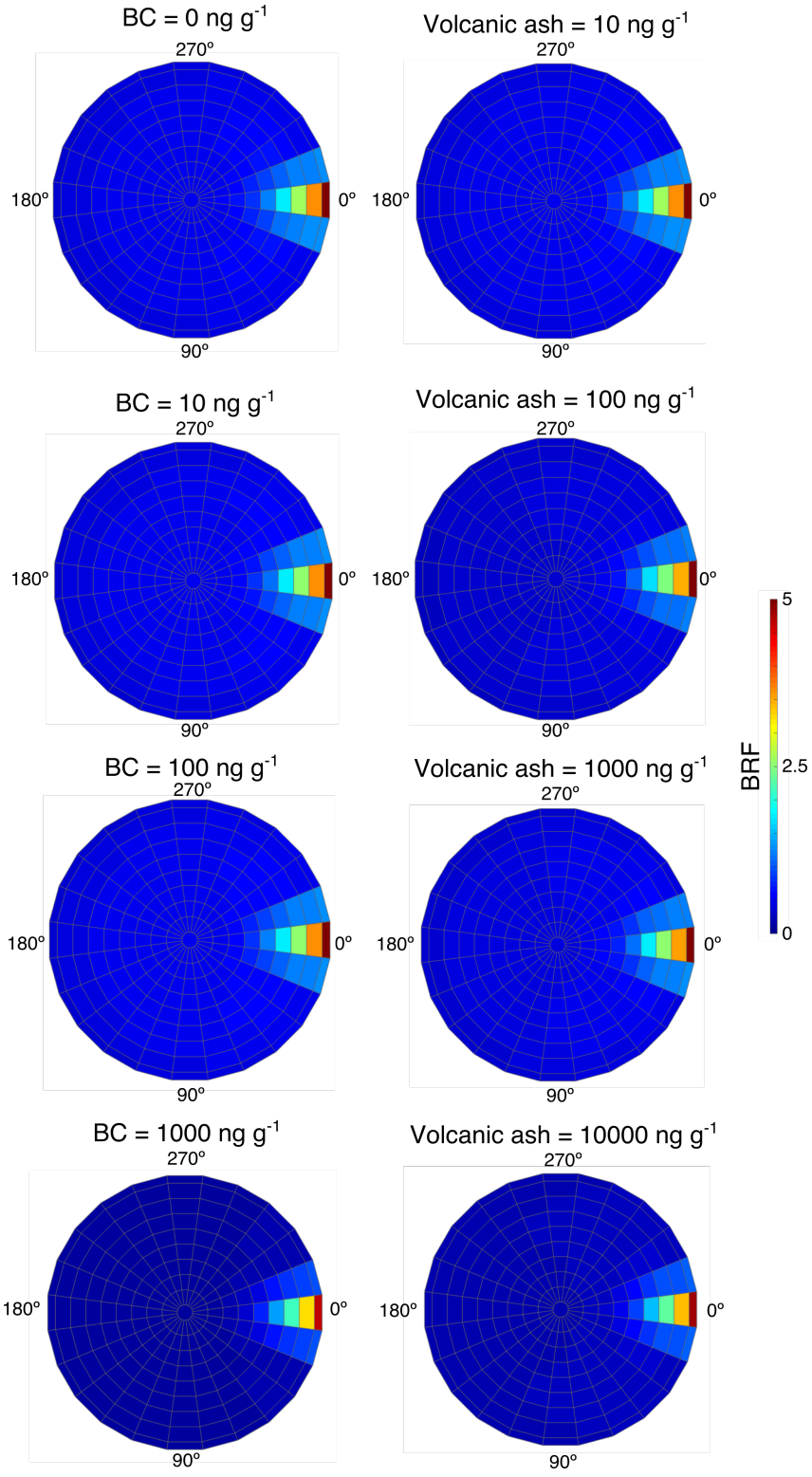

Figure 17. BRF of a clean sea ice layer with varying mass-ratios of black carbon and volcanic ash. A fixed sea ice layer was modelled with a thickness of 50 cm, a underlying diffuse reflectance of 0.1, and a scattering coefficient of 300 m^{-1} for an illumination zenith angle of 60 °. The results are presented here for a wavelength, λ = 550 nm. The mass-ratio of the black carbon was varied between 0 ng g^{-1} and 5000 ng g−1, and the mass-ratio of the volcanic ash was varied between 0 ng g^{-1} and 10000 ng g−1.

Supplementary information

Artificial sea ice thickness

The following figure shows the temperature profiles measured during each experiment in the sea ice laboratory, on the day the BRF measurements were performed. The plots are categorised by experiment with the blue lines representing the profile of the clean sea ice, and the red lines representing the temperature profile of the same clean sea ice with an additional 5 cm surface layer of impurity bearing sea ice. The horizontal dashed lines mark the change in gradient of the temperature profile, which was used as an indicator of the sea ice / seawater interface. The change in gradient of the profile is clearly marked for most of the measurements, defining the sea ice thickness. However, for profiles with a smoother transition (profile 4b, 5b, and 6a) between the linear temperatures in the seawater and the rapidly changing temperatures in the sea ice, the sea ice thickness was obtained with higher uncertainties. Indeed, the calculated sea ice thickness varies depending on the position of the transition considered to represent the water / ice interface. An example of the possible interpretations is plotted for experiment 5, where the sea ice thickness may lie between 42.0 and 49.5 cm. The average thicknesses of the upper and lower boundaries of the transition were used in the modelling study, presented in this chapter.

Note the unusual shape in the temperature profile for the experiment 4a. The temperature profile was measured after the BRF measurements was acquired. The blue line in the plot highlights the warmer surface of the sea ice owing to the heat generated by the tungsten-halogen lights.

FIGURE 7.1: Temperature profiles in the sea ice simulator tank for each BRF measurement.

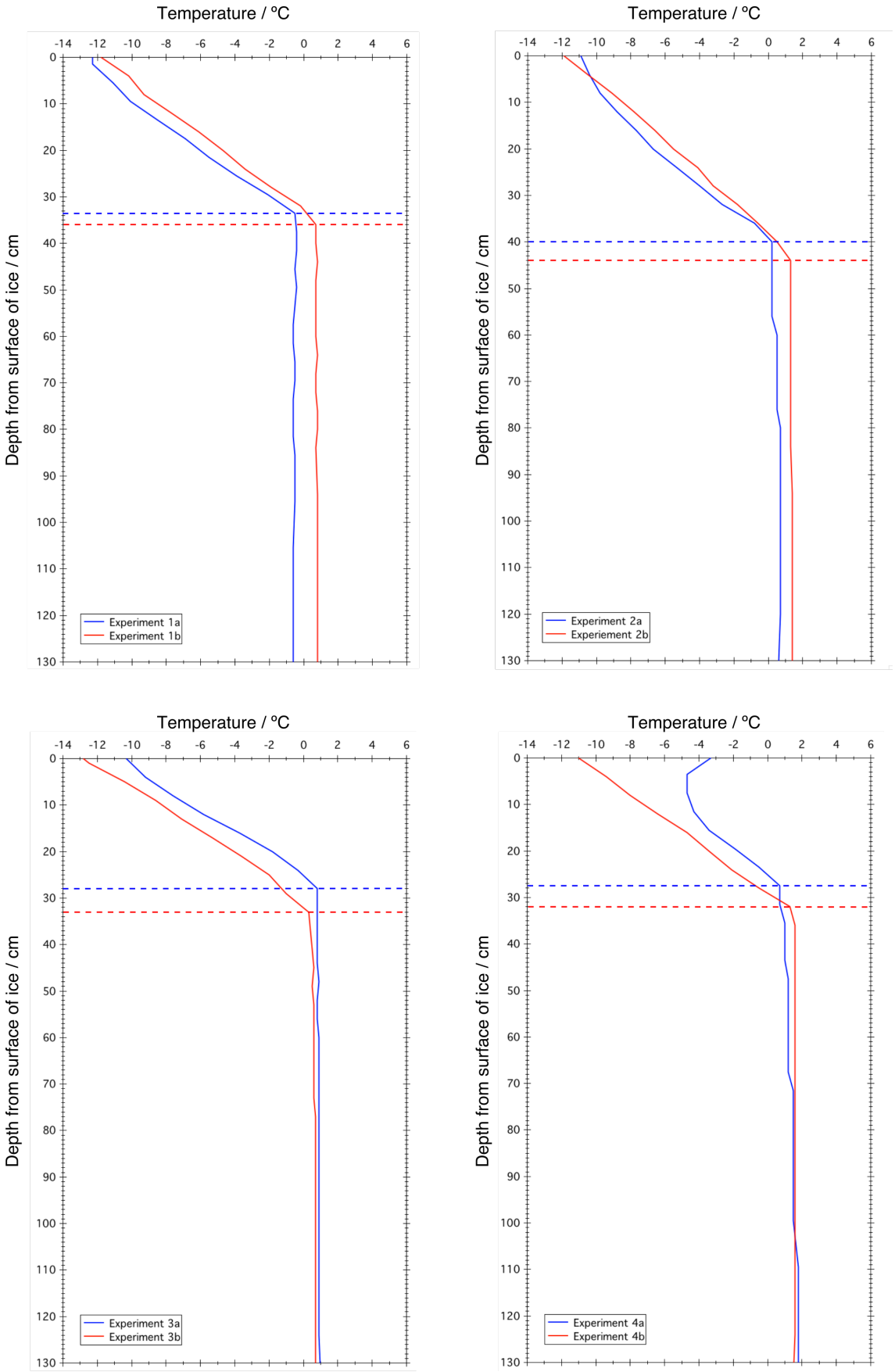

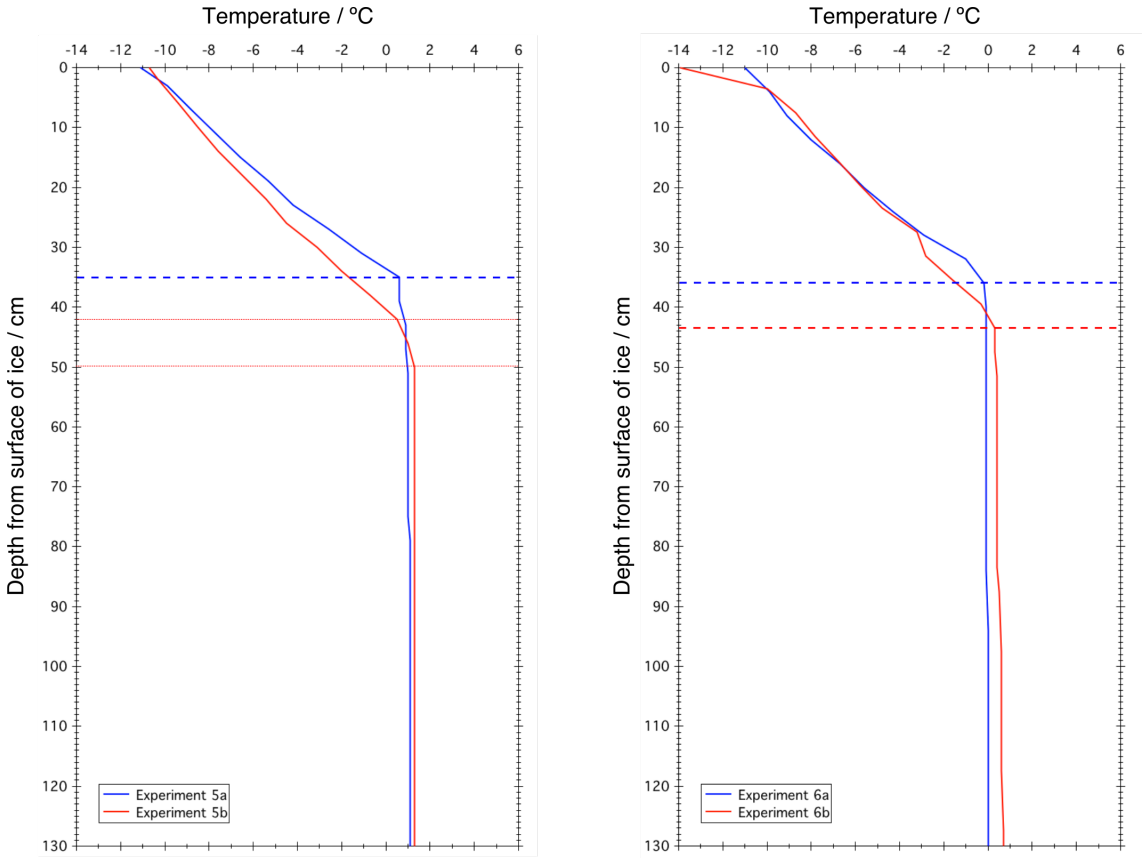
Temperature / °C
-14 -12 -10 -8 -6 -4 -2 0 2 4 6
0 10 20 30 40 50 60 70 80 90 100 110 120 130
Depth from surface of ice / cm
Experiment 5a
Experiment 5b
Temperature / °C
-14 -12 -10 -8 -6 -4 -2 0 2 4 6
0 10 20 30 40 50 60 70 80 90 100 110 120 130
Depth from surface of ice / cm
Experiment 6a
Experiment 6b

Chapter 8

Bidirectional reflectance measurements (HDRF) of thin first year sea ice at large solar zenith angles

Citation:
Lamare, M. L., Greenwell, C., Wang, F., King, M. D., & Fox, N. (2017). Bidirectional reflectance measurements (HDRF) of thin first-year sea ice at large solar zenith angles. In preparation for: Scientific Reports.

Author contributions:
Lamare, M. piloted the study, performed the experiments at the sea ice laboratory, did the data analysis, prepared the results and wrote the paper.

Greenwell, C. assisted with the experiments at the sea ice laboratory, and performed the data analysis of the ASD spectrometer.

Wang, F. was in charge of the sea ice facility in Winnipeg.

King, M.D. and Fox, N. oversaw the study, and proof-read the paper.

Bidirectional reflectance measurements (HDRF) of thin first-year sea ice at large solar zenith angles

Maxim L. Lamare[1,2], Claire Greenwell[2], Feiyue Wang[3], Martin D. King[1,*], and Nigel Fox[2]

[1]Royal Holloway University of London, Department of Earth Sciences, Egham, TW20 0EX, UK
[2]National Physical Laboratory, Teddington, TW11 0LW, UK
[3]University of Manitoba, Centre for Earth Observation Science, Winnipeg, MB R3T 2N2, Canada
[*]Corresponding author: m.king@es.rhul.ac.uk

ABSTRACT

Measurements of the Hemispherical Directional Reflectance Factor (HDRF) of 13 cm thick first-year sea ice were performed at the Sea-ice Environmental Research Facility (SERF) at the University of Manitoba, Canada. The HDRF data were acquired with the Gonio Radiometric Spectrometer System (GRASS) over a wavelength range of 400–1700 nm and over the viewing azimuth angles 0–360° and viewing zenith angles 0–60°. The measurements constitute the first full HDRF in-situ characterisation for bare first-year sea ice surfaces. The averaged HDRF was shown to be quasi-isotropic over the hemisphere, except for a strong forward scattering maxima (hotspot), centred over the solar zenith angle and 180° from the solar azimuth angle. The intensity of the HDRF measured at the hotspot were a factor of ten larger than at nadir over the measured wavelength range and showed less wavelength dependence than for nadir. Variations in the HDRF values outside the hotspot were negligible. The BRF of the first-year sea ice was simulated with the PlanarRad radiative-transfer model. By varying the parameters affecting reflectance in the sea ice and comparing the model outcomes to the measured data, a light scattering coefficient of 150 m^{-1} was determined for the sea ice at SERF, with particulate mass-ratios of 200 ng g^{-1} of black carbon and 10 mg m^{-3} of algae. The optical properties of the sea ice estimated with the model are typical of first year sea ice. The modelled BRF reproduced the measured HDRF pattern.

Introduction

Changes in the shortwave surface albedo of sea ice significantly impact the global climate system through the positive-feedback effect[1–4]. A shift in the type of sea ice present in the spring and summer in the Arctic, from thick multi-year sea ice to thin first-year sea ice has been observed over the past decades[5–7], impacting the energy budget of the sea ice cover. Indeed, the shortwave spectral albedo has been shown to be smaller for first-year sea ice than for multi-year sea ice[8–11], and the thinning of the ice[12–14] contributes to an increase in the absorption of solar radiation, as more light is transmitted through the ice[15] and absorbed by the underlying ocean. Observations of the drivers of radiative forcing are essential to provide insight into the rapid transformations on-going in polar regions[16–18]. Satellite remote sensing is widely used to monitor the temporal and spatial variability of the albedo of sea ice over vast polar expanses[19–23]. Although advances in remote sensing technology have facilitated the acquisition of multi-angular data[24], observations of the surface of the Earth are limited to a discrete number of narrow viewing geometries, defined by the solar zenith angle (SZA), the viewing zenith angle (VZA) and the relative azimuth angle between the sun and the sensor[25]. Owing to the anisotropy of the reflected radiation above sea ice[26], knowledge of the bidirectional reflectance distribution function (BRDF), which describes the angular distribution of reflectance, is necessary to normalise the radiance observed at different viewing angles and derive surface properties such as albedo. Field measurements of the angular reflectance provide empirical data that may be used as input parameters for BRDF models deriving surface albedo[27,28], or validate the performance of satellite BRDF algorithms[29,30].

In practise, field BRDF measurements are not achievable, as the definition of BRDF relies on radiance being measured with an infinitely small solid angle[31,32]. The bidirectional reflectance factor[32] (BRF) is a measurable quantity that is commonly used to describe the angular reflectance pattern of a surface. However, BRF relies on direct illumination only and does not account for the diffuse illumination provided by the atmosphere. Because of the technical difficulties linked to measuring BRF, field measurements report the hemispherical–directional reflectance factor (HDRF), which, for clear skies, provides an approximation for BRF[33]. HDRF, that accounts for direct and diffuse illumination can be expressed as[32]:

$$HDRF_\lambda(\theta_r,\phi_r,2\pi,\theta_i,\phi i) = \frac{L_\lambda(\theta_r,\phi_r,2\pi;\theta_i,\phi i)}{L_\lambda^{id}(\theta i,\phi i,2\pi)}, \quad (1)$$

where L_λ is the spectral radiant flux of the measurement surface and L_λ^{id} is the spectral radiant flux of an idea Lambertian target in the viewing azimuth angle ϕ_r and zenith angle θ_r, with the azimuth and zenith illumination angles, respectively ϕ_i and θ_i. Most instruments measuring reflectance anisotropy do so with a finite field of view, resulting in the hemispherical-conical reflectance factor (HCRF), described in Schaepman-Strub et al.[32](eq. 16). In this work, the radiance measure across the field of view of the sensor was considered isotropic and therefore measurements are referred to as HDRF[34,35]. The BRF / HDRF of snow on sea ice has been previously characterised through field measurements and modelling studies[36,37] and the BRF of bare sea ice has been modelled[38–40]. However, field measurements of the HDRF of bare sea ice, and in particular first-year sea ice are scarce[41,42].

In this study, the first complete HDRF measurements of thin first-year sea ice are presented. The HDRF acquisitions were carried out at the out at the Sea-ice Environmental Research Facility (SERF) located at the University of Manitoba, Winnipeg, Canada, using the Gonio RAdiometric Spectrometer System (GRASS). The physical properties of the sea ice observed during the measurements were used to simulate the BRF of first-year sea ice with a radiative-transfer model. By fitting the observational data, the scattering coefficient of the sea ice and impurities content (black carbon and algae) was derived.

Methods

Experimental site

SERF features an outdoor pool of 18.3 m long, 9.1 m wide and 2.6 m deep, filled with artificial seawater that replicates the chemical composition of natural seawater[53]. A detailed description of the facility can be found in Else et al[54]. Over the course of the experiment described in this study, the average water salinity recorded was 30.84 practical salinity units (PSU). The seawater in the pool is exposed to the ambient outdoor temperatures and freezes in the winter, forming sea ice. Measurements were performed during the second experiment of the 2016 campaign season, between the 16th February and 28th February 2016. The sea ice was formed from open water as of the 9th February 2016, when the heating system in the pool was turned off. At the start of the measurements, the ice in the SERF pool had grown to a thickness of 13 cm. Daily sea ice coring was performed, using a Kovacs Mark II coring system to assess the thickness of the sea ice. Owing to daily air temperature ranging from -11 to -0.18°C, the sea ice did not grow further, with an average thickness of 13.06 cm throughout the sampling campaign. A retractable roof was placed over the pool, during major snowfall events, to keep the sea ice snow-free for the duration of the measurements. A small snow fall event occurred on the 22nd February 2016, depositing approximately 0.5 cm of snow on the surface of the ice. The irregular deposition of snow was manually cleared the next day to maintain a bare sea ice surface. Because HDRF measurements require clear skies, acquisitions were limited by the atmospheric conditions. The sky conditions were monitored using a GoPro digital camera with a diagonal field-of-view of 149.2°. Only measurements without the presence of cumulus and less than 10% (visual assessment) cirrus were kept in this study. Because of a high number of overcast days, four complete sets of HDRF were measured over the duration of the experiment, on the 21st, 25th and 26th February 2016. The inter-calibration of the optics on GRASS (described in Instrumentation section) was destructive to the surface, therefore GRASS was displaced after each set of HDRF measurements. To avoid the influence of the sides of the pool, GRASS was kept as close to the centre of the pool as possible, whilst maintaining an untouched surface within the base ring of the goniometer.

Instrumentation

HDRF measurements were acquired out with a field goniometer, the Gonio RAdiometric Spectrometer System (GRASS)[55,56]. The structure of the goniometer is characterised by a hemispherical frame composed of three curved arms spaced apart by 30° and four structural arms for support. The upper part of the structure sits on a rail on a lower base ring of 2 m in radius and can be rotated by 360°. For the measurements in this study, four signal collectors were mounted on each curved arm at viewing zenith angles of 15, 40, 50 and 60°, and an additional signal collector was attached to the top of the hemisphere with an viewing zenith angle of 0°. Measurements were limited to a maximum 60° viewing zenith angle, as at higher zenith angles the elongated footprint would have included a section of the goniometer's base ring, corrupting the measurement. The signal collectors consist of a collimated lens with an 8° field of view, aimed at the centre of the goniometer's ring on the target surface. In the configuration described above, the footprint area of the nadir downward looking signal collector had an approximate diameter of 27.8 cm. The lenses were connected with optical fibres to a visible and shortwave infra-red (V-SWIR) spectrometer via a multiplexer. The custom built V-SWIR spectrometer system is composed of two separate spectrometers operating over the spectrum wavelength range 400 – 1700 nm with a spectral resolution of 1 nm. An Ocean Optics USB 2000+ spectrometer was used to measure incoming light between 400 and 969 nm, and a BWTEK Sol 1.7 spectrometer operated between 970 and 1700 nm . In order to correct for small changes in illumination conditions during the measurements, an upward looking integrating sphere was mounted on the top of the GRASS structure. The integrating sphere was connected to the spectrometer system with an optical fibre. A motorised mirror in the spectrometer, flipping between the signal from the integrating sphere and the multiplexer, allowed for a quasi-simultaneous measurement of the total downwelling irradiance for each angular surface

measurement. A further detailed description of GRASS can be found in Ball et al.[35] and Marks et al.[57].

Nadir sea water reflectance measurements were performed using an ASD FieldSpec portable spectral radiometer. A square section measuring 2 x 2 m, was cut out of the sea ice leaving the seawater exposed. Radiance measurements were made over the wavelength range 400 – 2400 nm, using an 8° field of view lens attached to the optical fibre. The lens was attached to the end of a 1m boom which was connected to a tripod, to avoid disturbance by the operator. The lens was placed at a height of 1m from the surface of the seawater over the centre of the hole in the ice. Although the height of the ASD lens was lower than GRASS nadir signal collector, measurements at multiple heights ranging between 25 cm and 1 m from water level showed a mean standard deviation of 1.05% in the visible and 2.43% in the shortwave infra-red. Thus, the height difference between the ASD and GRASS were not taken into account.

Field measurements and data processing

The HDRF of the sea ice at SERF was recorded in multiple steps. A single rotation was obtained from the 13 signal collectors over a period of 15 minutes, allowing a characterisation over a viewing azimuth angle of90° azimuth and a viewing zenith angle of 60°. The upper section of the structure was rotated four times over a sampling period of approximately 1 hour to achieve a complete HDRF set. However, because of the large solar zenith angles at the time of the measurements, the rotations were constrained by the shading of the structure on the measured surface of the sampling area, and the rotations were not carried out at equal intervals. Thereupon, measurements within 30° of the backward scattering solar principal plane (SPP) were not achieved. For each single rotation, four nadir measurements of the sea ice were obtained, producing twelve nadir measurements for each HDRF set. For each upwelling acquisition by the signal collectors, a downwelling irradiance measurement was obtained with the integration sphere, to account for variations in the atmospheric conditions, and the change in solar zenith angle. Measurements were performed close to solar noon to limit the effects of a changing solar zenith angle. The average variation in solar zenith angle was 0.14° for a full HDRF set performed at solar noon and 3.58° one hour after solar noon. The variation in solar azimuth angle was taken in account in the rotation of the structure. The change in solar azimuth angle over the period of a single rotation was less than 4° and considered within the azimuthal pointing accuracy of the instrument.
Preceding each full HDRF acquisition, the measurements were normalised against a pseudo lambertian reflector, as defined by equation 1. A Spectralon panel was placed on a horizontal frame across the base ring of GRASS. The structure allowed the panel to be aligned with the footprint of the nadir viewing signal collector at a constant surface level, without disrupting the target sea ice below. The 60 x 60 cm panel was approximately 20 cm above the surface of the sea ice. The radiance measured by the nadir signal collector was used to compute the HDRF for all the signal collectors, based on the assumption the the Spectralon panel was lambertian. Because the Spectralon panel was not perfectly lossless, a calibration was carried out at the National Physical Laboratory, UK using the National Reference Reflectometer (NRR). The absolutely calibrated spectrophotometer was used to evaluate the spectral reflectance of the Spectralon panel and provide a correction factor between 401 nm and 1001 nm. The correction factor was extrapolated over the full range of wavelengths measured by GRASS[35].
To account for the variations in the readings from each coupled signal collector / optical fibre, an inter-calibration of response from the signal collectors was realised after each HDRF set. The inter-calibration was performed by measuring the radiance from each signal collector against a stable light source[35] and dividing the raw target radiance measurements by the lamp's response. As the calibration process required the operators to enter the measurement area in order to access the signal collectors, GRASS had to be displaced to a new location on the sea ice surface after each calibration.
Following the previous steps, the HDRF was calculated as:

$$HDRF_{\lambda}(\theta_r, \phi r) = \left(\frac{\left(\frac{L^{raw}_{i,\lambda}(\theta_r, \phi r)}{L^{cal}_{i,\lambda}}\right)}{I_{r,\lambda}} \right) \frac{C_{f,\lambda}}{\left(\frac{L^{raw}_{id}}{L^{cal}_{nad,\lambda}}\right)}, \tag{2}$$

with L^{raw}_{i}, the raw surface radiance measured with each signal collector, L^{cal}_{i}, the radiance of the inter-calibration lamp measured for each signal collector, I_r the downwelling irradiance measured with the integrating sphere simultaneously with each upwelling radiance measurement, C_f, the Spectralon correction factor measured on the NRR, L^{raw}_{id}, the raw Spectralon panel radiance measured with the nadir signal collector and L^{cal}_{nad}, the radiance of the inter-calibration lamp measured with the nadir signal collector. In this study, the HDRF measurements are displayed using polar plots. For display purposes, the values were interpolated using the triangulation-based natural neighbour method. Where data was missing in the backscattering part of the the hemisphere, the HDRF was symmeterised.

Radiative-transfer modelling

The radiative-transfer calculations of the BRF of the sea ice were performed using PlanarRad[58]. PlanarRad is an open source radiative-transfer model that uses the invariant numerical integration technique to solve the radiative-transfer equations, based

on the algorithm described by Mobley[59]. A description of the parameters used by the model for sea ice can be found in Lamare et al.[40], who previously used PlanarRad to compute the BRDF of three types of characteristic bare sea ice as a function of surface roughness.
The scattering and absorption of light in sea ice are constrained in the model by the absorption coefficient, a, the attenuation coefficient α, the phase function, the solar zenith angle and the surface roughness. The solar zenith angle was fixed at 61.5°, to reproduce the mean sun angle during the measurements. The random surface roughness in the model[40] was fixed, with an elevation standard deviation of $\sigma = 1$ cm, to account for the estimated surface roughness at SERF. The Henyey-Greenstein phase function[60] was used to describe the directionality of the scattering within the sea ice. The asymmetry parameter, g, was fixed to a wavelength independent value of 0.98 for the sea ice in this study. The total absorption coefficient for the sea ice was calculated as:

$$\alpha_{total} = \alpha_{ice} + \alpha_{bc} + \alpha_{al}, \tag{3}$$

with α_{ice}, the absorption coefficient of pure ice, α_{bc}, the mass absorption coefficient of black carbon, and α_{al}, the mass absorption coefficient of algae. The absorption coefficient of pure ice was used for the sea ice, based on the values of Warren and Brandt[61]. The absorption coefficient of the black carbon was calculated using the mass absorption cross-section of black carbon[45], based on a black carbon particle size of 0.13 μm. For the purpose of this study, the mass-ratio of the black carbon in the sea ice was varied between 75 ng g^{-1} and 200 ng g^{-1}. The absorption coefficient of algae was calculated using chlorophyll a (Chl-a) measurements as a proxy for algae. The absorption cross-section of chlorophyll a (Chl-a) for the bottom 10 cm of sea ice was obtained from Mundy et al.[44] and mass concentrations of algae in the sea ice were varied between 1 mg m^{-3} and 50 mg m^{-3}.
The attenuation coefficient of the sea ice was expressed as:

$$A = \alpha_{total} + s, \tag{4}$$

with α_{total}, the total absorption coefficient described in equation 1, and s, the scattering coefficient. The scattering coefficient of sea ice was varied between realistic values to fit the observed data.

In order to model the field observations at SERF, a layer of 13 cm of sea ice was placed on an underlying optically thick layer of water. The diffuse reflectance of the water under the sea ice was obtained from the ASD measurements (described in the Instrumentation section). The parameter space was explored by varying the values of the scattering coefficient of the ice, whislt the black carbon mass-ratio and the algae content were varied. In a first step the averaged nadir HDRF measurements of the sea ice were reproduced by performing a visual fit, assessing the sensitivity of the parameters. In a second step, a chi-square test for goodness of fit was calculated for the different combinations of parameters to determine the best fit. The quantity of the chi-square used here is described by:

$$\chi^2 = \sum \frac{(O_i - C_i)^2}{\sigma_i^2}, \tag{5}$$

with O the observed data and C the modelled data at a wavelength i, and σ, the standard deviation of the observed data. Chi-square values were assessed for a range of scattering coefficients between 70 and 190 m^{-1}. For each scattering coefficient, a mass-ratio of black carbon of 75, 100, 150 and 200 ng g^{-1} was placed in the sea ice, with mass-ratios of 1, 10, 25 and 50 mg m^{-3} of algae. The combination of values yielding the lowest chi-square value were considered to best describe the observed sea ice parameters.

Results

HDRF measurements

A total of four full HDRF acquisitions were obtained during the field campaign. Further HDRF measurements were discarded owing to overcast sky illumination conditions, as measurements of the HDRF require clear skies. For a comparison with the radiative-transfer modelling, the HDRF sets were averaged, producing a representative HDRF of the sea ice conditions observed at SERF.

Nadir measurements

The average nadir for each HDRF set is shown in figure 2 a. The plotted HDRF nadirs are formed of 12 averaged nadir measurements acquired over four rotations. The plotted spectra display a strong wavelength dependance, with the nadir HDRF decreasing with between 575 and 1200 nm, owing to the absorption of ice dominating the signal at higher wavelengths. In the

visible wavelengths, the nadir HDRF decreases sharply as the wavelength decreases between 550 and 400 nm. The spectral albedo of young ice has been shown to be flat between 400 and 600 nm[43]. The observed trend for all nadir spectra suggests the presence of light-absorbing impurities in the sea ice. Indeed, Chlorophyll-*a* has a strong absorption between 400 and 700 nm, with very little absorption above 720 nm[44]. Additionally, the absorption of black carbon decreases with an increasing wavelength[45], which associated with the higher absorption of sea ice at longer wavelengths, makes the sea ice more sensitive to black carbon in the visible. Although the values of HDRF are much lower for the thin first-year sea ice observed at SERF, the spectral shape of the nadir HDRF is in agreement with measurements found in the literature: the overall decreasing values with larger wavelengths and a secondary maxima peaking at 1100 nm have been previously observed[10,46].

Nadir measurements of the sea ice surface show little variation over the duration of the field campaign. In the visible part of the spectrum, the error bars are larger than for the infrared. The observed difference was caused by the sensitivity difference between the two spectrometers in GRASS rather than a physical effect in the sea ice. Although the small difference observed between the HDRF measurements obtained on the 21st February 2016 and the measurements obtained on the 25th and 26th February 2015 could be explained by the light snowfall event that was subsequently removed on the 22nd February 2016, and therefore a change in the optical properties of the sea ice, most of the measurements lie within the 2 standard deviations error bar. Furthermore, the small variation in nadir HDRFs (approximately 0.01 across the visible) was considered to be negligible and consequently, for the purpose of this study, the conditions of the sea ice are considered identical throughout the campaign. Although the spectrometer recorded a signal above 1250 nm, the intensity of the HDRF was considered too low to be detected by the instrument and values above zero were considered as noise.

The average nadir HDRF over the measurement campaign is shown in figure 2 b, for comparison with the modelling results. The average nadir measurement is considered to be representative of the sea ice at SERF over the duration of the field campaign.

HDRF of first year sea ice

The polar plots of the averaged HDRF of the first year sea ice at SERF are shown in figure 3 for wavelengths 450, 600, 750, 900, 1050 and 1200 nm. The illumination azimuth angle of the sun was fixed at 180° out of convenience, meaning that the section of the plot between 90° and 270° represents the backscattering part of the hemisphere and the section between 270° and 90° represents forward scattering. The radius of the polar plot represents the viewing zenith angle, here plotted from 0° to 60°. The average solar zenith angle for all the plots was $61.57° \pm 0.43$ (1SD).

At all wavelengths, the HDRF of sea ice shows no significant departure from uniformity across the hemisphere, except for a strong forward scattering hotspot and is quasi-symmetrical along the solar principal plane. At 600 nm, the values outside the forward scattering peak vary by a maximum of 0.12 and a maximum of 0.047 at 1200 nm.The hotspot is centralised over the solar principal plane axis, spreading approximately across 30° in azimuth, with significantly larger values close to a viewing zenith angle of 60°, where the values of the HDRF are a factor of 10 higher than at nadir. The hotspot is observable at all wavelengths and the relative pattern of the HDRF has very little wavelength dependence. The values across the lambertian-like part of the hemisphere vary consistently with the nadir as a function of wavelength, as shown in figure 2. However, the hotspot varies to a lesser extent, maintaining large values across the range of wavelengths: at 1200 nm, the nadir HDRF is 99.32% lower than the value measured at 600 nm, whereas the HDRF only decreased by 11.04% for the strongest part of the hotspot over the same wavelength step. The anisotropic pattern of the HDRF of the first year sea ice observed at SERF is in good agreement with the measured BRF of melt season sea ice[37,41] found in the literature.

Modelling the BRF of sea ice

The BRF of sea ice was computed with a radiative-transfer model, using the physical properties of the measured sea ice as inputs. The scattering coefficient and impurities content in the sea ice were varied to reproduce the measured HDRF at nadir. Using the derived optical properties of the sea ice, the BRF and HDRF were compared.

Nadir fit

The modelled BRF values from the central nadir quad in PlanarRad were compared to the average nadir HDRF shown in figure 2 b. Figure 1 presents the calculated chi-square goodness of fit between the modelled BRF and measured HDRF as a function of the sea ice scattering coefficient, for varying mass loadings of black carbon and algae. The lowest chi-square number was considered to represent the best combination of parameters explaining the BRF of the observed sea ice. For all the different combinations of black carbon and algae mass-ratios, the chi-square values are distributed in a bowl shape, with a minima for the scattering coefficient located between 110 and 150 m^{-1}. The lower values of chi-square, between 110 and 150 m^{-1} show little variation, with no clear minima. The slightly flat minima indicates a lack of sensitivity of chi-square to the different combination of black carbon and algae. Therefore the scattering value of the observed first-year sea ice is considered to be between 110 and 150 m^{-1}. To fit the HDRF measurements, the combination of parameters yielding the lowest chi-square value were picked. In this study, a scattering coefficient of 150 m^{-1}, with a mass-ratio of 200 ng g^{-1} of black carbon and 10 mg m^{-3} of algae produced the best fit of the averaged nadir HDRF.

Figure 2 b shows the modelled wavelength dependent nadir BRF spectra, plotted with the nadir HDRF obtained at SERF. To limit computational resources, the BRF was calculated with a wavelength step of 100 nm. A comparison of the spectra at nadir shows a good agreement between the model results and the observations, with all the modelled points being within 2 standard deviations of the average nadir. Although the overall wavelength dependence at nadir is well reproduced, the model underestimates the secondary maxima at 1100 nm, and overestimates values between 600 and 800 nm by approximately 20%. The shape of the nadir HDRF spectrum at shorter wavelengths is correctly simulated by the model.

Comparison with HDRF

The BRF of first-year sea ice modelled with the parameters described in the previous section are compared to the averaged HDRF measurements of the sea ice surface at SERF in figure 4 for the wavelengths 400, 600, 800 and 1000 nm.. To enable the comparison of the quad averaged modelled BRF and the HDRF measurements performed at discrete points over the hemisphere, the HDRF shown in figure 4, was obtained by averaging the measurements over quads identical to the output of PlanarRad. For an easier comparison, the BRF colour scale was set to the same as the HDRF scale. Because measurements were not carried out above 60° VZA, the quads containing no data were left blank for the HDRF results. PlanarRad was used to compute the BRF over the entire hemisphere, therefore the BRF values are shown for all the quads for completeness.

The modelled BRF exhibits a similar pattern to the measured HDRF. The BRF of the modelled first-year sea ice is almost lambertian across the hemisphere, except for a forward scattering peak located in the same part of the hemisphere as for the HDRF measurements. However, the scattering peak of the BRF is narrower at the quad centered over 50° VZA and the values for the quads centered at 60 ° VZA and located at 15° in azimuth on each side of the solar principal plane are lower for the BRF than the HDRF. Additionally, the hotspot extends over larger viewing zeniths angles for the modelled BRF, but cannot be compared with the measurements owing to the lack of measurements at higher viewing zenith angles. The BRF and HDRF show a similar near symmetry along the solar principal plane at all wavelengths. The BRF of sea ice follows the same darkening trend for the quasi-lambertian part of the hemisphere between 600 and 1000 nm, as observed for nadir in figure 2. Furthermore, hotspot values decrease slower than the isotropic values on the hemisphere with an increasing wavelength, as it was shown in figure 3 for the HDRF measurements.

In figure 5, the comparison between the modelled BRF and measured HDRF over the solar principal plane, highlights the differences between the two quantities as a function of viewing zenith angle. Results are reported for the wavelengths 400, 600, 800 and 1000 nm. At all wavelengths, the model outputs and measurements show a good agreement between -40° VZA (equivalent to 40° VZA, 180° VAA on the polars plots) and +30° VZA (equivalent to 30° VZA and 0° VAA on the polars plots). For wavelengths at 400 and 600 nm, the measurements show a slight increase in HDRF for larger zenith angles in the backscatter direction, that the model did not predict. However, because of the shading of the instrument, measurements of the backscattering solar principal plane were not performed and the values presented in figure 5 were interpolated. For smaller viewing zenith angles, the interpolated values are considered to be representative, because of the proximity of measurement points on the hemisphere. However, for larger zenith angles, the interpolated values may be considered as artefacts. In the forward scattering part of the hemisphere, the model underestimates the BRF at 40° VZA but the values are within 0.1 of the measurements. Inversely, at 50° VZA, the model overestimates the BRF in comparison to HDRF for shorter wavelengths, and shows a close agreement for longer wavelengths. At the forward scattering maxima (60° VZA), the BRF values are largely overestimated, being a factor of 7 to 11 higher than the HDRF measurements.

Discussion and Conclusions

The HDRF of thin first year sea ice shows a uniform reflectance across the hemisphere, with a strong anisotropic foreword scattering peak, approximately located around the same zenith angle as the illumination from the sun. For the solar zenith angles reported in this study, which are representative of arctic spring conditions (60° SZA), the forward scattering hotpot is located around 60° VZA, and for VZAs lower than 45°, the sea ice may be assumed to have lambertian properties. Therefore, for the normalisation of multi-angular satellite remote sensing measurements of first-year sea ice, corrections for the anisotropic reflectance can be ignored outside the forward scattering peak direction. In the case presented here, with a SZA of 60°, measurements under 45° VZA or located at an azimuth further than 30° from each side of the forward solar principal plane do not require normalisation. Nevertheless, for satellite products requiring the characterisation of the distribution of reflectance across the entire hemisphere, such as albedo products, the knowledge of the location, size and strength of the forward scattering peak is essential. The field measurements of the sea ice surface at SERF were performed to provide detailed knowledge about the anisotropy of first-year sea ice for the remote sensing and climate modelling community. The meteorological conditions at the time of the field campaign were a limiting factor and only a preliminary characterisation of the HDRF of first-year sea ice was achieved. Hence, the authors recommend more extensive future field campaigns, to provide measurements of the HDRF for a wider variety of sea ice types and thicknesses. To overcome the limitations of this study and provide insight on the angular reflectance of sea ice for a wider range of conditions, the measurements were used to validate a BRF radiative-transfer model.

The modelling section of this study shows that the anisotropy of the reflectance of the first year sea was reproducible with radiative-transfer calculations. Furthermore, using measured physical parameters as input parameters, the model was used to determine the optical properties of the sea ice. The scattering coefficient of the sea ice at SERF was estimated to be between values of 110 and 150 m^{-1}, with a best fit at 150 m^{-1}. The range of values considered in this are consistent with scattering coefficients for first year sea ice found in the literature []. The scattering coefficient isn't sensitive to the mass-ratio of black carbon or algae in the sea ice between 110 and 150 m^{-1}. However the values are inter-dependent to explain the shape of the spectra of HDRF at nadir. The modelling study presented here shows that a scattering coefficient of 150 m^{-1} with a mass-ratio 200 ng g^{-1} of black carbon and 10 mg m^{-3} of algae, provide the best parameters to fit the observed data. Although the mass-ratio of black carbon is high, the value wasn't considered unrealistic. Global modelling of black carbon in snow reports concentrations between 100 ng g^{-1} and 200 ng g^{-1} for a 2.8° x 2.8° cell over Winnipeg[47]. Although measurements of black carbon mass-ratios deposited in snowpacks across Canada[48] found much lower values averaging between 19 and 22 ng g^{-1}, higher values of back carbon are not uncommon in urban or industrialised areas[49]. Furthermore, the sea ice facility is located on the campus of the university of Manitoba, close to car parking areas, and a major highway is located approximately 1 kilometre from the sea ice facility, the associated vehicle traffic being a major source of black carbon emissions[50]. A value of 10 mg m^{-3} of Chl-*a* is reasonable with quantities commonly observed in sea ice[51,52]. For modelling purposes, the algae was considered to be uniformly distributed throughout the sea ice and vertical variations of algae concentration were not taken into account, as such assumptions have been shown not to effect the Nadir reflectivity**?**.

The modelling of the first-year sea ice at SERF was able to describe the HDRF / BRF pattern over the hemisphere, as well as providing a good fit for the HDRF values of the isotropic part of the hemisphere. However, a discrepancy was observed between PlanarRad results and the observed data in the forward scattering peak, where the model consistently overestimated the values of HDRF. The quad with the highest HDRF value, centered over a viewing zenith angle of 60° on the solar principal plane, was approximately a factor of 7 higher than the measurements, for all wavelengths. A possible explanation for the differences between the modelled and observed data is that PlanarRad averages the BRF values over discrete segments of the hemisphere. Therefore, the value of the forward scattering peak in the quad centered over 60° VZA and 0° VAA, is an average of the values located between 55 and 65° VZA and between 352.5 and 7.5° VAA. The compared HDRF measurements were limited to the 60° VZA signal collector, and therefore when the data is represented as quads to match the PlanarRad output, the HDRF of the forward scattering peak is under-estimated. Furthermore, as shown in the results, the forward scattering maxima is located on the edge of the measured part of the hemisphere, and has not been entirely captured by the instrument. Indeed, the modelling results suggest that the hotspot extends up to 75° VZA, which was not recorded with GRASS. For a further characterisation of the forward scattering hotspot at high solar zenith angles, the authors recommend measurements with a field goniometer that can perform measurements at higher viewing zenith angles. A second explanation for the discrepancy between PlanarRad and GRASS outputs, is that although the HDRF was considered to be an approximation of BRF, the quantities measured differ[32]. The difference in the forward scattering peak values may be explained by the difference in the ratio of diffuse to direct illumination between the two quantities, as a higher ratio of diffuse to direct illumination causes the angular reflectance maxima to be smoothed out[32]. For the measurements to be useful for remote sensing purposes, the field measurements should corrected for atmospheric effects using an additional radiative-transfer code.

The results presented in this study provide the first field measurements of the HDRF of thin first-year sea ice. Radiative-transfer modelling of the solar radiation for the same sea ice conditions generally shows a good agreement with the measurements. However, large differences in values are observed for the forward scattering peak, which could be explained by the difference in the definitions of measured and modelled quantities. However, the overall pattern of the angular reflectance of sea ice is well reproduced. Although further in-situ work is required, the results presented here allow to estimate the extent of the bias introduced by the anisotropy of sea ice on multi-angular satellite measurements and contribute to better retrievals of albedo over sea ice.

Acknowledgements

M.L.L. and C.G. thank Dave Binne for his assistance at SERF. M.D.K. and M.L.L. thank NERC for support under Grant NE/K000770X/1. The authors would like to thank NERC FSF for the equipment loan (662.1112).

Author contributions statement

M.L.L. and M.D.K. conceived the experiment, M.L.L. and C.G. conducted the experiment and analysed the results. M.L.L. was the primary author of the paper. All authors reviewed the manuscript.

Additional information

The authors declare no competing financial interests.

References

1. Ebert, J. A. C. . J. L. S. . E. E. Sea Ice-Albedo Climate Feedback Mechanism. *Journal of Climate* **8**, 240–247 (1995). DOI 10.1175/1520-0442(1995)008¡0240:SIACFM¿2.0.CO;2.
2. Holland, M. M. & Bitz, C. M. Polar amplification of climate change in coupled models. *Climate Dynamics* **21**, 221–232 (2003). DOI 10.1007/s00382-003-0332-6.
3. Hall, A. The role of surface albedo feedback in climate. *Journal of Climate* **17**, 1550–1568 (2004). DOI 10.1175/1520-0442(2004)017¡1550:TROSAF¿2.0.CO;2.
4. Perovich, D. K. *et al.* Increasing solar heating of the arctic ocean and adjacent seas, 1979–2005: Attribution and role in the ice-albedo feedback. *Geophysical Research Letters* **34**, n/a–n/a (2007). DOI 10.1029/2007GL031480.
5. Fowler, C., Emery, W. J. & Maslanik, J. Satellite-derived evolution of arctic sea ice age: October 1978 to march 2003. *IEEE Geoscience and Remote Sensing Letters* **1**, 71–74 (2004). DOI 10.1109/LGRS.2004.824741.
6. Nghiem, S. V. *et al.* Rapid reduction of arctic perennial sea ice. *Geophysical Research Letters* **34** (2007). DOI 10.1029/2007GL031138.
7. Galley, R. J. *et al.* Replacement of multiyear sea ice and changes in the open water season duration in the beaufort sea since 2004. *Journal of Geophysical Research: Oceans* **121**, 1806–1823 (2016). DOI 10.1002/2015JC011583.
8. Grenfell, T. C. & Maykut, G. A. The optical properties of ice and snow in the Arctic Basin. *Journal of Glaciology* **18**, 445–463 (1977).
9. Barry, R. G. The parameterization of surface albedo for sea ice and its snow cover. *Progress in Physical Geography* **20**, 63–79 (1996). DOI 10.1177/030913339602000104.
10. Perovich, D. K. The optical properties of sea ice. Tech. Rep., DTIC Document (1996).
11. Perovich, D. K. & Polashenski, C. Albedo evolution of seasonal arctic sea ice. *Geophysical Research Letters* **39**, n/a–n/a (2012). DOI 10.1029/2012GL051432.
12. Rothrock, D. A., Yu, Y. & Maykut, G. A. Thinning of the arctic sea-ice cover. *Geophysical Research Letters* **26**, 3469–3472 (1999). DOI 10.1029/1999GL010863.
13. Haas, C. *et al.* Reduced ice thickness in arctic transpolar drift favors rapid ice retreat. *Geophysical Research Letters* **35**, n/a–n/a (2008). DOI 10.1029/2008GL034457.
14. Kwok, R. & Rothrock, D. A. Decline in arctic sea ice thickness from submarine and icesat records: 1958–2008. *Geophysical Research Letters* **36**, n/a–n/a (2009). DOI 10.1029/2009GL039035.
15. Perovich, D. K. On the aggregate-scale partitioning of solar radiation in arctic sea ice during the surface heat budget of the arctic ocean (sheba) field experiment. *Journal of Geophysical Research: Oceans* **110**, n/a–n/a (2005). DOI 10.1029/2004JC002512.
16. Stroeve, J. C. *et al.* Tracking the arctic's shrinking ice cover: Another extreme september minimum in 2004. *Geophysical Research Letters* **32**, n/a–n/a (2005). DOI 10.1029/2004GL021810.
17. Stroeve, J., Holland, M. M., Meier, W., Scambos, T. & Serreze, M. Arctic sea ice decline: Faster than forecast. *Geophysical Research Letters* **34**, n/a–n/a (2007). DOI 10.1029/2007GL029703.

18. Serreze, M. C., Holland, M. M. & Stroeve, J. Perspectives on the arctic's shrinking sea-ice cover. *Science* **315**, 1533–1536 (2007). DOI 10.1126/science.1139426. http://science.sciencemag.org/content/315/5818/1533.full.pdf.

19. Xiong, X., Stamnes, K. & Lubin, D. Surface albedo over the arctic ocean derived from avhrr and its validation with sheba data. *Journal of Applied Meteorology* **41**, 413–425 (2002). DOI 10.1175/1520-0450(2002)041¡0413:SAOTAO¿2.0.CO;2.

20. Wang, X. & Key, J. R. Arctic surface, cloud, and radiation properties based on the avhrr polar pathfinder dataset. part i: Spatial and temporal characteristics. *Journal of Climate* **18**, 2558–2574 (2005). DOI 10.1175/JCLI3438.1.

21. Riihelä, A., Manninen, T., Laine, V., Andersson, K. & Kaspar, F. Clara-sal: a global 28 yr timeseries of earth's black-sky surface albedo. *Atmospheric Chemistry and Physics* **13**, 3743–3762 (2013). DOI 10.5194/acp-13-3743-2013.

22. Riihelä, A., Manninen, T. & Laine, V. Observed changes in the albedo of the arctic sea-ice zone for the period 1982-2009. *Nature Clim. Change* **3**, 895–898 (2013).

23. Pistone, K., Eisenman, I. & Ramanathan, V. Observational determination of albedo decrease caused by vanishing arctic sea ice. *Proceedings of the National Academy of Sciences* **111**, 3322–3326 (2014). DOI 10.1073/pnas.1318201111.

24. Diner, D. J. *et al.* New directions in earth observing: Scientific applications ofmultiangle remote sensing. *Bulletin of the American Meteorological Society* **80**, 2209–2228 (1999). DOI 10.1175/1520-0477(1999)080¡2209:NDIEOS¿2.0.CO;2.

25. Luo, Y., Trishchenko, A. P., Latifovic, R. & Li, Z. Surface bidirectional reflectance and albedo properties derived using a land cover–based approach with moderate resolution imaging spectroradiometer observations. *Journal of Geophysical Research: Atmospheres* **110**, n/a–n/a (2005). DOI 10.1029/2004JD004741.

26. Schlosser, E. Optical studies of antarctic sea ice. *Cold Regions Science and Technology* **15**, 289–293 (1988). DOI http://dx.doi.org/10.1016/0165-232X(88)90075-4.

27. Strugnell, N. C. & Lucht, W. An algorithm to infer continental-scale albedo from avhrr data, land cover class, and field observations of typical brdfs. *Journal of Climate* **14**, 1360–1376 (2001). DOI 10.1175/1520-0442(2001)014¡1360:AATICS¿2.0.CO;2.

28. Li, X., Gao, F., Wang, J. & Strahler, A. A priori knowledge accumulation and its application to linear brdf model inversion. *Journal of Geophysical Research: Atmospheres* **106**, 11925–11935 (2001). DOI 10.1029/2000JD900639.

29. Wanner, W. *et al.* Global retrieval of bidirectional reflectance and albedo over land from eos modis and misr data: Theory and algorithm. *Journal of Geophysical Research: Atmospheres* **102**, 17143–17161 (1997). DOI 10.1029/96JD03295.

30. Susaki, J. *et al.* Validation of temporal brdfs of paddy fields estimated from modis reflectance data. *IEEE Transactions on Geoscience and Remote Sensing* **42**, 1262–1270 (2004). DOI 10.1109/TGRS.2004.826798.

31. of Standards, U. S. N. B. & Nicodemus, F. E. *Geometrical considerations and nomenclature for reflectance*, vol. 160 (US Department of Commerce, National Bureau of Standards, 1977).

32. Schaepman-Strub, G., Schaepman, M. E., Painter, T. H., Dangel, S. & Martonchik, J. V. Reflectance quantities in optical remote sensing—definitions and case studies. *Remote Sensing of Environment* **103**, 27–42 (2006). DOI http://dx.doi.org/10.1016/j.rse.2006.03.002.

33. Abdou, W. A. *et al.* Ground measurements of surface brf and hdrf using parabola iii. *Journal of Geophysical Research: Atmospheres* **106**, 11967–11976 (2001). DOI 10.1029/2000JD900654.

34. Bourgeois, C. S., Calanca, P. & Ohmura, A. A field study of the hemispherical directional reflectance factor and spectral albedo of dry snow. *Journal of Geophysical Research: Oceans* **111**, D20108 (2006).

35. Ball, C. P., Marks, A. A. & Green, P. D. Hemispherical-Directional Reflectance (HDRF) of windblown snow-covered Arctic tundra at large solar zenith angles. *Geoscience and Remote Sensing, IEEE Transactions on* (2015).

36. Li, S. & Zhou, X. Modelling and measuring the spectral bidirectional reflectance factor of snow-covered sea ice: an intercomparison study. *Hydrological processes* **18**, 3559–3581 (2004).

37. Arnold, G. T., Tsay, S. C., King, M. D., Li, J. Y. & Soulen, P. F. Airborne spectral measurements of surface-atmosphere anisotropy for arctic sea ice and tundra. *International Journal of ...* **23**, 3763–3781 (2010).

38. Jin, Z. & Simpson, J. J. Bidirectional anisotropic reflectance of snow and sea ice in AVHRR Channel 1 and 2 spectral regions. I. Theoretical analysis. *IEEE Transactions on Geoscience and Remote Sensing* **37**, 543–554 (1999).

39. Stamnes, K. *et al.* Modeling of radiation transport in coupled atmosphere-snow-ice-ocean systems. ... *and Radiative Transfer* **112**, 714–726 (2011).

40. D., M. L. L. . J. H. . K. M. The effects of surface roughness on the spectral (300 – 1400 nm) bidirectional reflectance distribution function (BRDF) of sea ice. *In preparation* (2017).

41. Perovich, D. K. Light reflection from sea ice during the onset of melt. *Journal of Geophysical Research: Oceans* **99**, 3351–3359 (1994). DOI 10.1029/93JC03397.

42. Zhou, X. & Li, S. Comparison between in situand MODIS-derived spectral reflectances of snow and sea ice in the Amundsen Sea, Antarctica. *International Journal of . . .* **24**, 5011–5032 (2003).

43. Allison, I., Brandt, R. E. & Warren, S. G. East Antarctic sea ice: Albedo, thickness distribution, and snow cover. *Journal of Geophysical Research: Oceans* **98**, 12417–12429 (1993).

44. Mundy, C. J. *et al.* Characteristics of two distinct high-light acclimated algal communities during advanced stages of sea ice melt. *Polar Biology* **34**, 1869–1886 (2011).

45. Dang, C., Brandt, R. E. & Warren, S. G. Parameterizations for narrowband and broadband albedo of pure snow and snow containing mineral dust and black carbon. *Journal of Geophysical . . .* **120**, 5446–5468 (2015).

46. Gerland, S., Winther, J.-G., Ørbœk, J. B. & Ivanov, B. V. Physical properties, spectral reflectance and thickness development of first year fast ice in Kongsfjorden, Svalbard. *Polar Research* **18**, 275–282 (1999).

47. Skeie, R. B. *et al.* Black carbon in the atmosphere and snow, from pre-industrial times until present. *Atmospheric Chemistry and Physics* **11**, 6809–6836 (2011).

48. Doherty, S. J., Dang, C., Hegg, D. A., Zhang, R. & Warren, S. G. Black carbon and other light-absorbing particles in snow of central North America. *Journal of Geophysical . . .* **119**, 12,807–12,831 (2014).

49. Wang, X., Doherty, S. J. & Huang, J. Black carbon and other light-absorbing impurities in snow across Northern China. *Journal of Geophysical . . .* **118**, 1471–1492 (2013).

50. Bond, T. C. *et al.* Bounding the role of black carbon in the climate system: A scientific assessment. *Journal of Geophysical . . .* **118**, 5380–5552 (2013).

51. Gosselin, M., Levasseur, M., Wheeler, P. A., Horner, R. A. & Booth, B. C. New measurements of phytoplankton and ice algal production in the Arctic Ocean. *Deep Sea Research . . .* **44**, 1623–1644 (1997).

52. Norman, L. *et al.* The characteristics of dissolved organic matter (DOM) and chromophoric dissolved organic matter (CDOM) in Antarctic sea ice. *Deep Sea Research . . .* **58**, 1075–1091 (2011).

53. Rysgaard, A. H. . F. W. . D. B. . N.-X. G. . R. G. . S. pH evolution in sea ice grown at an outdoor experimental facility. *Marine Chemistry* **154**, 46 – 54 (2013). DOI http://dx.doi.org/10.1016/j.marchem.2013.04.007.

54. Else, B. G. T. *et al.* Under-ice eddy covariance flux measurements of heat, salt, momentum, and dissolved oxygen in an artificial sea ice pool. *Cold Regions Science . . .* **119**, 158–169 (2015).

55. Milton, H. P. . N. F. . M. C. . E. Design and testing a new instrument to measure the angular reflectance of terrestrial surfaces. In *2006 IEEE International Symposium on Geoscience and Remote Sensing*, 1119–1122 (2006).

56. Milton, H. P.-B. . N. F. . E. The NPL Gonio RAdiometric Spectrometer System (GRASS). In *Proceedings of the Remote Sensing and Photogrammetry Society Conference: Measuring change in the Earth system. University of Exeter, 15-17 September 2008*, 1–3 (2008).

57. King, A. M. . C. F. . A. M. . G. Z. . N. F. . M. Characterisation of the HDRF (as a proxy for BRDF) of snow surfaces at Dome C, Antarctica, for the inter-calibration and inter-comparison of satellite optical data. *Remote Sensing of Environment* (2015).

58. Hedley, J. Planarrad. *www.planarrad.com* (2015). Last accessed: Jan. 2017.

59. Mobley, C. D. *Light and water: radiative transfer* (Natural Waters. Academic Press, 1994).

60. Henyey, L. C. & Greenstein, J. L. Diffuse radiation in the Galaxy. *The Astrophysical Journal* **93**, 70–83 (1941).

61. Warren, S. G. & Brandt, R. E. Optical constants of ice from the ultraviolet to the microwave: A revised compilation. *Journal of Geophysical Research: Oceans* **113**, D14220 (2008).

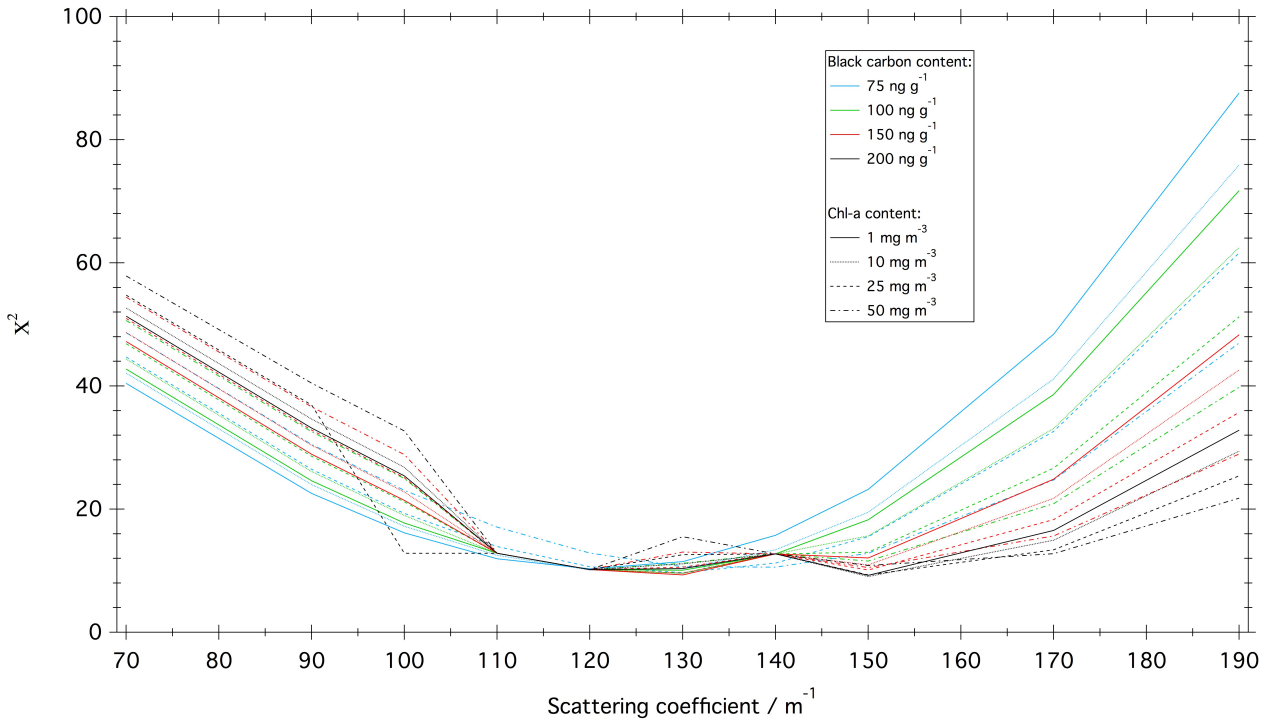

Figure 1. Chi-square (χ^2) goodness of fit test, as a function of the sea ice scattering coefficient for combinations of mass-absorption coefficients of black carbon between 75 and 200 ng g^{-1} and algae between 1 and 50 mg m^{-3}.

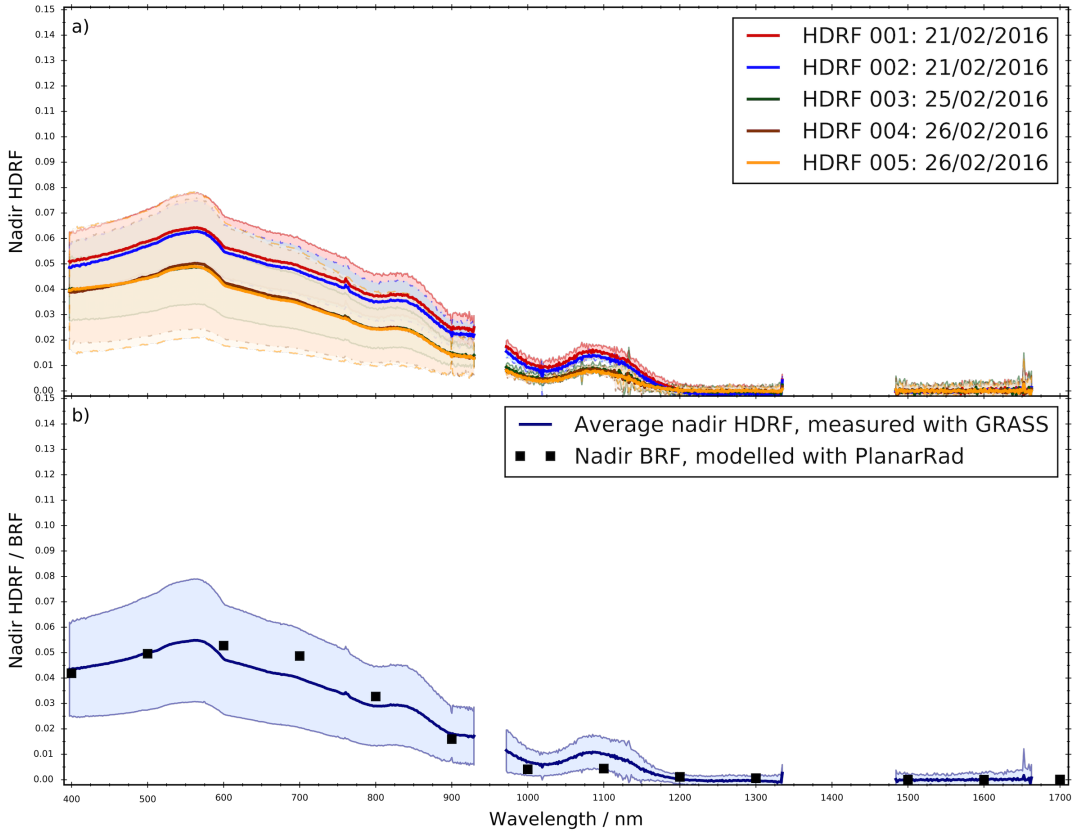

Figure 2. a) Average nadir HDRF of each complete set measured with GRASS over the wavelength range 400 – 1700 nm. For clarity, noisy spectra due to the join between the two spectrometers around 970 nm and the absorption band between 1340 and 1480 nm are not shown. The error bars represent 2 standard deviations. b) Average nadir HDRF of the sea ice surface measured at SERF (blue line) and modelled nadir BRF, with a scattering coefficient of 150 m^{-1}, and a black carbon mass-ratio of 200 ng g^{-1} and an algae mass-ratio of 10 mg m^{-3} calculated at an interval of 100 nm (black squares).

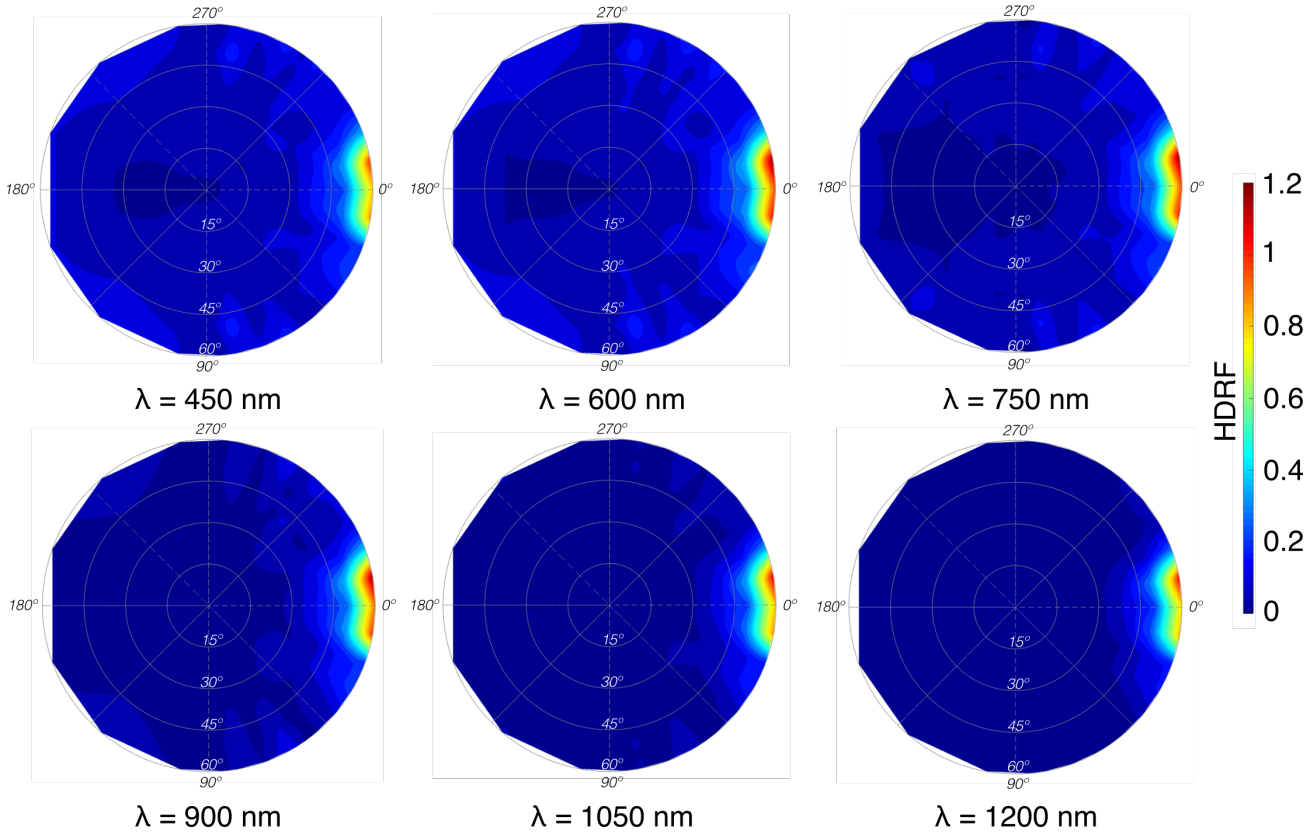

Figure 3. Polar plots of the averaged HDRF of 13 cm thick first-year sea ice at wavelengths 400 – 1200 nm. The average solar zenith angle was 61.57° ± 0.43 (1SD).

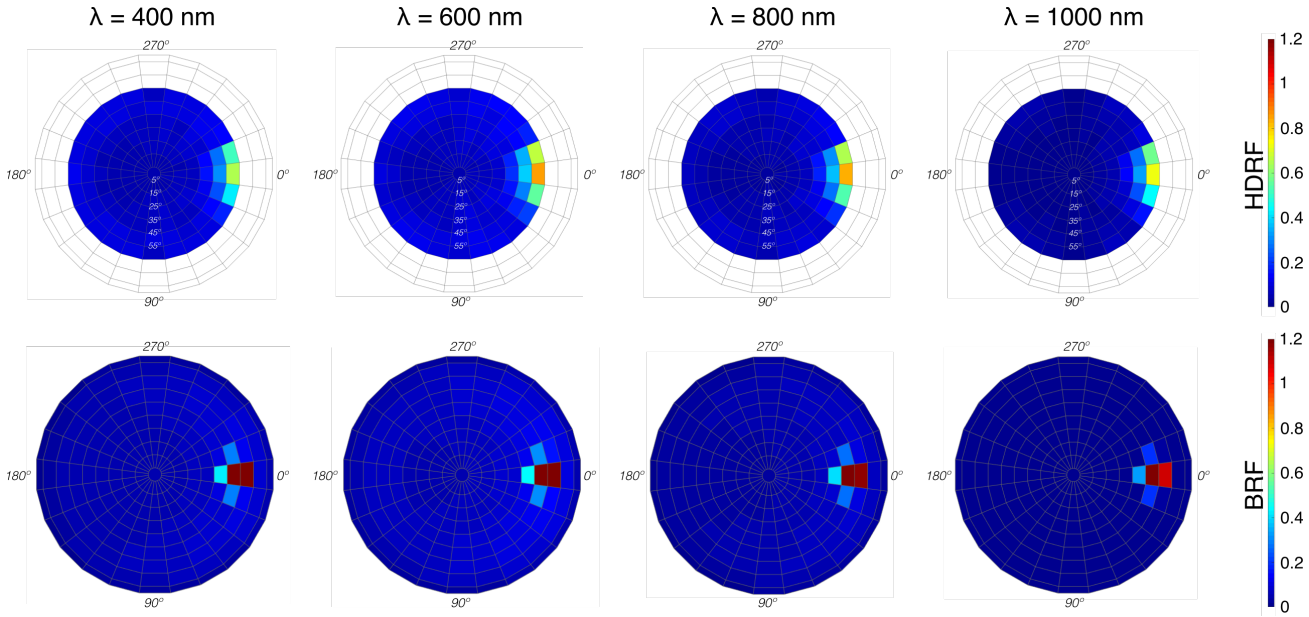

Figure 4. Top: HDRF polar plots of 13 cm first-year sea ice measured at SERF for wavelengths 400, 600, 800 and 1000 nm. For direct comparison with the PlanarRad model, the measurements were averaged over quads of the same dimension as the model. Bottom: BRF polar plot of 13 cm first-year sea ice with best-fit parameters for wavelengths 400, 600, 800 and 1000 nm.

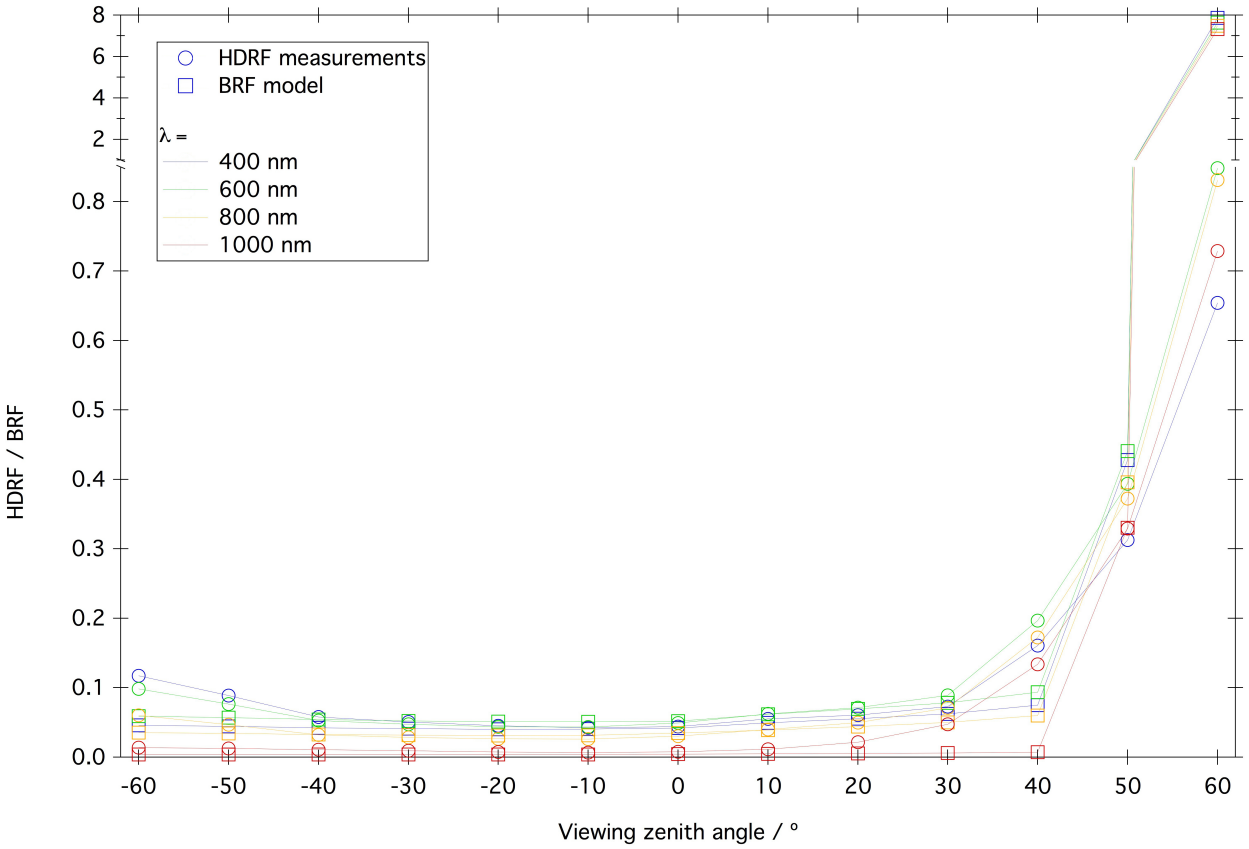

Figure 5. Comparison of the measured HDRF (circles) and the modelled BRF (squares) along the solar principal plane of 13 cm first-year sea ice for wavelengths 400, 600, 800 and 1000 nm.

Chapter 9

Synthesis and concluding remarks

The principal aim of the work presented in this thesis was to characterise the bidirectional reflectance distribution function of sea ice in response to deposited light-absorbing aerosols, for the calibration of satellite remote sensing products. In this final chapter, a summary of the findings of each individual chapter is presented, followed by a general discussion on the overall aims of the work, and finally suggestions for future research will be put forward.

9.1 Summary of the key finding for the individual studies

In this section, the key findings from each individual chapter are presented.

9.1.1 The impact of mineral aerosol deposits on the albedo of snow and sea ice

In chapter 3 calculations employing a coupled atmospheric and snow/sea ice model highlighted the effects of five different types of mineral aerosol deposits on characteristic snow and sea ice types. Firstly, the albedo of different snow and sea ice types was calculated with a fixed mass-ratio of different mineral aerosol deposits distributed evenly throughout the media. Secondly, the albedo of snow and sea ice containing varying mass-ratios of Asian dust was calculated. Thirdly, the mineral dust was placed in a surface layer, and in multiple layers with varying intervals throughout the snow. The main findings of the work are summarised below:

- The study confirms that much larger mass ratios of mineral aerosol deposits in snow or sea ice are necessary to reduce the albedo, compared to black carbon. To achieve the same decrease in albedo, a mass ratio of mineral aerosol deposits of a factor of 100 larger than the mass ratio of black carbon deposits is required. The wavelength-dependent effects of the mineral aerosol deposits on albedo are similar to black carbon, where the increase in absorption affects shorter wavelengths a lot more than in the infrared, owing to strong ice absorption at larger wavelengths.

- Despite differences in the absorption cross-section of the different mineral aerosol deposits reaching 77 %, variations in the type of mineral aerosol deposit in the snow or sea ice do not have a significant effect on the albedo. Indeed, the variation in the albedo of snow and sea ice more sensitive to the optical properties of the snow or sea ice than the optical properties of the different types of mineral aerosol type. Moreover, melting snow or sea ice are more sensitive to mineral aerosol deposits than fresh snow of multi-year sea ice, which participates in a positive-feedback loop entraining further melting. Therefore, it is more important to consider the optical properties of the snow or sea ice when studying the effects of light-absorbing impurities on the radiative budget of snow or sea ice.

- The mass-ratio of mineral aerosols deposits necessary to change the albedo of snow and sea ice significantly is larger than the quantities typically observed in the Arctic. However, large mass-ratios of mineral aerosol deposits can be found concentrated in layers through snowpacks, owing to deposition by storm events. The thickness of a surface layer containing mineral aerosol deposits has little impact on the albedo, with changes of less than 0.5 % between the albedo of a snowpack with a 1 cm surface layer and a 10 cm layer containing 100 ng g^{-1} of dust. When the mineral aerosol deposits are distributed in multiple layers throughout the snowpack, mass-ratios of mineral aerosols placed in closely spaced layers has a larger effect on the surface albedo than the same mass-ratios placed in a 1 cm thick surface layer. As the spacing between the layers increases, the effects on the surface albedo become similar to a single surface layer.

- The TUV-snow model was validated against the results of a widely used radiative-transfer model (**Flanner2007a**). The two models were shown to be in agreement for the calculation of volcanic ash mass-ratios in snow.

9.1.2 The optical properties of laboratory grown sea ice doped with black carbon

In chapter 4, the initial experiments using the first large scale sea ice laboratory in the UK. Realistic sea ice was grown in a tank in the sea ice laboratory, and the *e*-folding depths and nadir reflectance were measured. In a second step, a 5 cm layer of sea ice with varying mass-ratios of black carbon was grown on the surface of the previous sea ice, providing the first optical laboratory study of black carbon in sea ice. The reflectance data measured in the laboratory was compared with the modelled sea ice, using the TUV-snow model, that was previously used in chapter 3. The key results from the work were:

- The sea ice simulator was shown to create realistic sea ice conditions, with scattering cross-sections varying between 0.05 to 0.35 $m^2 kg^{-1}$. The reflectance of the sea ice measured in the laboratory was within the range of reflectance values of sea ice

measured in the field (Grenfell and Maykut, 1977). The physical parameters of the artificial sea ice were characteristic of a first year ice sea ice with the typical density, salinity profile and structure of natural sea ice.

- The calculations of the reflectance and *e*-folding depths of sea ice using the TUV-snow radiative-transfer model with the measured optical and physical properties of the artificial sea ice as inputs were able to reproduce the measurements within the uncertainty limits, showing that the sea ice simulator can be used as a model validation tool, rather than complex field measurements.

- A 5 cm surface layer of sea ice containing mass-ratios of 75, 150 and 300 ng g^{-1} of black carbon caused a decrease in reflectance of 3, 10 and 21% respectively. The model calculations were able to reproduce the absorption of black carbon in sea ice based on knowledge of the physical properties of the observed sea ice. The agreement between the results produced by the TUV-snow model and the measurements validated the model as a tool to accurately quantify the radiative forcing of polar regions, with the associated effects of black carbon in sea ice.

9.1.3 Changes in the optical properties of snow explaining an early onset of algae bloom

In chapter 5, the TUV-snow model was used to calculate downwelling irradiance through land-fast sea ice with an overlying snow cover. The radiative-transfer calculations were used to support the observations of an algae spring bloom in conditions that were previously thought to be insufficient to drive algae growth. The outcomes of the study were:

- A snow thickness of 40 cm on the surface of sea ice was previously considered to be a limiting factor for under-ice algae growth (Mundy et al., 2007b; Campbell et al., 2014). However, an early onset of under-ice algae growth was measured in the North East of Greenland, when a 1 m thick snow cover over a 1 m layer of sea ice was present. Increasing Chlorophyl *a* concentrations were recorded with no apparent change in the thickness of the snow.

- The measured downwelling irradiance at the bottom of the sea ice was on the limit of the sensor detection levels, with an under-ice photosynthetically active radiation of 0.17 μmol photons $m^{-2}\,s^{-1}$.

- Radiative-transfer calculations were performed to compute the downwelling photosynthetically active radiation through the snow and sea ice, showing that changing snow conditions (warming snowpack) affect the amount of light reaching the bottom of the sea ice. Based on the modelling results, a change in the optical properties of the snow layer was provided as an explanation for the ice algae growth in low light conditions.

- The observations support that the primary production beneath snow covered first-year sea ice is more widely spread than previously thought, and is an essential contributor to the overall primary production in the Arctic.

9.1.4 The effects of surface roughness on the spectral BRDF of sea ice

Chapter 6 looked at the anisotropic reflectance of sea ice, using a radiative-transfer model designed to compute directional radiance fluxes. The BRDF of sea ice was modelled for three characteristic sea ice types with varying thicknesses as a function of surface roughness. The modelling study provided the first extensive characterisation of the BRDF of sea ice for different conditions (illumination angles, sea ice type, sea ice thickness), and investigated the effects of increasing surface roughness. The main findings of the work are summarised below:

- Studies of the BRDF of bare sea ice are scarce in the literature. The outcome of the study was a large dataset parameterising the BRDF of bare sea ice, which can be used as a validation tool for General Circulation Models or remote sensing products.

- Radiative-transfer calculations showed that the surface roughness has a significant effect on the anisotropy of the BRDF, particularly affecting the forward scattering peak. An accurate characterisation of the forward scattering peak width and intensity was provided.

- Further efforts are necessary to increase the resolution of the radiative-transfer model to capture more accurately the rapidly changing intensities across the forward scattering part of the hemisphere.

- For satellite sensors viewing sea ice below a viewing zenith angle of 45° for typical illumination angles in the Arctic during spring and summer, corrections for the anisotropy of the radiation reflected from the sea ice are not critical, as the sea ice exhibits a quasi-lambertian response outside of the forward scattering peak.

- For small amounts of surface roughness, the quasi-lambertian part of the hemisphere was shown to be more sensitive to changes in sea ice thickness than the forward scattering peak, which is also less wavelength dependent than the quasi-lambertian part of the hemisphere. For larger amounts of surface roughness, the forward scattering peak is also affected by surface roughness, and becomes more wavelength dependent than for a smoother sea ice.

- The results showed that surface roughness is inter-dependent of the physical parameters affecting the BRDF of sea ice, and therefore cannot be considered separately or ignored in calculations of the radiation budget of the sea ice.

9.1.5 The effects of black carbon and mineral aerosols on the angular reflectance of sea ice

Chapter 7 expanded on the work in chapter 6, by investigating the effects of light-absorbing impurities on the BRF of sea ice. The BRF of realistic sea ice grown in the Royal Holloway laboratory, which was first presented in chapter 4, was measured. Based on the methods developed in chapter 4, a 5 cm surface layer containing particles representative of aerosol deposits was placed on the sea ice. Artificial black carbon was used to represent atmospheric black carbon particles, and based on the findings of chapter 3, a sample of volcanic ash represented mineral aerosol deposits. The BRF measurements performed with a laboratory goniometer were compared to the output of the model described in chapter 6. The key findings were the following:

- The radiative-transfer calculations based on the physical properties of the sea ice and the calculated optical properties of the impurities measured in the laboratory were able to reproduce the BRF of sea ice doped with black carbon.
- The spectral dependent effects of black carbon particles distributed in a surface layer of the sea ice on the nadir BRF are similar to the trends observed in the literature for reflectance and albedo (Grenfell and Light, 2002; Marks and King, 2013b). The absorption of mineral particles in the sea ice are more wavelength-dependent than black carbon, with enhanced absorption at shorter wavelengths. The quasi-lambertian part of the hemisphere was more sensitive to a varying mass loading of impurities than the forward scattering peak.
- Further work needs to be conducted on the effects of mineral aerosols deposits on the angular reflectance of sea ice in the forward scattering peak, as the model appeared to consistently overestimate the BRF in the forward scattering peak. Furthermore, the discrepancies between the model output and the measurements can be explained by the difference in sampling resolution between the two. When measuring the BRF of sea ice, a high angular sampling resolution is recommended.

9.1.6 Angular measurements of first-year sea ice in natural illumination conditions

In chapter 8, the first measurements of the HDRF bare sea ice with natural illumination conditions were presented. A field goniometer was deployed on an outdoor artificial sea ice layer of sea ice with a thickness of 13 cm, at the University of Manitoba, Winnipeg, Canada. The facility, has widely been used to study realistic sea ice in controlled conditions. The radiative-transfer model used in chapter 6 and validated in chapter 7, was employed to calculate the optical properties of the sea ice and derive the impurities mass-ratios in the sea ice. The main findings of the work were the following:

- The pattern of the HDRF of the sea ice measured at the sea ice facility, although not directly comparable, showed a similar trend to the modelling of sea ice presented in chapter 6, and the measurements of the BRF of indoor artificial sea ice measured in chapter 7.
- The study confirms that for large illumination zenith angles (above 60 °), the normalisation of reflectance is not necessary below viewing zenith angles of 45° for all viewing azimuth angles. However for satellite products necessitating knowledge of the reflected radiation across the hemisphere such as albedo, the characterisation of the forward scattering peak is essential.
- The study was limited by the thin layer of sea ice. Further studies are necessary to characterise the angular reflectance of sea ice for a varying sea ice thickness.
- The radiative-transfer calculations were used to derive the optical properties of the sea ice, as well as the impurities in the ice. The measured ice was calculate to have a scattering coefficient of 150 m^{-1}, which is representative of first year sea ice (Lamare et al., 2016). A mass-ratio of 200 $\mathrm{ng\,g}^{-1}$ of black carbon was present in the ice, which was indicative of the surrounding urban environment. Furthermore the absorption spectrum of Chlorophyl *a* was necessary to reproduce the observed data using the model, with an estimated 10 $\mathrm{mg\,m}^{-3}$ of algae present in the sea ice.
- Although the model was able to reproduce the HDRF measurements across the hemisphere, the model overestimated the intensity of the forward scattering peak, in a similar manner to chapter 7.
- The model did not include diffuse radiation, and although the BRF was shown to be correlated with the HDRF, further work is recommended to include a direct and a diffuse component to the radiative-transfer.

9.2 Conclusion

The results of the individual chapters have highlighted the importance of accurately characterising the angular response of reflected radiation from sea ice, to better monitor the radiative forcing of sea ice using satellite remote sensing products. The work in this thesis was governed by several overarching scientific questions, which the different chapters attempted to cover. Below, the knowledge from the different chapters is synthesised and combined in response to the questions.

1. Which parameters affect the BRDF of bare clean sea ice, and what are the individual effects of the parameters?

A review of the literature, presented throughout the introductions of the different chapters in this thesis has shown that the BRDF of sea ice has only been superficially characterised, through spare field measurements, limited laboratory experiments and radiative-transfer modelling. Previous studies have outlined the characteristic anisotropic pattern of the BRDF of sea ice, with a quasi-lambertian response across the major part of the hemisphere, and a strong scattering peak in the forward direction, located close to the illumination zenith angle. The surface roughness of sea ice was shown to diminish the intensity and diffuse the forward scattering peak. However, a comprehensive characterisation of the BRF of sea ice in response to varying physical and optical parameters that can be observed in nature has been lacking. The results presented in chapter 6 have shown that the principle parameters controlling the anisotropy of the sea ice are the thickness, the wavelength, the solar zenith angle, the scattering of the sea ice, and the surface roughness. The surface roughness of the sea ice was shown to be the principal parameter controlling the intensity size, and location of the forward scattering peak. However, the modelling outputs indicated that the surface roughness could not be parameterised separately from the physical parameters of the sea ice, being inter-dependent of the thickness of the sea ice, the solar zenith angle and wavelength. Indeed the forward scattering peak responds differently to varying physical parameters for smooth sea ice surfaces than for rougher surfaces. A decrease in the thickness of the sea ice lowers the BRF of the quasi-lambertian part of the hemisphere, hardly affecting the forward scattering peak for smooth sea ice, whereas the intensity of the forward scattering peak decreases strongly with a thinning sea ice for larger amounts of surface roughness. For a smooth sea ice, the size of the scattering peak across the hemisphere increases as a function of an increasing illumination zenith angle as the location of the forward scattering peak moves in a specular manner, and the intensity of the forward scattering peak increases. For rough sea ice, the size of the forward scattering peak does not change and the intensity does not increase as rapidly as for smooth sea ice. The wavelength dependence of the BRDF of the sea ice also differs for varying amounts of surface roughness, where with small amounts of surface roughness, the forward scattering peak does not change in size with an increasing wavelength, but decreases in size for larger surface roughness values. The surface roughness was used in the model as a fitting parameter to reproduce the measured BRF and HDRF of sea ice in chapters 7 and 8, and realistic values of surface roughness were used to provide a good fit of the observational data. Overall, the work has shown that surface roughness is an essential parameter in the determination of the forward scattering peak of the BRDF of sea ice, which needs to be accurately defined to correctly derive satellite products that rely on the knowledge of the angular distribution of reflected radiation.

2. How do impurities, which are know to strongly impact the nadir reflectance of sea

ice, affect the anisotropy of sea ice?

In the introduction, light-absorbing impurities were shown to significantly affect the radiation budget of the sea ice. However, no studies investigating the effects of aerosol deposits either natural or of anthropogenic nature on the BRDF of sea ice were found. The effects of black carbon deposits on the albedo and reflectance of sea ice have been widely discussed in the literature, and are still the object of ongoing publications. However, comprehensive studies on the effects of mineral aerosols deposits on the albedo of snow and sea ice were scarcer. Therefore, before addressing the effects of mineral aerosols on the BRDF of the ice, a study describing the impact of different types of mineral aerosol deposits was undertaken in chapter 3. As shown in the previous section, the main finding was that the type of sea ice or snow is more important than the type of mineral aerosol deposit when investigating the radiative forcing of mineral aerosol deposits in the cryosphere. Owing to the lack of data for the BRDF of sea ice containing aerosol deposits in the literature, the radiative-transfer model required empirical measurements to be compared against and validated. In chapter 4, a new large scale sea ice laboratory was presented, and used to validate reflectance measurements of sea ice containing a superficial layer doped with black carbon. The laboratory proved to be an ideal validation tool for the evaluation of sea ice models, providing a controlled environment where the different physical and optical parameters of the sea ice are monitored. The work paved the path for chapter 7, where the effects of black carbon particles and volcanic ash representing generic mineral aerosol particles on the BRF of sea ice were investigated. Owing to the variability in the sea ice fabric from an experiment to an other, the observations in the sea ice laboratory were reproduced using a radiative-transfer model. As it was the case in chapter 4, the sea ice laboratory served as a validation tool for the PlanarRad radiative-transfer model, showing the ability for the model to describe the angular characteristics of the reflected radiation above sea ice. The BRF pattern of the sea ice across the hemisphere was shown to remain similar as the mass-ratio of black carbon was increased, although the quasi-isotropic part of the hemisphere was more sensitive to the black carbon than the forward scattering peak. The effects of the volcanic ash on the BRF of sea ice were less clear, as the measurements seemed to indicate a diffusion of the forward scattering peak and a stronger reduction in the forward scattering peak, but the modelling results did not support the observations. Furthermore, the radiative-transfer model was employed to derive the parameters of thin young sea ice from observations in chapter 8. The values of black carbon estimated by the model were considered to be realistic, owing to the urban setting of the outdoor sea ice facility. However, no empirical measurements were available to confirm the results. Overall, the work presented in this thesis has contributed to a better understanding of the effects of

impurities on the BRDF of sea ice, although the findings have lead to further questions that need to be investigated, discussed in the following section.

3. Can radiative-transfer modelling provide an accurate representation of the BRDF of sea ice for varying physical and optical parameters, to provide the remote sensing community with better inputs for satellite products, and can radiative-transfer modelling replace in-situ measurements?

   Throughout the work in this thesis, the main objective was to parameterise aerosol deposits in sea ice using radiative-transfer models, that would in turn provide reliable inputs for empirical models that are used to derive surface albedo products from multi-angular satellite data, or for General Circulation Models that rely on accurate retrievals of albedo. Indeed, in-situ measurements of sea ice, particularly multi-angular measurements are complex, costly in resources and require substantial data processing, as shown in chapter 8. Measurements performed on artificial sea ice are easier to obtain, however the work in chapter 7 has shown that separating the effects of the impurities in the sea ice from the physical parameters of the sea ice was complex. Nevertheless, the experimental setup proved to be an excellent validation tool for two different radiative-transfer models. In chapter 4, the modelled reflectance was in good agreement with the measurements. However, although the trends and angular patterns of the BRDF of sea ice could be reproduced by the model in chapter 7, the model showed a consistent overestimation of the intensities in the forward scattering peak. Consequently, the radiative-transfer models cannot be used alone to describe the BRDF of sea ice, and further empirical validations are necessary.

9.3 Recommendations for future research

Based on the knowledge acquired during the work presented here, future recommendations are proposed:

- When further characterising the effects of mineral aerosol deposits on the BRDF of sea ice, a quantitative assessment of the surface roughness is required, in order to constrain the different parameters, that have similar attenuation effects on the BRDF. In the case of the sea ice laboratory measurements, experiments measuring the BRF of the artificial sea ice with varying amounts of generated surface roughness are recommended.
- Although the laboratory measurements were a good proxy for naturally occurring sea ice, the uncertainties could be further reduced by using a collimated illumination beam, and ensuring that the heat generated by the lamps does not affect the surface of the sea ice.

- The PlanarRad radiative-transfer model has shown potential in describing the BRDF of sea ice. The overestimation of the intensity of the forward scattering peak may me explained by the difference in resolution between the measurements and the model, which averages radiance over quads. Implementing a smaller quadrilateral discretisation is recommended. Moreover, the implementation of a diffuse illumination component in order to reproduce HDRF measurements should be investigated. Further comparisons with empirical data are required however. In that sense, an inter-comparison study between the model outputs, in-situ measurements in the field and overpassing satellite retrievals should be considered, to validate the model as a remote sensing calibration tool.

- The measurements of the HDRF of sea ice with the field goniometer at the sea ice facility in Winnipeg were complex and the measurements were limited by the structure of the instrument. Further uncertainties were introduced by the long acquisition times of the spectroradiometer. Recent developments in BRF acquisitions have provided novel tools with great potential for rapid measurements and easier deployments, which are essential for fieldwork in the Arctic. The latest technological advances in unmanned aerial vehicle technology provide a new platform for HDRF measurements. Furthermore, the investigation of the use of CCD arrays rather than cumbersome spectrometer systems is recommended.

- The outdoor measurements at the sea ice facility were limited by the thickness of the sea ice, owing to weather conditions. Further HDRF measurements of bare sea ice with varying sea ice thicknesses are suggested.

Appendix A

Citation:
Bialek, A., Greenwell, C., **Lamare, M.**, Meygret, A., Marcq, S., Lachérade, S., Wooliams E., Berthelot, B., Bouvet, M., King, M.D., Underwood C., Fox, N. (2016). New radiometric calibration site located at Gobabeb, Namib desert. *2016 IEEE International Geoscience and Remote Sensing Symposium (IGARSS)*, 6094–6097.

Author contributions:
Lamare, M. performed the HDRF measurements using the GRASS instrument, processed the HDRF data, performed the GRASS instrument post-campaign analysis, and wrote section 3.2.

Bialek, A., Greenwell, C., Meygret, A., Marcq, S., and Lachérade, S. performed the pre-campaign calibrations of the instrument, took nadir radiance measurements, processed the data from Cimel, the ASD and Pleiades.

Wooliams E., Berthelot, B., Bouvet, M., Fox, N. and Bialek, A. managed the project, set up the field campaign and will provide the project deliverables.

King, M.D. and Underwood C., provided guidance for the field characterisation.

NEW RADIOMETRIC CALIBRATION SITE LOCATED AT GOBABEB, NAMIB DESERT

Agnieszka Bialek[1,6], Claire Greenwell[1], Maxim Lamare[1,3], Aimé Meygret[2], Sebastien Marcq[2], Sophie Lachérade[2], Emma Woolliams[1], Béatrice Berthelot[4], Marc Bouvet[5], Martin King[3], Craig Underwood [6], Nigel Fox[1]*

[1]National Physical Laboratory, [2]CNES, [3]Royal Holloway University of London, [4]Magellium, [5]ESA, [6]University of Surrey

ABSTRACT

A new permanently instrumented radiometric calibration site for high/medium resolution imaging satellite sensors is currently under development, focussing on the visible and near infra-red parts of the spectrum. The site will become a European contribution to the Committee on Earth Observation Satellites (CEOS) initiative RadCalNet (Radiometric Calibration Network). This paper describes the site characterisation that was carried out, both to define the exact location of permanent monitoring instrumentation, and to provide an initial detailed assessment of the site's properties. The characterisation involved a range of tests, using an ASD FieldSpec spectroradiometer, and the Gonio Radiometric Spectrometer System, a hyperspectral, multi-angle HDRF instrument. Teams from NPL and CNES each performed parts of this characterisation, working together to acquire the data and generate the final outcome

Index Terms— RadCalNet, site characterisation, HDRF, vicarious calibration

1. INTRODUCTION

Vicarious calibration and validation using ground reference sites is a key technique in Earth Observation, both for the cross comparison of sensors (including calibration of lower accuracy sensors against sensors with better radiometric calibration) and for monitoring long-term drift (effectively by comparison against themselves using a stable ground reference). It is common to use accessible desert sites for -field-campaign measurements that are made to coincide with a satellite overpass.

CEOS, the space arm of GEO (Group on Earth Observations), is in the process of establishing RadCalNet, a network of instrumented test sites, where field-measurement campaigns are supplemented by permanent instrumentation which takes measurements of the ground throughout the day. In the prototype phase RadCalNet is being established with four reference sites: University of Arizona/NASA's site at Railroad Playa, Arizona, USA; AoE's site at Baotou, China; the CNES site at La Crau, France; and the new ESA/CNES site in Gobabeb, Namibia. It is hoped that once RadCalNet is fully established (during 2016), additional sites will be added.

In addition to the requirements of RadCalNet, which will initially be limited to nadir, the Gobabeb site will provide off-nadir measurements to increase the number of matching overpasses. The site is being established as part of a collaborative project between ESA and CNES, in conjunction with NPL and Magellium.

To achieve SI traceability for the new ESA/CNES RadCalNet site, NPL has performed a detailed characterisation and calibration of the instruments and artefacts to be used on the site.

This paper describes the establishment of the Gobabeb site, including how the site area and specific site locations were chosen, together with the results of measurements of a field campaign in November 2015.

2. PREPARATION

2.1. Area Selection

The location of the new ESA/CNES vicarious calibration site was selected following a comprehensive global study by Magellium for suitable RadCalNet sites. Scores were given to areas on Earth based on the following criteria: spatial homogeneity at 1 km^2 resolution; spatial homogeneity at 10 km^2 resolution; flatness; atmospheric aerosol content and percentage of cloud free days. These scores were used to establish regions of interest, which were then studied in greater detail including accessibility, GSM coverage and proximity to inhabited areas. In total 86 sites across the world were flagged as potential sites by the study. From this list the new ESA/CNES site was chosen to be based near the Gobabeb Research and Training Centre in Namibia.

Further surface homogeneity studies focusing on individual Gobabeb areas were performed by CNES using Sentinel 2 and PLEIADES data. The most important criterion for the test site is its homogeneity over different spatial scales, i.e. the representativeness of small scale areas (~10 m^2) compared with much larger ones (100 m^2), to enable calibration of several satellite sensors with different image resolutions.

2.2. Instrument Characterisation

To reduce the uncertainty in the field site characterisation, NPL performed a range of tests on the instruments that were be used on the site to provide traceability to SI. This was done for the instruments intended for the initial characterisation of

the site, for the in-situ calibration standards and for the permanent monitoring instrumentation. The site characterisation instrumentation included two ASD FieldSpec spectroradiometers for measuring nadir surface reflectance and GRASS (Gonio RAdiometric Spectrometer System), a system for measuring reflectance at different viewing angles. The in-situ SI traceable standards included Spectralon™ panels and tarpaulins. The instrument intended for permanent autonomous operation is a CIMEL sun photometer. The results of these laboratory tests are presented in [1].

3. SITE CHARACTERISATION

Several tests were conducted during a two week measurement campaign in Autumn 2015. This involved a visual assessment of the candidate test sites' surfaces, GSM coverage tests (to ensure the permanently installed instrument can use the GSM network as a means of data transmission), and a detailed characterisation study of the spectral reflectance and homogeneity of the chosen test site, as described in more detail in the following sections.

3.1. Nadir measurement

The nadir ground reflectance measurements were performed using ASD FieldSpec portable spectral radiometers. The ASD instrument has good sensitivity over a wavelength range of 400 nm to 2400 nm. It can be used with a bare fibre (with approximately 25° FOV) or with a lens, which has either an 8° FOV (NPL) or 5° FOV (CNES). Measurements taken with the ASD are in radiance units. For traceable reflectance values, measurements of a reference diffuser (Spectralon) are necessary, taken with the same measurement geometry and under the same illumination conditions as the ground measurements.

Figure 1: Measurements with the ASD spectrometer

3.1.1. Area Characterisation

Area characterisation was performed over a set of small squares. NPL took repeated measurements over the same small set of points to obtain an understanding of repeatability and stability, while CNES took measurements over a much wider area to understand surface homogeneity on different scales (from a few cm to a km).

Measurement of a single point consisted of a short sequence that approximately took 5 minutes: a Spectralon measurement, four ground measurements (eight for CNES) at slightly different positions, then a final Spectralon measurement. For NPL's method, each of these included 5 readings from the ASD at each position, which were then averaged. For CNES' method, each position included 20 scans - which were averaged by ASD's software.

3.1.2. Static test

In order to understand the ground BRF (Bidirectional Reflectance Factor) effects and to check that the solar zenith angle changes could be correctly accounted for in the area characterisation data, an investigation was carried out to study the variation in reflectance at a single ground point. Spectralon measurements were taken in quick sets of five, every half an hour, and between those times, a single reading from the ground was taken every two minutes, to provide a near continuous record of the ground reflectance. The Spectralon readings were interpolated, using BRF values every 10 degrees from laboratory calibration prior to the field campaign, on a smooth curve to give estimated BRF values for all times of ground measurements.

3.1.3. Tarpaulins

A set of three large, uniform reference tarpaulins was brought to the site. These were manufactured to have Lambertian reflectance properties and three different grey scale levels. They were previously calibrated for total diffuse reflectance and 0°:45° radiance factor at NPL. In the field they were used to provide a large uniform area over which we could perform comparisons of different measurement procedures, and investigate how much effect changing the ASD operator has on the results.

Figure 2: Measurements with tarpaulins

3.1.4. Downwelling Irradiance

In order to measure the downwelling irradiance (from the Sun and sky) at the site, the ASD was used with an alternative input optic. A diffuser replaced the lens at the end of the input fibre and the instrument was set up vertically upwards. The ASD and tripod were set up a short distance away from the

GRASS structure (far enough to ensure that it did not affect the GRASS measurements, but close enough to be comparable), and left monitoring for the entire morning. These data were intended to be used partly as validation of the downwelling measurements made using GRASS, and also to provide a representative idea of the variation in solar irradiance over a day.

Figure 3: Close-up of diffuser input

3.2. Multi-angular measurements

Ground-based measurements of the hemispherical directional reflectance factor (HDRF) of the site were carried out with the GRASS [2]. GRASS is designed to record quasi-simultaneous, multi-angle, hyperspectral measurements of the Earth's surface reflectance. Signal collectors mounted on a hemispherical frame and aiming at the same target area are connected with fibre optic cables to a V-SWIR spectroradiometer, operating over a wavelength range from 400 nm to 1700 nm. A full description of the system can be found in [3] and [4].

Figure 4: GRASS instrument in situ

3.2.1. GRASS measurements

During the campaign, measurements were made using GRASS with clear sky conditions over viewing zenith angles from 0º to 50º with a 10º interval and azimuth angles from 0º to 360º with a 30º interval. Changes in illumination were monitored with an integrating sphere mounted on the instrument and a reference measurement was recorded at nadir over a Spectralon panel. Random sampling points were chosen over an area of 300 m × 300 m that was selected in the first stage of the project based on criteria given in Section 2.1. Repeated measurements at different sampling points allowed HDRF datasets to be obtained over a range of solar zenith angles. Furthermore, measurements were timed to correspond to key satellite overpasses (Sentinel 2A MSI and Landsat 8 OLI).

3.2.2. ASD - GRASS nadir view comparison

As an additional check on the consistency of the ground reflectance measurements, the ASD was used in conjunction with GRASS. Measurements were taken of the ground as observed by GRASS nadir view and with the ASD spectrometer as well. This was repeated with both the Spectralon Panel and then the tarpaulins placed in the view of GRASS and the ASD. These data provided an alternative route to compare nadir view results of the same ground patch from two instruments that have different footprint on the surface (the ASD footprint is around 9 cm diameter while GRASS is about 20 cm).

3.3. Site Impact

The impact of continuous foot traffic on the site is a concern. As visible in Figure 5 (from images with the high resolution sensor PLEIADES), the paths where area characterisation was done, and particularly the GRASS positions, show a marked change compared with other areas. Any future visits to the site will have to be planned carefully so that any damage to the site is minimised.

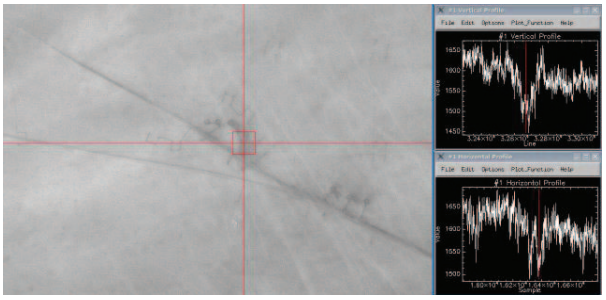

Figure 5: PLEIADES 70 cm-panchromatic image of the site, taken 18th December 2015, approximately two weeks after the field campaign darkened areas represent the surface damaged due to foot traffic and darkened circles GRASS positions (copyright CNES, Distribution Airbus Defence and Space)

4. EXPECTED OUTCOMES

4.1. Results from data

The data are currently being processed. They will provide information about surface homogeneity at the scale of a few square centimetres, which is equivalent to the footprint size of small zenith angles for the CIMEL Sun Photometer that will be used for the permanent instrumentation. The sparse measurements over larger areas of the test site will test the representativeness of the CIMEL sun photometer measurements over the overall area. In addition the ASD measurements will provide full hyperspectral information, which will be used to allow spectral interpolation of the 12 spectral bands provided by the CIMEL Sun Photometer.

The site characterisation included the necessary repetitions and additional testing required to establish a robust uncertainty budget for the reflectance values for the site. The characterisation and calibration of the instruments by NPL ensures rigorous traceability to SI.

GRASS measurements will produce HDRF information about the site, which can be compared with future CIMEL measurements.

4.2. Mast installation

The final stage of the site development will include the installation of the permanent instrumentation the mast and weather station. This will involve mounting the CIMEL instrument on top of a mast from which measurements of the atmosphere and surface will be taken. The original plan was to use the same type of mast at the new Gobabeb site as at the La Crau site [5]. This had to be modified as the Gobabeb site is located in the territory of the Namib-Naukluft National Park protected area, so the ground cannot be destroyed or permanently modified and only masts with guy ropes can be installed.

Taking into consideration surface damage during site characterisation (see fig 5), an additional set of mast installation practice runs will be performed in the UK to establish the least invasive method.

5. CONCLUSIONS AND SUMMARY

This paper presents a process for establishing a new radiometric calibration site for visible and NIR satellite sensor validation. The Gobabeb site is being developed as a European contribution to the RadCalNet network. This site was selected following an extensive study of the potential areas, based on a number of predefined criteria. The choice of the final position for the mast installation was supported by initial site characterisation campaign results. All instruments and artefacts used during the site characterisation were previously calibrated and/or characterised at NPL.

The in situ measurements on the site performed near the end of 2015 confirmed excellent environmental and surface homogeneity for this location. Due to surface dryness and moderate winds present, especially in the afternoon hours, the biggest challenge for the in situ measurements was to maintain a good state of the reference reflectance panels throughout the campaign duration. Several additional daily comparisons of standards were performed to monitor their stability. Site characterisation data processing is currently ongoing, and the results will be presented in the full version of this paper.

The installation of the permanent equipment is scheduled for Summer 2016. It is expected that the site will become operational soon after that.

6. ACKNOWLEDGEMENTS

This work was supported by the European Space Agency (ESA) funded ACTION project, and the European Union and European Metrology Programme through the European Metrology for Earth Observation and Climate Joint Research Project (MetEOC2). The EMRP is jointly funded by the EMRP participating countries within EURAMET and the European Union. M.D. King and M.L. Lamare thank NERC for support under Grant NE/K000770X/1 and NERC FSF (555.0608). The authors would like to thank NERC FSF for the equipment loan and Gobabeb Research and Training Centre for their support and hospitality.

7. REFERENCES

[1] C. Greenwell, A. Bialek*, et al.*, "Preparation of a new autonomous instrumented radiometric calibration site: Gobabeb, Namib Desert," 2015, pp. 963919-963919-14.

[2] H.M. Pegrum-Browning, Fox, N. and Milton, E., "The NPL Gonio Radiometric Spectrometer System (GRASS)," in *Remote Sensing and Photogrammetry Society Conference*, University of Exeter, 2008.

[3] C.P. Ball, A.A. Marks*, et al.*, "Hemispherical-Directional Reflectance (HDRF) of Windblown Snow-Covered Arctic Tundra at Large Solar Zenith Angles," *Geoscience and Remote Sensing, IEEE Transactions on,* vol. 53, pp. 5377-5387, 2015.

[4] A. Marks, C. Fragiacomo*, et al.*, "Characterisation of the HDRF (as a proxy for BRDF) of snow surfaces at Dome C, Antarctica, for the inter-calibration and inter-comparison of satellite optical data," *Remote Sensing of Environment,* vol. 158, pp. 407-416, 3/1/ 2015.

[5] A. Meygret, R.P. Santer*, et al.*, "ROSAS: a robotic station for atmosphere and surface characterization dedicated to on-orbit calibration," 2011, pp. 815311-815311-12.

Bibliography

Aagaard, K., L. K. Coachman, and E. Carmack (1981). "On the halocline of the Arctic Ocean". In: *Deep Sea Research Part A. Oceanographic Research Papers* 28.6, pp. 529–545.

Abràmoff, M D and P J Magalhães (2004). "Image processing with ImageJ". In: *Biophotonics international* 11.7, pp. 36–42.

Atkinson, M. J. and C. Bingman (1997). "Elemental composition of commercial seasalts". In: *J. Aquaric. Aquat. Sci* 8.2, pp. 39–43.

Ball, C. P. et al. (2015). "Hemispherical-Directional Reflectance (HDRF) of Windblown Snow-Covered Arctic Tundra at Large Solar Zenith Angles". In: *IEEE Transactions on Geoscience and Remote Sensing* 53.10, pp. 5377–5387.

Ball, Christopher (2015). "Bidirectional reflectance of snow and sea ice: field, laboratory and modeling studies". PhD thesis. Royal Holloway University of London, Egham, UK.

Bialek, A, C Greenwell, and M Lamare (2016). "New radiometric calibration site located at Gobabeb, Namib desert". In: *Geoscience and Remote Sensing Symposium (IGARSS), IEEE*.

Bialek, A. et al. (In preparation). "Characterisation of the reflectance of a New Radiometric Calibration Site in Gobabeb, Namib Desert ". In: *IEEE Transactions on Geoscience and Remote Sensing*, p. 11.

Bohren, C. F. and D. R. Huffman (2008). *Absorption and scattering of light by small particles*. John Wiley & Sons.

Bond, T. C. and R. W. Bergstrom (2006). "Light Absorption by Carbonaceous Particles: An Investigative Review". In: *Aerosol Science and Technology* 40.1, pp. 27–67.

Bond, T. C. et al. (2013a). "Bounding the role of black carbon in the climate system: A scientific assessment". In: *Journal of Geophysical Research Atmospheres* 118.11, pp. 5380–5552.

Bond, T. C. et al. (2013b). "Bounding the role of black carbon in the climate system: A scientific assessment". In: *Journal of Geophysical Research: Atmospheres* 118.11, pp. 5380–5552.

Born, Max and Emil Wolf (1980). "Principles of Optics (6th edition): Chapter XII - Diffraction of light by ultrasonic waves". In: *Principles of Optics (Sixth (corrected) Edition)*. Pergamon, pp. 593–610.

Campbell, Karley et al. (2014). "Remote estimates of ice algae biomass and their response to environmental conditions during spring melt". In: *Arctic* 67.3, pp. 375–387.

Cavalieri, D. J. (2003). "30-Year satellite record reveals contrasting Arctic and Antarctic decadal sea ice variability". In: *Geophysical Research Letters* 30.18, pp. 4–7.

Chu, B, HC McEvoy, and JW Andrews (1994). "The NPL reference sources of blackbody radiation". In: *Measurement Science and Technology* 5.1, p. 12.

Clarke, A D (1982). "Integrating sandwich: a new method of measurement of the light absorption coefficient for atmospheric particles." In: *Applied optics* 21.16, pp. 3011–3020.

Cox, C. and W. Munk (1954). "Measurement of the Roughness of the Sea Surface from Photographs of the Sun's Glitter". In: *JOSA* 44.11, pp. 838–850.

Curry, Judith A., Julie L. Schramm, and Elizabeth E. Ebert (1995). *Sea ice-albedo climate feedback mechanism*.

Dang, C., R. E. Brandt, and S. G. Warren (2015). "Parameterizations for narrowband and broadband albedo of pure snow and snow containing mineral dust and black carbon". In: *Journal of Geophysical Research: Atmospheres* 120.11, pp. 5446–5468.

Derimian, Y, O Dubovik, and D Tanre (2012). "Optical properties and radiative forcing of the Eyjafjallajökull volcanic ash layer observed over Lille, France, in 2010". In: *Journal of Geophysical Research: Atmospheres* 117.D20.

Deser, Clara et al. (2010). "The seasonal atmospheric response to projected Arctic sea ice loss in the late twenty-first century". In: *Journal of Climate* 23.2, pp. 333–351.

Doherty, S J et al. (2010a). "Light-absorbing impurities in Arctic snow". In: *Atmospheric Chemistry and Physics* 10.23, pp. 11647–11680.

Doherty, S. J. et al. (2010b). "Light-absorbing impurities in Arctic snow". In: *Atmospheric Chemistry and Physics* 10.23, pp. 11647–11680.

Doherty, S. J. et al. (2013). "Observed vertical redistribution of black carbon and other insoluble light-absorbing particles in melting snow". In: *Journal of Geophysical Research Atmospheres* 118.11, pp. 5553–5569.

Else, B G T et al. (2015). "Under-ice eddy covariance flux measurements of heat, salt, momentum, and dissolved oxygen in an artificial sea ice pool". In: *Cold Regions Science and Technology* 119, pp. 158–169.

Fisher, F N, M D King, and J Lee Taylor (2005). "Extinction of UV-visible radiation in wet midlatitude (maritime) snow: Implications for increased NOx emission". In: *Journal of Geophysical Research: Atmospheres* 110.D21.

Flanner, Mark G et al. (2007). "Present-day climate forcing and response from black carbon in snow". In: *Journal of Geophysical Research* 112.D11.

France, J L et al. (2012). "Hydroxyl radical and NO xproduction rates, black carbon concentrations and light-absorbing impurities in snow from field measurements of light penetration and nadir reflectivity of onshore and offshore coastal Alaskan snow". In: *Journal of Geophysical Research: Atmospheres* 117.D14.

Galley, R J et al. (2015). "Imaged brine inclusions in young sea ice—Shape, distribution and formation timing". In: *Cold Regions Science and Technology* 111, pp. 39–48.

Ginoux, Paul, Dmitri Garbuzov, and N. Christina Hsu (2010). "Identification of anthropogenic and natural dust sources using moderate resolution imaging spectroradiometer (MODIS) deep blue level 2 data". In: *Journal of Geophysical Research Atmospheres* 115.5, p. D05204.

Gottschalk, K (2016). "Trajectory Analysis of Black Carbon in the Arctic Region". In: *PSU McNair Scholars Online Journal* 10.1.

Greenwell, Claire et al. (2015). "Preparation of a new autonomous instrumented radiometric calibration site: Gobabeb, Namib Desert". In: *SPIE Remote Sensing*. Ed. by International Society for Optics and Photonics. Vol. 9639, pp. 963919–963919–14.

Grenfell, C G and G a Maykut (1977). "The optical properties of ice and snow in the Arctic Basin". In: *Journal of Glaciology* 18.80, pp. 445–463.

Grenfell, Thomas C (1983). "A theoretical model of the optical properties of sea ice in the visible and near infrared". In: *Journal of Geophysical Research: Oceans* 88.C14, pp. 9723–9735.

— (1991). "A radiative transfer model for sea ice with vertical structure variations". In: *Journal of Geophysical Research: Oceans* 96.C9, pp. 16991–17001.

Grenfell, Thomas C. and Bonnie Light (2002). "Spatial distribution and radiative effects of soot in the snow and sea ice during the SHEBA experiment". In: *Journal of Geophysical Research* 107.C10, pp. 1–7.

Grenfell, Thomas C et al. (2011). "Light absorption from particulate impurities in snow and ice determined by spectrophotometric analysis of filters." In: *Applied optics* 50.14, pp. 2037–2048.

Hanesiak, J M et al. (2001). "Local and regional albedo observations of arctic first-year sea ice during melt ponding". In: *Journal of Geophysical Research* 106.C1, p. 1005.

Hansen, James and Larissa Nazarenko (2004). "Soot climate forcing via snow and ice albedos." In: *Proceedings of the National Academy of Sciences of the United States of America* 101.2, pp. 423–8.

Hare, A A et al. (2013). "pH evolution in sea ice grown at an outdoor experimental facility". In: *Marine Chemistry* 154, pp. 46–54.

Hedley, John (2008). "A three-dimensional radiative transfer model for shallow water environments." In: *Optics express* 16.26, pp. 21887–21902.

Heilbronner, R and S Barrett (2013). *Image analysis in earth sciences: microstructures and textures of earth materials*. Springer Science & Business Media.

Henyey, Louis G and Jesse Leonard Greenstein (1941). "Diffuse radiation in the galaxy". In: *The Astrophysical Journal* 93, pp. 70–83.

Ho, Joshua (2010). "The implications of Arctic sea ice decline on shipping". In: *Marine Policy* 34.3, pp. 713–715.

Hudson, S R, S G Warren, and R E Brandt (2006). "Spectral bidirectional reflectance of Antarctic snow: Measurements and parameterization". In: *Journal of Geophysical Research: Atmospheres* 111.D18.

Jackson, R D, T R Clarke, and M S Moran (1992). "Bidirectional calibration results for 11 Spectralon and 16 BaSO4 reference reflectance panels". In: *Remote Sensing of Environment* 40.3, pp. 231–239.

Jacobson, Mark Z. (2004). "Climate response of fossil fuel and biofuel soot, accounting for soot's feedback to snow and sea ice albedo and emissivity". In: *Journal of Geophysical Research D: Atmospheres* 109.21, n/a–n/a.

Jeffrey, S. W. et al. (1999). "Occurrence of UVA- and UVB-absorbing compounds in 152 species (206 strains) of marine microalgae". In: *Marine Ecology Progress Series* 189, pp. 35–51.

Jin, Zhonghai et al. (2004). "A parameterization of ocean surface albedo". In: *Geophysical Research Letters* 31.22.

Johnson, Ben et al. (2012). "In situ observations of volcanic ash clouds from the FAAM aircraft during the eruption of Eyjafjallajökull in 2010". In: *Journal of Geophysical Research: Atmospheres* 117.D20.

Jones, E P and L G Anderson (1986). "On the origin of the chemical properties of the Arctic Ocean halocline". In: *Journal of Geophysical Research: Oceans* 91.C9, pp. 10759–10767.

Kimes, D S, Kirchner, J A, and Newcomb, W W (1983). "Spectral radiance errors in remote sensing ground studies due to nearby objects." In: *Applied optics* 22.1, pp. 8–10.

King, M D et al. (2005). "Measurement and modelling of UV radiation penetration and photolysis rates of nitrate and hydrogen peroxide in Antarctic sea ice: An estimate of the production rate of hydroxyl radicals in first-year sea ice". In: *Journal of Photochemistry and Photobiology A: Chemistry* 176.1-3, pp. 39–49.

Kirchmeier-Young, Megan C., Francis W. Zwiers, and Nathan P. Gillett (2016). "Attribution of Extreme Events in Arctic Sea Ice Extent". In: *Journal of Climate* 30.2, JCLI–D–16–0412.1.

Koch, Dorothy and James Hansen (2005a). "Distant origins of Arctic black carbon: A Goddard Institute for Space Studies ModelE experiment". In: *Journal of Geophysical Research D: Atmospheres* 110.4, pp. 1–14.

— (2005b). "Distant origins of Arctic black carbon: A Goddard Institute for Space Studies ModelE experiment". In: *Journal of Geophysical Research: Atmospheres* 110.D4.

Kuo-Nan, L (1973). *A numerical experiment on Chandrasekhar's discrete-ordinate method for radiative transfer: Application to cloudy and hazy atmospheres*. Vol. 30. 7. Journal of the Atmospheric Sciences, pp. 1303–1326.

Kwok, R. et al. (2009). "Thinning and volume loss of the Arctic Ocean sea ice cover: 2003-2008". In: *Journal of Geophysical Research: Oceans* 114.7, p. C07005.

Lamare, M. L., J. Lee-Taylor, and M. D. King (2016). "The impact of atmospheric mineral aerosol deposition on the albedo of snow & sea ice: are snow and sea ice optical properties more important than mineral aerosol optical properties?" In: *Atmospheric Chemistry and Physics* 16.2, pp. 843–860.

Landy, Jack C et al. (2015). "Parameterization of Centimeter-Scale Sea Ice Surface Roughness Using Terrestrial LiDAR". In: *IEEE Transactions on Geoscience and Remote Sensing* 53.3, pp. 1271–1286.

Laven, P (2006). *MiePlot: a computer program for scattering of light from a sphere using Mie theory & the Debye series*. PhilipLaven.com.

Lee-Taylor, Julia and Sasha Madronich (2002). "Calculation of actinic fluxes with a coupled atmosphere–snow radiative transfer model". In: *Journal of Geophysical Research: Atmospheres* 107.D24, ACH 22–1–ACH 22–10.

Leigh, L, D Helder, and I Behnert (2011). "Tuz Gölü site characteristics". In: *Geoscience and Remote Sensing Symposium (IGARSS), IEEE*.

Lucht, Wolfgang, Crystal Barker Schaaf, and Alan H. Strahler (2000). "An algorithm for the retrieval of albedo from space using semiempirical BRDF models". In: *IEEE Transactions on Geoscience and Remote Sensing* 38.2 II, pp. 977–998.

Maffione, Robert A., Jeff M. Voss, and Curtis D. Mobley (1998). "Theory and measurements of the complete beam spread function of sea ice1". In: *Limnology and Oceanography* 43.1, pp. 34–43.

Marks, A A and M D King (2013a). "The effects of additional black carbon on the albedo of Arctic sea ice: variation with sea ice type and snow cover". In: *The Cryosphere* 7.4, pp. 1193–1204.

Marks, A. A. and M. D. King (2013b). "The effects of additional black carbon on the albedo of Arctic sea ice: Variation with sea ice type and snow cover". In: *Cryosphere* 7.4, pp. 1193–1204.

Marks, A A and M D King (2014). "The effect of snow/sea ice type on the response of albedo and light penetration depth (*e*-folding depth) to increasing black carbon". In: *The Cryosphere* 8.5, pp. 1625–1638.

Marks, Amelia (2014). "Sea ice response to anthropogenic pollution: an experimental and modelling study". PhD thesis. Royal Holloway University of London, Egham, UK.

Marks, Amelia et al. (2015). "Characterisation of the HDRF (as a proxy for BRDF) of snow surfaces at Dome C, Antarctica, for the inter-calibration and inter-comparison of satellite optical data". In: *Remote Sensing of Environment* 158, pp. 407–416.

Maslanik, James A. et al. (2007). "A younger, thinner Arctic ice cover: Increased potential for rapid, extensive sea-ice loss". In: *Geophysical Research Letters* 34.24, p. L24501.

Meier, Walter N. et al. (2014). *Arctic sea ice in transformation: A review of recent observed changes and impacts on biology and human activity*.

Meister, G et al. (1996). "In situ BRDF measurements of selected surface materials to improve analysis of remotely sensed multispectral imagery". In: *International Archives of Photogrammetry and Remote Sensing* 31, pp. 493–498.

Mobley, C. D. (1994). *Light and water: radiative transfer*. Natural Waters. Academic Press.

Mobley, C. D. et al. (1998). "Modeling light propagation in sea ice". In: *IEEE Transactions on Geoscience and Remote Sensing* 36.5, pp. 1743–1749.

Morel, Anclré and Louis Prieur (1977). "Analysis of variations in ocean color". In: *Limnology and oceanography* 22.4, pp. 709–722.

Morel, André and Stéphane Maritorena (2001). "Bio-optical properties of oceanic waters: A reappraisal". In: *Journal of Geophysical Research: Oceans* 106.C4, pp. 7163–7180.

Mundy, C. J. et al. (2007a). "Influence of snow cover and algae on the spectral dependence of transmitted irradiance through Arctic landfast first-year sea ice". In: *Journal of Geophysical Research: Oceans* 112.C3.

— (2007b). "Influence of snow cover and algae on the spectral dependence of transmitted irradiance through Arctic landfast first-year sea ice". In: *Journal of Geophysical Research: Oceans* 112.3, p. C03007.

Mundy, C. J. et al. (2011). "Characteristics of two distinct high-light acclimated algal communities during advanced stages of sea ice melt". In: *Polar Biology* 34.12, pp. 1869–1886.

Nghiem, Son V. et al. (2007). "Rapid reduction of Arctic perennial sea ice". In: *Geophysical Research Letters* 34.19, p. L19504.

NOAA (2017). "Solar calculator". In: *https://www.esrl.noaa.gov/gmd/grad/solcalc/index.html*.

Overland, James E. and Muyin Wang (2010). "Large-scale atmospheric circulation changes are associated with the recent loss of Arctic sea ice". In: *Tellus, Series A: Dynamic Meteorology and Oceanography* 62.1, pp. 1–9.

Peddle, Derek R et al. (2001). "Reflectance processing of remote sensing spectroradiometer data". In: *Computers & Geosciences* 27.2, pp. 203–213.

Pegrum, H et al. (2006). "Design and Testing a New Instrument to Measure the Angular Reflectance of Terrestrial Surfaces". In: *2006 IEEE International Symposium on Geoscience and Remote Sensing*. IEEE, pp. 1119–1122.

Pegrum, Heather M et al. (2004). "Calibration of the NPL transfer standard absolute radiance source (TSARS) and its use with GOME 2-FM3 spectral radiance measurements". In: *Remote Sensing*. International Society for Optics and Photonics, pp. 503–514.

Pegrum-Browning, H, N Fox, and E Milton (2008). *The NPL Gonio RAdiometric Spectrometer System (GRASS)*. Tech. rep. National Physical Laboratory, Teddington, UK.

Peltoniemi, Jouni I et al. (2005). "BRDF measurement of understory vegetation in pine forests: dwarf shrubs, lichen, and moss". In: *Remote Sensing of the Environment* 94.3, pp. 343–354.

Penner, Joyce E. and T. Novakov (1996). "Carbonaceous particles in the atmosphere: A historical perspective to the Fifth International Conference on Carbonaceous Particles in the Atmosphere". In: *Journal of Geophysical Research: Atmospheres* 101.D14, pp. 19373–19378.

Perovich, D. K. (1991). "Seasonal changes in sea ice optical properties during fall freeze-up ". In: *Cold Regions Science and Technology* 19, pp. 261–273.

— (1996). *The optical properties of sea ice*. Tech. rep. US Army Cold Regions Research and Engineering Laboratory (CRREL).

Perovich, Donald K. and Christopher Polashenski (2012). "Albedo evolution of seasonal Arctic sea ice". In: *Geophysical Research Letters* 39.8, n/a–n/a.

Petrich, Chris and Hajo Eicken (2010). "Growth, structure and properties of sea ice". In: *Sea Ice* 2, pp. 23–77.

Petty, G.W. (2006). *A first course in atmospheric radiation*. Sundog Publishing.

Post, Eric et al. (2013). "Ecological Consequences of Sea-Ice Decline". In: *Science* 341.6145, pp. 519–524.

Ramanathan, R., G. Carmichael, and V. Ramanathan and G. Carmichael (2008). "Global and regional climate changes due to black carbon". In: *Nature Geoscience* 1.4, pp. 221 –227.

Rigor, Ignatius G. and John M. Wallace (2004). "Variations in the age of Arctic sea-ice and summer sea-ice extent". In: *Geophysical Research Letters* 31.9, n/a–n/a.

Rösel, A., L. Kaleschke, and G. Birnbaum (2012). "Melt ponds on Arctic sea ice determined from MODIS satellite data using an artificial neural network". In: *The Cryosphere* 6.2, pp. 431–446.

Rysgaard, S et al. (2014). "Temporal dynamics of ikaite in experimental sea ice". In: *The Cryosphere* 8.4, pp. 1469–1478.

Sandmeier, S R and A H Strahler (2000). "BRDF laboratory measurements". In: *Remote Sensing Reviews* 18.2-4, pp. 481–502.

Sandmeier, St et al. (1998). "Sensitivity Analysis and Quality Assessment of Laboratory BRDF Data". In: *Remote Sensing of the Environment* 64.2, pp. 176–191.

Schaepman-Strub, G et al. (2006). "Reflectance quantities in optical remote sensing—definitions and case studies". In: *Remote Sensing of the Environment* 103.1, pp. 27–42.

Schopfer, J et al. (2007). "Dual field-of-view goniometer system FIGOS". In: *International. Archives of Photogrammetry Remote Sensing and Spatial Information Sciences*, pp. 493–498.

Serreze, Mark C., Marika M. Holland, and Julienne C. Stroeve (2007). "Perspectives on the Arctic's Shrinking Sea-Ice Cover". In: *Science* 315.5818, pp. 1533–1536.

Serreze, Mark C. et al. (2016). "Summer atmospheric circulation anomalies over the Arctic Ocean and their influences on September sea ice extent: A cautionary tale". In: *Journal of Geophysical Research: Atmospheres* 121.19, pp. 11463–11485.

Sibson, Robin et al. (1981). "A brief description of natural neighbour interpolation". In: *Interpreting multivariate data* 21, pp. 21–36.

Siegel, H et al. (2005). "Ocean colour remote sensing relevant water constituents and optical properties of the Baltic Sea". In: *International Journal of Remote Sensing* 26.2, pp. 315–330.

Siegel, Herbert, Monika Gerth, and Marko Beckert (1994). "The variation of optical properties in the Baltic Sea and algorithms for the application of remote sensing data". In: *SPIE Vol. 2258 Ocean Optics XII*, pp. 894–905.

Simmonds, Ian and Kevin Keay (2009). "Extraordinary September Arctic sea ice reductions and their relationships with storm behavior over 1979-2008". In: *Geophysical Research Letters* 36.19, p. L19715.

Simpson, William R et al. (2002). "Radiation-transfer modeling of snow-pack photochemical processes during ALERT 2000". In: *Atmospheric Environment* 36.15, pp. 2663–2670.

Snedecor, George W. and William G. Cochran (1967). *Statistical Methods*. Iowa State University Press.

Stamnes, K, S C Tsay, and T Nakajima (1988a). "Computation of eigenvalues and eigenvectors for the discrete ordinate and matrix operator methods in radiative transfer". In: *Journal of Quantitative Spectroscopy ...* 39.5, pp. 415–419.

Stamnes, K et al. (1988b). "Numerically stable algorithm for discrete-ordinate-method radiative transfer in multiple scattering and emitting layered media." In: *Applied optics* 27.12, pp. 2502–2509.

Stroeve, Julienne et al. (2007). "Arctic sea ice decline: Faster than forecast". In: *Geophysical Research Letters* 34.9.

Stroeve, Julienne C. et al. (2012). "Trends in Arctic sea ice extent from CMIP5, CMIP3 and observations". In: *Geophysical Research Letters* 39.16, n/a–n/a.

Tschudi, Mark A., James A. Maslanik, and Donald K. Perovich (2008). "Derivation of melt pond coverage on Arctic sea ice using MODIS observations". In: *Remote Sensing of Environment* 112.5, pp. 2605 –2614.

Tucker III, W B, A J Gow, and J A Richter (1984). "On small-scale horizontal variations of salinity in first-year sea ice". In: *Journal of Geophysical Research: Oceans* 89.C4, pp. 6505–6514.

VanCuren, Richard A. et al. (2012). "Aerosols and their sources at Summit Greenland –First results of continuous size- and time-resolved sampling". In: *Atmospheric Environment* 52, pp. 82–97.

Vihma, Timo (2014). "Effects of Arctic Sea Ice Decline on Weather and Climate: A Review". In: *Surveys in Geophysics* 35.5, pp. 1175–1214.

Wang, Muyin and James E. Overland (2012). "A sea ice free summer Arctic within 30 years: An update from CMIP5 models". In: *Geophysical Research Letters* 39.17, n/a–n/a.

Waquet, F et al. (2014). "Retrieval of the Eyjafjallajökull volcanic aerosol optical and microphysical properties from POLDER/PARASOL measurements". In: *Atmospheric Chemistry and Physics* 14.4, pp. 1755–1768.

Warren, Stephen G. and Richard E. Brandt (2008). "Optical constants of ice from the ultraviolet to the microwave: A revised compilation". In: *Journal of Geophysical Research: Atmospheres* 113.D14.

Warren, Stephen G. and Warren J. Wiscombe (1980). "A Model for the Spectral Albedo of Snow. II: Snow Containing Atmospheric Aerosols". In: *Journal of the Atmospheric Sciences* 37.12, pp. 2734–2745.

Weeks, W F and O S Lee (1962). "The Salinity Distribution in Young Sea-Ice". In: *ARCTIC* 15.2.

Weeks, Willy (2010). *On sea ice*. University of Alaska Press.

Williams, David C (1999). "Establishment of absolute diffuse reflectance scales using the NPL Reference Reflectometer". In: *Analytica chimica acta* 380.2-3, pp. 165–172.

Wiscombe, Warren J. and Stephen G. Warren (1980a). *A model for the spectral albedo of snow. I: Pure snow*.

Wiscombe, Warren J and Stephen G Warren (1980b). "A Model for the Spectral Albedo of Snow. I: Pure Snow". In: *Journal of the Atmospheric Sciences* 37.12, pp. 2712–2733.

Wong, Samuel SM (1997). *Computational methods in physics and engineering*. World Scientific Publishing Co Inc.

Woolliams, Emma et al. (2005). *Final Report of the CCPR K1-a Key Comparison of Spectral Irradiance 250 nm to 2500 nm*. Tech. rep. National Physical Laboratory, Teddington, UK.

Young, C L, I N Sokolik, and J Dufek (2012). "Regional radiative impact of volcanic aerosol from the 2009 eruption of Mt. Redoubt". In: *Atmospheric Chemistry and Physics* 12.8, pp. 3699–3715.

Zdanowicz, C. M., G. A. Zielinski, and C. P. Wake (1998). "Characteristics of modern atmospheric dust deposition on the Penny Ice cap, Baffin Island, Arctic Canada". In: *Tellus, Series B: Chemical and Physical Meteorology* 50.5, pp. 506–520.

Zdanowicz, C M, G A Zielinski, and C P Wake (2016). "Characteristics of modern atmospheric dust deposition in snow on the Penny Ice Cap, Baffin Island, Arctic Canada". In: *Tellus B: Chemical and Physical Meteorology* 50.5, pp. 506–520.